OCS Study
MMS 2000-060

DeSoto Canyon Eddy Intrusion Study

Final Report

Volume II: Technical Report

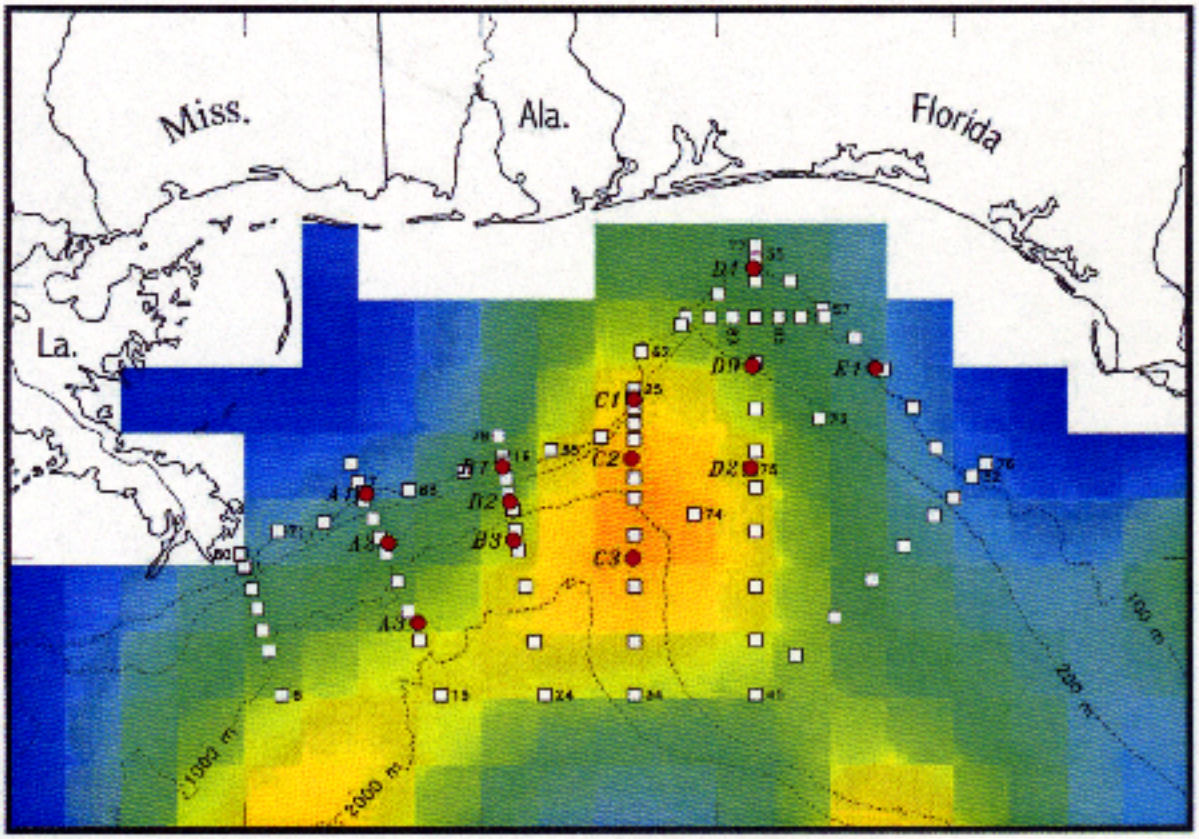

MMS U.S. Department of the Interior
Minerals Management Service
Gulf of Mexico OCS Region

OCS Study
MMS 2000-080

DeSoto Canyon Eddy Intrusion Study

Final Report

Volume II: Technical Report

Authors

Thomas J. Berger
Peter Hamilton
James J. Singer
Evans Waddell
Science Applications International Corporation

James H. Churchill
Woods Hole Oceanographic Institute

Robert R. Leben
University of Colorado

Thomas N. Lee
University of Miami

Wilton Sturges
Florida State University

Prepared under MMS Contract
1435-01-96-CT-30825
by
Science Applications International Corporation
615 Oberlin Rd., Suite 300
Raleigh, North Carolina 27605

Published by

U.S. Department of the Interior
Minerals Management Service
Gulf of Mexico OCS Region

New Orleans
November 2000

DISCLAIMER

This report was prepared under contract between the Minerals Management Service (MMS) and Science Applications International Corporation (SAIC). This report has been technically reviewed by the MMS and approved for publication. Approval does not signify that the contents necessarily reflect the views and policies of the Service, nor does mention of trade names or commercial products constitute endorsement or recommendation for use. It is, however, exempt from review and compliance with the MMS editorial standards.

REPORT AVAILABILITY

Extra copies of the report may be obtained from the Public Information Office (Mail Stop 5034) at the following address:

U.S. Department of the Interior
Minerals Management Service
Gulf of Mexico OCS Region
Public Information Office (MS 5034)
1201 Elmwood Park Boulevard
New Orleans, Louisiana 70123-2394

Telephone Number: 1-800-200-GULF or
504-736-2519

CITATION

Suggested Citation:

Hamilton, P., T. J. Berger, J.J. Singer, E. Waddell, J.H. Churchill, R.R. Leben, T.N. Lee, and W. Sturges. Desoto Canyon Eddy Intrusion Study, Final Report, Volume II: Technical Report. OCS Study MMS 2000-080. U.S. Dept. of the Interior, Minerals Management Service, Gulf of Mexico OCS Region, New Orleans, LA. 275 pp.

ABOUT THE COVER

The map of the northeastern Gulf of Mexico on the cover of this report shows the locations of moorings (red dots) and hydrographic stations (white squares) occupied during the DeSoto Canyon Eddy Intrusion Study. These locations are overlaid on a color-coded map of sea surface height (SSH) as determined from satellite altimetry. The warmer colors (yellow/orange) indicate a higher SSH. This grades through green to blue in going to lower SSH. Note the horizontal scale of the yellow/orange colored feature that was centered among the moorings. Such a relative high is associated with anticyclonic (clockwise rotating) surface currents.

ACKNOWLEDGEMENTS

The Program Manager wishes to extend thanks to the captain and crew of the *R/V Pelican* for their continued support and conscientious effort during the many cruises conducted during the study. During data processing, Paul Blankinship provided excellent data processing and analysis support to the program principal investigators. Carol Harris did an outstanding job in the general production of this and many other project reports. For the duration of the program, Sharon Goodhart provided administrative and project support that has been key to the successful and timely completion of the study.

The continuing, enthusiastic and timely support of Dr. Alexis Lugo-Fernandez, the MMS Contract Officer's Technical Representative, during all phases of this project is gratefully acknowledged.

TABLE OF CONTENTS
VOLUME II

TABLE OF CONTENTS (continued)

VOLUME II

TABLE OF CONTENTS (continued)

VOLUME II

LIST OF FIGURES

LIST OF FIGURES (continued)

LIST OF FIGURES (continued)

LIST OF FIGURES (continued)

LIST OF FIGURES (continued)

LIST OF FIGURES (continued)

LIST OF FIGURES (continued)

LIST OF FIGURES (continued)

LIST OF FIGURES (continued)

LIST OF FIGURES (continued)

LIST OF FIGURES (continued)

LIST OF FIGURES (continued)

LIST OF TABLES

LIST OF TABLES (continued)

LIST OF TABLES (continued)

ACRONYMS AND ABBREVIATIONS

AA	Aanderaa
A,B,C,D,E	Mooring Identifier
ACE	Anticyclonic Eddy
ALTOPR	Altimeter Ocean Products
AVHRR	Advanced Very High Resolution Radiometry
C	Centigrade (temperature scale)
CCW	Counterclockwise
C-MAN	Coastal-Marine Automated Network
cpd	Cycles per day
CST	Central Standard Time
CUPOM	Colorado Princeton Ocean Model
D,D	Divergence, depth
df,DF	Degrees of Freedom
DLP	Day Low Pass
EOF	Empirical Orthogonal Function
ESI	Environmental Sensors, Inc.
F	Flux
f	Coriolis Parameter
FC	Florida Current
FEOF	Frequency EOF
g	Gravitational acceleration
GDR	Geophysical Data Records
GEOSAT	
H	Water depth
HLP	Hour Low Pass
kHz	Kilohertz (1000 cycles/sec.)
L	Shelf width, alongshore length scale
LCFE	Loop Current Frontal Eddy(ies)
MAB	Mid-Atlantic Bight
NDBC	National Data Buoy Office
NOAA	National Ocean and Atmospheric Administration
NE	Northeastern
NOS	National Ocean Service
OEI	Oregon Environmental Instruments
PODBM	Physical Oceanography Data Base Management
ppt	Parts per thousand
psu	Practical Salinity Units
R	Correlation Coefficient
r	Bottom resistance
S	Average cross shelf slope
SAB	South Atlantic Bight
SD	Standard Deviation
SSF	Southern Straits of Florida
SSH	Sea Surface Height
SST	Sea Surface Temperature
T	Momentum Transport, temperature
t	Time
TEOF	Temporal EOF
TRW	Topographic Rossby Wave
USGS	United States Geological Survey
u,v	Velocity component

v,V	Velocity component
w	Width of outershelf band
x,X	Horizontal component direction
y,Y	Horizontal component direction
z,Z	Vertical direction
ζ	Vorticity

I. INTRODUCTION

1.1 Introduction

The DeSoto Canyon Eddy Intrusion Study will provide the Minerals Management Service (MMS) with information and analyses which expands the understanding of physical oceanographic conditions and processes in the northeastern Gulf of Mexico. In turn, these insights will support an enhanced basis for developing sound, rationally based environmental assessments. The threat of a spill contacting land in the northeastern Gulf of Mexico is of great concern to the MMS. To estimate the potential for such a spill coming into contact with resources in the region, a robust "climatological" circulation, which includes the means and dominant oceanographic phenomena is needed. On the northeastern Gulf slope, Loop Current (LC) and eddy intrusions are two important processes to be included in any climatological circulation characterization of the area (see Figure 1.1-1 as an example).

To gather the data needed to assemble the oceanographic climatological database for oil spill trajectory analysis, the MMS funded the present DeSoto Canyon Eddy Intrusion Study. Knowledge acquired through this study will facilitate MMS's understanding of the outer shelf circulation, e.g., how the LC and associated eddies exchange momentum and mass with the shelf. The role of the DeSoto Canyon as a route that facilitates these intrusions and as a conduit of mass exchange between the deep Gulf and the shelf will be further elucidated by characterizing processes and conditions over the adjacent slope. As described below, results and data from this study will also be useful to other concurrent oceanographic studies that the MMS and others are sponsoring in the northeastern Gulf.

1.2 Project Objectives

The general objectives of this study are:

- Use *in-situ* current measurements, hydrographic data, and satellite images to document and characterize LC intrusions and interactions with the northeastern Gulf slope (Figure 1.2-1, for illustration). This study shall examine the frequency and horizontal and vertical extent of these interactions and intrusions. Through the use of dynamical principles, a conceptual model will be used to help explain the character and evolution of LC-slope interactions observed in the course of the study.

- Document and examine the dynamical processes of momentum, mass and vertical vorticity exchanges occurring during LC-slope interactions. These analyses shall be based on the *in-situ* current measurements and hydrographic data.

- Estimate the frequency of LC, LC rings and secondary eddies' interactions with the northeastern slope, and conduct an assessment of the vertical and horizontal shears, exchanges of vorticity, momentum, and mass fields associated with the eddy-slope interactions.

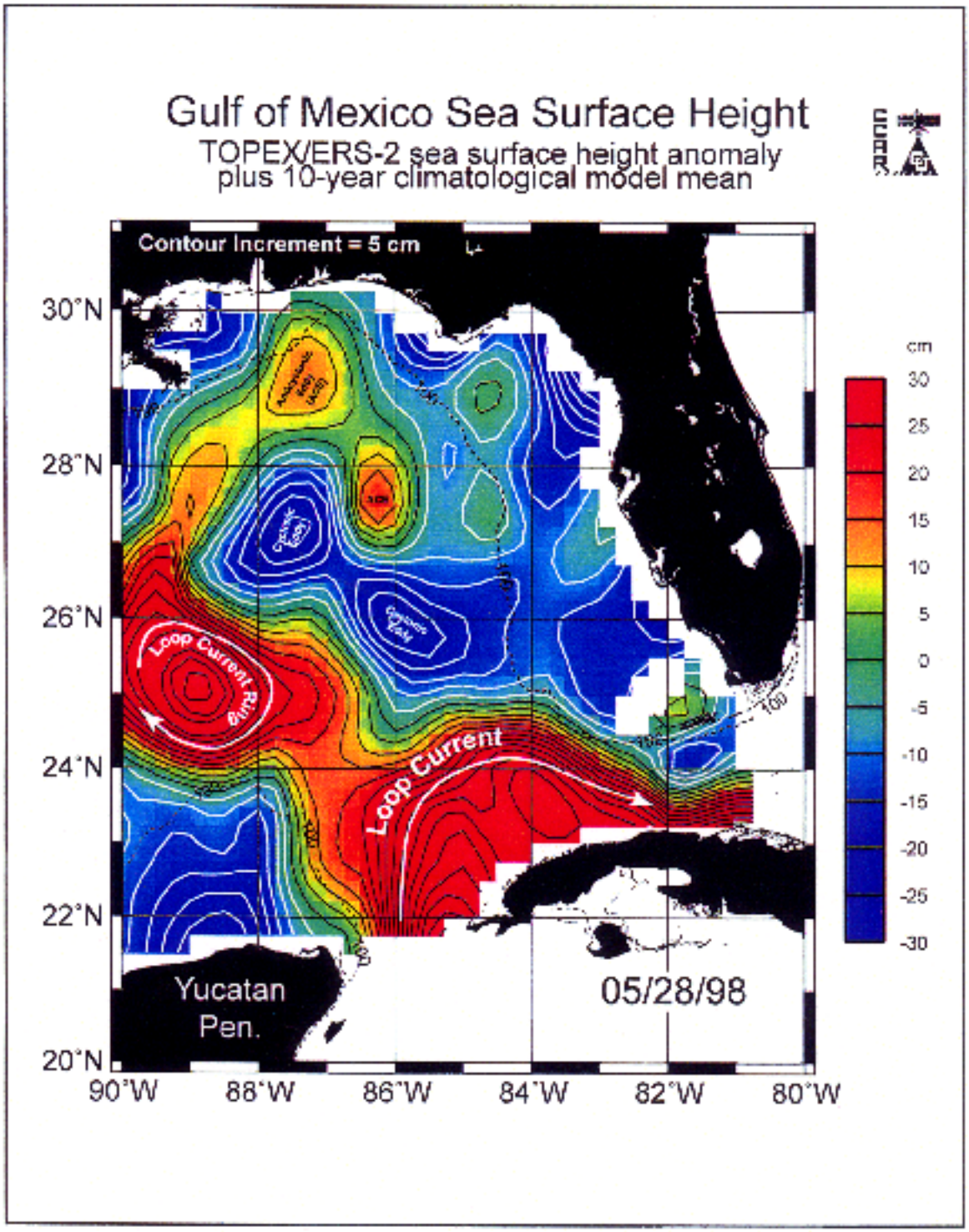

Figure 1.1-1. Image showing contours of sea surface height with examples of the types and scales of eddy-like features that can occur in the eastern and northeastern Gulf of Mexico.

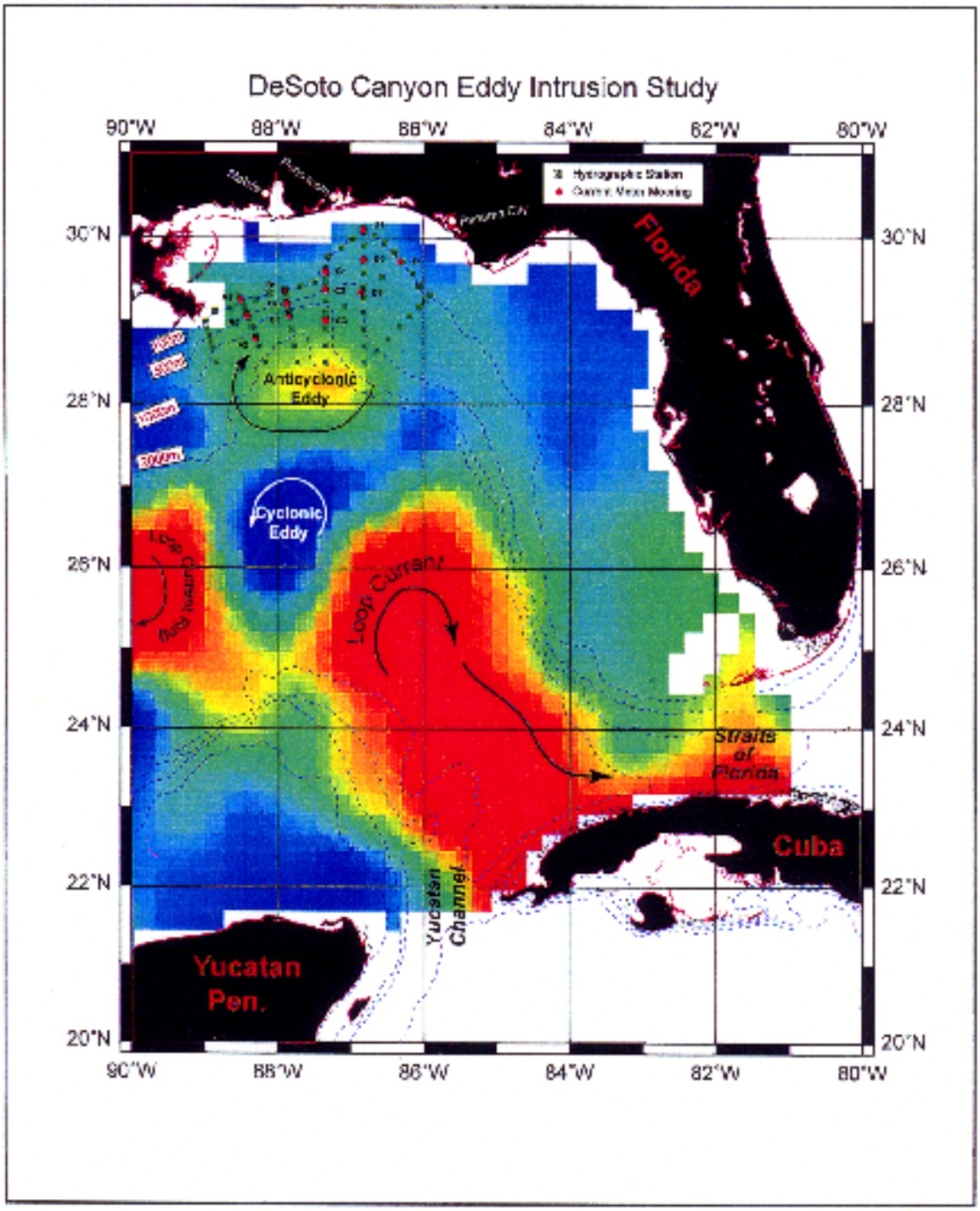

Figura 1.3-1. Base map of the study area with color coded image of the height of the sea surface (warmer colors are higher/taller) as determined by satellite altimeter. Several key oceanographic features are labeled. On the slope (seaward of 100m isobath) off Alabama and the Florida Panhandle are shown the locations of current meter moorings and hydrographic stations occupied during the DeSoto Canyon Eddy Intrusion Study.

- Elucidate the role of the DeSoto Canyon in LC and eddy processes as a mechanism and as well as a route of mass and momentum exchange between the shelf and deep water of the northeastern Gulf.

The overall program was to last 4 years with two complete years of field observations in the general study area (enclosed by solid lines in Figure 1.1-1). The general location and configuration of moorings were specified in the Scope of Work provided by the MMS. The general area for the hydrographic sampling scheme was also specified. SAIC proposed some limited modifications that were incorporated into the overall design that produced the observational database used for this report. It is important to note that several concurrent and complementary programs involving physical oceanographic measurements were conducted in this general study area. The MMS is funding Texas A&M University to conduct a study titled " Northeastern Gulf of Mexico Chemical Oceanography and Hydrography Study" (Contract No. 1435-01-97-CT-30851). Additionally, selected physical oceanographic measurements are being made in the pinnacle area near and at the shelf break offshore of Alabama as part of an NBR/USGS-funded study being conducted by Continental Shelf Associates.

Members of the program's scientific team (Principal Investigators - PIs) and their primary areas of investigation on this project are presented below in alphabetical order:

- James Churchill (Woods Hole Oceanographic Institute - WHOI) - Canyon processes; atmospheric forcing due to hurricanes; shelf-slope exchange processes.

- Peter Hamilton (Science Applications International Corporation - SAIC) - Slope eddy dynamics; scales of motion; atmospheric forcing.

- Robert Leben (University of Colorado - UCol) - Loop Current, dynamics and metrics, ringshedding patterns and characteristics.

- Thomas Lee (University of Miami - UMiami) - Slope eddy kinematics; shelf-slope exchange processes and mechanisms.

- Wilton Sturges (Florida State University - FSU) - LC and LC ring dynamics.

An important support function was provided by James Singer (SAIC) who was responsible for the planning and conduct of all field operations and logistics and served as Program Chief Scientist on all cruises. Throughout most of the program, Thomas J. Berger was the Program Manager. Although recently retired, he was responsible for the oversight and guidance of activities during all but the creation of this final report.

1.3 Report Organization

The report is composed of eight chapters covering the topics listed below:

Chapter 1: Introduction – General overview of program rationale.

Chapter 2: Data Acquisition – Instruments, procedures and methods by which data used in this project was acquired.

Chapter 3: Data Processing and Management – Procedures for data handling, analysis and management of the various types of data used during the study.

Chapter 4: Loop Current and its Intrusions – Characteristics of Loop Current, cycle of ring shedding, various metrics and dynamics associated with the intrusion and ring shedding process.

Chapter 5: Slope Circulation Patterns – Describing specific circulation patterns measured and documented on the slope. The analytical tools used in this description help isolate relation and patterns.

Chapter 6: Slope Response to Atmospheric Forcing – Characterizing slope circulation patterns as a response to atmospheric forcing mechanisms at a wide range of periods.

Chapter 7: Conceptual Model and Characterization – Effort at synthesizing some of the LC and slope circulation relationships and patterns deduced from this program.

Chapter 8: References

II. DATA ACQUISITION AND PRESENTATION

2.1 Introduction

Data collection during the DeSoto Canyon Eddy Intrusion Study included shipboard Conductivity/Temperature/Depth (CTD), Acoustic Doppler Current Profiler (ADCP) and Expendable Bathythermograph (XBT) surveys; in-situ moored current, temperature, conductivity and pressure time series measurements and the collection of GeoSat altimeter data. Available ancillary data from other coincidental programs include drifting buoy data from Davis-type Argos drifters, hydrographic data from the GulfCet II and Northeastern Gulf of Mexico Chemical Oceanography and Hydrography studies, and near-bottom current measurements from the Northeastern Gulf of Mexico Coastal Marine and Ecosystem Program. Additional ancillary data from various government or government-funded entities include meteorological, water-level, river-runoff, satellite-imagery and hurricane-tracking data, all of which were evaluated or used in this study.

2.2 CTD Data

2.2.1 Introduction

CTD data were collected during each of seven mooring deployment/rotation cruises aboard the R/V PELICAN (at approximately four-month intervals), beginning in March 1997 and concluding in April 1999. Initially, a standard grid with 75 stations was occupied. This was increased to 80 stations in November 1997 to obtain additional shelf/slope observations along five of the seven onshore/offshore sections. Seven additional stations were added for the December 1998 cruise, as part of a Feature Survey. Figure 2.2-1 shows the standard grid for this latter survey with the Feature Survey stations (Stations 81-87) and all 13 current meter mooring locations included.

2.2.2 CTD Data Acquisition System

The primary CTD data acquisition system was a SeaBird 911 Plus CTD System provided and operated by the technical staff at Louisiana Universities Marine Consortium (LUMCON). The CTD fish was equipped with two sets of conductivity and temperature sensors for redundant CT data collection, a Datasonics altimeter and a SeaBird Carousel Water Sampler with General Oceanics Niskin water sample bottles. A SeaBird 19 SeaCat Profiler was also used during brief periods when the main CTD system was not available. To eliminate or significantly reduce the possibility of sensor mismatch (salinity spiking) when passing through a sharp thermocline, the lowering speed of the CTD was adjusted from 15 meters per minute for the first 90 meters of descent to 30 meters per minute from 90 meters to 200 meters depth and then to 60 meters per minute below 200 meters.

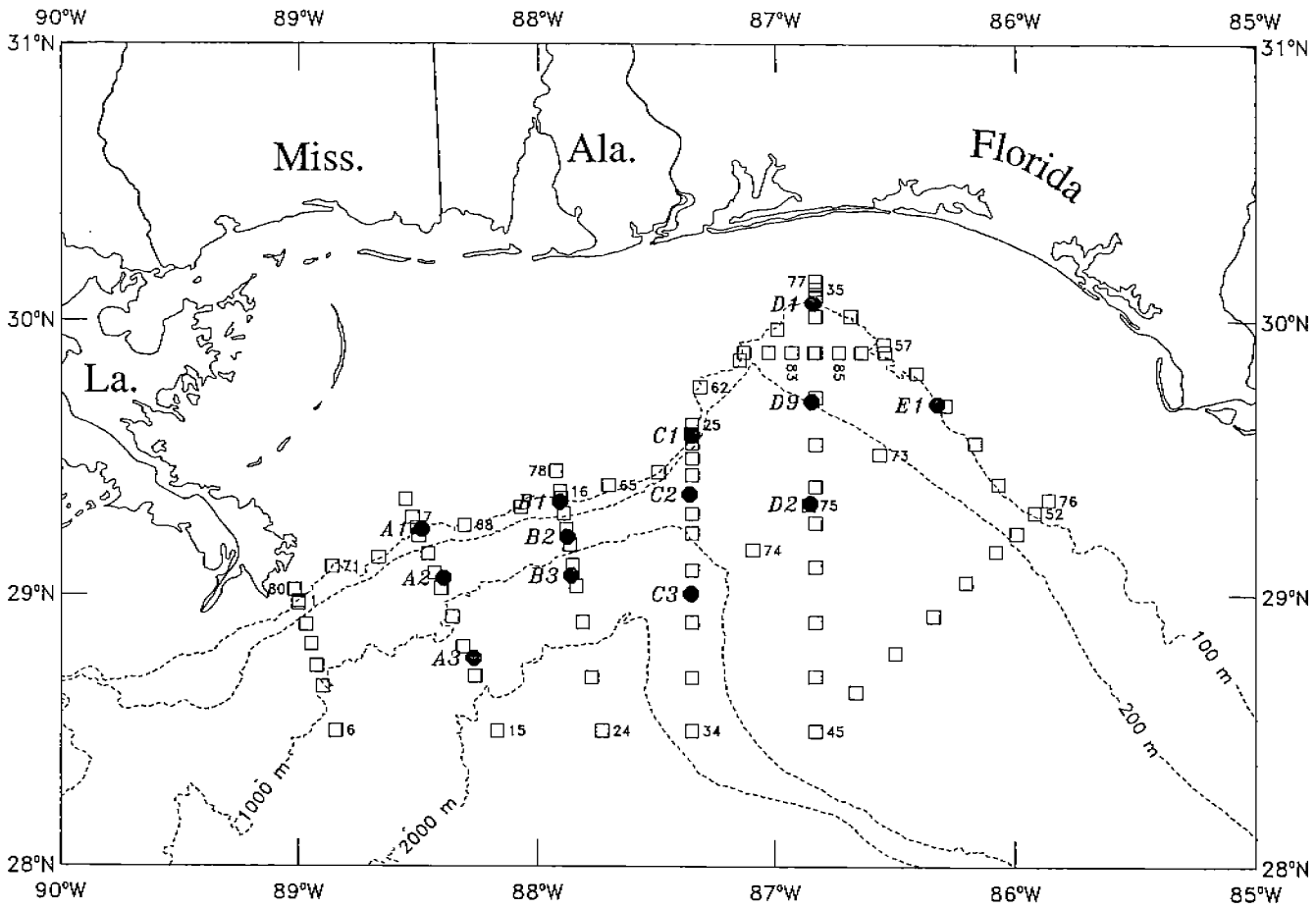

Figure 2.2-1 Map showing standard hydrographic grid for the DeSoto Canyon Eddy Intrusion Study with feature survey stations for December 1998 cruise (Stations 81-87) and all 13 current meter mooring locations (solid circles).

2.2.3 CTD Performance and Data Return

Over ninety-eight percent of the planned CTD stations were completed during the two-year field program. In addition, on occasion, some stations were sampled twice during a particular cruise. All but two of the unsampled stations were lost due to the passage of Tropical Storm Danny during the July 1997 cruise when Stations 66-72 along the 90 meter isobath section were not sampled. The remaining two unsampled stations were due to time/redundancy considerations (Station 75 in November 1997) and termination problems (Station 6 in March 1999). The actual useful data return was reduced by a pump plumbing problem on the CTD fish during the December 1998 cruise which caused the conductivity data, and subsequently the calculated salinity data, while profiling, to be noisy. These salinity data were discarded as it was not possible to smooth and adjust the data with any confidence that the adjustments were valid at shallower depths, particularly near the shelf break. Table 2.2-1 summarizes the CTD data return.

Table 2.2-1. Summary of CTD data collected during the DeSoto Canyon Eddy Intrusion Study.

Cruise ID	Dates	CTD Stations Planned	CTD Stations Completed
PE 9722	03/18/97 - 03/28/97	75	75
PE 9803	07/08/97 - 07/19/97	75	69*
PE 9820	11/10/97 - 11/22/97	80	79
PE 9830	03/31/98 - 04/10/98	80	81
PE 9908	08/03/98 - 08/14/98	80	81
PE 9923	12/01/98 - 12/13/98	87	93**
PE 9932	03/29/99 - 04/06/99	80	79
TOTALS	03/18/97 - 04/06/99	557	557

* Tropical Storm Danny prevented completion of CTD Stations 66-72 along the 90 meter isobath.

** Problem with CTD pump plumbing resulting in noisy salinity data. Temperature data ok. Salinity data discarded.

2.3 XBT Data

2.3.1 Introduction

XBT data were collected in conjunction with two Feature Surveys conducted on 20-22 November 1997 and 10-11 December 1998. In November

1997, eighteen T-7 XBTs were deployed along two east-west sections offshore of and parallel to the 100m sections (Stations 101-109 and 111-119) are shown in Figure 2.3-1. In December 1998, twenty-one XBT stations were sampled along three transits of an east-west section across the mouth of the DeSoto Canyon and repeated at approximately 12-hour intervals at the same station locations as shown for CTD Stations 81-87. This section is also shown in Figure 2.3-1.

2.3.2 XBT Data Acquisition System

Data from T-7, XBTs were collected using a Sippican LM-3A handheld launcher and a Sippican MK-12 Oceanographic Data Acquisition System. All probes were manufactured by Sippican.

2.3.3 XBT Performance and Data Return

Fifteen of eighteen XBTs provided useful data during the November 1997 cruise, but only fifteen of twenty-six drops (from probes deployed at twenty-one stations) provided useful data in December 1998. The poor data return in December 1998 was due to the receipt of defective probes from the manufacturer. The insulating film on the signal wire from the probe to the data logger was of poor quality and did not provide a reliable insulation against shorting when the wire came in contact with the ocean. These probes had been received in March.

2.4 Vessel-Mounted ADCP Data

2.4.1 Introduction

Underway ADCP data were collected as part of the two Feature Surveys (approximately 24 hours on 20-22 November 1997, and approximately 48 hours on 10-11 December 1998). The November 1997 survey consisted of three east-west sections crossing the A-Line and B-Line moorings, and the December 1998 survey consisted of four transits of a triangular grid at the mouth of the DeSoto Canyon (see Figure 2.3-1). This second survey was 48 hours long instead of 24 hours as it combined the time of two separate surveys into one longer one. An April 1998 Feature Survey was not done as available satellite imagery gave no indication of anything of interest, so the saved time was added to the December 1998 survey.

2.4.2 Vessel-Mounted ADCP Data Acquisition System

The ADCP data acquisition system was provided by LUMCON and was operated by their technical staff during each cruise aboard the R/V PELICAN. The system consisted of two narrowband RDI hull-mounted VM-ADCP systems (150 KHz and 600 KHz) configured so that both could operate at the same time. DGPS navigation data were input from the vessel's navigation system and ADCP data were processed using RDI Transect software. The data acquisition setup for each instrument is presented in Table 2.4-1.

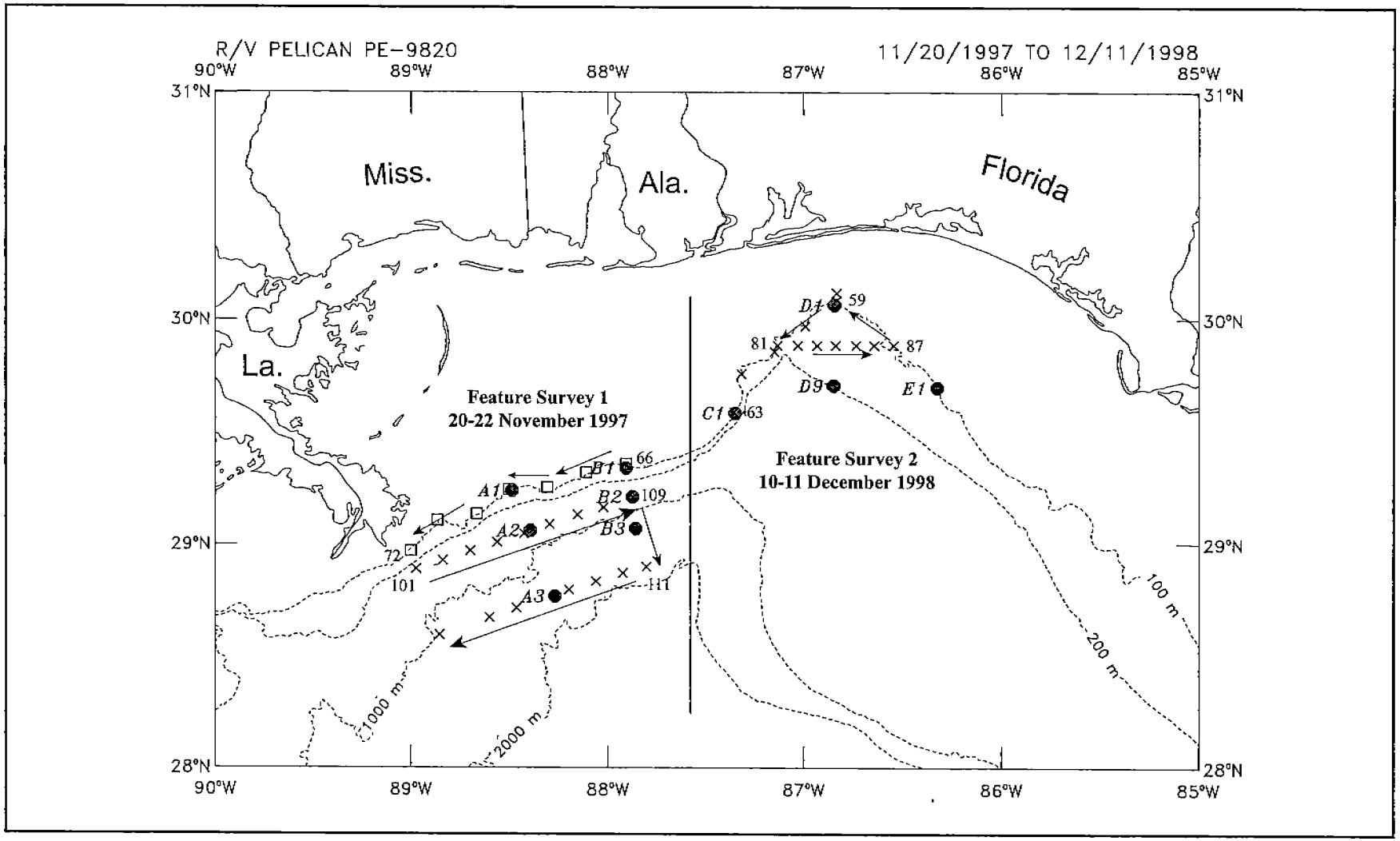

Figure 2.3-1. Map showing the two ADCP/XBT Feature Surveys conducted in November 1997 and December 1998 with nearby mooring locations.

Table 2.4-1. Data acquisition setup for vessel-mounted ADCPs used during the DeSoto Canyon Eddy Intrusion Study Feature Surveys.

ADCP	150 KHz	600 KHz
Time Between Pings (seconds)	0.65	0.16
Depth Cell Length (meters)	8	4
Transmit Pulse Length (meters)	8	4
Blanking (meters)	4	4
Number of Depth Cells	40	40
Number of Pings Per Ensemble	10	10

2.4.3 Vessel-Mounted ADCP Performance and Data Return

Data were collected from both ADCPs simultaneously during the two Feature Surveys. This amounted to a total of approximately 72 hours of continuous operations during which the data were displayed on the monitor and stored as 5-minute averages. Due to the greater range of the 150 KHz ADCP, which permitted bottom track for more extended periods during the surveys, only the 150 KHz data were considered for later processing.

2.5 Moored Instrument Data

2.5.1 Introduction

Moored current, temperature, conductivity and pressure measurements were made from thirteen mooring sites in the study area along the 100, 200, 500 and 1300m isobaths. These sites were previously identified in Figure 2.2-1. Measurements were made continuously from March 1997 to April 1999 with six mooring deployments at approximately four-month intervals (see Table 2.5-1).

Table 2.5-1. Approximate mooring deployment periods for the DeSoto Canyon Eddy Intrusion Study.

Deployment	Approximate Deployment Dates*
1 (March 1997)	03/19/97 - 07/17/97**
2 (July 1997)	07/09/97 - 11/20/97
3 (November 1997)	11/13/97 - 04/08/98
4 (April 1998)	04/02/98 - 08/12/98
5 (August 1998)	08/05/98 - 12/12/98
6 (December 1998)	12/03/98 - 04/06/99

* The overlap in dates from the end of one deployment to the beginning of the next is due to the actual time the last and first moorings were actually deployed and recovered during each cruise.

** Except Mooring B1 (03/27/97 - 08/22/97) and Mooring D1 (03/25/97 - 08/21/97).

The mooring configurations remained unchanged for the entirety of the study except that a Trawl Resistant Bottom Mount (TRBM) at Mooring D1 was replaced in August 1997 with an inline mooring configuration similar to that at the other 100m sites. Also, at various times, the level of the upper measurements of conductivity and temperature at the 100m sites moved up or down (between 62 and 20m) depending on the availability of a

surface marker buoy for that site. This was because the Coast Guard required surface markers for all subsurface moorings extending to within 200 feet (61m) of the surface. Three of the five 100m sites (B1, C1 and E1) were initially configured with surface markers and the B1 marker was shifted to the A1 site in August 1998. Also, in August 1998, the 20m level on the A1 and C1 moorings was shifted upward to 16m at the request of the Review Board and program Principal Investigators (PIs).

2.5.2 Moored Instrumentation

The moorings consisted of a variety of current measuring instruments. These included Aanderaa RCM-7's and 8's, General Oceanics Mk2s, InterOcean S4s, and RD Instruments 300 kHz Workhorse and 150 kHz Narrowband ADCPs. Additional measurements were made using Hugrún Seamon Mini Temperature Recorders and SeaBird MicroCat and SeaCat Conductivity and Temperature Recorders. The Aanderaa, General Oceanics and InterOcean instruments were outfitted with conductivity sensors and some, but not all, of the Aanderaa, General Oceanics and SeaBird instruments were outfitted with pressure.

As a general rule (by the end of the field program), Aanderaa current meters were deployed at the 200 and 300 meter levels on the 500m moorings (A2, B2, C2, and D2) and at 500 meters on the 1300m moorings (A3, B3, and C3); General Oceanics current meters were deployed approximately 10m above bottom on the 500m and 1300m moorings, and InterOcean current meters were deployed approximately six meters above bottom on the 100m moorings (A1, B1, C1, D1, and E1). RD Instruments Workhorse ADCPs were deployed at 80m or 90m depth on each of the above moorings and the 150 kHz Narrowband ADCP was deployed at 180m depth on the 200m D9 mooring. Hugrún Mini Temperature Recorders were deployed at 62, 150 and 250m depths on the 500m moorings and the SeaBird Conductivity and Temperature Recorders were deployed at 16m (or 20m), and/or 62m and/or 82m depth on the 100m moorings. Table 2.5-2 summarizes this information for the last four-month deployment period.

2.5.3 Moored Instrument Performance and Data Return

A total of 322 instrument deployments were made over the course of the two-year field program as approximately 54 instruments were deployed or rotated every four months. The total 'good data' data return was approximately 95.6%. This return was calculated based on the maximum number of data points expected for the various type instruments at their respective settings. However, since an ADCP generally works or doesn't work, the data return for these instruments reflects only that 'good data' were obtained for at least one level, though up to 19 or 20 levels may have provided useful data.

Initially, no data were obtained from the April-August 1998 deployment of the B1 Mooring as it was lost in its entirety, except that the surface marker buoy and one of the subsurface steel buoys were found

Table 2.5-2. Mooring instrumentation and deployment levels during the last deployment period (December 1998 - April 1999) of the DeSoto Canyon Eddy Instrusion Study.

MOORING	LOCATION	WATER DEPTH (M)	INSTRUMENT DEPTH (M)	INSTRUMENT TYPE (SERIAL NO.)
A1	29°14.521'N 88°29.068'W	100	16 20 80 94	C/T (1719) MK2 (452) ADCP (214) S4 (08161753)
A2	29°03.565'N 88°23.352'W	500	62 90 150 200 250 300 490	Mini TR (C929) ADCP (197) Mini TR (C932) RCM-7 (10350) Mini TR (C933) RCM-7 (6892) S4 (08161758)
A3	28°46.051'N 88°17.327'W	1300	80 500 1290	ADCP (196) RCM-8 (10533) MK2 (447)
B1	29°20.565'N 87°54.539'W	100	62 94	RCM-7 (9950) S4 (07801745)
B2	29°12.720'N 87°52.279'W	500	62 90 150 200 250 300 490	Mini TR (C937) ADCP (206) Mini TR (C939) RCM-7 (9524) Mini TR (C940) RCM-7 (9525) MK2 (443)
B3	29°04.285'N 87°51.502'W	1300	80 500 1290	ADCP (211) RCM-5/8 (7582) MK2 (450)
C1	29°35.157'N 87°20.993'W	100	16 80 94	C/T/D (0059) ADCP (200) S4 (08161755)
C2	29°22.309'N 87°21.412'W	500	62 90 150 200 250 300 490	Mini TR (C946) ADCP (224) Mini TR (C947) RCM-7 (9949) Mini TR (C950) RCM-5/8 (7528) MK2 (453)
C3	29°00.327'N 87°21.260'W	1300	80 500 1290	ADCP (207) RCM-4/7 (6922) MK2 (444)
D1	30°04.128'N 86°50.507'W	100	62 80 94	C/T/D (0057) ADCP (209) S4 (08111746)
D2	29°20.144'N 86°51.149'W	500	62 90 150 200 250 300 490	Mini TR (C919) ADCP (212) Mini TR (C959) RCM-7 (10881) Mini TR (C960) RCM-7 (9948) MK2 (457)
D9	29°42.450'N 86°50.819'W	200	180	ADCP (322)
E1	29°42.001'N 86°19.734'W	100	20 80 94	C/T (1720) ADCP (213) S4 (08161757)

adrift in the Gulf of Mexico and recovered by other parties in July and October 1998, respectively. Surprisingly, in January 2000, some 16 months after this mooring was verified as missing, its bottom steel buoy element and an S4 current meter were recovered off Key Largo, FL. Approximately 2.5 months of useful data were recovered from this instrument. Also, in March 1999, about one month before the end of the field program, a replacement for this same B1 Mooring was trawled up (in

its entirety, including the anchor) by a commercial shrimping vessel. In this latter case, these instruments and the corresponding data were retrieved a few months after the field program was concluded.

Approximately 22.5% of the 4.4% data loss, was due to the missing B1 Mooring. The remaining data loss was due to various instrument malfunctions including defective DSUs (3), fouled or broken rotors (2), defective tilt channels (2), stuck wings (3), leaks (1), and battery failures (2). The 72 Hugrún temperature recorder deployments provided 100% data return as did 75 of 76 RDI ADCP deployments, the data loss here being due to the loss of the WorkHorse ADCP at the B1 Mooring site. The worst instrument data return (89.3%) was for the InterOcean S4 current meter where two units had battery pack failures early in their deployments and only 2.5 months (out of four months) of useful data were obtained from the S4 recovered in January 2000 from the missing April-August 1998 deployment of the B1 Mooring. Table 2.5-3 provides a complete summary of the data return for all of the instruments deployed during this program, and Figure 2.5-1a,b provides a time line of the data return by instrument level on each mooring.

2.6 GeoSat Altimeter Data

Since 1993, tandem sampling of the Gulf of Mexico by satellite altimeters has allowed continuous mapping of the mesoscale circulation in the region at unprecedented resolution. This operational capability has been used during the DeSoto Canyon field program to monitor the Loop Current and Loop Current intrusions into the eastern Gulf of Mexico. The altimeter missions and the data acquired for this study are described below.

2.6.1 TOPEX/POSEIDON

TOPEX/POSEIDON(T/P) is a joint U.S.-France satellite mission managed in partnership by the National Aeronautics and Space Administration (NASA) and the Centre National d'Etudes Spatiales (CNES). The T/P satellite was launched aboard an Ariane 42P launch vehicle on August 10, 1992 from Kourou, French Guiana. Two altimeters are carried aboard the satellite but only one is active at any one time because of on-board sharing of the altimeter antenna. The primary instrument is the dual-frequency NASA altimeter, commonly referred to as TOPEX. TOPEX sends microwave pulses to the ocean surface at two frequencies so that a correction can be made to the altimeter range to account for the delay caused by free electrons in the ionosphere. The CNES altimeter, commonly referred to as POSEIDON, is a single frequency, solid-state, low-power, low-mass sensor. The antenna sharing agreement between NASA and CNES provides for the POSEIDON altimeter to be turned on approximately 10% of the time. The current operational procedure is to turn on POSEIDON for a complete cycle (10 days) approximately every 10 cycles, though not exactly every 10 cycles to prevent aliasing problems.

After an initial assessment phase (Table 2.6-1), the satellite was placed into a 10-day exact repeat orbit in late September 1992 to begin operational sampling of the ocean and has remained in this orbit through

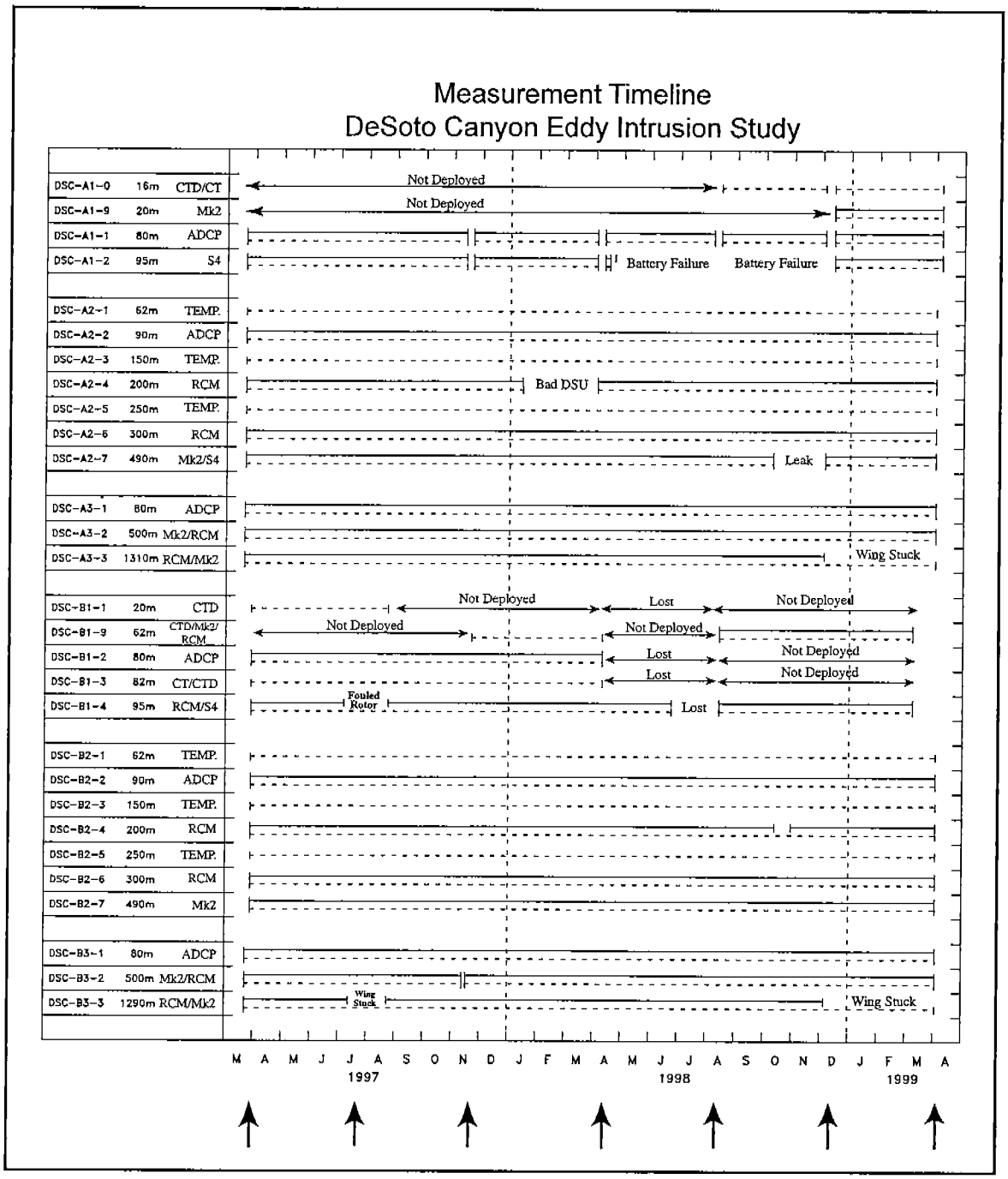

Figure 2.5-1a. Timeline of data return by instrument level for the indicated DeSoto Canyon Eddy Intrusion Study moorings. Arrows indicate the approximate dates of the hydrographic cruises.

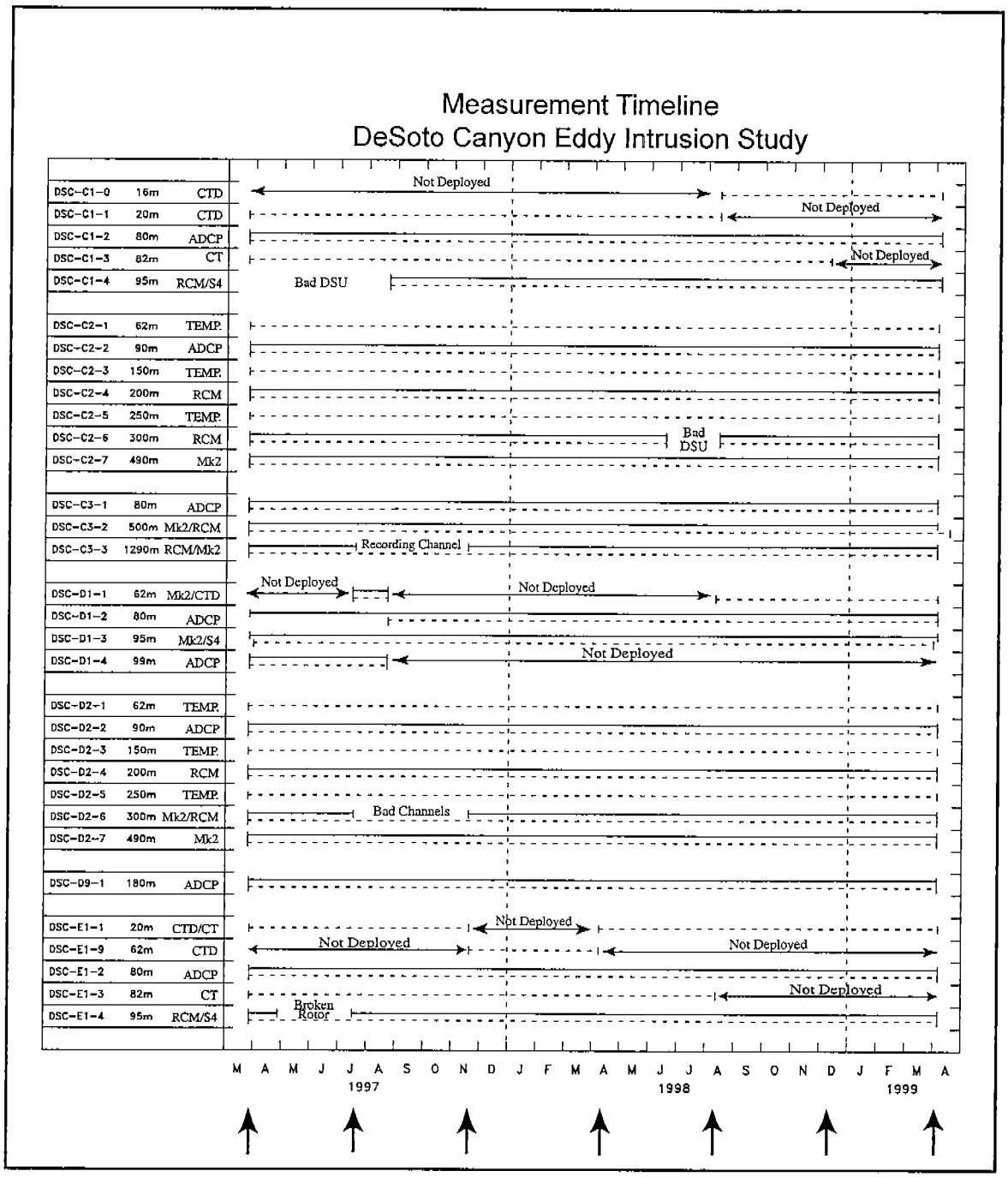

Figure 2.5-1b. Timeline of data return by instrument level on indicated moorings for the DeSoto Canyon Eddy Intrusion Study. Arrows indicate the approximate dates of the hydrographic cruises.

Table 2.5-3. Moored instrument data return (by good record count) during the DeSoto Canyon Eddy Intrusion Study.

Deployment	Aanderaa RCM-7/8	General Oceanics MK2	Hugrún Seamon Mini
1	223565/246355 (13)	74452/75359 (10)	64038/64038 (12)
2	209215/216395 (11)	73778/83631 (9)	72120/72120 (12)
3	256274/274213 (12)	63484/63484 (6)	80267/80267 (12)
4	213975/228239 (11)	63045/66049 (7)	72117/72117 (12)
5	209905/216469 (11)	66097/74206 (8)	68389/68389 (12)
6	214273/214273 (12)	50594/61821 (7)	67206/67206 (12)
TOTALS	1327207/1395944 (70)	391450/424550 (47)	424137/424137 (72)
Percent Good	95.08%	92.20%	100%
Deployment	**InterOcean S4**	**Sea-Bird MicroCat/SeaCat**	**RD Instruments ADCP***
1	7977/7977 (1)	49905/49905 (6)	146571/146571 (13)
2	24532/24532 (3)	58932/60944 (5)	148537/148537 (13)
3	49692/49692 (5)	80317/80317 (6)	173190/173190 (13)
4	32817/44628 (5)	48181/72181 (6)	143576/155576 (13)
5	34515/42366 (5)	52993/52993 (5)	135942/135942 (12)
6	44458/48168 (6)	44927/44927 (4)	134780/134780 (12)
TOTALS	193991/217363 (25)	335255/361267 (32)	882596/894596 (76)
Percent Good	89.25%	92.80%	98.66%

Grand TOTAL 3,554,636/3,717,857 = 95.61%

* All ADCP levels for each instrument counted as one (1) time series record.
(#) = Number of Instruments

the entire mission to date. The primary science objective of the T/P mission is to observe accurately basin-scale to global-scale circulation variability. The operational orbit, which repeats every 10 days along the ground track (Figure 2.6-1), does not result in sufficiently dense spatial sampling for accurate mapping of mesoscale circulation variability. As a result, data from TOPEX must be combined with altimeter data from other satellites for mesoscale circulation monitoring.

2.6.2 ERS-1&2

The first and second European Remote-Sensing (ERS) satellites, ERS-1 and ERS-2, were developed by the European Space Agency (ESA) as a sequence of multidisciplinary earth observing satellites devoted to remote sensing from a polar orbit. These two satellites are nearly identical and have identical payload instruments including satellite altimeters. The only difference in the payloads is an ozone mapping instrument that was added to ERS-2, which was not available on ERS-1. By flying a sequence of identical instruments, ESA has been able to cross-calibrate and extend a very useful time series of global remote sensing observations. Only ERS-2 is currently operational. ERS-1 was placed in

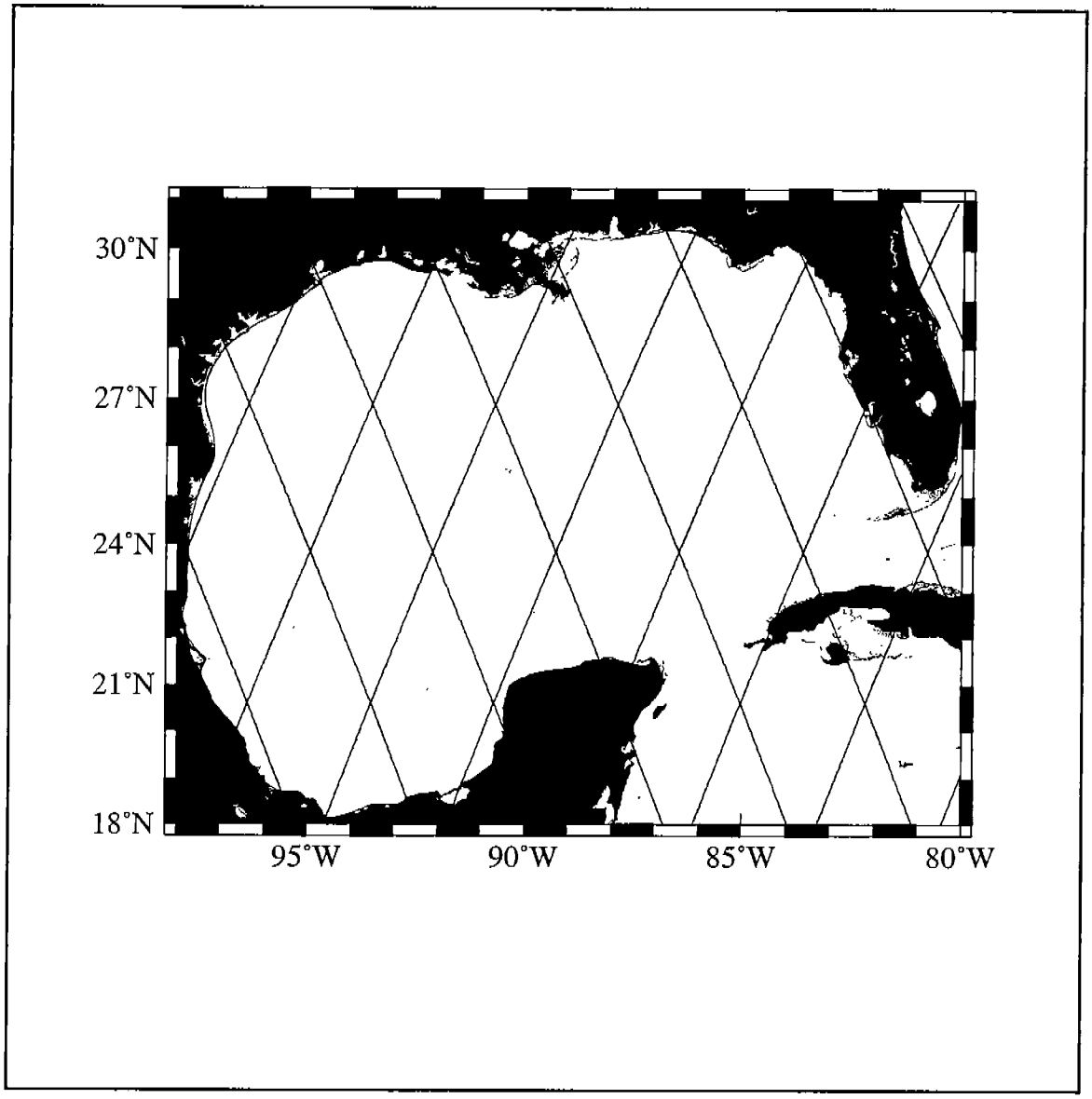

Figure 2.6-1. TOPEX/POSEIDON ground track over the Gulf of Mexico from the operational 10-day exact repeat orbit.

a safe-hold state in May 1995 and served as a backup satellite until it failed in January 2000.

Table 2.6-1. TOPEX/POSEIDON Mission Phases

Mission Phase	Duration	Repeat period	Description
Maneuver	8/10/92 to 9/23/92		Initial phase to maneuver into operational orbit.
Assessment	8/10/92 to 12/31/92	10-day	Assessment phase to evaluate the performance of the satellite.
Primary and Extended Missions	1/1/93 to EOM	10-day	Primary and extended mission phase dedicated to collection of an extended time series of altimeter data from the TOPEX/POSEIDON operational 10-day repeat orbit.

ERS-1 was launched on July 17, 1991. Several observational periods, called "mission phases", were flown from orbits designed to meet the multidisciplinary objectives of the mission and optimize the scientific usefulness of the data collected (Table 2.6-2). Only the 3-day repeat orbits used during the commissioning and ice mission phases are unsuitable for mesoscale mapping. Both the multidisciplinary and geodetic phases provide altimeter data at sufficiently dense spatial sampling to be useful for mesoscale monitoring. During the multidisciplinary mission phases, both ERS-1 and ERS-2 sample along the 35-day repeat ground track shown in Figure 2.6-2. The 168-day repeat orbits flown during the geodetic phases can also be exploited for mesoscale mapping by using the 37-day near-repeat cycles within this orbit. An example of this spatial sampling over the Gulf of Mexico is shown in the ground track/coverage map for ERS-1 during the second cycle of the first geodetic phase (Figure 2.6-3).

ERS-2 was launched on April 21, 1995 and immediately placed into the 35-day repeat orbit used for the multidisciplinary phases of the ERS missions (Table 2.6-3). The satellite has remained in this orbit throughout the entire mission, which simplifies the processing of ERS-2 altimeter data.

2.6.3 Data Sources

TOPEX data are distributed by the Physical Oceanography Distributed Active Archive Center (PO.DAAC) at the Jet Propulsion Laboratory. ERS data are distributed by "Centre ERS d'Archivage et de Traitement"(CERSAT), the French Processing and Archiving Facility for ERS-1 and ERS-2.

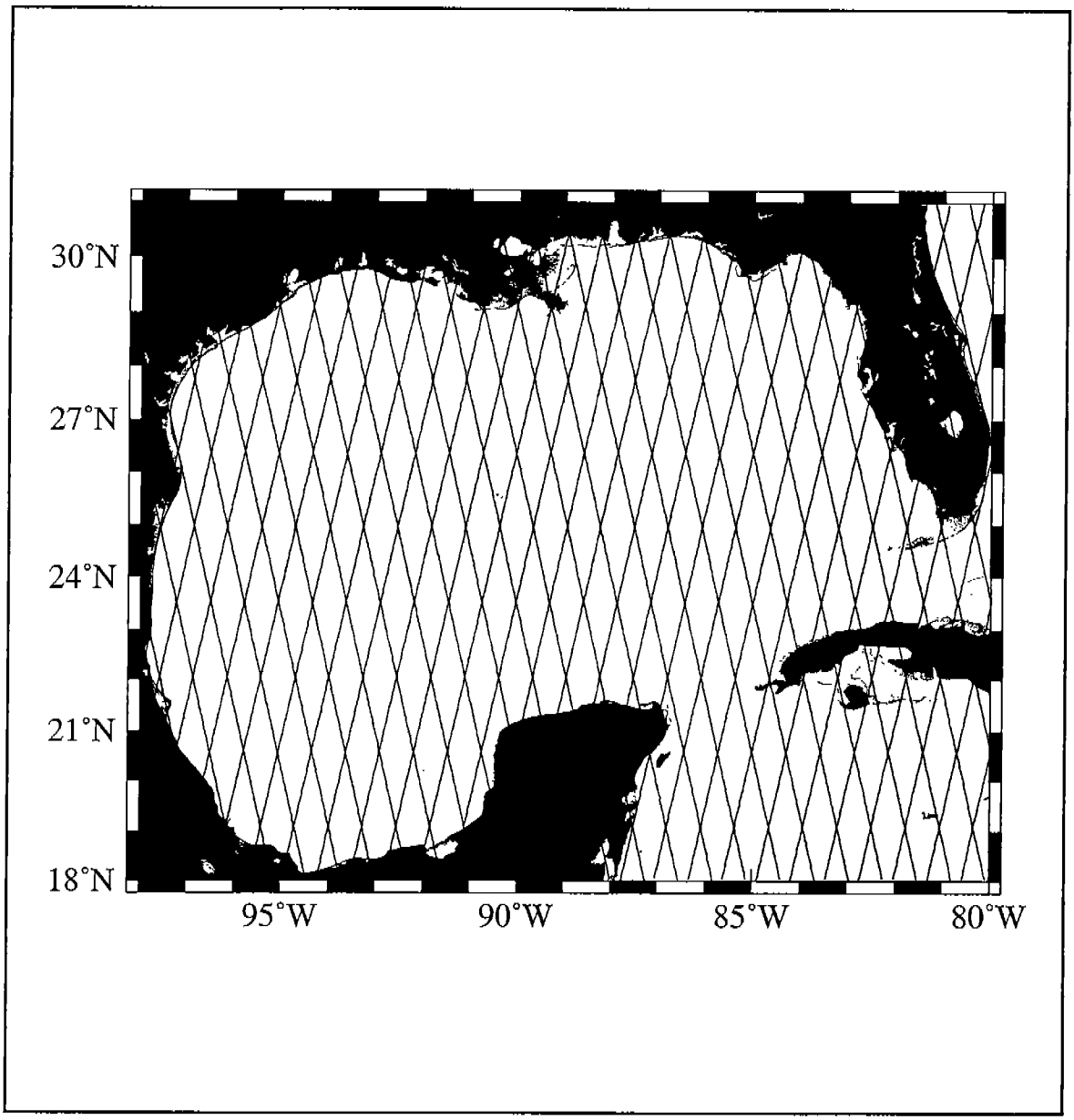

Figure 2.6-2. ERS-1 and ERS-2 ground track over the Gulf of Mexico from the 35-day exact repeat orbit used during multidisciplinary mission phases. ERS-2 was in this orbit during the entire DeSoto Canyon field program.

Table 2.6-2. ERS-1 Mission Phases

Mission Phase	Duration	Repeat Period	Description
Commissioning	7/31/91 to 12/20/91	3-day	Phase dedicated to observing very frequently the calibration sites.
Ice 1	12/28/91 to 3/30/92	3-day	Phase dedicated to observing specific ice zones.
Multidisciplinary 1	4/14/92 to 12/20/93	35-day	Multidisciplinary phase dedicated to satisfying most of the applications including land/ice mapping with SAR and ocean circulation mapping with altimetry.
Ice 2	12/23/93 to 3/10/94	3-day	Phase dedicated to resampling ice zones after two years.
Geodetic 1	4/10/94 to 9/27/94	168-day	Phase dedicated to providing very dense spatial observations from the altimeter for mapping the geoid.
Geodetic 2	9/27/94 to 3/21/95	168-day	Second phase of geoid mapping with the 168-day ground track shifted longitudinally by 8 km to double spatial resolution.
Multidisciplinary 2	3/21/95 to 5/16/96	35-day	Final phase to perform multidisciplinary mission and permit cross-calibration and tandem operation with ERS-2.

Table 2.6-3. ERS-2 Mission Phases

Mission Phase	Duration	Repeat Period	Description
Commissioning	5/1/95 to 11/1/95	35-day	Phase dedicated to commissioning satellite.
Tandem	11/1/95 to 5/15/96	35-day	Phase flown in tandem with ERS-1 for tandem SAR
Multidisciplinary	5/16/96 to EOM	35-day	Phase dedicated to performing multidisciplinary mission. The satellite is expected to remain in the 35-day repeat orbit to the end of mission (EOM).

2.7 Ancillary Data

2.7.1 Introduction

A number of ancillary data sets are available from other programs coincident in time with the DeSoto Canyon Eddy Intrusion Study. The applicable data from these programs are identified below.

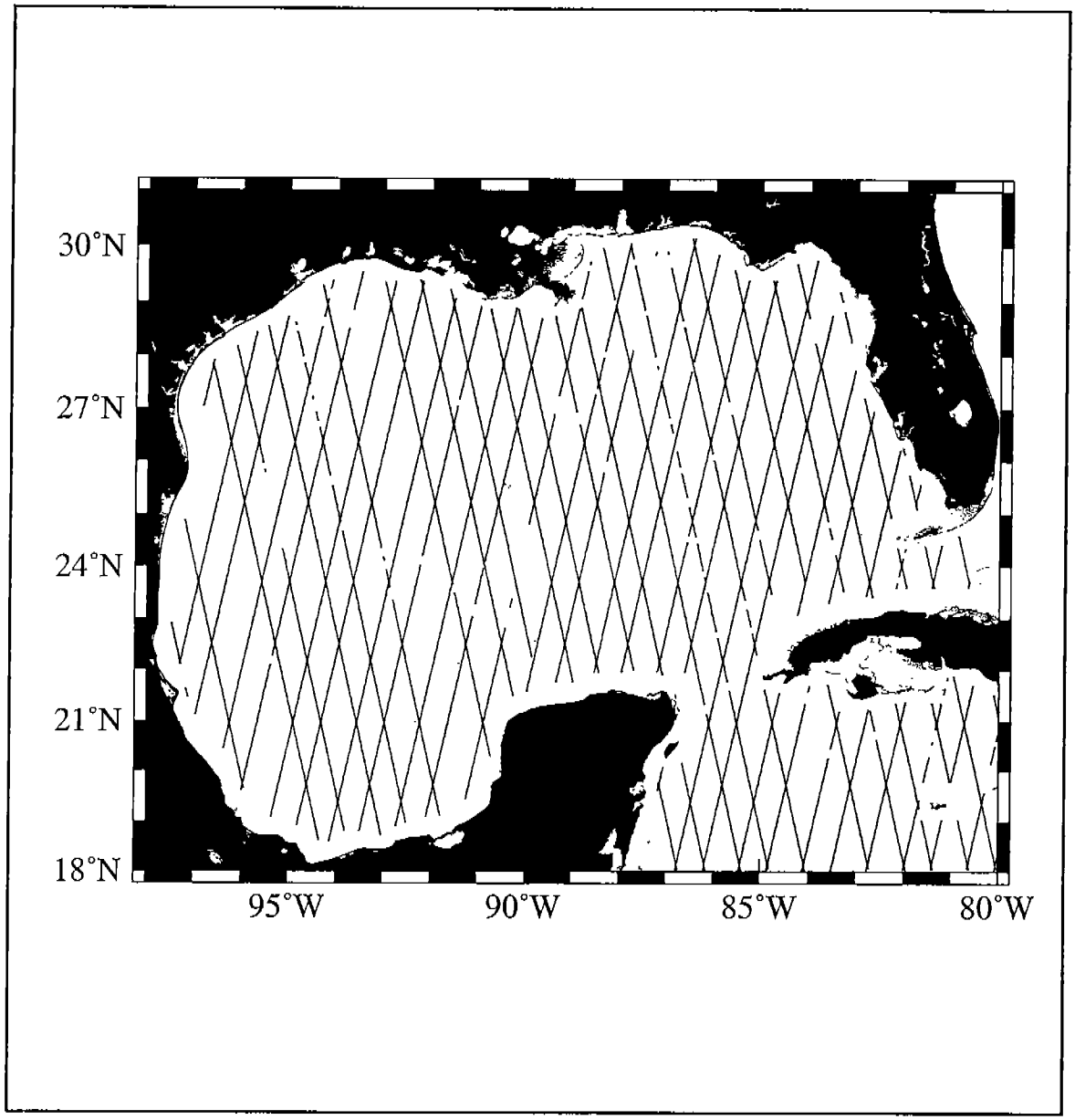

Figure 2.6-3. ERS-1 ground track showing data coverage for the first 37-day near repeat from the 168-day exact repeat orbit used during the ERS-1 Geodetic 1 mission phase.

2.7.2 Ancillary Data - SCULP drifters

The Surface Current and Lagrangian-drift Program (SCULP) was developed to improve the understanding of ocean circulation over continental margins in the northern Gulf of Mexico. Drifters deployed during SCULP are similar in design to those used during the U.S. Coastal Dynamics Experiment (Davis, 1985). The drifters are composed of four rectangular vanes (50 cm wide, 90 cm tall) extending radially from a thin, vertically oriented, tube held in place at a depth of 0.5 meters by four small surface floats. The drifters are initially packaged in soluble cardboard boxes with attached parachutes and dropped from aircraft. Continuous position transmissions are through service ARGOS for a period of 90 days. Drifter slip has previously been observed to be less than 3 cm/s (Davis, 1985). The data were collected and processed by Carter Ohlmann and Peter Niiler of the Scripps Institution of Oceanography.

The SCULP field program consists of three distinct segments identified here as SCULP-I, -II, and -III. The SCULP-I drifters were deployed primarily at 15 stations (distributed as a 3 by 5 grid) within a 125-km square on the Louisiana-Texas shelf from October 1993 through July 1994. The grid was reinitialized weekly for the first three months, then biweekly for three months, and finally monthly, giving roughly one year of data. The SCULP-II drifters were deployed within a ~400 by 150 km rectangle on the northwest Florida shelf to investigate cross-shore flows. The initial SCULP-II deployment occurred in February 1996, and consisted of 15 units. The grid was reinitialized every two weeks for roughly a year. The SCULP-III study was specifically concerned with eddies on the shelf-rise of the Louisiana and north Florida coasts. Four deployments of 20 drifters seeded the edge of warm eddies identified with remotely sensed sea-surface temperature (AVHRR) and the near real-time T/P and ERS-2 SSH data. Drifters were released during April 1998, on the Louisiana shelf, and during July 1998, on the continental margin south of the Florida-Louisiana border.

Drifter positions, recorded at various times throughout each day, were ordered in time and edited by eliminating displacements requiring velocities greater than 250 cm/sec. Data points recorded within 15 minutes were averaged together to eliminate erroneous displacements associated with observations by multiple satellites. The data were then interpolated onto a uniform time grid and daily averaged values were computed. This was done by calculating an analytic correlation function for each day from the Fourier transform of a model spectrum obtained from ten days of unequally spaced observations centered on the day of interest (Van Meurs, 1995). Each correlation function was then used to produce an interpolated location time series. Interpolated values were sub-sampled every three hours and daily averaged velocities calculated. Tidal and inertial signals are effectively removed in the daily averages.

2.7.2.1 Argos-Tracked Drifting Buoys

Thirty-two Davis-type Argos drifters were deployed in the study area between March 1997 and December 1998 as part of an internal MMS-funded oil spill model verification effort. The deployments were made in conjunction with scheduled cruises of the MMS-sponsored NEGOM Chemical Oceanography and Hydrography Study and the present DeSoto Canyon Eddy Intrusion Study. These data are identified in Table 2.7-1 and a composite of all of the Davis-type drifter tracks is shown in Figure 2.7-1. Additional oil-following drifters were deployed as part of this internal MMS effort, but these data are not considered useful to the present study.

Table 2.7-1. MMS Davis-type Argos drifting buoys deployed during the DeSoto Canyon Eddy Intrusion Study.

Drifter ID	Begin Date	End Date	No. Drifting Days
14709	03/24/97	04/23/97	30
14701	07/13/97	08/10/97	28
14702D	07/13/97	08/10/97	28
14703	07/13/97	07/18/97	28
14710	11/16/97	12/15/97	29
14711	11/16/97	12/14/97	28
17445	11/25/97	12/25/97	30
18814	11/22/97	02/19/98	89
18840	11/24/97	01/27/98	64
20505	11/24/97	03/30/98	126
20011	05/11/98	08/20/98	101
20012	05/12/98	08/19/98	99
20013	05/12/98	09/29/98	140
20014	05/16/98	08/12/98	88
20015D	05/15/98	09/23/98	131
20016	05/13/98	08/26/98	105
20017	05/13/98	09/22/98	132
20018	05/14/98	09/23/98	132
20019	05/15/98	08/11/98	88
11887	08/05/98	09/04/98	30
11888	08/03/98	09/02/98	30
11889	08/01/98	08/31/98	30
11890	08/02/98	09/01/98	30
11895	08/03/98	09/02/98	30
11896	08/05/98	09/04/98	30
11897	08/05/98	09/03/98	29
11898	08/04/98	09/03/98	30
20562	08/03/98	09/03/98	31
09700	11/21/98	12/21/98	30
09702	11/22/98	12/22/98	30
12061	11/21/98	04/01/99	131
20019D	11/23/98	01/06/99	44

2.7.3 GulfCet II Study

Two MMS/USGS-sponsored cruises were conducted in the study area in May-June and August 1997 (OREGON II Cruise 225, Leg 3 and GYRE Cruise 97G-08, respectively). These cruises were made as part of an effort to

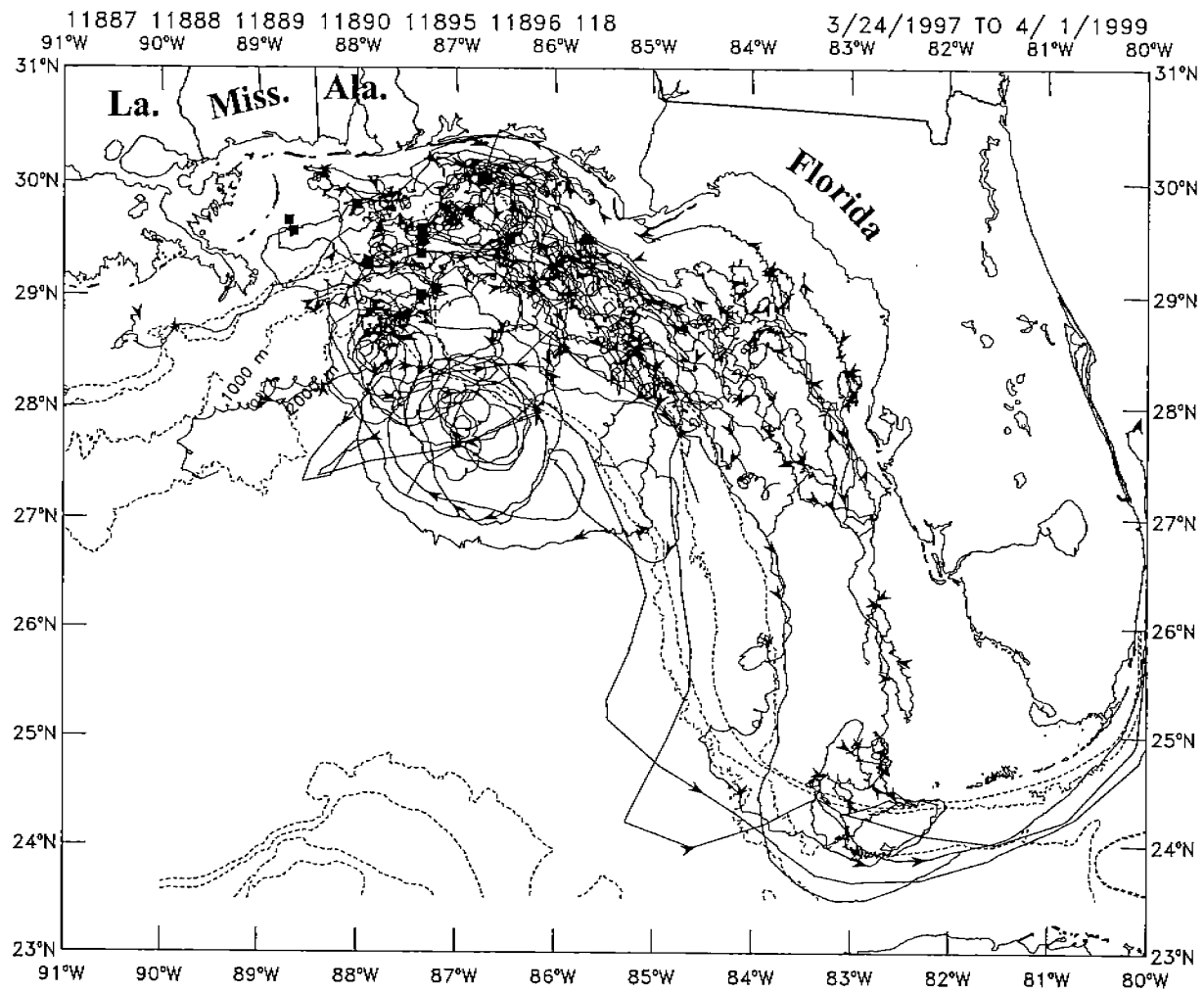

Figure 2.7-1. Composite track plot of all Davis-type ARGOS drifters deployed by MMS contractors in the study area during the DeSoto Canyon Eddy Intrusion Study.

assess the effects of oil and gas exploration and production on the distribution and abundance of marine mammals in the Northern Gulf of Mexico. Table 2.7-2 summarizes this hydrographic data collection.

Table 2.7-2. MMS/USGS GulfCet II cruises.

Cruise ID	Dates		CTDs	XBTs
	From	To		
OREGON II-225	05/29/97	06/09/97	4	77
97G-08	08/06/97	08/21/97	12	169

2.7.4 Northeastern Gulf of Mexico Chemical Oceanography and Hydrography Study

As part of a separate MMS-supported study of chemical and hydropgraphic conditions in the NEGOM being conducted by Texas A&M University, four chemical oceanography and hydrography cruises were conducted in the study area in November 1997 and May, July-August and November 1998. These cruises included a sampling grid of CTD and XBT stations. Many of the sections coincided with the same sections sampled as part of the DeSoto Canyon Eddy Intrusion Study, except that they extended much further up onto the shelf, but offshore only out to the 1000 meter isobath. In addition, underway thermosalinograph and ADCP data were collected during each cruise. Table 2.7-3 summarizes the data collection and Figure 2.7-2 shows the hydrographic grid for the CTD casts. XBT stations (not shown) were generally made between most, but not all, of the CTD stations.

Table 2.7-3. MMS Chemical Oceanography and Hydrography cruises.

Cruise ID	Dates		CTDs	XBTs	Underway Thermosalingraph & ADCP
	From	To			
N1	11/16/97	11/27/97	96	79	Yes
N2	05/04/98	05/15/98	99	96	Yes
N3	07/25/98	08/09/98	100	102	Yes
N4	11/12/98	11/25/98	99	114	Yes

2.7.5 NEGOM Marine Ecosystem Program: MAMES III

As part of the MAMES III being conducted by Continental Shelf Associates and Texas A&M University, four sites (1, 4, 5, and 9) along the Mississippi/Alabama shelf break were instrumented with near bottom current meters (4 and 16m above the bottom) from May 1997 to July 1999. These moorings were maintained near features (pinnacles) of varying heights rising up out of the bottom. Table 2.7-4 lists the mooring locations, CTD casts were also made at these four mooring sites during each deployment/rotation cruise.

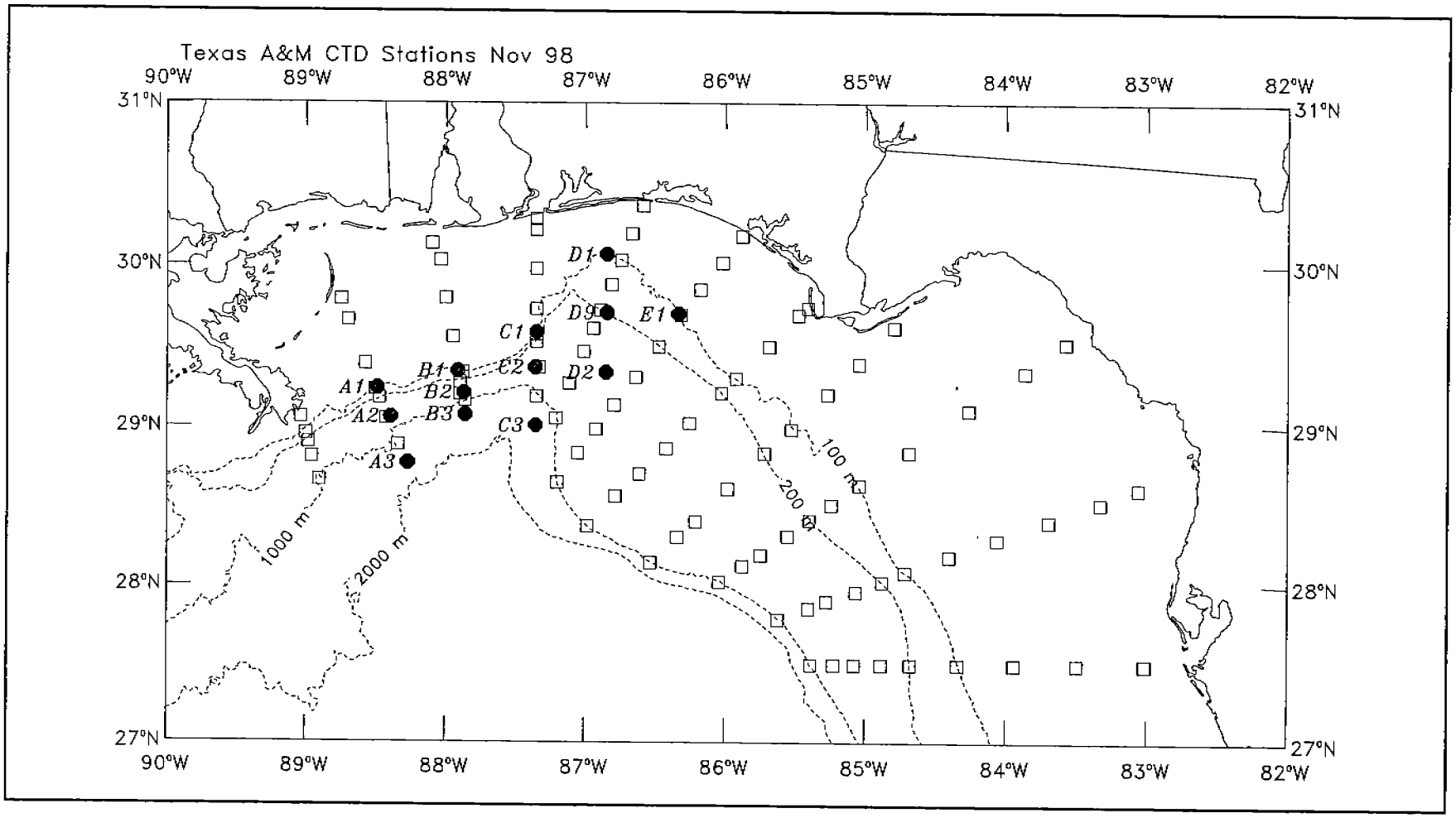

Figure 2.7-2. Map showing CTD station locations for the indicated cruise on the MMS-funded NE Gulf of Mexico Chemical Oceanography and Hydrography Study being done by Texas A&M University with DeSoto moorings locations suuperimposed.

Table 2.7-4. Northeastern Gulf of Mexico Coastal Marine and Ecosystem Program: Ecosystem Monitoring Mississippi/Alabama Shelf moorings.

Site	Instrument Type	Latitude	Longitude	Approximate Water Depth	Instrument Distance Above Bottom
1A	(AA/OEI)	29°26.479'N	87°34.322'W	75m	(16m/4m)
1B	(AA/OEI)	29°26.113'N	87°34.305'W	80m	(16m/4m)
1C	(AA/OEI)	29°26.243'N	87°34.791'W	80m	(16m/4m)
4	(AA/OEI)	29°19.860'N	87°45.360'W	115m	(16m/4m)
5	(AA/OEI)	29°23.516'N	87°58.660'W	80m	(16m/4m)
9	(AA/OEI)	29°14.415'N	88°19.388'W	95m	(16m/4m)

AA = Aanderaa RCM current meter
OEI = Oregon Environmental Instruments current meter

2.7.6 Meteorological Data

Meteorological data came from the National Data Buoy Center (NDBC). There were two types of stations used, the shore/platform based C-MAN stations and the moored 3-meter discus buoys.

2.7.6.1 C-MAN

Six coastal C-MAN stations were available to provide data in the NEGOM region. They are listed in Table 2.7-5. All stations reported wind speed and direction, air temperature and atmospheric pressure. The sensor height above mean sea level varied from station to station. Grand Isle, LA also reported water level data.

Table 2.7-5. C-MAN stations used during DeSoto Canyon Eddy Intrusion Study.

Station Name	Station ID	Sensor Heights above mean sea level (m)		
		Anemometer	Air Temperature	Atm. Pressure
Cape San Blas, FL	CSBF1	11.6	7.9	5.2
Keaton Beach, FL	KTNF1	11.8	10.9	4.8
Cedar Key, FL	CDRF1	11.8	10.9	4.8
Dauphin Island, AL	DPIA1	17.4	9.1	8.5
Southwest Pass, LA	BURL1	30.5	11.9	12.5
Grand Isle, LA	GDIL1	17.6	17.0	10.9

2.7.6.2 3-Meter Buoy

Four moored 3-meter discus buoy stations were used to provide offshore meteorological and wave data in the NEGOM region (Table 2.7-6). All stations reported wind speed and direction (5m), air temperature (5m), sea surface temperature (-0.6m), atmospheric pressure (0m) and wave data [height, average period, direction (only at 42007 and 42036) and dominant period]. Wave directional data were only available for 42007 (OTP) and 42036 (W. Tampa) and both had short gaps. Wind data were unavailable for 42007 (OTP) during Hurricane Georges in late-September 1998. The anemometer apparently was damaged as the hurricane approached. Station 42039 (Pensacola S.) had a two-month outage of all data from early February to early March 1998, and its barometer data never returned. Station 42040 (Mobile South) had a three-month outage of its wind data from mid-November 1998 through mid-January 1999.

Table 2.7-6. Offshore meteorological buoys used during the DeSoto Canyon Eddy Intrusion Study.

Station Name	Station ID
Pensacola S.	42039
W. Tampa	42036
Mobile South	42040
OTP	42007

2.7.7 Water Level Data

Hourly water-level data were obtained from the National Ocean Service (NOS) and the National Data Buoy Center (NDBC). The stations are listed in Table 2.7-7.

Table 2.7-7. Water-level stations used during the DeSoto Canyon Eddy Intrusion Study.

Station Name	Station ID	Source of Data
Cedar Key, FL (CE)	8727520	NOS
Panama City Beach, FL (PA1)	8729210	NOS
Panama City Beach, FL (PA2)	8735180	NOS
Dauphin Island, AL (DA)	DPIA1	NDBC
South Pass, LA (SO)	8760551	NOS
Grand Isle, LA (GR1)	8761724	NOS
Grand Isle, LA (GR2)	GDIL1	NDBC

At the start of this field program, seven water-level stations were reporting data in the NEGOM region. By the end of the program, only three were still active and two of those were located at Grand Isle, LA. The NOS station at Grand Isle, LA was the only one that had a continuous record for the study period.

2.7.8 River Runoff Data

River discharge data for eight rivers were obtained from the U.S. Army Corps of Engineers (New Orleans District) and the U.S. Geological Survey. These rivers are listed in Table 2.7-8. The Mississippi River dominates the region for discharge rate.

Table 2.7-8. River discharge stations used during the DeSoto Canyon Eddy Intrusion Study.

River Name	Station Number	Source of Data	Drainage Area (mi^2)
Mississippi (MI)	Tarbert Landing	USACOE	1,129,940
Atchafalaya (AT)	07381490	USGS	87,570
Bogue Chitto (BO)	02792000	USGS	1,213
Pearl (PE)	02489500	USGS	8,494
Pascagoula (PA)	02479310	USGS	8,204
Perdido (PR)	02376500	USGS	394
Apalachicola (AP)	02359230	USGS	19,500
Suwannee (SU)	02323500	USGS	9,640

2.7.9 Satellite Imagery

Satellite sea surface temperature imagery was provided by the USGS via an online collection of real time and archived images. Several images per day in GeoTiff format were available through the following web site:

http://coastal.er.usps.gov/east_gulf/html/sst.html.

Each image had been calibrated and navigated. More information concerning the processing procedures are available from this web site.

2.7.10 Hurricanes

Three hurricanes passed through the Desoto Canyon region during this study. These were Hurricanes Danny, Earl and Georges (Table 2.7-9). Data on their position and intensity were obtained from Johns Hopkins University, Applied Physics Laboratory.

Table 2.7-9. Hurricanes that passed through the study area during the DeSoto Canyon Eddy Intrusion Study.

Hurricane	Dates in Study Area	Wind Speed While in Study Area (mph)
Danny	18-20 July 1997	60-80
Earl	2-3 September 1998	60-100
Georges	27-29 September 1998	105-110

III. DATA QUALITY ASSURANCE AND PROCESSING

3.1 Introduction

Data quality assurance and processing techniques are discussed in this chapter. Where possible, detailed calibration and/or processing methods are described. Applicable methods for ancillary data are presented from the point in processing at which the data were obtained.

3.2 CTD Systems

3.2.1 CTD Sensor Calibration

Sea-Bird Electronics, Inc. CTD systems are designed in such a way as to permit easy processing and reprocessing of the raw data with new calibration coefficients. Subsequently, following a cruise, if the sensor calibration is in question, or the calibration is rather old, the raw data can be easily reprocessed with new calibration coefficients.

During this study, the Sea-Bird 911 Plus CTD sensors were calibrated at the manufacturer's facilities on numerous occasions. The primary and/or secondary temperature and conductivity sensors were calibrated in December 1996, March 1997, February and May 1998, and again in February/March 1999. In all cases, the conductivity and temperature sensors were found to be within the manufacturer's specifications. Pressure sensor calibrations were done in August 1996 and again in January 1999. Table 3.2-1 summarizes the manufacturer's specifications.

Table 3.2-1. Manufacturer's specifications for SeaBird Electronics,Inc., 911 Plus CTD.

Sensor	Initial Accuracy	Stability (per month)	Resolution
Conductivity	0.003 mmho/cm	0.002 mmho/cm	0.0004 mmho/cm
Temperature	0.002ºC	0.0003ºC	0.0002ºC
Pressure 10,000 psia	0.015% FS (1.02M)	0.0015% FS (0.102M)	0.001% FS

As a further CTD calibration check, water samples were drawn from mixed layers (where possible) for each cast for each cruise to determine a separate calculated CTD salinity minus bottle salinity intercomparison. These results (by cruise) for the 911 Plus CTD are presented in Table 3.2-2. The bottle salinities were run at Texas A&M University. The resulting data reveal that the calculated mean salinity differences for these mixed-layer comparisons for each cruise (including the pump plumbing plagued cruise of December 1998) ranged between +0.009 and -0.014 psu. Subsequently, no additional processing or reprocessing of the 911 Plus CTD data was required. Unfortunately, efforts to overcome the December 1998 pump plumbing problem by various means of lagging and offsetting the data were unsuccessful in eliminating the noisy salinity signal. Subsequently, these salinity data were discarded. A Sea-Bird SBE 19 SeaCat CTD was used, but only for a small number of casts (Stations 12-15 and Station 41) during the last cruise (March-April 1999) when the 911 Plus CTD was unavailable due to wire termination

problems. The SeaCat's specifications are presented in Table 3.2-3. This instrument had previously been calibrated in January 1998, but was post calibrated in May 1999. Prior to recalibration, a TS plot revealed a significant offset in the data. Following processing and recalibration, the corrected data plot compared favorably with the TS plot for the 911 Plus. This comparison is shown in Figure 3.2-1.

Table 3.2-2. Time (in months) of most recent calibration of 911 Plus CTD sensors before and after each cruise during the DeSoto Canyon Eddy Intrusion Study.

Cruise Dates	10,000 psia Pressure	Primary Temp.	Primary Conduct.	Secondary Temp.	Secondary Conduct.
03/18/97 - 03/28/97	7/22	3/11	3/11	0/11	0/11
07/08/97 - 07/19/97	11/18	7/7	7/7	4/7	4/7
11/11/97 - 11/22/97	15/14	8/NA	8/NA	8/3	8/3
03/31/98 - 04/11/98	20/9	1/NA	1/3	1/3	1/NA
08/04/98 - 08/15/98	24/5	3/6	3/7	1/6	1/7
12/01/98 - 12/13/98	28/1	7/2	7/3	5/2	5/3
03/30/99 - 04/06/99	2/NA	1/NA	1/NA	1/NA	1/NA

NA = NotAvailable

Table 3.2-3. Mixed layer 911 Plus CTD salinity minus Bottle salinity comparisons by cruise during the DeSoto Canyon Eddy Intrusion Study.

Cruise ID	Dates	CTD - Bottle ΔS (psu)	Std. Dev. (psu)
PE 9722	03/18/97 - 03/28/97	-0.014	±0.007
PE 9803	07/08/97 - 07/19/97	-0.009	±0.008
PE 9820	11/10/97 - 11/22/97	-0.007	±0.008
PE 9830	03/31/98 - 04/10/98	-0.002	±0.007
PE 9908	08/03/98 - 08/14/98	0.001	±0.010
PE 9923	12/01/98 - 12/13/98	0.009	±0.013
PE 9932	03/29/99 - 04/06/99	-0.002	±0.006

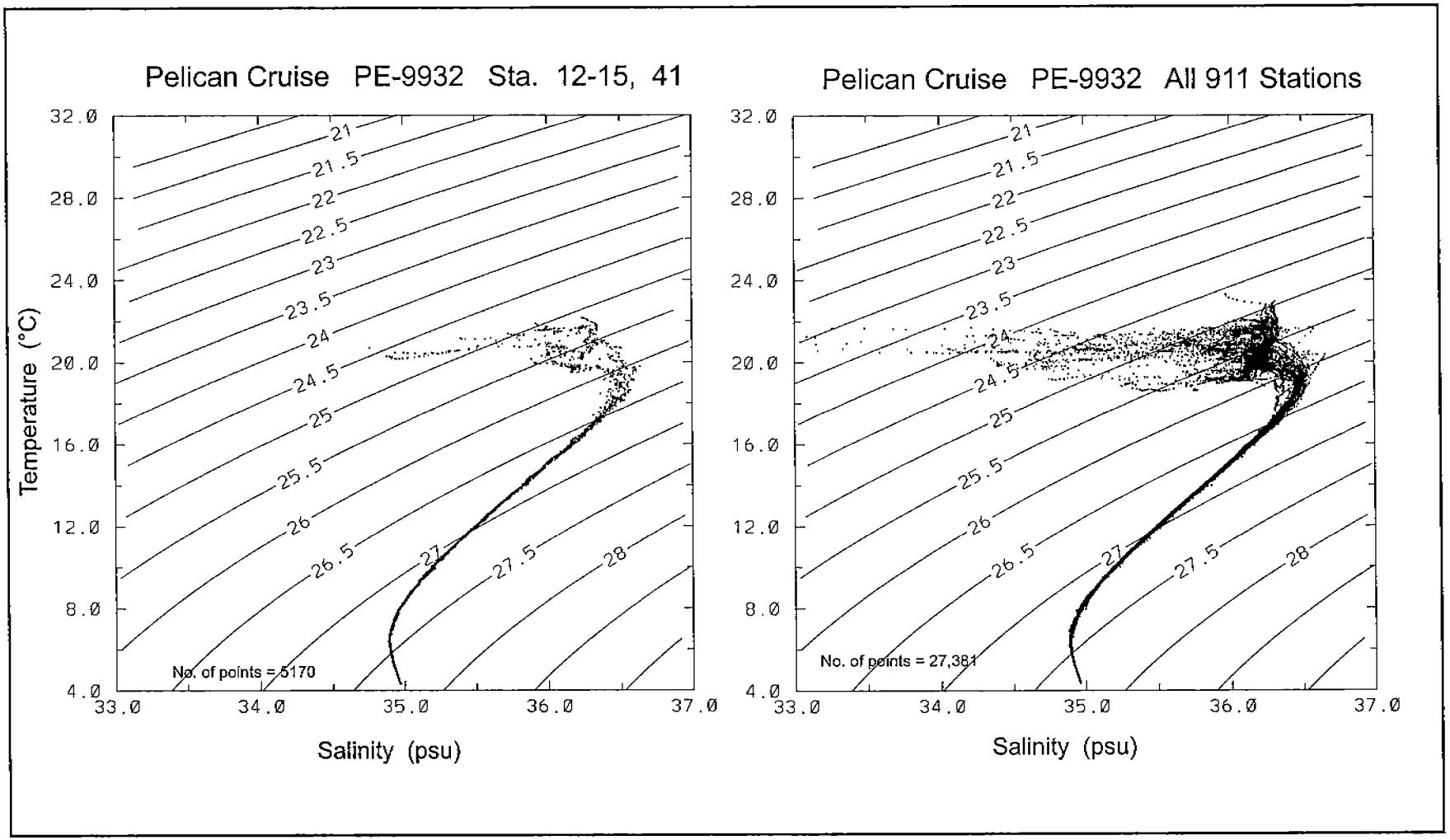

Figure 3.2-1. Final temperature/salinity (T/S) plots of CTD data from the Sea-Bird SeaCat 19 (left panel) and 911 Plus CTD (right panel) during the March-April 1999 cruise.

3.2.2 CTD Data Processing

Raw CTD data files were ingested into SAIC's Physical Oceanographic Data Base Management (PODBM) system. In this database the type of station (CTD or XBT) was identified as well as the latitude, longitude, depth of cast and water depth for each cast. These data were then averaged to one-meter levels and sigma-t, temperature and salinity data were plotted versus depth for each cast to serve as an initial quality check. Finally, a composite Temperature-Salinity (T-S) plot was produced for each cruise.

3.3 XBT System

3.3.1 XBT Probe Calibration

The T-7 XBT probe is rated by the manufacturer as having a temperature accuracy of ± 0.2 °C over the range -2 to +35 °C. No effort was made to provide an independent calibration check of this accuracy, but CTD data collected at the same location as XBT data (but not at the same time) during the second Feature Survey in December 1998 ranged from 0.1°C to 0.7°C lower in temperature than the corresponding XBT data. These results were derived from a comparison of temperatures at 25 and 40m depth in a 50 meter thick mixed layer along a repeated section that was sampled twice over twelve hours.

Separately, it has been well documented (Hanawa et al. 1995) that the manufacturer's original drop-rate equation ($z = 6.472\ t - 0.00216\ t^2$) under-estimates the actual drop rate of the T-7 XBT probe, tending to artificially lift the isotherms approximately 3.4 % from their actual depths. The data obtained in this program were collected using this same historical standard equation: Subsequently, in processing, a linear correction ($Z_1 = 1.0336\ z$ (from Hanawa et al. 1995)) was applied to more accurately present the depth/temperature pairs.

3.3.2 XBT Data Processing

SAIC uses a systematic procedure for the processing of CTD and XBT profiles. The following list summarizes the processing steps for CTD/XBT profile data respectively.

Data are logged into the SAIC Physical Oceanographic Data Base and the cruise is assigned a unique cruise ID. Next, the data are read into binary disk files on the local server. These files are created by storing the data scans as ASCII characters in a sequential file using the system file utility program. During sequential file creation, checks are made on the input parameters (temperature, conductivity and depth) for large spikes, data gaps and number of data scans for each individual cast.

Vertical profiles of temperature and conductivity are plotted and checked for spikes or obviously questionable data. The bad data scans are removed or the entire cast is discarded depending on the number of bad data points. T/S diagrams are created for each cast to assure consistency with known characteristics of water masses in the Gulf.

From the corrected data set, both vertical and horizontal contour maps are produced for individual sections and the entire cruise, respectively. These maps are checked visually against the profiles as a quality control measure. Other data products (geostrophic velocity, integrated transports, dynamic heights) are produced as required for further analysis.

3.4 Altimetry

Sea surface height (SSH) analysis maps were produced from archival altimetric measurements based on the latest versions of the TOPEX and ERS geophysical data records (GDRs). TOPEX data were obtained from the Physical Oceanography Distributed Active Archive Center (PO DAAC) at the Jet Propulsion Laboratory, and ERS data from the "Centre ERS d'Archivage et de Traitement"(CERSAT), the French Processing and Archiving Facility for ERS-1 and ERS-2. Both data sets are processed in as consistent a fashion as possible to produce accurate analysis maps based on the blended tandem altimetric observations.

3.4.1 Data Processing

The TOPEX data were corrected using standard corrections supplied on the JPL/PO.DAAC TOPEX GDRs, including inverted barometer, electromagnetic bias, ionosphere and wet/dry tropospheric corrections, as recommended in the GDR handbook (Callahan, 1993). The mean sea surface included on the GDRs (Basic and Rapp, 1992) was subtracted from each sub-satellite data point to apply an implicit cross-track geoid gradient correction. Ocean tides were removed using the tidal solution derived from the Colorado Center for Astrodynamics Research (CCAR) barotropic tide model (version 1.0) assimilating TOPEX data (Tierney et al., 1998).

The ERS-1 and ERS-2 Altimeter Ocean Products (ALTOPR) CD-ROMs were obtained from CERSAT. The ERS altimeter data were corrected using standard corrections supplied on the ALTOPR GDRs, including inverted barometer, electromagnetic bias, ionosphere and wet/dry tropospheric corrections. The data were also corrected using the CCAR Version 1.0 tide model to be consistent with the TOPEX processing.

Each cycle of corrected 10-day repeat TOPEX and 35-day repeat ERS data was linearly interpolated to reference ground tracks based on computed orbits for the satellites. The TOPEX reference track was based on a ground track computed for cycle 18, with a fixed spacing of the sub-satellite reference points at once per second along-track which is approximately a 5.77 km spacing over the Gulf of Mexico. The ERS 35-day reference ground track is based on 1/second along-track points computed for cycle 6 of the ERS-1 Multidisciplinary 1 mission phase. No gridding of the non-repeat ERS-1 data was performed. An empirical orbit error correction was applied to the ERS along-track data, after gridding when appropriate, to remove residual ERS orbit error. An empirical correction of the TOPEX data was not needed; however, to consistently "filter" both data sets the empirical correction was also applied to the TOPEX data. This correction was based on an along-track "loess" filter, which

removed a running least squares fit of a tilt plus bias within a sliding window from the along-track data. The filter window is approximately 15 degrees of latitude (200 second along-track), passing the short wavelength mesoscale signals while filtering the longer wavelength orbit and environmental correction errors.

This processing procedure references the along-track data to an accurate high resolution mean sea surface based on altimeter data collected from the TOPEX/POSEIDON, ERS-1 and GEOSAT Exact Repeat missions (Yi, 1995). By referencing the data to an independent mean sea surface, a climatology based on multiple altimeter mission data sets can be developed to include past, present and future altimeter data referenced in the same manner. This includes the historical GEOSAT data (Berger et al., 1996) and the TOPEX/POSEIDON and ERS-2 data available during the DeSoto Canyon field program.

3.4.2 Blended T/P and ERS 1&2 Climatology

An archive of the Gulf of Mexico SSH maps from January 1, 1993 to April 30, 1999 has been produced from the corrected sea surface height anomalies from TOPEX/POSEIDON and ERS-1&-2. Daily analysis maps of height anomaly relative to the mean sea surface have been created using an obective analysis procedure (Cressman, 1959) to interpolate the along-track data to a 1/4 degree grid over the Gulf. The method used an iterative difference-correction scheme to update an initial guess field and converge to a final gridded map. A multigrid procedure was used to provide the initial guess. The complete multigrid procedure is described in an appendix to Hendricks et al. (1996). Five Cressman iterations were used with radii of influences of 200, 175, 150, 125 and 100km, while employing a 100 km spatial decorrelation length scale in the isotropic Cressman weighting function. Data were also weighted in time using a 12-day decorrelation time scale relative to the analysis date. A model mean is added the sea surface height anomaly maps to estimate the total dynamic topography. This mean was computed for the time period 1993 through 1998 from a data assimilation hindcast of the general circulation in the Gulf. The 1993 through 1998 hindcast was made for the MMS Deepwater Reanalysis and Synthesis Project by Lakshmi Kantha and Jei Choi using the University of Colorado Princeton Ocean Model (CUPOM). The residual mean in the sea surface height anomaly maps over the time period 1993-1998 is removed before adding the model mean to produce the synthetic height estimate. A sample map is shown in Figure 3.4-1.

3.5 Moored Instrumentation

3.5.1 Moored Instrumentation Calibration

Each of the moored instruments deployed in this program, with the exception of the Aanderaa RCM current meters, was calibrated and serviced by its manufacturer prior to initial deployment. The Aanderaa instruments were serviced and recalibrated by Environmental Sensors, Inc., (ESI) formerly the Canadian distributor and service provider

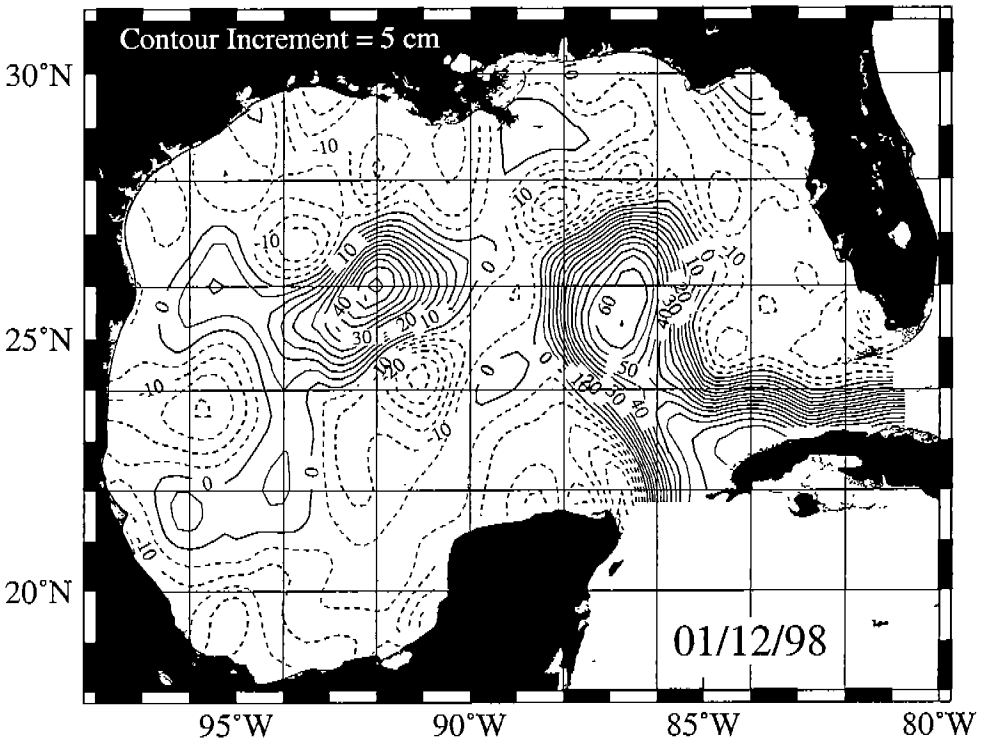

Figure 3.4-1. Sea surface height map for January 12, 1998. Sea surface height anomalies referenced to the 1993-1998 time period have been added to a model mean based on an assimilation hindcast for the same time interval.

for Aanderaa instruments in North America. In the cases of the Hugrún Seamon Mini Temperature Recorders, the RDI 300 KHz WorkHorse ADCPs and the Sea-Bird MicroCats, these instruments were all newly purchased for the program. Periodically, over the course of the program, a number of instruments were returned to the various manufacturers or ESI for servicing and/or re-calibration. At the conclusion of the field effort, most instruments were returned to the same entities for a post-program servicing and recalibration. Table 3.5-1 summarizes the manufacturer's specifications and the following sections discuss specific calibration issues for each type instrument.

In addition to the above, the conductivity data from the Aanderaa, General Oceanics and InterOcean current meters, when deployed in the upper 200m of the water column, tended to show some data quality degradation over the four-month deployment period due to fouling. Subsequently, the calculated salinity data obtained from the temperature and conductivity data collected by these current meters were adjusted following comparisons with nearby CTD casts taken at the beginning and end of each mooring deployment.

3.5.1.1 Aanderaa Current Meters

All of the Aanderaa current meters were calibrated at ESI for wide range temperature, wide range conductivity and direction as well as an operational test of speed in February or July 1997 and again at the conclusion of the field program in June or July 1999. Temperature calibration stability over the study period was excellent for all but two of the instruments. These two fell just outside the rated accuracy (±0.05°C) with differences on the order of ±0.07°C when compared at the high end (near 28°C) of the calibration scale. Conductivity calibration stability was significantly worse, as only three instruments were within the rated accuracy (±0.074 mmho/cm) at the conclusion of the program. Seven sensors had drifted producing conductivity differences ranging from ±0.078 to ±0.230 mmho/cm and one sensor had drifted by as much as 1.241 mmho/cm. Two conductivity sensors had failed during the program and were replaced with newly calibrated sensors. A compass calibration check revealed that all of the instruments were within the stated calibration accuracy (within ±5°) over the course of the program, and an operational test of speed (counting rotor turns) revealed that all of the instruments were functioning properly prior to their initial deployment and following final recovery.

3.5.1.2 General Oceanics Current Meters

The Niskin winged current meters were calibrated by the manufacturer in January or February 1997 and again in August 1999. Three units were removed from service due to malfunctions or a leak prior to the final calibration check and two units still require a final servicing. To date, all of the tested instruments were within their respective sensor specifications at the conclusion of the field program.

Table 3.5-1. Manufacturer's specifications for moored instruments used during DeSoto Canyon Eddy Intrusion Study.

	Temp Range (°C)	Temp. Accuracy/ Resolution (°C)	Conduct. Range (mmho/cm)	Conduct. Accuracy/ Resolution (mmho/cm)	Speed Range (cm/s)	Speed Accuracy/ Resolution (cm/s)	Direction Accuracy/ Resolution (Degrees)	Pressure Range (psia)	Pressure Accuracy/ Resolution (psia)
Aanderaa RCM 7/8 Current Meter	-0.34 to 32.17	±0.05/0.1% Range	0-74	±0.074/0.074	2-295	±1 cm/s or ±2% of speed/ starting speed is 2 cm/s	±5 for 5-100 cm/s ±7.5 for 2.5 to 5 and 100 to 200 cm/s/0.35	0-3000 0-5000	±1% Range/ 0.1% Range
General Oceanics MK2 Current Meter	-5 to 45	±0.25/0.016	0-75	±2.5/0.1	0-300	±1/1	±2/1	0-2000	±0.5% Range/ 0.1% Range
Hugrûn Temperature Recorder	-2 to 40	±0.1/0.025	---	---	---	---	---	---	---
InterOcean S4 Current Meter	-5 to 45	Thermistor ±0.05/0.003 Standard ±0.2/0.05	5-65	±0.2/0.01	0-350	±2% of reading ±1cm/s/0.2 cm/s	±2/0.5	---	---
RDI Narrowband ADCP	-5 to 45	±0.2/0.012	---	---	0-1000	±0.2% of measured velocity ±0.5cm/s	±5/0.005	---	---
RDI Workhorse ADCP	-5 to 45	±0.4/0.01	---	---	0-1000	±0.5% of measured velocity ±0.5cm/s	±5/0.01	---	---
SeaBird MicroCat CT Recorder	-5 to 40	±0.002/0.0001	0-100	±0.003/month Res 0.0001	---	---	---	0-300	±0.15%Range/ 0.002%Range
SeaBird SeaCat CT Recorder	-5 to 35	±0.01/0.001	0-70	±0.01/0.001	---	---	---	0-300	±0.15%Range/ 0.002%Range

3.5.1.3 Hugrún Temperature Recorders

These instruments were calibrated by the manufacturer in January 1997 and again in July 1999. A comparison of reprocessed data from the last deployment with both the new and old calibration coefficients revealed that there had been no significant change/drift in calibration over the study period. All comparisons were found to be within the instrument's rated accuracy, generally varying by no more than ± 0.025°C. Subsequently, no adjustments were made in these data following instrument recalibration.

3.5.1.4 InterOcean Current Meters

The S4 current meters were initially calibrated by the manufacturer between March 1997 and March 1998. Two were recalibrated in July and November 1998 and one of these same units (that had been recovered by a shrimping vessel) was recalibrated again in June 1999 following final recovery. Two other units were returned to MMS after only one deployment. All of the instruments were equipped with conductivity sensors.

3.5.1.5 RDI ADCPs

All of the instruments were calibrated/serviced by the manufacturer in January or February 1997, and all but one of the recovered units were serviced again in June or November 1999. One instrument is yet to be serviced. The remaining eleven instruments were found to be within specification, except that four of the WorkHorse units (197, 200, 209 and 211) were found to exceed the manufacturer suggested accuracy of less than ±5 degrees for compass error when tested in a downward-looking mode. However, these same compasses were within specifications when tested in an upward-looking mode, which is how each was used in this study. Subsequently, all of the ADCP data are considered to be within instrument specifications, and there is no indication of any problem with data from the unit which is still awaiting servicing at RDI.

3.5.1.6 SeaBird CT Recorders

The SeaCat and MicroCat instruments were calibrated between December 1996 and June 1997, prior to initial deployment, and again in May or June 1999 following final recovery. Three of the SeaCat units were borrowed from the manufacturer and only deployed once during the initial deployment period, and a fourth borrowed unit was only deployed once during the fifth deployment period. The conductivity cells on all of these instruments were protected by antifouling cylinders which were replaced after a maximum of eight months use (two deployments). These cylinders appear to have worked well as there was no buildup of biological material inside the conductivity cells. In addition, the post-program calibrations reveal that the total conductivity sensor drift over the two-year field effort was less than 0.045 mmho/cm at 60 mmho/cm and less than 0.020 mmho/cm at 30 mmho/cm. Temperature drift on these same units was less than 0.003°C. Subsequently, the salinity drift is on the order of 0.020 to 0.050 psu.

3.5.2 Moored Instrumentation Data Processing

The following instruments were used on the moorings: InterOcean's S-4, Hugrun's Seamon-mini, Sea-Bird's SeaCat and MicroCat, RDI's ADCP, Aanderaa's RCM-7&8 and General Oceanics' MK2. Each required a somewhat different processing scheme to bring the data into SAIC's database. Some instruments, such as the S4, have their calibrations internally recorded. Others, like the Aanderaas, have the calibrations applied during data processing.

The SAIC database utilizes a consistent format whereby each filename has two data fields representing either vector or scalar data. For a vector, the u-v components are presented. Scalar data may be either a single parameter in each of the two fields, such as temperature, or two different parameters, such as temperature and salinity. Times for all data are in GMT.

Once in SAIC's database, each file for each deployment is analyzed for proper processing, missing or erroneous data, calibration errors or trends in the data. Missing data may be patched using similar data. Erroneous data may be bridged by interpolation. Data, such as salinity, may require detrending due to drift of the sensor. This is accomplished by applying an offset to the time series by comparison to adjacent CTD records, as required. Once the raw time series files have been cleaned up, they are filtered using 3-HLP and 40-HLP filters. The vector data are rotated to align the data with the local bathymetry.

All time series data for all deployments are concatenated into a single record covering the entire two-year study period. Where data are missing, the existing files are concatenated into as long a record as possible. Some single deployment files remain due to data gaps.

3.6 Drifting-Buoy Data

Drifter data from MMS included all transmissions received from each drifter and each position of the drifter as determined by Service Argos. Interactive procedures were then used to remove all duplicate positions, verify the validity of each position fix, sort the data into a time-ordered sequence and archive the data into the PODBM system. Once loaded onto the system, a final visual check was made of the data by plotting each individual buoy trajectory on a high-resolution map of the study area containing detailed bathymetry and coastline. This was used to identify spurious changes in the buoy's movement which could then be removed.

IV. LOOP CURRENT AND ITS INTRUSIONS

4.1 Introduction

The Loop Current (LC) and related processes are the primary sources of energy and momentum for circulation features in the NE Gulf of Mexico. With this as background a concerted effort was made to develop a more complete description of the morphology (boundary length, enclosed area, etc.) of the LC, the recent history of change associated with ring shedding and some possible dynamics associated with ring assimilation into Gulf waters. This information is basic to developing and understanding processes affecting circulation patterns in the study area.

4.2 Loop Current/Loop Current Intrusions from Altimetry

4.2.1 Introduction

Continuous monitoring of the Loop Current is possible from January 1993 to the present using the tandem sampling provided by microwave altimeters aboard the T/P and ERS-1&2 satellites. Satellite altimetry is a unique remote sensing technique because it is an all-weather observing system that directly measures a dynamic variable of the ocean state, the sea surface height (SSH). A number of useful metrics can be derived from altimeter data that allow quantitative and continuous monitoring of the Loop Current intrusions into the Gulf. In this report, we describe the techniques and altimeter-derived metrics that were developed for monitoring the Loop Current and Loop Current intrusions.

4.2.2 Loop Current Monitoring

Altimetric monitoring of the LC is difficult because of the large contribution of the mean circulation to the total dynamic topography in the eastern Gulf of Mexico. Although altimeter systems measure variations in SSH very accurately, imprecise knowledge of the marine geoid makes accurate absolute measurements of the total sea surface topography associated with ocean circulation impossible at this time. Synthetic observations of the total dynamic topography can be constructed by adding an independent estimate of the mean height to the height deviation measured by the satellites relative to a long-term altimetric mean.

For this study, we have selected a model mean SSH computed for the time period 1993 through 1998 from a data assimilation hindcast of the general circulation in the Gulf (Figure 4.2-1). The 1993 through 1998 hindcast was made for the MMS-funded Deepwater Physical Oceanography Reanalysis and Synthesis Program by Lakshmi Kantha and Jei Choi using the University of Colorado-Princeton Ocean Model(CUPOM). Along-track TOPEX and ERS-1&2 SSH anomalies are assimilated into CUPOM on a track-by-track basis as subsurface temperature anomalies. Before adding the mean to the gridded SSH anomaly fields, we averaged the 1993 through 1998 fields and removed any residual mean. By following this procedure, we have referenced the anomaly fields to a mean spanning the same time period as computed from the hindcast assimilation. The qualitative differences in synthetic maps created using various model means and

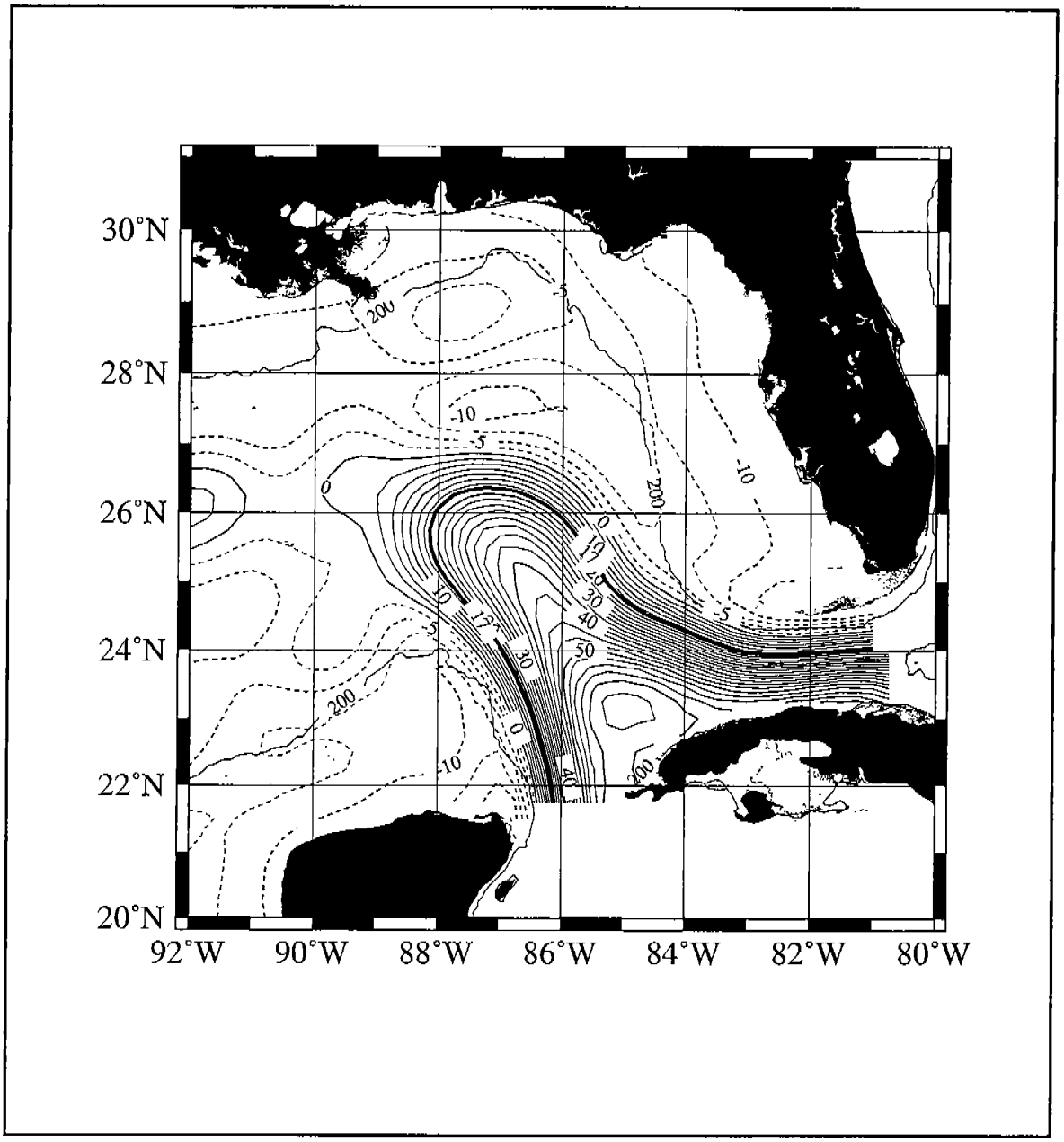

Figure 4.2-1. 1993-1998 mean sea surface height from a hindcast data assimilation experiment for the MMS Deepwater Physical Oceanography Reanalysis and Synthesis Project by Lakshmi Kantha and Jei Choi using the University of Colorado Princeton Ocean Model (CUPOM). The contour increment is 2.5 cm with positive and negative contours shown as solid and dashed lines, respectively. The 17-cm contour, which approximates the high velocity core of the LC, is shown as a thick solid line.

climatological means are not very remarkable, however, the derived quantitative metrics can be quite sensitive to the mean selected. For example, the sensitivity of the analysis of eddy shedding using the altimetric record discussed in Chapter 3 of this report has been checked and found to have little dependence on the mean. The quantitative metrics show much more sensitivity to the mean used to estimate a synthetic height, however, using the data assimilation model mean and referencing the altimeter data to a mean over the same time period produced robust results.

Altimetric monitoring of LC rings in the western Gulf of Mexico relied on the small contribution of the mean circulation to the total dynamic topography (Berger et al., 1996a,b). For that study, the 17-cm SSH anomaly contour was selected to derive quantitative metrics for the LC because the contour closely matched the location of maximum gradients in the topography, and allowed continuous tracking of LC rings during their translation through the western Gulf of Mexico. The 17-cm contour of total dynamic topography also works well as a definition for the high velocity core of the LC in the eastern Gulf of Mexico (Figure 4.2-2).

A direct comparison of the location of the 17-cm contour relative to the sea surface temperature (SST) front can be made at the northernmost point of the LC intrusion into the Gulf (Figure 4.2-3). SST images coincident with the altimeter maps were sampled along longitude meridians within +3° and -2° degrees of the 17-cm contour. The time series of coincident data over the time period of the DeSoto Canyon program shows a consistent bias between the two estimates of the LC location. In general, the agreement is good during times of strong thermal contrast, however, the 17-cm contour of SSH is consistently south of the SST front by about one degree of latitude or approximately 100 km. This is to be expected because of the difference in location between the high velocity core of the current and the surface thermal fronts. The variability about this bias offset is remarkably small given the occurrence of warm water filaments and other fine scale frontal variations on the periphery of the LC that are not well sampled by the altimeters. No comparison can be made during much of the time period, which highlights the difficulty of continuously monitoring the LC with thermal imagery.

4.2.3 Loop Current Metrics and Statistics

A variety of LC metrics can be computed from the SSH maps given the reliability of the 17-cm contour as a proxy for the location of the LC in the eastern Gulf of Mexico. These metrics include the length, area, volume and circulation associated with the LC within the Gulf of Mexico, and its maximum northward and westward extent.

The procedure for computing the metrics from the SSH fields has been automated by a MATLAB program that accesses the altimeter data archive and objectively computes the values. Daily values for each metric are computed as follows:

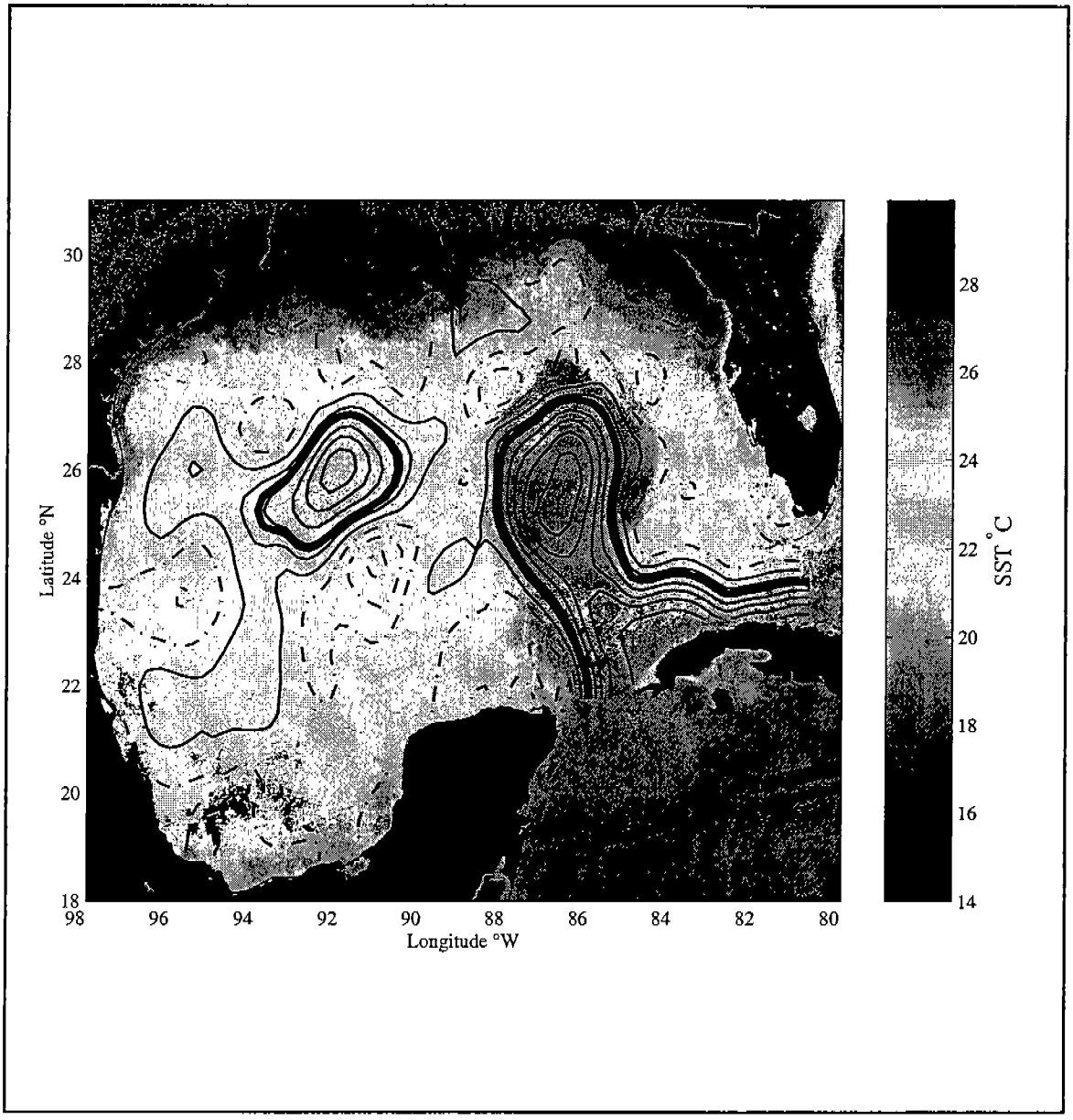

Figure 4.2-2. The 17-cm sea surface height contour from the altimetry map for January 12, 1998 overlaid on the composite SST imagery from the 2.98 days ending January 12, 1998 at 6:40 UT. SST data courtesy of the Johns Hopkins University Applied Physics Laboratory Ocean Remote Sensing Group.

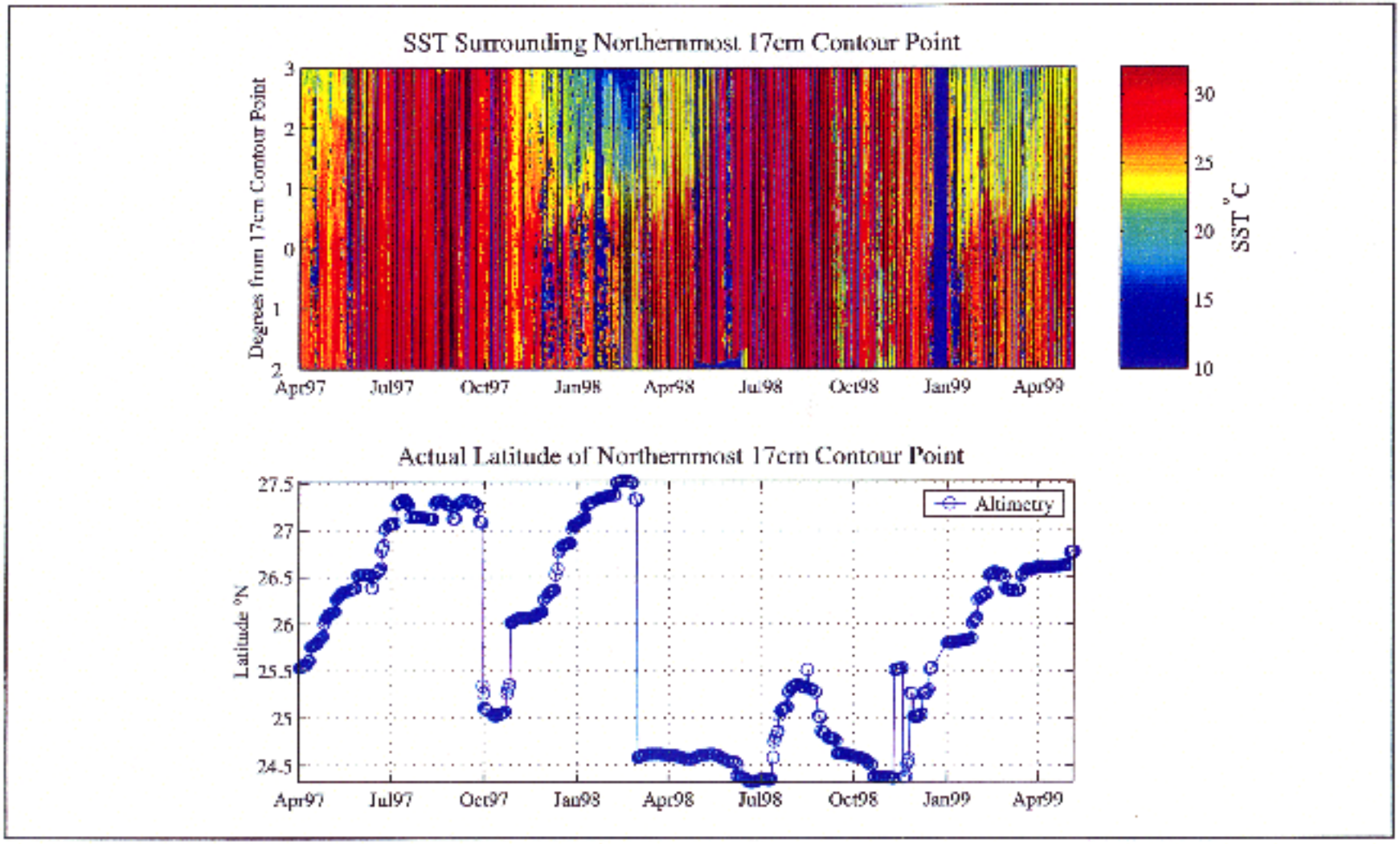

Figure 4.2-3. SST pixel values from coincident imagery are shown for the 3° north and 2° south of the northernmost point on the 17-cm sea surface height contour defining the IC core. The upper panel is color coded to provide the measured SST in the X-S region surrounding the actual northernmost, 17 cm contour point.

1. Load the 0.25° gridded SSH field and generate the coordinates of the 17-cm contours within the Gulf.
2. Identify the LC core, which is defined as the continuous 17-cm contour that enters the Gulf through the Yucatan Channel and exits through the Florida Straits.
3. Find the maximum west longitude and north latitude coordinates to determine the extent of westward and northward penetration of the LC.
4. Compute the length of the LC by summing the distances between the coordinates on the 17-cm contour.
5. Identify all 0.25° grid cells bounded by the 17-cm contour and compute the total Loop Current area by summing the areas of the individual cells.
6. Estimate the LC volume, assuming a one and a half layer ocean and a reduced gravity approximation, by evaluating the following area integral over the region bounded by the 17-cm contour:

$$\iint \frac{g}{g'} h dx dy$$

   where h is the sea surface height; g is the acceleration of gravity; and g' the reduced gravity. (A value of 0.03 m/s^2 was used for g'.)
7. Estimate the LC circulation by the line integral of the geostrophic velocity along the 17-cm contour:

$$\oint \vec{V} \cdot ds = \int u dx + v dy$$

   where u and v are the geostrophic velocity components and dx and dy are the coordinate spacing in the east/west and north/south directions respectively. The geostrophic velocity components at the midpoint locations are found by bilinear interpolation from the gridded geostrophic velocity components computed from the height field. (The sign convention employed is such that the anticyclonic vorticity associated with the LC is positive.)

The metric values have been computed for the time period from January 1, 1993 to April 30, 1999 and are shown in Figures 4.2-4 and 4.2-5. Summary statistics for this time interval are shown in Table 4.2-1. The total area of open water on the 0.25° grid in the Gulf of Mexico is 1,512,000 km^2. During this time interval, the average area covered by the LC was 142,000 km^2 or approximately 9% of the Gulf. The average length was 1390 km and average circulation was 1,271,000 m^2/s. The total estimated LC volume was 2.17 x 10^{13} m^3. This volume would take over 8 days to fill assuming an average inflow of 30 Sv, which is typical of the transport into the Gulf through the Yucatan Channel. The average maximum northward and westward extension of the LC intrusion was 26.1°N and 87.7°W. The maximum and minimum northward extension into the Gulf observed during the time interval was 28°N and 24.1°N, respectively. The maximum and minimum westward extension was 92°W and 85.8°W.

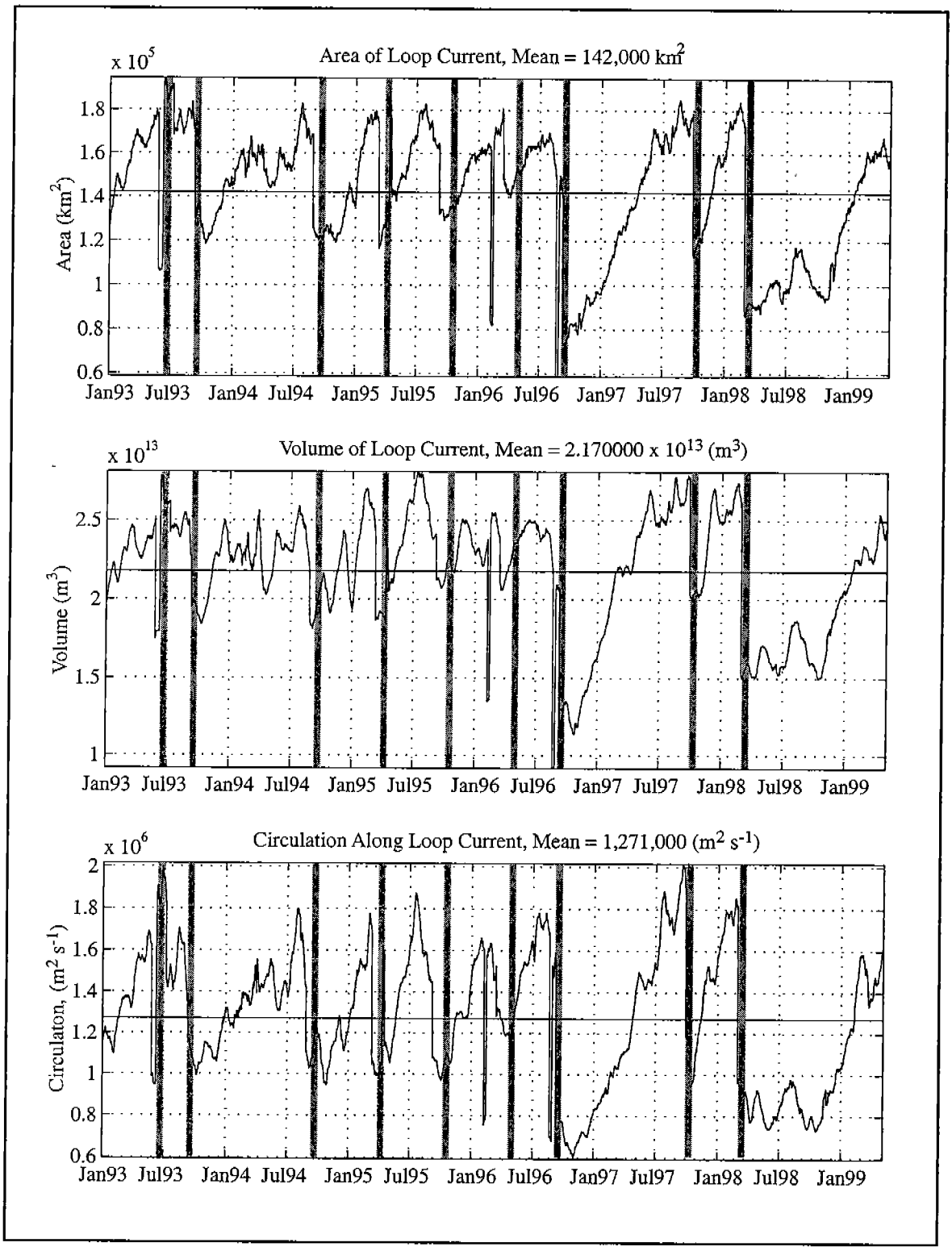

Figure 4.2-4. Time series of LC area, volume, and circulation for 1/1/1993 through 4/30/1999. Ring shedding events are shown by vertical gray lines immediately following the separation.

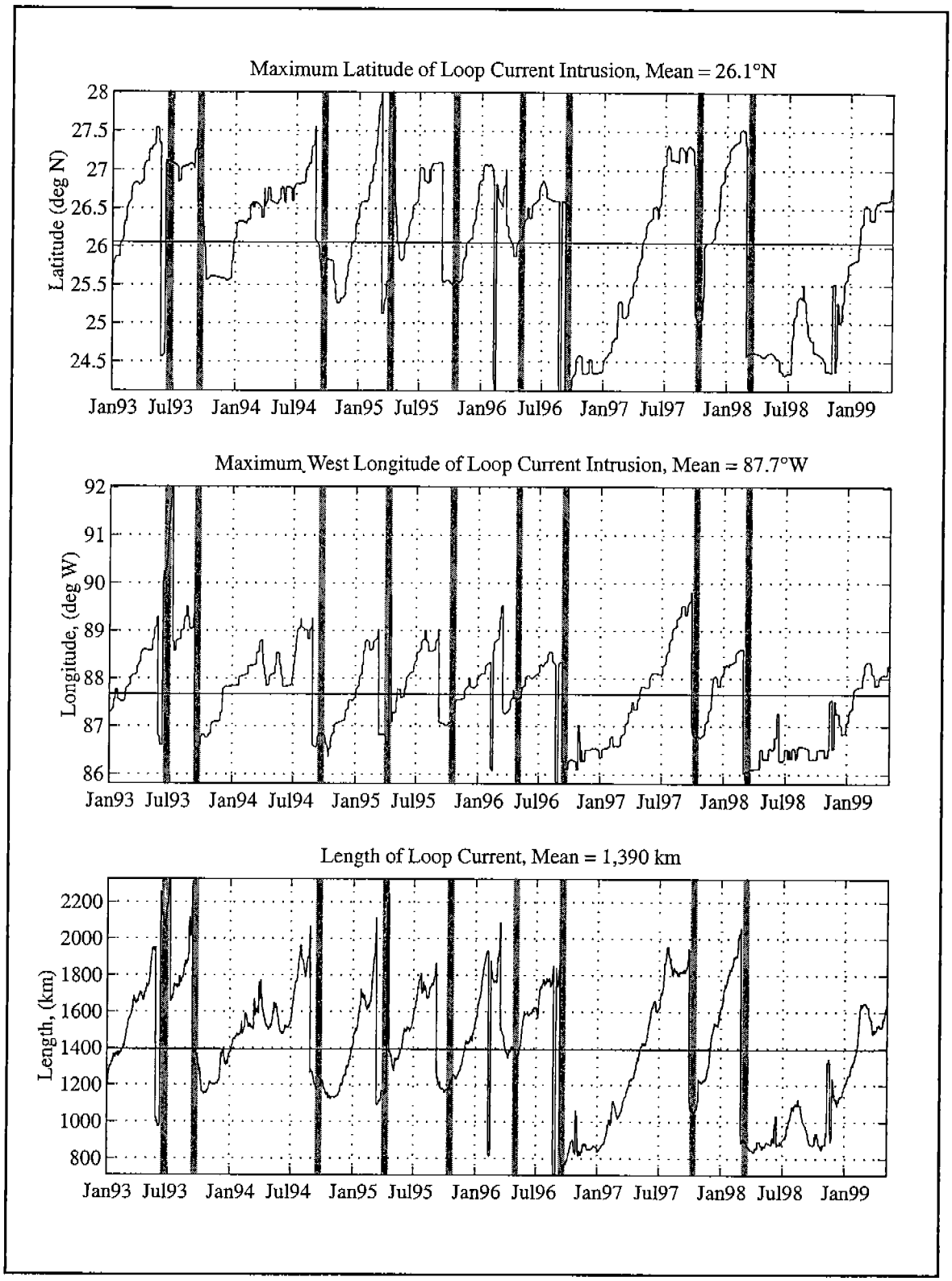

Figure 4.2-5. Time series of Loop Current northward and westward penetration, and length for 1/1/1993 through 4/30/1999. Ring shedding events are shown by vertical gray lines.

Table 4.2-1. Statistics for Loop Current Metrics (1/1/1993 -4/30/1999).

	West Longitude	North Latitude	Length	Area	Volume	Circulation
Mean	87.7°W	26.1°N	1390 km	142,000 km^2	2.17x10^13 m^3	1,271,000 m^2/sec
Std. Dev.	0.97°	0.93°	321 km	28,300 km^2	0.37x10^13 m^3	321,190 m^2/sec
Maximum	92.0°W	28.0°N	2016 km	194,600 km^2	2.81x10^13 m^3	2,016,200 m^2/sec
Minimum	85.8°W	24.1°N	593 km	58,600 km^2	0.91x10^13 m^3	593,480 m^2/sec

Similar statistics were derived from 10 years (1976-1985) of monthly frontal analysis maps based on AVHRR thermal images (MMS 89-0068). The summary LC statistics from that study reported an average area of 210,000 km^2 and 29.75°N and 91.25°W for the maximum northward and westward extension. The average area derived from thermal imagery was nearly 50% larger than the altimetric estimate reported here. This difference is attributable to the offset between the surface thermal fronts and the location of the core of the LC determined from altimetry. A similar offset of 50 to 100 km was found between the surface frontal analysis maps and subsurface temperature gradients at 125 meters determined from coincident XBT survey transects. Assuming the mean statistics over the two time intervals are comparable, we can estimate the relative offset by the difference of the averages divided by the average length of the Loop Current. This gives an estimate of approximately 50 km, which is comparable to the other estimates of the relative offset. The integrated effect of this offset is to increase estimates of the areal extent of the LC from thermal imagery relative to the value determined from altimetry.

The percent occurrence maps for the 17-cm contour and waters associated with the LC from altimetry are shown in Figures 4.2-6 and 4.2-7. These maps can be compared to the occurrence maps computed from the monthly frontal analysis maps from AVHRR thermal imagery (Figures 4.2-6&7 from MMS 89-0068). The occurrence of the 17-cm contour and waters associated with the LC from altimetry is well within the 200-meter isobath, unlike the estimates from thermal imagery that show significant probabilities of the front and LC waters being on the west Florida and Campeche shelves. This again is likely a result of warm filaments or shallow thermal features in the frontal analysis derived from the thermal imagery being interpreted as the main front of the LC.

4.2.4 Loop Current Ring Shedding Cycle

A primary reason for computing objective metrics for the LC and its penetration into the Gulf is to monitor the time-dependent behavior of the LC as it sheds rings that affect currents in the DeSoto Canyon study area. The LC ring shedding cycle has been studied extensively and an updated list of individual shedding events and spectrum are discussed in this report. The identified shedding events during the altimetric monitoring time period are plotted on each of the subplots of the metric time series. A

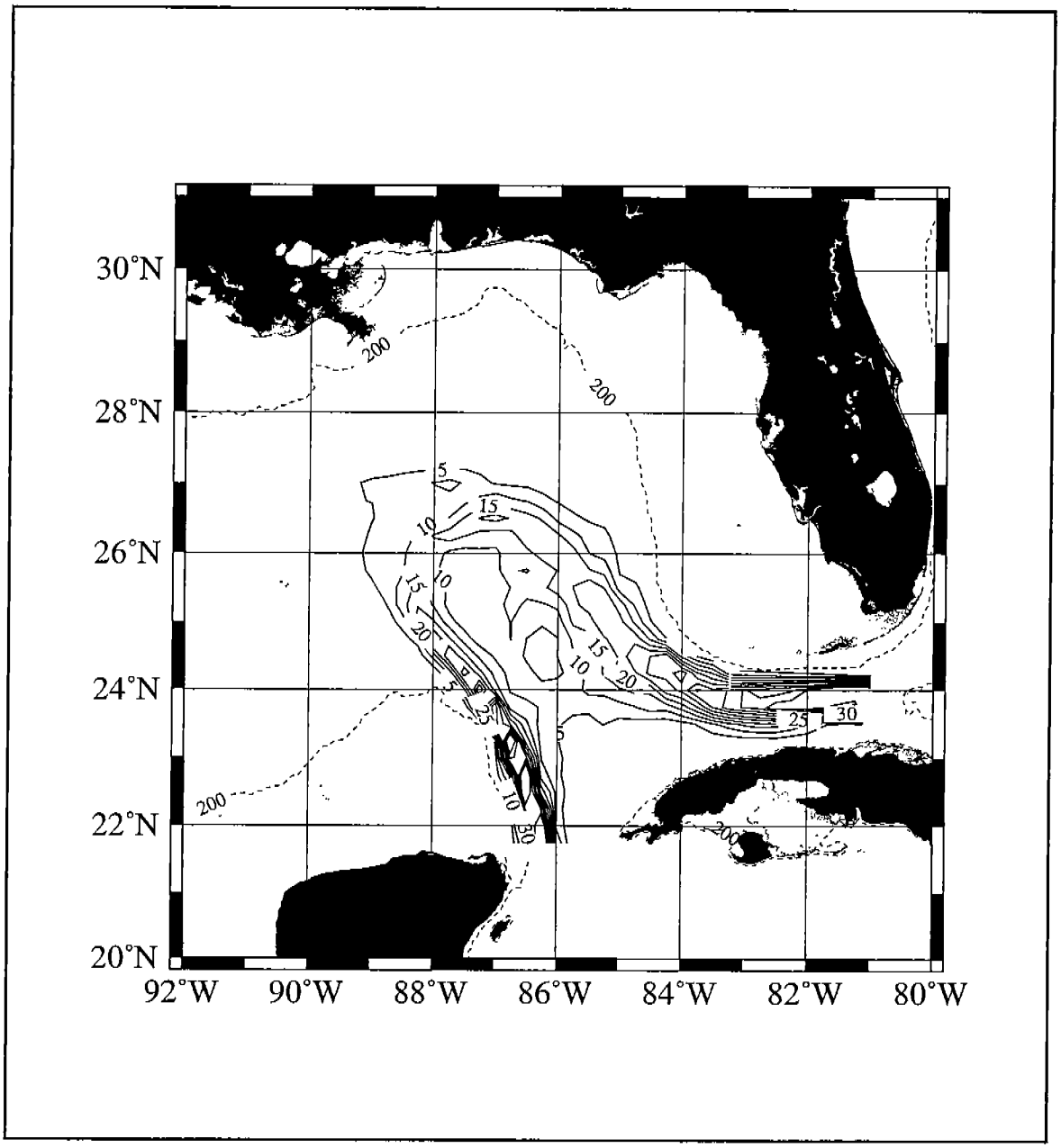

Figure 4.2-6. Percent occurence of 17-cm contour defining the high velocity core of the LC for the interval from 1/1/1993 through 4/30/1999.

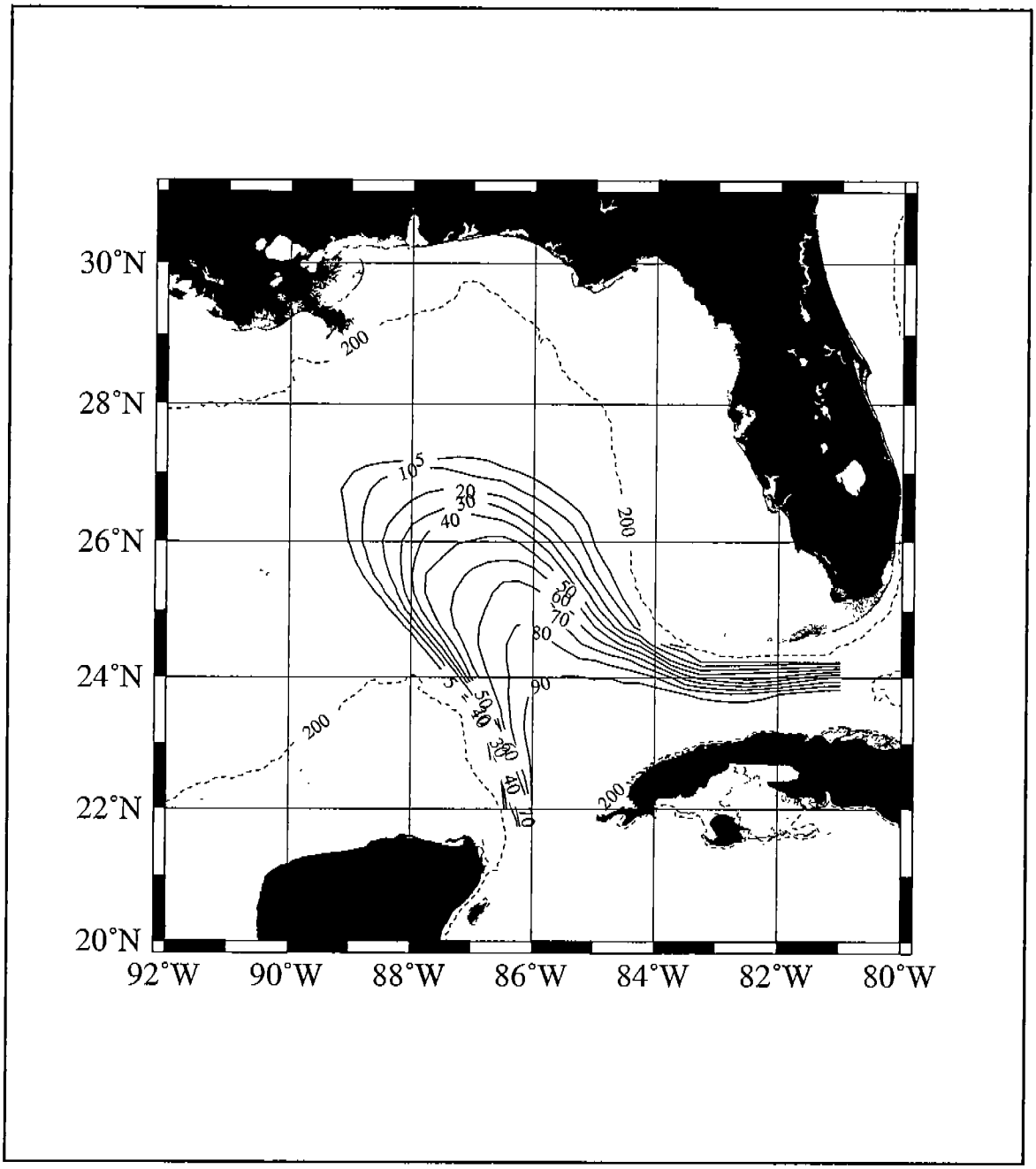

Figure 4.2-7. Percent occurrence of LC waters for the interval from 1/1/1993 through 4/30/1999.

shedding event is associated with each of the dominant peaks in the time series. The exact timing, however, is dependent on the criteria selected for the definition of separation and is complicated by the ambiguity of associating a discrete time with what is clearly a continuous process. The method employed to identify separation tends to select the times of minimums in the metric time series immediately after an extended intrusion, which is a conservative estimate that is unlikely to over count shedding events.

The matrix of correlation coefficients computed from the altimetric estimates of LC metrics is shown in Table 4.2-2. Identifying a "best" metric for monitoring the LC is difficult because of the high correlation between the individual time series. Dynamical considerations may favor the circulation metric, which shows the most consistent growth throughout an intrusion event and the greatest increase just before separation. The volume of the LC is the least correlated with the other metrics and exhibits large variations independent of shedding events. There has been a single estimate of the correlation coefficient between area and northward extend of the LC reported, based on frontal analysis derived from the thermal imagery. The value found was 0.76, which is significantly less than the 0.955 determined from the altimetric analysis and may be related to the difficulties associated with identifying frontal boundaries in thermal imagery. The high correlation found between the altimeter-derived metrics support the use of surrogate time series from the historical record as proxies for shedding events. For example, there is very high correlation between area, length and circulation and the northward penetration of the LC, a metric that is available from the historical record.

Table 4.2-2. Correlation Matrix for Loop Current Metrics

	Area	Volume	Circulation	Maximum North Latitude	Maximum West Longitude	Length
Area	1.000	0.950	0.932	0.955	0.917	0.948
Volume	0.950	1.000	0.891	0.872	0.828	0.846
Circulation	0.932	0.891	1.000	0.931	0.908	0.948
Max. North Lat.	0.955	0.872	0.931	1.000	0.876	0.955
Max. West Lon.	0.917	0.828	0.908	0.876	1.000	0.950
Length	0.948	0.846	0.948	0.955	0.950	1.000

4.2.5 Geostrophic vs. SCULP Drifter Velocities

The SSH maps were used to monitor the LC, LC rings and secondary eddies in the northeastern Gulf of Mexico during the field program. To assess the accuracy of the altimetry, we compared geostrophic velocities calculated from the objectively analyzed maps of SSH to the coincident drifter estimates. The daily 0.25° resolution gridded SSH anomaly fields, based on archival TOPEX and ERS-2 altimeter data, were added to the hindcast model mean to give an estimate of the total SSH. Geostrophic velocities were calculated from the height fields using finite differences. Similar comparisons have been made of the gridded

altimeter geostrophic velocities to drifters velocities (Ohlmann et al., submitted to JGR Oceans), and found that surface currents from drifting buoys agreed well with geostrophic velocities derived from the gridded (0.25°) SSH maps over the deep basin. In that study, however, 14-day averages of the daily drifter velocities within a cell were used for the comparisons. Here, we directly compared the daily averaged values.

The total number of daily average surface velocities from the combined SCULP-I, -II and -III data sets is 39,362, with 52% (20,517) located in 0-50m depths, 16% (6,203) in 50-100m depths, 22% (8,801) in 100 to 1500m depths, and 10% (3,841) in depths greater than 1500m. The map of the vector correlation coefficient (Crosby et al., 1993) between the altimeter-derived velocities and the daily-averaged surface velocities from the drifters is shown in Figure 4.2-8. The two estimates are in better agreement over the deep Gulf and along the continental slope in water depths greater than 100m, but not on the continental shelf.

4.2.6 Loop Current Characteristics During Field Measurements

The over 6-year long time series of LC metrics can be used to characterize the LC behavior during the present field program: March, 1997 through April, 1999. Metric time series for the 2-year time period are shown in Figures 4.2-9 and 4.2-10.

Only one LC metric achieved an extremum during the field program - the circulation, which reached a maximum for the over 6-year time period in late September 1997 during the first intrusion in the first year of the DeSoto program. Two ring shedding events occurred during the field program, both in the first year. This is in contrast to the second year of field measurements during which the LC retreated to a far more southerly position for nearly 9 months, the longest time period of retreat observed in the altimetric record.

The mean SSH over the two-year record is shown in Figure 4.2-11. The two-year mean differs little from the hindcast model assimilation mean (Figure 4.2-1) added to altimeter data to produce an estimate of the synthetic height field. The anticyclonic circulation over the DeSoto Canyon study area was only slightly stronger than that during the 6-year mean time period. A distinct region of cyclonic circulation, between the study area and the mean LC, can be discerned in both means, though the feature is displaced to the west during the field program time intervals. Caution should be exercised when interpreting subtle differences in these maps since most of the "signal" is dependent on the fidelity of the model assimilation hindcast.

Significantly stronger differences were found over the study region in the 1-year means from April 1997 through April 1998 (Figure 4.2-12) and April 1998 through April 1999 (Figure 4.2-13). The distinct behavior of the LC in each year of the two-year field program clearly affected the circulation structure captured in the 1-year mean SSH fields. Weaker anticyclonic circulation in the study area and stronger cyclonic circulation to the south of the study area are seen in the first year mean, associated with a stronger and slightly intruded LC. The cyclonic circulation, just north of the mean LC, also displaced to the east. When

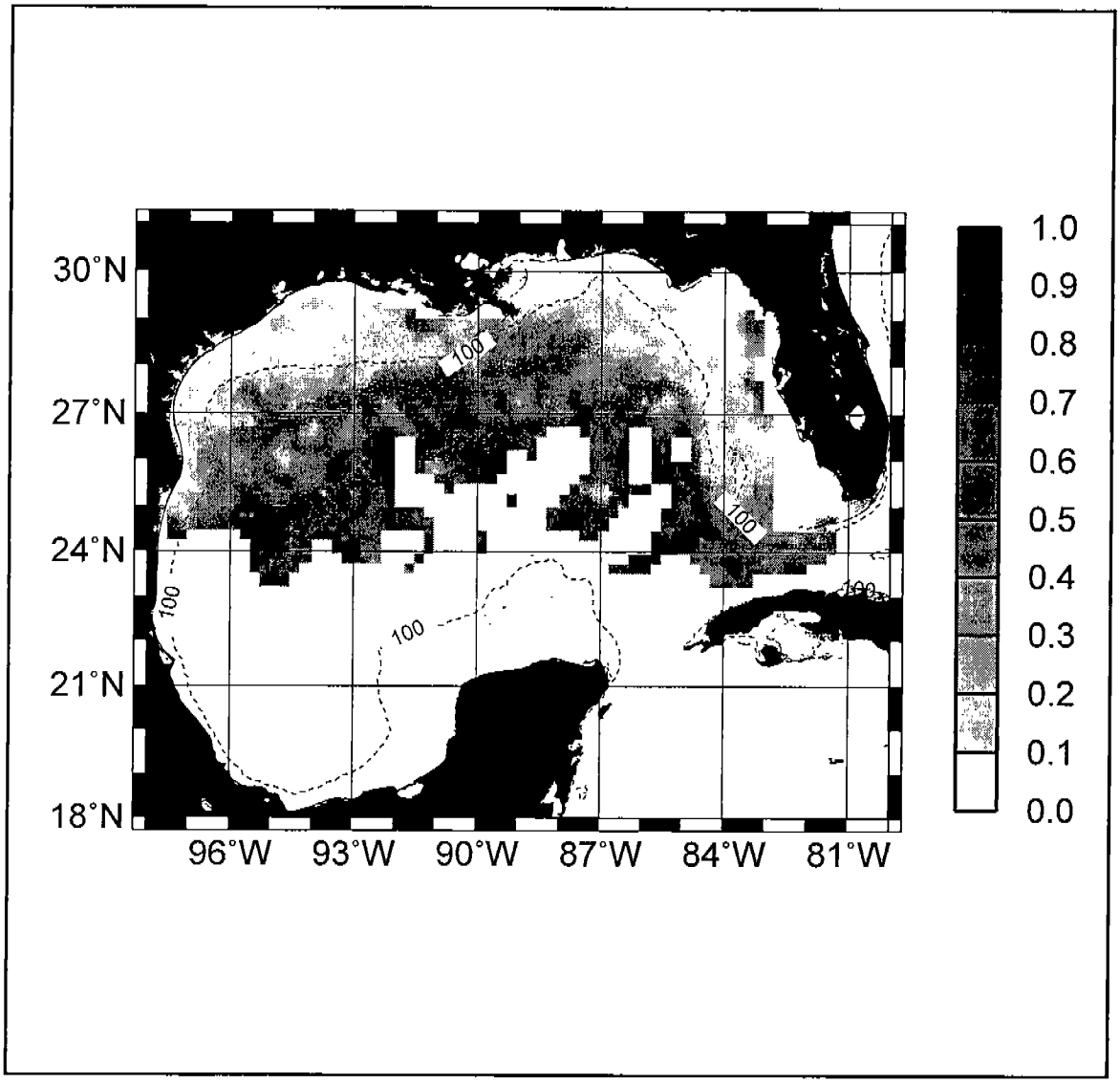

Figure 4.2-8. Map of the vector correlation coefficient between daily averaged drifter velocities and coincident geostrophic velocities computed from maps of sea surface heights.

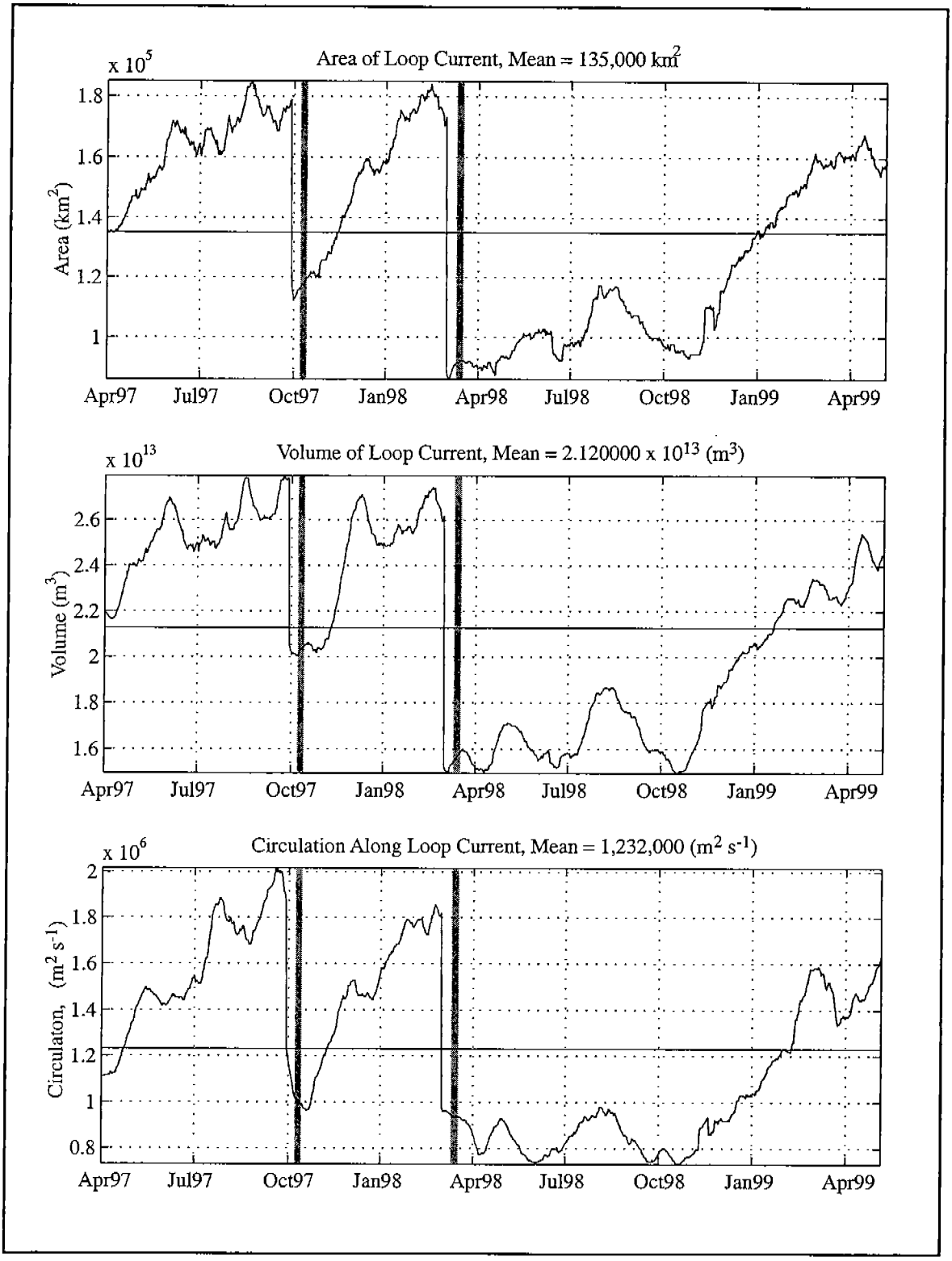

Figure 4.2-9. Time series of LC northward and westward penetration, and length during the field program. Ring shedding events are shown by vertical gray lines.

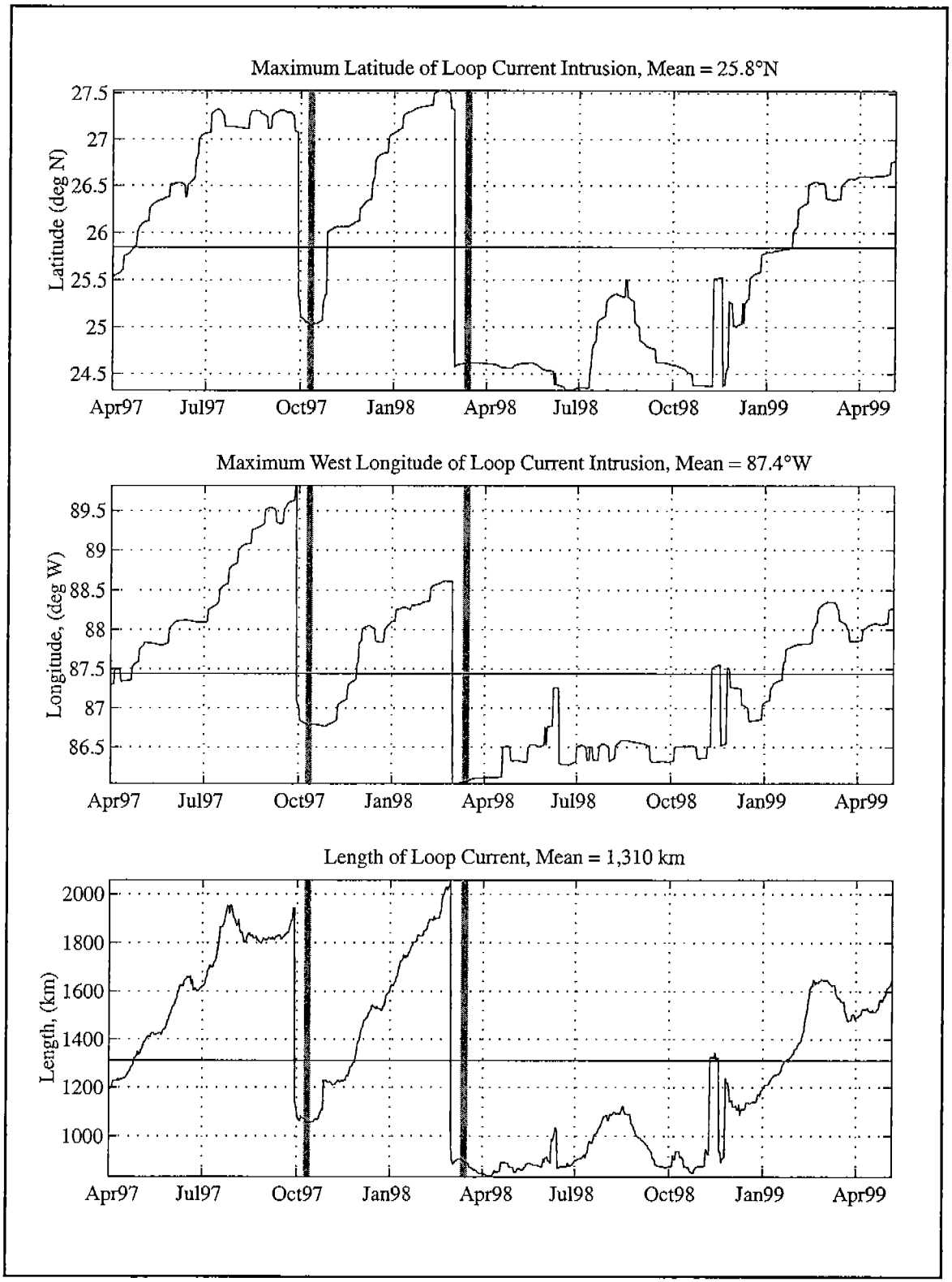

Figure 4.2-10. Time series of LC northward and westward penetration, and length during the field program. Ring shedding events are shown by vertical gray lines.

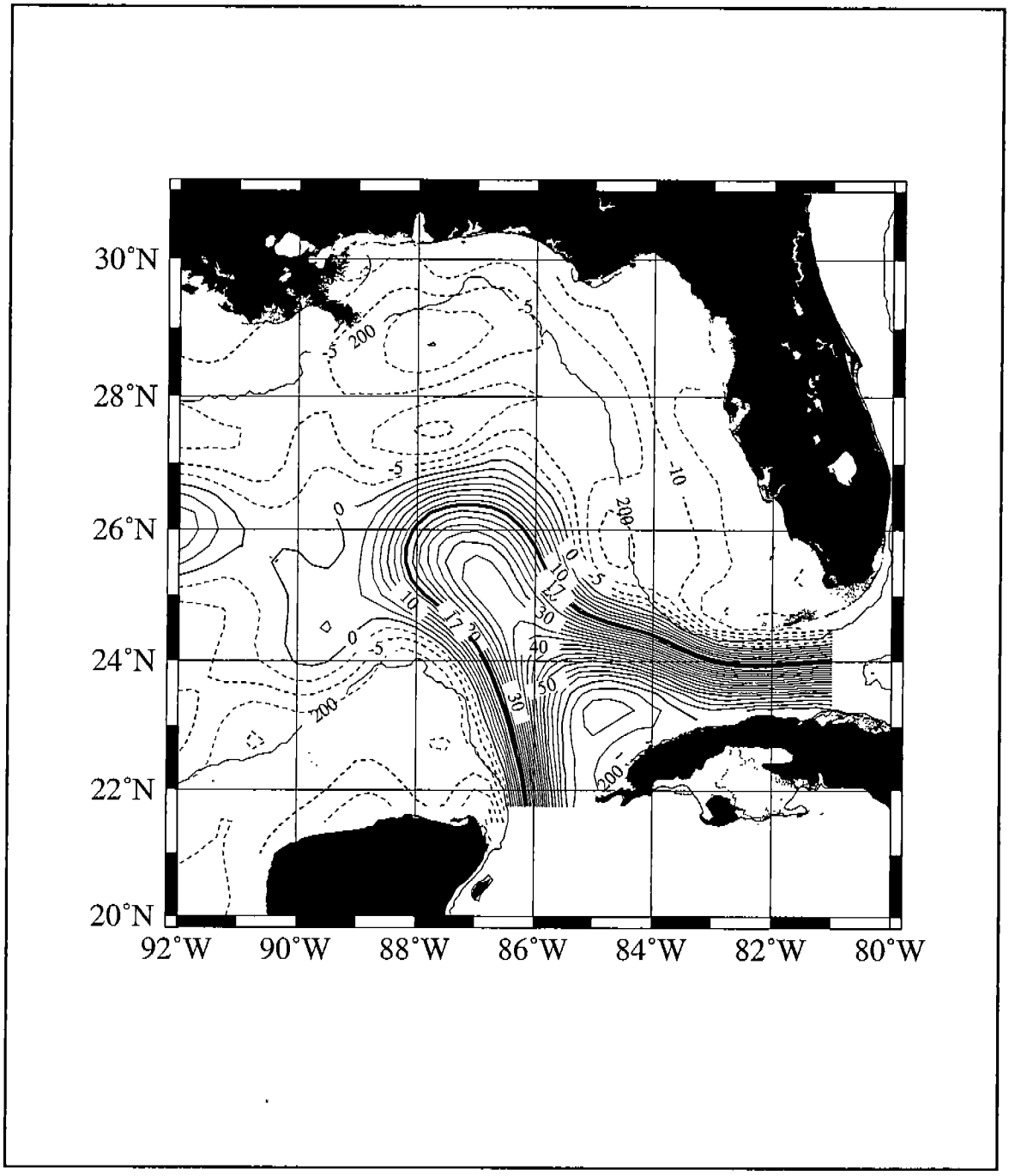

Figure 4.2-11. Mean SSH for interval from April 1997 to April 1999.

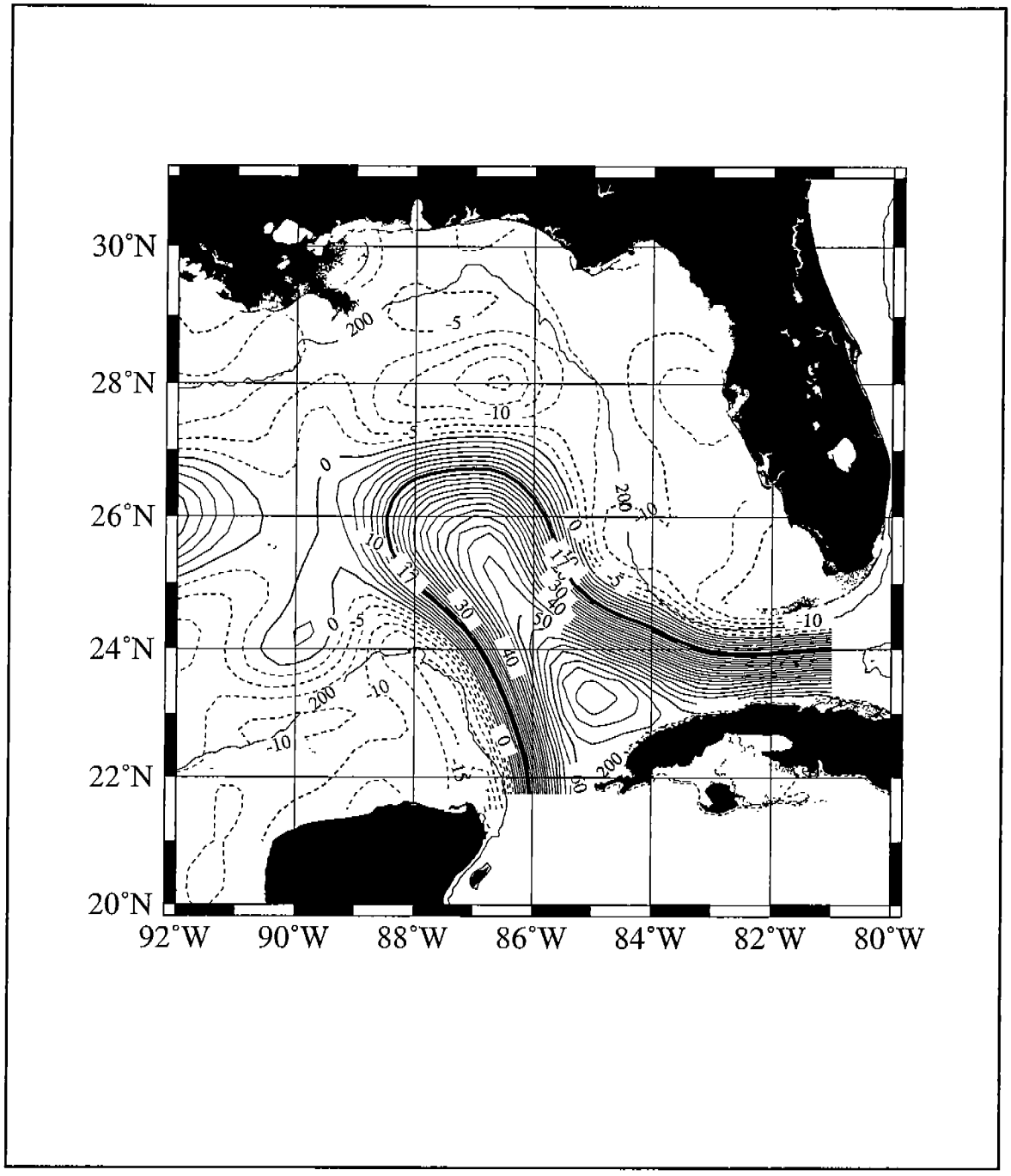

Figure 4.2-12. Mean SSH for the interval from April 1997 to April 1998.

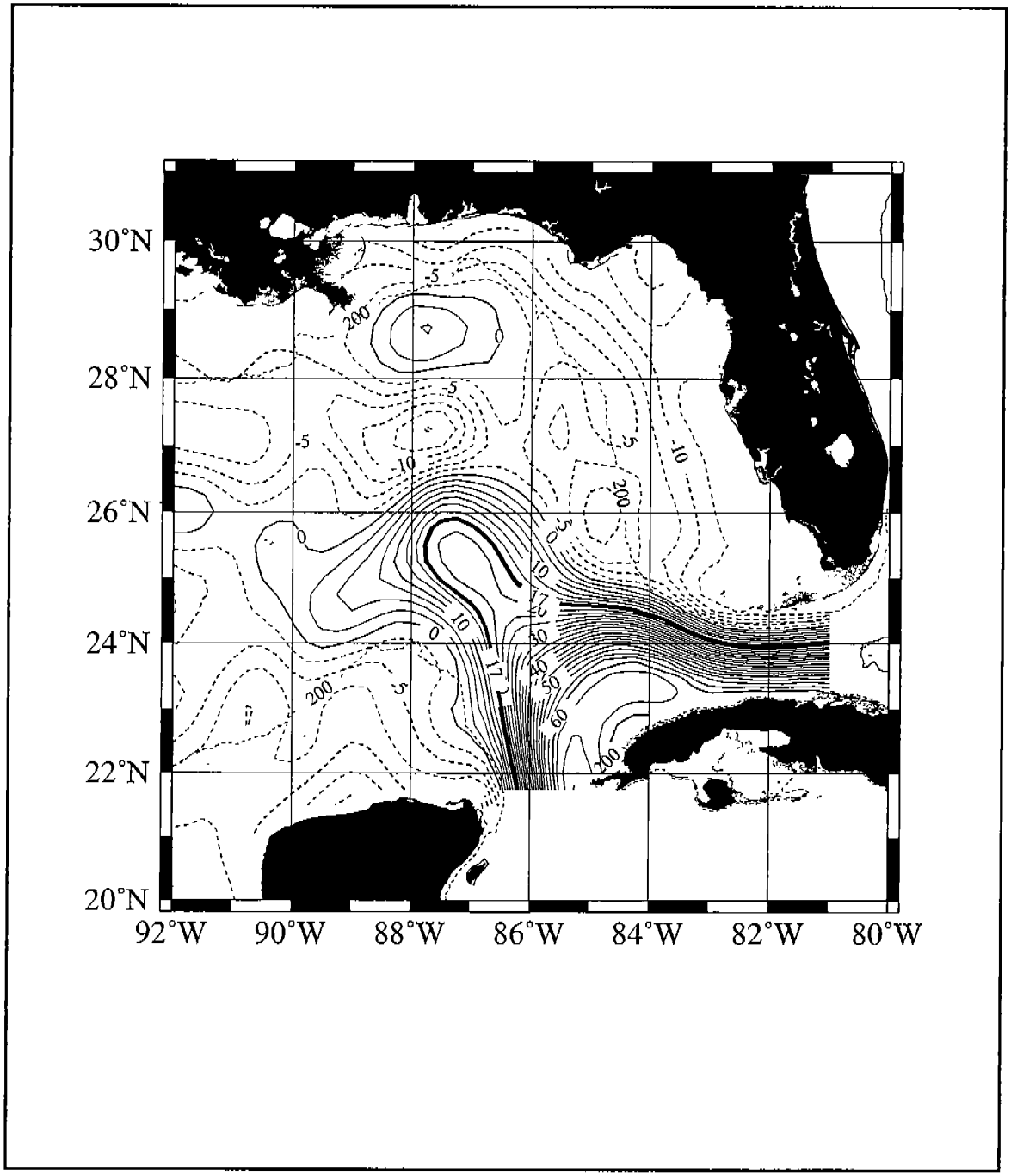

Figure 4.2-13. Mean SSH for the interval from April 1998 to April 1999.

the LC is retreated during the second year of the field program, the circulation pattern in the mean field showed stronger anticyclonic circulation over the study region and a displacement of the cyclonic circulation south to the west.

4.3 Loop Current and LC Rings - Energetics and Dynamics

4.3.1 Introduction

The most energetic events in the circulation of the Gulf of Mexico are the separation of large anticyclonic rings from the LC. The discussion below about the LC and its rings consists of two parts. The first part is analysis, based on a much longer and improved dataset, of the frequency of ring shedding. The second is a discussion of the forcing of LC variability by the wind curl. We find a remarkable coherence between the variability of the LC and that of wind curl over the whole Gulf. The coherence is near the ~95% confidence limits in several bands at which there is power in both signals.

Building on previous work, we examined all the apparent rings since July, 1973. This new data set includes using satellite altimetry since 1992 and provides a set of 34 known ring formations. The primary advantage of altimetry is that the data remain available in the summer. One finding is that the ambiguity of whether or not a ring has separated is reduced, but not eliminated; the uncertainty with which separation "events" can be specified remains approximately 4 weeks, even with nearly-continuous data. The distribution of separation intervals has peaks near 11 and 14 months; if the distribution is smoothed, as in the usual spectral analysis, a large peak in the distribution of separation intervals is formed near, but not exactly at, 12 months. A large secondary peak is at 6 months, with a smaller peak at 9 months.

4.3.2 Background and Procedures

4.3.2.1 Historical Analysis

Before the main flow from the Caribbean Sea becomes the Florida Current and then the Gulf Stream, it first passes through the Gulf of Mexico. When this powerful current from the Caribbean first comes into the Gulf, the flow is directed primarily towards the north. This flow must accomplish a 90° turn to the east to pass between Cuba and the Florida Keys. The dynamical balance of this turn has been discussed by Pichevin and Nof (1997). In the course of making this turn, the current pattern takes the shape of a portion of a large circle, or loop. Over the course of several months, the part of the flow field in this loop extends farther into the Gulf (see, for example, Reid, 1972) until it becomes sufficiently unstable. At this point a large anti-cyclonic ring gradually separates from the main flow and drifts to the west. In many respects these rings are analogous to Gulf-Stream rings.

There are several puzzling features of these ring separation events. They are not quick, simple events, but can be long and drawn out; the separation process generally taking several months or more. It is not unusual for observers of some satellite IR images to conclude "The ring

has now separated," yet an image several months later may show the ring still attached to the main flow. Clearly, we do not understand the separation process well. Nevertheless, for any representation of Gulf circulation (whether analytical or numerical) to be capable of modeling the circulation competently, it should be able to handle ring separation events correctly. It seems important to us, therefore, to determine this fundamental time scale of ring separation events as accurately as can be done based on the available data.

Since the 1970s, much of our knowledge of ring-shedding behavior has been based heavily on satellite infra-red (i.e. SST) data (see, for example, Maul and Vukovich, 1993). SST data continue to be extremely valuable, because the horizontal resolution is unsurpassed. However, SST data suffer from a major limitation: the uniformly warm surface temperatures in the Gulf of Mexico during summer (i.e. no thermal gradients) allow no inferences about the flow field for 3-4 months in the summer.

Data from satellite altimeters, however, are not subject to this seasonal limitation. Some unresolved problems with determining a proper geoid surface for interpreting the altimetry data remain, but these are gradually being reduced to an uncertainty level of a few cm. The present level of accuracy suggests that, while there may be details of the SSH field that cannot be resolved exactly, large-scale features such as whether a ring has separated from the LC can now be determined unambiguously.

Satellite altimeter data are now routinely available in both near-real-time (Lillibridge et al., 1997) and as archival data records. Leben maintains a web page (http://www-ccar.colorado.edu/~altimetry/) on which daily maps of the Gulf of Mexico sea surface topography have been posted since 1996. Multi-satellite sampling by the altimeters aboard the TOPEX/POSEIDON and ERS 1 and 2 satellites has been used to map the Gulf of Mexico sea surface topography over the interval from April 1992 to the present. As an example, these maps have been useful for the study of LC rings in the western Gulf (Biggs et al., 1996).

Previously, a data set based on ring separations between 1973-1993 (Sturges, 1994) suggested that the time intervals between ring shedding events had two modes, one at 8-9 months and the second at 13-14 months. These data were based heavily on satellite IR data. It is possible that some separations included on that list, particularly those in the spring or early summer, may not have separated. Since that analysis was completed, three changes have taken place. First, the earlier "community approved consensus" list has been subject to several corrections. Second, the satellite altimetry data has made it possible to insure that summer-time events are followed reliably. And third, several years elapsed during which more separation events have taken place. Consequently this new data set contains over 50% more ring events than in the previous compilation. This new, expanded data set is a key focus of this presentation.

4.3.2.2 New Data and Processing

We have reviewed maps of SSH in the Gulf to estimate the times of ring separation events. These maps are based on geophysical data records (GDR) from the TOPEX/POSEIDON (T/P) and ERS 1 and 2 satellite altimeters, processed in a manner consistent with the near real-time monitoring described by Lillibridge et al., (1997).

TOPEX data were adjusted using standard corrections supplied on the JPL/PO.DAAC TOPEX GDRs, including inverted barometer, electromagnetic bias, ionosphere and wet/dry tropospheric corrections, as recommended in the GDR handbook (Callahan, 1993). Several additional corrections not found on the original GDRs were also applied to the TOPEX data. These corrections included orbits based on the JGM-3 gravity model and an empirical ocean tide model (Desai and Wahr, 1995) based on TOPEX altimeter data computed using the JGM-3 orbits. The ERS-1 and ERS-2 Altimeter Ocean Products (ALTOPR) CD-ROMs were obtained from CERSAT. The ERS altimeter data were corrected using standard corrections supplied on the ALTOPR GDRs, including inverted barometer, electromagnetic bias, ionosphere and wet/dry tropospheric corrections. The data were also corrected using JGM-3 orbits and the Desai and Wahr (1995) tide model to be consistent with the TOPEX processing. After extracting the data from the GDRs and applying corrections, the corrected SSHs from both satellites were referenced to an accurate high resolution mean sea surface based on altimeter data collected from the TOPEX/POSEIDON, ERS-1 and GEOSAT Exact Repeat missions (Yi, 1995).

These corrections allow data from both repeat and non-repeat ground tracks to be combined by objective analysis, so that the non-repeating ground tracks covered during Geodetic Phase 1 and 2 of the ERS-1 mission (April 10, 1994 to March 21 1995) can be used to augment T/P sampling for more accurate mesoscale mapping.

The final step in the along-track processing is to apply an empirical orbit error correction to the ERS 1 and 2 along-track data to remove residual ERS orbit error. An empirical correction of the TOPEX orbits is not needed; however, to "filter" both data sets consistently, the empirical correction is also applied to the TOPEX data. This correction was based on an along-track "loess" filter, which removed a running least squares fit of a tilt plus bias within a sliding window from the along-track data. The filter window is approximately 15 degrees of latitude (200 seconds along-track), passing the ocean mesoscale signals much shorter than this, while removing the longer wavelength orbit and environmental correction errors.

Daily maps of the Gulf of Mexico SSH anomaly relative to the mean sea surface were created using an objective analysis procedure (Cressman, 1959). This method interpolates the along-track data to a 0.25° grid over the Gulf. The method uses an iterative difference-correction scheme to update an "initial guess" field and then converges to a final gridded map. A multigrid procedure was used to provide the initial guess, as described in the appendix to Hendricks et al. (1996). Five Cressman iterations are used with radii-of-influence of 200, 175, 150 , 125 and 100 km, while employing a 100 km spatial decorrelation length scale in

the isotropic Cressman weighting function. Data were also weighted in time using a 12-day decorrelation time scale relative to the analysis date.

The altimetry data are used here to determine only departures from the mean SSH. To estimate the full SSH, or total dynamic topography, relative to a level surface, the mean surface from a 10-year numerical ocean model (courtesy of L. Kantha and J.K. Choi), has been added to the height anomaly maps. To test the reliability of this surface for the purposes of this work, we found that the timing of ring-shedding events was insensitive to the mean used to produce the synthetic product, though the local structure of the LC was affected by differences in the mean fields on the order 10 cm.

Altimetric mapping provides all-weather and all-season data. While it shows less horizontal detail than the IR data, the altimetric data used here are less likely to miss the shedding or re-attachment of a ring. The primary advantages of the new list of sheddings, obviously, are that there are no data losses from clouds, or from the usual summertime spatial uniformity of SST in the Gulf.

4.3.2.3 Methods

The method used in this analyses is similar to that employed by Sturges (1974). By examining the maps as a time sequence, it is clear when ring begins to separate. However, new rings often begin the separation process, only to reconnect with the LC as much as a month or more later. To tell for certain that a ring will separate, it is necessary to observe the nascent ring as it continues to form, pulling away clearly and drifting to the west as a separate feature. One advantage of this altimetry-based data set, never obscured by summertime problems, is that the continued examination of the rings as they pull away allows us to be certain that the separation process goes to completion.

All available frames of contoured data since the spring of 1992 were evaluated. The method was simply to examine each map to determine subjectively whether the ring appeared to be separating, and continue to track it as the separation process continued. A surprising feature of these results is that, even with a significantly improved data set, the exact time of separation of a ring remains elusive. As has been reported earlier, based on numerical modeling results (e.g., Sturges et al., 1995) the separation process is not a single abrupt event, but a gradual pulling away, with parts of the flow connecting the main portion of the LC to the separating ring for a significant part of its travel time to the west. When the time sequence of maps are examined, it is clear that this separation process takes many weeks. It is rarely possible, on the basis even of this new data set, to point to a particular time in the separation sequence and say "At this point the separation is complete."

The most striking example of this ambiguity took place during 1996. It appeared that a ring was beginning to separate, and over the course of nearly a year the "ring" hovered in essentially the same general location. On the basis of many subjective viewings, we conclude that a

ring did separate in September 1996, but the ambiguity is bothersome. Awareness of this phenomenon is certainly not new, as it has been observed to take place previously in the Gulf of Mexico and for Gulf Stream rings as well.

To review briefly the method used earlier by Sturges (1974), the separation times shown in Table 4.3-1 were used to determine a histogram. To make the results more nearly in keeping with the usual analyses of time-series data, however, the *inverse* of the separation interval is plotted; the resulting values were then smoothed with 5 Hanning passes to give the form of a power spectrum. The basis for this procedure was described by Silverman (1986).

Table 4.3-1. A compilation of ring-separation events; i.e., times when data are available to show a ring separating reliably from the Loop Current.

Year	Month	Separation Period, months	Estimated uncertainty, weeks
1973	July		
1974	April	9	
1975	January	9	
1975	July	6	
1976	August	13	
1977	March	7	
1978	June	15	
1979	April	10	
1980	January	9	
1981	March	14	
1981	November	8	
1982	May	6	
1983	March	10	
1984	February	11	
1984	August	6	
1985	July	11	
1986	January	6	
1986	October	9	
1987	September	11	
1988	May	8	
1989	May -June (?)	12.5	
1990	August	14.5	
1991	Aug - Sept	12.5	
1992	July 19	11.5	4
1993	June 22	11	4
1993	Sept 19	3	1
1994	Sept 22	12	4
1995	April 8	7	4
1995	October 18	6	4
1996	April 30	6	5
1996	September	5	4
1997	October 11	13	3
1998	March 14	5	2.5
1999	August 22	17	2

Entries through Oct. 1986 are from Vukovich (1988 a&b); other entries prior to July 1992 are from Table 1 of Sturges (1994) using corrections based on Berger (1993). Data beginning 1992 are from satellite altimetry, this work.

Nevertheless we emphasize that what is recorded in Table 4.3-1 is not a time series and Figure 4.3-1 is not based on the usual spectral calculations.

4.3.3 Discussion of Ring Shedding Frequency

The complete list of ring separation times is shown in Table 4.3-1. Other ring separation events were recorded a decade or more earlier, but we show here only those for which we believe that *successive* separations are reliably known. There are 34 separation events in the 26-year interval July 1973 - August 1999. For the recent separations, beginning in 1992, the apparent uncertainty interval is shown explicitly. The separation times listed are the midpoint of that interval.

Figure 4.3-1 shows the frequency distribution of ring separations in the form of a spectrum. The results shown provide conclusions that are somewhat more reliable than in the previous, similar calculation. The most noticeable region of power is near one year. The peak in the low-frequency mode is at 11.6 mo; this specific peak does not change if smoothing is done by only 3 Hanning passes for higher resolution. We attach no significance to the precise value 11.6 mo, as most of the separations are unknown to +/- at least a month. The 80% confidence limits, estimated by many iterations with a bootstrap method, extend to 1.7 times the power found in any peak. The mean value, for 33 separation intervals in 313 months, is near 9.5 months, yet there is little power at that value. The distribution has one major mode near annual, with half the separations at periods shorter and longer than ~10.5 months.

Figure 4.3-2 shows a slightly different version of the same calculation. The smoothed "spectrum" from Figure 4.3-1 is shown together with the original data of the exact times of the individual separations from Table 4.3-1. It is obvious that the smoothing process, while desirable for many reasons, has formed a peak where none exists in the basic data. Thus, we should be careful to note that there is no "annual cycle" in the LC in the way that there is such a strong annual cycle in most other variables, such as the wind forcing, temperature, etc.

One difficulty with the data of Table 4.3-1 is that the uncertainties are perhaps large but unknown for the values based on the older data. Even with the satellite altimetry, the separation of September, 1996 remains elusive. But by following the images carefully, we conclude that a ring did separate. Its motion was slow, and by the following late April or early May the ring appears almost to have been re-absorbed by the LC. However, a ring emerges at about 93°W when this ring disappears, leading us to the conclusion that the ring actually separated.

What one does, when faced with such uncertainty, of course, is to try the calculation both ways to see if it makes any significant difference. By computing the "spectrum" of Figure 4.3-1 with and without the elusive ring, one finds that the differences are negligible. A small bump at ~30 months will appear, but the effect on the rest of the spectrum is

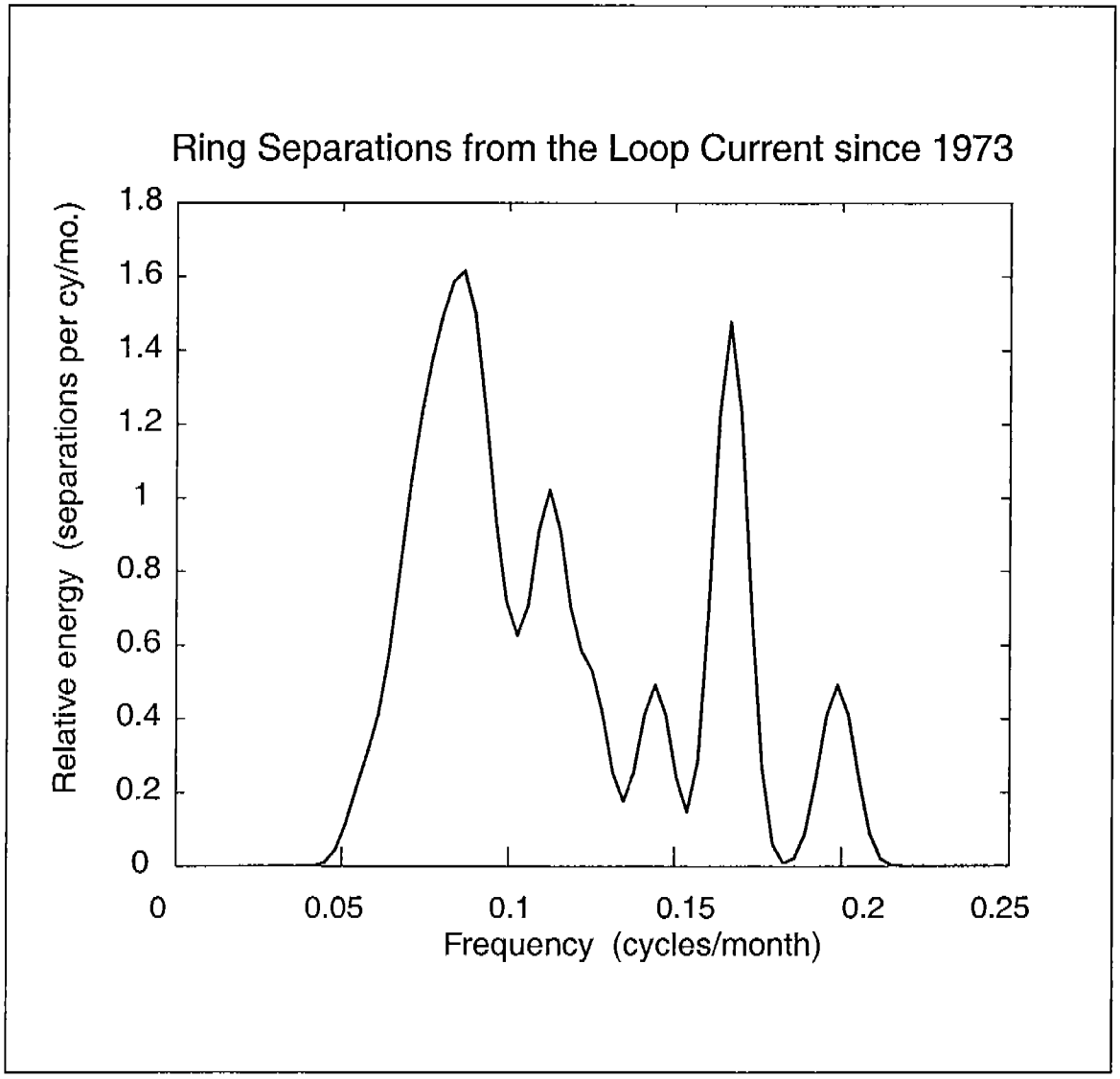

Figure 4.3-1. Periodicity of ring separations from the Loop Current. This figure is actually a histogram, plotted to resemble the usual power spectrum; both scales are linear. All known separations since July 1973 - Aug. 1999 are included; see Table 4.3-1. The original histogram has been smoothed by 5 Hanning passes. A single value at (3 mo) is omitted for clarity, and is offscale. Confidence limits of 80%, are obtained by multiplying (or dividing) any value by 1.7; determined by a bootstrap technique.

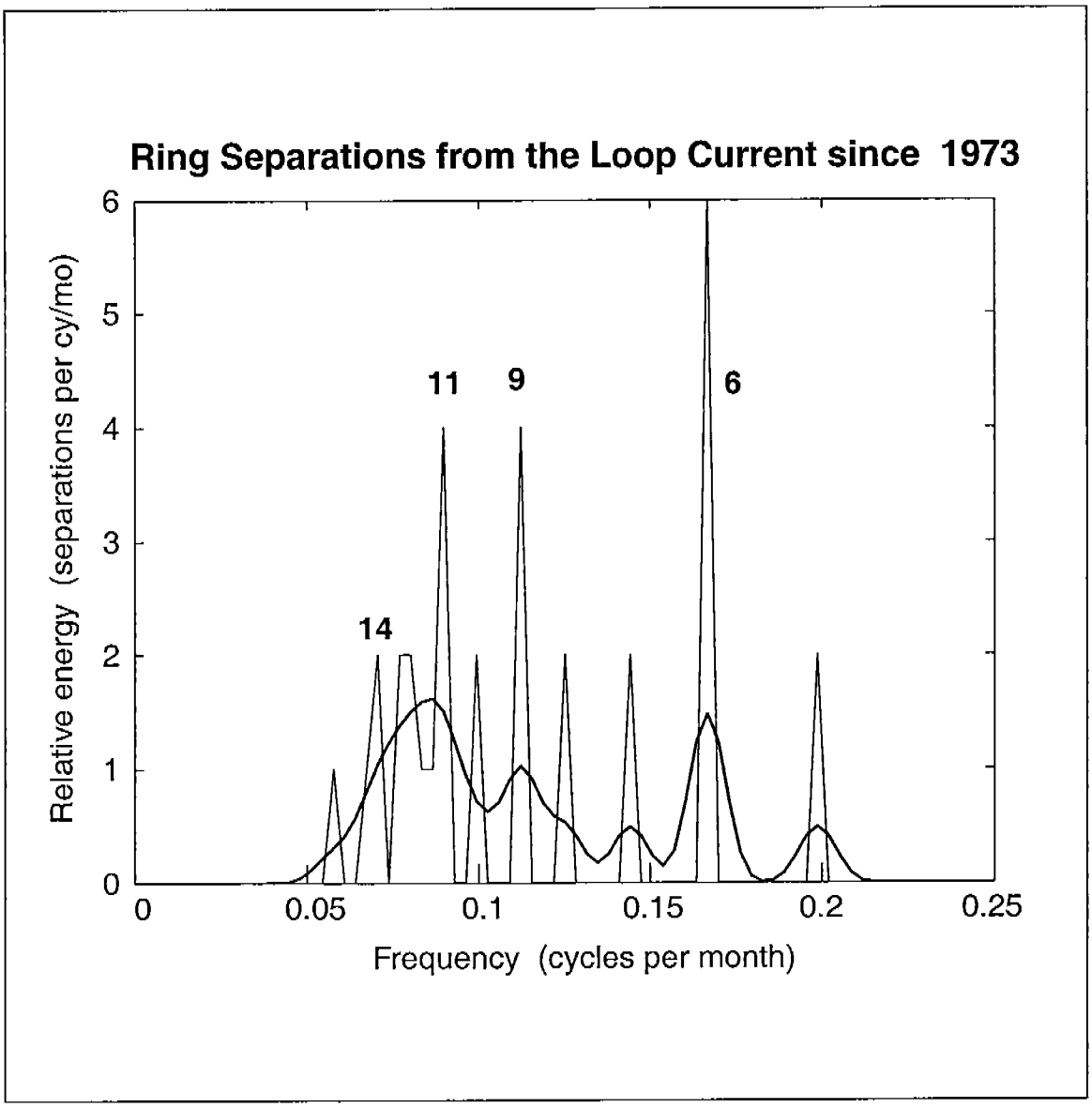

Figure 4.3-2. Periodicity of ring separations from the Loop Current; similar to Figure 4.3-1, except that the original, unsmoothed separation data values are shown in addition to the smoothed curve from Figure 4.3-1

hard to see by eye. The peak at 11.6 months is broadened slightly, but otherwise unmoved, and the peaks at 6 and 9 months are unaffected.

It is well known that determining the true uncertainty of geophysical spectra is fraught with problems. We often deal more with hope than with confidence. The primary power peak here is near one year, so a 31-year data set might seem relatively "long" in some sense. However, a major uncertainty is that the wind system over the North Atlantic forces a decadal-scale variability in the flow. The "typical" low-frequency variability in winds, sea level, and transport of the Gulf Stream seems to be at periods of the order of 100-200 months. We may thus suppose that, if the climate system has substantial variability at such long periods, the data of Table 4.3-1 may in fact now provide only two or three "looks" at the process, rather than 31. The error bars may thus be larger than we think. The essential result is that the primary power lies near a period of 12 months, but there is almost no power at exactly 12.0 months There are smaller peaks at 9 and 6 months.

When the wind forcing is averaged over many years it has a very clear annual cycle. It is surprising, therefore, that the peak here is *near* one year, but quite distinctly *not* precisely at 12.0 months. This feature is explored in Section 4.3.4.

4.3.4 Forcing of LC Variability by the Wind Curl

4.3.4.1 Background

Two aspects of the LC's behavior have long been a puzzle. First, even though the wind forcing of the ocean has a pronounced annual cycle, there seems to be no annual cycle to the LC nor to the shedding of rings. Data from the early 1960s, when ring shedding was first discovered, suggested an annual cycle. However, the duration of observations is now long enough to provide much higher resolution. At periods just shorter and just longer than annual, there is a large amount of power, but essentially no power at exactly a year, as shown in the preceding section.

The second point is more subtle. As the LC intrudes from its more southerly position, around ~24°N, to a more extreme northerly position near ~28°N, its front advances several hundred kilometers and a large amount of upper-layer water is displaced. Except for the entrance and exit ports, the LC is totally surrounded by the Gulf of Mexico. Therefore, the displaced volume ~6 x 10^4 km^3, of displaced water must somehow "go away,"yet it is not clear just where it goes. Initially the most likely option might appear to be that this upper-layer fluid is forced out through the Florida Straits, or back through the Yucatan channel, but at present we have no evidence documenting such a flow pattern. The amount of "extra" flow that must be associated with the intrusion phase of the LC cycle can easily be estimated to be as great as ~10 Sv, during times when the LC grows quickly over an interval of only ~2 months.

The idea we wish to put forward hinges on a new and perhaps surprising bypothesis, which admittedly is contrary to the ideas of the way the

ocean responds to Ekman pumping in the large mid-ocean gyres *in the open ocean*. We propose that, to accommodate the inflowing Loop Current, the displaced upper layer waters of the Gulf may be largely balanced by outflow of deep water in Yucatan Channel. This flow takes place on two time scales: first, on the one-to-several month time scale of Loop Current intrusions, the mass fluxes of order 5-10 Sv.; and second, on the long-term-mean time scales associated with the decay of old rings (~one per year), with a mass flux of order 2 Sv. This second value is presumably the time mean of the fluctuations of the first. We will show (following section) that this second value is consistent both in mean value and in energetics with the Ekman pumping over the interior of the basin.

The large mass fluxes associated with the shorter time scale intrusions are consistent with recent numerical modeling experiements (for the MICOM, E. Chassignet, personal communication; for the Navy Ocean Model, W. Schmitz, personal communication; for the Princeton Ocean Model, T. Ezer, personal communication; for the Bryan-Cox model, Y. Hsueh, Y. Golubev, personal communication). It is startling to see large compensating flows of deep water *to the south* during the times of a Loop Current intrusion. All the models referred to are full-ocean, wind-forced, and do not specify input boundary conditions at Yucatan; the fact that such flows are consistent among the different models lends a bit of credence to the idea we have put forward, although it surely is not proof. This information is offered to support the plausibility of our suggested method, but a full discussion is clearly beyond the scope of this report.

For most of the year, the majority of the surface area of the Gulf of Mexico is forced by convergent surface wind stresses. Because the net Ekman pumping at the surface is downward, there must be a net inflow in the upper layers that is balanced by a net outflow. The sign of the deep Sverdrup interior flow would be to the south, and this flow would presumably leave the Gulf by flowing back through the wider, deep, Yucatan Channel. We propose that this outflow is deep water.

In the more usual case of Sverdrup flow in the main subtropical gyres of the open ocean, one usually assumes that the resulting southerly flow goes down, to the south and, somehow, "away." Because this transport in the Gulf is confined and the exit through the Florida Straits is only ~850m deep, the logical outflow port is through the 2000-m deep Yucatan Channel. We recognize that this is a novel and perhaps controversial hypothesis; the proof will rest initially, on two ideas that can be demonstrated. First, the energetics make it highly plausible; second, the remarkably good agreement between wind curl variability (or Ekman pumping) and the LC position is quite persuasive.

One of the first thing that comes to mind, when discussing such a flow path, is whether the water mass properties make such an idea possible. Elliott (1982) made a careful study of the decay of anticyclonic rings, making the argument that the salty upper-layer waters in rings could be diluted by river water to make less salty Gulf water. If upper-layer waters are pumped down, it is likely that over the course of decades there will be a very great deal of mixing not only with river inflow but

also with inflowing *deep* Caribbean water. We do not give the details here, but assert that a balance of water properties can be demonstrated.

4.3.4.2 Energetics of the Forcing

We first estimate the amount of energy required to pump near-surface fluid down to depths below the main thermocline. The suggestion put forward here is that the upper waters are forced downward, below the inflowing water, or to depths of roughly 900m and deeper. There are two related ways to estimate the work required. First, we can estimate directly the work required to force a given volume of upper-layer fluid down through the known stratification of the Gulf. Second, we can determine the available potential energy (APE) of a detached ring. To within the assumptions used for an order-of-magnitude calculation, these two methods give the same value. While it is possible to make these calculations much more precisely, it will turn out to be adequate here to determine merely the order-of-magnitude.

The APE in rings has been studied carefully by Reid et al. (1981), Bray and Fofonoff (1981), and others. Reid et al. show (their Table 2) a collection of rings for which the APE above 1000m is ~8 x 10^{15} J. We will take this value to be typical for rings here.

Next we estimate the energy available by the work done by the winds on the surface of the Gulf. Stern (1975) shows that the rate at which energy is supplied to the ocean is given by the product of wind stress and the near-surface *geostrophic* velocity. That is, the energy rate, E, is

$$E = \tau \bullet v = \text{Mean}\ (\tau \bullet v) + \text{Mean} < \tau' \bullet v' > \quad (4.1)$$

where the first term on the right is the product of the mean values, and the second is the mean of the product of the fluctuating parts. It is quite possible to determine the fluctuating component of the wind stress, but we are able to determine the velocity only poorly in the mean, and even worse for the fluctuating parts. It is our suspicion that the second term on the right will add to the first term on the right, but the error bars are quite large. We therefore estimate only the first term on the right.

It is well known that the central and western Gulf, away from the LC, is dominated by an anticyclone. Averaging the presence of LC rings, we take the central high to be of order ~30 cm, or somewhat less than half the magnitude in the center of the LC itself. Over a horizontal distance of ~500 km the slope would give a surface current of ~6 cm/sec. This is a conservative estimate, assuming continuity with the observed flow in the western boundary discussed by Sturges (1993).

The general pattern of winds over the Gulf of Mexico is dominated by the trade winds blowing from east to west. The winds are much stronger in the south, with velocities decreasing steadily toward the north. There is a rotation in the far west, so that the winds blow more from southeast toward the northwest, but this is a secondary effect. We take 1 dyne/cm^2 as a typical value over the *southern half* of the Gulf, where

the trade winds are strong. To determine the amount of work supplied by the wind, the product $\tau \bullet v$, the instantaneous value, must be integrated in time for about one year, the time scale of ring formation. The result is easily shown to be 12×10^{16} J.

The winds are lighter over the northern half of the Gulf, but still to the west, while the geostrophic return flow must be of opposite sign. So the product $\tau \bullet v$ in the northern half will be of opposite sign from that in the south. Assuming for simplicity a mean wind stress in the north of about half that over the south, the net work done by the winds over the whole Gulf is thus very roughly estimated as $\sim 6 \times 10^{16}$ J. Recall that the APE in a ring is only $\sim 8 \times 10^{15}$ J.

These rough estimates suggest that the work done by the wind is not only adequate but is ample by an order-of-magnitude to force down the volume of one detached ring per year. We have tried to be conservative in the estimate of wind forcing, but even if we are in error by a factor of 2 or 3 the argument holds. While this is certainly not conclusive proof, but seems a necessary condition. A more convincing argument is provided by the high coherence between the variability of wind curl and LC, as described below.

- **LC Data**

The monthly position of the northernmost extension of the LC front used in these calculations is largely from the prior studies already identified. The earlier location data were taken from the set shown by Sturges (1992); the more recent are from satellite altimetry results provided by Leben (see Section 4.2 for addition discussion of these recent data). In some previous studies the variability of this position has been used as a surrogate for the times of LC separations, although this is only an approximate measure. A better metric for the present purpose would be the area enclosed by the full LC, but such data are not reliably available over a sufficient interval. The newer data allow locations of the northernmost extensions to be determined on an approximately weekly basis, but we have used monthly positions to be consistent with the older data.

- **Wind Curl Data**

The wind data we have used is from the NCEP Reanalysis Project, available at their NOAA web page (http://www.cpc.ncep.noaa.gov). We computed the stress using a constant drag coefficient. The more involved method of a variable drag coefficient may be useful, but we are interested here primarily in whether the curl forcing and the LC variability are coherent. We suspect that the presumed reduced reliability of the LC positions in earlier years obviates the need for more sophisticated calculations of wind curl.

To determine the curl, we computed the line integral of stress along the outer edge of the Gulf, but are restricted by the 2.5° resolution of the NCEP winds. We computed the curl over two regions: first, the basic area of the Gulf, including the Bay of Campeche; second, as a trial calculation, we added an area to the west of Cuba, north of 20°N,

between Cuba and S. America. The northward Ekman transport in this region is also constrained by the coastal boundaries to be forced downward with the rest of the Gulf, so it would seem that this pumping should also be included. As it turns out, the details of the results from the two approaches were changed negligibly.

4.3.4.3 Comparison of LC Variability and Wind Curl Forcing

Figure 4.3-3 shows the power spectra of the LC variability and wind stress curl variations. Because of the assumed physical behavior of the system, the signal we call "LC" here is the time derivative of the LC front position, used to determine the N-S motion of the intrusion of the LC. The lack of power at the annual period in LC position is an odd but clear result. To make these signals comparable, the wind curl shown in Figure 4.3-3 has been pre-filtered to remove the mean annual cycle from the curl. It is obvious that the two spectra are quite similar.

Figure 4.3-4 shows the cross spectra between these two. The three panels show the cross-spectral power, the coherence, and phase. The coherence between the wind curl over the whole Gulf plus the added region to the west of Cuba is only slightly higher than without the added region, and that calculation is shown here. The coherence is above the 90% confidence limits at all frequencies where there appears to be substantial amounts of power in either signal. In other words, at periods other than near annual, the two signals are highly coherent.

The coherence of the two signals is a surprising result. One important aspect, with regard to our basic hypothesis, is that the curl forcing and the motion of the LC front for the frequency region where most of the power lies (periods of ~9 - 14 months) are 180° out-of-phase. That is, when the curl forcing was most strongly negative, the LC motion had its maximum rate of advance to the north. This result is consistent with, but does not prove, the notion that the curl forcing (or Ekman pumping) was responsible for the variability of LC intrusions. We should emphasize that the high coherence shown in Figure 4.3-3 is found with the signals determined from the curl over a basic box around the Gulf, with and without the small region in the Bay of Campeche, and with and without the region west of Cuba. In other words, this result seems robust.

- **The Annual Cycle**

We introduced a new mechanism of exchange between the LC waters and the Caribbean Sea via a deep outflow; we have tried to explain here the observation that the motion of the LC front is coherent with the curl forcing over the whole basin. It may be more difficult to explain "something that does not happen," namely the lack of coherence at the annual period. We offer the following argument which may be plausible, if highly speculative.

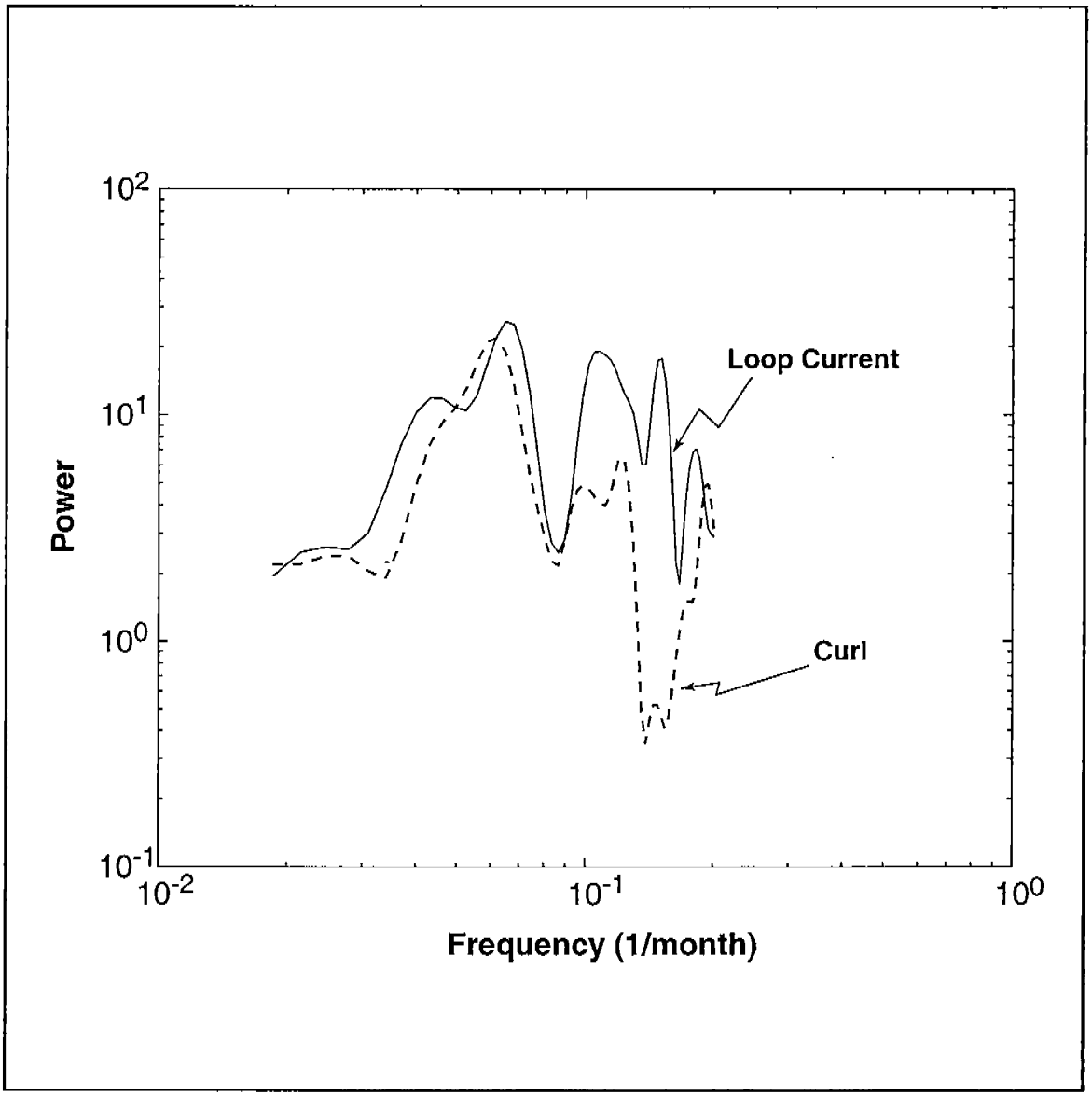

Figure 4.3-3. Power spectra of the north-south motion of the Loop Current and of wind stress curl over the full Gulf of Mexico. The Loop Current signal is from the time derivative of the northern-most position of the Loop Current front, from a variety of data sources. The wind curl is computed from the NCEP reanalysis wind data over the Gulf of Mexico plus a small region south of Yucatan Channel and west of Cuba. Smoothing is by 5 Hanning passes. The mean annual cycle of the curl was removed from the signal before computing the spectrum. The monthly data begin in July 1973.

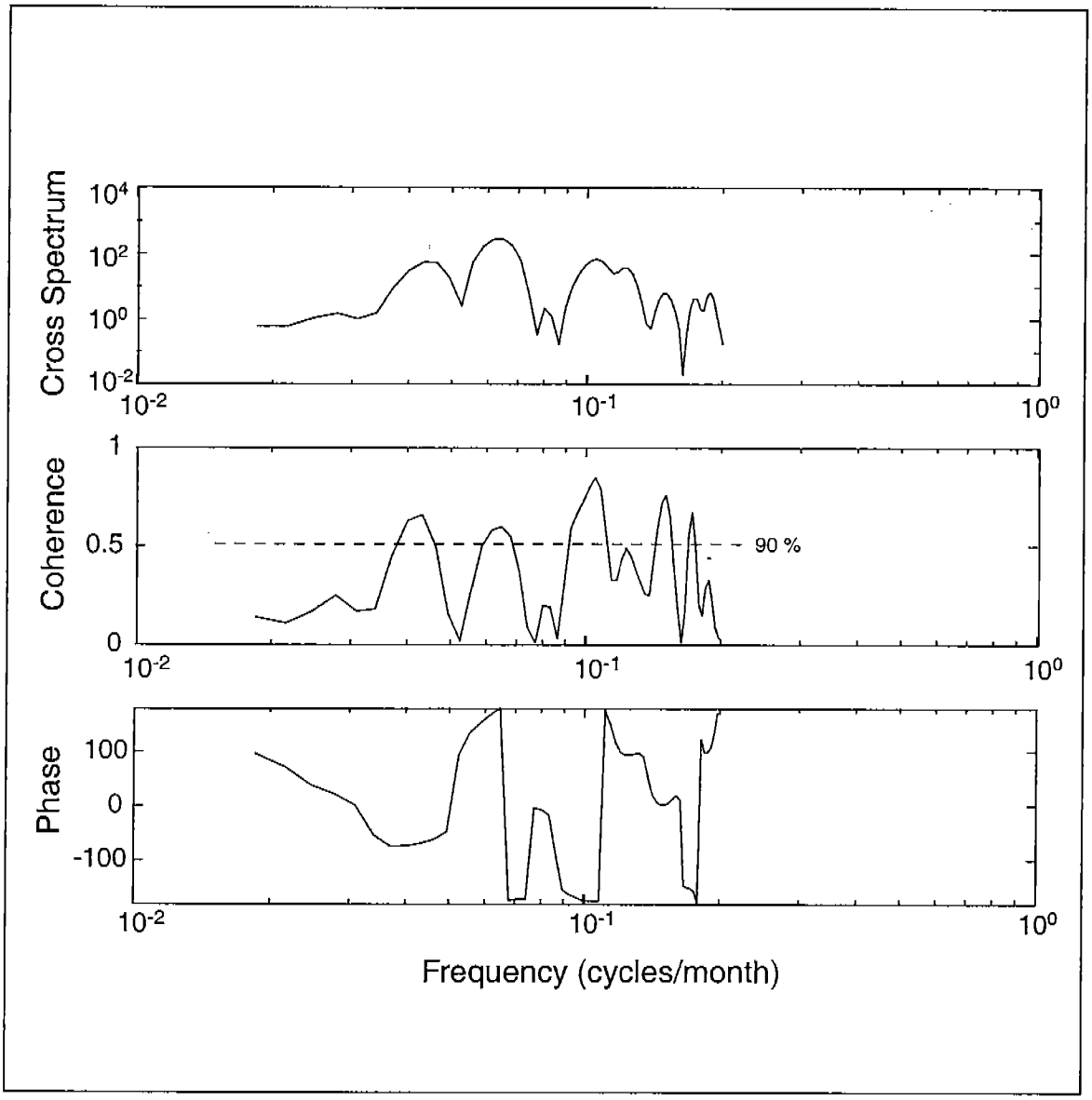

Figure 4.3-4. Cross spectra between the wind curl and Loop Current variability (the signals of 4.3-3). The upper panel shows cross spectral power; middle panel, coherence squared, and lower panel phase. Smoothing is by 5 Hanning passes. The 90% confidence limits are shown.

The arguments in the preceding sections have been made with the implicit understanding that the Ekman pumping forces upper-layer water down and ultimately out via some deep exit route. In a *steady* circulation pattern, this would be a complete set of ideas. But the wind forcing over the open Atlantic gives rise to the well-known annual cycle of the Florida Current transport. The flow in the Caribbean and Gulf is the result of the wind forcing over the whole Atlantic; the Gulf Stream is the *return flow*. As the transport into the Caribbean Sea - Gulf of Mexico increases as a result of the annual cycle of wind forcing, more water is forced into the Gulf as LC inflow. As the flow increases, the initial response to this increased flow through Yucatan Channel would be for the LC to penetrate farther into the Gulf of Mexico.

If the Ekman pumping over the surface of the Gulf were constant, we speculate that the LC might indeed have an annual cycle. However, the Ekman pumping over the Gulf also has a substantial annual cycle, separate from the annual cycle over the open Atlantic. Therefore we suggest that the deep outflow associated with the annual cycle of Ekman pumping perhaps balances (to a first approximation) the changes in flow associated with the annual cycle of the Gulf Stream transport.

It is appropriate to compare the phases and the amplitudes of the annual cycles of these two flow patterns. Figure 4.3-5 shows three versions of the annual cycle of the wind curl: one over a basic rectangle covering most of the Gulf (the box determined largely by the 2.5°-degree resolution of the NCEP data (22.5° - 27.5°N, 85-97°W); the second, including the curl forcing over the Bay of Campeche; and the third including the forcing in an area west of Cuba, as described above. The reason for showing all three curves is to emphasize the fact that the phase of the forcing signal is insensitive to the details of the area selected.

The maximum downward pumping occurs during July. Recall that the annual cycle of the Gulf Stream transport also has its maximum in approximately July and minimum in October, despite the fact that the wind forcing over the Atlantic is phase shifted considerably from this timing. The annual cycle has been very well documented, from the early work of Fuglister (1951), through the studies of Niiler and Richardson (1973), more recently by Sato and Rossby (1995), and others. These two seemingly unrelated processes, the curl over the Gulf and the annual transport of the Gulf Stream, are approximately in-phase on the average; there will be large variations from this on a year-to-year basis.

The magnitudes of the variability of various parts of the flow can be estimated as well. The magnitude of the annual cycle of the Gulf Stream in the Florida Straits was estimated by Niiler and Richardson (1973) to be a peak of ~33.6 Sv in early summer and a minimum of ~25.4 Sv in early winter. Sato and Rossby also find that the fluctuations are plus or minus ~4 Sv, peak to peak; the standard deviation of the monthly means, however, is ~3 Sv, despite having a large dataset based on many years of observations.

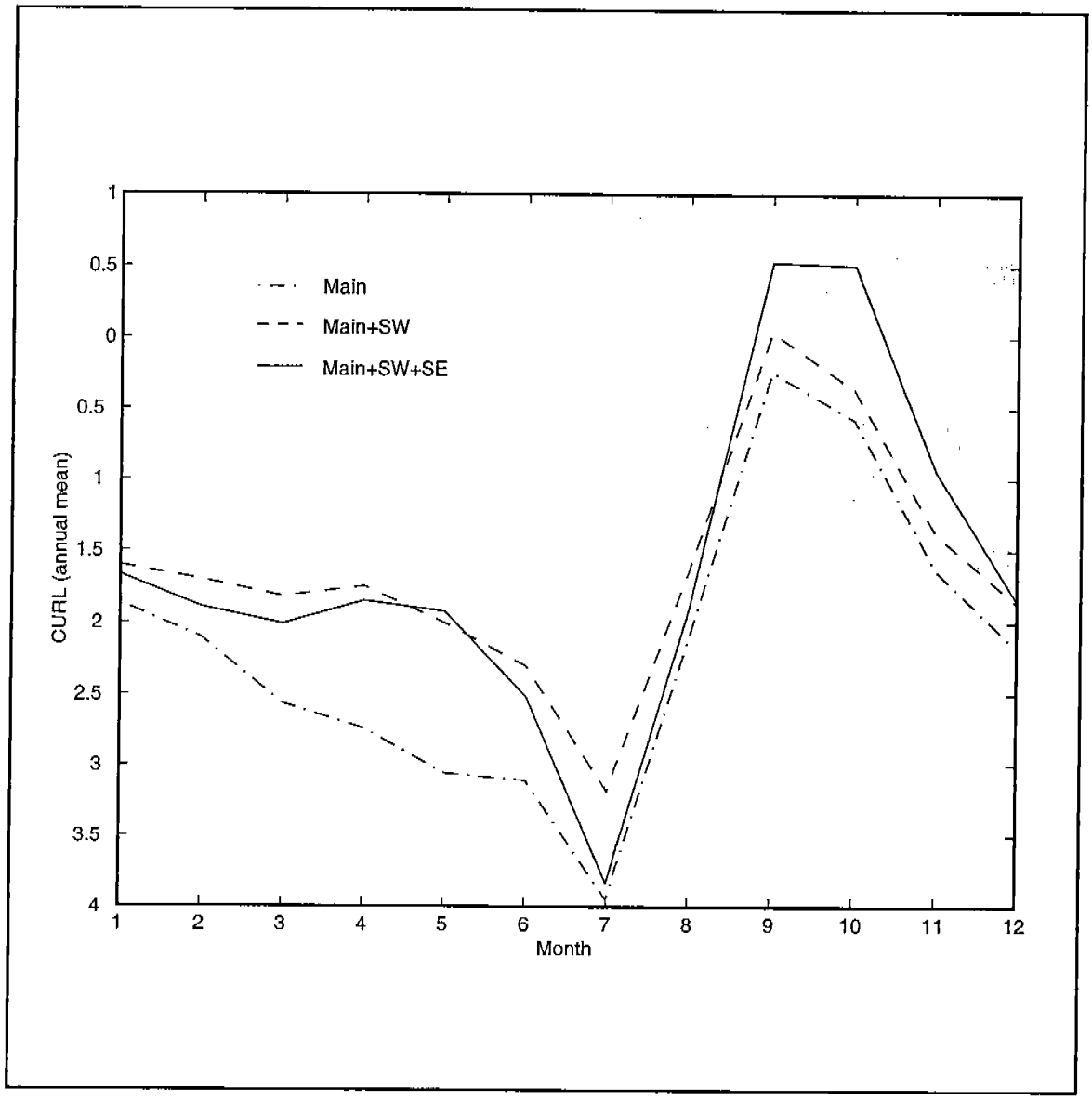

Figure 4.3-5. The mean annual cycle of wind curl over the Gulf of Mexico from the NCEP data. The dash-dot curve labelled "Main" is for a basic rectangle extending from 22.5°N to 27.5°N, 85°W to 97.5°W. The dashed curve labeled "Main & SW" also includes the region over the Bay of Campeche; the full curve labeled "Main & SW & SE" also includes a region to the west of Cuba that also confines the northward-directed Ekman transport.

For comparison, the magnitude of the annual cycle of wind curl over Gulf, shown in Figure 4.3-5, has a peak (negative) value of ~-5.5 and a minimum of ~-1.4. Thus, we can estimate that the forcing changes by plus or minus ~2 over its mean value of ~-3.5.

There is a simple and nearly independent way to estimate the downward transport associated with the Ekman pumping; we estimate the magnitude of the flow forced by winds over the Gulf in comparison with the equivalent forcing over the North Atlantic. Most maps of open ocean wind curl show the line of maximum curl going over Bermuda and extending into the Gulf. We can *estimate* the Ekman pumping in the Gulf merely by knowing the ratio of the width of the Gulf to the width of the Atlantic, and by the relative magnitudes of the curl in the Gulf to the curl over the open Atlantic. The analyses of the COADS winds by Mayer and Weisberg (1993) show that the curl forcing over the Gulf in summer is essentially the same as in the western N. Atlantic. During the winter the curl in the Gulf is roughly half that over the Atlantic. The ratio of the width of the Gulf to the width of the Atlantic is (in degrees of longitude) ~15°/70°, or 0.2. Therefore, we may use a ratio of 0.5 - 0.75 for the curl, and estimate the Sverdrup transport in the Gulf as ~[0.2 * (.5-.75) * 30] Sv, or ~3-4.5 Sv, depending on the fraction of the curl one chooses.

Thus, by this order of magnitude calculation, the variability in wind curl pumping over the Gulf can easily be determined. Given a mean value of ~3.5 Sv, with a seasonal variability of 2, we estimate that the variability of the curl-forced transport over the whole Gulf that could be associated with an annual cycle would be on the order of ±2 - 3 Sv. While this is not *exactly* the same value as the annual cycle of Gulf Stream transport, it seems close enough to provide an interesting basis for further study into the relationship between these important variables.

4.3.5 Discussion and Conclusions

The arguments presented *support* the suggestion that the curl of the wind stress is the major contributing factor to the irregular behavior of the northward advance of the LC front. The issue requires further study for a clear proof and thorough understanding. The lack of an annual cycle in the LC, as demonstrated in Figure 4.3-2, despite the strong annual cycle in the wind forcing remains an elusive issue.

A final point to mention is the time scale of the downward pumping. The net vertical motion forced by the Ekman pumping is on the order of 50 m/year. Thus, to force surface water down beneath the incoming current, to ~1000m, will take a time on the order of decades. It is worth pointing out that after about a year, the "old ring" in the western Gulf has been sheared apart and lost its identity. The tattered remnants of many old rings must remain in the Gulf, being flushed out at about one per year. There is ample time for mixing.

V. SLOPE CIRCULATION PATTERNS

5.1 Introduction

The prior chapters of this report begin establishing the complex nature of the often concurrent circulation producing mechanisms as well as the three-dimensional complexity of the resulting circulation patterns. Chapter 5 beings to describe both the documented patterns of currents as well as the associated dynamical features that appear to produce these patterns.

A broad range of horizontal scales-of-motion were evident in the DeSoto Canyon during the field measurement period. The presence of oceanographic features producing circulation patterns in the DeSoto Canyon have been documented for at least 35 years (Figure 5.1-1), however, access to synoptic documentation of broad regions of the Gulf of Mexico became possible with the availability of satellite imagery and altimetry (Chapter 4). These remotely sensed geophysical measurements in combination with in-situ current/temperature time series and ship-survey observations begin to provide a basis for a systematic descriptions, in spite of the limitations in the remotely sensed data that result from seasonal availability (thermal) or horizontal resolution (altimetry).

The following material in Chapter 5 presents a reconstruction of features present in the study area during the two-year field measurement effort, as well as a description of current and hydrographic patterns associated with these features. Observations were analyzed to characterize currents and transport at a number of time scales. Additionally, the in-situ current and temperature data have been used to describe slope and shelf break dynamics as well as fluxes of temperature and momentum.

5.2 Event Description

The following is a chronological description of the more significant events observed during the two-years of field observations. The measurements are subdivided into eight intervals representing times when a particular process appears to have had a controlling influence on the observed flow field. Time series of current vectors from the upper 8 to 40 m at all sites are shown with winds at buoy 42040 located on the A mooring transect and coastal sea level at Panama City in Figures 5.2-1a-1d. Currents at the 300m depth from all sites are shown in Figures 5.2-2a-2d.

Period 1: March 21 - May 1, 1997

Satellite derived sea surface temperature (SST) and sea surface height (SSH) fields indicate that during this interval the southwest portion of the array was influenced by a warm intrusion from a streamer trailing a former cyclonic Loop Current (LC) frontal eddy (LCFE) that had moved southeast of the array around a Loop Current ring (Figure 5.2-3a) This streamer apparently spun-up into a warm anticyclonic eddy (ACE) that caused strong eastward flow over the upper 500m at A3 (Figure 5.2-2a).

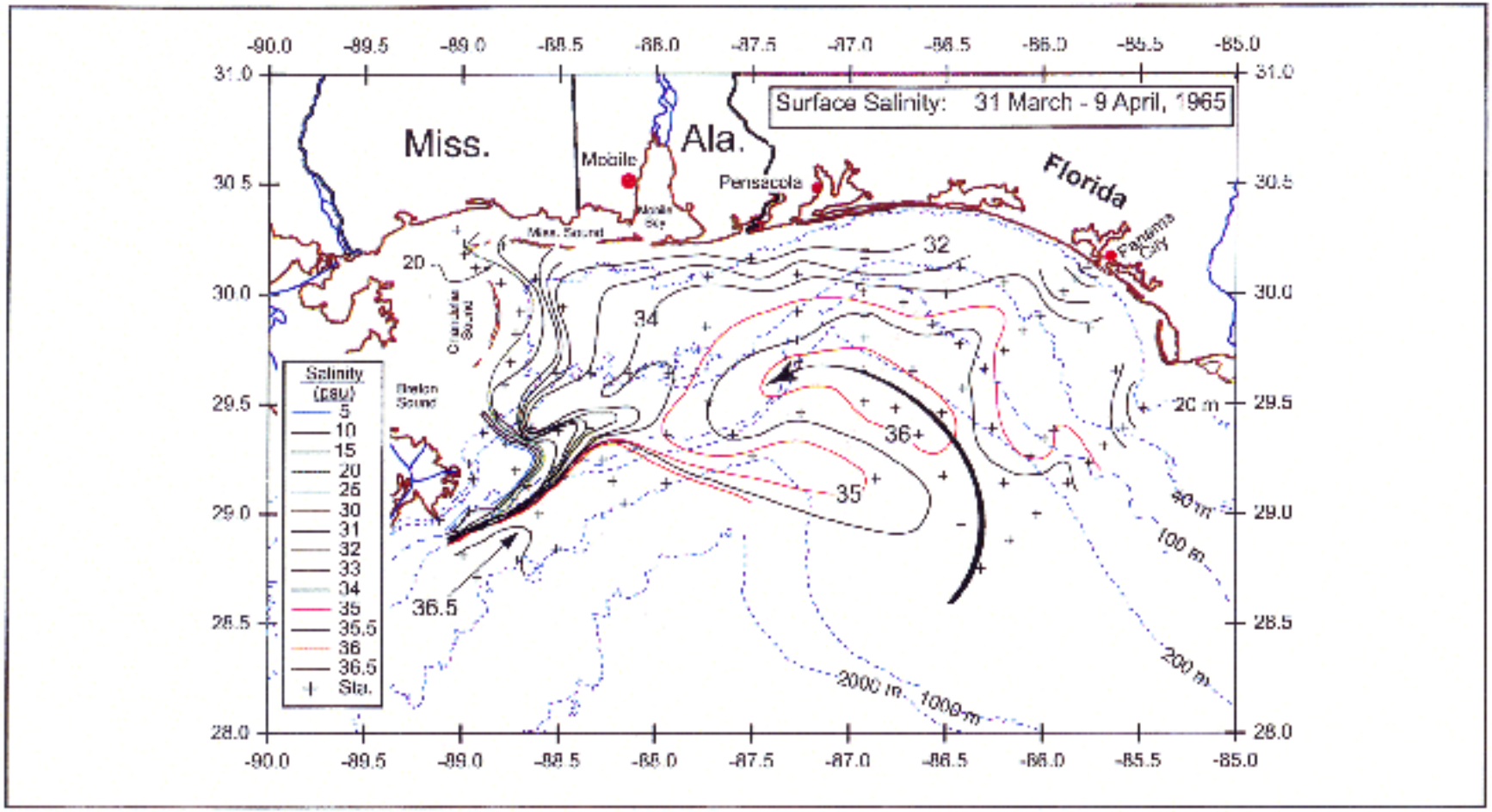

Figure 5.1-1 Contours of sea surface salinity as measured by Drennan (1968) during a survey in the general area of this project. Note the apparent intrusion of saline water from over the deeper slope up the the vicinity of the shelf break (200m isobath). Lower salinity water is coming from the west and being moved out over the slope by the cyclonic (counterclockwise) eddy in the upper canyon. The Mississippi River is putting very low salinity on to the shelf into relative deep water.

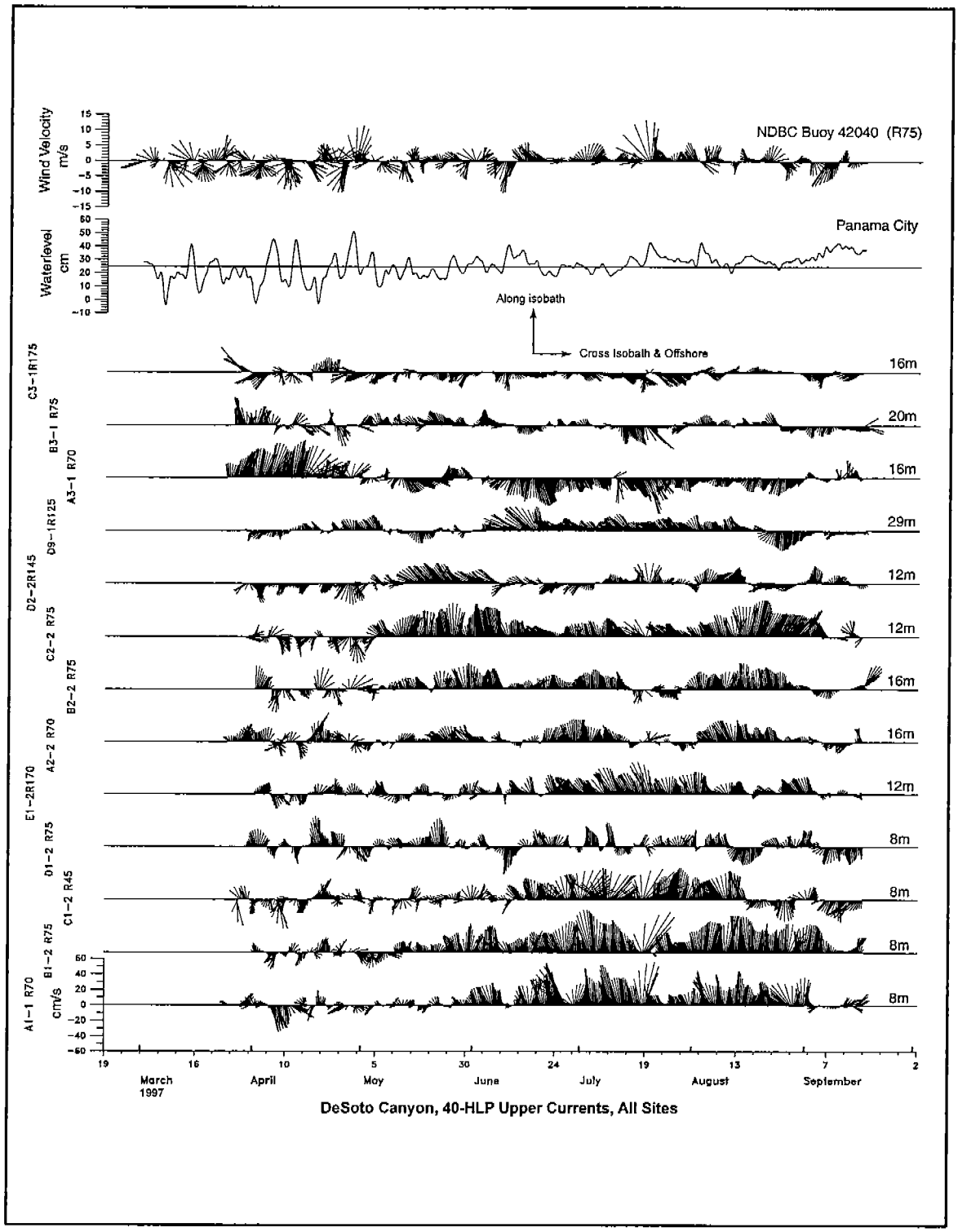

Figure 5.2-1a. Subtidal current vectors from depths of 8 to 40 m for all mooring sites from March to September 1997. Frame of reference has been rotated so that for each mooring, vectors directed upward represent along isobath flow with an easterly component.

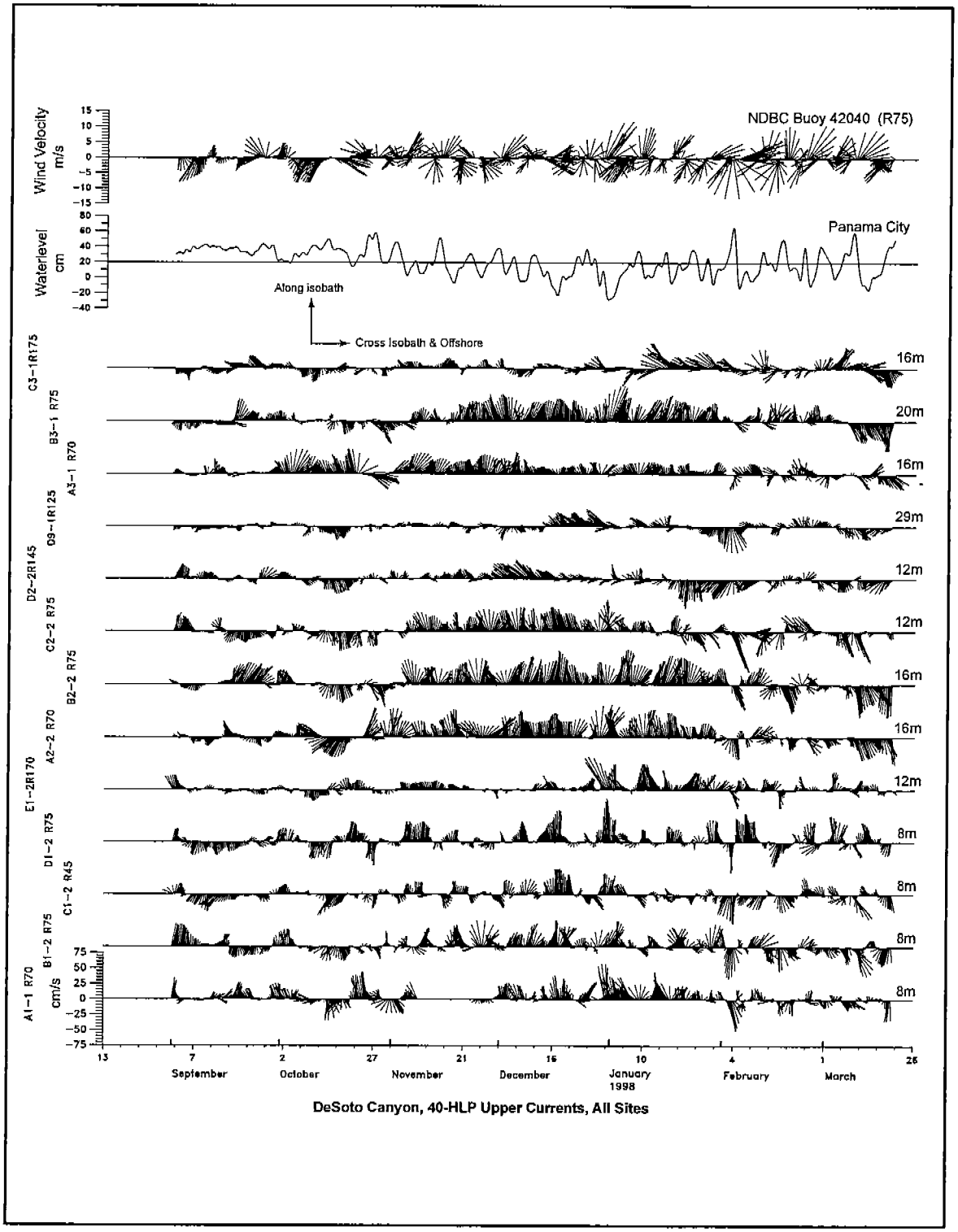

Figure 5.2-1b. Subtidal current vectors from depths of 8 to 40m for all mooring sites from September 1997 to March 1998.

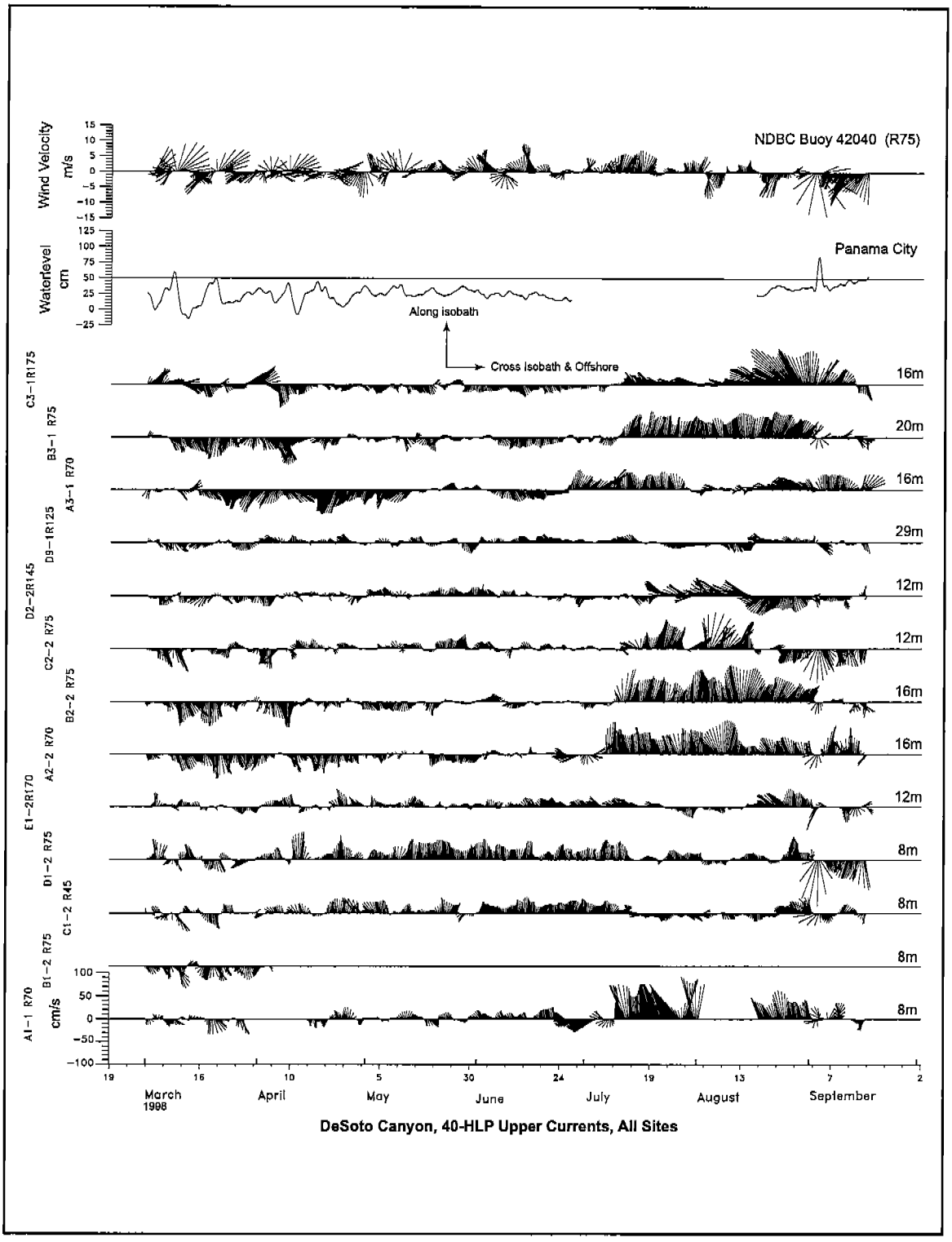

Figure 5.2-1c. Subtidal current vectors from depths of 8 to 40m for all mooring sites from March to September 1998.

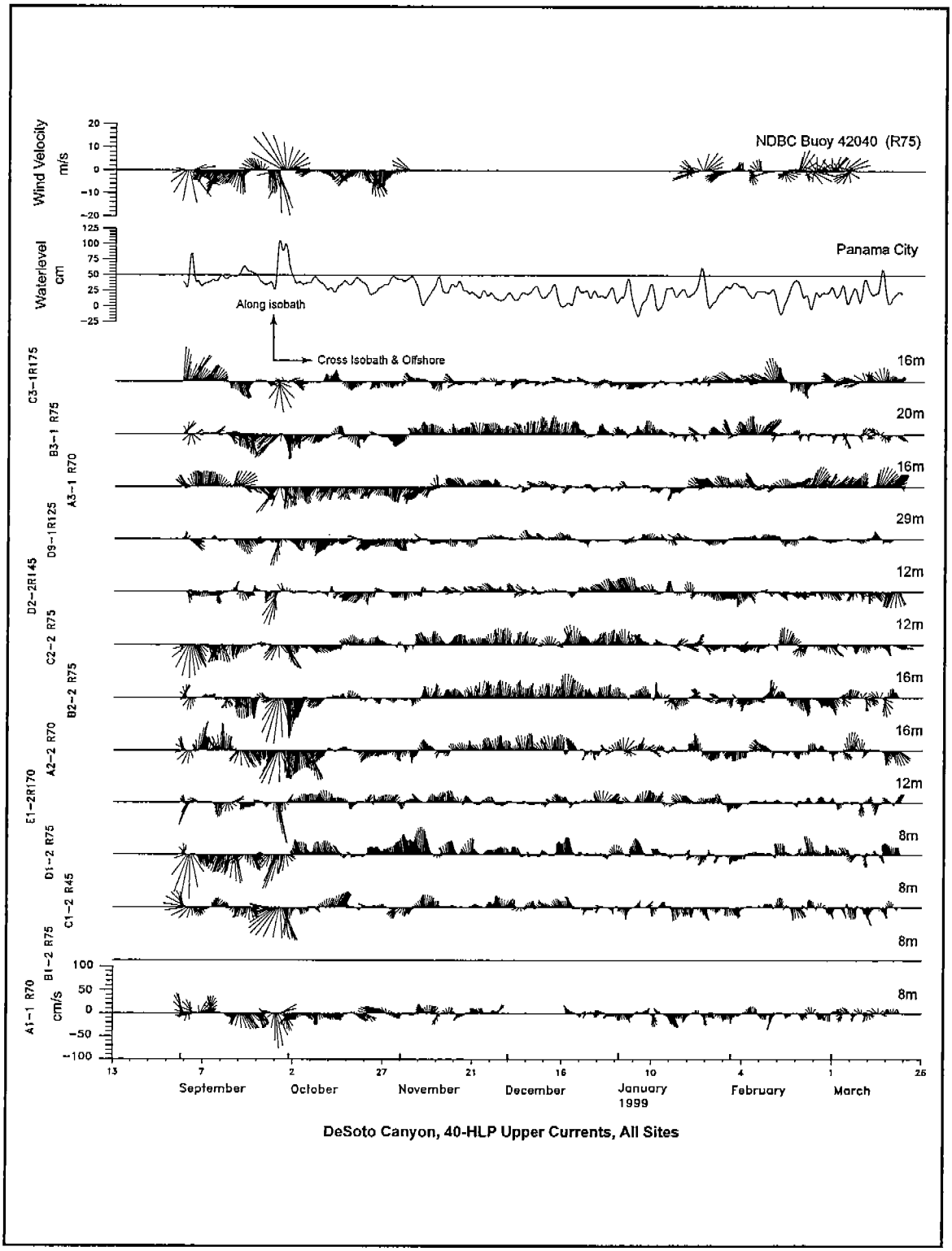

Figure 5.2-1d. Subtidal current vectors from depths of 8 to 40m for all mooring sites from September 1998 to March 1999.

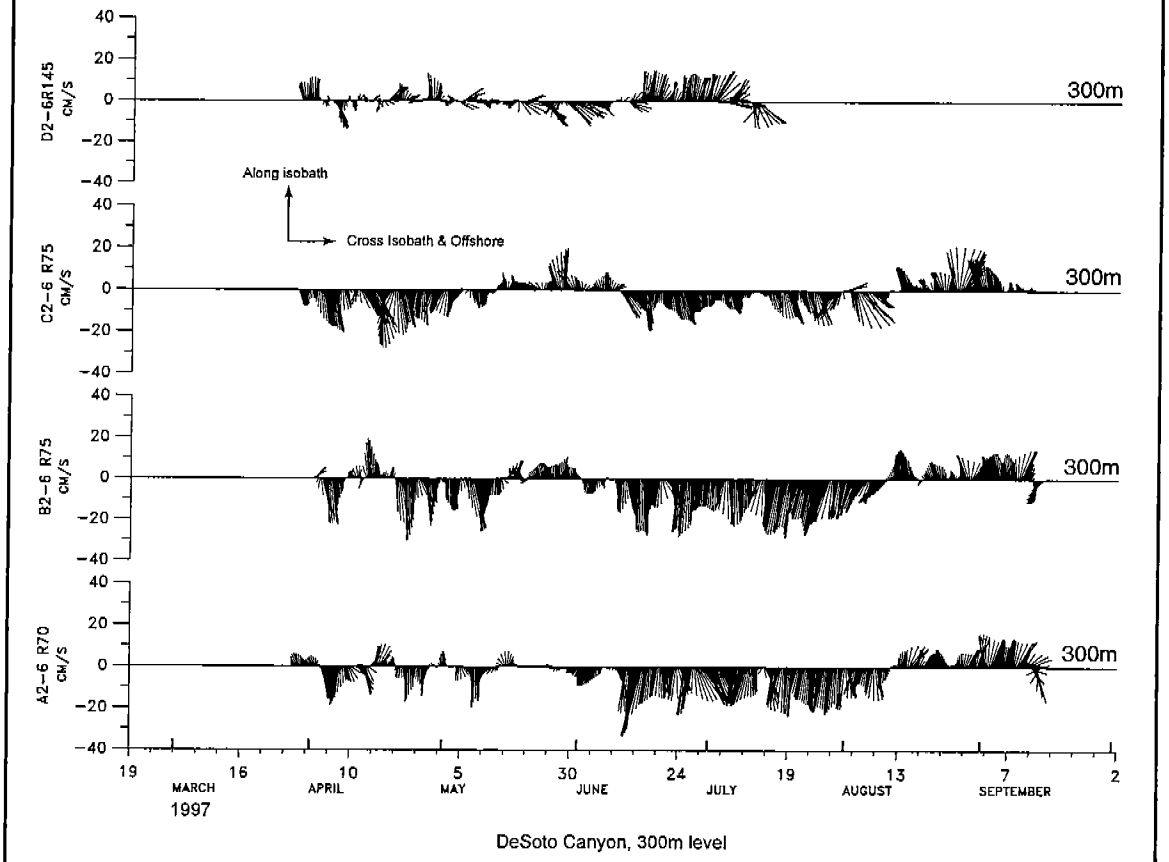

Figure 5.2-2a. Subtidal current vectors from 300m depths at mid-slope moorings (A2, B2, C2 and D2) from March to September 1997.

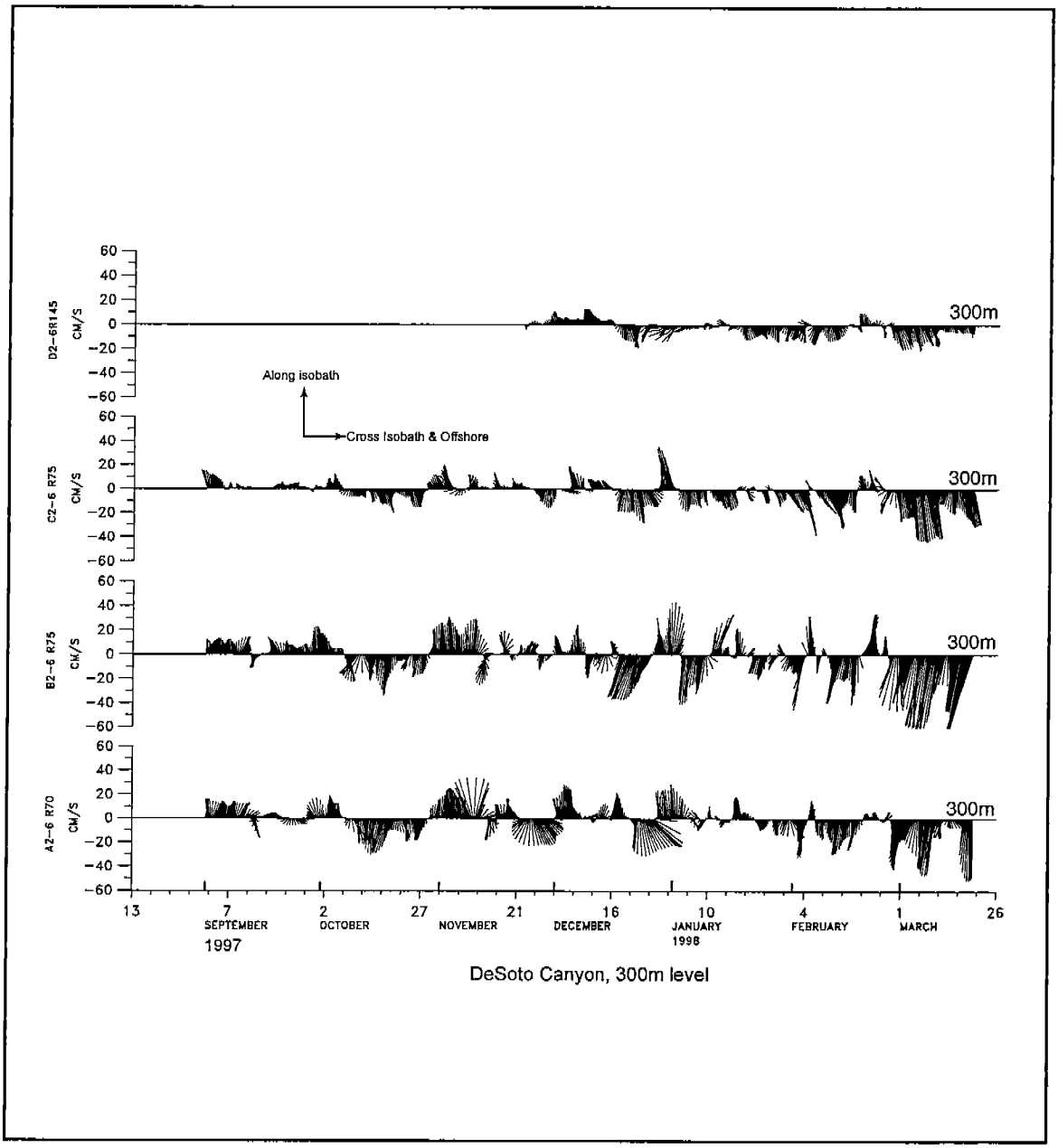

Figure 5.2-2b. Subtidal current vectors from 300m depth at mid-slope moorings (A2, B2, C2 and D2) from September 1997 to March 1998

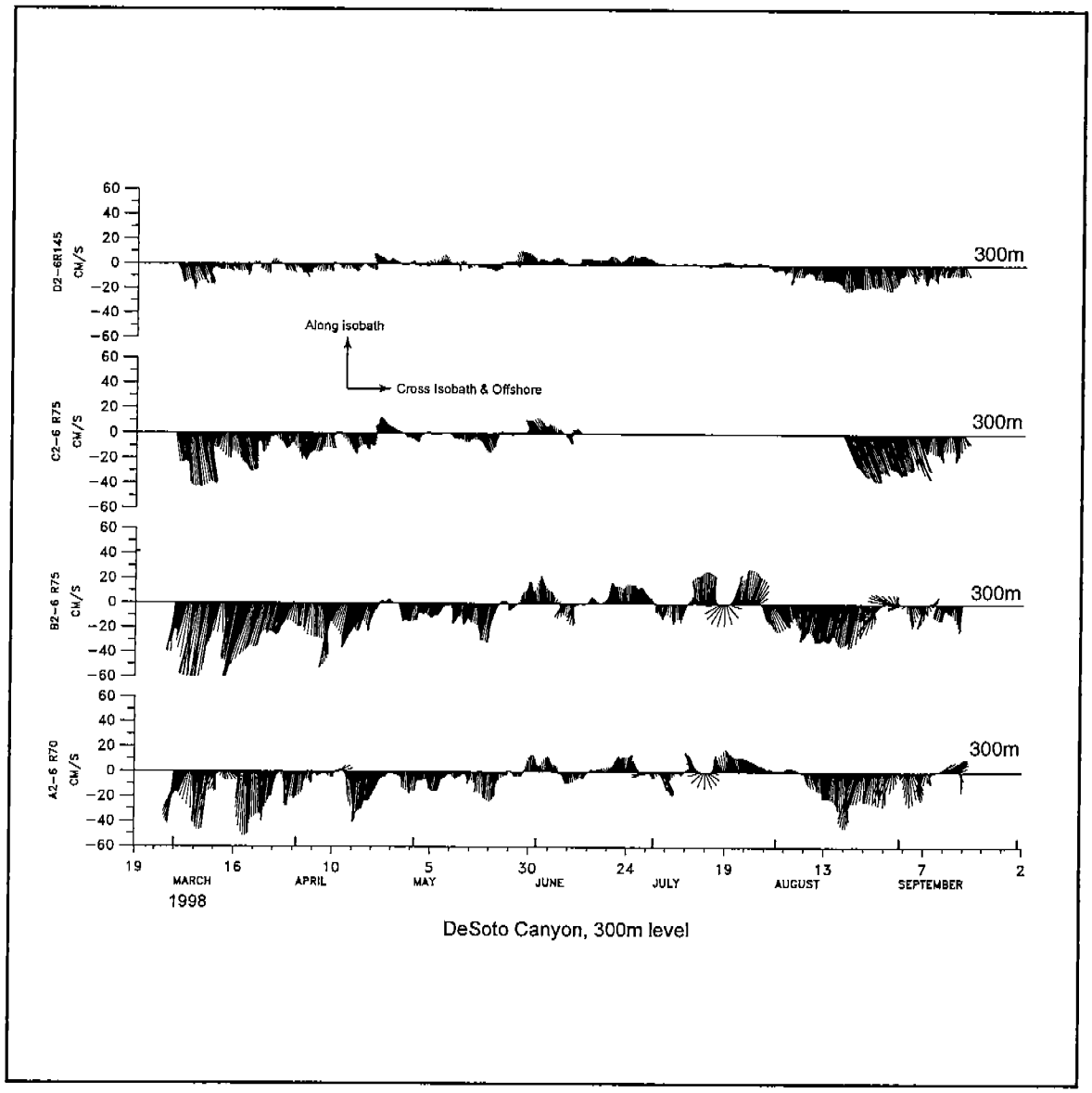

Figure 5.2-2c. Subtidal current vectors from 300m depth at mid-slope moorings (A2, B2, C2 and D2) from March to September 1998.

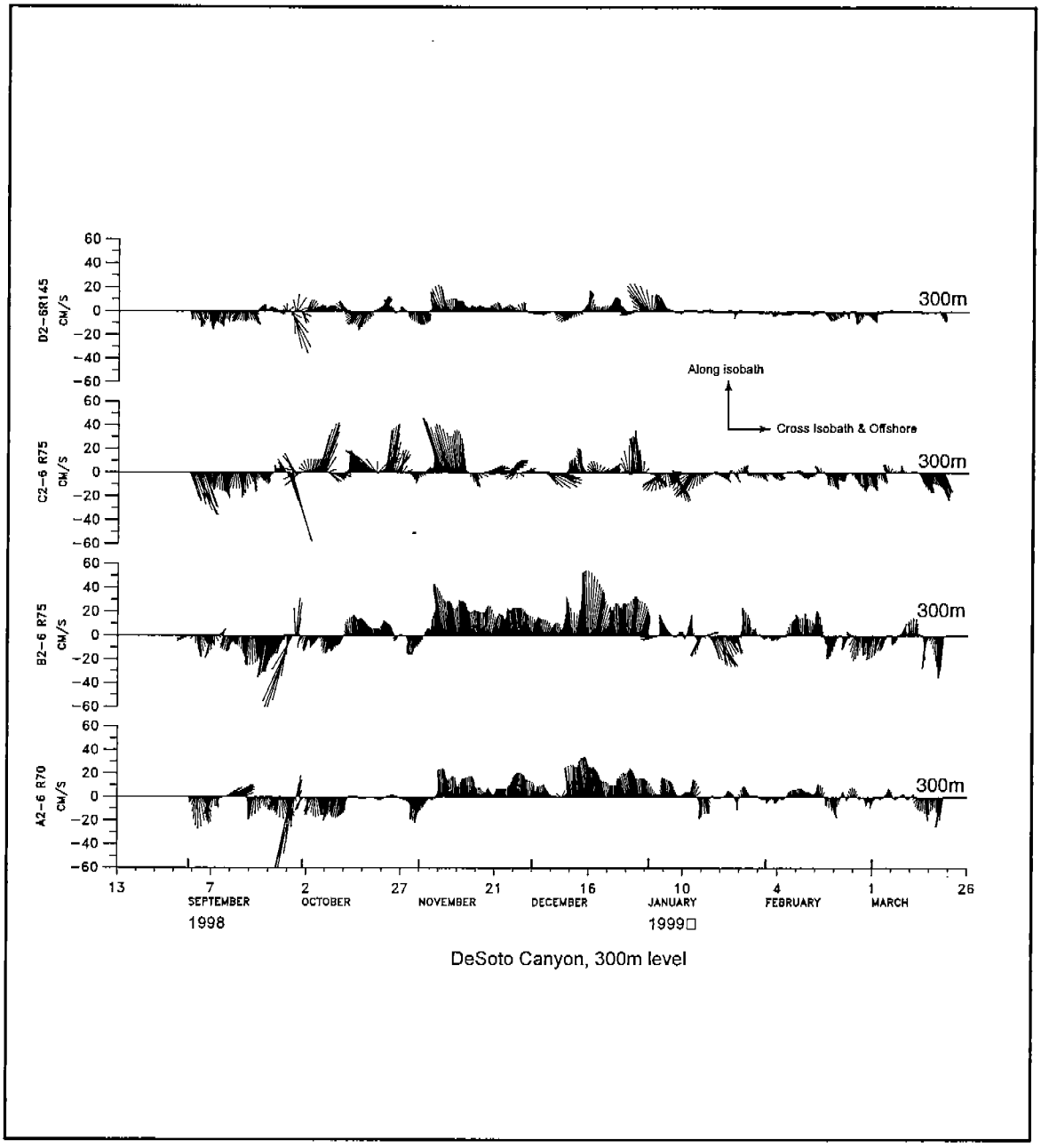

Figure 5.2-2d. Subtidal current vectors from 300m depths at mid-slope moorings from September 1998 to March 1999.

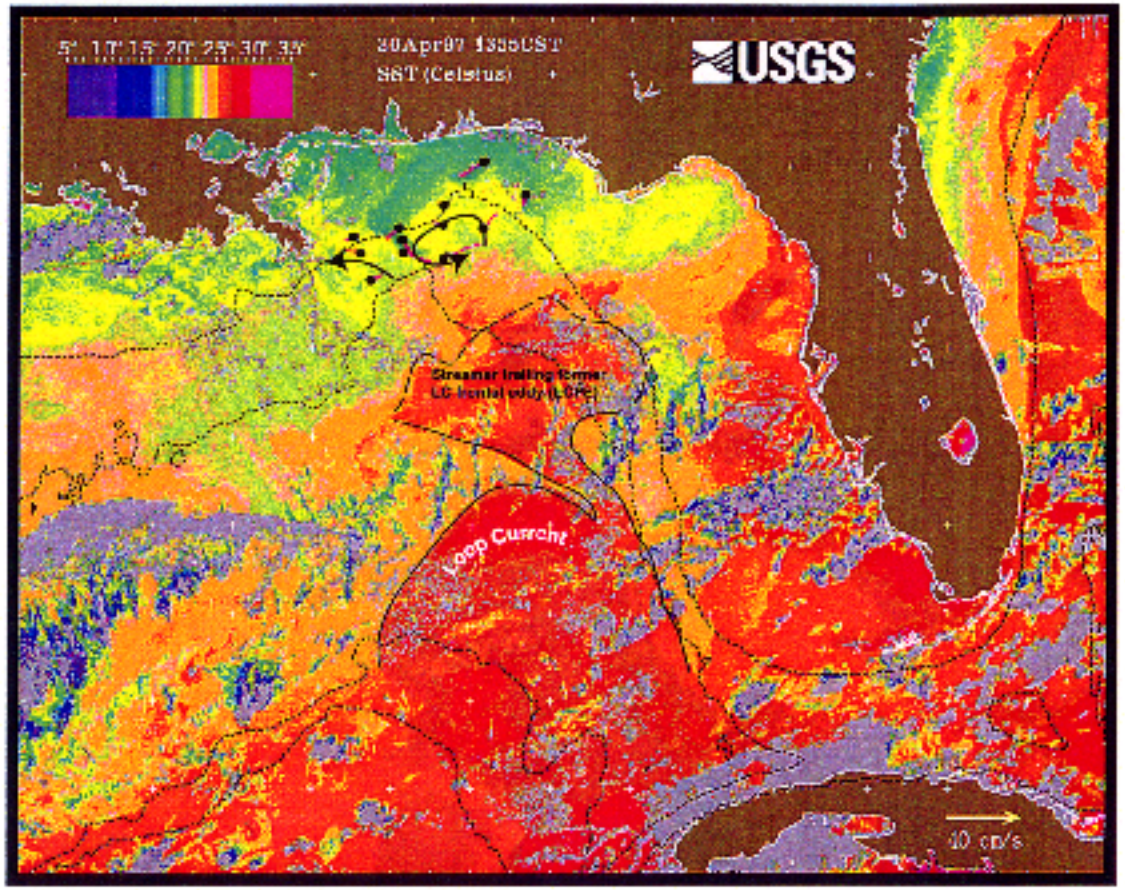

Figure 5.2-3a. SST image for April 30, 1997 (1355 CST). Measured surface current vectors are overlaid on the image in the study area. A streamer trailing a former LC frontal eddy is labelled, as is the Loop Current proper.

In the SSH fields this warm streamer is shown as a surface ridge that wrapped around the surface low from the LCFE (Figure 5.2-3b). Contributing to the flow variability during this time was the development of a 100 km scale cyclonic shelf eddy (CSE) that produced a cyclonic flow pattern from mooring lines A-D and resulted in offshore exchange of cool shelf water at line B (Figure 5.2-3a). Currents along the shelf break also appear to have a significant wind influence during this time with alongshore flow events following alongshore wind events and in-phase with coastal sea level changes. Flows deeper than 200m were mostly westward, although variable and there was a positive offshore temperature gradient at depth that further supports the finding of a cold eddy offshore that was responsible for entraining the warm streamer into the array in the upper layer.

Period 2: May 1 - September 9, 1997

Period 2 is characterized by strong eastward flow at shelf break and mid-slope sites and westward flow in the offshore (1500m) and at depths below 200m (Figures 5.2-1a and -2a). Although satellite SST images were not useful during summer SSH fields show the Loop Current merging with the ring from Period 1 and extending northward to about 27.5°N. A trough extends north of the Loop to 28.7°N and a ridge extends north of the trough into the moored array (Figure 5.2-4a). The trough appears to develop from a LCFE and causes the strong westward flow at offshore and deeper sites. The ridge most likely comes from a warm streamer that extends into the array and evolves into an ACE that supports the strong eastward flow in the upper layer at the shelf break and mid-slope. Shipboard hydrographic data of July 8-16, 1997 are consistent with this above description. A tongue of high salinity LC water extends into the DeSoto Canyon region from offshore. Near surface geostrophic currents showed this as an onshore intrusion of LC water (Figure 5.2-4b). A significant eastward jet along the salinity and temperature front at the shelfbreak and westward flowed offshore and at 500m (Figure 5.2-4c). Cross-shelf temperature gradients from the array and shipboard data are mostly negative in the upper layer during this time and indicate a warm intrusion from the south. Persistent eastward winds developed over the period June 14 to August 3 and may also have contributed to the eastward flow in the upper layer of the shelf break.

Period 3: November 1, 1997 - February 4, 1998

Period 3 is associated with persistent eastward flow over most of the array. The eastward flow was stronger and more persistent in the western part of the array where it extended to depths of 300 to 500m at the offshore stations on lines A and B. (Figure 5.2-1b and -2b) At lines C and D the flow was more variable with strong onshore and up-canyon flows during the last half of this period. The eastward flow continued to follow the topography to the south in the eastern part of the array causing southward alongshore flow at mooring E. Shipboard derived geostrophic currents also show the eastward jet during November 11-19, 1997 (Figures 5.2-5a and -5b) to have been stronger in the western part of the array. The jet extended along the slope throughout the array and followed the topography toward the south in the eastern part of the array. The vertical extent of the jet was at least 500m.

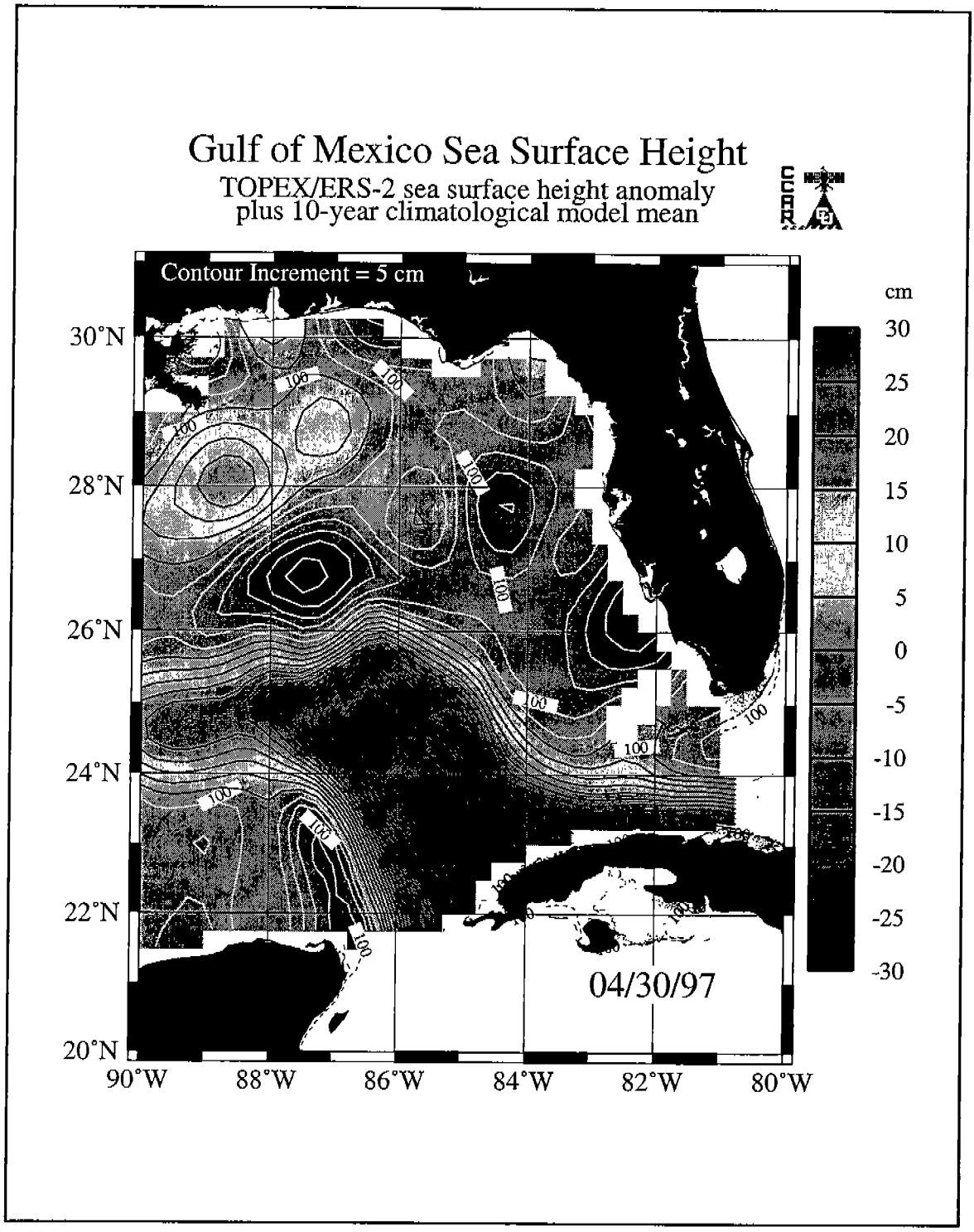

Figure 5.2-3b. SSH for April 30, 1997 derived from TOPEX/ERS-2 plus model mean. Dark contours are for SSHs that are greater than zero; white contours are for SSHs less than zero.

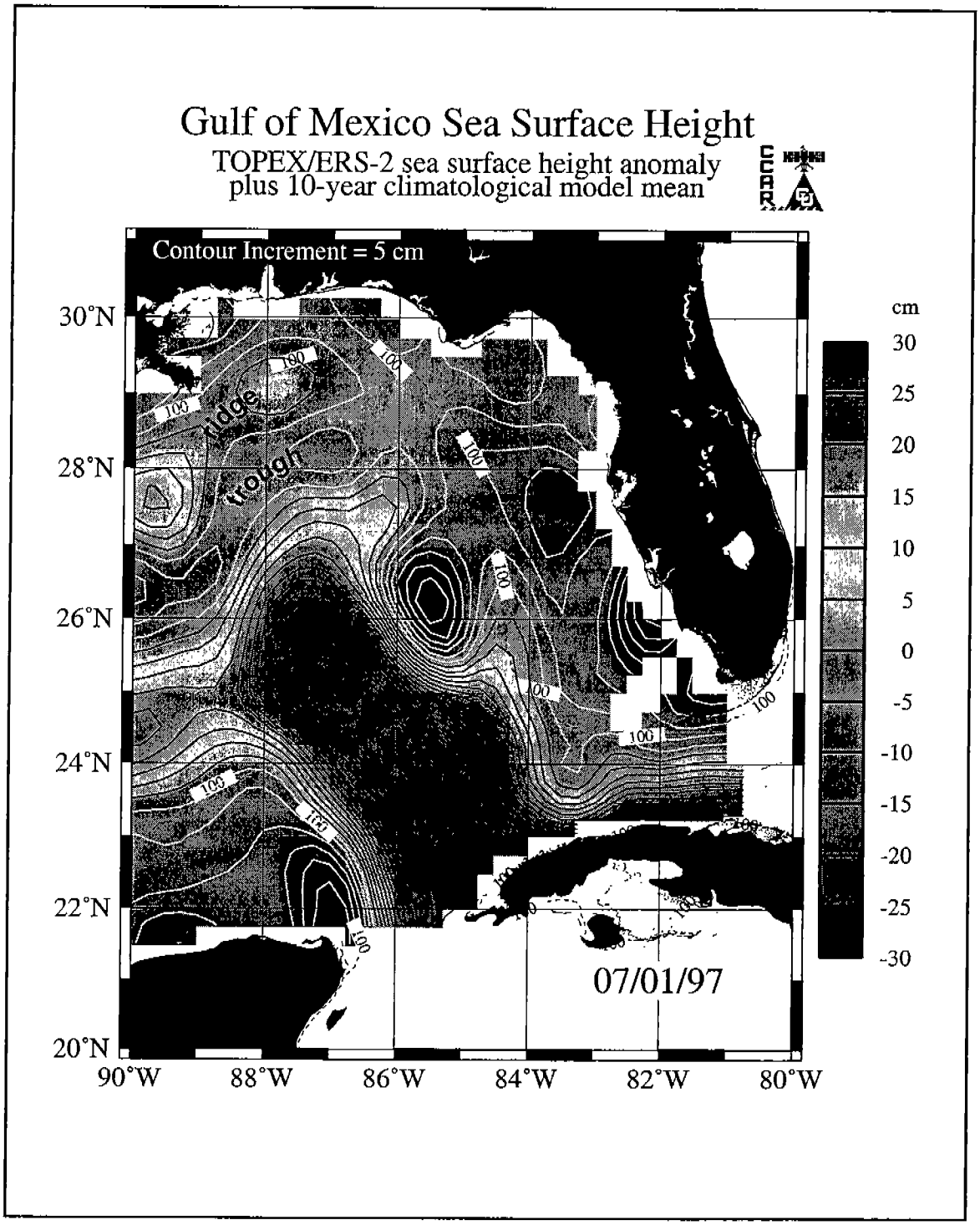

Figure 5.2-4a. SSH for July 1, 1997 derived from TOPEX/ERS-2 plus model mean. Dark contours are for SSHs that are greater than zero; white contours are for SSHs less than zero.

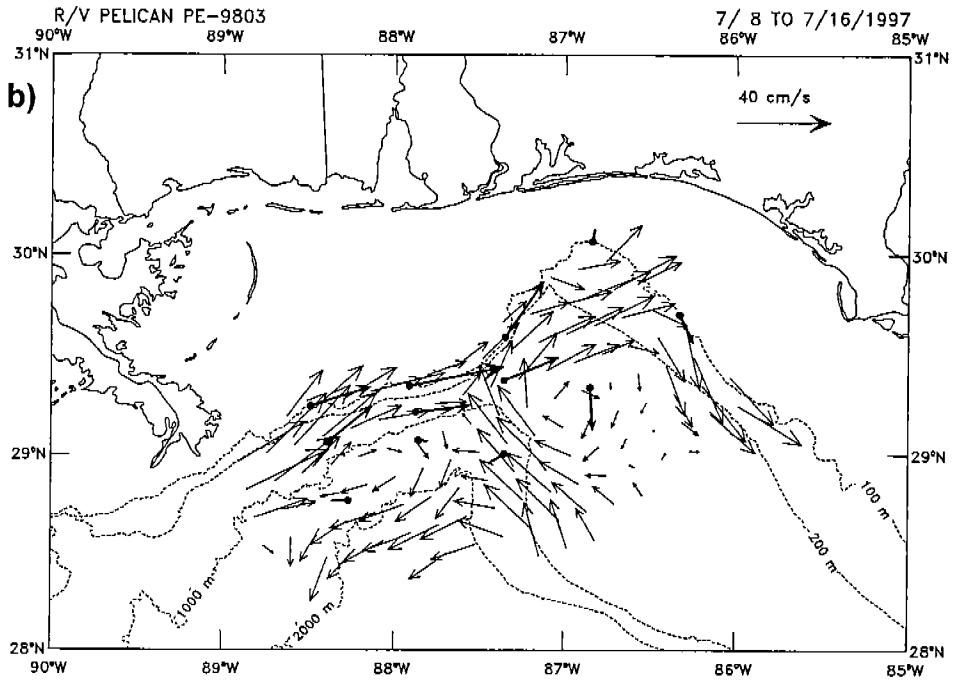

6 - 1000m Geostrophic Velocity

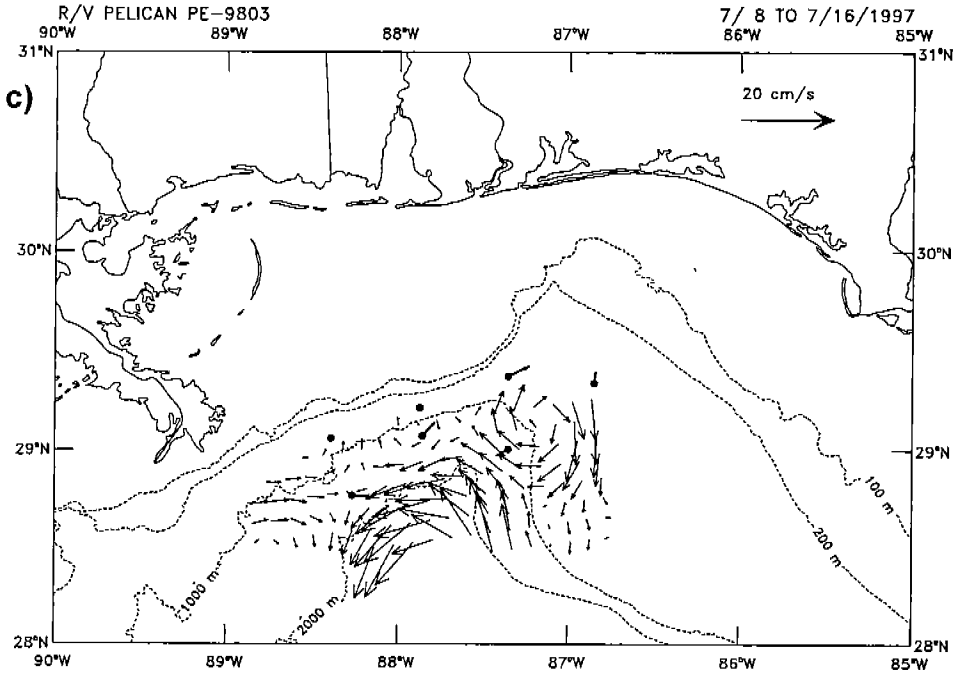

500 - 1000m Geostrophic Velocity

Figure 5.2-4b,c. Geostrophic currents at b) 6m and c) 500m, based on a level of no motion at 1000 m using CTD profiles taken during the July 8-16, 1997 cruise. Heavier vectors are for currents measured at the mooring sites indicated by dots.

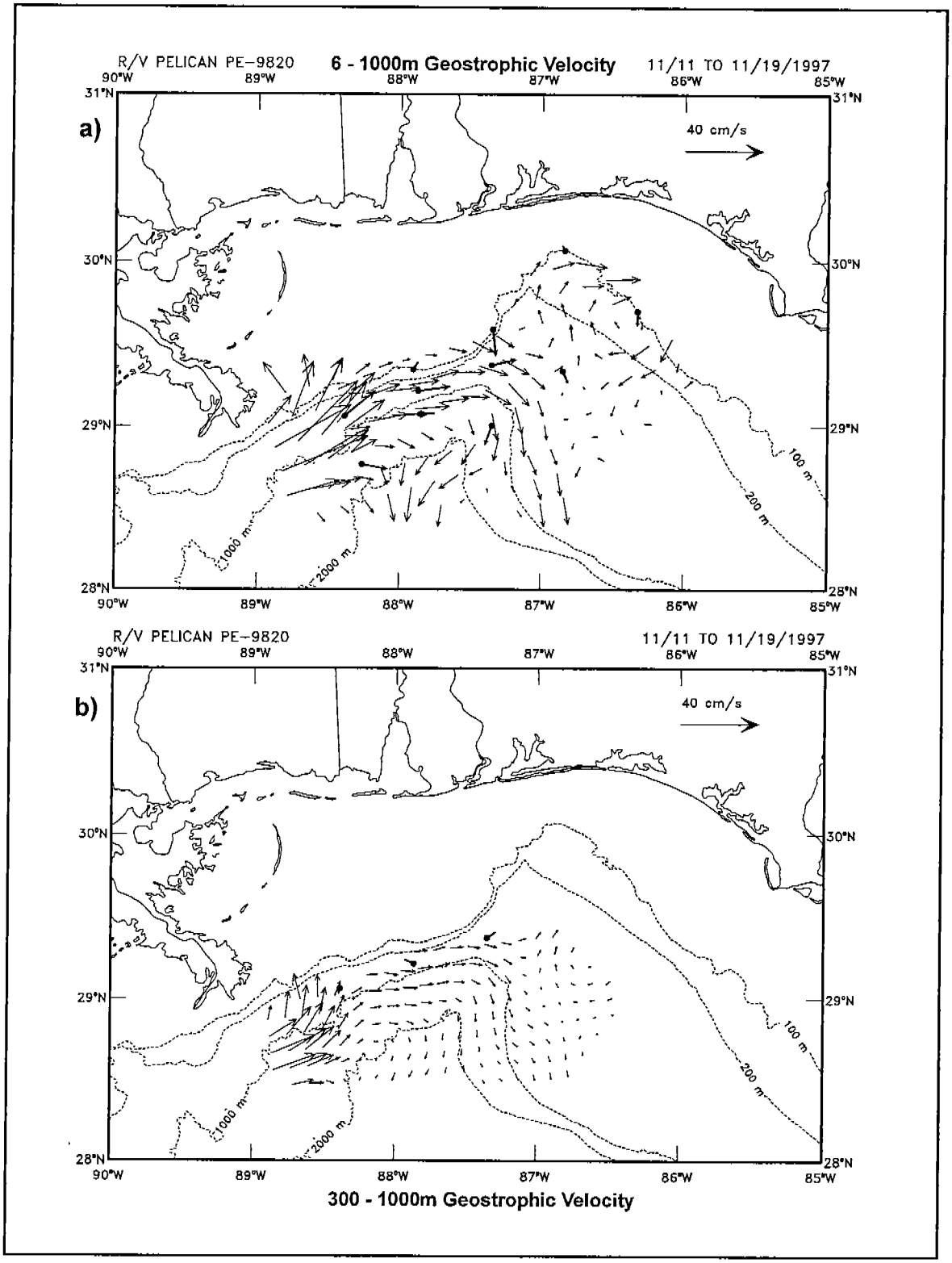

Figure 5.2-5a,b. Geostrophic currents for a) 6m and b) 300m, based on a level of no motion at 1000m using CTD profiles taken during the November 11-19, 1997 cruise. Heavier vectors are for currents measured at the mooring sites indicated by dots.

The SSH fields indicate that a large LC ring formed in October just prior to this period (Figure 5.2-5c). A LCFE was present northeast of the ring, with a filament ridge wrapping around the eddy and into the array. By mid-December when strong east flows were widespread, this ridge had spun-up into an ACE over the array, with a cyclonic feature located offshore separating the ACE from the LC ring and the LC (Figure 5.2-6). These features continued while the LC extended northward into the eastern Gulf, eventually reaching 28°N with a trough at its northern extreme that extends into the array. Apparently, the northward intrusion of the LC and trough caused the ACE over the array to move to the west ending the eastward flow event.

Satellite derived SST patterns in early December clearly show the presence of a warm eastward jet over the array, as well as the LC ring southwest of the Mississippi River delta and the immerging new LC south of the array (Figure 5.2-7). Also shown is a long streamer of slope water that was entrained offshore along the east side of the ring south of the delta. In addition, the SST patterns indicate the presence of 50 km scale cold, cyclonic eddies that developed on the temperature front on the north side of the warm jet. These features can enlarge up to 100 km over time and appear to have been active in shelf/slope exchange judging from their association with offshore streamers or squirts of cold shelf waters. Near the end of the period, SST images clearly show the LC extended near 28°N with a LCFE at the northern extreme and just south of the instrument array (Figure 5.2-8). Also visible in the image is the cold shelf eddy that had enlarged to about 100 km and caused a cyclonic circulation pattern between mooring lines B to D. The ring had moved further to the west increasing the separation from the LC. A strong LCFE was present southwest of the Tortugas, producing a narrowing of the LC.

Winter wind forcing patterns apparently contributed to the increased flow variability at the shelf break although many times overshadowed by the eddy-induced flow changes. A particularly strong westward wind event occurred near the end of the period from February 2-4 that caused westward flow through the array coupled to a coastal sea level rise (Figure 5.2-1b).

Period 4: February 4 - July 7, 1998

During Period 4, flow was generally westward throughout the array, except in the upper 30 to 40m along the shelf break where the flow was eastward, although with more variability. SST was especially clear up until early May and shows strong influence of frontal eddies and filaments that extended into the array from a recently separated ring, resulting in the westward flow at the offshore sites (Figure 5.2-9). Considerable offshore exchange is indicated during this time as shown by the presence of elongated offshore squirts of cold shelf water in the vicinity of the array. The young LC showed strong interaction with the southwest Florida shelf near the Tortugas and a Tortugas cyclonic eddy was well-developed south of the western Florida Keys. By mid-April the frontal eddy south of the array was well-developed and a warm streamer wrapped around the eastern side of the eddy and into the array (Figure 5.2-10a). The streamer appears to have caused the westward flow to split

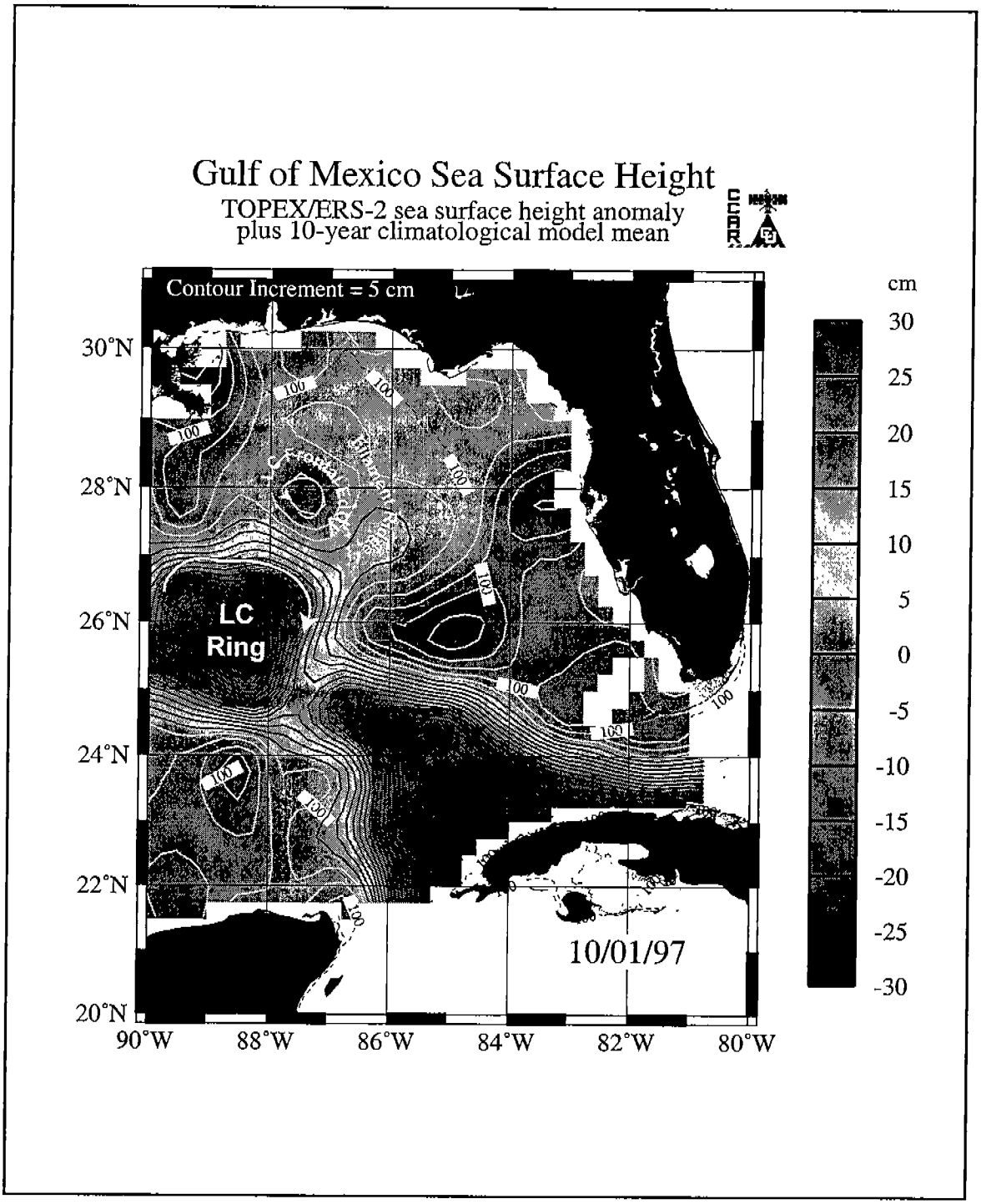

Figure 5.2-5c. SSH for October 1, 1997 derived from TOPEX/ERS-2 plus model mean. Dark contours are for SSHs that are greater than zero; white contours are for SSHs less than zero.

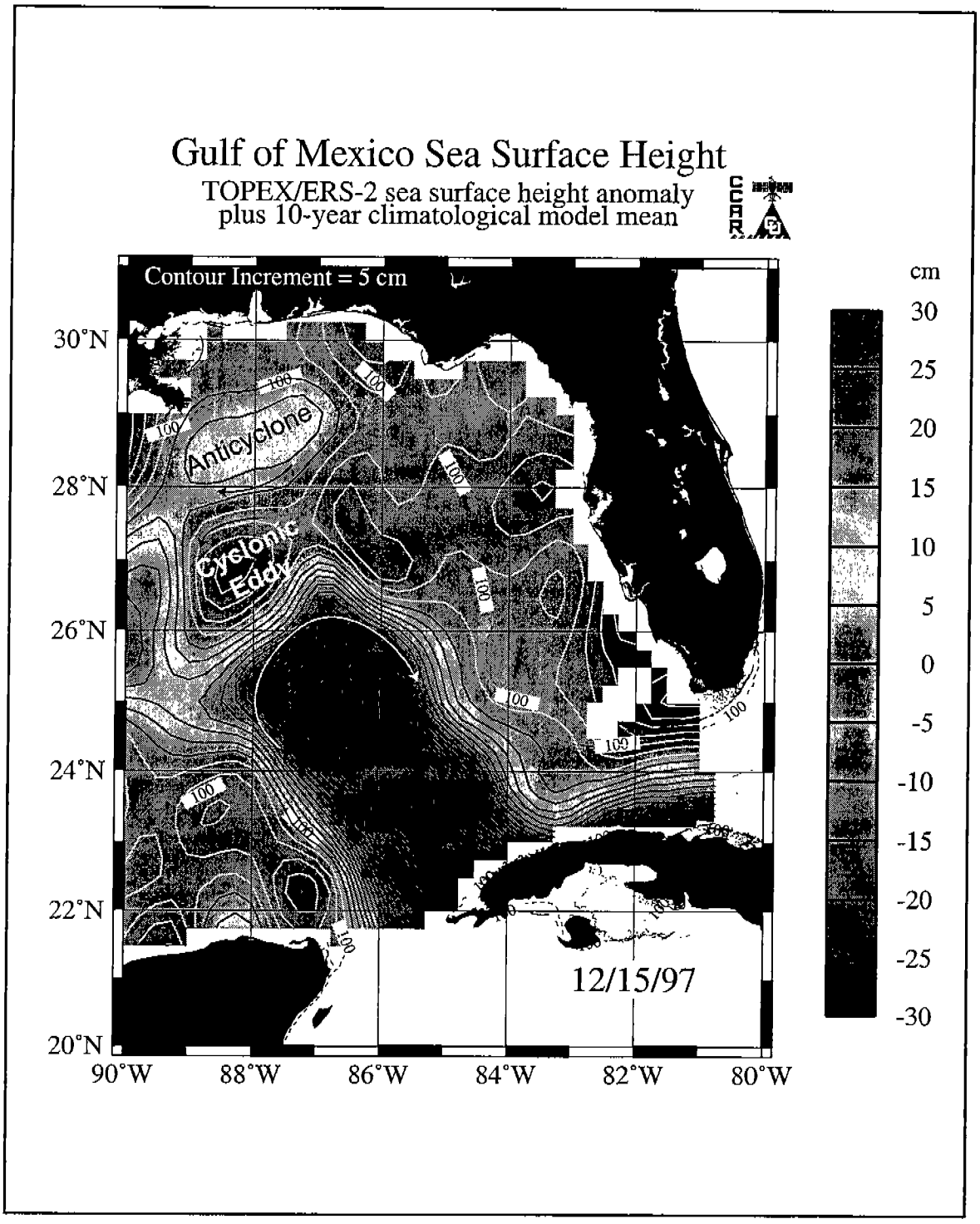

Figure 5.2-6. SSH for December 15, 1997 derived from TOPEX/ERS-2 plus model mean. Dark contours are for SSHs that are greater than zero; white contours are for SSHs less than zero.

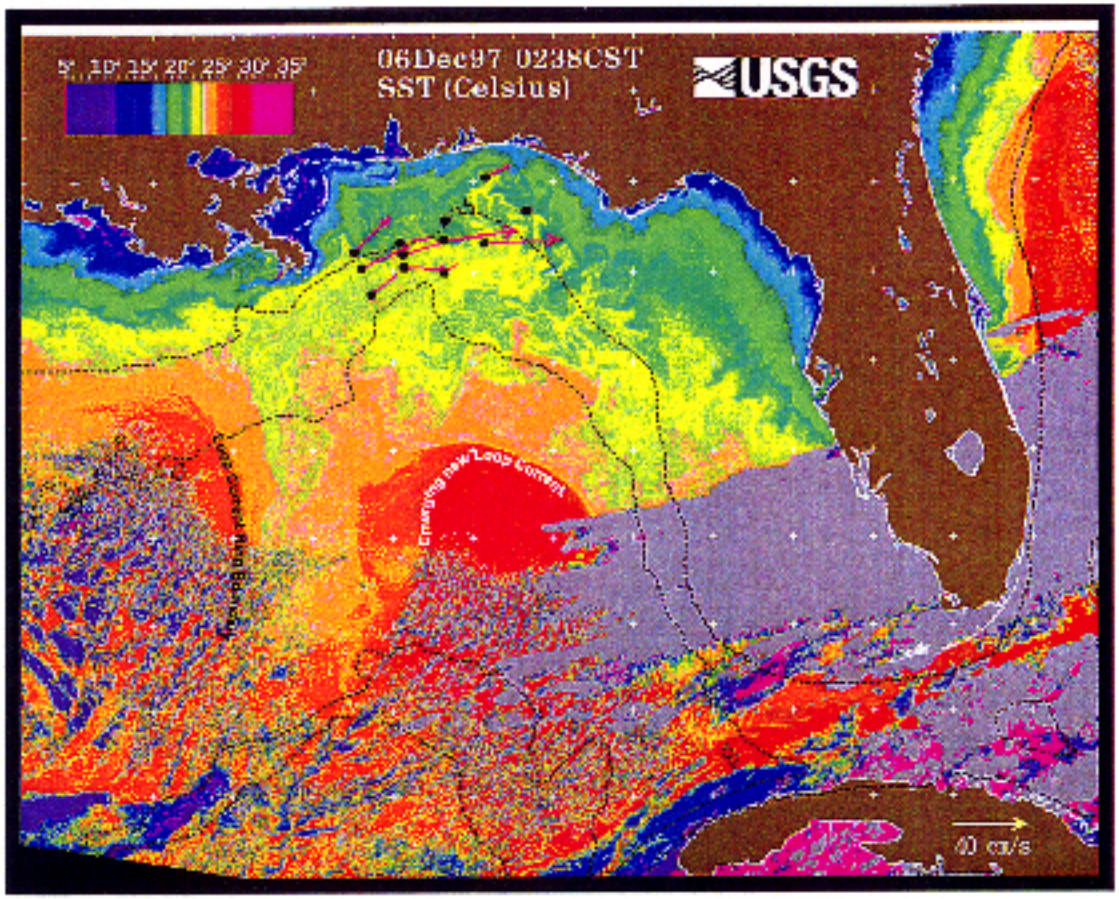

Figure 5.2-7. SST image for December 6, 1997 (0238 CST). Measured near surface currents have been overlaid on the image. Features mentioned in the text have been labelled for clarity. The eastward directed jet is evidenced by the relatively strong currents measured at each mooring.

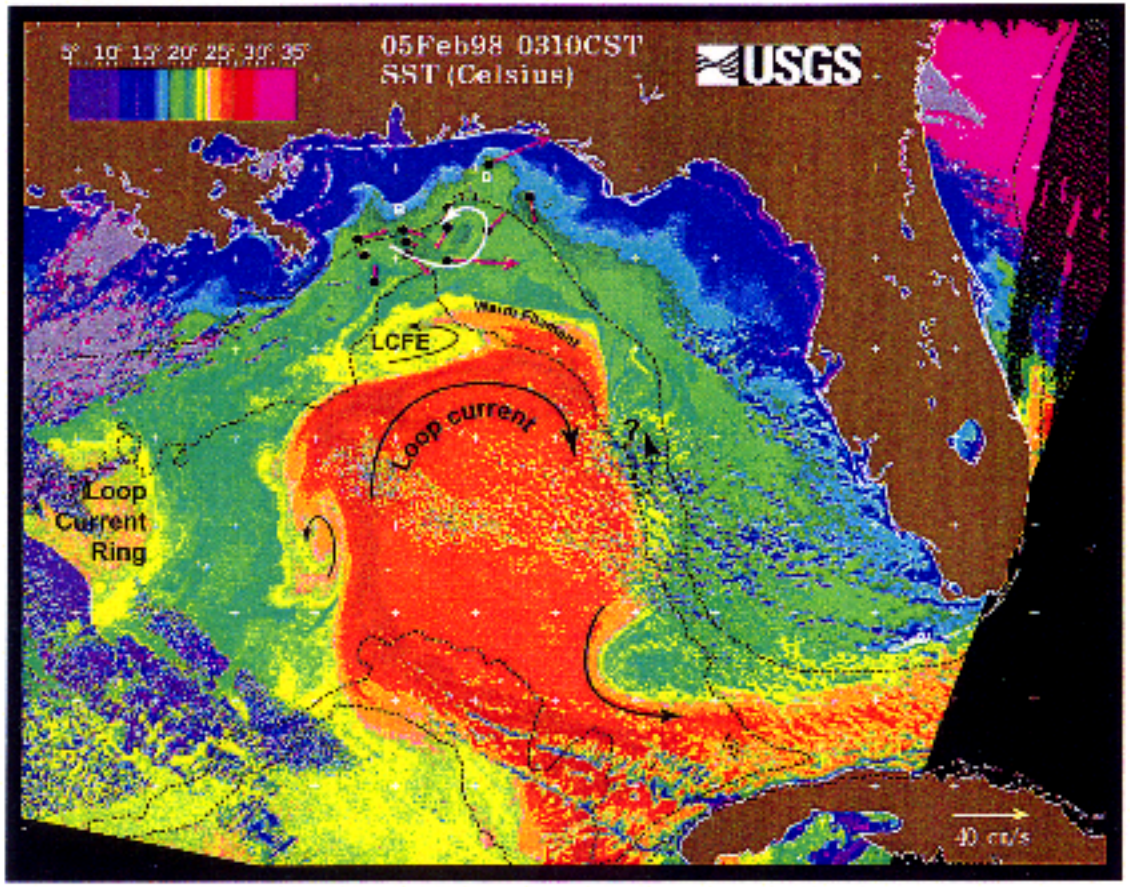

Figure 5.2-8. SST image for February 5, 1998 (0310 CST). Near surface currents measured in the study area are overlaid on the image. Features mentioned in the text have been

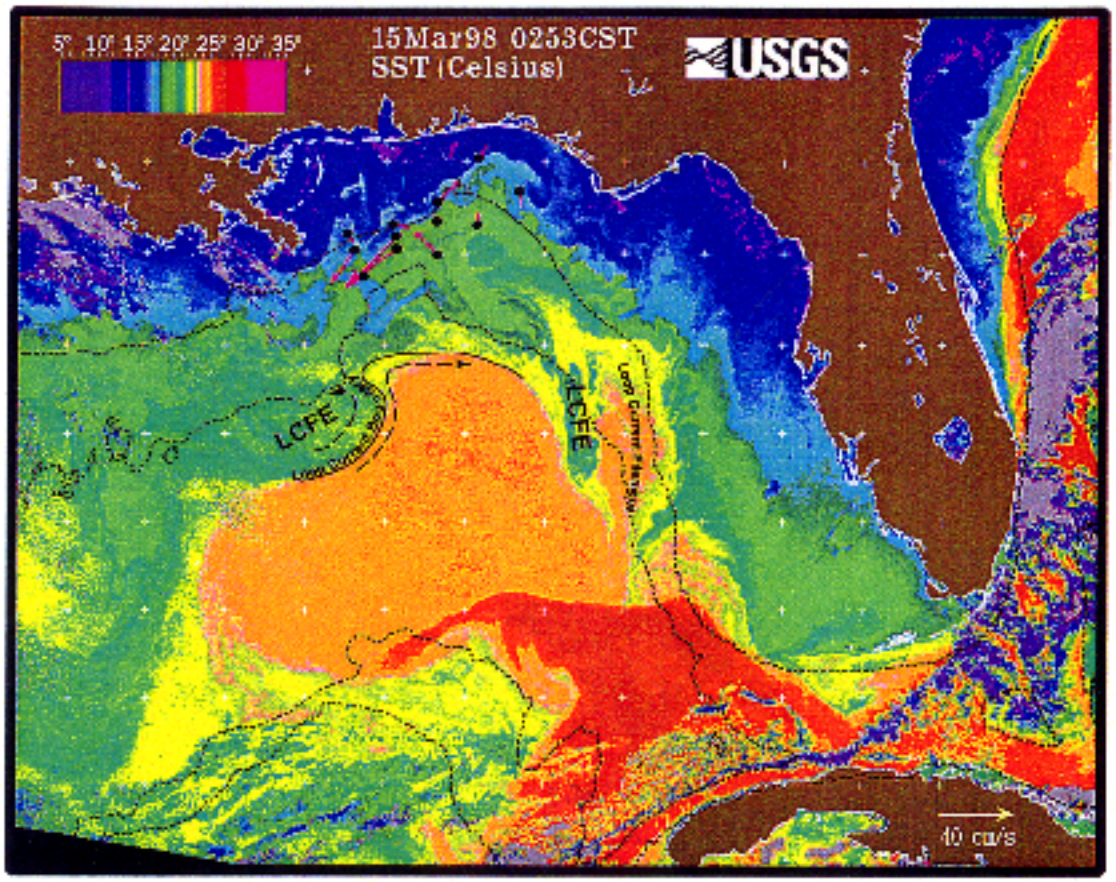

Figure 5.2-9. SST image from March 15, 1998 (0253 CST). Measured near surface current vectors in the study area are overlaid on the image. Some portions of the Loop Current and associated boundary features are also labelled.

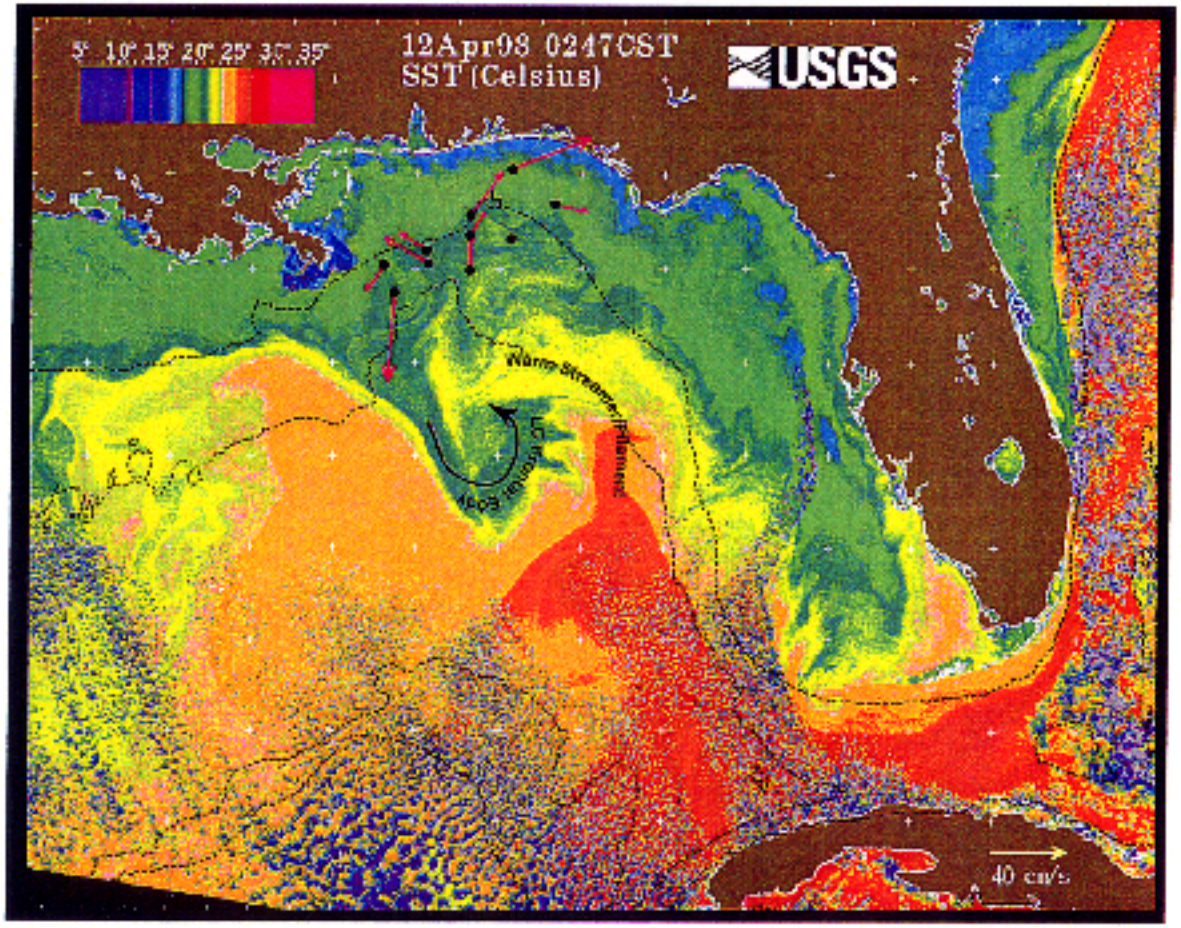

Figure 5.2-10a. SST image for April 12, 1998 (0247 CST). Measured current vectors are overlaid on the image in the study area. Features mentioned in the text have been labelled for clarity.

within the array with up-canyon and eastward flow on C, D and E lines and westward and offshore flow on A and B lines. Similar flow properties were observed for geostrophic currents derived from shipboard data (Figures 5.2-10b and -10c), where westward flow extended to at least 500m in the western part of the array and up-canyon flow was estimated for the eastern part. The young LC was located near 25°N west of the Tortugas. A band of cold shelf water appears to have been moving southward all along the west Florida shelf and into the inner shelf. The SSH and SST fields for mid-April show similar patterns with a large cyclonic eddy on the northeast side of a newly formed ring and a ridge (streamer) that wrapped around the eddy and into the array (Figure 5.2-11). This pattern continued throughout Period 4.

Period 5: July 7 - August 29, 1998

Period 5 is characterized by eastward currents in the upper layer at most of the mooring sites, except for C1, which had westward flow (Figure 5.2-1c). At 300m the flow was also eastward until late July when it shifted to be mostly westward (Figure 5.2-2c). SST images are not available for this period, however, the SSH fields indicate that a LCFE was located offshore of the array on the boundary of the previously separated ring. A ridge wrapped around the east side of the LCFE and appears to spin-up into a ACE close to the array (Figure 5.2-12a). Eastward flow that is expected to develop on the north side of the ACE would be consistent with the observed eastward flow pattern in the upper layer, where as at 300m the flow was more influenced by the offshore cyclonic eddy. Shipboard measurements during August 4-12, 1998 further support this interpretation. Geostrophic currents near the surface show a strong eastward jet along the shelfbreak and mid-slope, with a small cyclonic eddy in the nearshore part of the canyon (Figure 5.2-12b). The eastward flow decreased below 300m and was replaced by westward flow over the deeper region of the slope (Figure 5.2-12c). The clockwise circulation within the ACE was also shown by near surface drifter patterns from two drifters launched in early August east of the Mississippi delta and later entrained in the ACE, making several clockwise circuits from August 10-30 (Figure 5.2-12d). This interval is also noted for a time of prolonged eastward winds. However, winds speeds were not strong and did not appear to have a significant influence on observed currents.

Period 6: August 29 - October 29, 1998

Period 6 is noted for its strong wind forcing resulting from two hurricanes that passed over the array. Hurricane Earl moved from west to east through the outer part of the array on September 2 and 3. Hurricane Georges moved from south to north directly over line A on September 27-28. A strong current response was observed at inertial frequencies for the deeper sites and is discussed elsewhere in this report. The subinertial currents were generally westward over most of the array during this period (Figure 5.2-1d and -2d). The two hurricanes are indicated by strong westward flow events during their passage over the array. Surprisingly, little eastward flow occurred. SSH fields indicate that there was a weak ridge over the array with a stronger offshore trough that may have had a controlling influence on the persistent westward flow. Although the winds were also westward, except during the

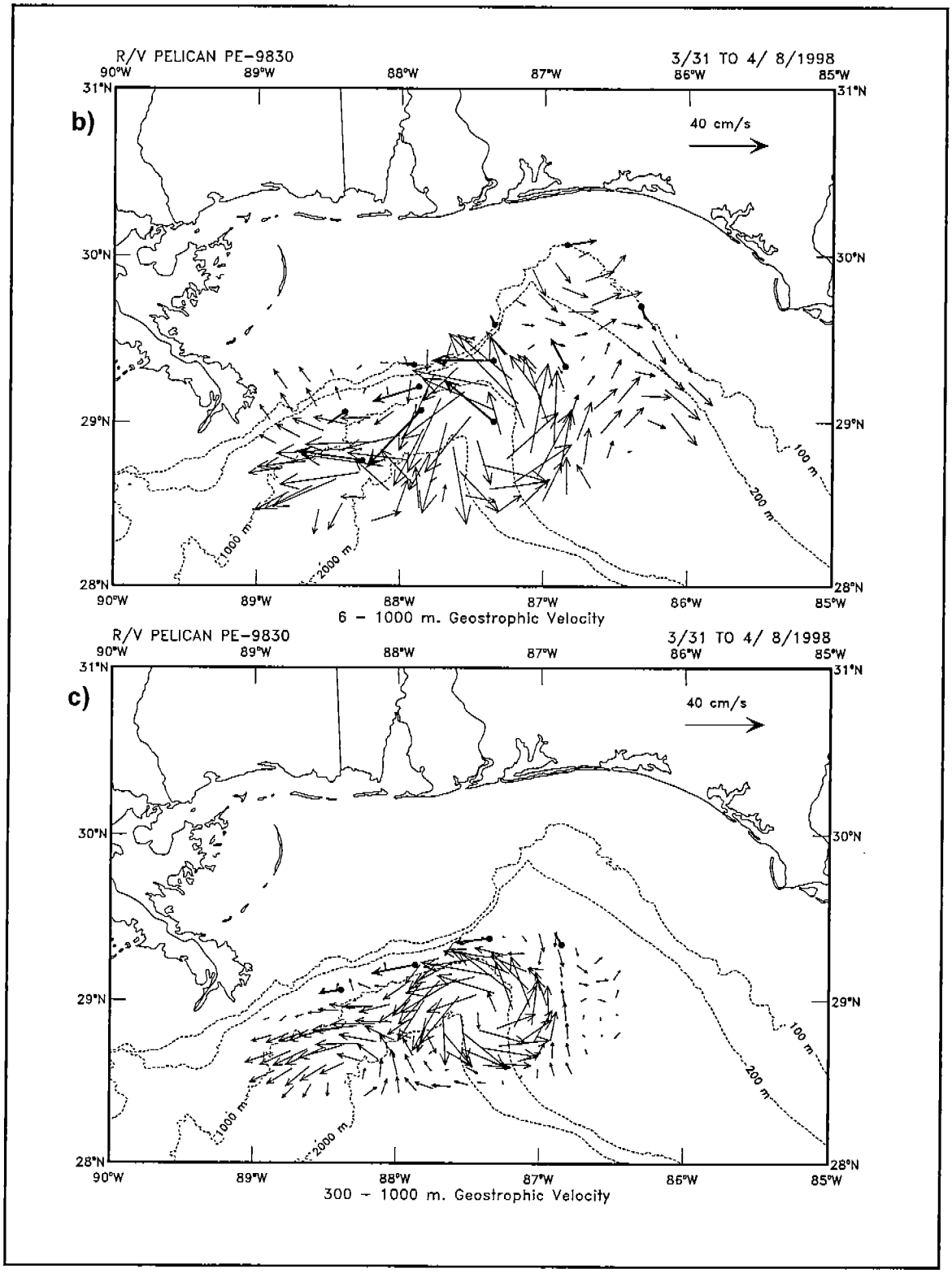

Figure 5.2-10b,c. Shipboard geostrophic currents for b) 6m depth and c) 300m depth, based on a level of no motion at 1000m for March 31 - April 8, 1998. Heavier vectors represent currents measured at the mooring sites indicated by dots.

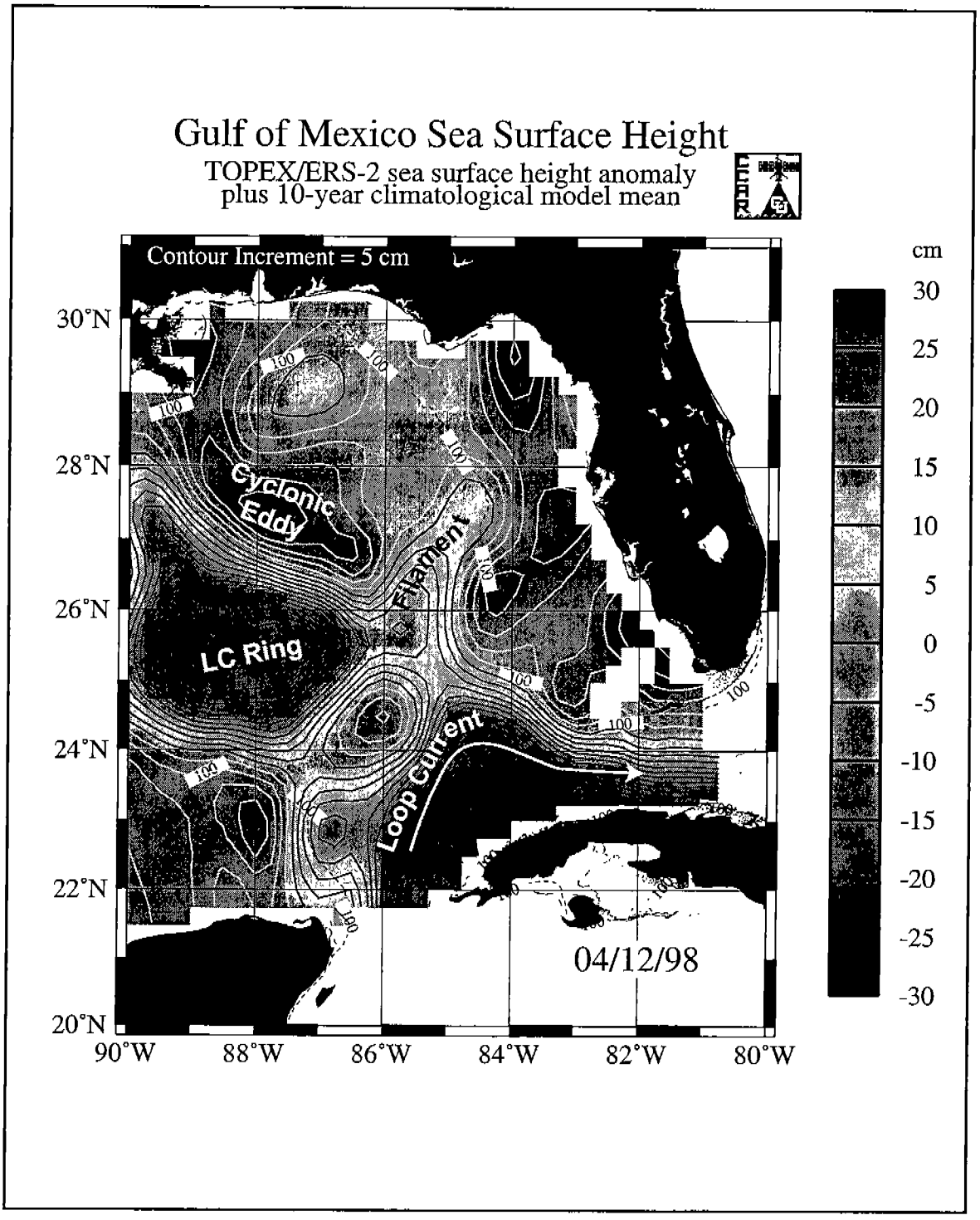

Figure 5.2-11. SSH for April 12, 1998 derived from TOPEX/ERS-2 plus model mean. Dark contours are for SSHs that are greater than zero; white contours are for SSHs less than zero.

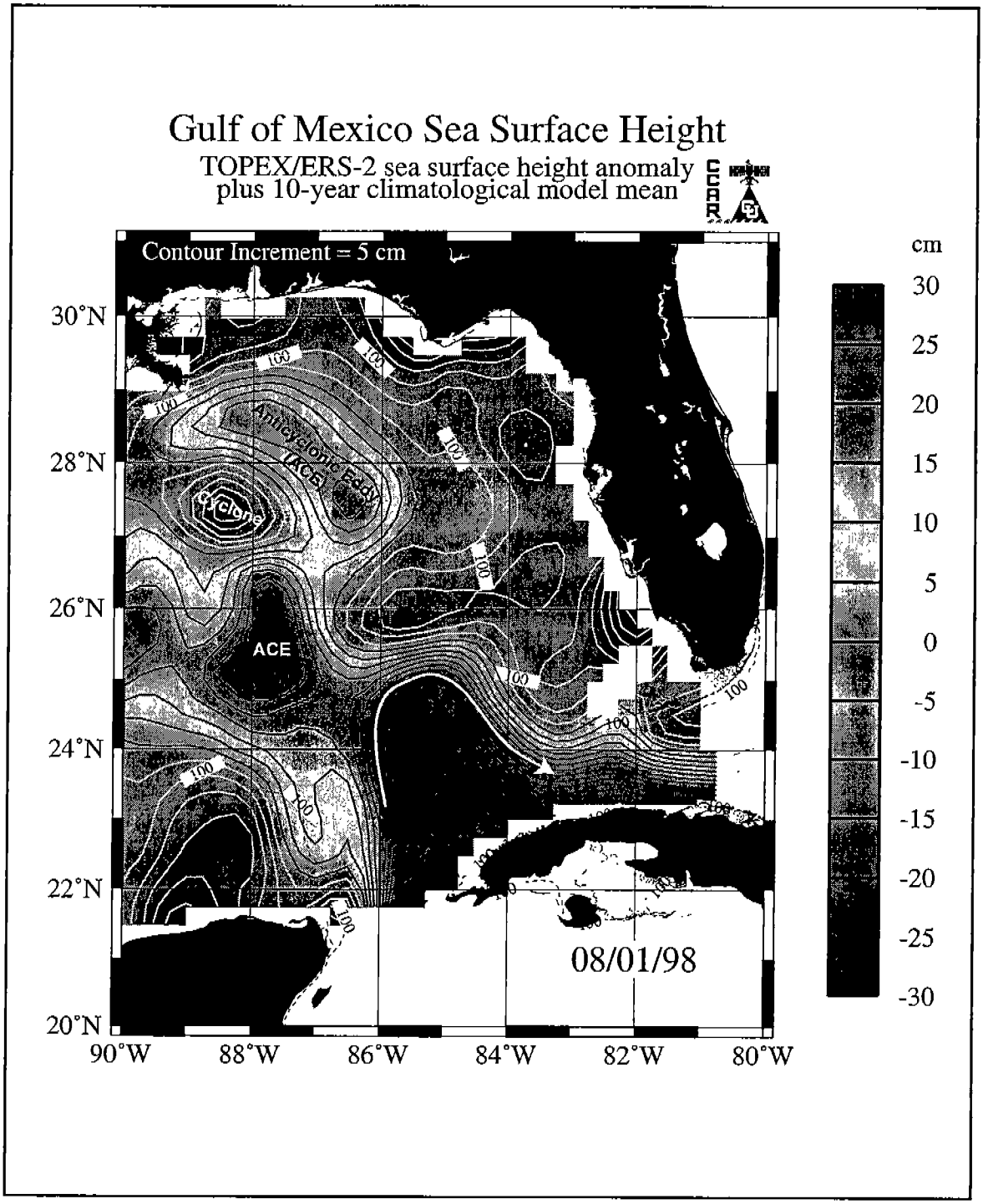

Figure 5.2-12a. SSH for August 1, 1998 derived from TOPEX/ERS-2 plus model mean. Dark contours are for SSHs that are greater than zero; white contours are for SSHs less than zero.

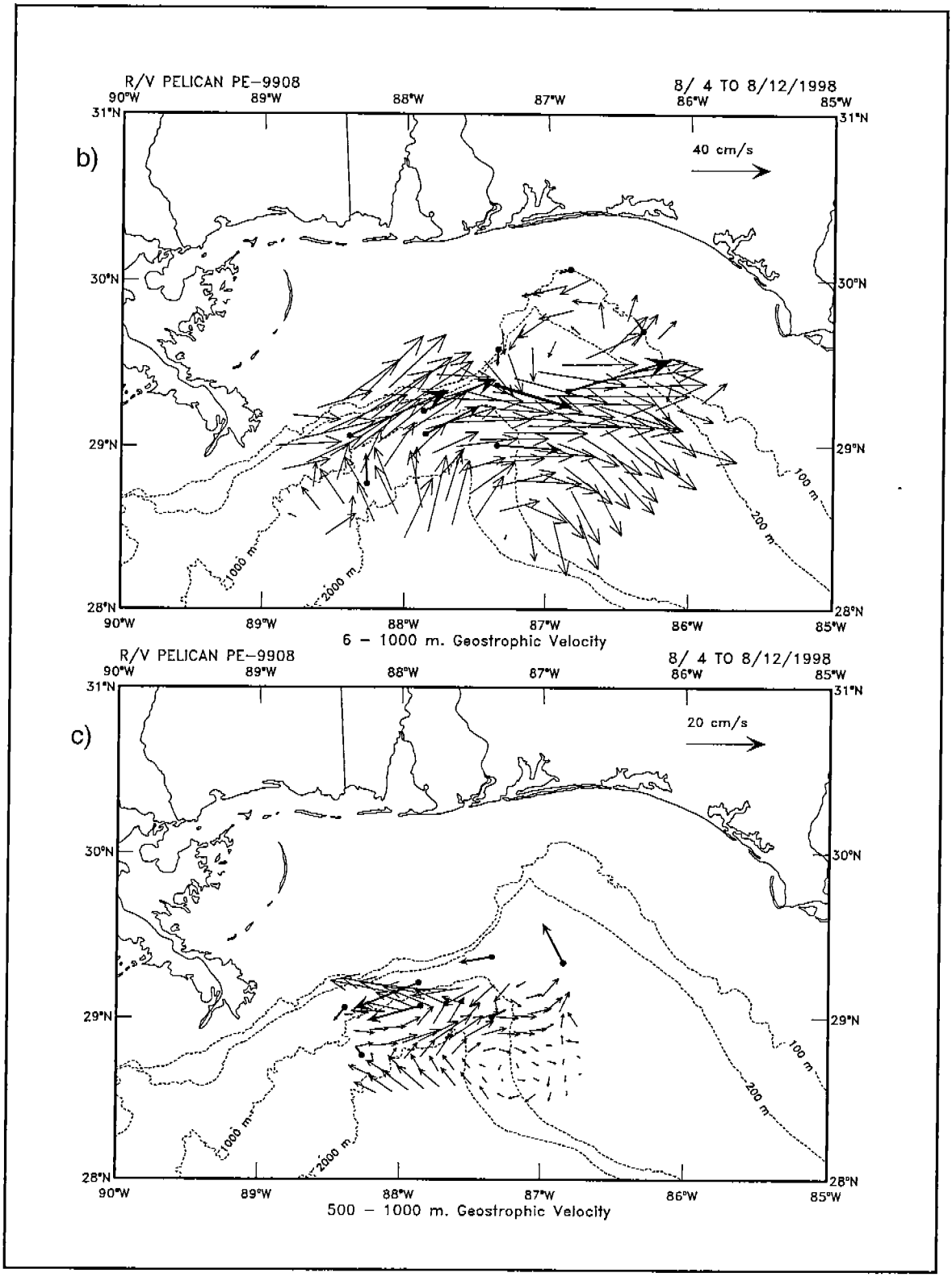

Figure 5.2-12b,c. Shipboard geostrophic currents for b) 6m depth and c) 500m depth, based on a level of no motion at 1000m for August 4-12, 1998. Heavier vectors represent currents measured at the mooring sites indicated by dots.

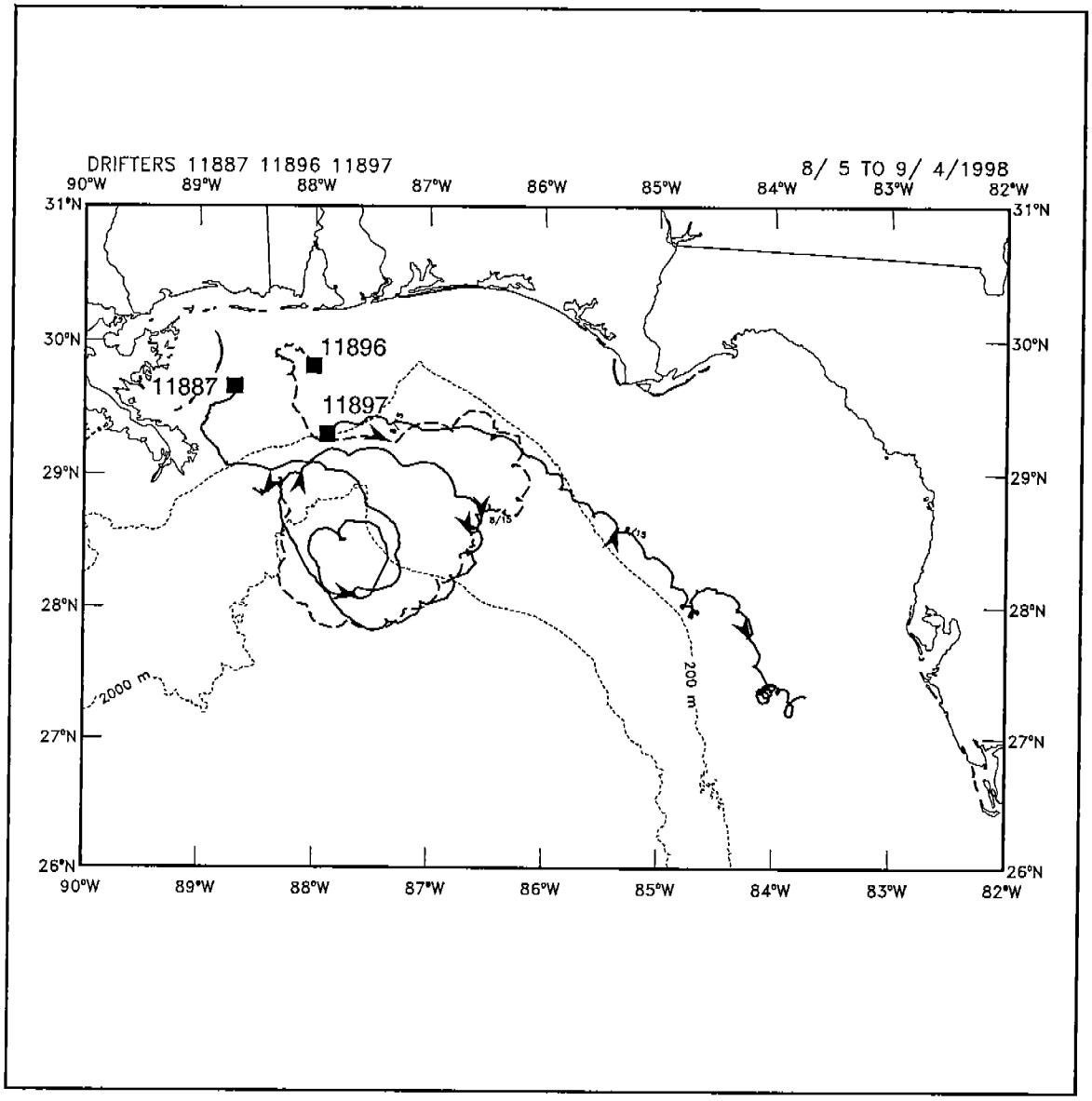

Figure 5.2-12d. Trajectories of satellite tracked near surface drifters 11887, 11896 and 11897 from August 5 – September 4, 1998. Arrow heads are placed every ten days of the plotted trajectories.

second half of Hurricane Georges, which could also have contributed to the westward flow at the shelf break.

Period 7: October 29, 1998 - January 15, 1999

During Period 7, flow was generally eastward over the upper 300m for most of the array (Figures 5.2-1d and -2d). The shelf break stations displayed more variability than offshore sites. This pattern may have been partly due to local wind forcing. Satellite SST imagery shows a warm 200 km scale eddy or remnant ring to the south of the array during this time that appears to have been influential in driving the eastward flow (Figure 5.2-13). The SSH and SST fields generally show similar ACE and LC patterns (Figure 5.2-14a). Shipboard derived geostrophic currents between December 1-9, 1998 show the strong eastward currents over the upper 500m of the slope (Figure 5.2-14b and -14c). A satellite tracked near surface drifter, launched near the head of the Desoto Canyon on November 21, was entrained by this warm eddy in mid-December off the middle of the west Florida shelf (Figure 5.2-14d). The drifter was carried around the eddy in a clockwise direction over the next several weeks and then moved back to the north into the eastern region of the array. This northward intrusion into the array appears to have been assisted with a warm streamer that extended into the array from a frontal eddy moving around the remnant ring. In March, the drifter moved back onshore close to the region where it was originally launched. A strong negative cross-shelf temperature gradient occured over the array with considerable small-scale structure indicating water mass interaction and cross-shelf exchange. The LC had begun to reform and extended northward to about 26.3°N just south of the warm eddy.

Period 8: January 15 - March 15, 1999

Period 8 was a somewhat confusing interval with variable flows over the array. At mooring A3, currents were eastward over the upper 500m for the whole period, whereas at the shelf break and mid-slope, the flow was more often toward the west although with occasional eastward flow (Figures 5.2-1d and -2d). Fortunately, there were many days with clear SST images during the period that helps explain the observed variability. Apparently, the warm eddy, mentioned above, continued to influence currents in the array and caused the persistent flow at A3 (Figure 5.2-15). A series of small (50-60 km) cyclonic eddies developed on the shoreward thermal front of the warm intrusion causing flow variability within the array. The LC extended north to about 26.7°N in late January, with a large frontal eddy centered near 26°N on its eastern border, trailing a filament into the region of the warm eddy. This pattern continued for most of February. By the end of February and early March the warm eddy moved to the southwest away from the array and caused strong offshore flow to the southeast at A3 (Figure 5.2-16a). Shipboard estimates of geostrophic currents for March 28 - April 5, 1999 also show generally offshore flow near the surface in the western half of the array with a cyclonic shelf eddy in the DeSoto Canyon that caused up-canyon flow (Figure 5.2-16b). Geostrophic currents at 300 and 500m depths were weaker and toward the west (Figure 5.2-16c). The LC extended to about 27°N at this time and apparently forced the

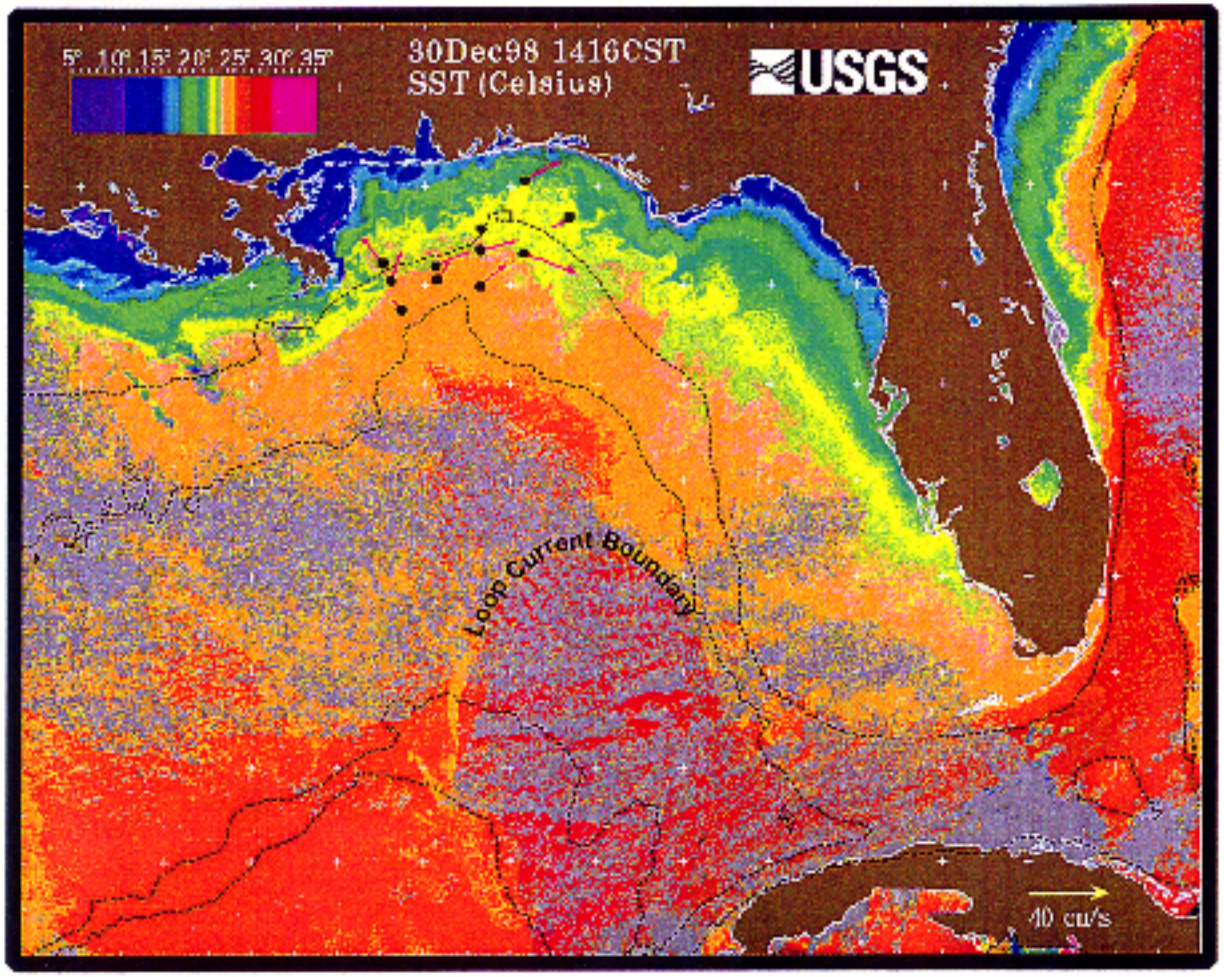

Figure 5.2-13. SST image for December 30, 1998 (1416 CST). Measured near surface current vectors are overlaid on this image. Note the LC is not extended very far to the north.

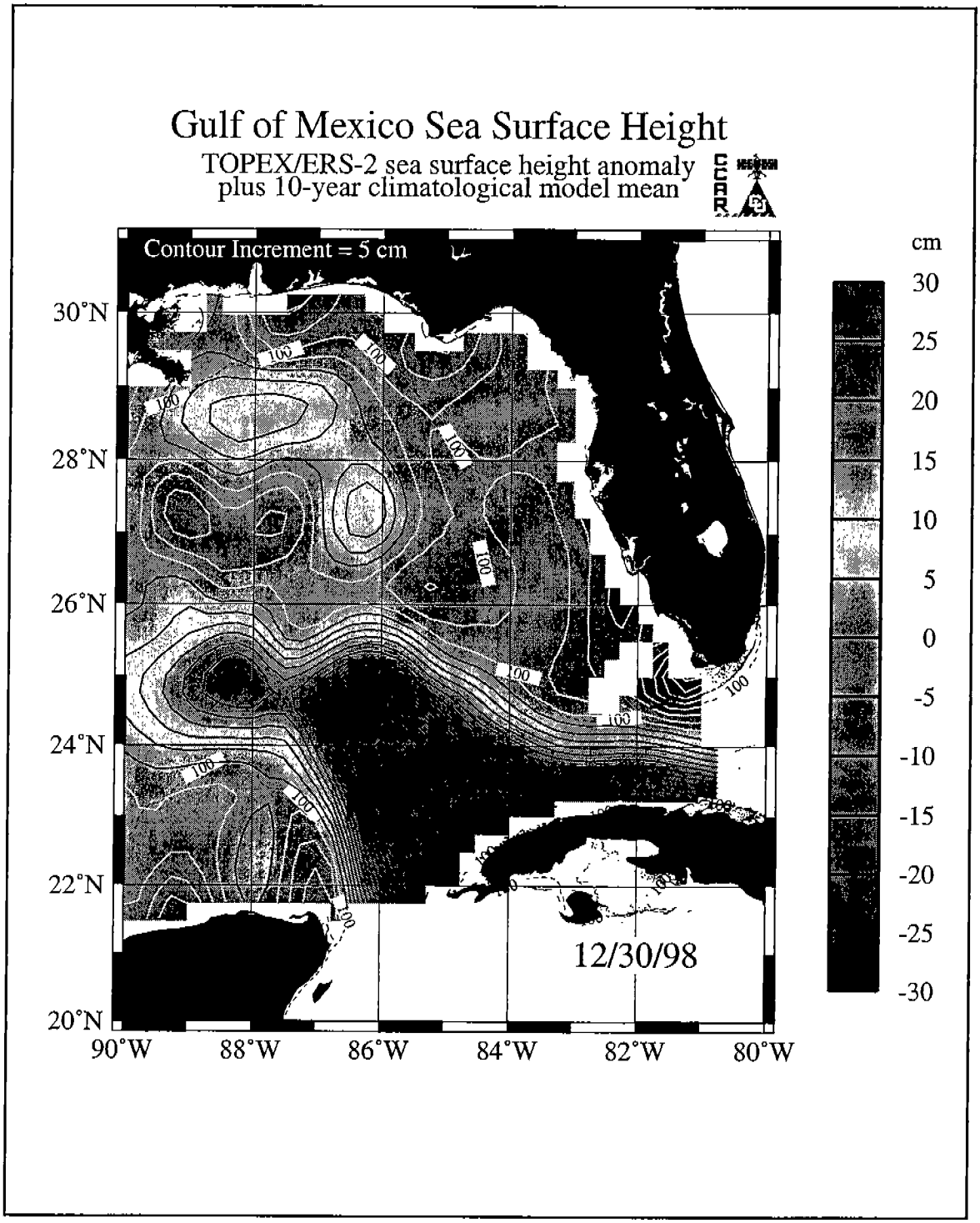

Figure 5.2-14a. SSH for December 30, 1998 derived from TOPEX/ERS-2 plus model mean. Dark contours are for SSHs that are greater than zero; white contours are for SSHs less than zero.

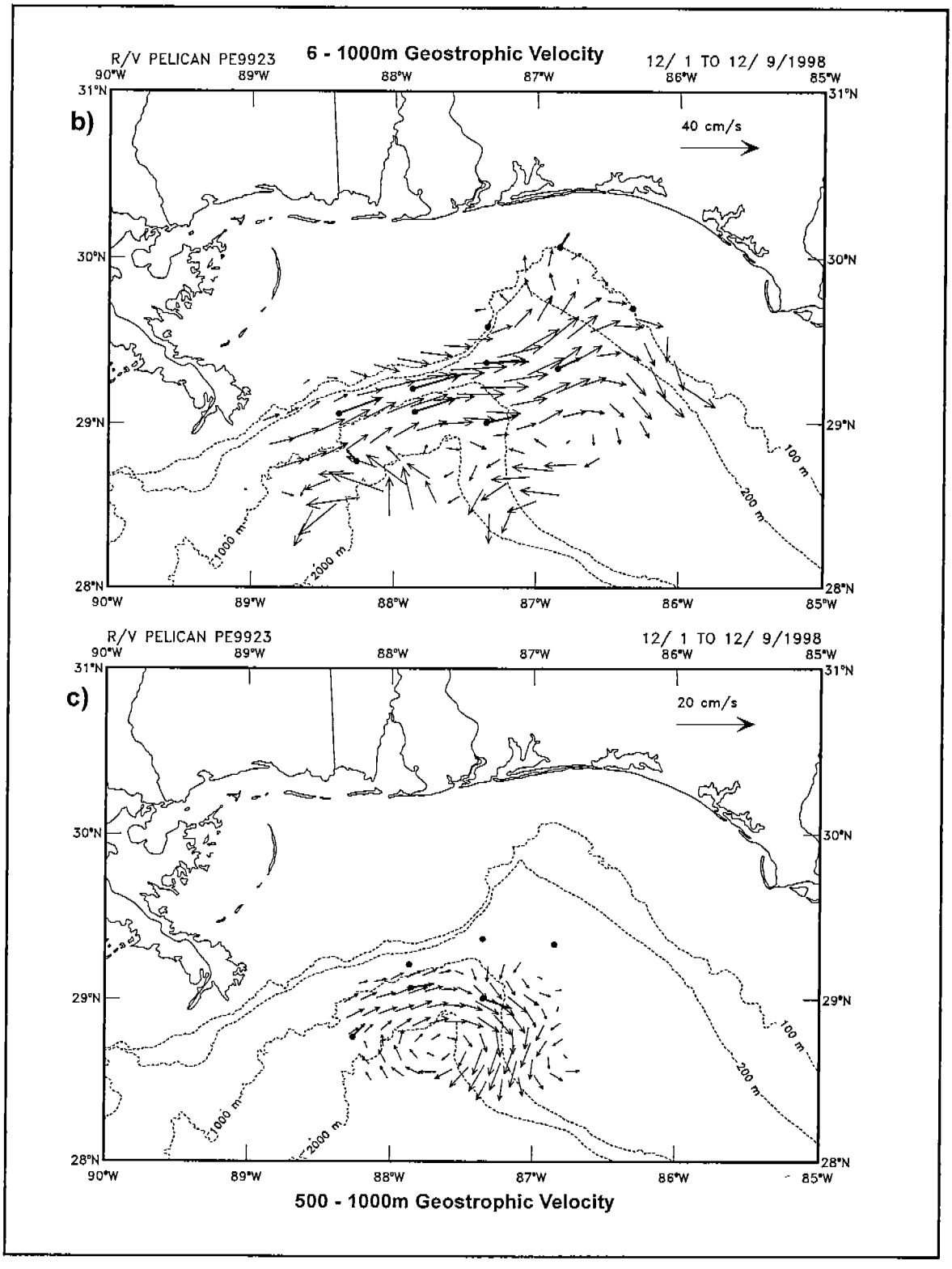

Figure 5.2-14b,c. Shipboard geostrophic currents for b) 6m depth and c) 500m depth, based on a level of no motion at 1000m for December 1-9, 1998. Heavier vectors represent currents measured at the mooring sites indicated by dots.

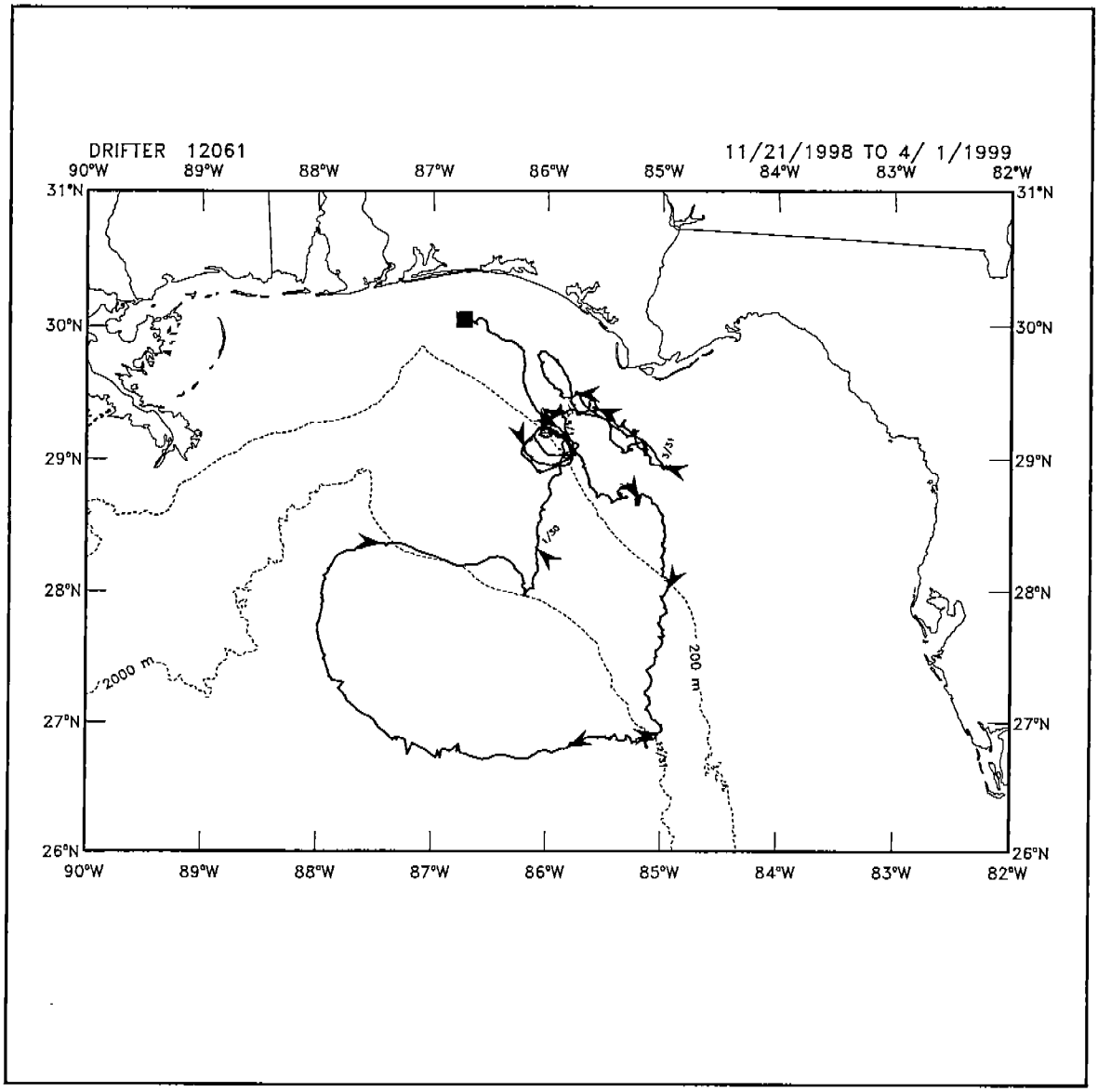

Figure 5.2-14d. Trajectories of satellite tracked near surface drifter 12061 from November 21, 1998 - April 1, 1999. Arrow heads are plotted at trajectory locations occuring every ten days.

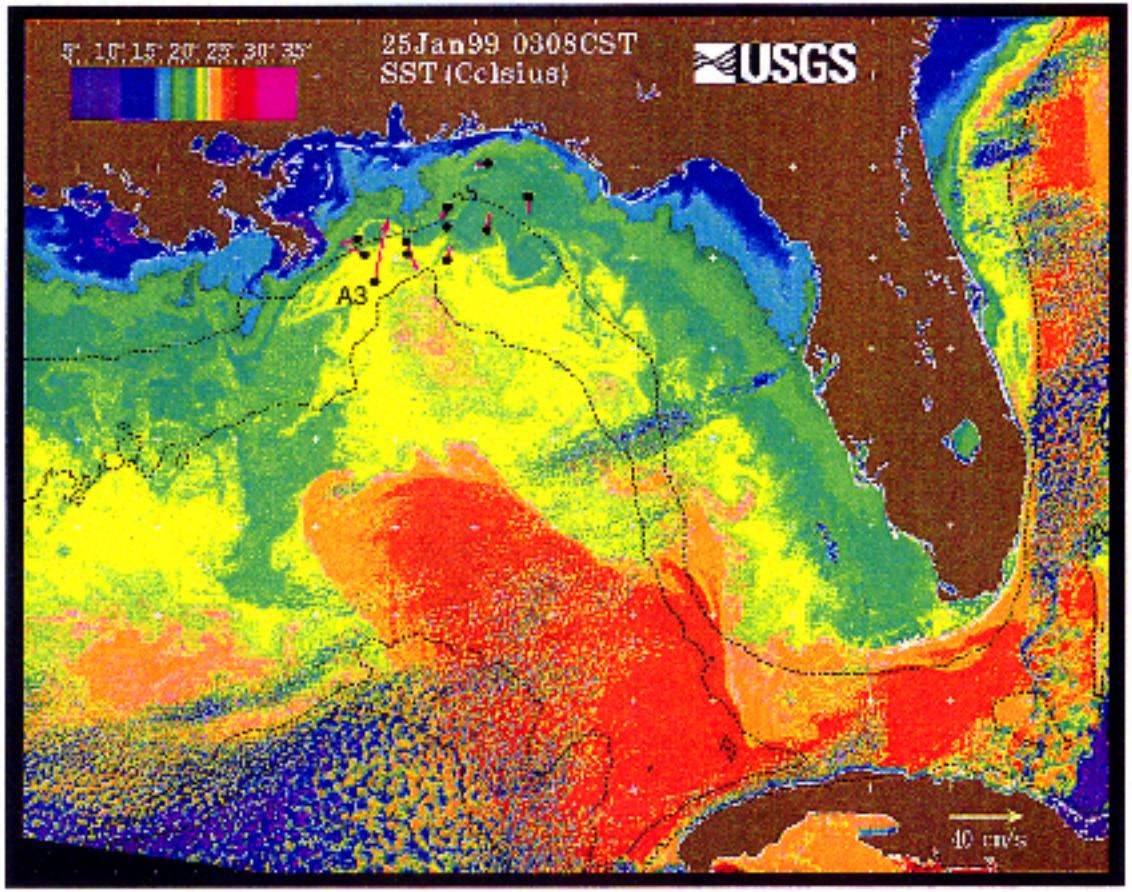

Figure 5.2-15. SST for January 25, 1999 at 0308CST derived from satellite AVHRR together with upper level currents from the moored array at the time of the image.

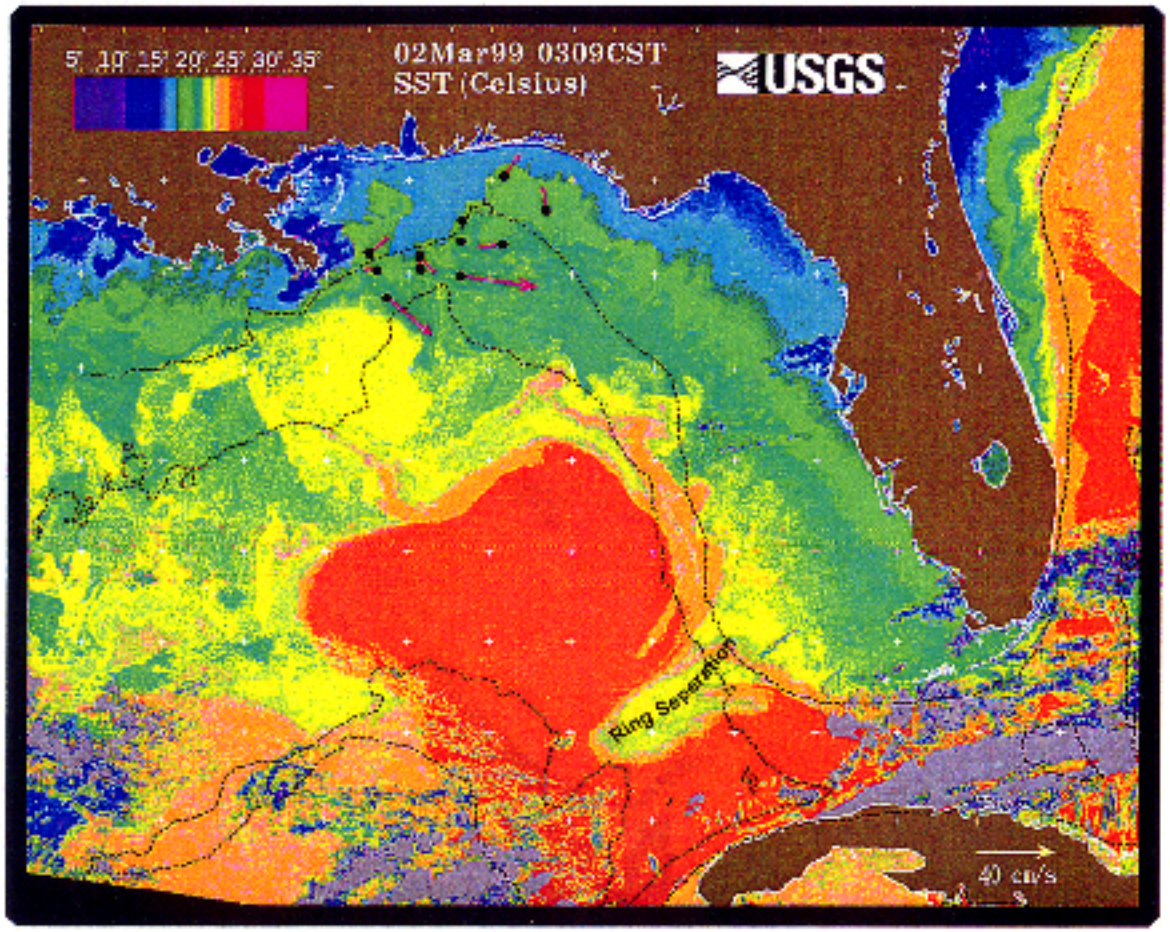

Figure 5.2-16a. Sea surface temperature image for March 2, 1999 (0309 CST). Measured near surface currents are superimposed on the image. A Loop Current ring appears to be separating, however, this configuration can occur without complete seperation actually occuring.

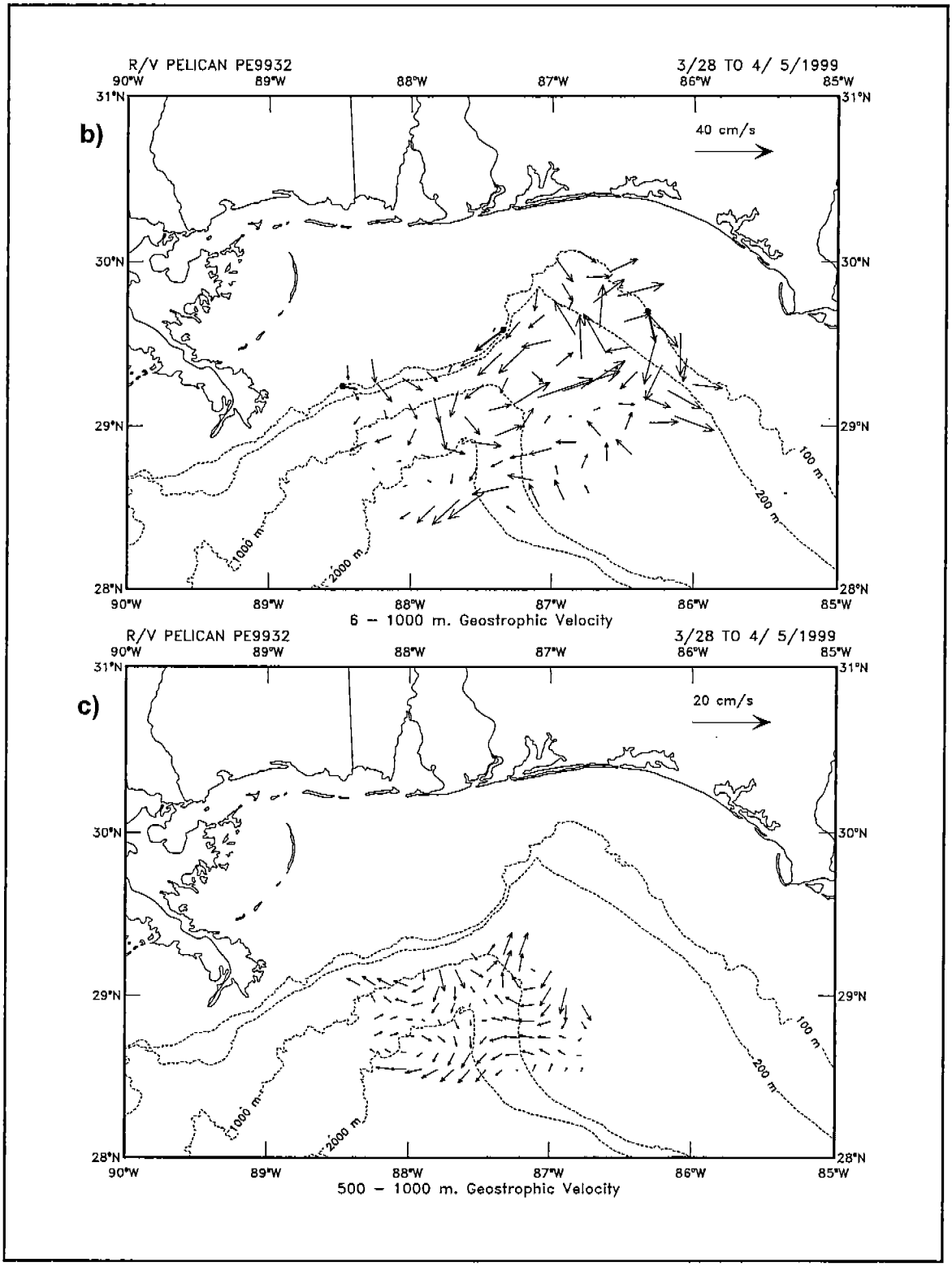

Figure 5.2-16b,c. Shipboard geostrophic currents for b) 6m depth and c) 500m depth, based on a level of no motion at 1000m for March 28 - April 6, 1999. Heavier vectors represent currents measured at the mooring sites indicated by dots.

warm eddy near the array to move westward to allow for further growth. Frontal eddies and streamers are obvious around the perimeter of the LC. A large frontal eddy was southwest of the Tortugas, appears to have had a role in the narrowing of the LC neck, which can be a forerunner of ring separation. Similar patterns of eddy structures and LC extension are shown by the SSH fields (Figures 5.2-17 and -18).

5.3 Loop Current Frontal Eddies

5.3.1 Background

Flow in the eastern Gulf of Mexico and southern Straits of Florida (SSF) is constrained by the configuration of the two broad shallow shelves, the Campeche Bank and the west Florida shelf (Figure 5.3-1). The Campeche Bank extends approximately 280 km north of the Yucatan Peninsula, bounding the flow entering the Gulf of Mexico through the Yucatan Channel. Likewise, the west Florida shelf steers the flow along the west coast of Florida. Both shelves are clearly marked by steep escarpments on their seaward edge, plunging to depths beyond 3000m in the central Gulf of Mexico. Sill depths in the Yucatan Channel, the channel connecting the Caribbean with the Gulf of Mexico, reach approximately 2000 m. The SSF is bounded on the north by the Florida Keys and on the south by the coast of Cuba. The width of the SSF decreases from 150 km at the western entrance to approximately 85 km near Cay Sal Bank, while water depths decrease from 2000 m at the western entrance to 800 m in the east.

Circulation in the eastern Gulf of Mexico is dominated by the LC, a portion of the Gulf Stream system that closes the subtropical gyre in the north Atlantic. Warm water flows from the Caribbean through the Yucatan Channel, where it is called the Yucatan Current, "loops" anticyclonically through the northeastern Gulf of Mexico, and exits through the SSF, where it becomes the Florida Current (FC). The LC penetrates into the northeastern Gulf of Mexico to varying degrees throughout the year, and occasionally an anticyclonic ring will separate from the LC [Leipper, 1970; Maul, 1977; Muller-Karger et al., 1991; Sturges, 1992; Sturges and Leben, 2000]. Typically, ring separation causes an abrupt southward retreat of the northern LC boundary and, consequently, the establishment of more direct flow between the Yucatan Channel and the SSF [Leipper, 1970; Ichiye et al.,1973; Hurlburt and Thompson,1980; Muller-Karger et al., 1991, see also Chapter 4 of this report]. After a ring separates, the LC may take several months to reestablish its anticyclonic circulation in the northeastern Gulf of Mexico. However, occasionally, anticyclonic rings with diameters less than 250 km separate from the LC and do not produce a significant change in the northern position of the LC boundary [Vukovich, 1995]. In this scenario the current still penetrates into the northeastern Gulf of Mexico, even after the ring has separated. The northward penetration of the LC has significant variability with a mean period around 12 months [Sturges and Leben, 2000].

Early observational programs in the Gulf of Mexico were primarily focused on quantifying the cycle of northward penetration and anticyclonic ring shedding by the LC. However, observations revealed a

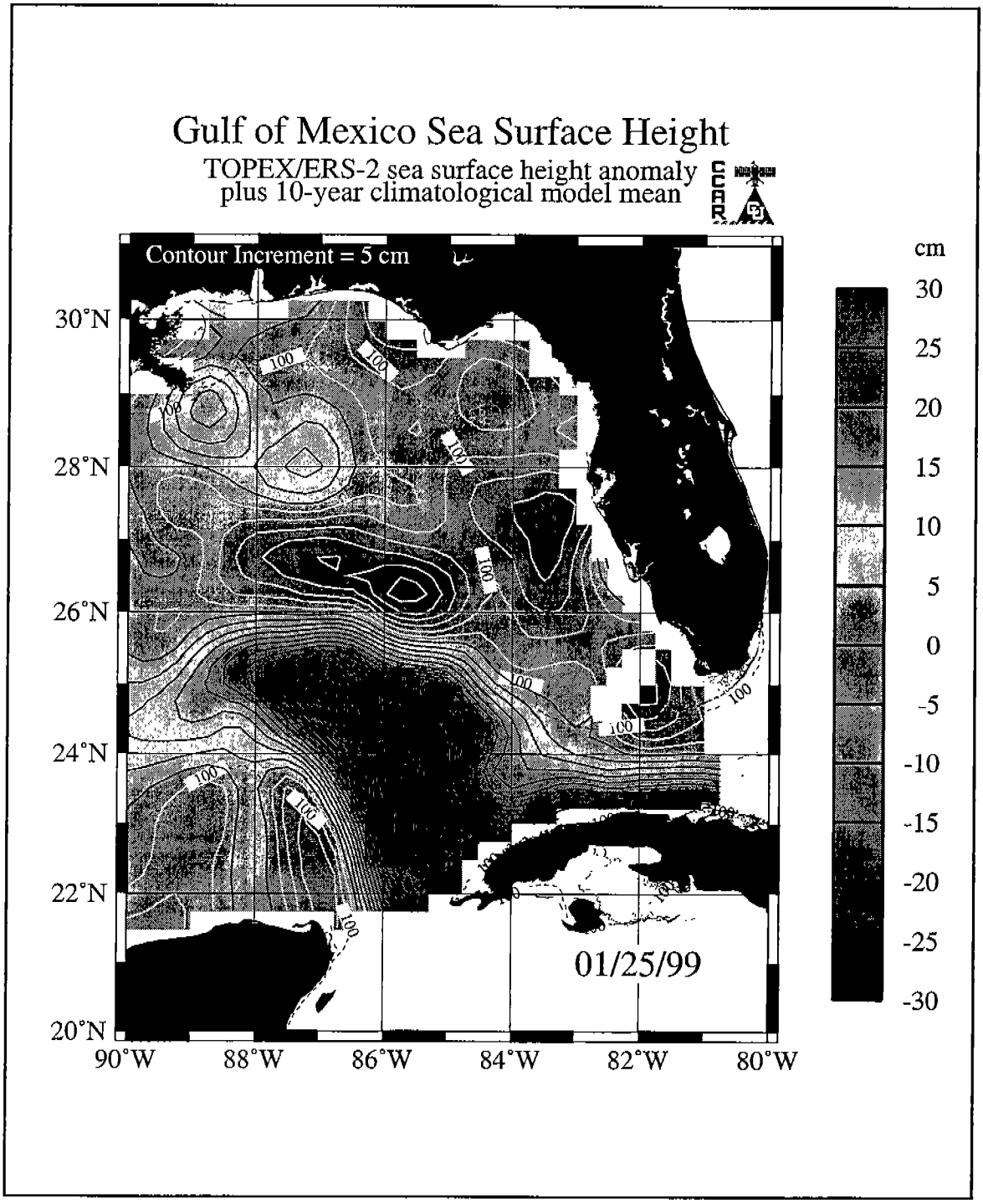

Figure 5.2-17. SSH for January 25, 1999 derived from TOPEX/ERS-2 plus model mean. Dark contours are for SSHs that are greater than zero; white contours are for SSHs less than zero.

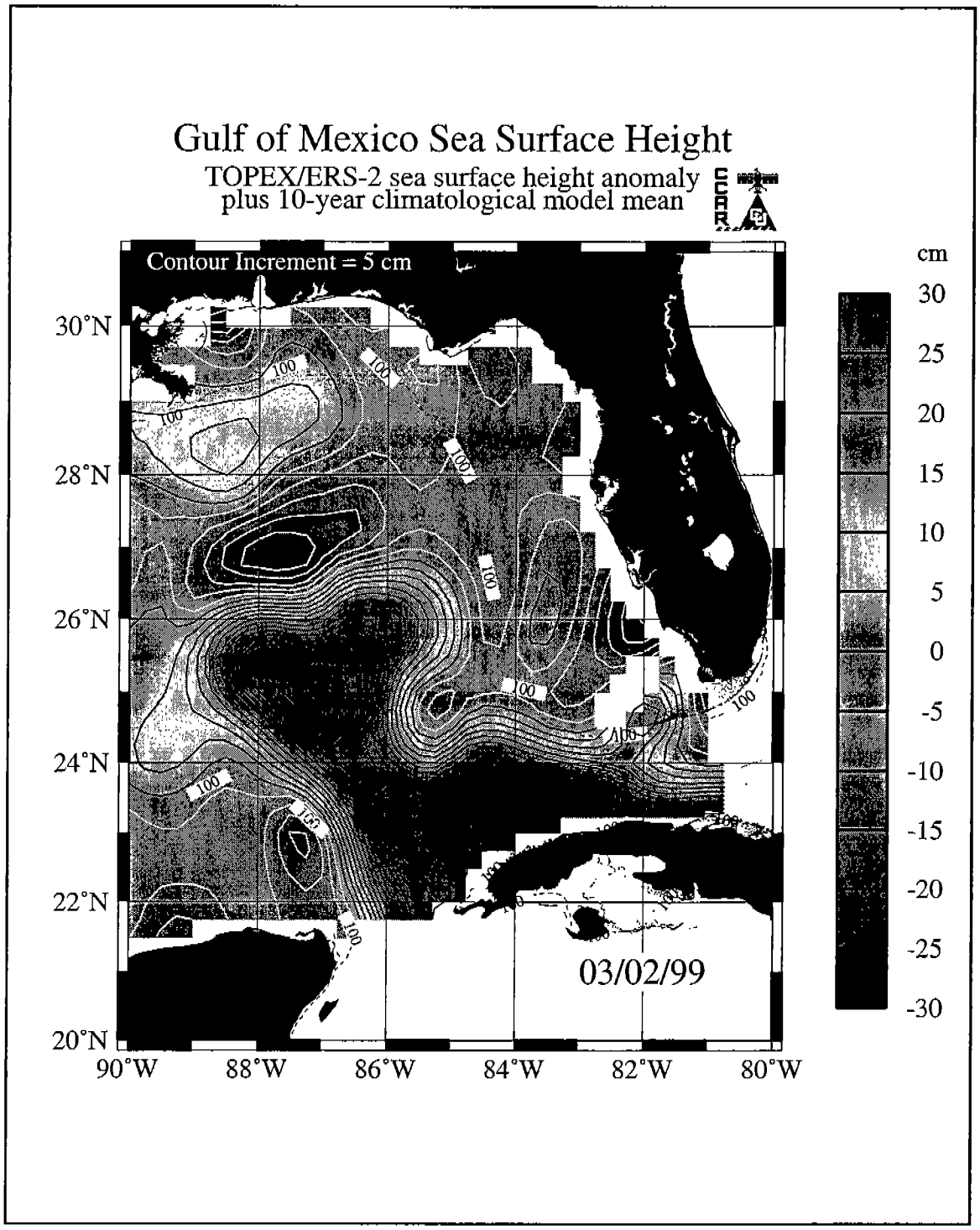

Figure 5.2-18. SSH for March 2, 1999 derived from TOPEX/ERS-2 plus model mean. Dark contours are for SSHs that are greater than zero; white contours are for SSHs less than zero.

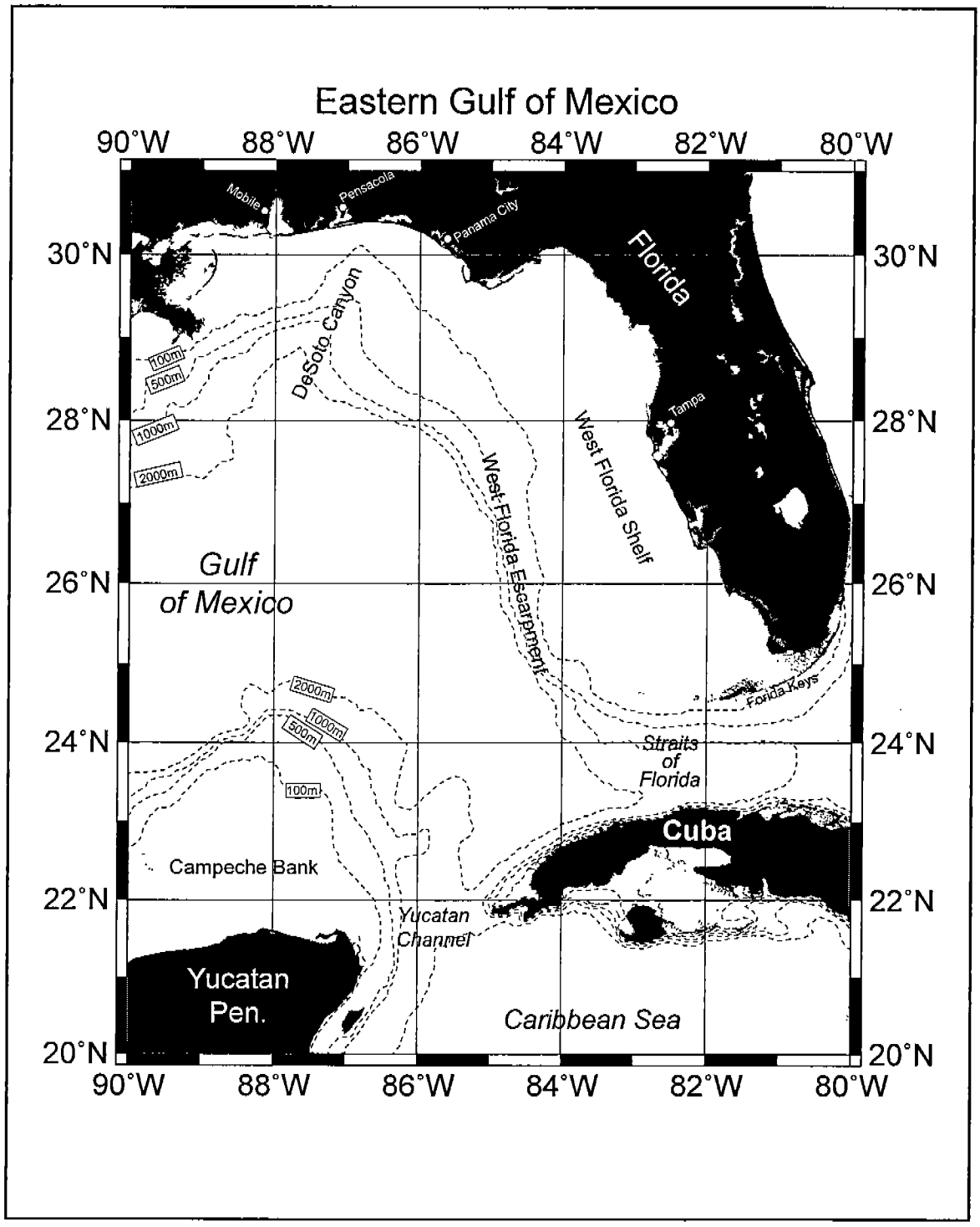

Figure 5.3-1. Bathymetry of the eastern Gulf of Mexico and southern Straits of Florida.

wide range of smaller-scale features that were related to the large-scale processes. For instance, Leipper [1970] investigated current patterns in the northeastern Gulf of Mexico and found meanders and eddies located along the northern and eastern edges of the LC. This led to the first evidence that anticyclonic ring shedding may be preceded by the westward propagation of cyclonic eddies across the Yucatan Channel [Cochrane, 1972]. Several investigators have presented hydrographic data showing a closed cyclonic feature near the Dry Tortugas, which occasionally appears during ring separation of a LC ring [Nowlin and McLellan, 1967; Molinari, 1977]. The dynamic height maps of Ichiye et al. [1973] in the northeastern Gulf show evidence of cyclonic eddies embedded in the edge of the LC just north of the Campeche Bank. No mention of the eddies is made by the authors, but they appear to have diameters of approximately 50-100 km.

Curiously, although the Gulf of Mexico and SSF are geographically and dynamically connected by the LC, previous studies concerning the mesoscale variability associated with each have remained independent. The most comprehensive studies of LC frontal eddies (LCFE's) and perturbations took place in the late 1970s to early 1980s with the studies of Maul [1977], Vukovich et al. [1979], Paluszkiewicz et al. [1983], and Vukovich and Maul [1985]. Vukovich and Maul [1985], combining more than 10 years of satellite infrared data and several years of coincident hydrographic measurements, identified large cold perturbations on the northern extreme of the LC that moved southward along the LC boundary, adjacent to the west Florida shelf. These meanders eventually grew into stationary meanders with closed cyclonic streamlines and cold cores near the Dry Tortugas. Upon reaching the SSF, they were observed in one of two possible configurations: A large southwestward oriented protrusion of cold water near the Dry Tortugas [e.g., Maul et al., 1984] or a cold tongue, bounded to the west by the southward flowing LC and to the east by a ridge of warm water extending over the west Florida shelf to as far north as 26°N [cf. Vukovich and Maul, 1985, Figure 2a]. The cold tongue and the cold meander events observed by Vukovich et al. [1979], Maul et al. [1984], and Vukovich and Maul [1985] always displayed the signatures of closed cyclonic circulation. Geostrophic estimates of velocities within the LCFE exceeded 100 cm/s on the LC side of the features where horizontal density gradients were maximized, while velocities reached 20 cm/s over the west Florida shelf. Diameters varied from 80 to 120 km, and subsurface signatures extended to 1000m [Vukovich and Maul, 1985]. Surprisingly, in 10 years of observations, the features were never observed moving into the SSF. Once the perturbations reached the Dry Tortugas, they either dissipated or grew westward across the width of the LC. Vukovich and Maul [1985] postulated that dissipation of LCFE may involve kinetic energy transfer to the mean flow, similar to the behavior of spin-off eddies described by Lee [1975] in the northern Straits of Florida. The lack of prior observations of such propagations may be an artifact due to aliasing of an imperfect sea surface temperature time series derived from early satellite images.

In a subsequent study, Vukovich [1988a] used a wave-staff technique on 5 years of infrared satellite data to quantify the boundary variations associated with the LCFE. Perturbations along the northward flowing limb

of the LC were 20-30 km near 25°N and grew to 90 km near 27°N, suggesting that perturbations generated at or entering through the Yucatan Channel grow as they propagate toward the northern section of the LC. The eddies observed by Maul et al. [1974] and Maul [1977], proposed to be generated by shear instabilities, and by Cochrane [1972], proposed to be a result of topographic vortex generation, were all of the order of 10-20 km. Two-layer model experiments generated cyclonic eddies downstream of the Yucatan Channel, east of the Campeche Bank [Hurlburt, 1986]. The model eddies were generated by baroclinic instabilities in the vicinity of the steep topography of Campeche Bank [Hurlburt, 1986].

To summarize, cyclonic eddies are common along the outer LC boundary, and observations have suggested that they may be important in the LC anticyclonic ring-shedding process. Model studies and observations suggest that these LCFE's form along the northward flowing branch of the LC and grow in an unstable manner as they propagate downstream along the frontal boundary. Recent studies (Fratantoni *et al.*, 1998) have shown that these eddies can continue around the Loop Current and enter the SSF where they have been termed Tortugas eddies (Lee *et al.*, 1995). Fratantoni *et al.* (1998) used AVHRR imagery to show that Tortugas eddies are LCFE's that become nearly stationary off the Dry Tortugas. Fratantoni also identified two modes of interaction of LCFE's with the Tortugas eddies: mode-1, a southward advancing LCFE forces the Tortugas eddy downstream into the Straits of Florida; and mode-2 the LCFE takes part in a ring separation without interaction with the Tortugas eddy which results in stationary Tortugas eddies for periods up to 140 days.

5.3.2 Influence of Loop Current Frontal Eddies on the Study Area

Due to their large spatial scales and rapid evolution LCFE are best observed with synoptic, satellite derived SST images. A good example is shown in Figure 5.2-8 for February 5, 1998. At that time there were three well-developed LCFE's visible in the image: one at the northern extreme of the Loop Current just south of the array; another at the northwest corner of the Loop; and a third over the outer part of the Campeche Bank. These eddies are identified by the warm streamers of LC water that wrapped cyclonically around and into their cold cores. There was also a fourth LCFE on the eastern side of the LC, somewhat hidden by the clouds, and a fifth LCFE southwest of the Tortugas that is participating in the narrowing of the LC neck that can be a forerunner of ring separation. As mentioned in the previous section, SSH fields are also useful in identifying LCFE and their filament structures. Typically, a LCFE will appear as a closed low near the boundary of the LC high. Comparison of LCFE signatures in same day SST and SSH fields show generally good agreement in location and size of features (Figures 5.2-6, -7, -10 and -11 are good examples). The warm filaments are generally shown as ridges wrapping around the closed lows.

Investigation of the evolution of LCFE from a succession of SST images, SSH fields and movies of the same, shows that these features travel around the LC at speeds of 2 to 24 km/d. It generally takes several months for a LCFE to travel completely around the LC from the Yucatan Channel to the southern Straits of Florida. However, the features can

shear apart before they accomplish the complete circuit around the LC. LCFE's are commonly observed to form along the outer edge of the Campeche Bank as the Yucatan Current enters the eastern Gulf of Mexico and perturbations of the flow are no longer constrained by topography. It is also possible for LCFE to form anywhere along the LC frontal zone. After formation they go through a rapid growth stage along the western and northern frontal boundaries of the LC reaching dimensions of 100 to 300 km in about one month. The decay stage of LCFE is indicated by the elongation of the warm streamers that trail in their wake. This often occurs along the eastern side of the LC where the LCFE's merge onto the steep escarpment of the west Florida shelf. Interestingly, the warm filaments trailing the LCFE's as they move off to the south are often observed to extend into the DeSoto Canyon moored array area.

Available SST and SSH imagery for the study area indicate that there were at least 12 LCFE's in the vicinity of the moored array during the study period, 11 of which either directly or indirectly influenced the observed flow and temperature variability. Table 5.3-1 summarizes the relevant information pertaining to each eddy as estimated from the evolution of SST and SSH fields. During the warm summer months (June - September) only SSH data were used due to the absence of surface thermal gradients. A more detailed description of these LCFE is provided in Appendix A.

Table 5.3-1. Characteristics of Loop Current frontal eddies (LCFE) that influence the study area as determined from satellite derived SST and SSH fields.

LCFE	Period Observed	Eddy Duration (Months)	Period of Influence on Study Area	Estimated Max. Size E-W x N-S (km)	Estimated Translation Speed (km/d)
1	1/1-8/15/97	3.8	3/21-7/14/97	300 x 200	5
2	7/1-10/15/97	1.8	7/14-9/9/97	270 x 140	4
3	8/10/97-1/15/98	5	9/9-12/15/97	110 x 75	12
4	12/6/97-2/10/98	2	12/19/97-2/1/98	140 x 60	17
5	1/11-2/25/98	1.5	2/5-2/18/98	130 x 75	17
6	1/16-3/25/98	2.3	3/1-3/24/98	280 x 140	20
7	2/5-3/14/98	1.3	No Influence Detected	110 x 55	24
8	3/4-6/1/98	2.9	3/16-5/1/98	300 x 245	2.4
9	3/23-6/15/98	2.8	5/1-6/24/98	110 x 110	10-16
10	7/1/98-2/1/99	8	7/7-9/1/98	200 x 200	Stationary
11	1/7-3/2/99	1.8	1/6-2/8/99	150 x 110	10
12	2/15-4/30/99	2.5	2/20-3/10/99	110 x 110	9

5.4 Characteristic Slope Circulation Patterns

5.4.1 Geostrophic Current Patterns

Data from hydrographic surveys during this project provide a basis for computing several high resolution snapshots of the upper layer circulation in the study area. Patterns observed during these cruises are similar to mean circulations obtained from the moored

instrumentation during a number of different periods (1 to 3 months long) of sustained flows as discussed in Section 5.4.4. Thus, the geostrophic flows, derived from the CTD surveys, reveal some of the details of the eddy field over the Northeastern Gulf of Mexico slope. Figure 5.4-1 and 5.4-2 show the near surface and 500m level geostrophic flows (relative to 1000 m) for each of the seven surveys. These geostrophic velocities compare well with the 5-day averaged, 40-HLP currents from the moorings, centered on the cruise periods, that are overlaid on the maps. The near-surface velocity maps show complex eddy circulations with diameters of order the width of the slope (~50 to 100 km). Smaller scale features may have been present on the upper slope and at the head of the canyon.

Five of the seven maps (Figures 5.4-1a,b,c,e & f) show predominantly eastward flows along the upper slope, south of Mobile Bay, apparently driven by the circulation features located offshore of the area. These eastward jet-like flows had differing configurations depending on the sense of rotation of circulation patterns further south. In March 1997 (Figure 5.4-1a), the eastward flow, south of Mobile, diverged from the shelf break to bypass the head of Desoto Canyon. A weak cyclone-anticyclone pair of small eddies occupied the canyon. A SST image for March 24, 1997 shows a streamer of cold shelf water that moved southeast along the northern edge of the jet as it turned away from the shelf break. The image shows two moderately-sized warm eddies centered at 28°N, 88.7°W (LC ring D - for "Deviant") and 28°N, 87°W, respectively. The survey documented the northern part of this latter circulation. The northern front of the LC was south of 26°N at that time. Similar circulations occurred during the November 1997 and August 1998 surveys (Figure 5.4-1c & e). In the former, the eastward flow turned sharply to the south at approximately 87°W. In the latter, the flow was driven by a vigorous anticyclone to the south, and the canyon circulation was cyclonic. According to the map of SSH, an elongated warm anomaly formed parallel to the west Florida escarpment in the wake of the detachment of ring F ("Fourchon" ~400 km diameter) from the LC in April 1998. This anomaly remained for most of the year and was probably a direct contributor to the strong anticyclonic flows observed in the August survey (see Sections 4.2.2 and 5.2).

The remaining two surveys that show eastward flows (Figures 5.4-1b & f) are similar in that the jet-like flow roughly followed the shelf break around to the eastern side of the canyon and, cyclonic flows were present over the deep water south of Mobile Bay. In July 1997, the cyclone and anticyclone on the west Florida slope appears to have generated strong flows toward the shelf break that enhanced flow around the head of the canyon. In December, however, the interaction of the deep water cyclone and a weaker west Florida slope anticyclone (Figure 5.4-1f) did not generate onshore flow that could transport warm salty water to the outer shelf.

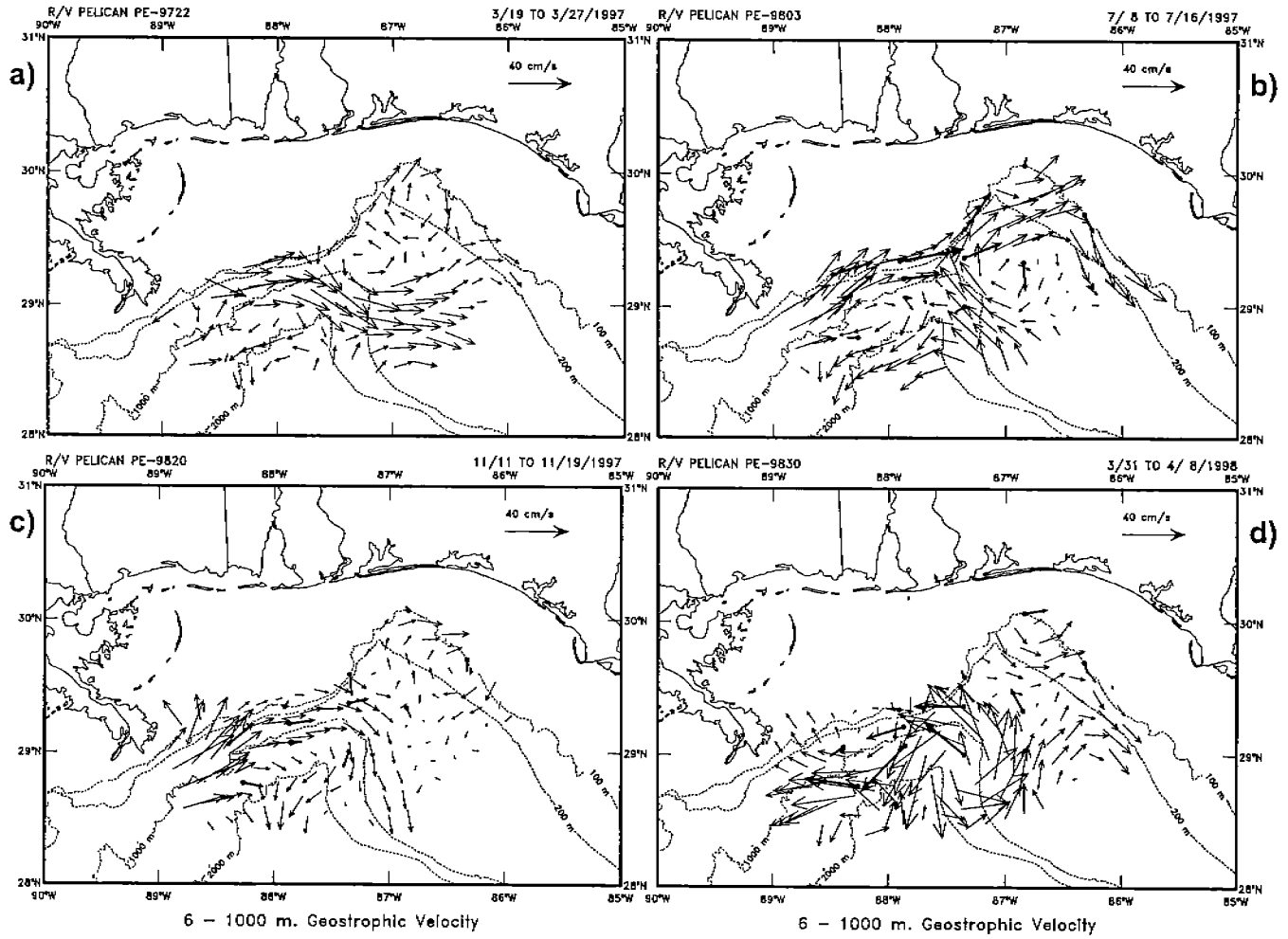

Figure 5.4-1. Geostrophic velocities at 6m depth from the hydrographic surveys. 5-day average velocity vectors (heavy arrows) from the 8m depth of the ADCP's are shown at stations marked with a dot.

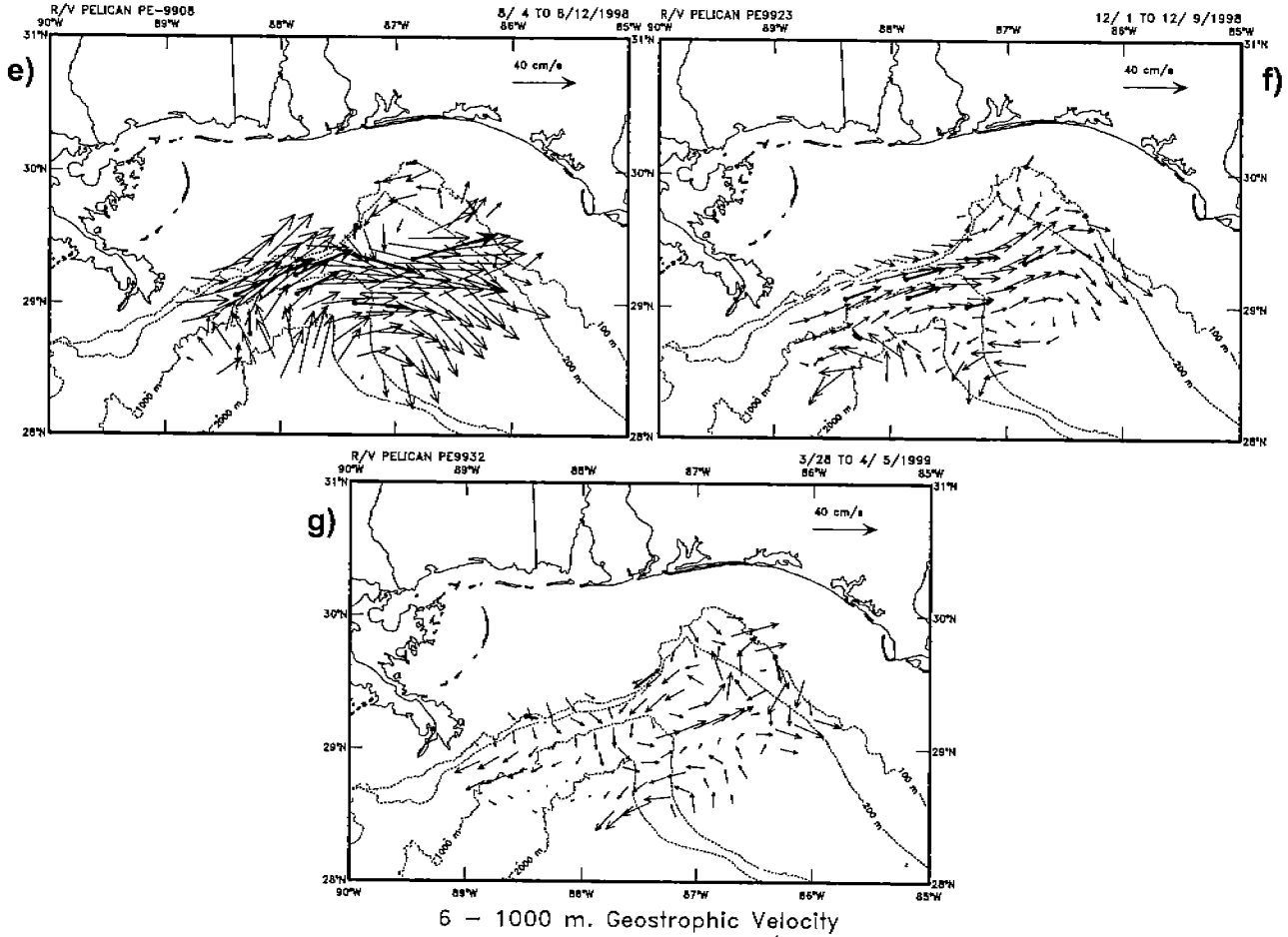

Figure 5.4-1(cont'd). Geostrophic velocities at 6m from the hydrographic surveys. 5-day average velocity vectors (heavy arrows) from the 8m depth of the ADCP's are shown at stations marked with a dot.

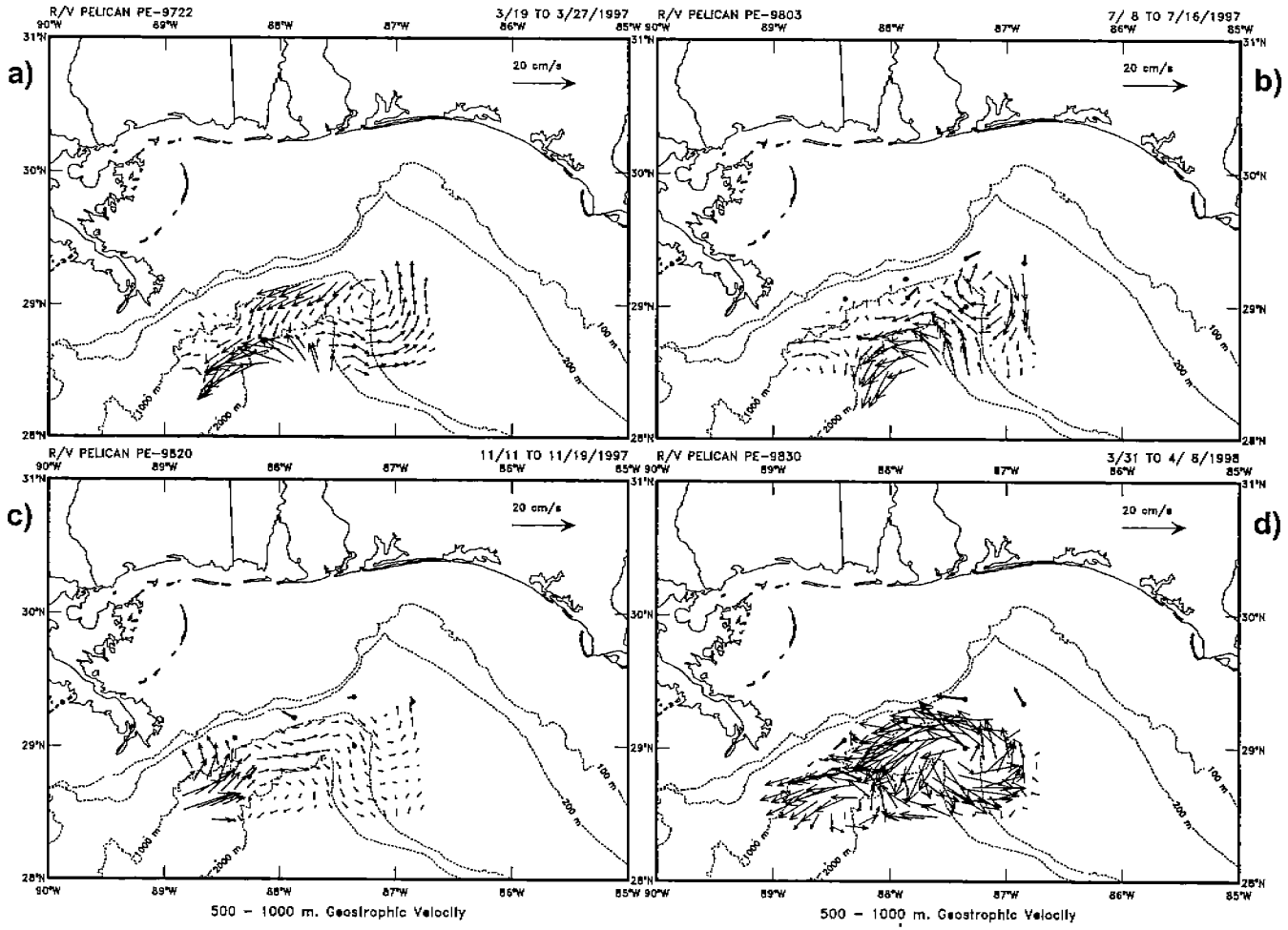

Figure 5.4-2 Geostrophic velocities at 500m from the hydrographic surveys. 5-day average velocity vectors (heavy arrows)from the 500m level current meters are shown at stations marked with a dot.

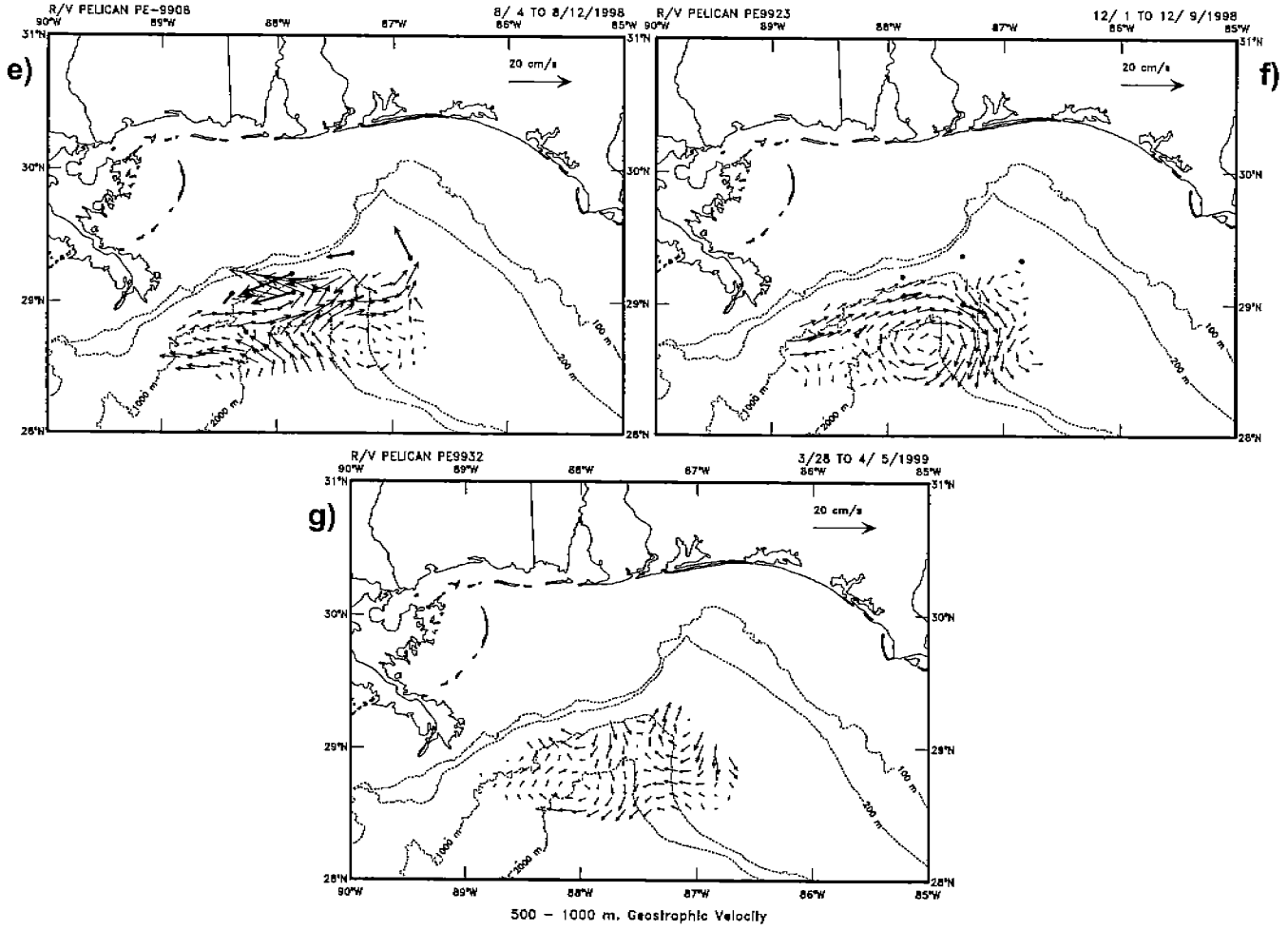

Figure 5.4-2(cont'd) Geostrophic velocities at 500m from the hydrographic surveys.(See previous figure for complete caption.)

The map from March 1998 (Figure 5.4-1d) shows flow to the west that is driven by a compact and vigorous slope cyclone in the center of the study area. There was another region of cyclonic flow to the west that appears in the altimetry as a cold frontal eddy on the northern periphery of ring F. Ring F was in the process of detaching from the LC. In the SST image for April 4 (16h CST) the two cyclones can be identified clearly. There was also an anticyclone over the west Florida slope that interacted with the cyclone to the west to promote onshore flow toward mooring C1. The March 1999 survey, however, shows a situation with weak, confused flows consisting of small scale cyclones and anticyclones along the upper slope on both sides of the canyon (Figure 5.4-1g).

The 500m geostrophic velocity maps (Figure 5.4-2) do not always have the currents flowing in the same direction as in the upper layer. A westward current in opposition to surface eastward flows was observed close to the Alabama slope (Figures 5.4-2a,c & e). In deeper water, the 500m level flows were often in the same direction as the surface flows. Examples are the westward cyclonic flows in March and July 1997, and March 1999 (Figures 5.4-2a, b & g). In other cases, the circulation at depth was similar to the near-surface flows across the slope. The two vigorous cyclones were observed at both levels in March 1998 (Figures 5.4-1d and 5.4-2d). The opposite case is found in December 1998 (Figures 5.4-1f and 5.4-2f) where slope flow to the east occurred at both levels. The 500m flows, however, turned south along the west Florida escarpment at a more westerly position than the near-surface jet. An important feature of all these 500m depth velocity maps is the presence of eddy motions with smaller length scales than at the surface. It is also noteworthy that the smaller scale eddies that were present at both depths, such as the canyon anticyclones in Figures 5.4-1a & b and 5.4-2a & b, had their centers displaced towards deeper water at the lower level. This was presumably the influence of the slope topography on the eddy circulations. The tilting of the vertical axis of peripheral eddies has been observed on the LATEX slope and attributed to the interaction of the smaller eddy with the larger (Berger et al., 1996; Hamilton et al., 2000).

Perhaps the clearest picture of the generation of a westward slope countercurrent at depth are shown in maps for August 1998 (Figures 5.4-1e and 5.4-2e). The anticyclonic flow over the canyon was observed at both depths. At the surface, the flow turned south. At depth, the flow was blocked by the eastern side of the canyon and turned north and joined a cyclonic circulation which then fed a countercurrent along the slope. The westward flowing countercurrent seems to have become entrained into the anticyclone south of the Mississippi Delta that was observed in the southwest corner of the study area. A similar circulation pattern was also observed in March 1997 (Figures 5.4-1a and 5.4-2a)

The depth dependence of the slope flow patterns is illustrated in Figure 5.4-3 where the geostrophic velocity component parallel to the isobaths is contoured for section B. This section, due south of Mobile Bay, often crossed the jet-like flows, discussed above, and extended into offshore waters deeper than 2000m. Observations from March 1997 and

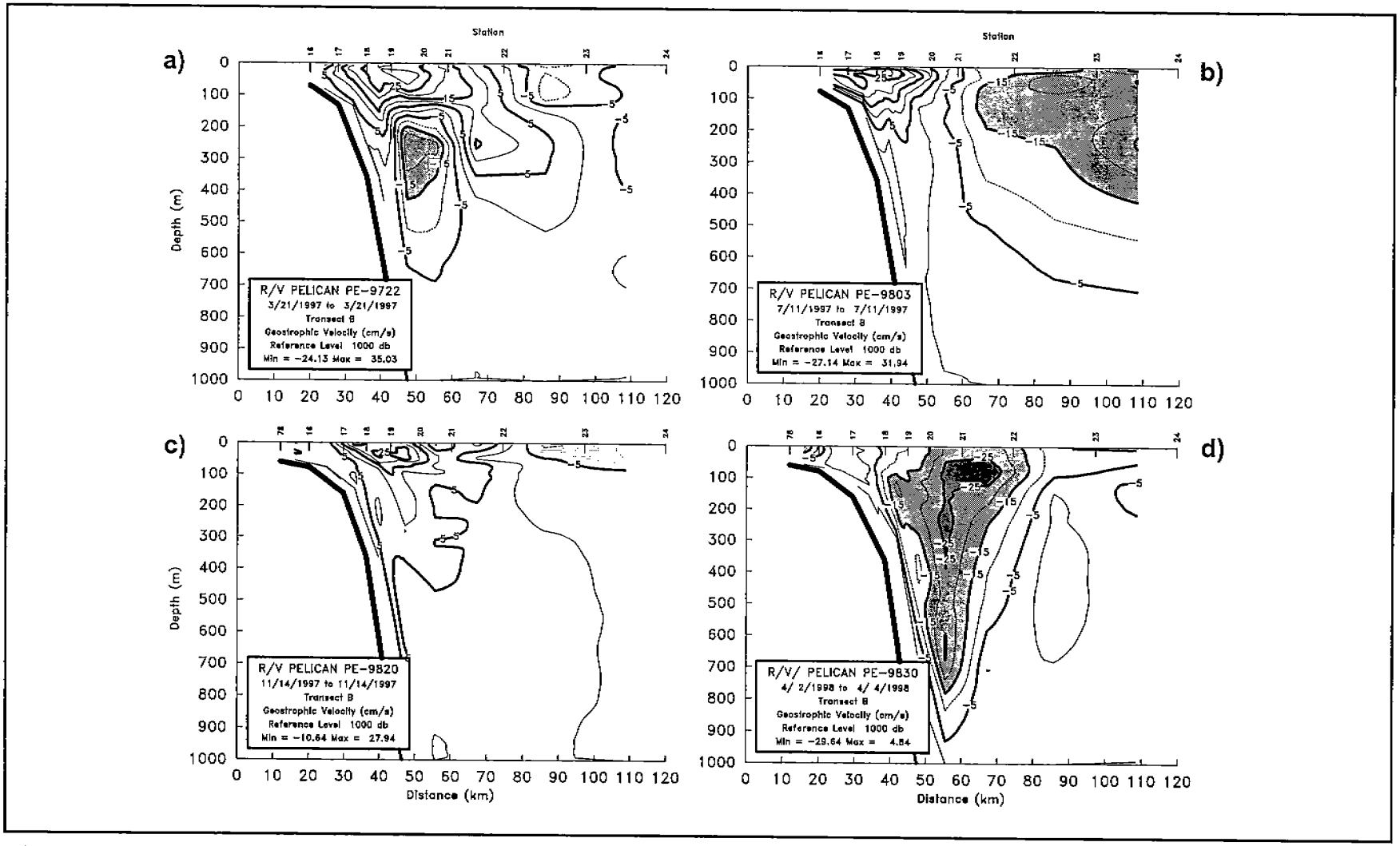

Figure 5.4-3 Geostrophic velocities on Section B for the indicated surveys. Positive velocities are eastward, normal to the section. Higher westward (negative) velocities are shaded. The bold line on the left of each section indicates the depth of the local bottom.

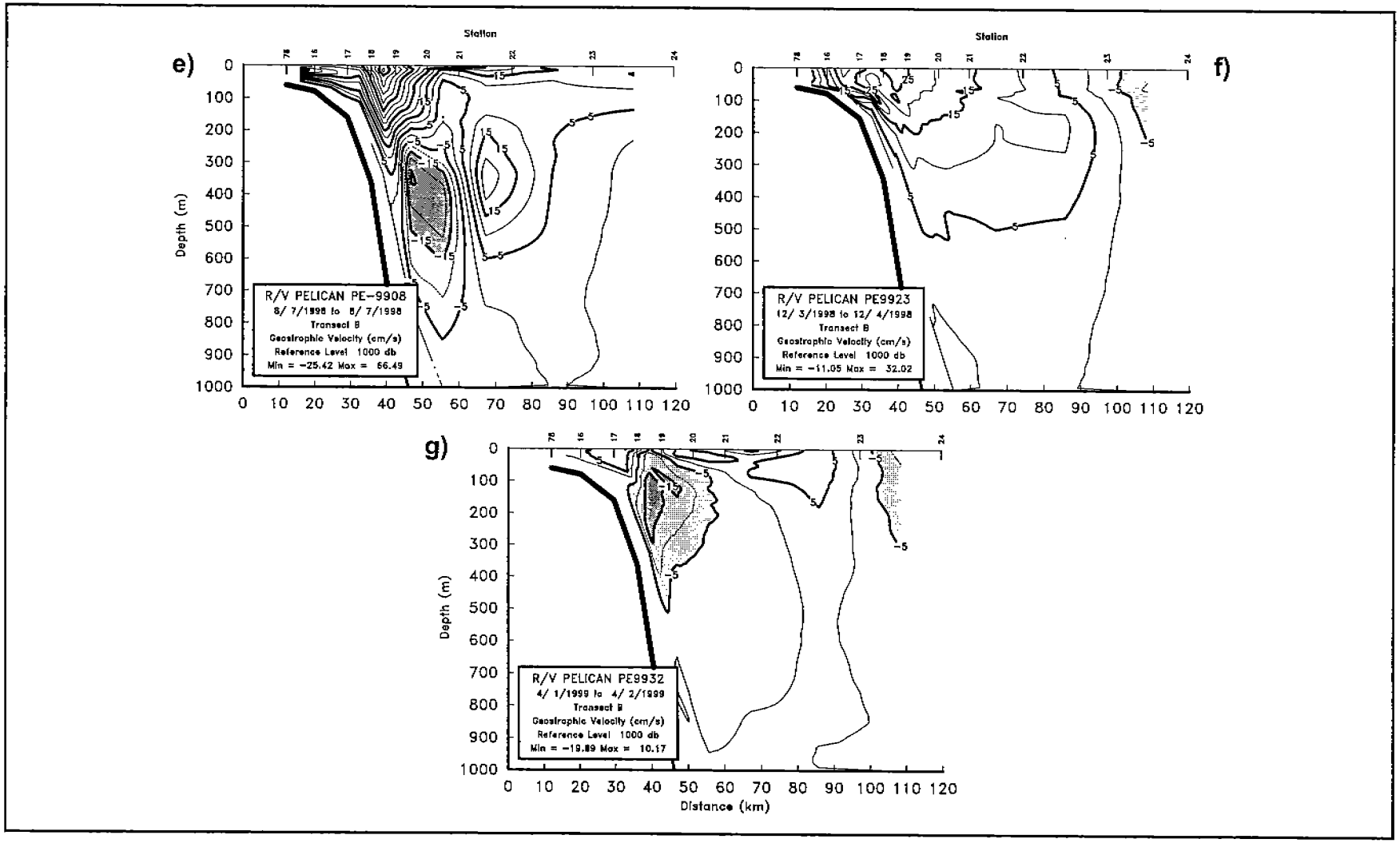

Figure 5.4-3(cont'd) Geostrophic velocities on Section B for the indicated surveys. Positive velocities are eastward, normal to the section. Higher westward velocities are shaded. The bold line on the left of each section indicates the depth of the local bottom.

August 1998 (Figures 5.4-3a & e) most clearly show the surface jet and the slope counter current below 200 to 300m. The core of the westward flow was at a depth of about 300 and 400m and had a vertical extent of 500 to 600m for March 1997 and August 1998, respectively. Further offshore the observed eastward flow had a subsurface maximum at a depth similar to the maximum westward flow, that was part of the deeper cyclonic flow discussed above. The last survey in April 1999 (Figure 5.4-3g) documented a weak two-layer structure with the westward current maximum at the shallow depth of 200m. Similarly, a two-layer structure is suggested for November 1997 by the mean, westward current velocity vectors at 500m in Figure 5.4-2c that occurred close to the slope but were missed by the geostrophic calculations (Figure 5.4-3c).

In contrast, the purely cyclonic and anticyclonic cases (Figures 5.4-3d & f, respectively) showed no reversals with depth. The velocity maximum, over the upper slope, was near-surface and eastward for the anticyclone, and subsurface, at about 100m, and westward for the cyclone as expected for these type of eddies. The July 1997 section (Figure 5.4-3b) seems similar, showing eastward and westward flows over the slope. However, the eastward upper slope jet was separate from the westward flow offshore. The latter resulted from the northern part of an offshore cyclonic eddy as Figure 5.4-1b makes clear.

The description of the geostrophic flows indicates that an eastward near-surface, jet-like flow often occurred along the upper slope offshore of Mississippi and Alabama. Further east on the slope this flow took various paths, including following the canyon rim, depending on the configuration of the eddies. This jet-like flow was sometimes accompanied by a westward countercurrent at depth. The depth of the countercurrent seems to have varied with different circulation patterns. However, it generally coincided with the occurrence of a small-scale cyclonic circulation at depth over the west Florida escarpment. The upper slope jet was often opposed by westward flows over deep water that were caused by cyclonic eddies related to the LC or LC ring fronts (see Section 5.2). In other situations, the circulation was dominated by one or more cyclones or anticyclones that occupied the slope. In these cases the direction of flow at the shelf break was controlled by these eddies.

Consequences of these circulation patterns included the transport of low salinity water from the shelf to the slope, and the transport of warm, salty offshore water toward the shelf break. Figure 5.4-4a shows the near-surface salinity for July 1997. The eastward shelf break flow (Figure 5.4-1b), assisted by eastward flow on the shelf that was driven by the prevailing westerly winds, distributed brackish water from the Mississippi delta along the canyon rim. This could be an important mechanism by which nutrient-laden, river-derived water was input to the shelf on the east side of the canyon. There are no major river discharges into the shelf on the east side of the DeSoto Canyon. The northward flow between the two counter rotating eddies (Figure 5.4-1b) caused a warm salty intrusion to approach the shelf break.

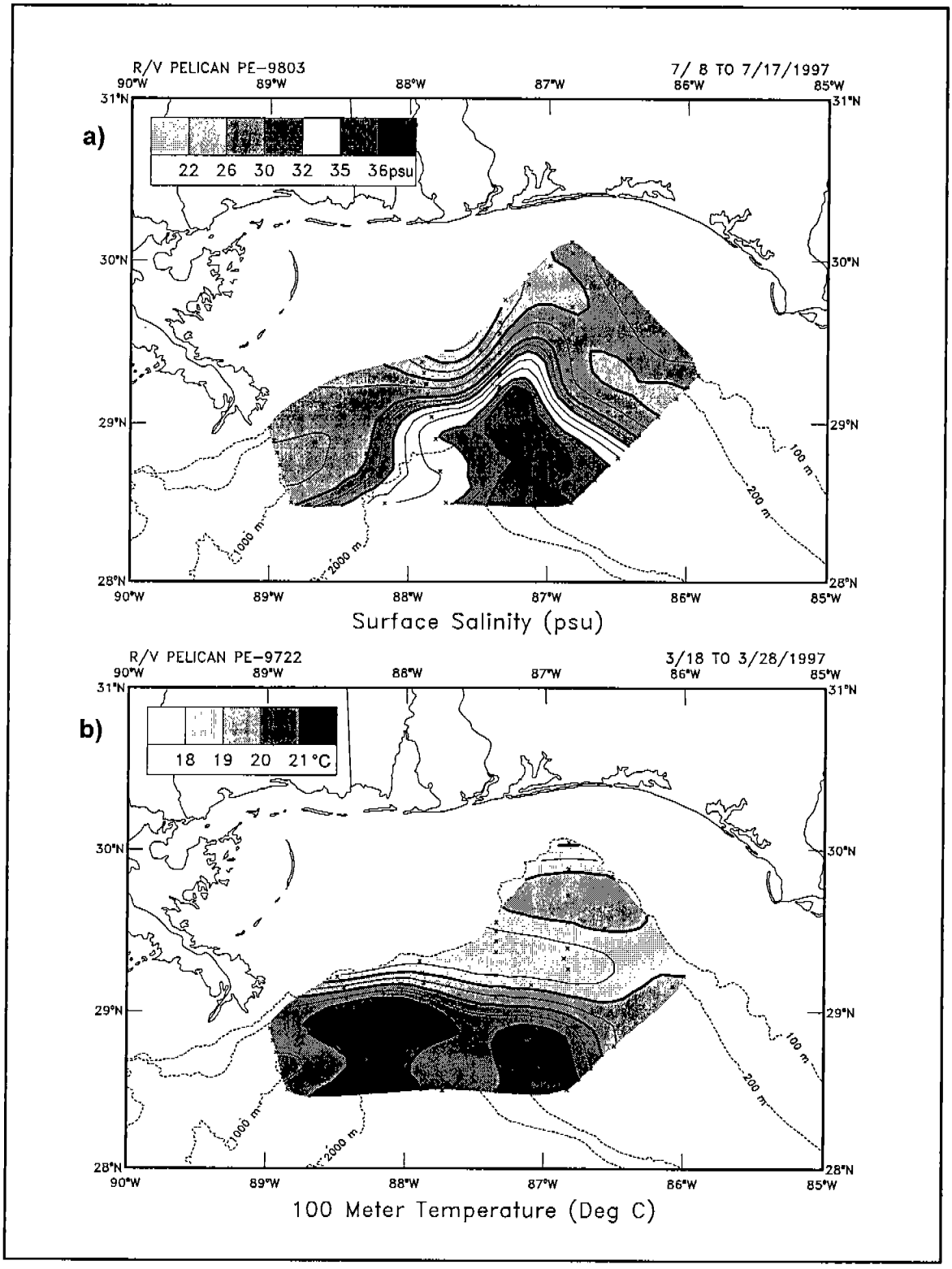

Figure 5.4-4 (a) surface salinity from July 1997 (PE-9803), and (b) temperature at 100m from March 1997 (Cruise PE-9722).

The eastward flow that prevailed along the shelf break in the western portion the study area, and the occurrence of small scale anticyclones around the head of the canyon, caused isotherms to be upwelled over the upper slope. Figure 5.4-4b shows contours of the temperature at 100m for the March 1997 survey. Figure 5.4-1a gives the surface velocity vectors. Cooler water was present on the northern edge of the eastward current that, in this case, bypassed the canyon head. However, the small anticyclone in the canyon also raised the isotherms to produce water colder than 18°C.

5.4.2 Long Period Events

Snapshots of the slope circulation raise questions on the persistence of various flow patterns and their frequency of occurrence. This section examines the moored data in order to derive some characteristic time scales and select appropriate periods for the calculation of useful mean flow patterns. The emphasis is on flows that have some degree of persistence over periods of a few months with higher frequency motions being discussed in later sections.

The middle slope (500m) moorings were the most heavily instrumented and allow both the temperature and velocity structure to be documented for the upper 300m of the water column. Figure 5.4-5 shows the 7-day low pass (DLP) temperature and velocity profiles at C2 over the entire two years of the study. The records from the 500m moorings at C2 are similar to the data from the other three 500m moorings. During the study, three periods appear to have had sustained flows to the east or west, or both at different depths. The isotherms at different depths had similar displacements indicating that the whole of the upper water column warmed and cooled in response to the advection of the barotropic flows. A small amount of seasonal warming and cooling was evident at the 62m level. It is noted that the first year of the study (March 1987 - March 1998) was cooler than the second year when the mean depth of the 15°C isotherm was about 50m deeper. The difference in the flows is that eastward, upper layer currents predominated in the first year whereas more sustained episodes of westward flow occurred in the second year. Generally, eastward and westward flow events raised and lowered the 15°C isotherm, respectively. Presumably, the cyclonic flow episodes were effective in advecting warmer water from the deep eastern basin to the northeastern slope.

As shown in Figure 5.4-5 the first period of sustained flows occurred in the summer of 1997 (S97 in Figure 5.4-5) with eastward flow above 200m and weaker westward currents at depth. The July 1997 survey occurred in the middle of this period (Figures 5.4-1b and 5.4-2b) and documented westward flow further offshore resulting from the northern edge of a cyclone. The means and standard deviations (plotted as ellipses) are given for this period in Figure 5.4-6. The 15m and 70m levels show eastward flow following the trend of the upper slope isobaths with westward flow further offshore. The mean currents at A3, B3 and C3 indicate that some of this westward flow was being entrained into the upper slope jet. At depths of 200, 300 and 500m the flow was westward with the 300m level giving the maximum mean currents of ~10 cm/s. The 500m mean flows (Figure 5.4-6c) should be compared with Figures 5.4-2a,

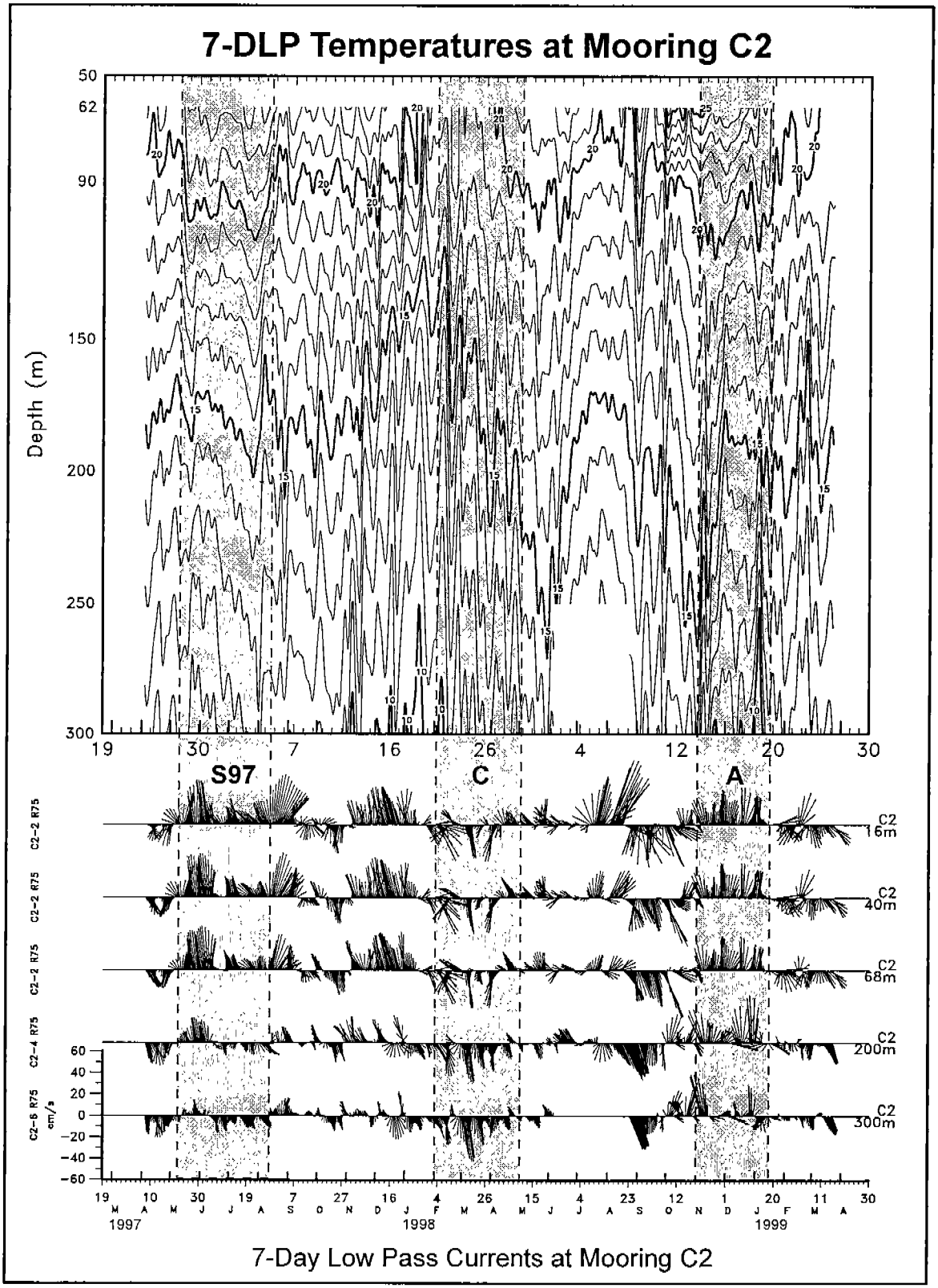

Figure 5.4-5 Seven-DLP current vectors and isotherm depths for the upper 300m of C2. Vertically upward vectors are directed along isobath with an easterly component.

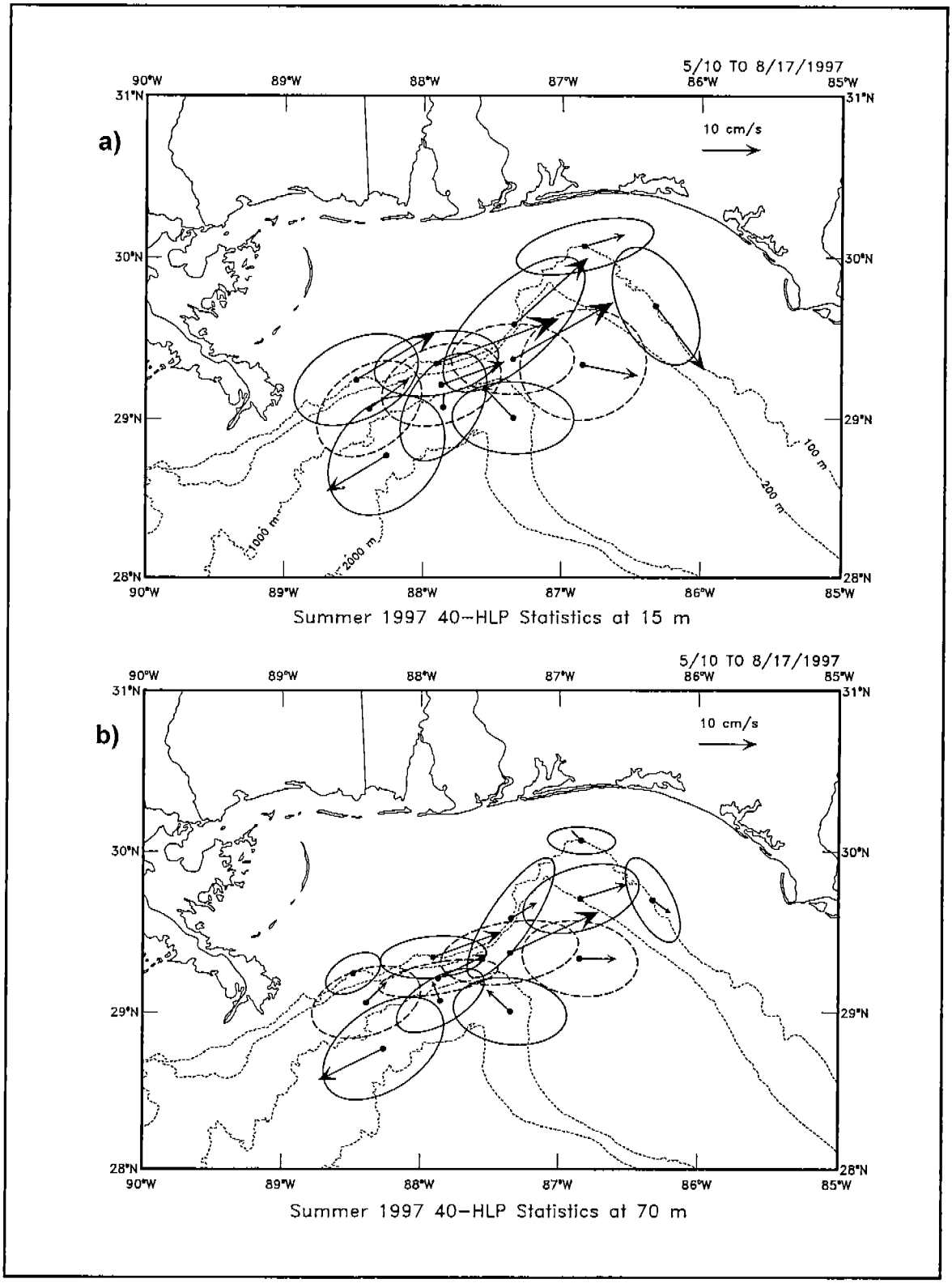

Figure 5.4-6a,b. Mean currents and standard deviation ellipses for summer 1997 (5/10 to 8/16/97) for: (a) 15m, (b) 70m (c) 200m (solid) and 300m (dashed), and (d) 500m (solid) and 1290m (dashed) depths.

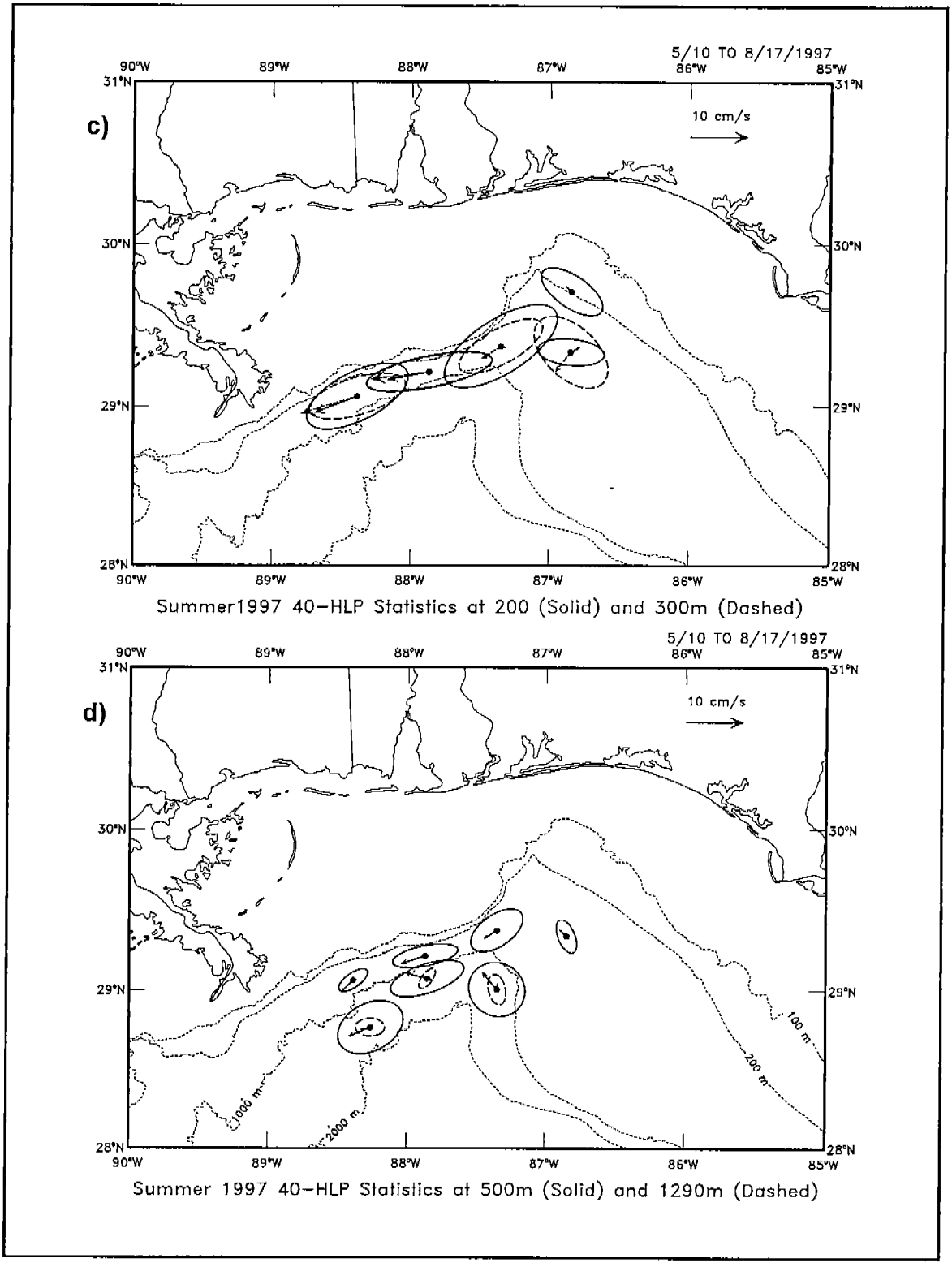

Figure 5.4-6c,d. Means and standard deviation ellipses at indicated depth.

b & e. Though in general the means were comparable to the standard deviations it is noteworthy that the cross-slope variances were a substantial fraction of the along-isobath variances, particularly offshore and in the canyon. The fluctuation kinetic energy, which is proportional to the area of the ellipses, showed no marked variation across the array at any given depth level. However, there was a strong decrease with increasing depth. This representative mean flow pattern had an upper slope eastward jet opposed by reverse flows below 200m and westward flow over the lower slope caused by a cyclone. It occurred at other times in the array such as December 1997 to January 1998, and July 1998 (Figure 5.4-5) and was related to the occurrence of LCFE being present in the region to the south between 28°N and 29°N (see Section 5.2).

Between February 1 and April 30, 1998, an interval denoted by C in Figure 5.4-5, flow was westward at all depths with speeds at 300m equaling or slightly exceeding those at the surface. The early April 1998 survey showed a vigorous cyclone over the western part of the canyon (Figure 5.4-1d). Velocities, and also temperatures, had energetic short time-scale (~10 to 20 days) fluctuations that rarely reversed the direction of the prevailing westward currents (Figure 5.4-5). Similar periods with all flows at C2 toward the west included August and September 1998 and February and March 1999. The short period fluctuations in the latter interval were not as energetic as during interval C.

The mean and standard deviation ellipses, for the standard depth levels, are given in Figure 5.4-7. Mean flows at 16m and 40m below the surface were toward the west with a magnitude of approximately about 10 cm/s over the Alabama slope and an anticyclonic circulation over the head of the canyon. The smallest westward velocities were at the shelf break. The standard deviation ellipses, in the upper 100m, show that the kinetic energy increased from the shelf break toward deeper water. The energy levels were also greater in the western part of the array than for the summer 1997 interval (compare Figures 5.4-6a and 5.4-7a). In the canyon, upper layer mean flows were northward. At the 16m level, flow turned east, with some returning to the offshore at E1. At 70m, the flow turned westward towards Pensacola. Thus, cyclonic flows in deep water can generated onshore velocities along the axis of the canyon (transect D). At 200m and 300m, the westward means exceeded 25 cm/s in the center of the slope (B2) and approached 10 cm/s at 500m depths. This period is characterized by a rapid succession of cyclonic frontal eddies propagating around a well extended LC or ring F which at this time was in the process of forming and detaching from the LC (see Section 5.2). This explains the predominance of cyclonic flow and the presence of short period fluctuations during the February to April 1998 interval. The intrusion of LCFE onto the slope during this period caused the steady deepening of the 15°C isotherm at mid-slope locations (Figure 5.4-5).

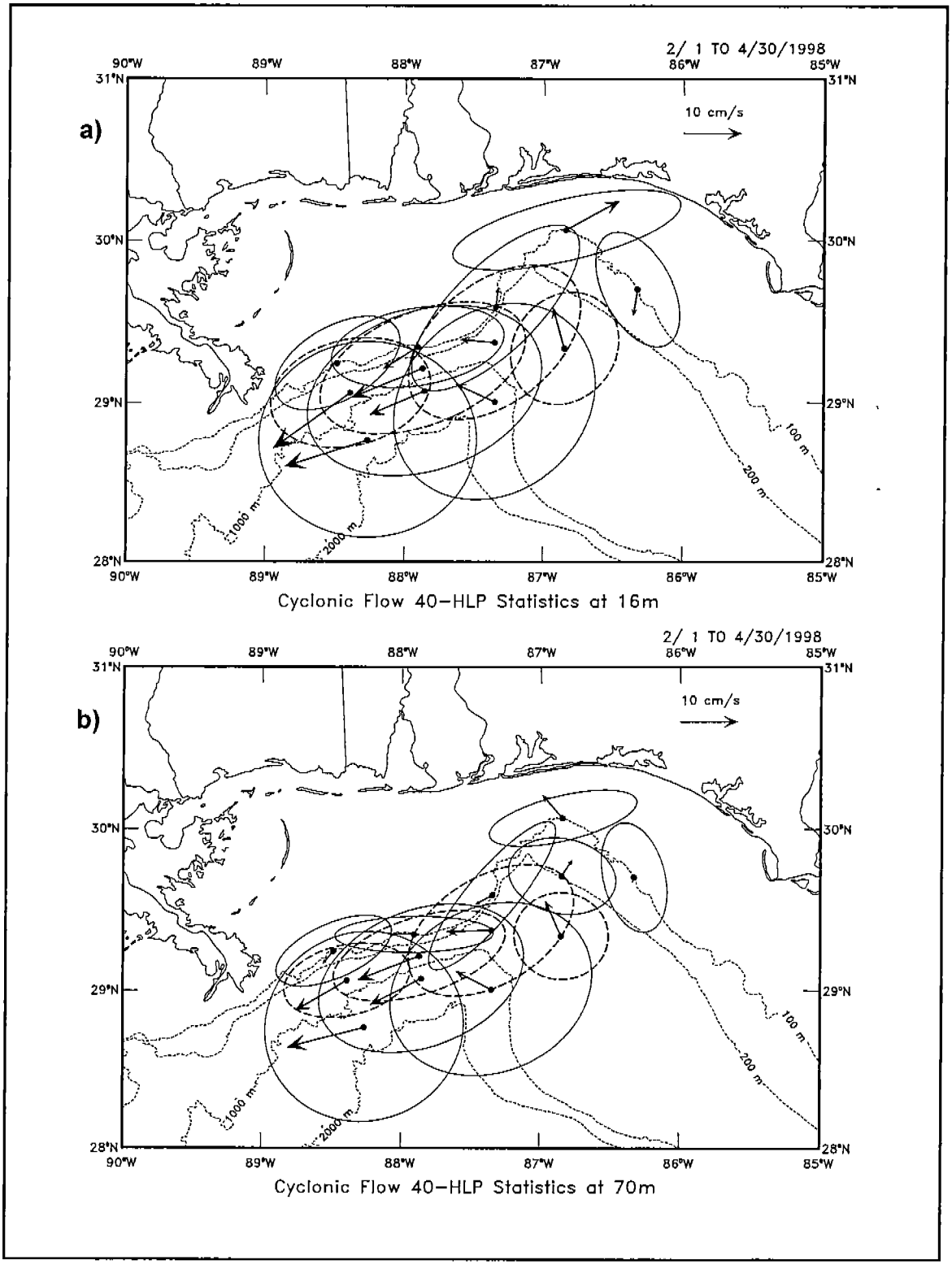

Figure 5.4-7a,b. Mean currents and standard deviation ellipses for the cyclonic flow period (2/1 to 4/30/98) at (a) 16 m, (b) 70m, (c) 200m(solid) and 300m(dashed), and (d) 500m(solid) and 1290m(dashed) depths.

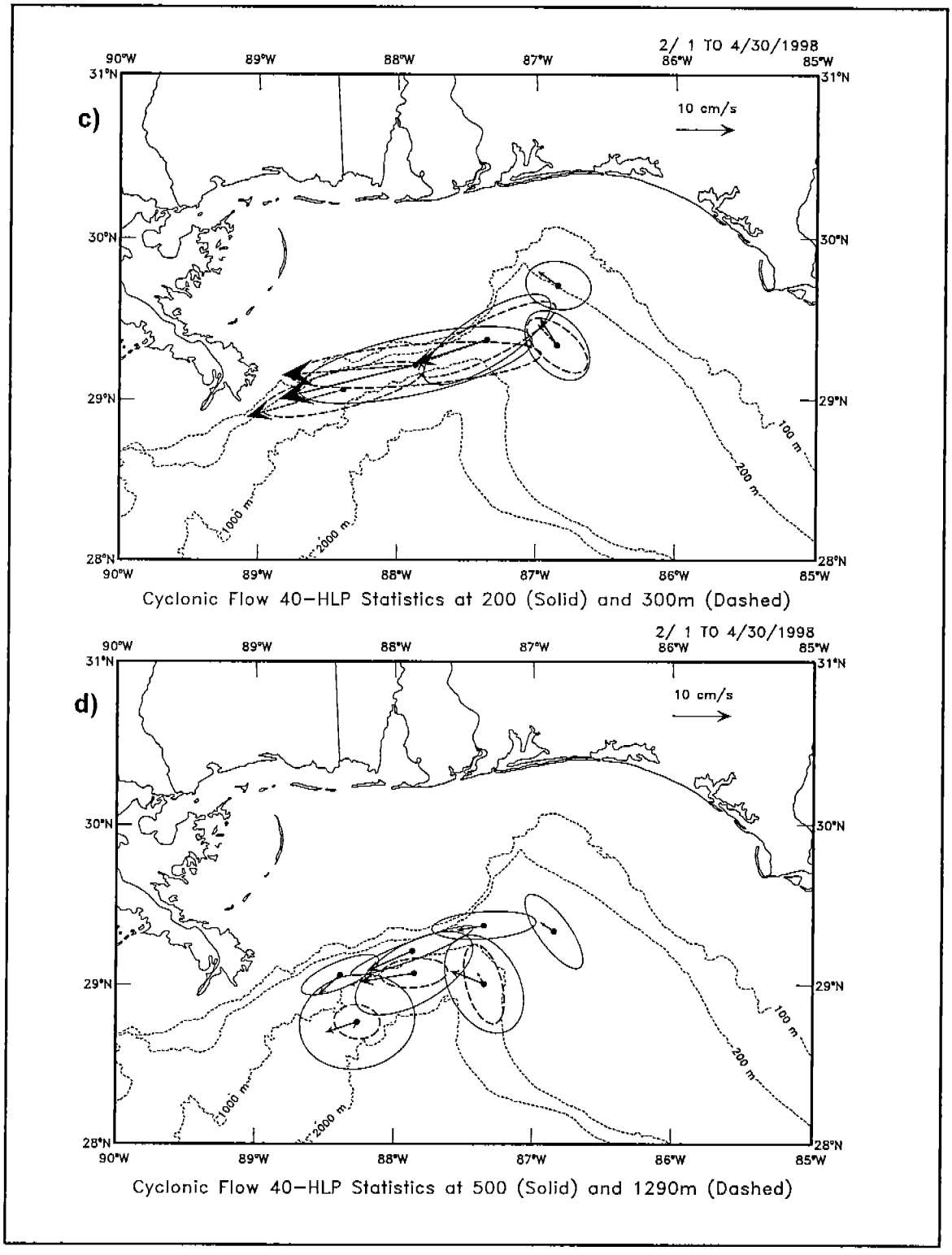

Figure 5.4-7c,d. Mean currents and standard deviation ellipses for the indicated depths.

The last interval, (interval A in Figure 5.4-5), was also characterized by along slope flows toward the east. The difference from the S97 period is that flows decreased little with depth and no undercurrent was present. Observations from the December 1998 survey (Figures 5.4-1f and 5.4-2f) show an anticyclonic circulation extending vertically through the water column over the central part of the canyon. The mean velocities and standard deviation ellipses for this period are plotted in Figure 5.4-8. The mean velocities in the upper 100m were eastward with northward inflow occurring on the western edge. The main current bypassed the head of the canyon but a subsidiary loop maintained the anticyclonic flow along the rim.

A similar situation is illustrated by the geostrophic currents in Figure 5.4-1f. At the 70m level, there is a suggestion that the canyon subsidiary loop may have become a cyclonic recirculation eddy. This again induces northward currents at D9 and D1. Unlike the cyclonic flow case, the sources for these onshore flows is the Alabama slope rather than deep eastern basin water. Eddy kinetic energy was again relatively uniform across the array, but the energy levels were less than for the S97 interval. At 200m and 300m depths, the means were eastward but, at B2, they exceeded the means in the upper 100m. At 500m (Figure 5.4-8d), however, a narrow region of westward flow existed next to the slope. The eastward mean flow over the 1200m isobath appears to have been blocked by the west Florida slope and was partly returned to the west via a cyclonic circulation in the canyon. Thus, the circulation was similar to, but less energetic than that occurring during the S97 interval, except that there was no cyclonic circulation offshore and the undercurrent was restricted to a narrow region close to the bottom at the 500m isobath. The anticyclonic circulation implies uplifted isotherms on the outer edges of the eddy. The water at 200m rapidly cooled during this event (Figure 5.4-5). This particular anticyclone was not directly associated with the LC. SSH and SST images show the LC mostly south of 25°N at this time. Examination of the time series at C2 (Figure 5.4-5) shows a few similar periods in the record but they were of short duration. Similar events include the latter halves of May and August 1997.

Analysis of these three mean circulation patterns show that the eddy circulations derived from the geostrophic currents may have been persistent for periods on the order of months. The large-scale features, such as the upper slope jet and its deep counter current, occurred in more than one survey. They have been shown to be general features of the northeast Gulf slope circulation. Forcing for these flows seems to depend on the presence of eddies over the lower slope. These deep water eddies may sometimes be related to LCFE, however, even when the LC was not present in the northeast Gulf, similar eddies were still present. For example, in the last nine months of the field observations, the LC front did not extend north of 26°N and Ring F was west of the delta. However, cyclonic and anticyclonic flow regimes were still observed over the northeast Gulf slope. These eddies may sometimes be still related to peripheral circulations of a major LC ring even after it has moved out of the eastern basin.

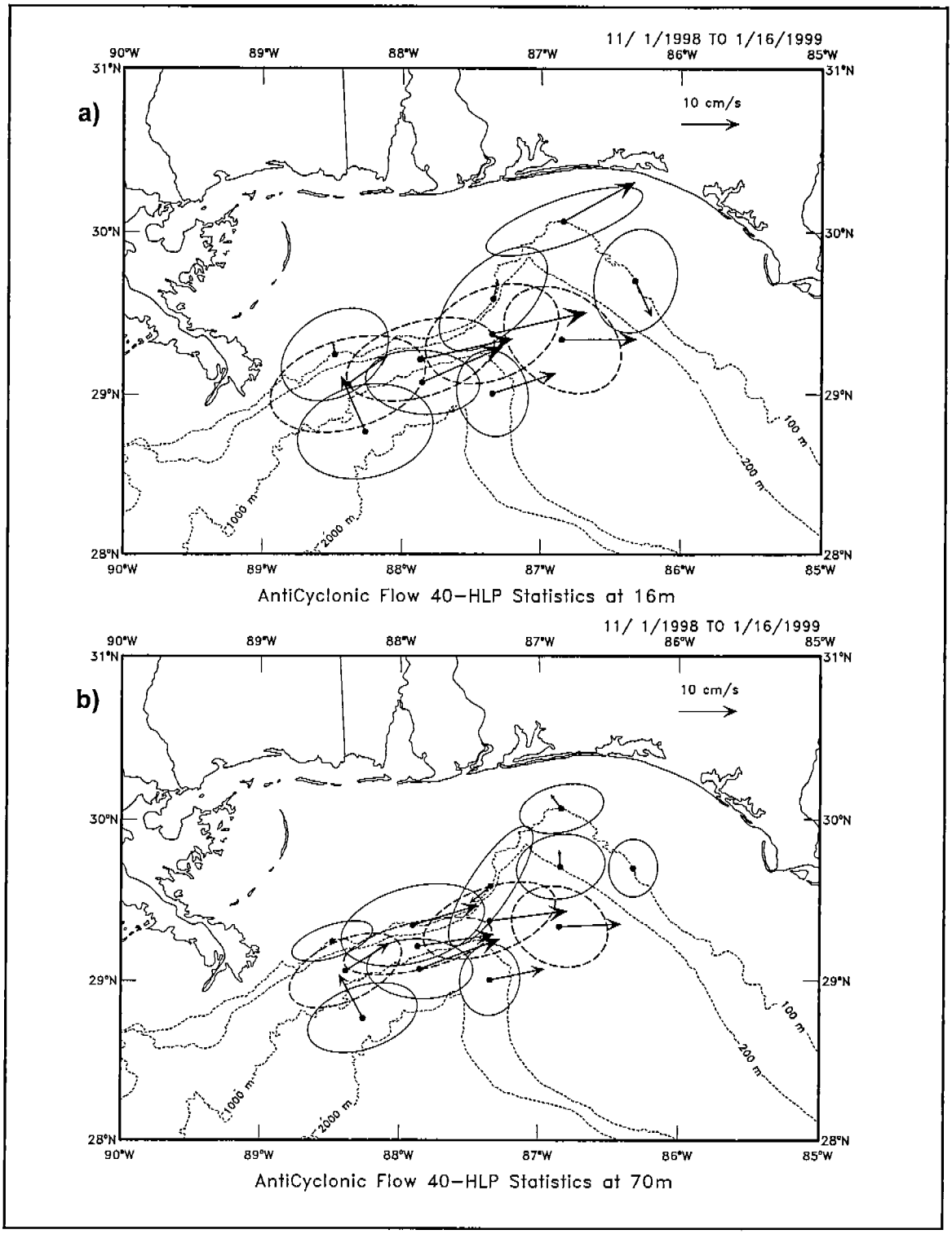

Figure 5.4-8a,b. Mean currents and standard deviation ellipses for the anticyclonic flow period (11/1/98 to 1/16/99) for (a) 16m, (b) 70m, (c) 200m (solid) and 300m (dashed), and (d) 500m (solid) and 1290m (dashed) depths.

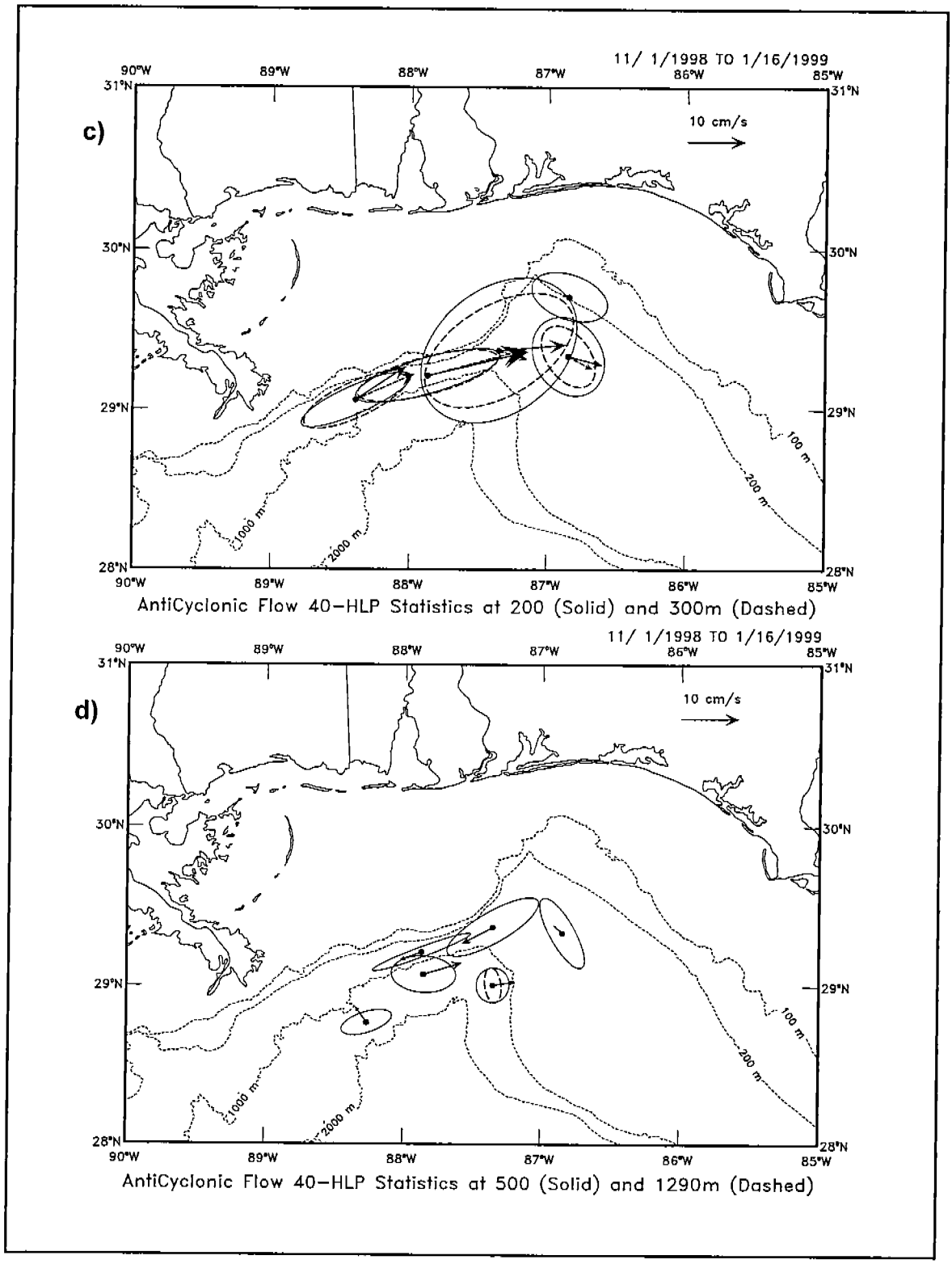

Figure 5.4-8c,d. Mean currents and standard deviation ellipses for the anticyclonic flow period (11/1/98 to 1/16/99) at indicated depths.

5.4.3 Two-Year Statistic Properties

After the analysis of means and standard deviations for specific kinds of flow episodes, it is useful to present statistics for the complete two-year study period. Figure 5.4-9 gives the means and standard deviations for the currents at various depths. The standard deviations greatly exceeded the means at all depth. Unlike the episode statistics, however, the two-year records contained both eastward and westward flow events. The means were quite robust, and subdividing the record into two separate 12-month periods produced very similar statistics. Upper layer means were eastward and tended to follow the isobaths at the surface. At 70m, the eastward flow was a little weaker and had an indication of a residual cyclonic circulation over the head of the canyon. There was a similar splitting of upper and lower layers at D1 into eastward means that occurred in Figure 5.4-8 during the anticyclonic flow period. Mean flows at 70m along transect D were directed northward across isobath. Therefore, it seems that both cyclonic and anticyclonic episodes contribute to the upper layer, northward mean velocities along transect D in the canyon. Mean flows at D9 had a up-slope component above about 120m. At 200m and below, the flow was all to the west with slightly larger magnitudes at the 500m isobath than at the 1300m isobath. Therefore, the counter current at depth was a distinct feature of the mean slope circulation.

The anticyclonic and cyclonic nature of the upper and lower layer flows, respectively, are also reflected in the two-year mean temperature fields at 90m and 500m (Figure 5.4-10). The 90m temperatures had a strong cross-slope gradient with the warmest water on the offshore side of the Alabama slope. The water at the head of the canyon was more than 2°C colder. Thus, persistent anticyclonic flows caused upwelling at the head of the canyon to a greater degree than elsewhere along the shelf break. At 500m, the mean, cross-slope temperature gradient, though small, had the opposite sign consistent with the westward flows found in the lower layer. The mean anticyclonic, upper layer circulation over the slope was consistent with the SSH data. A two-year mean SSH anomaly for the study period is given in Figure 5.4-11. A positive anomaly was found over the slope and separated from the mean LC by a negative anomaly. The latter resulted from the frequent passage of LC frontal eddies (see Section 5.2). These cyclones were an important forcing to, as well as a direct influence on, the slope circulation.

5.4.4 Long Period Variability

Spectra were calculated for the two-year long velocity records. Examples of the kinetic energy spectra are given for the 40m level in the upper water column (Figure 5.4-12a, b & c), and 200m and deeper (Figure 5.4-12c, d & e). The spectra are in variance preserving form such that equal areas under the curve have equal contributions to the total kinetic energy. Attention is restricted to periodicities longer than 15 days (0.065 cpd). Higher frequency motions are discussed in the context of seasonal variability in Section 6 of this report.

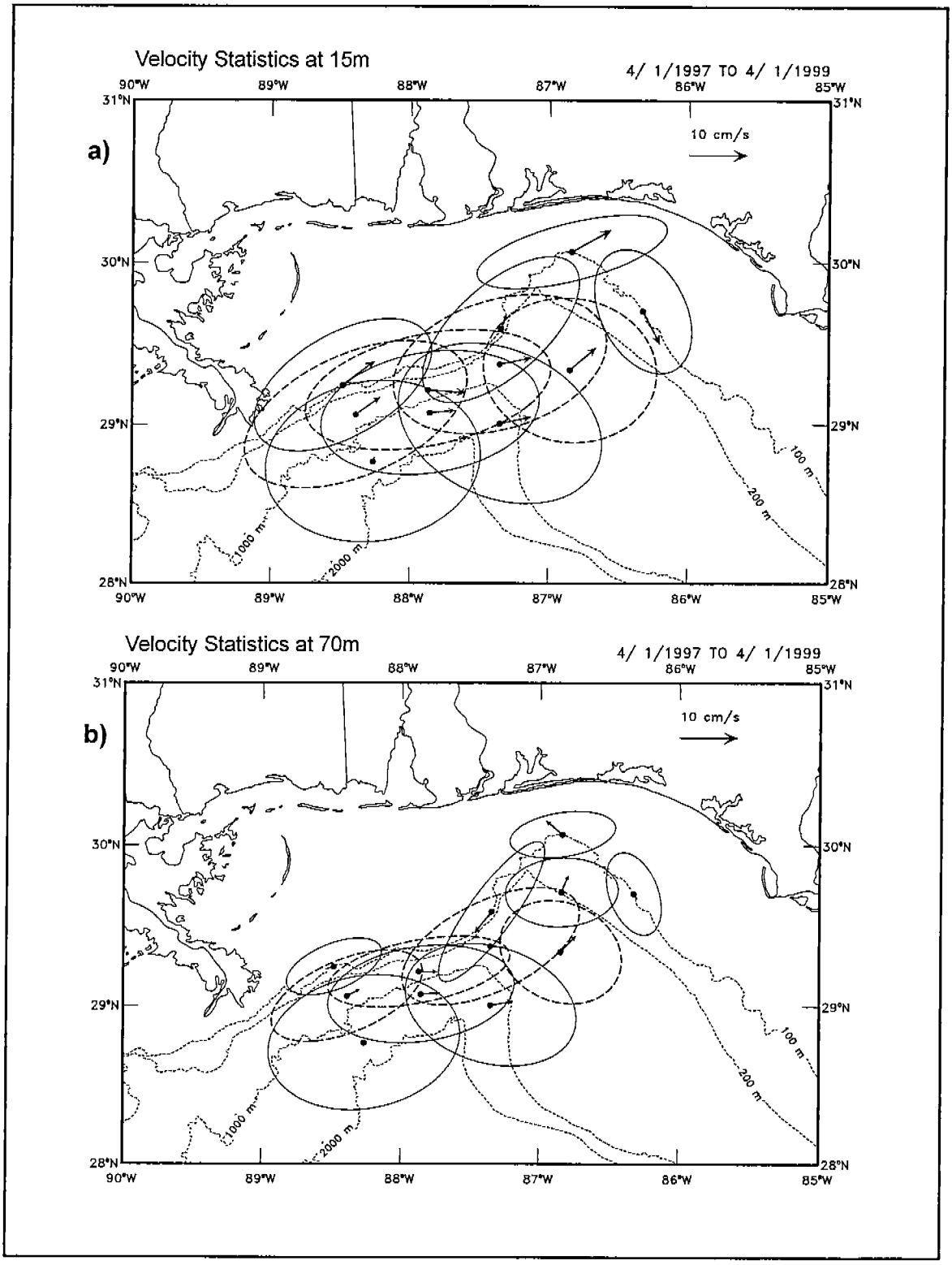

Figure 5.4-9a,b. Mean current vectors and standard deviation ellipses for the two-year study period at the indicated depths.

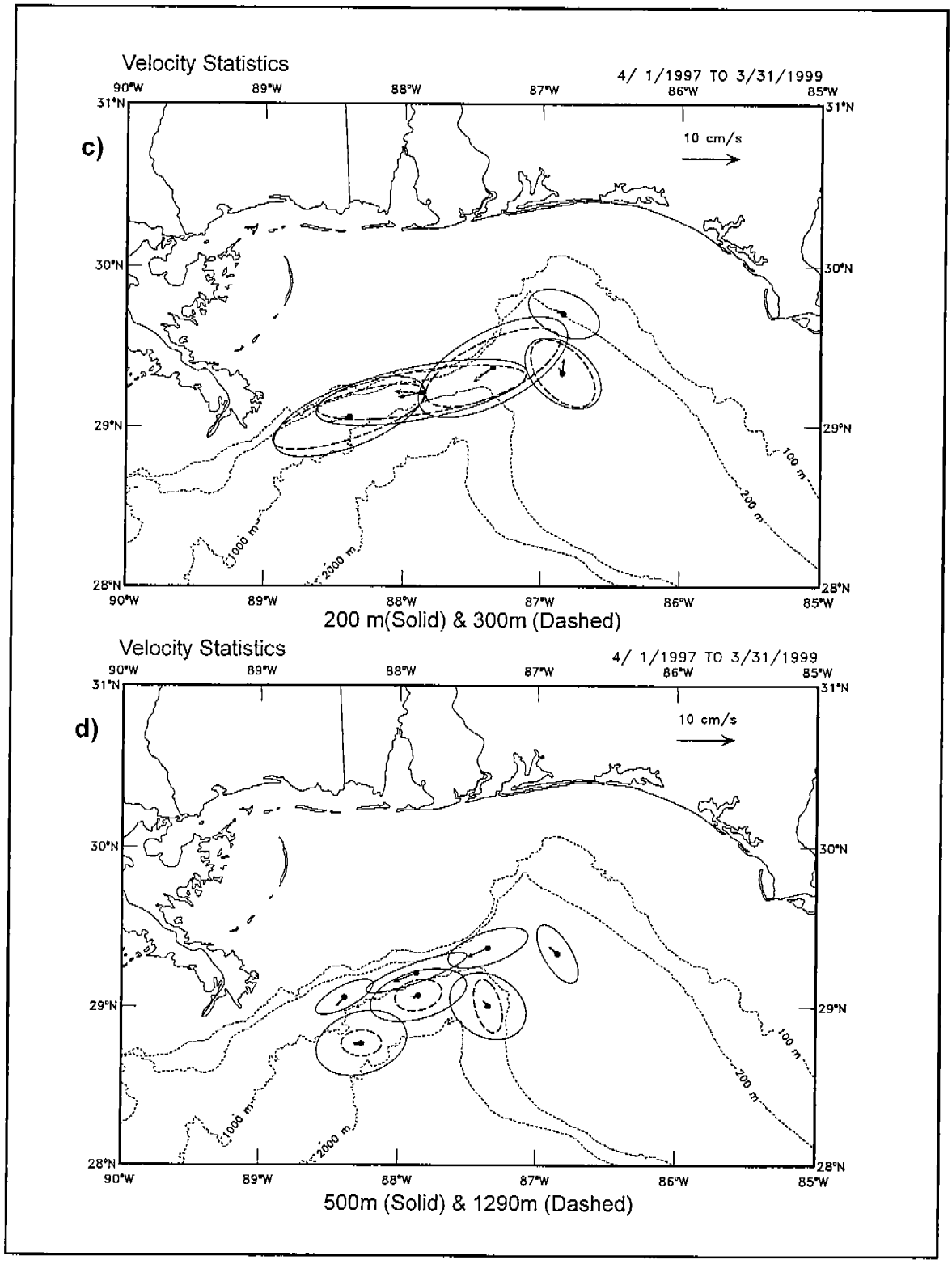

Figure 5.4-9c,d. Mean current vectors and standard deviation ellipses for the two-year study period at the indicated depths.

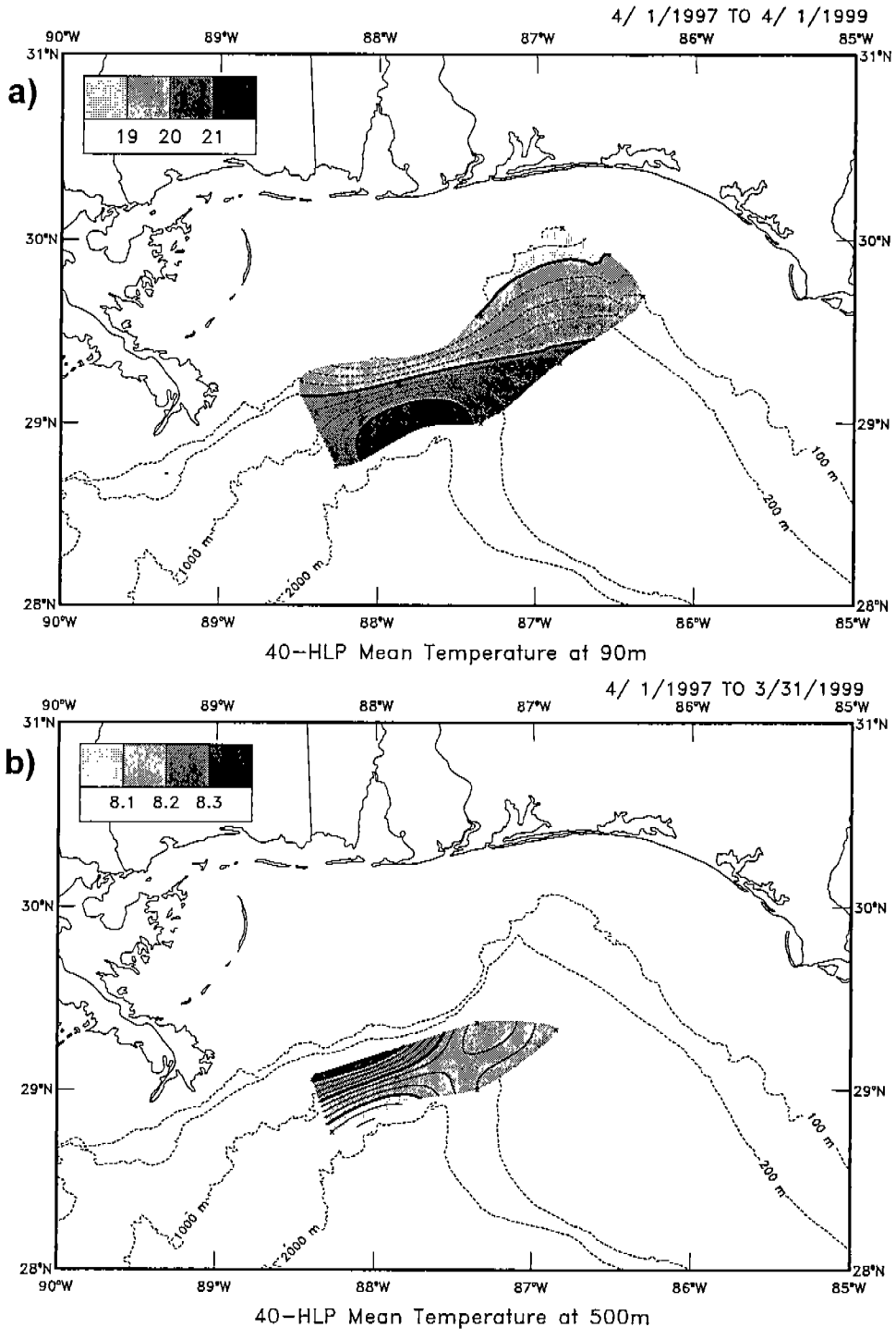

Figure 5.4-10 Contours of mean temperatures for the two-year study period (4/2/97 to 3/31/99) at (a) 90m and (b) 500m.

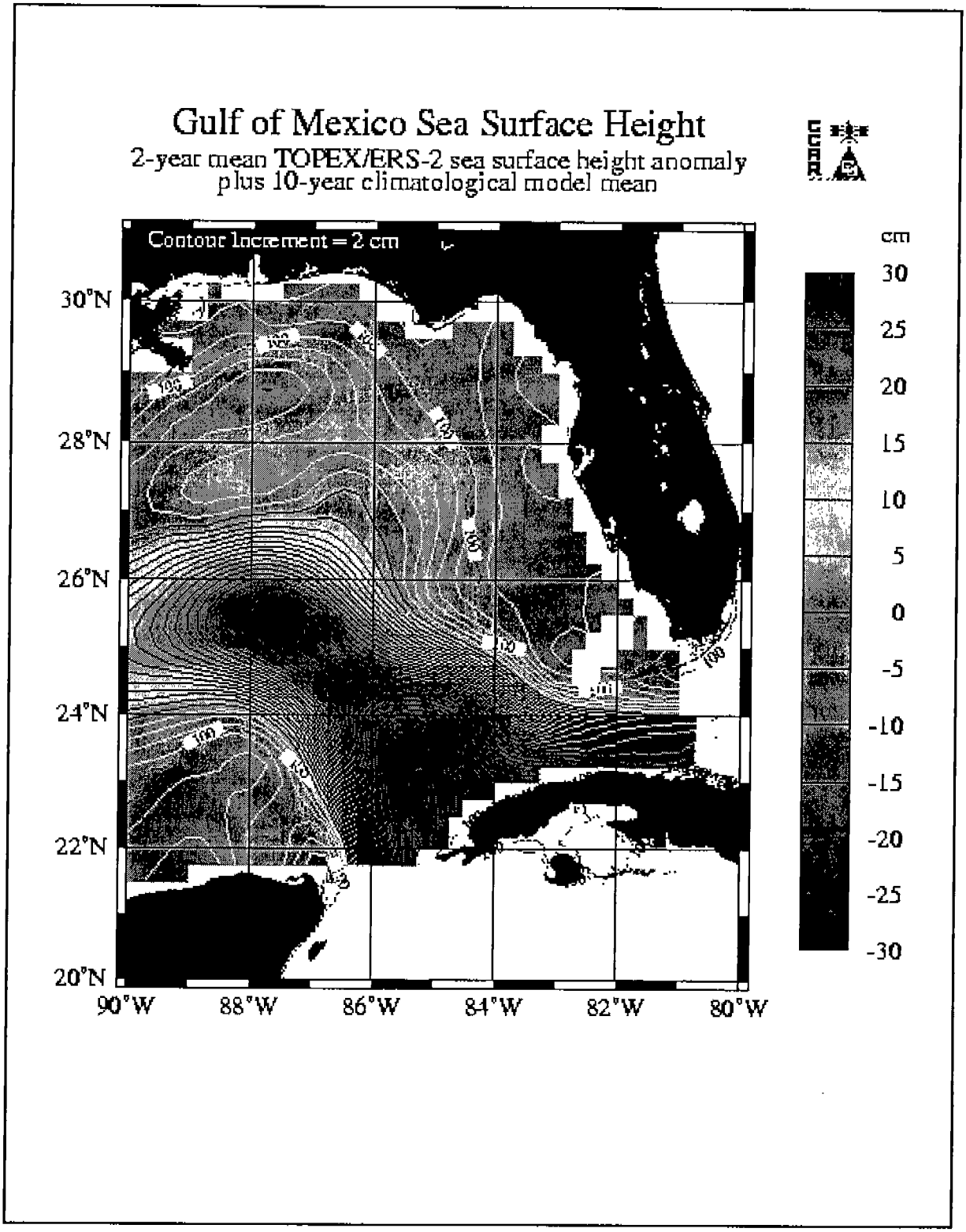

Figure 5.4-11 Two-year mean TOPEX/ERS-2 SSH anomaly added to a 10-year climatological LC derived from numerical model studies.

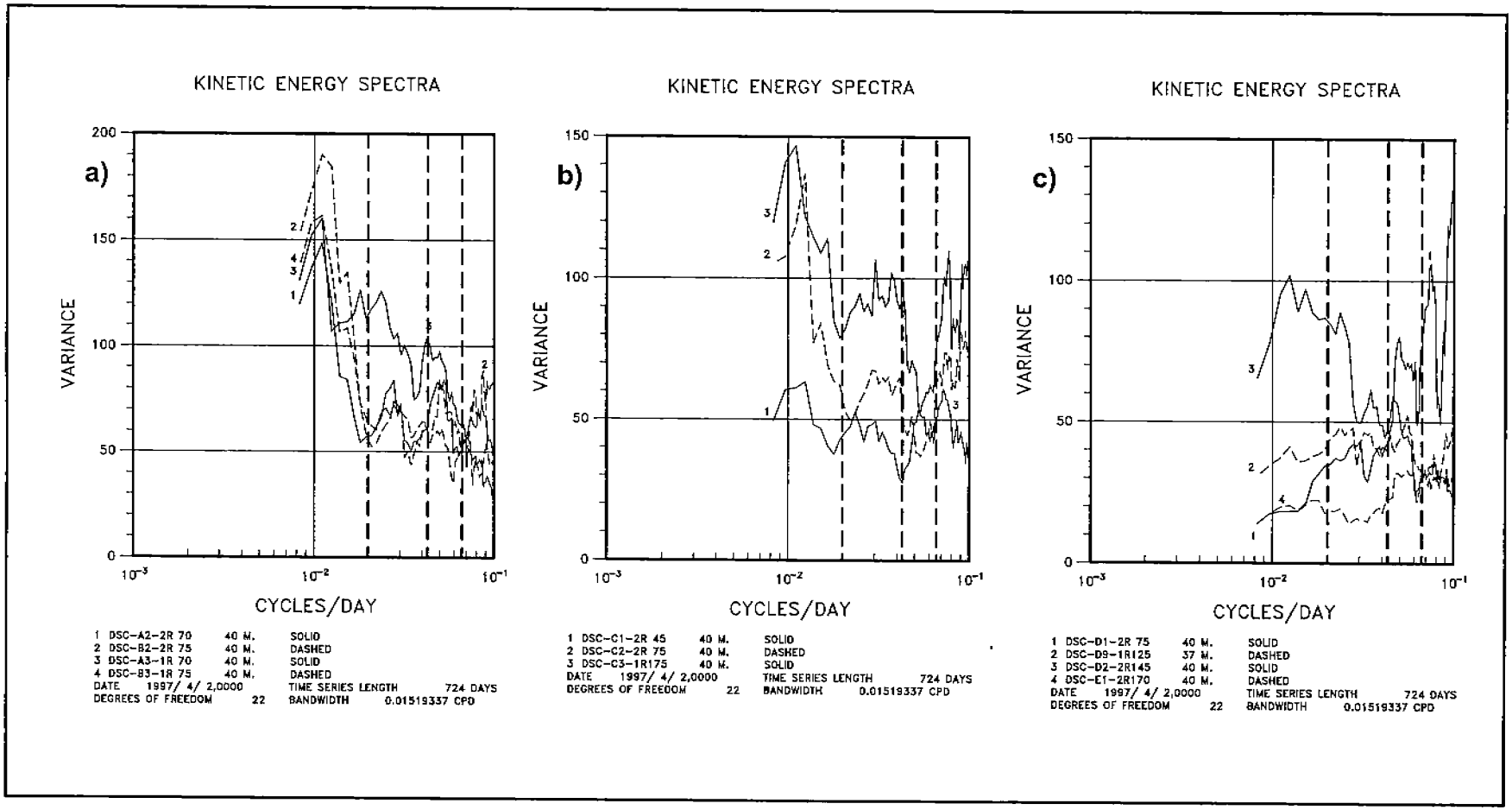

Figure 5.4-12. Kinetic energy spectra in variance preserving form for two-year velocity records at 40m (in panels a, b and c), (d) 200m and 300m, (e) 490m, and (f) 500m. The boundaries of the frequency bands used for the EOF analysis are shown by heavy dashed lines.

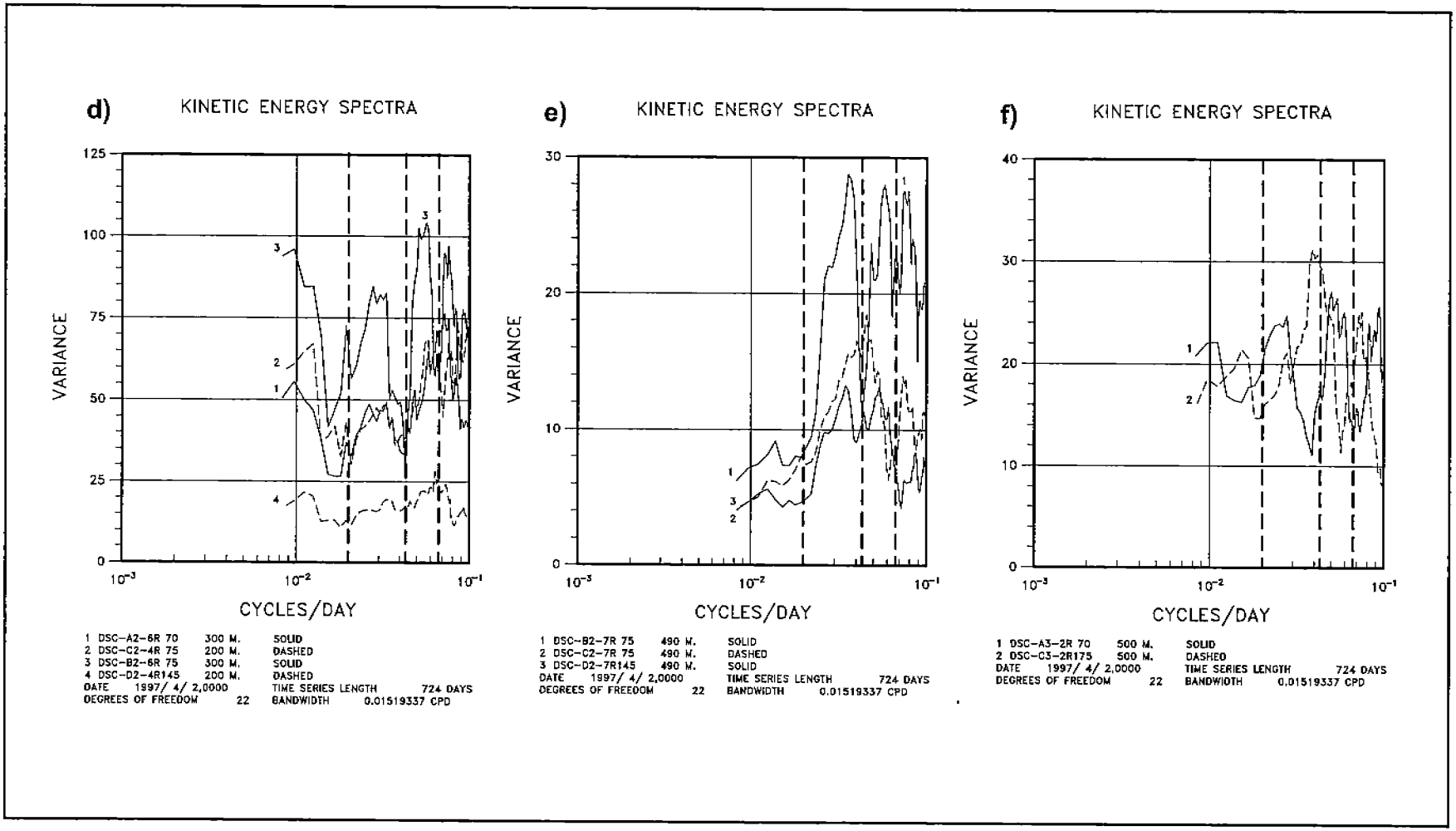

Figure 5.4-12. Kinetic energy spectra in variance preserving form for two-year velocity records at 40m (in panels a, b and c), (d) 200m and 300m, (e) 490m, and (f) 500m. The boundaries of the frequency bands used for the EOF analysis are shown by heavy dashed lines.

These spectra have prominent peaks that do not always appear at the same frequencies. This seems to be caused by movement of eddies on the slope. Moorings near the edge and center of eddy circulations have different spectra with the former having more energy at higher frequencies. Even so, three frequency bands were chosen so that they spanned the major spectral peaks for the majority of the records. These are 0-0.02 (724-50 day period), 0.02-0.043 (50-24 days), 0.43-0.65 (24-15 days) cpd. The boundaries of these bands are marked on Figure 5.4-12.

In the lowest band (0-0.022 cpd), energetic motions were found between ~70 and 100 days at the mid-and offshore moorings at and above 300m. The shelf-break and deep slope (500m) velocities had less energy in this band. The B2 mooring had the most energetic fluctuations and energy decreased in both along slope directions. The canyon region had less energy than over the Alabama slope. These motions, with periods longer than 45 days, corresponded to some of the major events discussed in the previous sections. The two higher frequency bands had prominent peaks at 200m and below. At the upper levels, motions at 25 to 35 days and 16. to 20 days were not as prevalent and organized as at depth (compare Figure 5.4-12a & b with 5.4-12 d & e).

EOF analysis was performed for the three, equal-width frequency bands using all available velocity records (both U and V-components) that spanned the two-years of measurements. Three levels (16, 40 and 68m) were used from the 300 kHz ADCP's (all moorings except D9), and four levels (37, 72, 98 and 168m) from the 150 kHz ADCP on D9. Analysis using all the levels of individual ADCP's has shown a high degree of coherence between levels. The various levels at C2 are seen to have been visually coherent in Figure 5.4-5. This analysis showed that the two higher frequency bands had very similar patterns and therefore they were combined in order to increase the significance of the modes. The EOF analysis presented here is for the two frequency bands 0-0.02 and 0.02-0.065 cpd, respectively. The eigenvector components were multiplied by the square root of the eigenvalue to give amplitudes in velocity units (cm/s). The significant modes and their eigenvalues are summarized in Table 5.4-1. Error estimates for the eigenvalues were determined from the number of degrees-of-freedom in each band and the requirement that the eigenvalues not overlap, and thus, be considered distinct (North et al. 1982). Under this strict criteria modes 2 and higher, and modes 3 and higher are not significant for the lower and higher frequency bands, respectively.

For 50- to 15-day period (0.02-0.065 cpd) motions, more than half the variance was not accounted for by the two significant modes. This implies that a majority of the energy was contained in small-scale motions that were not coherent across the array. At longer periods, the first mode dominated and accounted for slightly more than half the observed variance. The structure of the modes was examined by decomposing the amplitude and phases of the U and V components at each position into vector hodographs. Essentially, these EOF hodographs use the same formulation as tidal current ellipses (Foreman 1979) where the phase is relative to the major axis. The ellipses represent coherent

current fluctuations at the central period of the band about the two-year mean flow.

Table 5.4-1 Frequency domain EOF analysis of two-year velocity records.

Center Frequency: 0.01036 Bandwidth = 0.01934 cpd				
No.	Eigenvalue (cm^2/s^2)	Percent of Total Variance	Cumulative Percent	Error
1	487.2	57.7	57.7	130.2
2	128.1	15.2	72.9	34.2
3	80.3	9.5	82.4	21.5
4	57.6	6.8	89.2	15.4
Center Frequency: 0.04282 Bandwidth = 0.04558 cpd				
No.	Eigenvalue	Percent of Total Variance	Cumulative Percent	Error
1	41.32	27.6	27.6	7.19
2	23.24	15.5	43.1	4.05
3	17.31	11.6	54.6	3.01
4	14.22	9.5	64.1	2.48
5	10.06	6.7	70.8	1.75

Figure 5.4-13 shows the EOF ellipses at selected upper and lower layer depths for mode 1 of the lower frequency band. The fluctuations did not have a great deal of variability with depth. For this first mode, the fluctuations followed the trend of the isobaths and were most energetic along the Alabama slope. These fluctuations had little or no influence on the canyon and shelf break moorings C1, D1, D9 and E1 and thus represent large scale, low-frequency (~100-day period) eastward and westward flows along the slope. Phase changes from east to west were small but show some interesting features. Along the 500m isobath, the east side led the west at both the 40m and deeper depths, but for the 1300m moorings the west had a small lead or was nearly in-phase with the east. This implies offshore and westward propagation of phase which in turn suggests propagating topographic waves (Hogg 1981). Unlike topographic Rossby waves, these propagating topographic wave motions have the largest amplitudes near the surface.

A similar EOF analysis using the same 0-0.02 cpd frequency band was performed for all the temperature records at 90m. The mode structure was similar to that given in Table 5.4-1 with the first mode accounting for 63.6% of the total normalized variance. The amplitude and phase of mode 1 of the 90m temperatures are given in Figure 5.4-14. The amplitudes of the fluctuations were quite uniform with the maxima on the western rim of the canyon and the offshore side of the Alabama slope. Again, the phase changes indicate offshore and westward propagation of the coherent signals. A least squares fit of wave numbers to the array of phases obtained from the velocity and temperature modes (Hamilton 1984) are given in Table 5.4-2. Estimates of wavelengths range from 250 to 600 km with the wave vector directed approximately due south. This

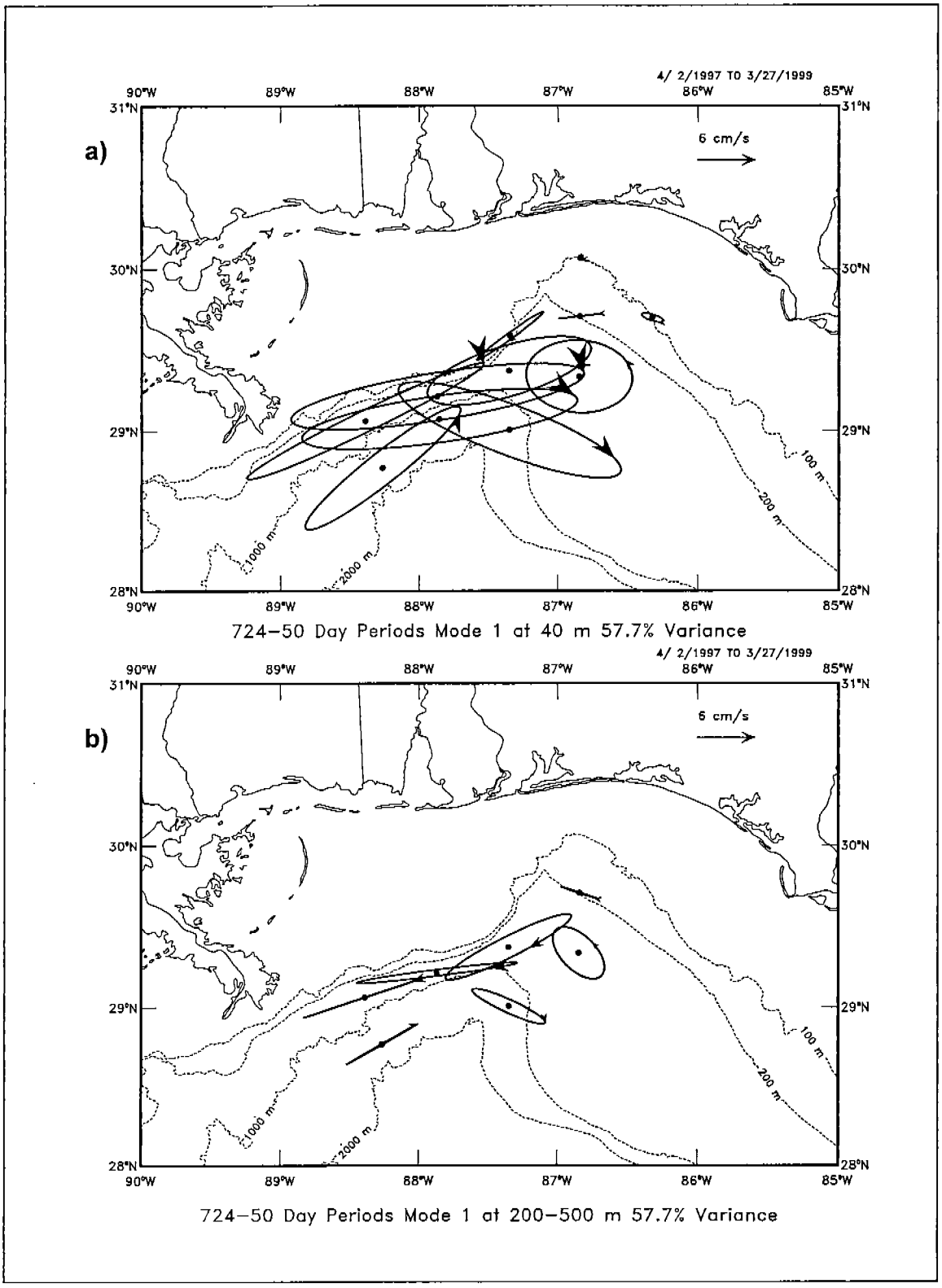

Figure 5.4-13 EOF ellipses for mode 1 of the 724 to 50-day period band. (a) is the subset for 40m depth, and (b) for 200m (C2 and D2), 300m (A2 and B2) and 500m (A3 and C3) depths. The relative phase of the motions is given by the arrow heads.

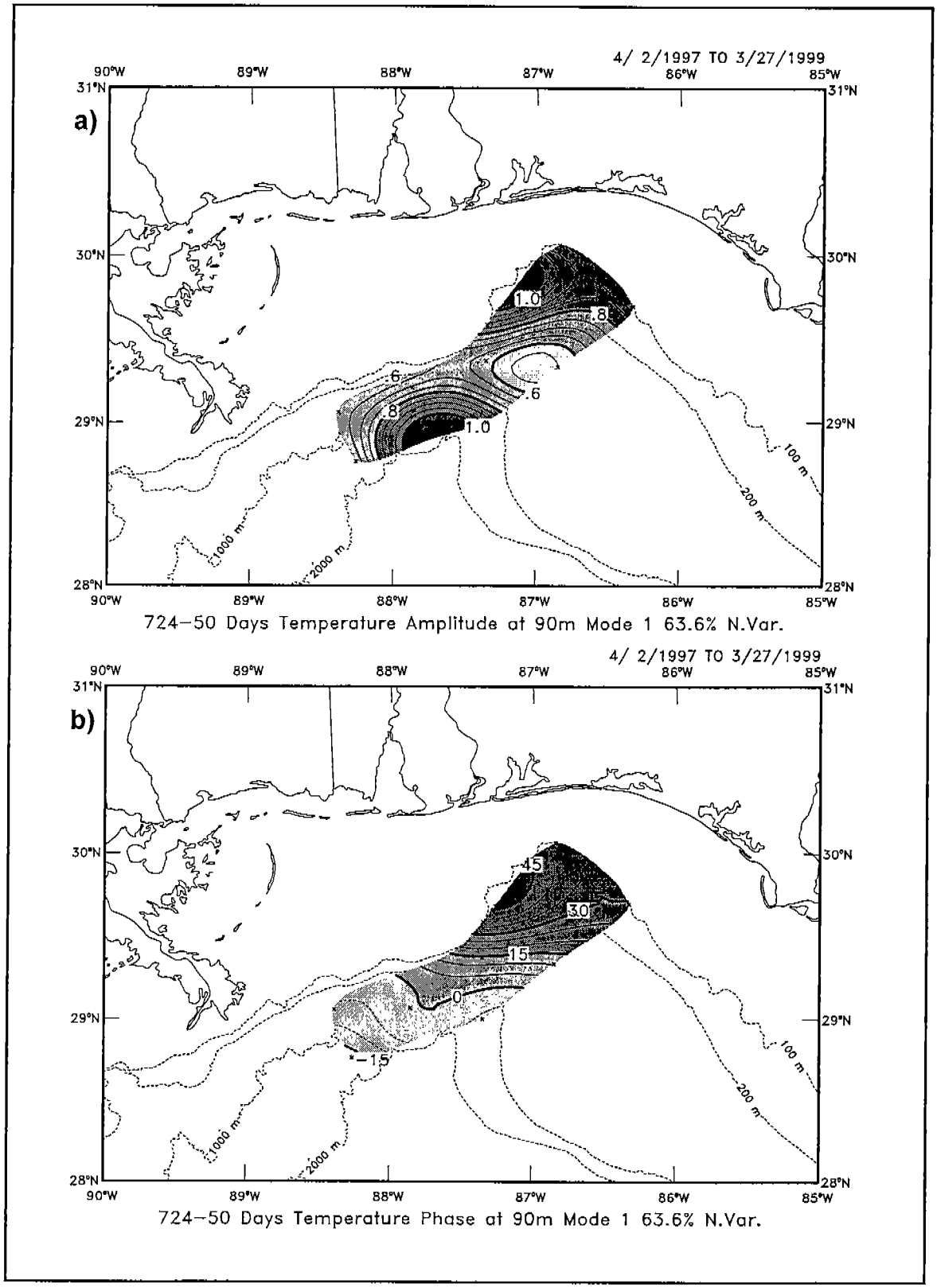

Figure 5.4-14 EOF Mode 1 (a) amplitude (°C), and (b) phase (degrees) of the 90m temperatures for the 724-50 day period band. Positive phase angles lead.

is consistent with the energy of planetary waves propagating westward along the slope. This could be an indication that the slope acted as a topographic waveguide for long period (~100 day) disturbances. The time and length scales are appropriate to LC or LC ring induced motions.

Table 5.4-2 Wave numbers from EOF Mode 1 phases for 724 to 50-day period fluctuations

Variables	East Wave Number, k, (km^{-1})	North Wave Number, l (km^{-1})	Wavelength (km)	Direction of Phase Propagation (Degs. True)
U, V-Cmpts at 40 m	0.000046	-0.002597	385	179
U, V-Cmpts at 200 to 500 m	0.000305	-0.004348	229	176
Temperature at 90 m	0.000014	-0.001637	611	180

The 50- to 15-day period band was much less energetic than the low frequency fluctuations discussed above. Mode 1 ellipses for the upper and lower layers are given in Figure 5.4-15. For this mode, the velocity fluctuations were essentially in-phase, both horizontally and with depth. Therefore, there is little evidence of propagating signals.

At the start of the cycle (e.g. ~0° phase angle) the flow consisted of two similar-sized (~100 km diameter) anticyclones, one over the Alabama slope with a center over or seaward of the 2000m isobath, and the other weaker circulation over the head of the canyon with a center between D9 and D2 (Figure 5.4-15a). At ~180° phase angle the situation was reversed with two cyclones present. At depth, only the slope anticyclonic/ cyclonic circulation was present (Figure 5.4-15b). Mode 2 (Figure 5.4-16) reversed the sign of the slope circulation such that there was cyclonic flow when there was anticyclonic flow over the head of the canyon and vice-versa. The flows were also more perpendicular to the isobaths on the lower slope (1300m moorings) than for the first mode. Because the second mode accounted for less of the total variance, the occurrence of counter rotating eddies was less prevalent than eddies of the same sign. The flow patterns for both modes indicate that the two eddies were interacting through flows along the upper Alabama slope. The implication of this analysis is that slope and canyon eddy circulations were relatively short lived (~10 to 25 days) and of considerable complexity. This may account for the shifting position of the peaks in this 0.02-0.065 frequency band. The relatively low percentage of the total variance accounted for by the significant modes also implies that smaller scale eddies were poorly resolved by the array. This is in contrast with the more organized, energetic, large-scale wave-like motions diagnosed in the 0-0.02 cpd frequency range.

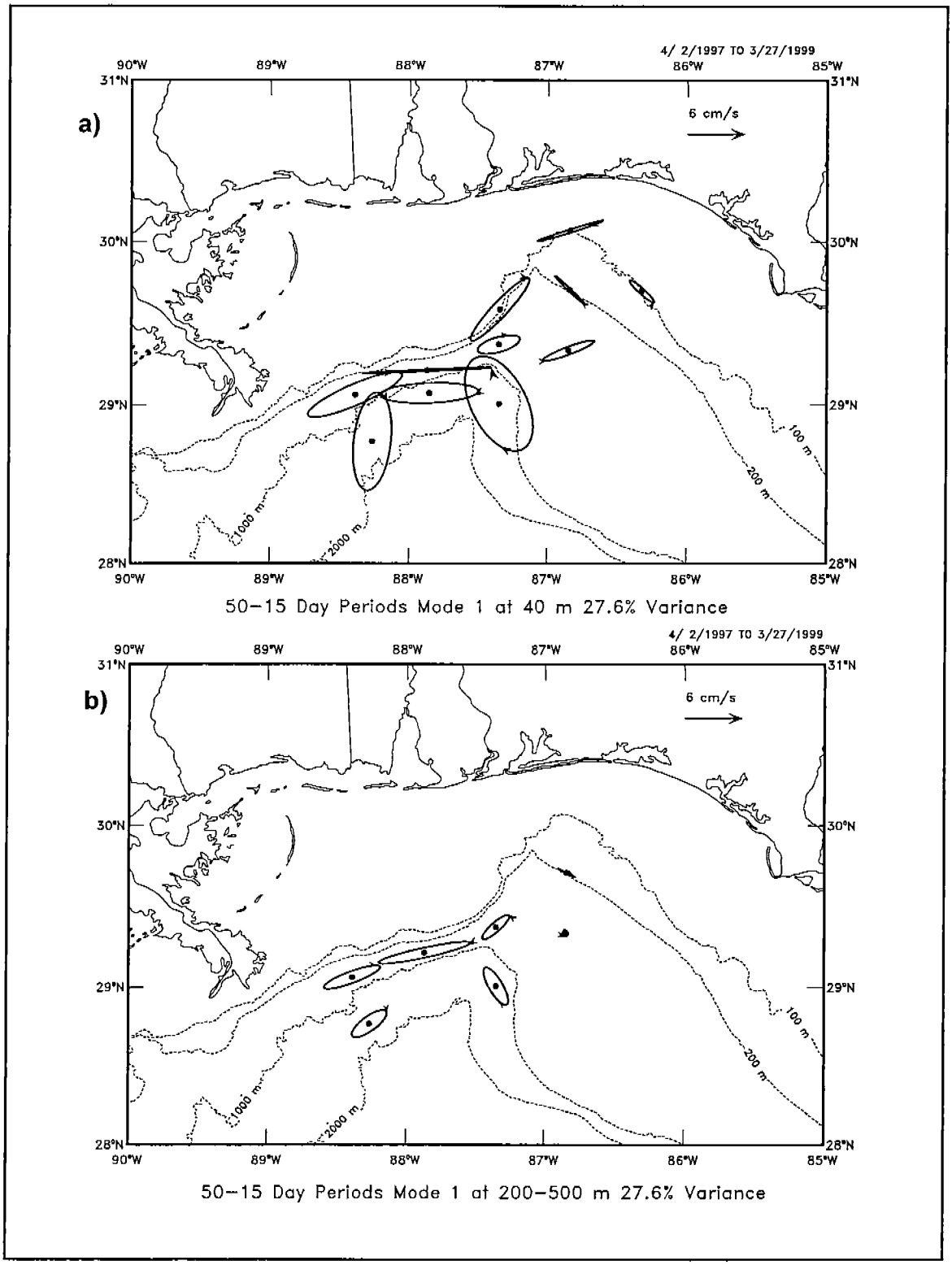

Figure 5.4-15 EOF ellipses for mode 1 of the 50 to 15-day period band. (a) is the subset for 40m depth, and (b) for 200m (C2 and D2), 300m (A2 and B2) and 500m (A3 and C3) depths. The relative phase of the motions is given by the arrow heads.

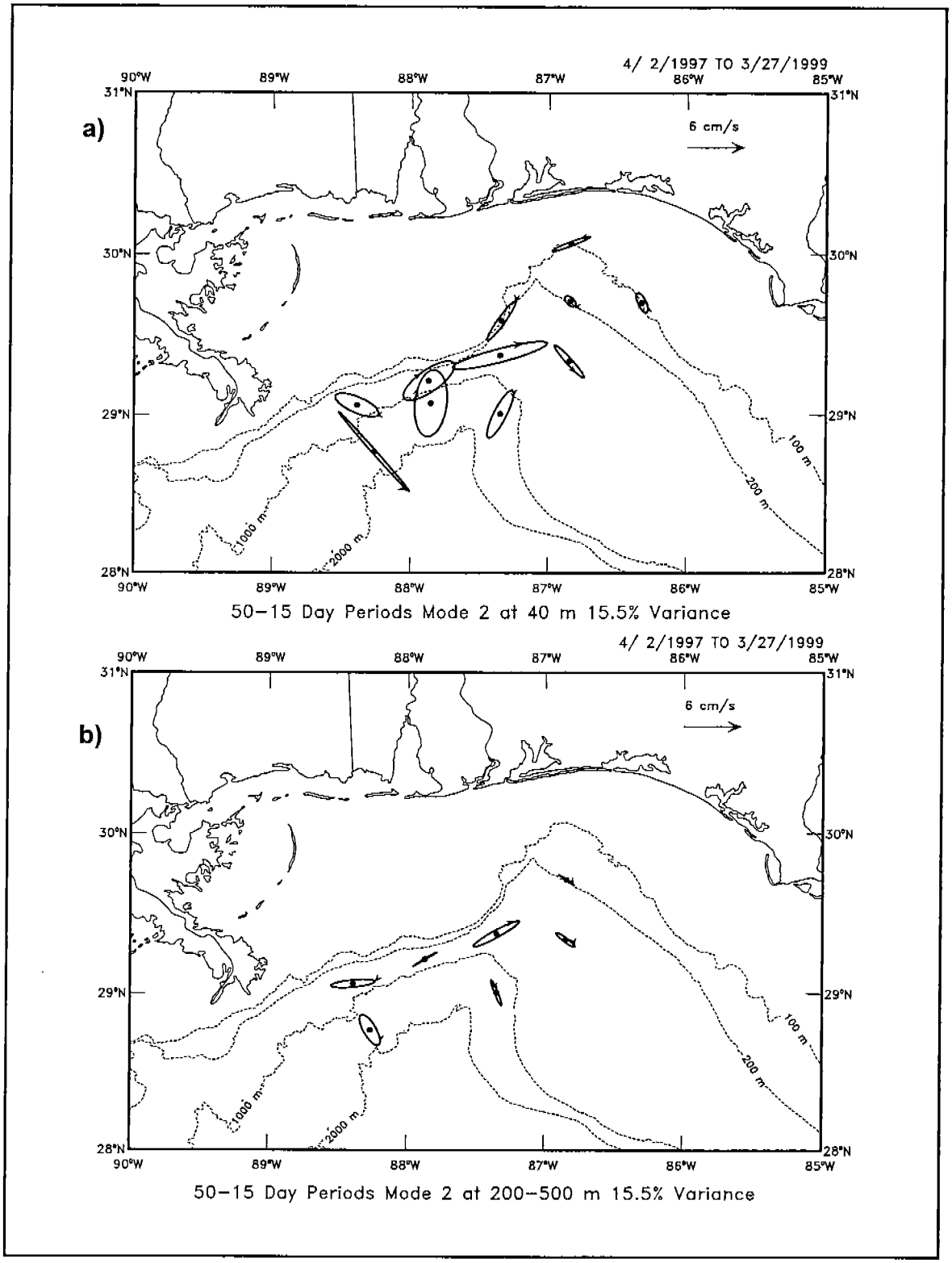

Figure 5.4-16 EOF ellipses for Mode 2 of the 50 to 15-day period band. (a) is the subset for 40m depth, and (b) for 200m (C2 and D2), 300m (A2 and B2) and 500m (A3 and C3) depths. The relative phase of the motions is given by the arrow heads.

5.5 Slope Dynamics and Fluxes

5.5.1 Divergence and Relative Vorticity

The arrangement of the moored array allowed resolution of both north-south and east-west spatial gradients of velocity. The divergence (D) and relative vorticity (ζ) are given by:

$$D = \partial u/\partial x + \partial v/\partial y, \text{ and } \zeta = \partial v/\partial x - \partial u/\partial y,$$

respectively, where (u,v) and (x,y) refer to the geographic coordinate system. Direct calculation of these quantities is expected to be noisy. Therefore, following Chereskin et al. (2000), least square planes were fitted to arrays of 4 to 6 velocity components at a given depth level. Thus,

$$u(x,y,t) = u_o + x \cdot \partial u/\partial x + y \cdot \partial u/\partial y + HOT, \text{ etc.},$$

where (x,y) were measured from the center position of the array. In the least square fit, the velocity components were weighted by their standard deviations. The resulting standard deviations of the gradient terms in the plane model were of order 0.05 to 0.09f, where f is the Coriolis parameter (~0.7 10^{-4} s^{-1}). Standard least square methods (Chapter 15, Press et al., 1992), rather than the matrix inversion method described by Chereskin et al. (2000) were used for these calculations. The array positions used in the calculation of D and ζ for various depth levels at B3, C2 and D9 are shown in Figure 5.5-1. The time series of divergence and relative vorticity at 40, 70 and 500m depths are given in Figures 5.5-2 and 5.5-3, respectively. Substantial fluctuations of D and ζ occurred at both the 40 and 70m level for B3 and C2. The signals were coherent with depth except at D9 where both D and ζ fluctuations were small. Vorticity was also coherent between the upper levels of B3 and C2. The divergence at the upper levels of B3 and C2 were weakly positively correlated (R = ~0.25 and 0.35, respectively) with temperature records at the same positions. The 80m temperature record at B3 was, however, negatively correlated (R ≈-0.48) with the vorticity. The same relation does not hold at C2. The implication is that only a small part of the temperature signal could be attributed to local vertical velocities. At B3, there was a stronger relationship to whether a cold or warm eddy (positive or negative vorticity, respectively) was present on the lower slope. The same relation did not hold for C2 because it was often situated in the outer parts of different eddy flows.

It is clear from Figure 5.5-3 that the vorticity fluctuations at B3 were closely related to the along-slope currents. Thus, eastward flow corresponded to negative vorticity and vice-versa. The large negative anomaly in July and August 1998 corresponded to the intense anticyclonic circulation observed over the slope (see Figure 5.4-1e). Even though the vorticity at C2 was similar to that at B3, it was much less closely related to the C2 currents. Again, this most likely occurred because of the position of C2 on the edges of the major deep-water eddy circulations (Figure 5.4-1). The small magnitude

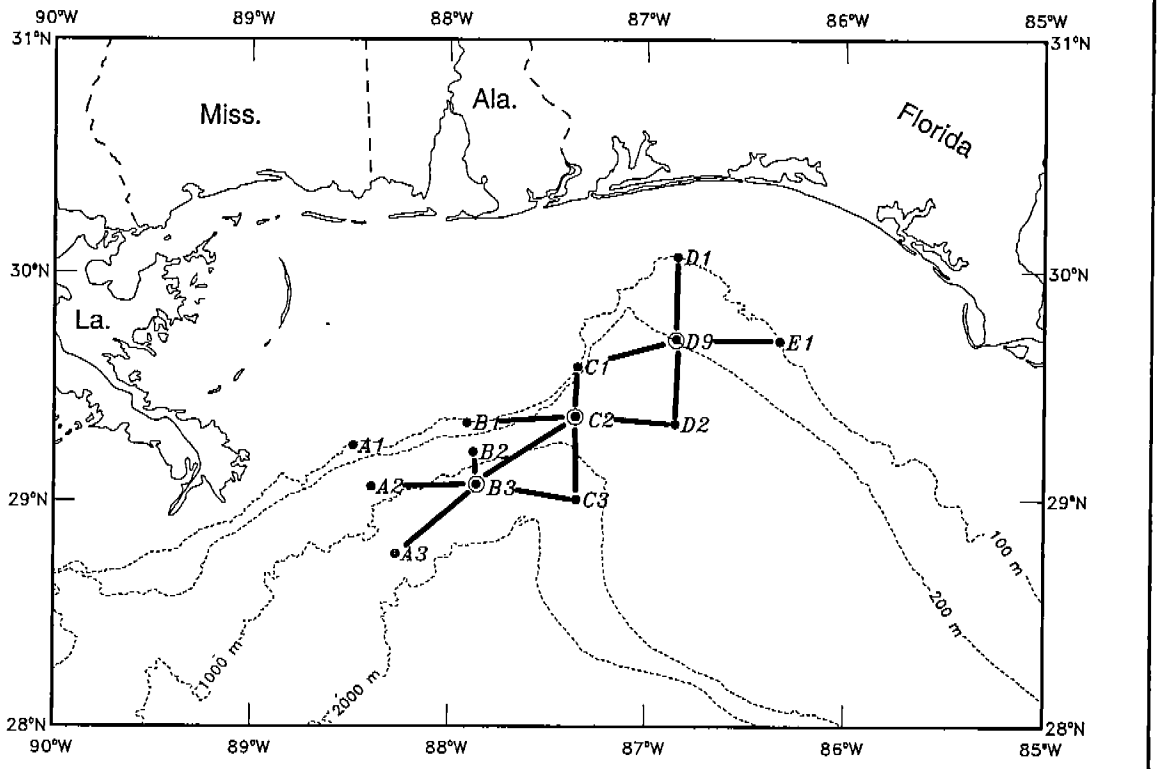

Figure 5.5-1 Positions used for divergence and vorticity calculated at the circled points.

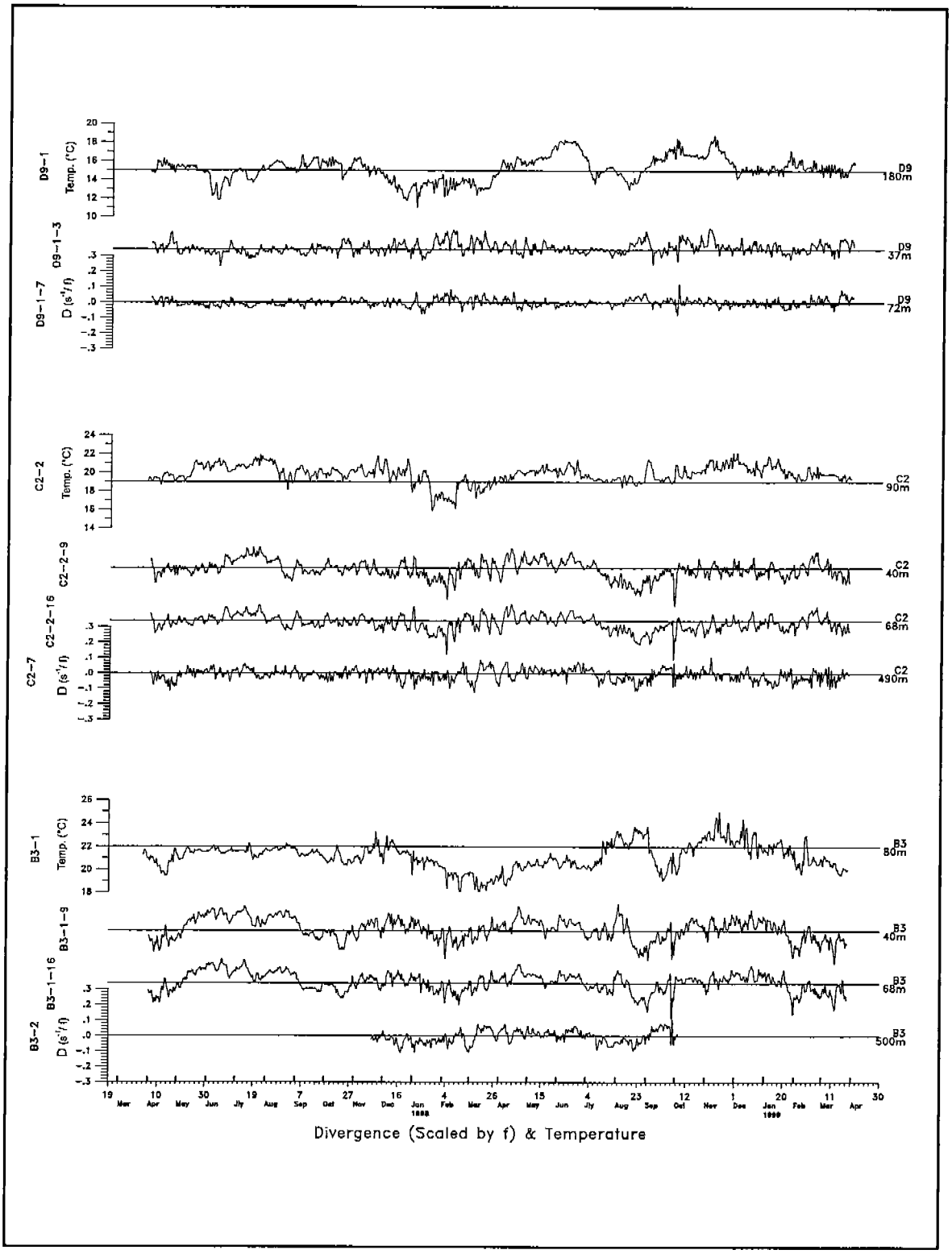

Figure 5.5-2. Divergence (normalized by f) and 40-HLP temperature time series for the indicated positions.

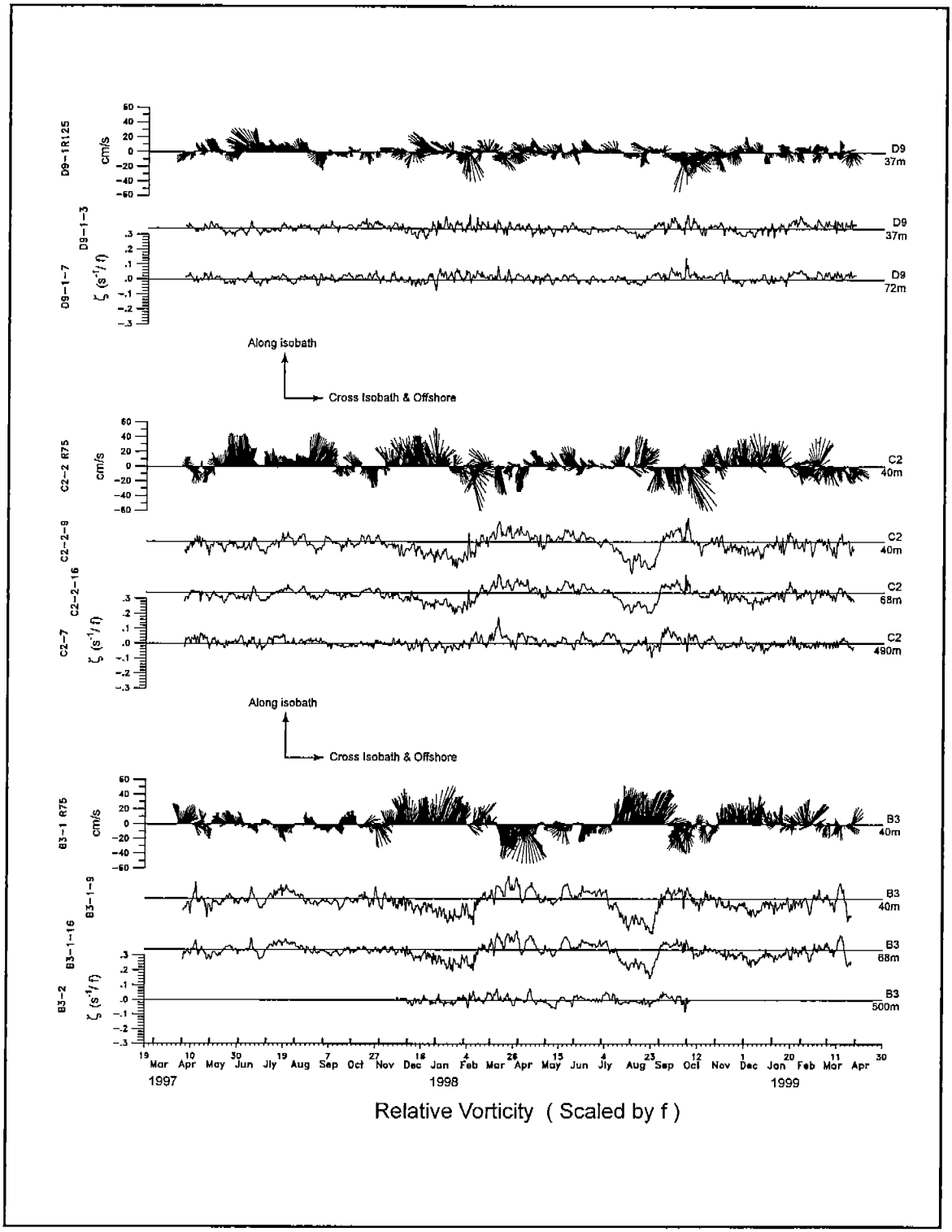

Figure 5.5-3. Relative vorticity (normalized by f) and 40-HLP current vectors for the indicated moorings and measurement depths. Relative vorticity is such that a positive value indicates a tendency for counterclockwise rotation and a negative value for clockwise rotation.

of the vorticity fluctuations at D9 is somewhat surprising given that flows following the rim of the canyon should have considerable curvature. However, major flow events often bypassed the head of the canyon, and the eddy scales were often smaller than the separation between the moorings used for these calculations (Figure 5.5-1).

The spectra of D and ζ show that most of the energy was at periods longer than 50 days (Figure 5.5-4a). The peak at ~100 days is similar to those found in the velocity spectra (Figure 5.4-12) and suggests that the major vorticity fluctuations were associated with the long period propagating slope waves that are probably related to LC and LC ring effects. Figure 5.5-4 also shows the coherence squared and phase differences of the most coherent records with D and ζ at B3 and C2 (40m depth). At long periods, the vorticity was coherent and 180° out-of-phase with the along-slope current at B3. This confirms the visual correlations of the time series in Figure 5.5-3. However, D and B3 were coherent and in-phase with the along-slope current at C2 at both long periods and periods of order 10 days. D and ζ were not significantly correlated at B3 and because ζ at B3 and C2 were highly correlated (Figure 5.5-4c), ζ at C2 was only weakly correlated with the along-slope currents at C2. A dynamical explanation of why the divergence of the eddy circulations over the lower slope were closely related to the current over the middle slope is not apparent at the present time. The other interesting relation to come from the coherence analysis is that the divergence at C2 was most strongly related to the across-slope current at C2 (Figure 5.5-4c). This seems to indicate that part of the up- and downwelling that occurs along the edge of eddies on the lower slope was induced by cross-slope exchange.

5.5.2 Across Margin Transport of Momentum at the Canyon Edge

Cross-margin flows at the canyon edge can also result in exchange of momentum between the canyon and the adjacent shelf. Using the velocity data from canyon edge moorings, the total cross-margin fluxes of along-isobath velocity, and its eddy contribution were computed according to:

$$F_M = uv, \text{ and } F_{Me} = u'v'$$

where F_M and F_{Me} are the total and eddy fluxes, respectively; u is along-isobath velocity; and u' and v' are fluctuations about the means of u and v. Hereafter, F_M and F_{Me} are referred to as momentum fluxes (although, technically, they are related to actual momentum fluxes through sea water density). The velocity rich data set from the canyon edge moorings allowed for the computations of momentum fluxes throughout most of the water column. These data further enabled us to compute "momentum transport" at each of the moorings by integrating the momentum fluxes over depth, i.e.

$$T_M = \int F_M dz, \text{ and } T_{Me} = \int F_{Me} dz$$

where T_M and T_{Me} are referred to as the total and eddy cross-margin momentum transports, respectively. The ADCP data from each of the shelf-edge moorings were used to compute these T_M and T_{Me} time series. These data spanned a depth range of roughly 12-72m.

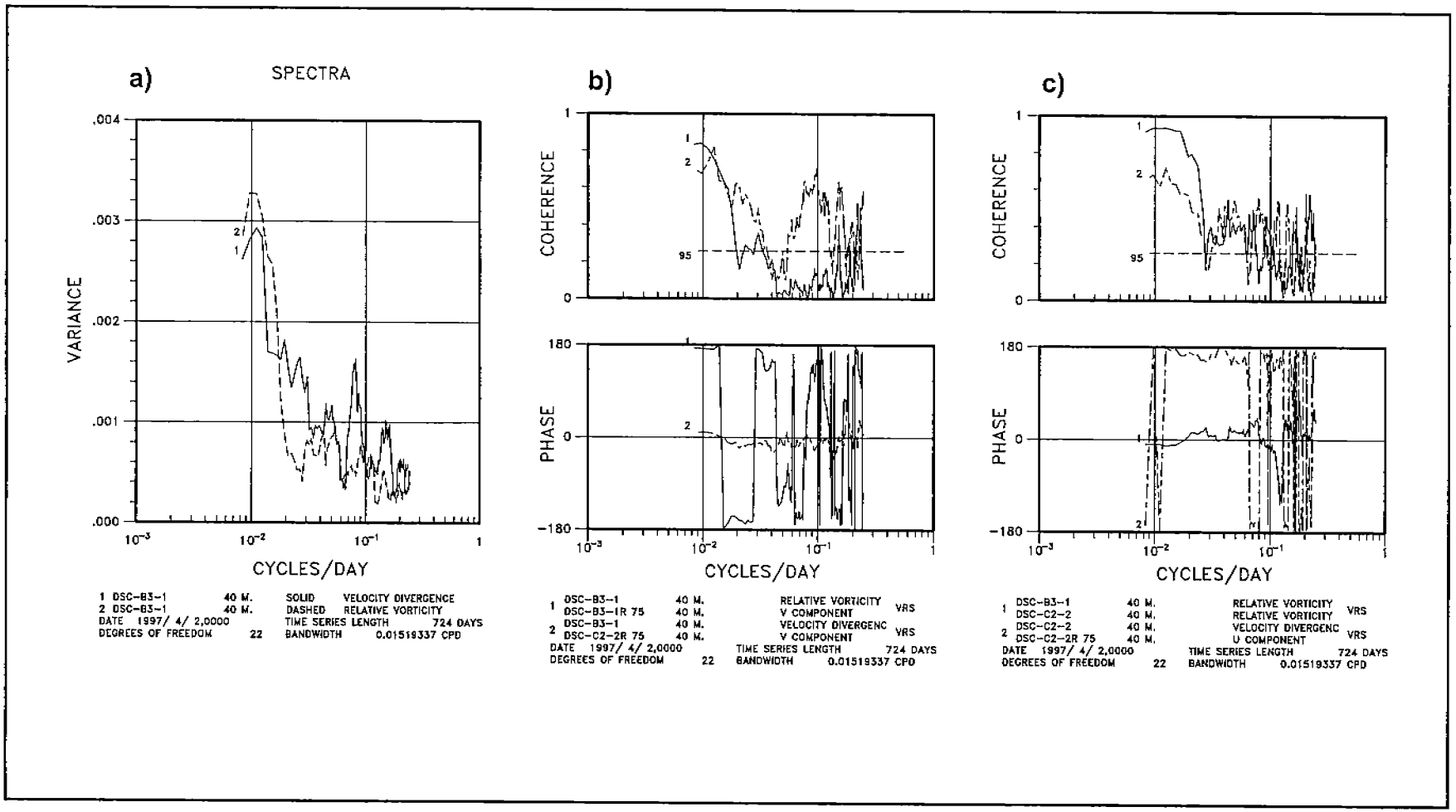

Figure 5.5-4 (a) Spectra of the divergence and relative vorticity at B3. Coherence squared and phase differences between the indicated records at (b) B3 and (c) C2.

Integration of T_M over time gives an estimate of the quantity of momentum transferred across the canyon edge per unit along-canyon distance. When considering the direction of this momentum transport, it is necessary to take into account the direction of the along-isobath flow, u. The coordinate system used in these calculations has the positive u direction set such that deeper water is to its right(i.e., to the northeast at moorings A1, B1 and C1; and to the southeast at mooring E1). With this convention, the positive v direction is always onshelf. In this rotated coordinate system, positive momentum fluxes and transports represent the onshelf flow of positive along-isobath momentum (positive u) or the offshelf flow of negative along-isobath momentum. Consider, for example, momentum fluxes occurring at mooring C1 when the flow at the mooring is northeastward (positive u). Positive momentum fluxes represent an onshelf transfer of the momentum of this flow. However, if the flow at the mooring is to the southwest (negative u), then a positive momentum flux represents an offshelf transfer of momentum from this flow (because, in this case, [uv] is positive for an offshelf velocity).

Unlike the cross-margin fluxes of temperature and salinity discussed later in Section 5.5.3, the cross-margin momentum fluxes and transports computed from the canyon edge mooring data were dominated by the eddy contributions. For all computed momentum transport time series, the ratio of T_{Me} to T_M variance was 0.82-0.95.

Time series of vertically averaged along-isobath current and T_M, computed from the canyon edge ADCP velocity profiles (Figure 5.5-5) reveal a number of events of strong along-isobath flow coupled with large cross-margin momentum transports. At all canyon-edge moorings, the largest vertically averaged along-margin flows occurred during Hurricane Georges (late September 1998). These flows were in the negative u direction (having an alongshore westerly component) at all canyon edge moorings, indicating a hurricane-induced flow moving counterclockwise along the canyon rim. As with the cross-margin salinity and temperature fluxes discussed in Section 5.5.3, the computed canyon edge momentum transports differed greatly from mooring to mooring during the hurricane.

Large along-isobath currents and cross-margin momentum transports were also observed during the winter of 1997-1998. As noted in Section 6.4, this was a period when intense storms passed over the canyon and when a vigorous eddy was seen at the western canyon edge. The vertically averaged velocities and cross-margin momentum transports from this period (Figure 5.5-6) reveal a response to wind forcing which varied from storm to storm; and, for each storm, from mooring to mooring. The late December 1997 storm generated positive along-isobath flows along the canyon rim. Computed cross-margin momentum transports associated with these flows were relatively large and directed onshelf at moorings A1 and E1, but were negligible at mooring C1. By contrast, the storm of early February 1998 generated strong negative along-isobath flows along the canyon rim. Computed cross-margin momentum transports during this storm were unusually large only at mooring C1. These very large momentum transports at C1 would have carried the storm-generated momentum onshelf. Relatively large cross-margin momentum transports

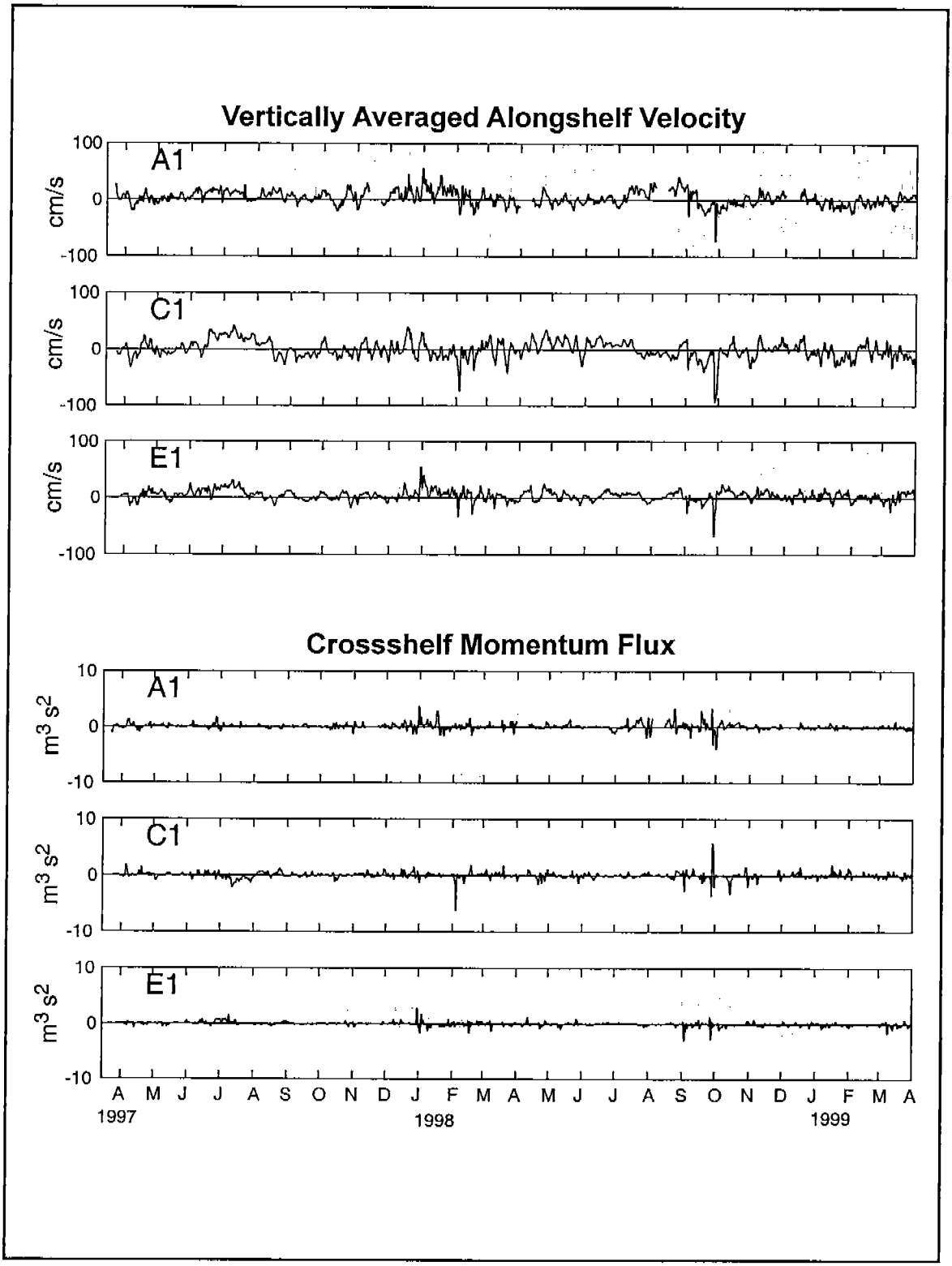

Figure 5.5-5. The top three panels show vertically averaged along-isobath velocity at the indicated moorings. The lower three panels show estimated cross-isobath momentum transport at the indicated moorings.

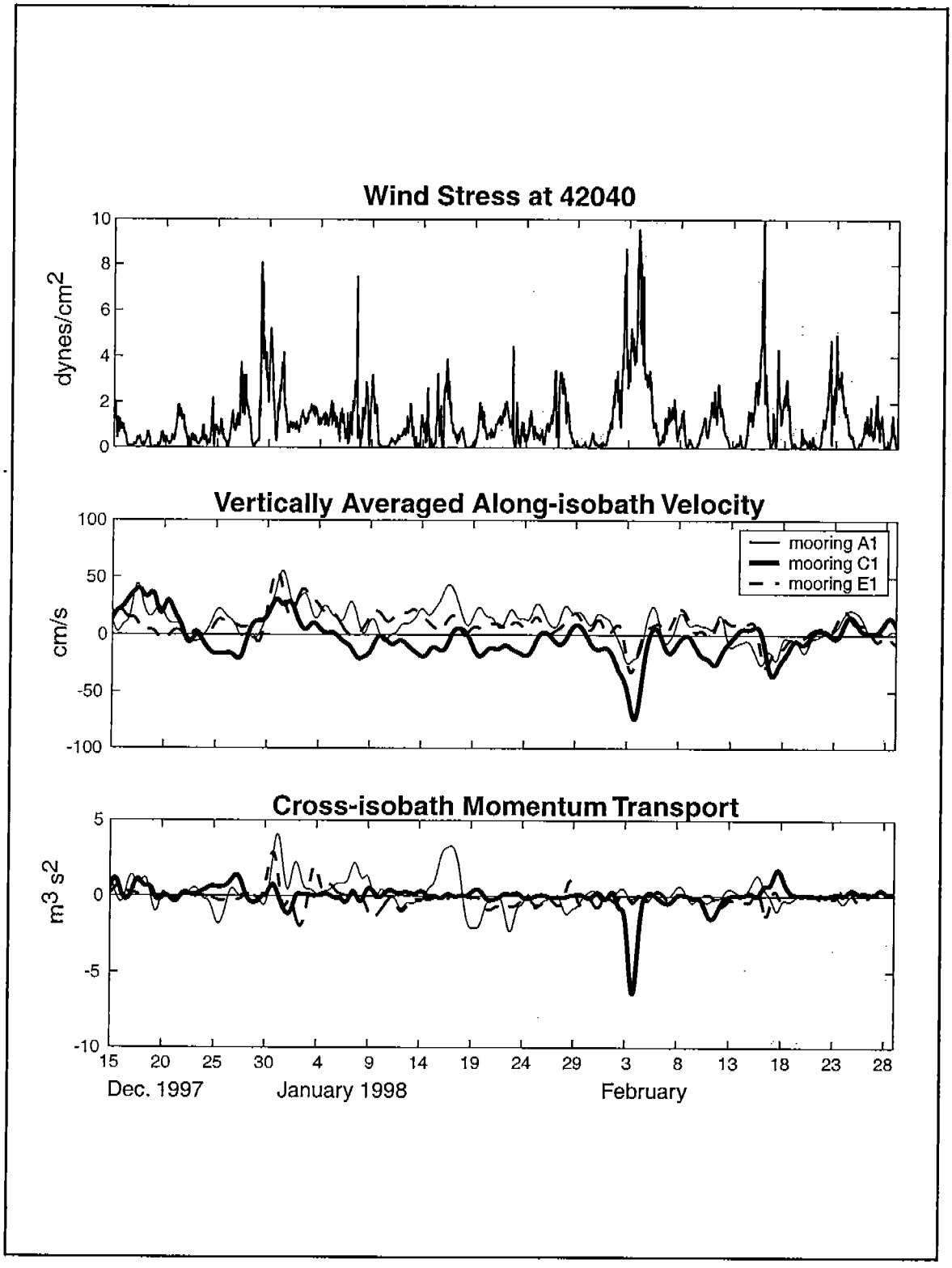

Figure 5.5-6. For the winter of 1997-1998, computed surface wind stress at buoy 42040 (top panel), vertically-averaged along-isobath velocity (middle panel) and cross-isobath momentum transport (bottom panel).

were also observed during mid-January 1998 when the winds were mild and an eddy was observed at the canyon edge. These large momentum transports were confined to moorings A1 and B1, which is consistent with satellite imagery which show the eddy in the area of these mooring during mid-January (see Figure 6.4-14,15). The computed transports at A1 changed sign (from onshelf to offshelf) on January 18, presumably due translation of the eddy by the mooring.

To assess the possible influence of the computed momentum transport "pulses" on the canyon-edge velocity field, consider an idealized situation in which the onshore momentum flux is confined to an outer shelf band of width, W, and mean depth, D. In the absence of friction, the average velocity in this band will be changed by:

$$\Delta v = \int_{t_1}^{t_2} T_M dt / (DW)$$

Integrating over the successive onshelf and offshelf momentum transport pulses seen at A1 during mid-January 1998 (associated with the eddy encounter with the canyon edge) and setting D and W to 60m and 20 km, respectively, gives a Δv of 20 cm/s. Using the same D and W values and integrating over the onshelf momentum pulse seen at mooring C1 during the early February 1998 storm, gives a Δv of 50 cm/s. Clearly, results of these over-idealized calculations are not robust in a quantitative sense. Nevertheless, they provide evidence that cross-margin momentum fluxes during storms and times of eddy contact with the canyon edge may significantly influence flows over the shelf near the canyon edge.

To estimate the overall extent to which wind-forcing contributed to the cross-margin momentum fluxes, we computed a wind-driven component of the fluxes using the method outlined in Section 5.5. The relationship of the estimated wind-driven fluxes at various depths was investigated through cross-spectral analysis. For a particular mooring, cross-spectra were computed between the shallowest and all other flux time series. Coherence and phase relative to the shallowest flux series was determined according to standard formulae (Bendat and Piersol, 1971; p 32) and by frequency band averaging over the entire cross-spectra. As demonstrated here by the results for mooring C1 (Figure 5.5-7), the estimated wind-driven fluxes accounted for roughly one half of the total flux variance. The wind-driven fluxes were highly coherent over the water column, with coherence always exceeding the 99% confidence interval. Their relative phases suggest a two-layer structure to the wind-driven momentum flux, with near-bottom fluxes nearly 180° out-of-phase with fluxes above (Figure 5.5-7). The zone separating the layers was relatively narrow and deep, extending over the 55-60 m depth range at mooring C1.

Because the cross-margin momentum fluxes were determined from both along and across-isobath velocity components, an obvious concern is their sensitivity to the choice of along-isobath orientation. To test this, we computed across-margin fluxes and transports at each canyon

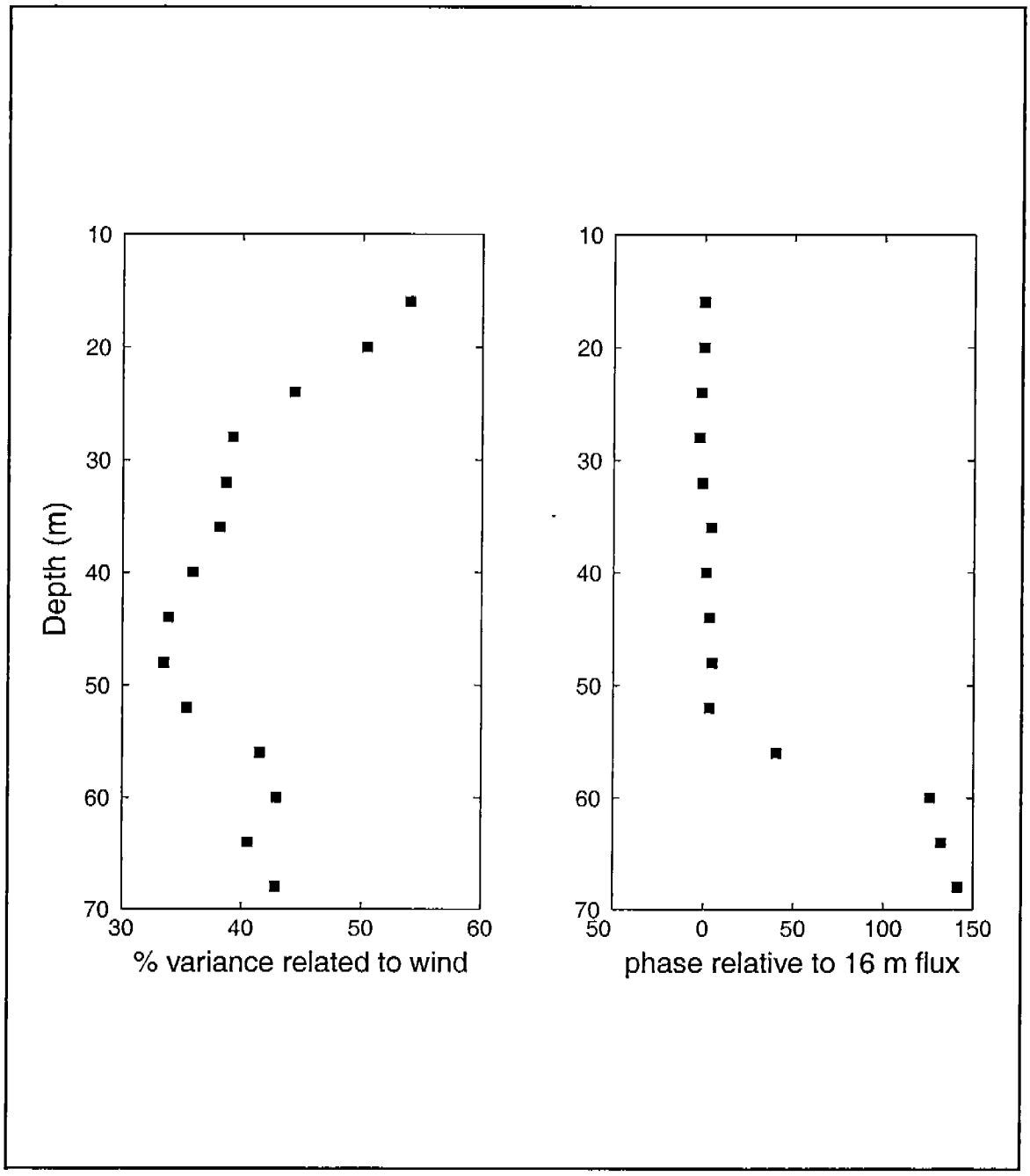

Figure 5.5-7. Characteristics of the estimated wind-driven cross-margin fluxes of momentum at mooring C1. The left panel shows the ratio of the estimated wind-driven to total flux variance. Shown in the right panel is the relative phase of the wind-driven flux as a function of depth.

edge mooring using along-isobath orientations differing by ± 5° of the orientation chosen for the calculations which produced the results discussed above (these orientations are given in Table 6.4-2). Although the details of the momentum fluxes and transports changed with varying orientation, all of the features discussed above were seen at all orientations tested.

5.5.3 Across Margin Heat and Salt Fluxes at the Canyon Edge

Cross-margin flows at the canyon edge can effect an exchange of warm, saline within the canyon with the fresher and cooler coastal water onshore. Using temperature, salinity and velocity time series from the canyon edge moorings, cross-margin fluxes of temperature and salinity were computed using:

$$F_T = vT, \qquad F_S = vS$$

where T, S and v represent temperature, salinity and the across-isobath component of velocity. F_T and F_S can be converted to heat and salt fluxes by multiplying by seawater heat capacity and density, respectively. The portion of the property fluxes produced by random, "eddy" motions, was estimated in the typical fashion as the product of property and velocity fluctuations about their means. For example, eddy fluxes of temperature were calculated as:

$$F_{Te} = v'T', \text{ with } v' = v - \langle v \rangle, \text{ and } T' = T - \langle T \rangle$$

Where <> denote time averaging. With this convention, total mean fluxes could be divided into eddy and advective components, i.e.

$$\langle F_T \rangle = \langle v \rangle \langle T \rangle \langle v'T' \rangle$$

Computation of temperature and salinity fluxes at the canyon edge was limited by the paucity of temperature and salinity data from the canyon edge moorings. These allowed for determination of coincident temperature and salinity fluxes at only 11 points over the canyon-edge (Tables 5.5-1 and 5.5-2), concentrated near the bottom and near the surface. In addition, times over which the fluxes could be calculated were limited by sensor failure, and varied greatly from point to point.

At all locations, eddy fluxes made a relatively small contribution to the total cross-margin flux of temperature and salinity (e.g. Figure 5.5-8) keeping in mind that both salinity and temperature are always positive and always greater than some minimum value, thus the total fluxes may be large due to the contribution of temperature and salinity above the local minimum values. Certainly the sign of this total flux is the sign of the cross isobath velocity. For salinity fluxes, variance of the eddy flux was 0.1-2% of the total flux variance. Eddy fluxes of temperature made a somewhat larger, 4-14%, contribution to the total variance of temperature flux.

Of particular note is the strong linear relationship between temperature and salinity fluxes, demonstrated here by the plot of all salinity fluxes against all temperature fluxes at the canyon edge moorings (Figure 5.5-9). Slope of the least-squares linear regression line

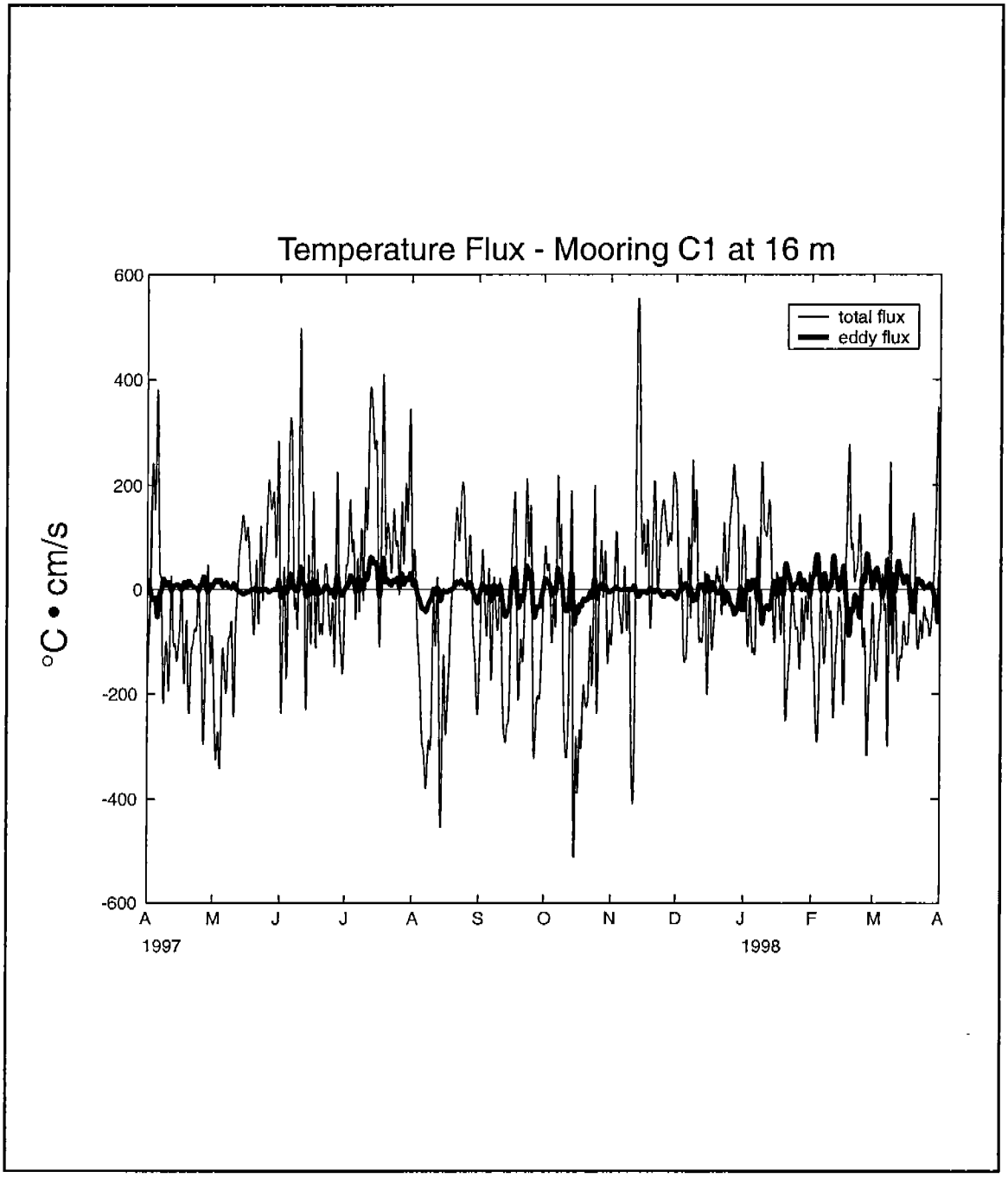

Figure 5.5-8. Time series of cross-isobath temperature flux at 16 m depth at mooring C1. Total flux and eddy flux are shown by the thin and bold lines,respectively.

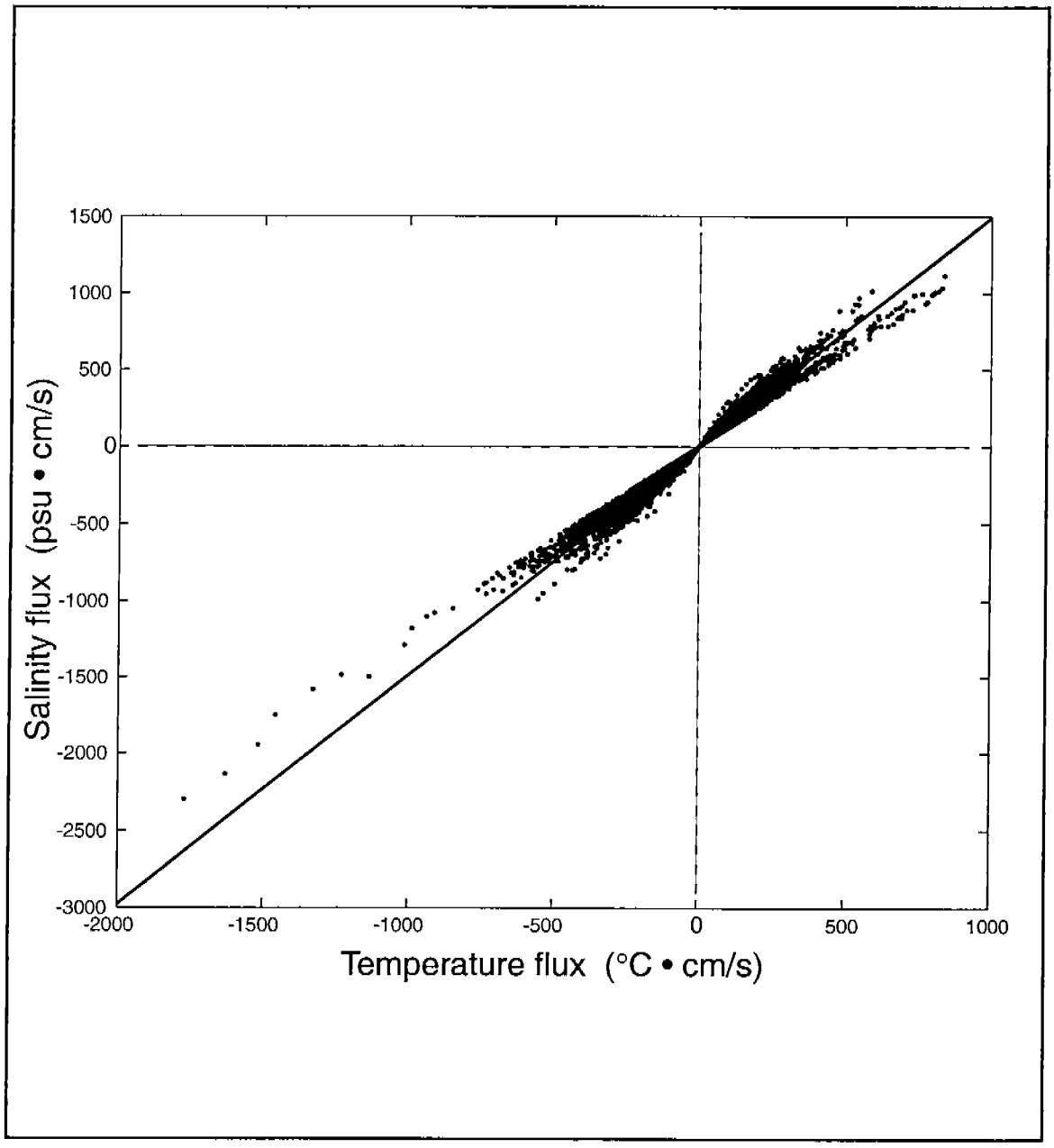

Figure 5.5-9. Plot of cross-margin salinity flux against cross-margin temperature flux. Fluxes were computed using data from canyon edge moorings (A1, B1, C1, D1 and E1). The line was fit to the points by least-squares.

relating these fluxes was 1.49 psu/°C with a 95% confidence interval of only 0.004 psu/°C. In view of the much lower costs of acquiring temperature vs salinity measurements, this result may be of value in designing future studies in the area. Water mass fluxes may be adequately determined from temperature and velocity measurements alone.

When judged by their statistical errors, the computed mean fluxes of temperature and salinity across the canyon edge were significant at moorings C1, D1 and E1, and not at A1 and B1 (Tables 5.5-1 and 5.5-2). The mean fluxes at C1, D1 and E1 were dominated by their advective components. These means suggest that, in the long term, the water mass exchange at the canyon edge may be something of a two-layer phenomenon, with onshelf flux near the surface and offshore flux near the bottom.

Unfortunately, the limitations in available mooring data does not support an evaluation of how fluxes in the center of the canyon edge water column may conform to, or clash with, this view.

Table 5.5-1. Estimated cross-margin temperature fluxes at DeSoto Canyon edge moorings (at 100 m isobath). Positive fluxes are onshelf.

Mooring	Sensor Depth (m)	Dates	Total Fluxes °C cm/s		Eddy Fluxes °C cm/s	
			Mean	Std. Err.*	Mean	Std. Err.*
A1	16	08/18/1998 - 01/28/1998	1.1	49.6	-1.33	2.73
A1	16	12/17/1998 - 04/01/1999	-28.2	20.9	-1.97	1.2
B1	20	04/01/1997- 08/18/1997	-26.9	18.9	-4.66	1.98
B1	62	11/25/1997 - 04/04/1998	16.5	15.5	0.79	0.81
B1	82	11/25/1997 - 04/04/1998	1.0	9.7	1.11	0.76
B1	82	04/01/1997 - 07/01/1997	-0.8	12.6	0.92	0.57
C1	16	08/17/1998 - 04/01/1999	-51.2	25.9	-6.79	3.62
C1	20	03/27/1997 - 08/08/1998	-16.5	11.2	1.16	1.39
C1	82	08/27/1997 - 12/05/1998	40.0	5.1	-0.82	0.58
D1	62	08/14/1998 - 03/30/1999	-66.1	8.1	-0.09	0.88
E1	20	03/31/1997 - 11/14/1997	-85.7	19.1	-3.58	1.78
E1	20	04/12/1998 - 03/31/1999	-49.7	15.3	-5.73	1.93
E1	62	11/23/1997 - 04/03/1998	8.1	16.5	-1.15	1.02
E1	82	07/20/1997 - 08/07/1998	5.4	5.2	-0.39	0.42

* Standard Errors were computed as Std. Err. = $SD/(df)^{1/2}$, where SD is the standard deviation of the fluxes about the estimated mean and df are the number of independent flux measurements from which the mean was calculated. df were approximated as T/T_c, where T is the length of the flux series and T_c is the correlation time scale of the series. Based on autocorrelation functions of the flux series T_c was set to 60 hrs. 90 % confidence limits of the means are roughly twice the standard errors (see Bendat and Piersol, 1971; p 115).

An issue of importance is the extent to which canyon edge fluxes were the product of wind-induced flow or the result of other types of

motions, such as those generated by LC eddies. To address this issue, a standard statistical technique was employed to extract that portion of a salinity or temperature flux series that was statistically related to the surface wind stress. The procedure was carried out in two steps. In the first, the relation between flux and wind stress was quantified by computing a spectral transfer function with east and north wind stress components as inputs and cross-margin flux as the output (see Bendat and Piersol, 1971; pp 151-153). In the second step, this function was combined with the wind stress components to produce the estimated wind-driven component of the flux series.

In Figure 5.5-10, supports a comparison of the total and estimated wind-driven component of cross-margin temperature flux at moorings C1, D1 and E1. Also shown are the ratios of the wind-driven flux variance to the total flux variance, a rough estimate of the proportion of flux generated by wind motions. These ratios suggest that wind-forced flows may have accounted for a significantly higher proportion of the cross-margin temperature flux near the bottom than at the surface. This disparity is best evidenced by the mooring C1 flux variance ratios. The admittedly sparse time series suggest a seasonality in the importance of wind-induced fluxes. The greatest mismatch between total and wind-forced temperature fluxes tended to occur in the spring and summer. Of note are the large temperature fluxes seen at the 20m level of mooring E1 during May-July 1998, which coincided with negligible estimates of wind-driven temperature flux. At all moorings, the largest cross-margin temperature fluxes occurred during Hurricanes Earl and Georges (in September 1998). However, the character of the fluxes during these storms was not the same at all moorings. At mooring C1, they were offshore near the surface and onshore near the bottom, while the reverse was observed at moorings D1 and E1.

Table 5.5-2. Estimated cross-margin salinity fluxes at DeSoto Canyon edge moorings (at 100 m isobath). Positive fluxes are onshelf.

Mooring	Sensor Depth (M)	Dates	Total Fluxes psu cm/s		Eddy Fluxes psu cm/s	
			Mean	Std. Err.*	Mean	Std. Err.*
A1	16	08/18/1998 - 01/28/1998	1.2	64.3	-1.97	1.09
A1	16	12/17/1998 - 04/01/1999	-44.0	34.3	-0.39	0.51
B1	20	04/01/1997- 08/18/1997	-33.7	28.0	-0.98	0.45
B1	62	11/25/1997 - 04/04/1998	27.9	27.2	-0.04	0.16
B1	82	11/25/1997 - 04/04/1998	-0.2	19.1	0.01	0.12
B1	82	04/01/1997 - 07/01/1997	-3.2	23.2	-0.03	0.03
C1	16	08/17/1998 - 04/01/1999	-66.9	35.0	-0.07	0.68
C1	20	03/27/1997 - 08/08/1998	-27.6	17.0	-0.55	0.27
C1	82	08/27/1997 - 12/05/1998	78.5	9.8	-0.07	0.07
D1	62	08/14/1998 - 03/30/1999	-114.8	13.9	0.02	0.10
E1	20	03/31/1997 - 11/14/1997	-119.3	27.2	-1.07	0.43
E1	20	04/12/1998 - 03/31/1999	-68.6	23.1	-0.24	0.25
E1	62	11/23/1997 - 04/03/1998	17.1	31.1	0.40	0.19
E1	82	07/20/1997 - 08/07/1998	10.8	10.3	-0.21	0.09

* See Table 5.5-1 for an explanation of the standard errors.

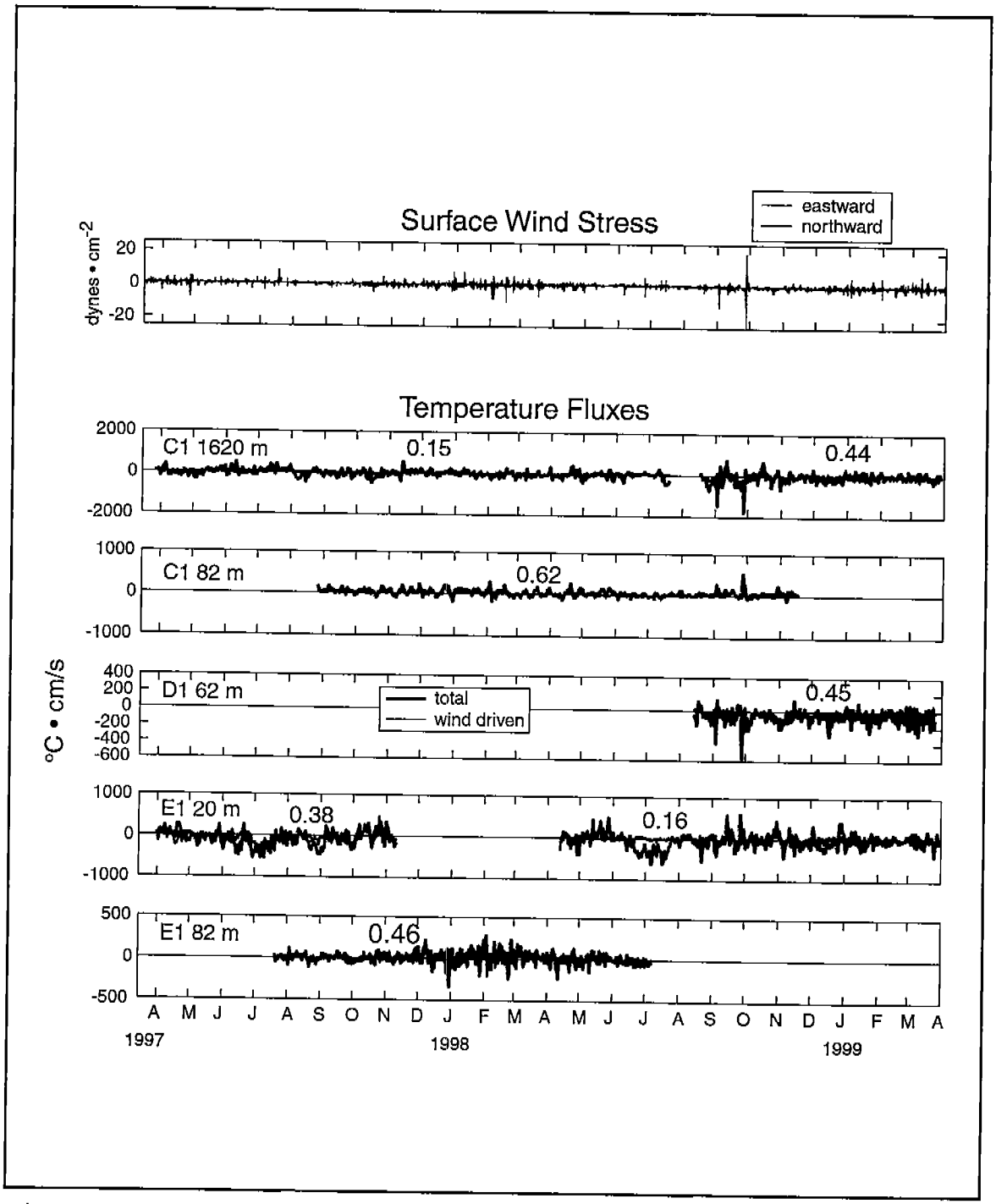

Figure 5.5-10. Time series of cross-margin temperature flux at the indicated moorings and depths together the with surface wind stress components (top panel). Total fluxes are shown by the blue lines. The red lines are the portion of the total flux coherent with the surface wind stress. The number above each time series is the ratio of the wind-driven flux variance to the total flux variance.

5.6 Deep Currents

Previous sections have described the circulation in the upper 500m of the water column. Over the slope, the circulation was dominated by eddies and an eastward flowing current with reversed flows at depths below about 200m. A major source of energy for these flows appears to have been eddy circulations, including LC/LCFE, in the deep eastern basin of the Gulf. The LC and LC rings penetrate to depths of 800 to 1000m. Below these depths, lower-layer currents have been observed to have the characteristics of topographic Rossby waves (TRW) (Hamilton 1990) with periods ranging from about 10 to 100 days. TRW motions are columnar, slightly bottom intensified, have wavelengths of order 50 to 250 km and propagate with group velocities of order 10 to 20 km/day. The majority of studies of TRW's have been in the Middle Atlantic Bight (e.g. Thompson 1977; Hogg 1981) where there has been some success in relating deep TRW motions to Gulf Stream meanders (Pickart 1995). The source of TRW motions in the Gulf is presumed to be the LC though the generation mechanisms have not been established. Numerical model studies, on the other hand, have predicted deep eddy circulations associated with the detachment and westward propagation of LC rings. These lower water column eddies have similar propagation speeds to their overlying LC anticyclone (Welsh and Inoue 2000). The existence of these eddies has not yet been established from observations. If the source of TRW's is primarily in deep water, then wave motions propagating towards the slope will tend to be refracted by the increasing bottom slope back into deep water (Shaw and Csanady 1988). Limited observations of near-bottom currents in depths of about 1000m on the northern slope have shown very small velocities (<10 cm/s) compared to current magnitudes of order 30 cm/s under the LC (Hamilton 1990).

The present study made velocity and temperature measurements at 10m above the bottom at three positions (A3, B3 and C3) on the 1300 m isobath along the northeast Gulf slope. The 40-HLP time series for the two-year study period are shown in Figure 5.6-1. These velocity records were not significantly correlated with the 500m level currents on the same moorings and, therefore, they have been analyzed separately. There were differences between the first six months (April to September 1997) of the A3 velocities and the remainder of the record. In the first six months there was a westward mean flow of 2.1 ± 0.5 cm/s which was similar to the mean at 500m. The fluctuations were not significantly correlated between the two levels of A3. The significant westward mean could be attributed to the cyclonic circulation that was present on the lower slope for most of this period (see Figure 5.4-6 for the summer 1997 mean currents and Figure 5.4-2a & b for the 500m level geostrophic flows in March and July 1997). After October 1997, flows at all three positions had more variability in direction and became more energetic. The eastern most station (C3) and the western most (A3) had the highest and least fluctuation energy, respectively. In examining these figures, there is also visual coherence of some of the events in both the currents and temperature fluctuations.

The kinetic energy and temperature spectra are given in Figure 5.6-2a and b. For the analyzed interval, there was a peak in the spectra for C3 at about 20 days. Hamilton (1990) showed that the 20- to 30-day

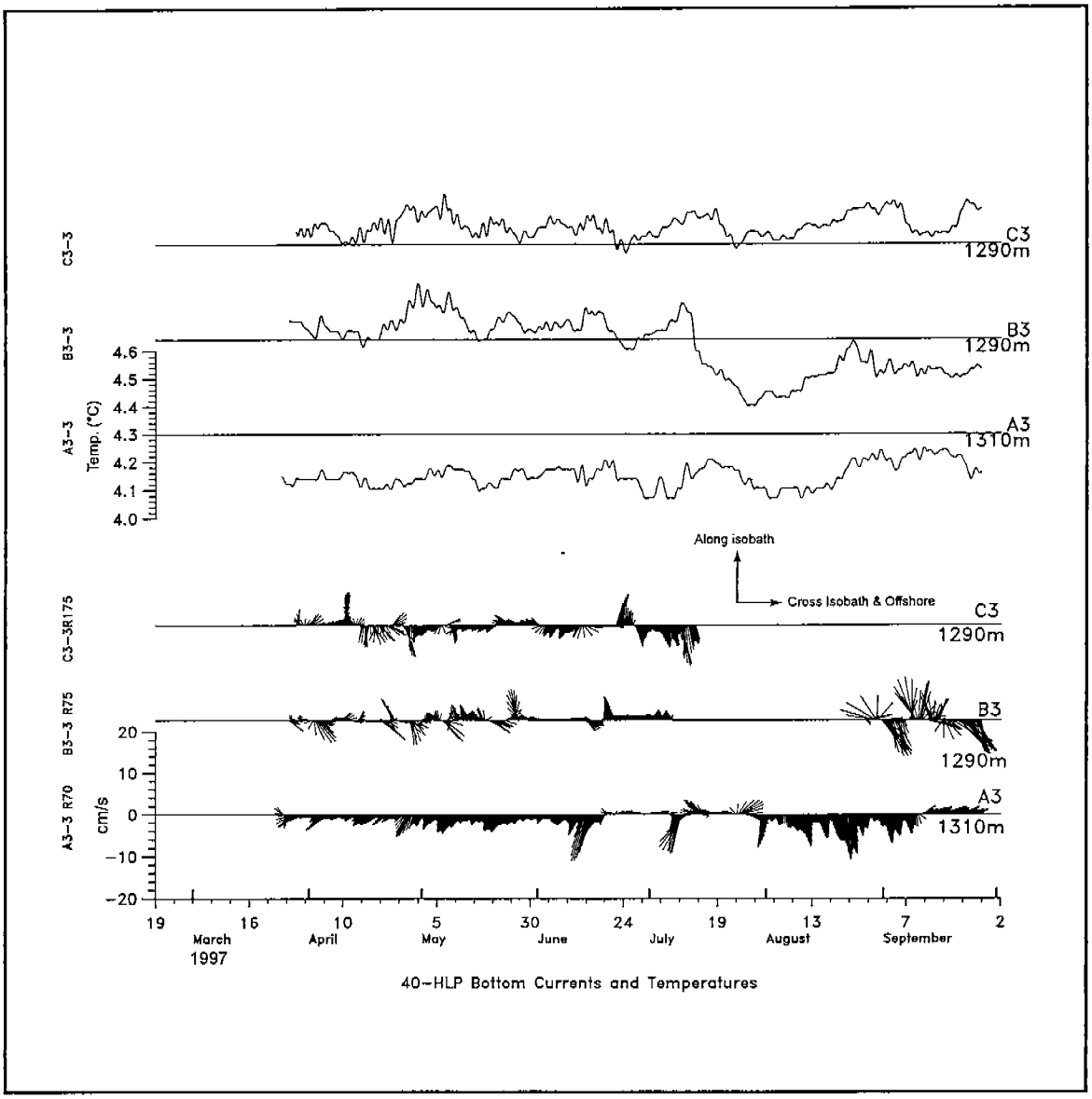

Figure 5.6-1a 40-HLP velocity vectors and temperatures for the bottom current meters on the 1300m moorings. Plotted in four, six-month segments (a-d). Vectors directed vertically upward are along isobath with an easterly component.

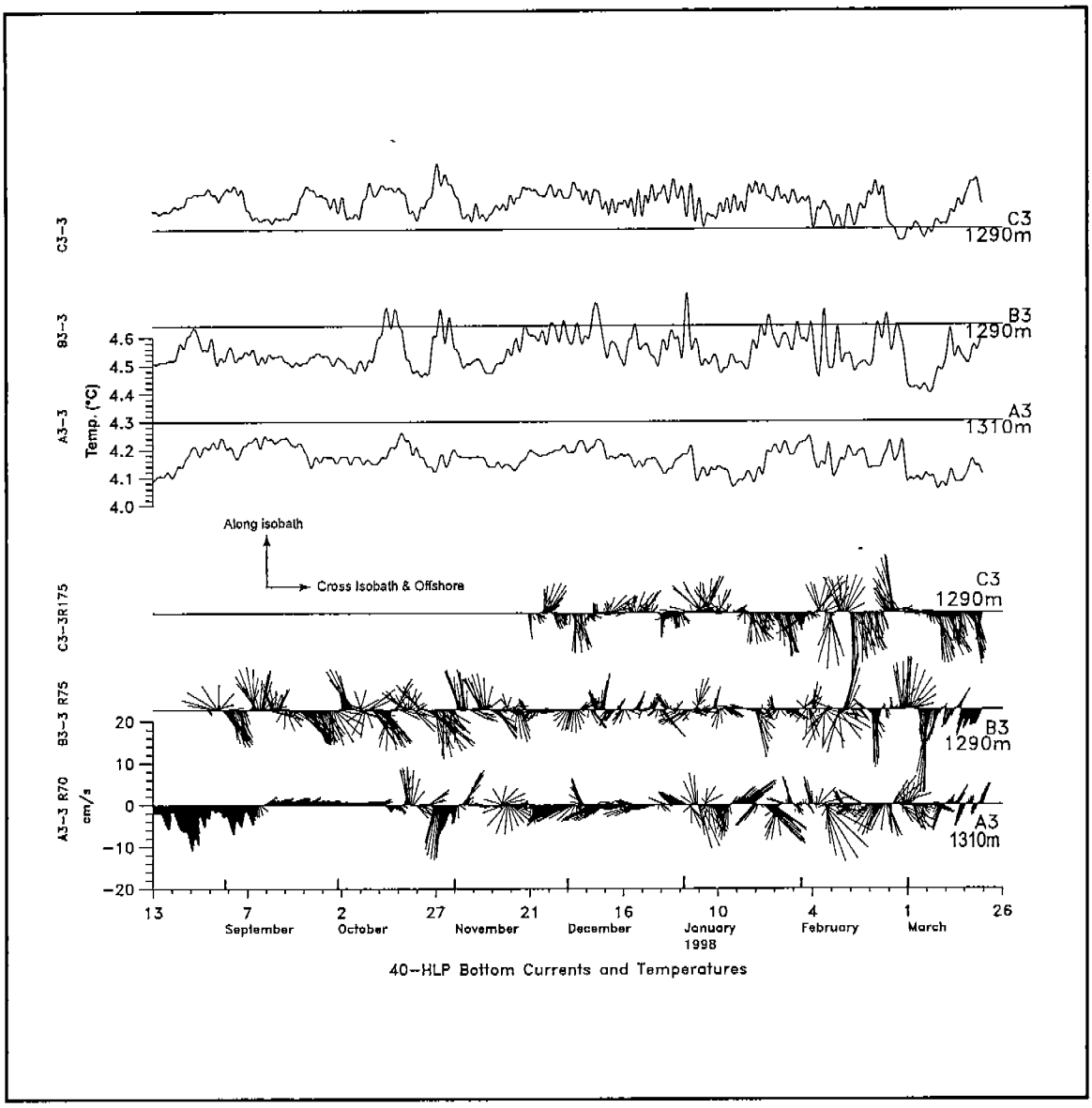

Figure 5.6-1b. 40-HLP velocity vectors and temperatures for the bottom current meters on the 1300m moorings. Plotted in four, six-month segments (a-d).

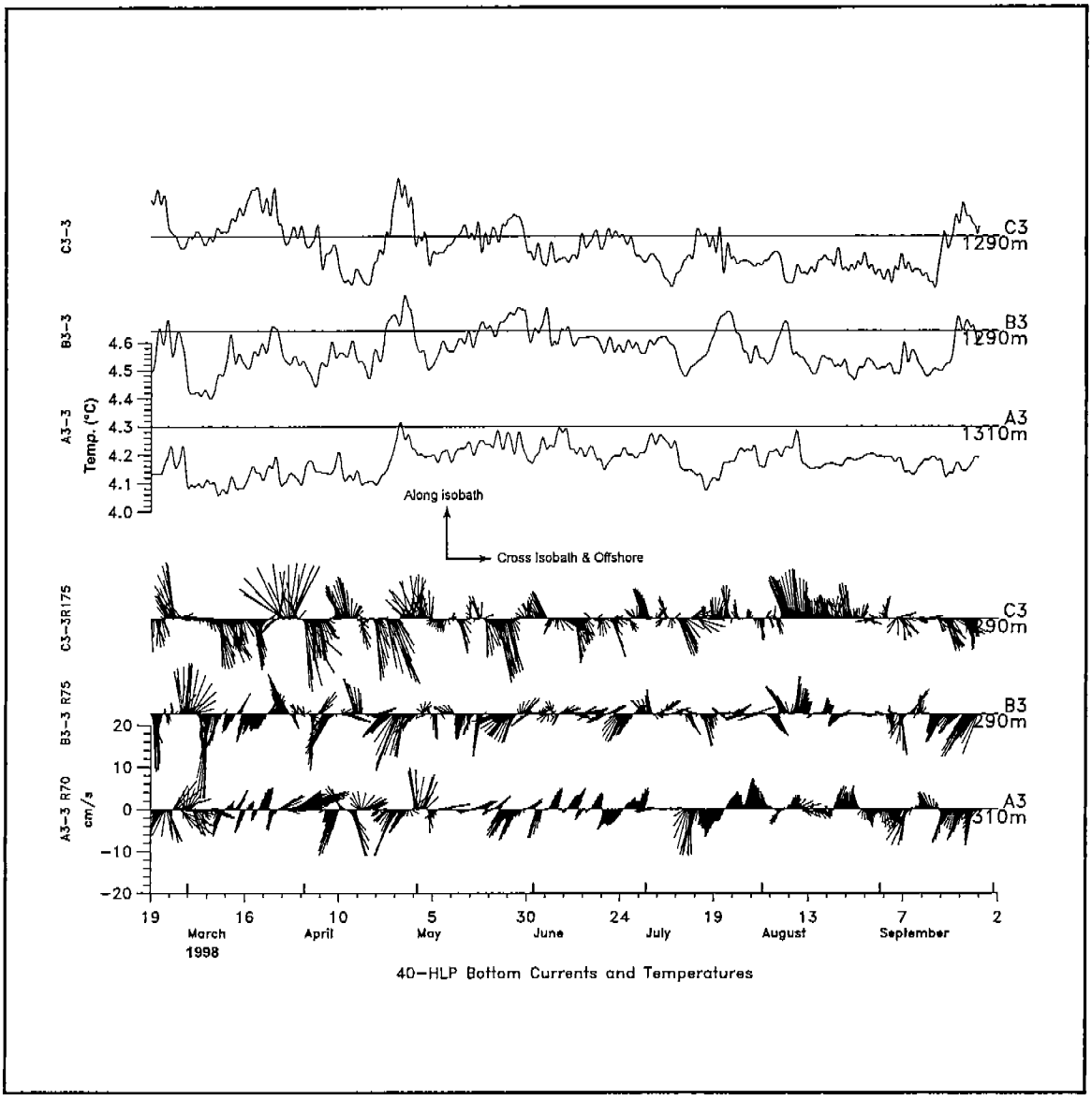

Figure 5.6-1c 40-HLP velocity vectors and temperatures for the bottom current meters on the 1300m moorings. Plotted in four, six-month segments (a-d).

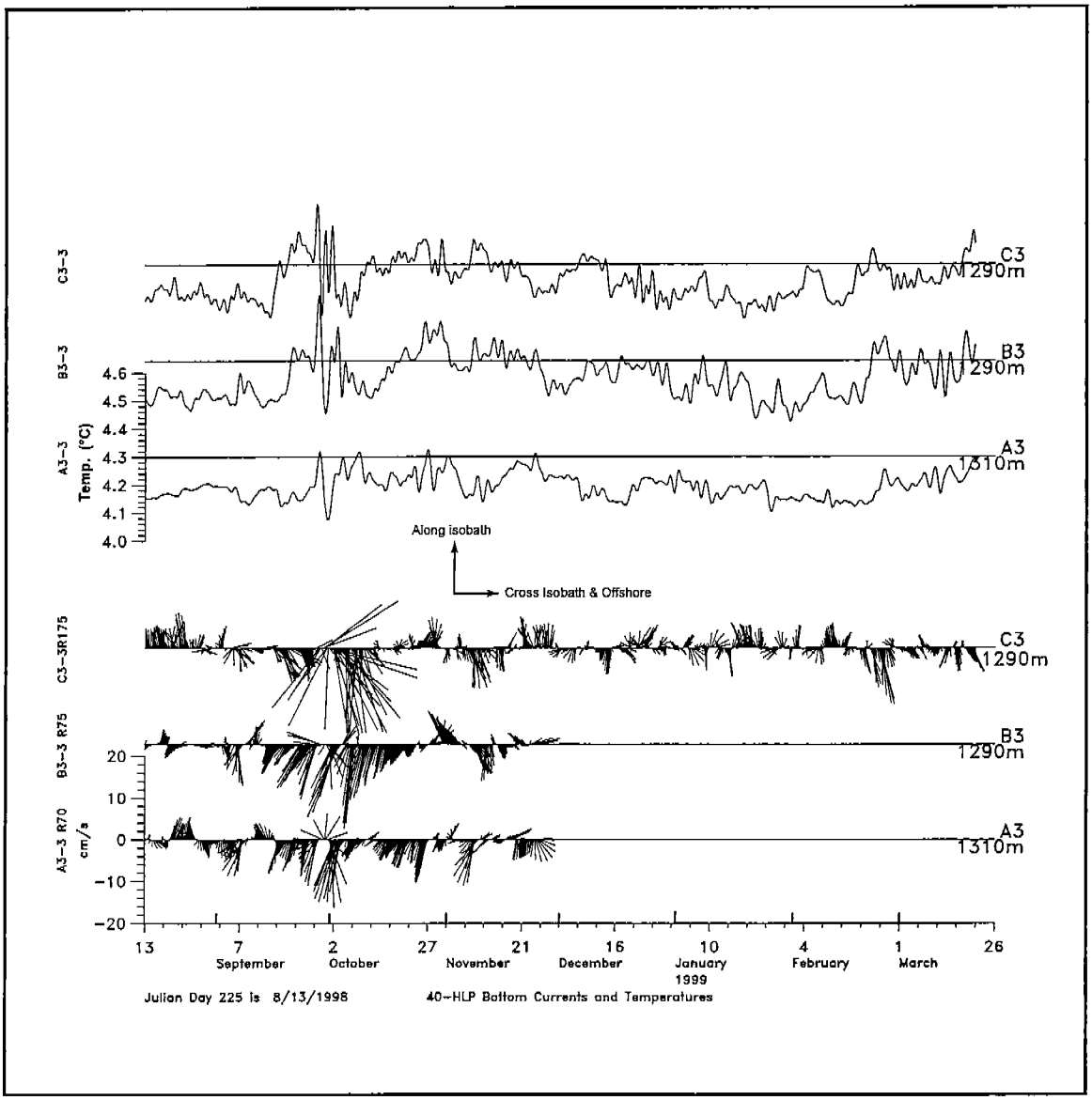

Figure 5.6-1d 40-HLP velocity vectors and temperatures for the bottom current meters on the 1300m moorings. Plotted in four, six-month segments (a-d).

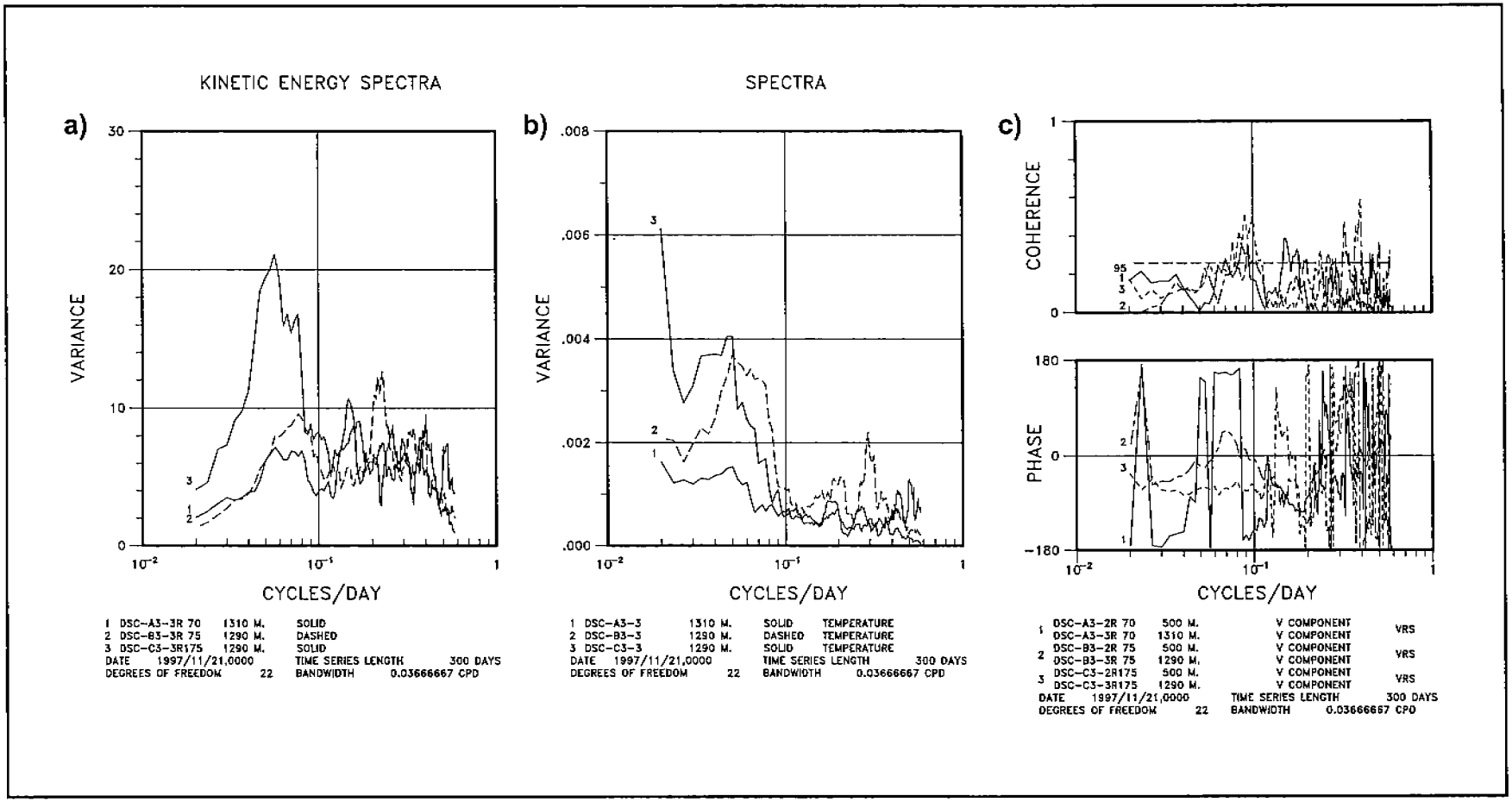

Figure 5.6-2 For bottom instruments on 1300m moorings: (a) Kinetic energy spectra (b) temperature spectra. In panel (c), coherence squared and phase differences are shown between the along isobath (V) components at 500m and 1300m for the three offshore moorings.

period TRW's dominate the spectra in water depths greater than 2000m, particularly in the central and western Gulf. On the northeast Gulf slope, the energy at these periods decreased rapidly towards the west indicating that the source could have been further to the south along the west Florida escarpment and thus may have been related to LC frontal eddies on the east side of the LC. At higher frequencies the spectra had a number of small peaks. There was little energy associated with these motions though there were intervals in the records when short period fluctuations (amplitudes ~5 cm/s) dominated at one or two of the moorings. An example is the May-June 1998 period at A3 and B3 (Figure 5.6-1c). The phase and coherence between the 500 and 1300m along-isobath (V) components (Figure 5.6-2c) confirms that the lower slope bottom currents were largely decoupled from flows in the upper layers.

An EOF analysis for the 10- to 50-day fluctuations (0.02 to 0.1 cpd) was performed for the bottom velocity and temperature records at the three moorings. A common interval of 300 days beginning on November 21, 1997 was used for the analysis. This avoids the period at the end of September 1998 where relatively large velocities of ~20-25 cm/s (Figure 5.6-1d) caused by Hurricane Georges were observed (see Section 6.3). The spectra were normalized by the variance of the frequency band so that U, V and T had equal weight in the EOF decomposition. The results are given in Figure 5.6-3 where the top panel shows mode 1 velocity ellipses and the lower panel the normalized amplitude and phase of temperature (T), and the cross (U) and along (V) isobath velocity components. Only the first mode, which accounts for 48.8% of the normalized variance in the frequency band, was significant. The velocity ellipses show the rapid decay of kinetic energy from east to west with the signal at A3 lagging that of C3. The major axes also rotated clockwise with respect to the local isobath direction. In the east, at C3, the major axis of the ellipse was at a small angle to the north-south trend of the west Florida escarpment isobaths. In the west, at A3, the fluctuations were almost perpendicular to the slope. If these motions were TRW's, then this must have been caused by changing bottom slopes from steep to less steep so that the wave frequency moved closer to the cut-off frequency (Rhines 1970) above which TRW motions were not supported.

The phase of T and V show a linear increase with distance along the isobath (Figure 5.6-3b) where positive phase differences lead. Thus, westward propagation is clearly indicated with an average phase difference between C3 and A3 of 58°. This results in an along-isobath wavelength of 620 km. The across-isobath wave number is the larger component for short-wavelength TRW's. Therefore, the true wavelength will have been less than 620 km. These westward propagating wave-like motions appear similar to TRW's found in deeper water. There is no information on the variability with depth in the bottom few hundred meters of the water column, and therefore, it is not known if there was any bottom trapping of these fluctuations that is characteristic of TRW's. It is however noted that the EOF analyses of the upper-layer currents at these frequencies showed no indication of any westward propagating signals. In this upper layer, propagating wave-like fluctuations were restricted to periods longer than 50 days. This

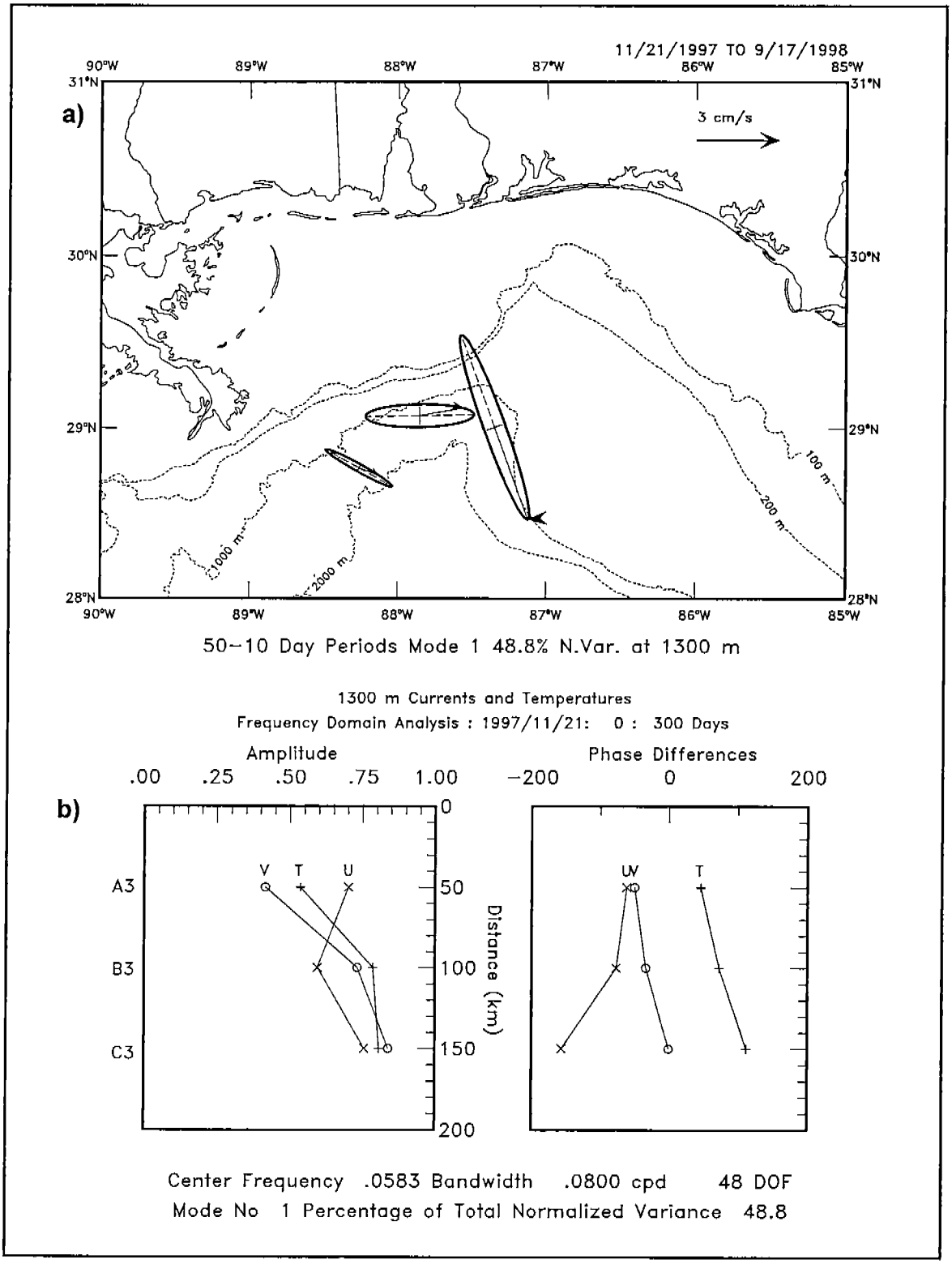

Figure 5.6-3 50 to 10-day frequency domain EOF analysis. The upper panel (a) shows mode 1 velocity ellipses. The lower panels (b) show normalized amplitude and phase versus distance along the isobath for the bottom instruments on the 1300m moorings.

separation by frequency and characteristics of upper and lower layer waves indicates that they had different sources and generation mechanisms. These are unknown at the present time.

VI. SLOPE RESPONSE TO ATMOSPHERIC FORCING

6.1 Introduction

A detailed evaluation of the *in-situ* and survey data revealed that atmospheric processes at the ocean surface appeared to have influenced to varying degrees the circulation and transport patterns in the study area. As evidenced from the presentation in Chapter 5, eddy-like features having several origins were present and affecting the observed currents. The actions of multiple forcings by these eddy motions as well as atmospheric forcing tends to complicate isolation of particular process-response models. When the meteorological forcing is large as it was when Hurricanes Earl and Georges traversed the study area, linkages between forcing and response can be clearer, although understanding the movement throughout the water column to this forcing remains a substantial undertaking. Strong storm systems are not uncommon in the northeastern Gulf. Figure 6.1-1 shows the number of storms with tropical status or greater per decade that moved through two subregions (Florida Panhandle and Big Bend) of the NE Gulf over a 110-year interval. Most of the storms contributing to this total could have had an effect on circulation patterns in the study area.

Chapter 6 examines several time scales as well as the spatial extent of an oceanographic response to atmospheric forcing. With the increased distance to the shoreline and the increased water depth, the relative importance of wind stress to circulation over the slope is often assumed to be lessened. Results from the present study will indicate that wind stress often had a significant influence seaward of the shelf, i.e. over the slope.

6.2 Slope Response to Synoptic Wind Forcing

The typical response of shelf currents to synoptic scale wind forcing is an energetic barotropic response of alongshelf currents to local alongshelf winds that are coherent over the shelf domain. This response is known as the arrested topographic wave (Csanady, 1978) and generally dominates the low-frequency current variability at most mid- and inner shelf locations (Beardsley and Butman, 1974 for the Middle Atlantic Bight, MAB; Mitchum and Sturges, 1982 for the west Florida shelf; and Lee et al., 1989 for the South Atlantic Bight, SAB). The response is different from a propagating continental shelf wave in that the forcing is local and the response is phase-locked to the forcing. The resulting amplitude of alongshore currents are uniform in the vertical and over the domain of the forcing, which is generally larger than the shelf scale for synoptic forcing events. The phase response of alongshore currents is also uniform over the water column and along isobaths, but increases with water depth. Upwelling (downwelling) alongshore winds will accelerate offshore (onshore) flows in the upper Ekman layer that are near in-phase with the wind forcing. Due to the coastal constraint these cross-shelf flows will cause a onshore (offshore) "adjustment drift" below the Ekman layer that in turn drives a uniform alongshore flow in the same adjusted geostrophically to the alongshore flows resulting in a set-down (set-up) of coastal sea level from the upwelling (downwelling) wind-driven alongshore currents. This is referred to as

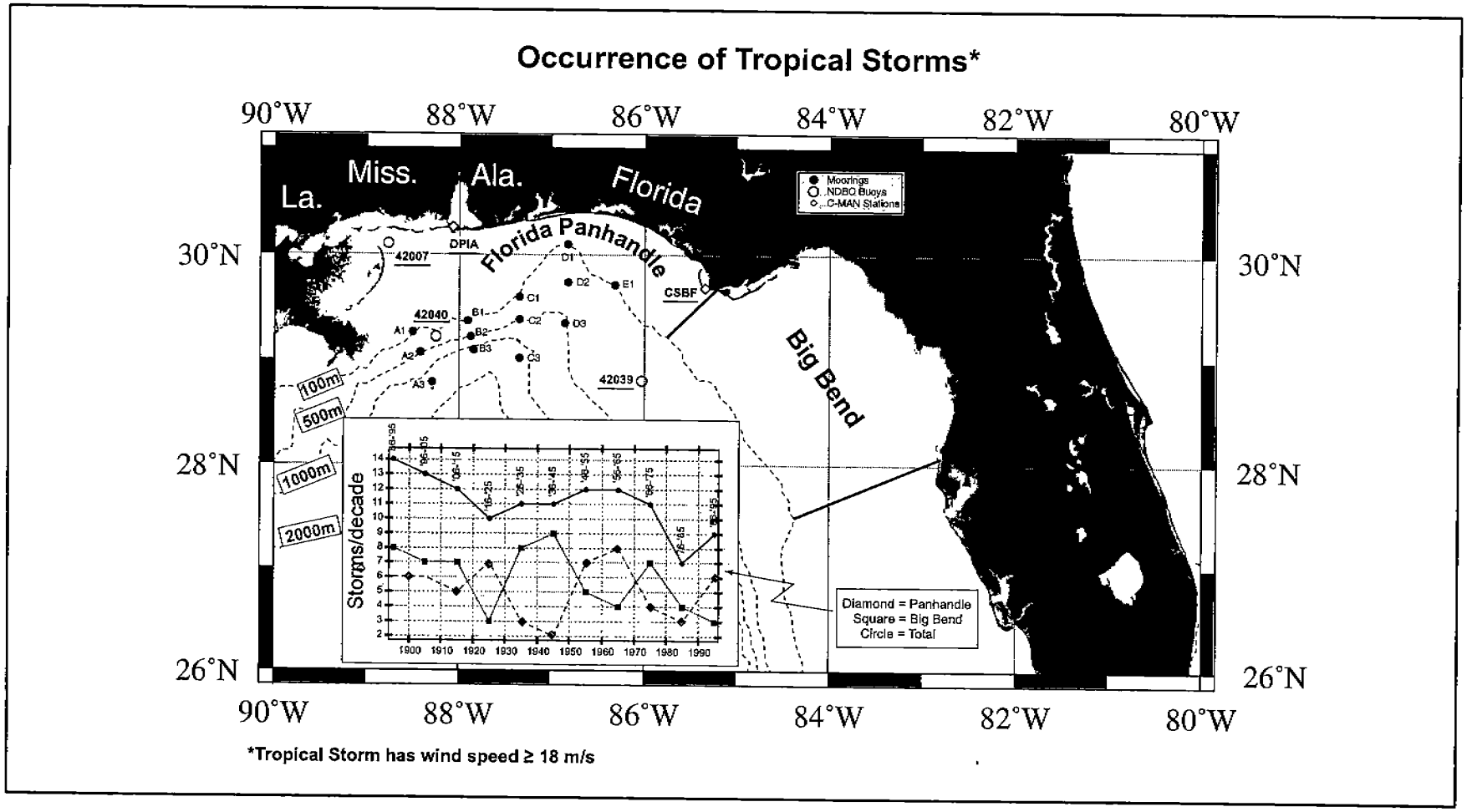

Figure 6.1-1. Map which partitions the NE Gulf of Mexico and indicates the number of tropical storms occurring in each partition per decade. Also shown are DeSoto Canyon moorings and present key meteorological measurement sites. The number of storms represents storms that reached tropical storm status or stronger.

the "Ekman frictional equilibrium response" (Beardsley and Butman, 1974; Scott and Csanady, 1976). Typically, the response is limited to the shelf and pressure fluctuations at the shelfbreak are assumed zero. However, Lee et al. (1989) observed this response at the shelf break and over the slope in the SAB with strongest response in the lower layer. They attributed the spread of the response over the slope to the weaker bottom gradient in the SAB slope, which resulted in the cross-shelf scale of the slope being equivalent to that of the shelf. The arrested topographic wave response is often difficult to observe at shelfbreak or slope locations due to the strong influences from boundary currents and their eddies. Certainly, the SAB is no exception and the influence of eddies there is notorious and well observed. However, the first-order influences of boundary currents and their eddies tend to be baroclinic so that the barotropic response to alongshore wind forcing becomes relatively stronger closer to the bottom.

In the DeSoto Canyon study area, the shelfbreak and slope region are subject to strong influences from the Loop Current, rings, cyclonic frontal eddies, anticyclonic eddies (ACE) evolving from warm streamers and smaller scale cyclonic shelf eddies that can develop on intruding warm fronts. This mixture of eddy processes produces strong current and temperature variability over the slope and can account for considerable cross-slope exchange. The time scale of variability from forcing by the LC and mesoscale eddies (LC frontal eddies (LCFE) and ACEs) tends to be longer than the synoptic wind event band of 5 to 15 days. Thus, current and temperature variability within the synoptic band are more likely due to a combination of wind forcing and submesoscale shelf eddies that are observed to develop on thermal fronts in the array. Also one would expect the wind response to be stronger and more observable at the shelfbreak sites compared to mid-slope or offshore moorings where the influence of mesoscale eddies is proportionally greater.

The shelf region, shoreward of the present mooring array, is generally oriented in an east-west direction, but is closed at its western end by the Mississippi River delta and curves toward the southeast at its eastern end, although still open. The shelfbreak tends to be oriented in a northeast to southwest direction from moorings A to D and then curves to the southeast past site E. The slope tends to follow the orientation of the shelfbreak, although the slope is narrower in the western region of the array at sites A-C and widens out as the shelf curves to the southeast near D and E. Due to the general east-west orientation of the shelf one would expect the strongest response to occur for east-west (alongshore) wind events and that this response would be strongest toward the center of the shelf where the topography is more uniform, i.e. near sites B, C and D. The most observable wind response should be found at site D, which is furthest from the influence of mesoscale eddies and at the narrowest section of the shelf, where alongshelf flows could be amplified. The weakest response should occur at sites A and E, near the western boundary of the shelf and southerly alignment, respectively.

Visual inspection of the upper level current vectors from all measurement sites together with the winds from offshore buoy 42040 near mooring line A and coastal sea level time series at Panama City, FL,

generally support the above expectations (Figures 6.2-1a-1d). There are at times significant correlations between alongshore wind, current and sea level events in agreement with the arrested topographic wave response. This response appears to be better defined at the shelfbreak, particularly at sites D and C and less so at shelfbreak (A and E) and offshore sites. The response is stronger during winter and spring seasons when wind forcing is greater due to the passage of strong cold fronts and winter storms. The winter of 1998 is a good example, wherein a storm in early February caused strong westward alongshore wind forcing and westward currents at most of the mooring sites together with a sharp rise in coastal sea level.

Seasonal wind forcing showing an interesting pattern in which winds shift from their strong oscillatory nature in winter and spring to a more persistent eastward direction in summer and southwestward direction in fall. The shelfbreak currents also tend to show these seasonal shifts, especially at site D1. The barotropic nature of the alongshore current response at the shelfbreak and the high correlation to wind forcing and coastal sea level is clearly displayed in the first year of current data from mooring D1 (Figure 6.2-1a and -1b). Alongshore currents are coherent over the water column and tend to lag alongshore winds on the order of one day. Coastal sea level is near in-phase with the alongshore currents as expected from local wind forcing. Also, a clear shift to persistent eastward flow occured during the summer consistent with the eastward winds.

The vertically averaged current vectors from each shelf break site plotted together with buoy winds near line A and Panama City coastal sea level are shown in Figures 6.2-2a to 2d. There are numerous examples of coherent, uniform current events that occured at all shelfbreak sites following strong alongshore wind events, as well as the seasonal shifts reported earlier.

6.2.1 Time Domain EOF's (TEOF)

Spectral analyses generally show significant energy peaks in the 5-15 day period band for subtidal current records from shelfbreak locations that were strongest during winter and in the lower part of the water column (example Figure 6.2-3a). Similar energy peaks were also observed in the 5-15 day period band for wind and coastal sea level records. In comparison, energy spectra for stations further offshore typically show the strongest current variability to be associated with motions at periods longer than 20 days (Figure 6.2-3b). Time domain EOF analysis was used to extract the coherent part of the total ensemble of wind stress from all wind stations and also for the ensemble of currents from all shelfbreak moorings. The EOF's were computed separately for the alongshelf and cross-shelf wind stress components and current components and also for each summer and winter season.

During all seasons the 1st mode EOF of the alongshelf wind stress components were nearly equal in amplitude and similar in phase at all stations and accounted for 70 to 80% of the total variance. The same can be said for the amplitude and phase of the 1st mode EOF of cross-shelf wind stress from all stations, which also explained about 70 to 80% of

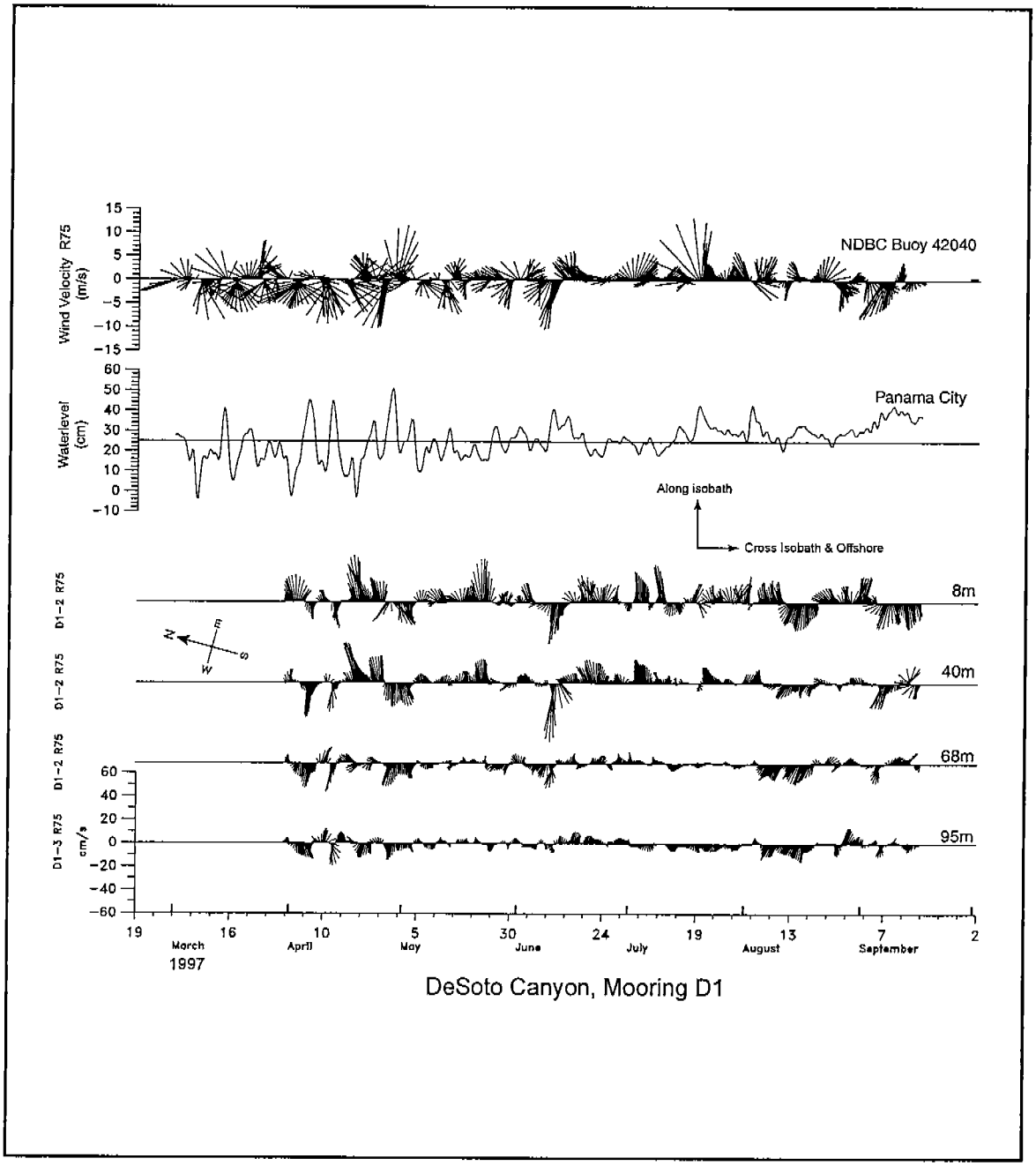

Figure 6.2-1a. Subtidal current vectors between 8 to 95m at mooring site D1 during March to September 1997 together with subtidal winds from buoy 42040, located near the A mooring line, and coastal sea level at Panama City, FL. See notations for directions of velocity vectors relative to isobaths and geographic frame-of-reference.

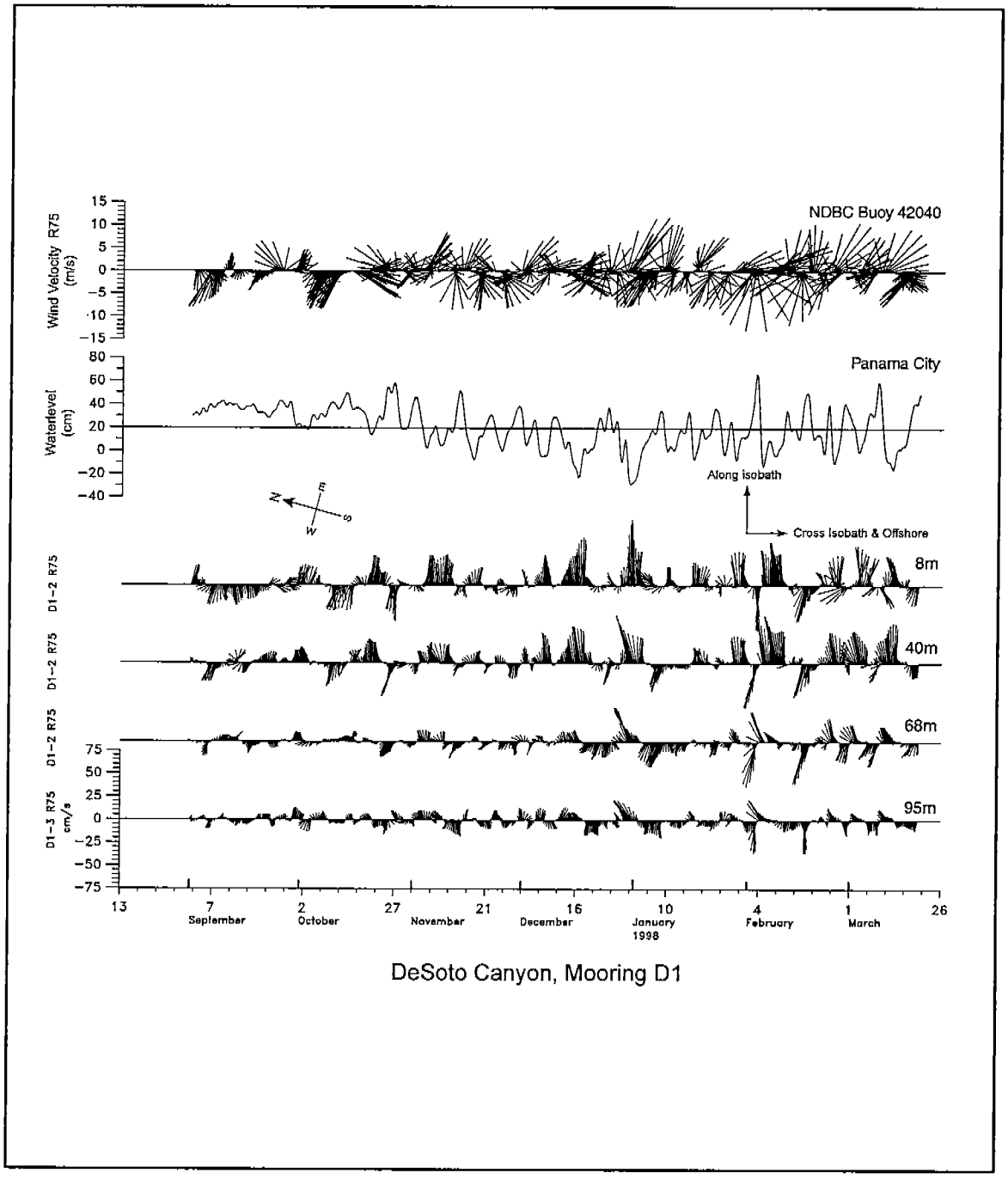

Figure 6.2-1b. Subtidal current vectors between 8 and 95m depth at mooring site D1 from September 1997 to March 1998 together with subtidal winds from buoy 42040, located near mooring line A, and coastal sea level at Panama City, FL. See notations for directions of velocity vectors relative to isobaths and geographic frame-of-reference.

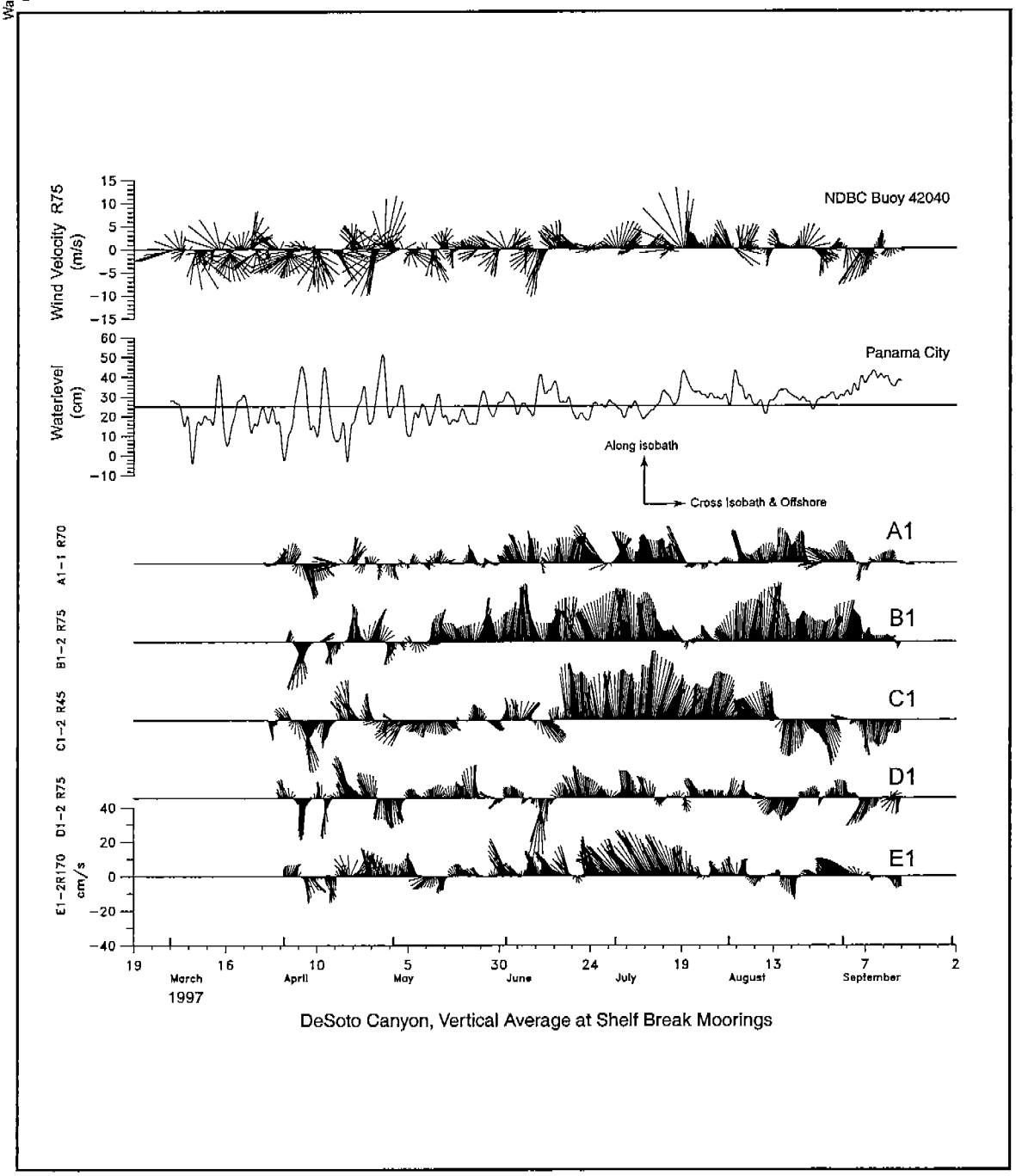

Figure 6.2-2a. Vertically averaged, rotated, subtidal current vectors from all shelf break moorings together with subtidal winds from buoy 42040 located near mooring line A, and coastal sea level at Panama City, FL. for the interval from March to September 1997.

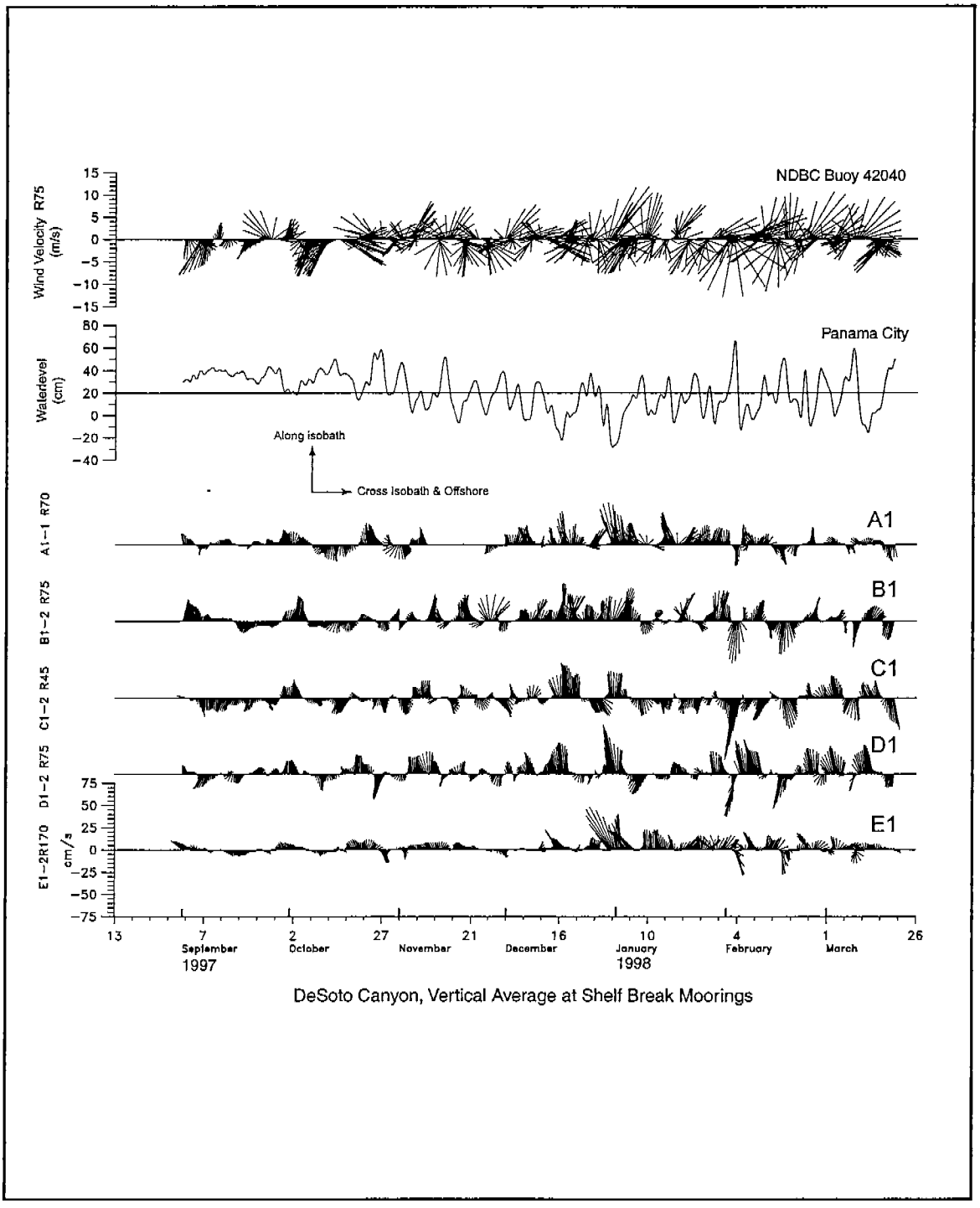

Figure 6.2-2b. Vertically averaged, rotated, subtidal current vectors from all shelf break moorings together with subtidal winds from buoy 42040, located near mooring line A, and coastal sea level at Panama City, FL. for the interval from September 1997 to March 1998.

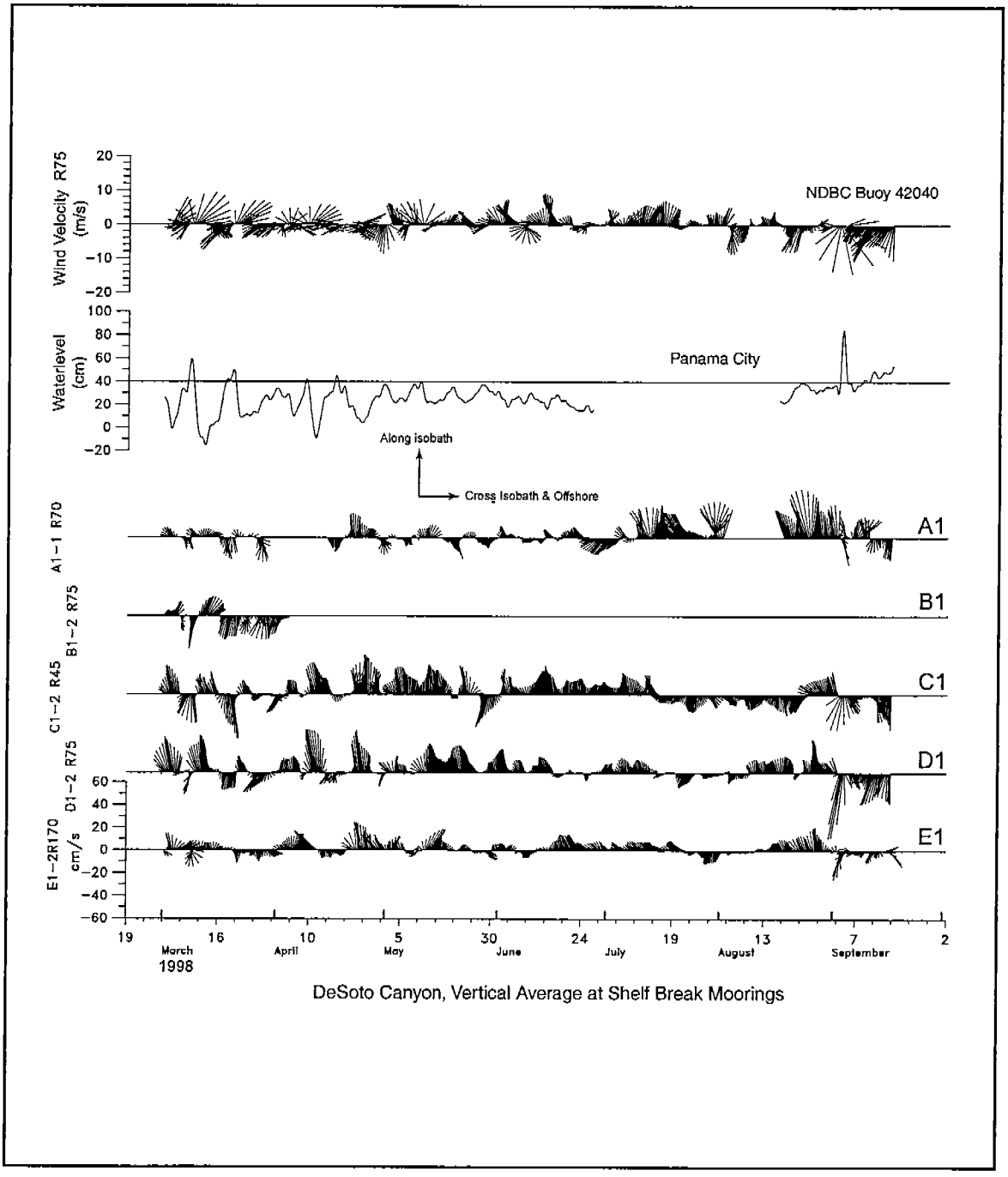

Figure 6.2-2c. Vertically averaged, rotated, subtidal current vectors from all shelfbreak moorings together with subtidal winds from buoy 42040 located near mooring line A, and coastal sea level at Panama City, FL. for the interval from March to September 1998.

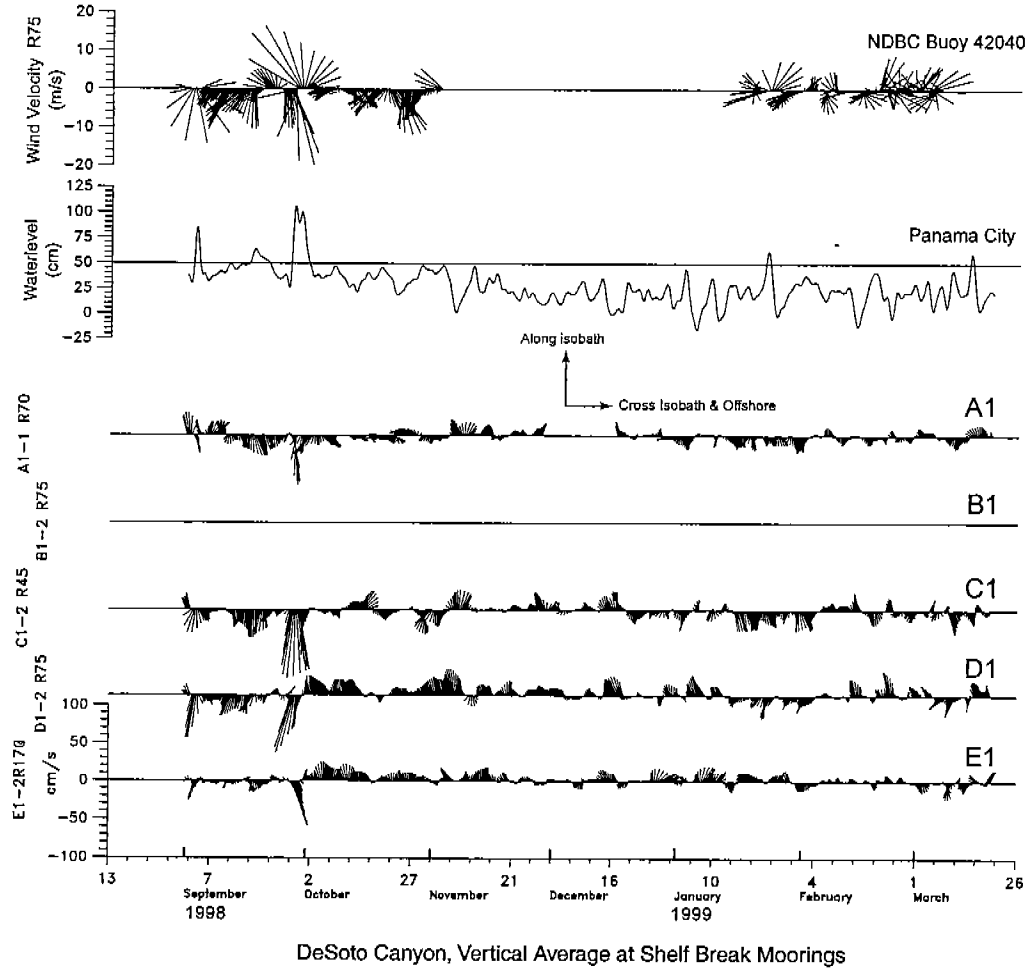

DeSoto Canyon, Vertical Average at Shelf Break Moorings

Figure 6.2-2d. Vertically averaged, rotated, subtidal current vectors from all shelf break moorings together with subtidal winds from buoy 42040, located near mooring line A, and coastal sealevel at Panama City, FL. for the interval from September 1998 to March 1999.

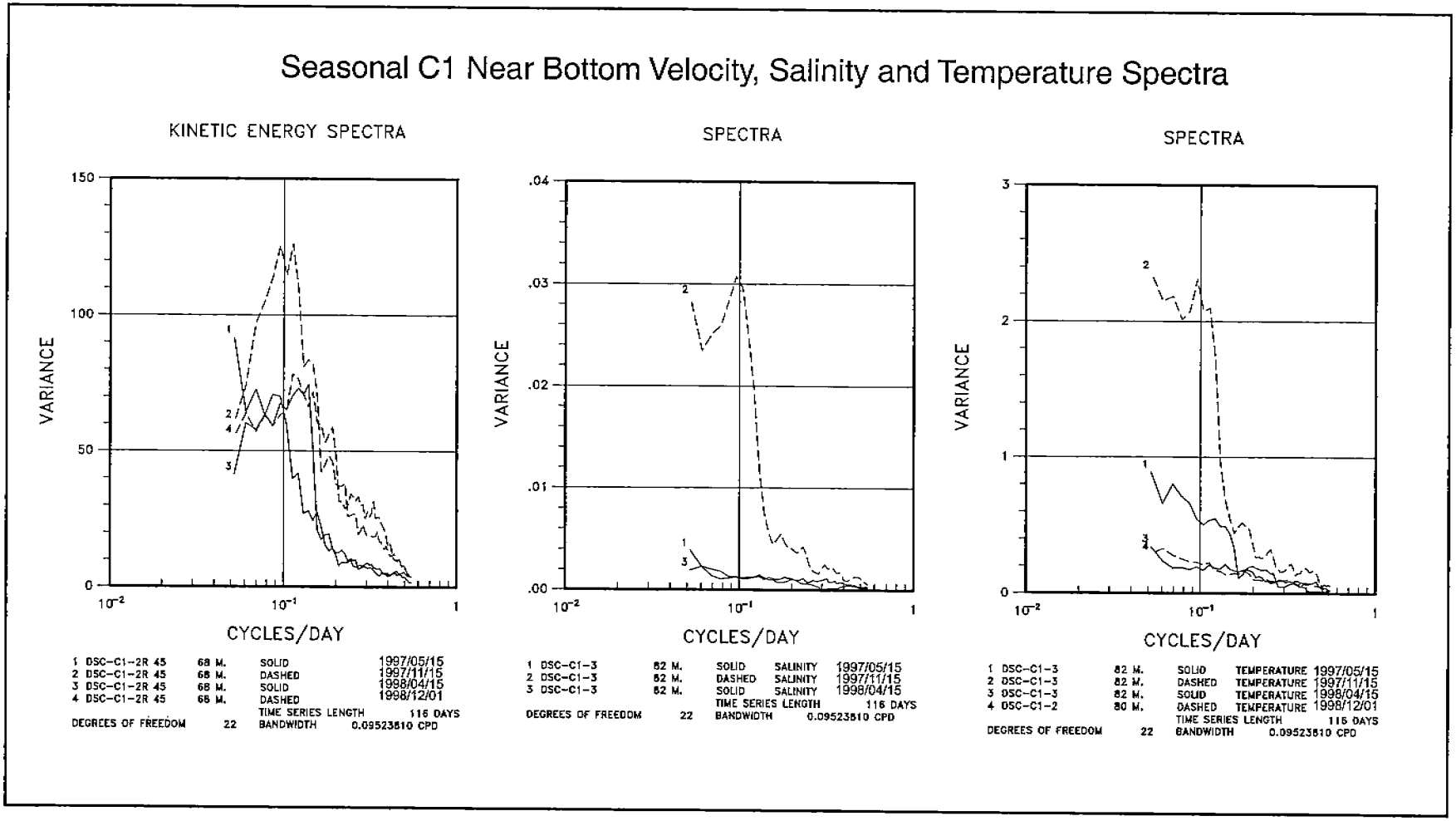

Figure 6.2-3a. Kinetic energy spectra at C1 for different depths and seasons during the two-year study.

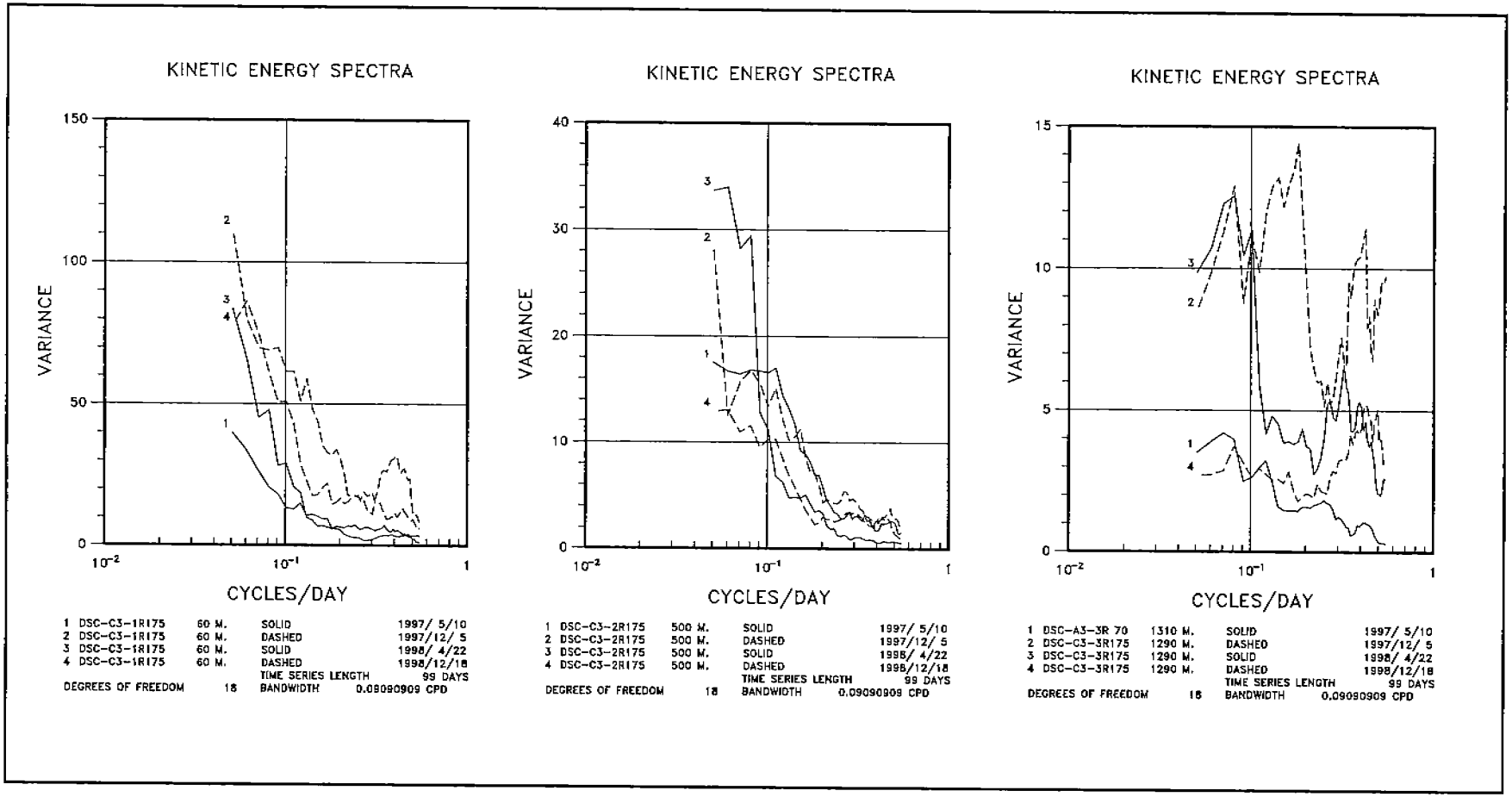

Figure 6.2-3b. Kinetic energy spectra at C3 for different depths and seasons during the two-year study.

the total variance for all seasons, except for a 54% variance in the summer 1997.

For alongshelf currents at the shelf break, the 1st mode EOF explained about 60% of the total variance in winter and 45% in summer seasons. This mode was generally barotropic at all stations. Currents at stations B1, C1 and D1 were generally more highly correlated with the mode than at stations A1 and E1, with stations C1 and D1 usually showing the higher correlations and amplitudes. During summer seasons, a 2nd mode EOF for the alongshore currents accounted for 20 to 30% of the variance. The 1st mode EOF of the cross-shelf currents was also barotropic and explained about 30% of the total variability in winter and 24 to 46% in summer seasons. The larger amplitudes and correlations with this mode occurred at stations A and E. The 2nd mode EOF generally accounted for about 20% of the total variability in cross-shelf currents, but with much smaller amplitudes than mode 1 and weaker correlation between sites. Including currents from mid-slope stations for depths less than 100m together with the shelfbreak currents generally reduced the percent of total variance explained by the 1st mode to 30 to 50% for the different seasons for either current component and spread more variability into 2nd and 3rd modes.

As an example of the TEOF analysis we show time series of the TEOF modes of cross-shelf and alongshelf wind and current components from the shelfbreak for the period of significant wind forcing, winter 1998 (Figure 6.2-4a and -4b). Also shown is the Panama City coastal sea level. The 1st mode alongshore currents have much greater amplitude than the 2nd or 3rd modes and also greater than any of the cross-shelf current modes; whereas, the amplitudes of the 1st mode alongshelf and cross-shelf winds are about equal. The 1st mode alongshelf current EOF is visually well correlated with the 1st mode alongshelf wind stress and with the coastal sea level.

Spectra of the 1st mode alongshelf current has a well-defined energy peak centered at 10 days, whereas, energy peaks of the 1st mode wind stress EOF's are spread over a period band of 8-10 days (Figure 6.2-5). The 1st mode alongshelf current EOF is highly coherent with the 1st mode alongshelf wind stress over a wide period band with a phase lag that increases with frequency, suggesting a near constant time lag on the order of one day (Figure 6.2-6). Even greater coherence occurred between the 1st and 2nd mode cross-shelf wind stress EOF's with the 1st mode alongshelf current. This may be explained by the curving nature of the shelfbreak study area where cross-shelf winds (toward 155°T) would have a significant alongshelf component over the eastern portion of the shelfbreak that could add to the alongshelf current modal variability. A similar response of alongshelf current modes to alongshelf and cross-shelf wind stress modes was observed when mid-slope currents in the upper 100m were included in the TEOF analysis indicating that the current response to synoptic wind forcing extends over the slope.

6.2.2 Frequency Domain EOF's (FEOF)

Energy spectra of shelfbreak currents and wind stress records and their 1st mode TEOF's consistently show well-defined spectral peaks centered

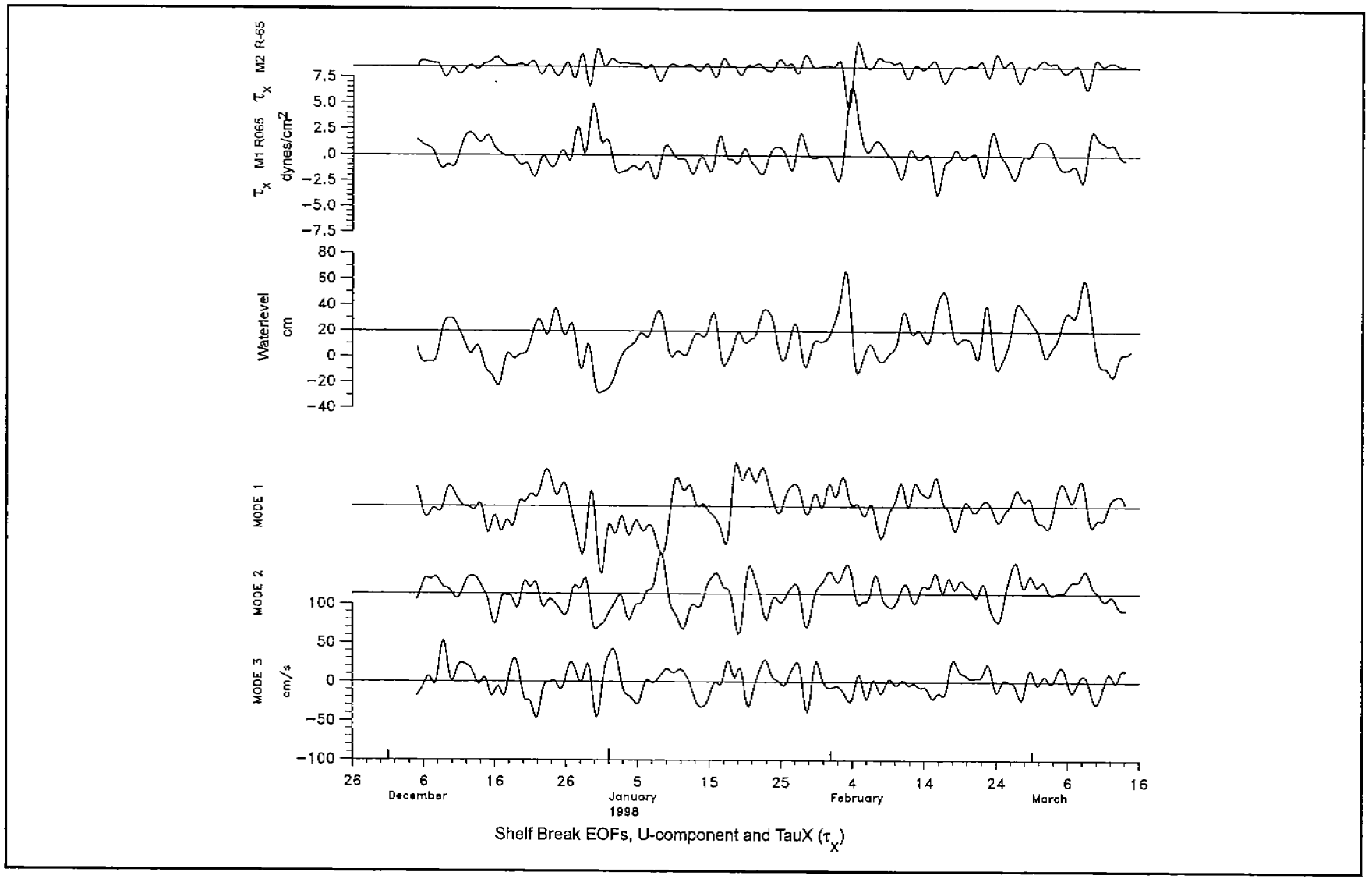

Figure 6.2-4a. Cross-shelf components of TEOF modes of shelf break currents and wind stress and Panama City, FL coastal sea level for winter 1998.

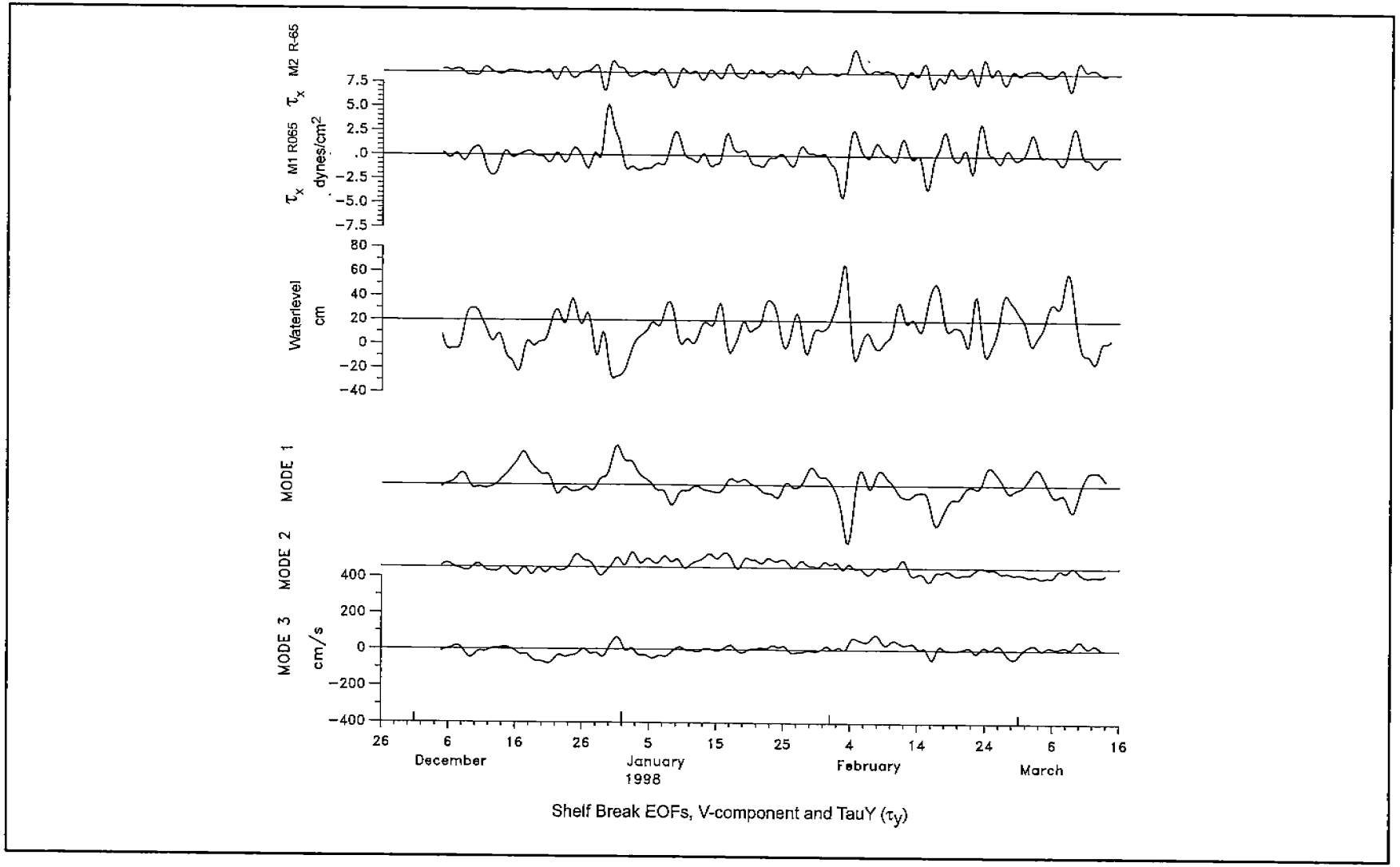

Figure 6.2-4b. Alongshelf components of TEOF modes of shelf break currents and wind stress and Panama City, FL coastal sea level for winter 1998.

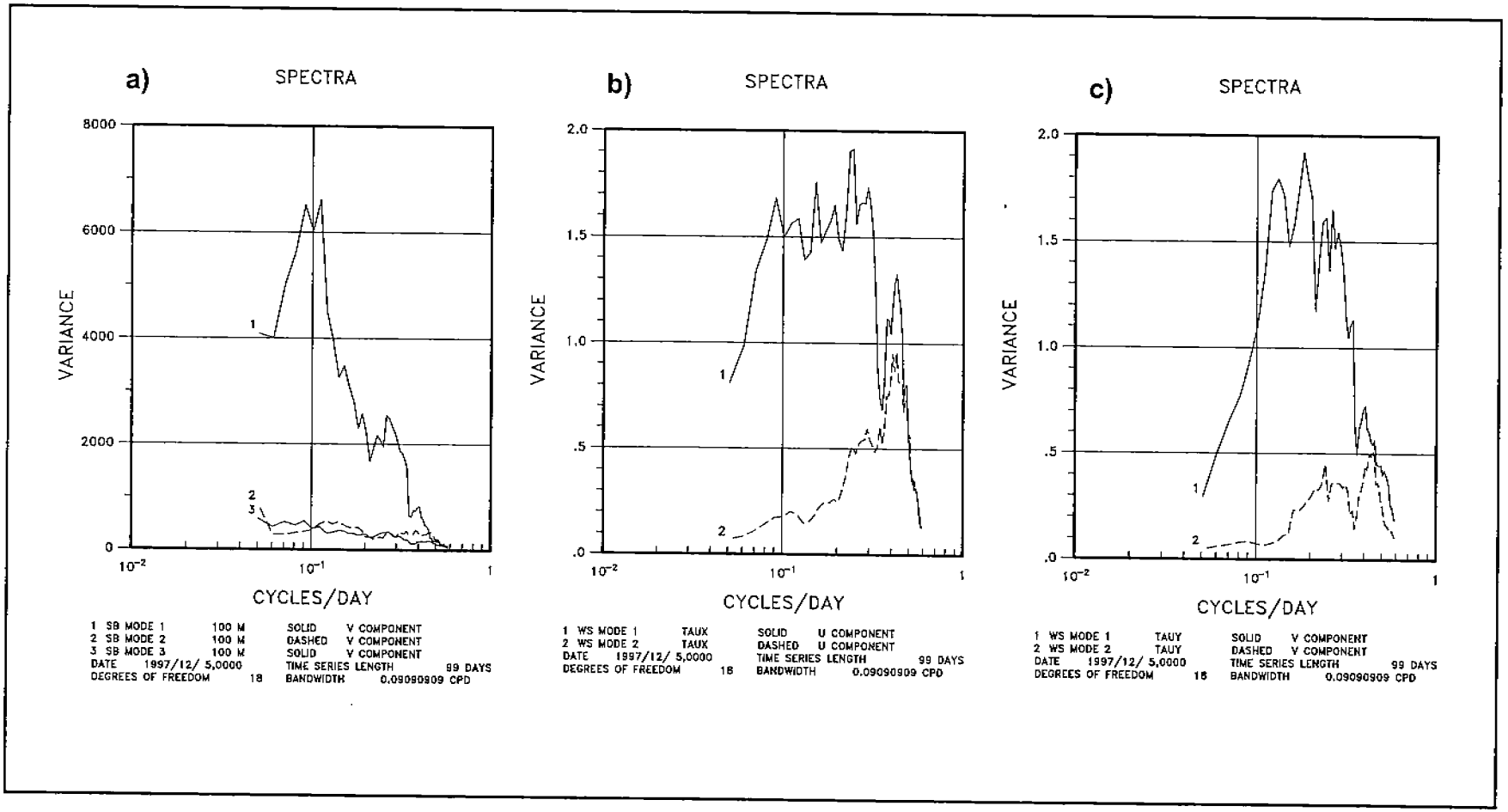

Figure 6.2-5. Spectra of TEOF modes of shelf break alongshelf currents and τ_x and τ_y, wind stress components for winter 1998.

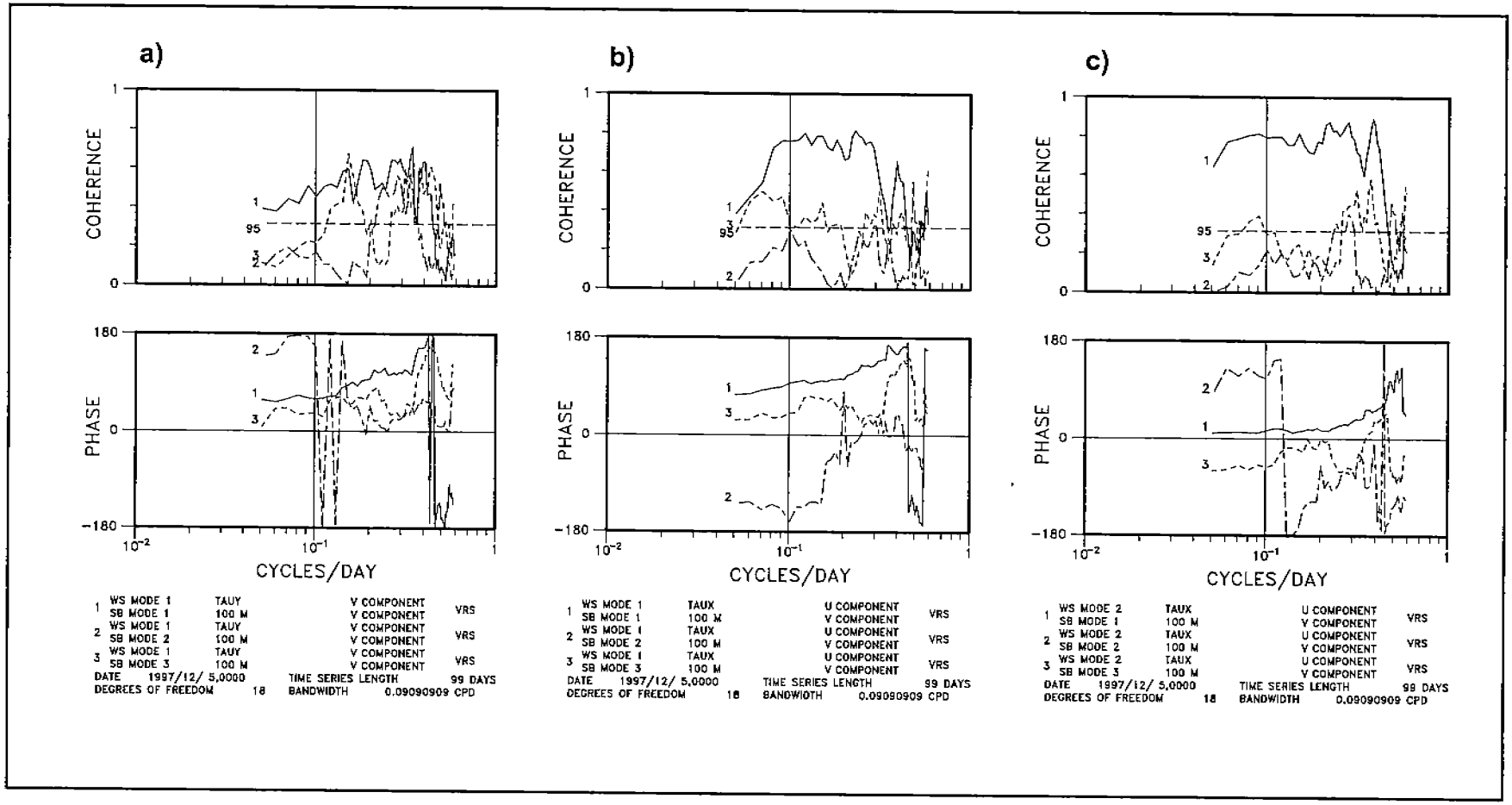

Figure 6.2-6. Coherence and phase spectra of TEOF modes of a) alongshelf wind stress and currents; b) mode 1 cross-shelf wind stress and alongshelf currents; and c) mode 2 cross-shelf wind stress and alongshelf currents for winter 1998.

within a 5-15 day period band. Frequency domain EOF (FEOF) analysis was conducted on the combined along isobath (v) and cross-isobath (u) current component time series within this band. The analysis was done separately for each mooring over the upper 100m for each of the four seasons of measurements.

Results of this analysis are summarized as ellipses in Figures 6.2-7a to -7d for the 1st mode FEOF's at selected depths on the shelfbreak moorings and for each season. Mode 1 has a barotropic structure at all shelfbreak sites with near constant phase with depth and small decrease in amplitude near the bottom. The orientations of the ellipses are aligned with the shelfbreak isobaths and indicates that largest amplitude occurs with the alongshelf component of the mode. The 1st mode explains a large percentage of the total variance at each site. The percentage of the total variance explained is greater in winter than summer and is maximized at sites C1 and D1, where approximately 90% of the variance was explained during winter seasons and 60 to 80% was explained during summer. At station A1 and E1, the 1st mode FEOF accounted for about 60 - 70% of the total variance during winter and 50 - 70% in summer. The percentage of total variance explained generally decreased with offshore distance, but still there was 50 - 70% of the variance explained by the 1st mode from all sites for the upper 100m.

6.2.3 Discussion

The above analyses indicate that shelfbreak currents and upper level slope currents had a significant response to coherent synotpic-scale wind events similar to that observed on other wide, shallow continental shelves, the so called "Ekman frictional equilibrium response" to local alongshelf wind forcing (Beardsley and Butman, 1974; Scott and Csanady, 1976). Alongshelf winds that were coherent over the shelf domain, generated cross-shelf Ekman transports in the surface layer with opposite return flows beneath which accelerated barotropic alongshore currents that were balanced by cross-shelf pressure gradients from cross-shelf sea level slopes. The geostrophic adjustment time needed for sea level to balance alongshore flow is $t_g = L/(gh)^{1/2}$ (Winant, 1980). For the DeSoto Canyon shelf region with shelf width (L) of 100 km and mean shelf depth (h) of 40m, the geostrophic adjustment time is less than 2 hours, which is in good agreement with the observations. The time necessary for the alongshelf currents to reach equilibrium with the alongshelf wind stress is the frictional adjustment time $t_f = H/r$, where "H" is the water depth and "r" is the bottom resistance coefficient. At similar outer shelf locations, "r" has been found to be approximately 0.1 (cm/s) (Lee et al., 1989). Using this value for r at the shelfbreak (100m) gives a frictional adjustment time of about 28 hours. This adjustment time is in reasonable agreement with the time lag of about 33 hours estimated from the phase lag of the 1st mode TEOF of shelfbreak alongshelf currents to alongshelf wind stress at the 10-day energetic period during winter 1998 (Figure 6.2-6)

This type of barotropic response to wind forcing is often observed to be trapped over the shelf on wide, shallow shelves with steep bottom slopes seaward of the shelf break like the Middle Atlantic Bight and South Australian shelf (Clark and Brink, 1985). Csanady (1978) found that the

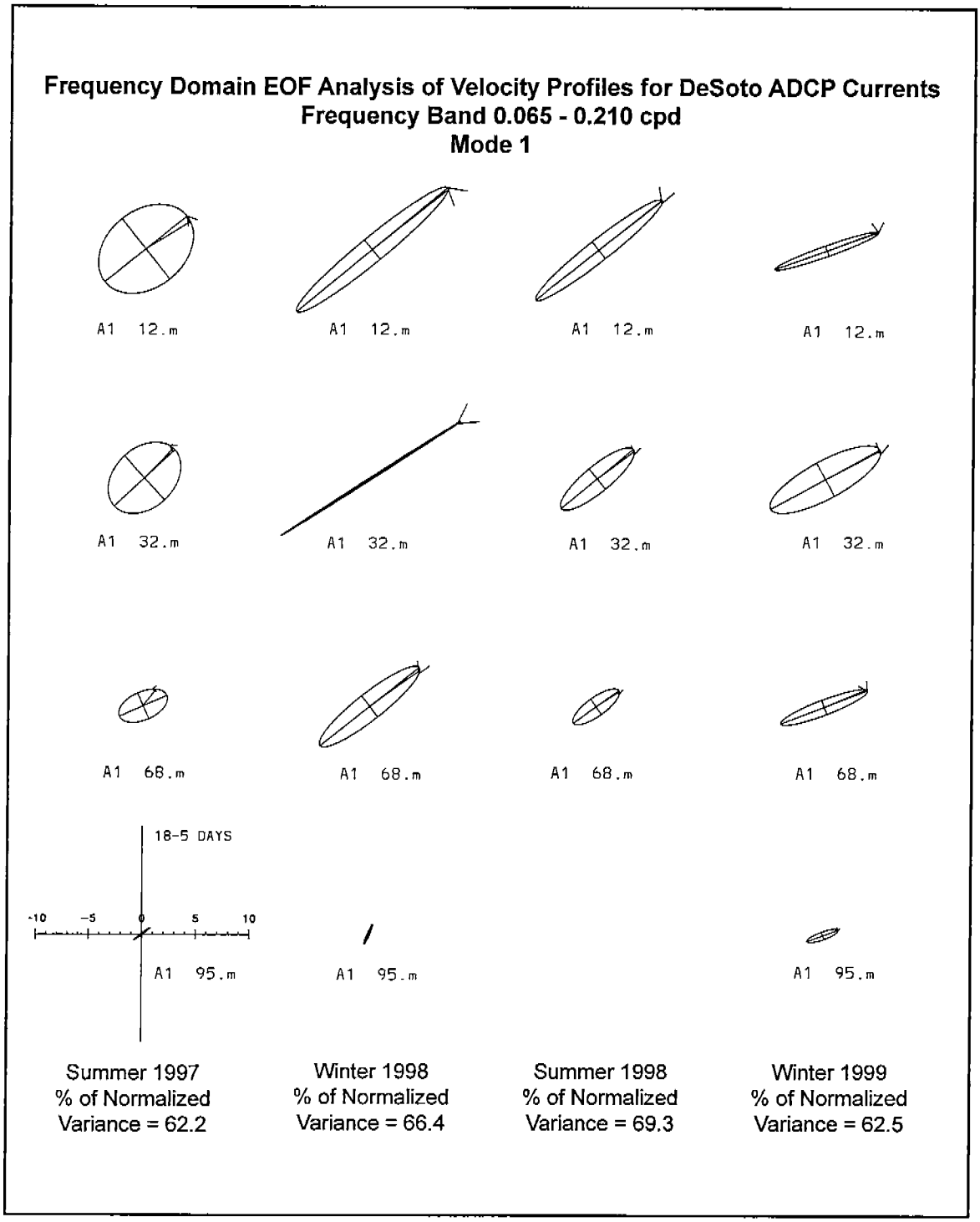

Figure 6.2-7a. Results of FEOF analyis for mode 1 at mooring A1 for summer and winter seasons presented as ellipses for selected depths. The length of the major/minor axes represent the amplitudes of the mode for the v and u current components. The arrow gives the relative phase of the mode.

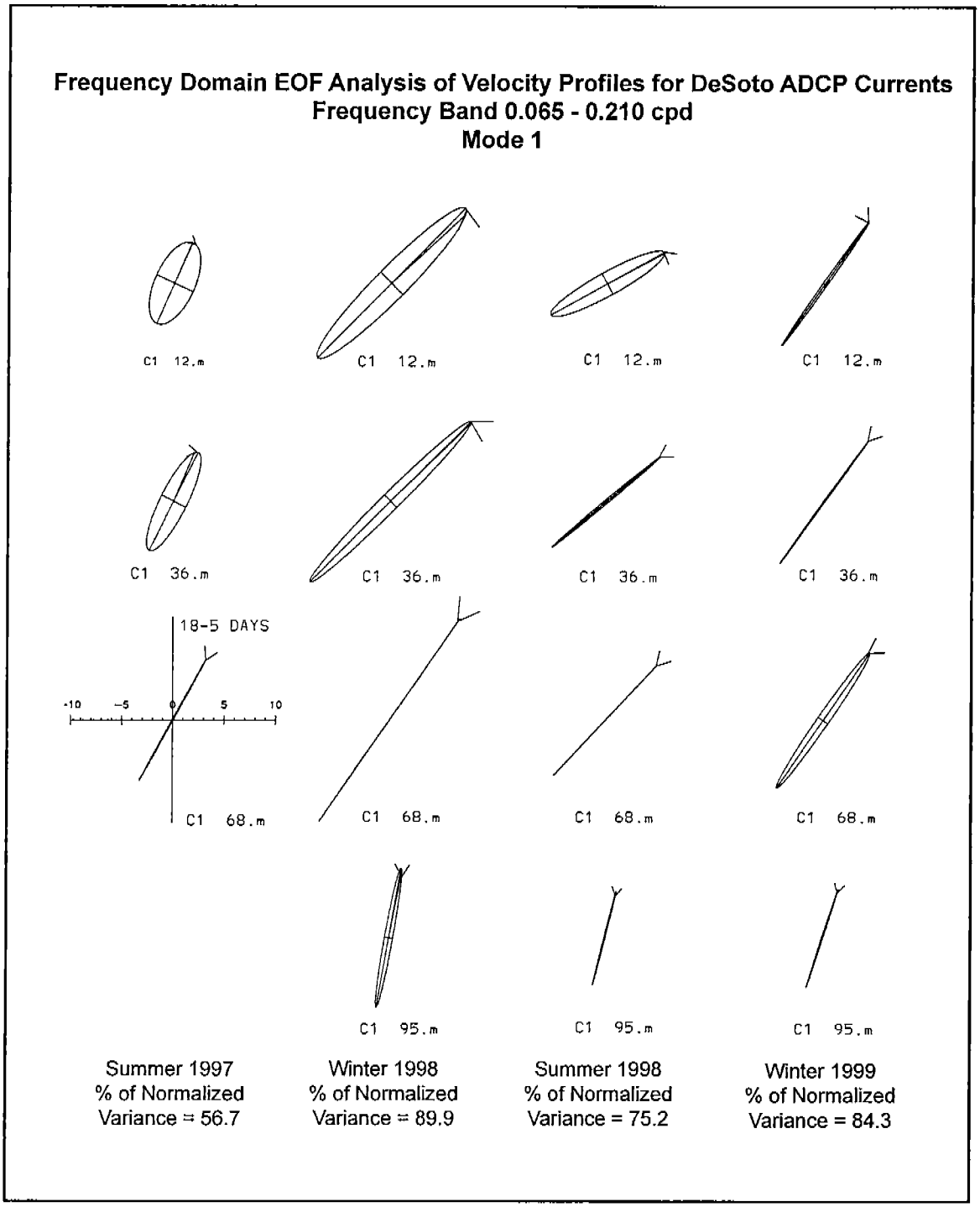

Figure 6.2-7b. Results of FEOF analyis for mode 1 at mooring C1 for summer and winter seasons presented as ellipses for selected depths. The length of the major/minor axes represent the amplitudes of the mode for the v/u current components. The arrow give the relative phase of the mode.

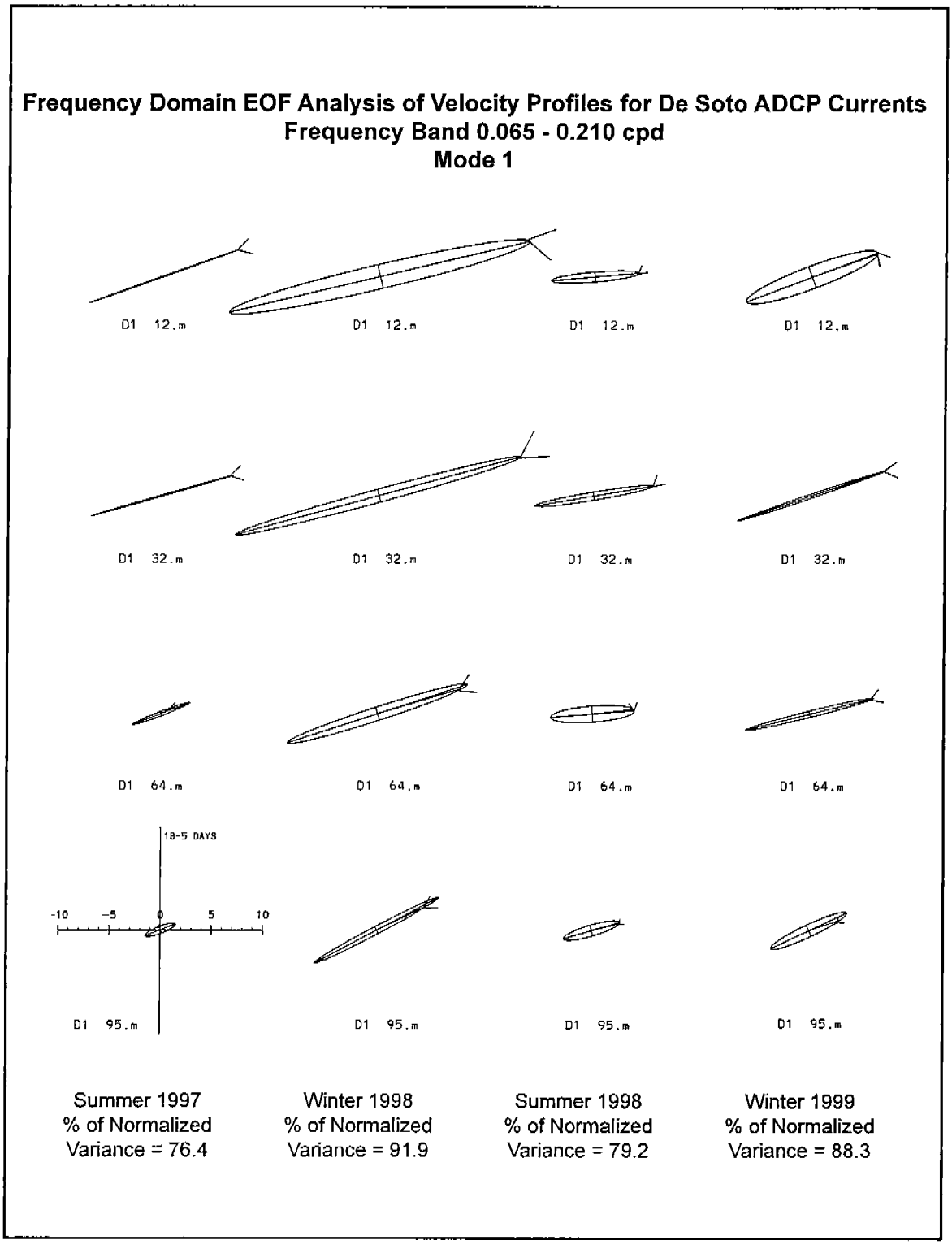

Figure 6.2-7c. Results of FEOF analyis for mode 1 at mooring D1 for summer and winter seasons presented as ellipses for selected depths. The length of the major/minor axes represent the amplitudes of the mode for the v/u current components. The arrow give the relative phase of the mode.

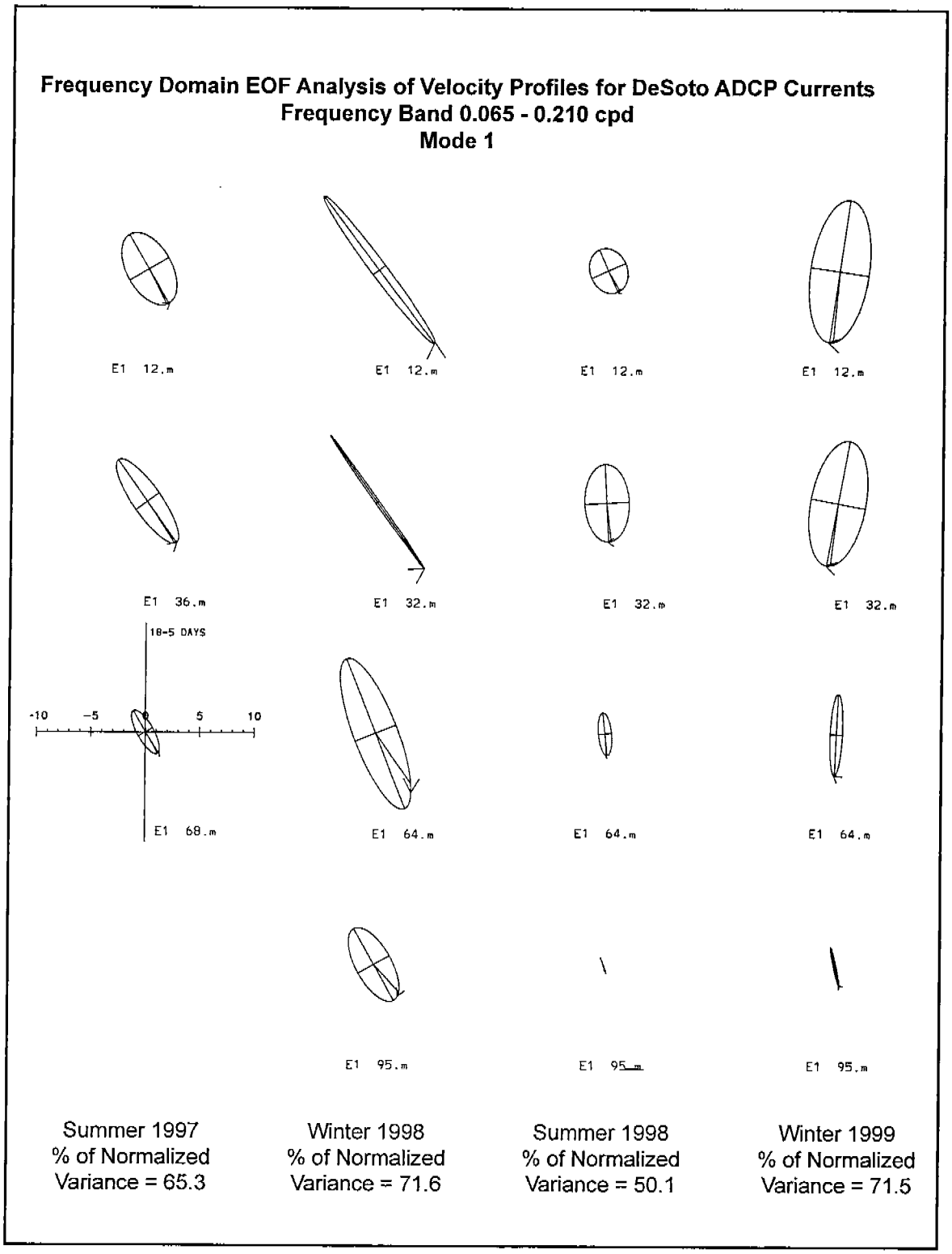

Figure 6.2-7d. Results of FEOF analyis for mode 1 at mooring E1 for summer and winter seasons presented as ellipses for selected depths. The length of the major/minor axes represent the amplitudes of the mode for the v/u current components. The arrow give the relative phase of the mode.

trapping width (L_x) associated with the arrested topographic wave (the barotropic response) could be estimated from $L_x = (2rL_y/fS)^{1/2}$, where L_y is the alongshore length scale of the wind forcing and S is the average cross-shelf bottom slope. For the shelf in the DeSoto Canyon study area L_y = 800 km and $S = 10^{-3}$, which gives a trapping width for the barotropic response on the order of 170 km. This trapping width is almost twice the shelf width and may explain why barotropic currents at the shelfbreak and even over the slope were coherent with the alongshore wind stress and coastal sea level variations. A similar finding of significant barotropic response to alongshelf wind stress was reported for the shelfbreak region of the South Atlantic Bight (Lee et al., 1989). However, in the SAB the Gulf Stream influence occurs within the same period band as the wind forcing, making it difficult to separate wind and Gulf Stream forcing. In the DeSoto Canyon shelf area the offshore Loop Current and eddy forcing generally occurred at periods greater than 20 days, whereas, the synoptic wind forcing band is 5 to 15 days. In the DeSoto Canyon study area, the primary forcing mechanism in the 5 - 15-day period band appears to have been synoptic wind events, which makes the current response at the outer shelf and slope relatively more observable.

6.3 Seasonal Wind Response on the Slope

Seasonal EOF analyses were performed for four 99-day segments of the two-year study period. Two summer (1997 and 1998) and two winter periods (1998 and 1999) were used. They were chosen to avoid the short, rather ill-defined, spring and fall transitions in the wind regimes as well as hurricanes Earl and Georges, and to capture major differences in the current velocity characteristics. As has already been noted, 5 - 15 day period fluctuations were much more prominent in the winter than the summer periods. There were also differences in the offshore deep-water circulation between seasons. For example, LC was well extended into the eastern Gulf from the beginning of the study to the end of summer 1998. In fall 1998, the LC retreated south of 25°N and remained there until the end of the study in April 1999.

The time and frequency domain EOF analyses performed for each mooring separately, using the individual velocity records from the upper 100m, showed a strong wind-forced response over the slope in the two winter periods (see Section 6.2). Similar analysis for the two summer periods showed no significant coherence between the along- and cross-slope wind stress modes and the principal velocity modes for the shelf-break and upper-slope moorings.

The present section examines the current patterns for the summer and winter seasons to see if there were significant differences between weak and strong wind-forcing, respectively. Because the previous analyses have shown that the current fluctuations were primarily barotropic in the upper 100m, the time domain EOF analysis uses the 0 to 100m depth mean U- and V-components of the velocity records for all 13 moorings. The eigenvectors (multiplied by the square root of the eigenvalue to give units of cm/s) are represented by vectors in a similar manner to Merrifield and Winant (1989). The time variation of each spatial

pattern is both positive and negative. Therefore, the mode amplitude vectors are reversed for about half of the total period.

The first two modes for the two summer periods are given in Figure 6.3-1. Though they differ in details, all these modes show fluctuations parallel to the isobaths over the Alabama slope. The major differences occurred in the east, over the head of the canyon, where suggestions of eddy-like circulations generate flows in opposition to the general trends of the slope currents. These patterns are similar to the 50 to 15-day period frequency domain EOF modes, derived from the two-year long velocity data, that are discussed in Section 5.4 (see Figures 5.4-15a and 16a). The two modes for summer 1998 have similar patterns to the modes for summer 1997, if the signs of the vectors are reversed in the latter. Mode 1 for summer 1998 accounts for 52.3% of the total variance with mode 2 being barely significant. Both modes are significant for summer 1997. This suggests that these type of patterns were typical, to some extent, but the degree to which they dominated at different seasons seems to depend upon the characteristics of the offshore eddy circulations. Recall that cyclonic and anticyclonic eddies dominated in the 1997 and 1998 summer periods, respectively. In both periods, the mean flow was eastward along the slope (see Figure 5.4-6 for summer 1997). Thus, eastward and westward fluctuations reinforced and reduced, respectively, the prevailing eastward flows. The first mode for summer 1998 accounts for the greatest fraction of the total variance (52.3%) for any of the seasons. When the fluctuations were eastward over the Alabama slope, a cyclonic flow was generated encompassing C1, C2, D2, D9 and D1. The strong northward flow through the canyon (D2 and D9) bifurcated producing strong onshore flow on the eastern canyon rim around E1. When the flow is reversed, the canyon circulation would be clockwise and the slope flow to the west. This flow pattern could be responsible for large on-off shelf exchanges on the eastern canyon rim.

Mode 1 for the two winters (Figure 6.3-2) shows that the fluctuations generally followed the trend of the isobaths along the slope and onto the west Florida slope. Unlike the summer periods, the canyon head was not separated from this flow pattern. Mode 2 on the other hand, has more complicated structures with opposing fluctuations and across isobath flows in the canyon. Mode 1 for winter 1998 accounts for 42.8% of the total variance and is clearly much more energetic than mode 1 for winter 1999. Winter 1999 had the highest total variance of any of the four seasons that were analyzed. The highest amplitudes range from 15 to 20 cm/s along the 500m isobath. The time series of normalized mode amplitudes for the four seasons (Figure 6.3-3) also show strong differences between summer and winter. The mode 1 amplitudes for the summer show relatively slow changes with time that are more consistent with slowly changing eddy-driven circulations. Mode 2 is similar with a little more variability at shorter periods. In winter, the slow underlying changes were still present but they were accompanied by more energetic fluctuations with short periods of order three to ten days. The short period fluctuations also had some degree of visual coherence between modes 1 and 2 for each winter period. This would indicate that they had similar forcing and the long period variability was the primary reason that the modes were not correlated over the 99-day record. The analysis of the winter wind-forced response, discussed in Section 6.2,

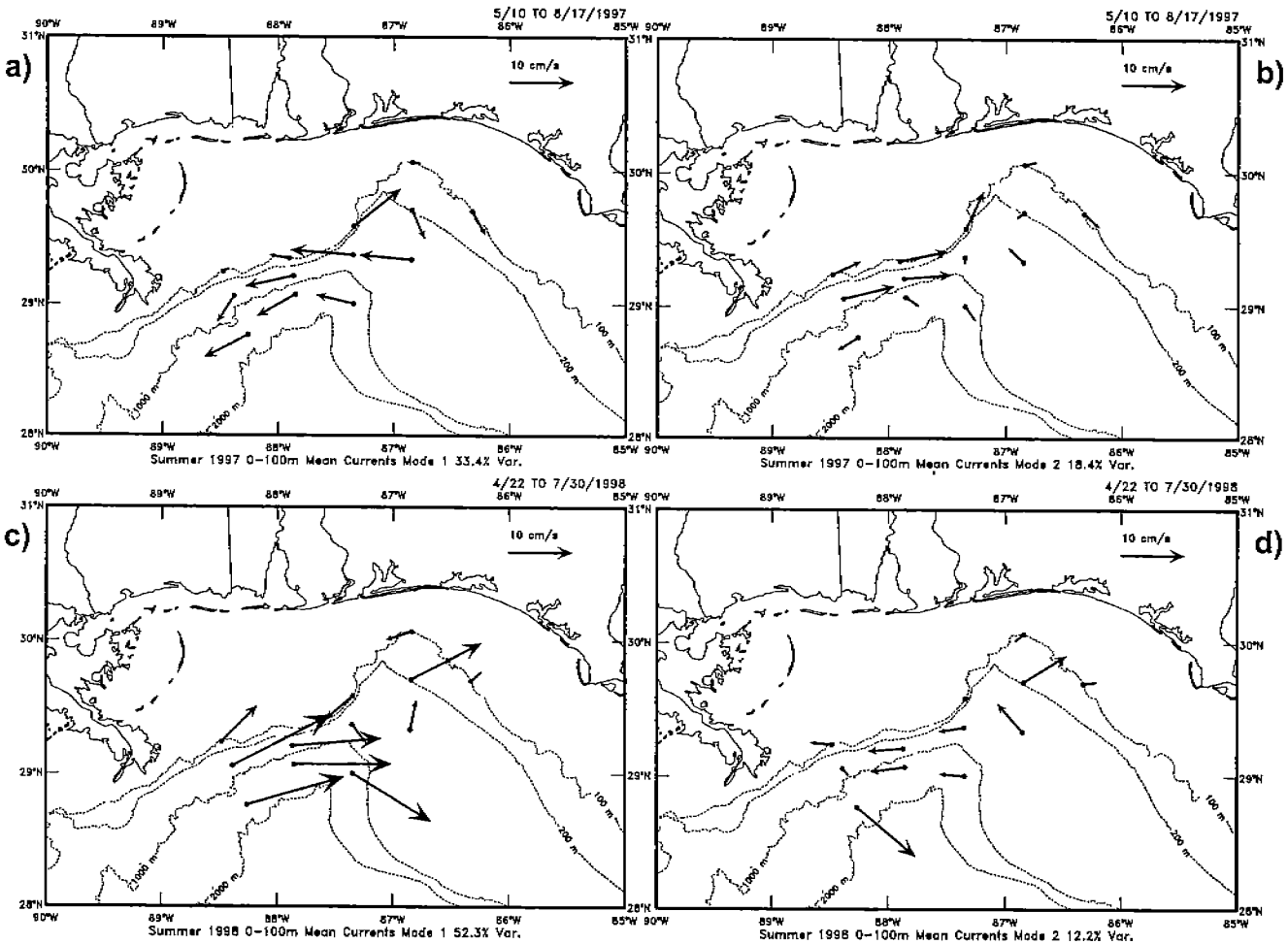

Figure 6.3-1. Time domain EOF eigenvector components represented as vectors multiplied by the standard deviation of the modes. Analysis is for the 40-HLP, 0 to 100m depth mean currents. Summer 1997 modes 1 (a) and 2 (b), and summer 1998 modes 1 (c) and 2)d).

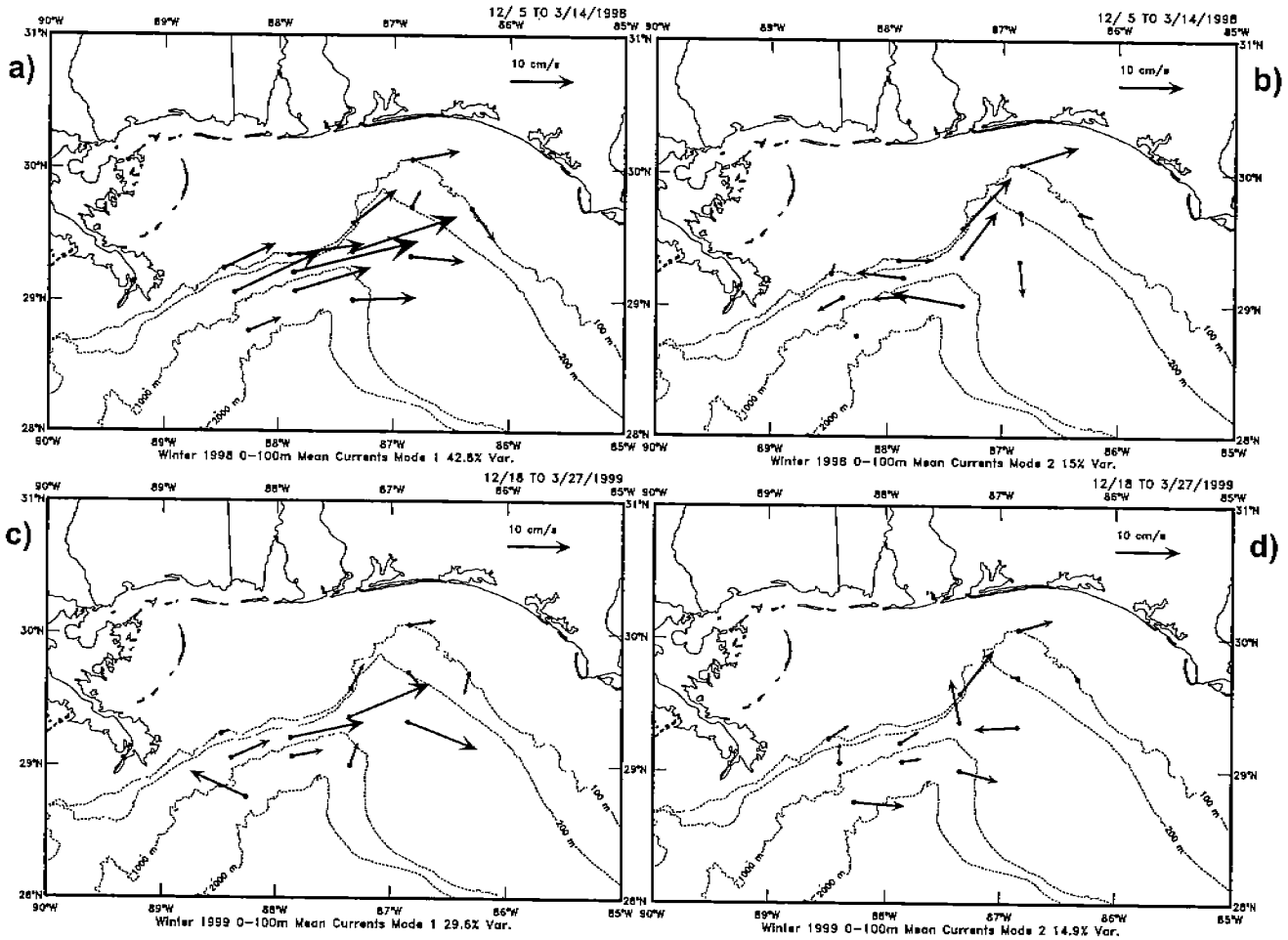

Figure 6.3-2. Time domain EOF eigenvector components represented as vectors multiplied by the standard deviation of the modes. Analysis is for the 40-HLP, 0 to 100m depth mean currents. Winter 1998 modes 1 (a) and 2 (b), and winter 1999 modes 1 (c) and 2)d).

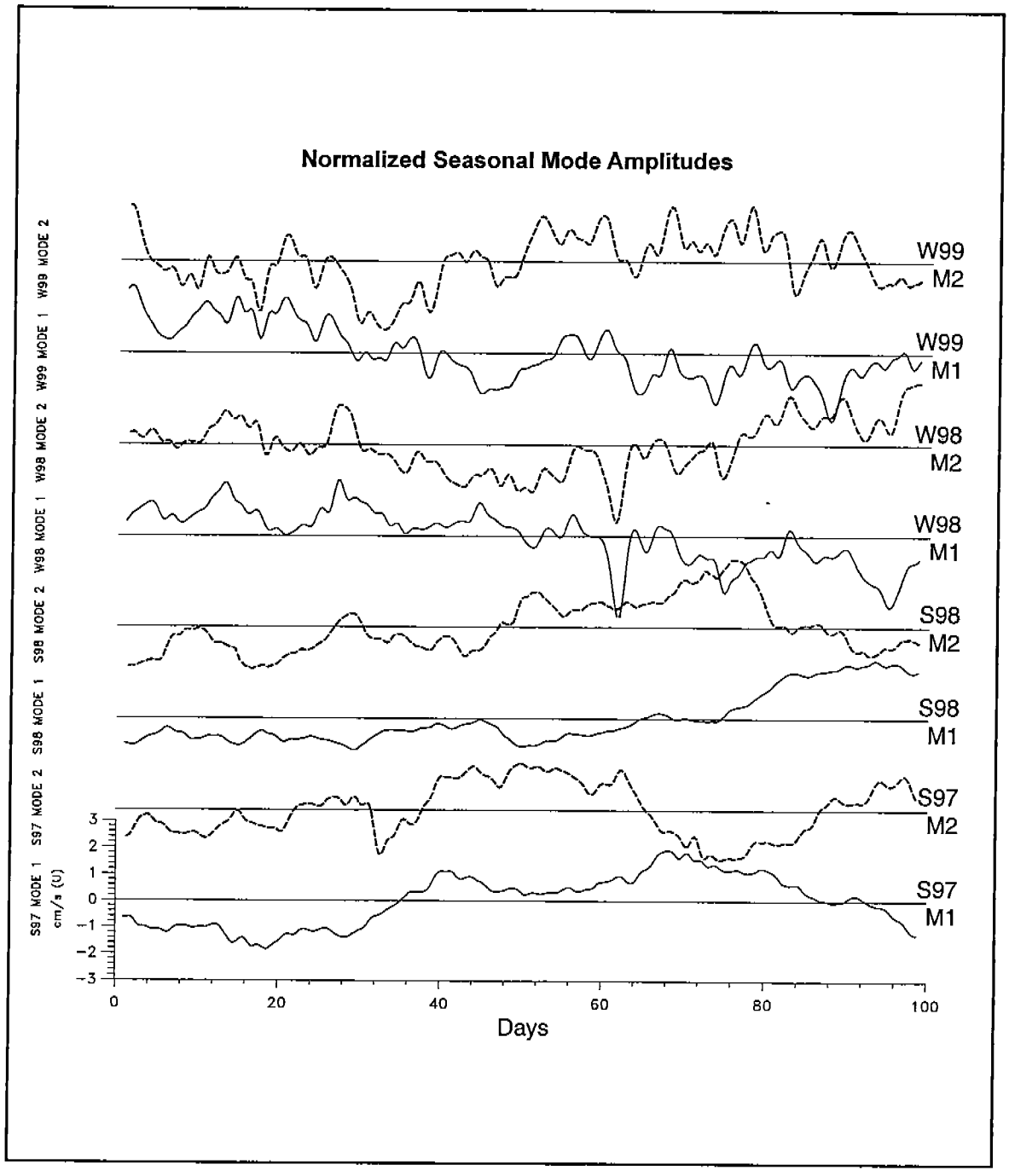

Figure 6.3-3. Time series of the normalized amplitudes of modes 1 (solid) and 2 (dashed) for the two summer and two winter seasons.

found high correlations with the currents at individual shelf-break and 500m isobath moorings. It will be demonstrated that the coherent wind-forced response was applicable to the shorter period motions of both modes in the winter seasons and thus, wind-driven currents were important across the slope in the upper layer.

EOF's were calculated for the east and north components of the wind-stress considered together. The eigenvectors for mode 1 in both winters account for more than 60% of the variance of the four shelf and slope wind stations used in the analysis (Figure 6.3-4). In both seasons, the fluctuations were directed across the Alabama slope and approximately parallel to the west Florida slope. The differences are that the amplitudes were slightly larger in winter 1998 than in winter 1999, and the vectors were rotated a little more to the east-west direction and so had a larger component parallel to the Alabama slope. This may explain why there are larger eigenvector amplitudes parallel to the Alabama slope in winter 1998 than in winter 1999 (Figure 6.3-2). The spectra, coherence squared and phase differences for the wind stress mode 1 and the 0-100m mean current modes are given in Figure 6.3-5. The wind stress spectra have energy from ~3 to 12 and ~3 to 7-day periods for the winters of 1998 and 1999, respectively. The winter of 1998 was also the more energetic, particularly at longer periods. This is reflected in the mode 1 spectra for the winter 1998 currents which has peaks around 10 and 3 days which are not observed in the other modes (Figure 6.3-5b). The coherences between wind stress and current modes were high where the wind stress modes have energy. The phase differences show that the wind stress led by greater than 90° which implies a lag of the currents of about 1 to 2 days. This is probably a reflection of the ~500m average water depth of the moored array, and the topography of the canyon with respect to the direction of the wind stress fluctuations. The lag could also be interpreted as the result of an arrested topographic wave generated by the along-slope wind stress over the west Florida side of the canyon. The propagation of this response is to the west where the along-slope wind stress fluctuations were small.

6.4 Canyon Response to Storms

6.4.1 Overview

Time series of surface wind stress computed from wind speeds measured at NOAA buoys 42040 and 42039 (Figure 6.4-1) reveal that, by far, the strongest wind stresses influencing DeSoto Canyon during this study were generated by Hurricane Earl, which passed the mooring array in early September, and Hurricane Georges, which traversed the array at the end of September. Another Earl and Georges superlative is revealed by the results of canyon edge flux calculations presented in Section 5.5.3. The largest cross-margin fluxes of temperature and salinity were observed during the hurricanes. In the present section, details of the current and temperature response to the Hurricanes Earl and Georges are examined, concentrating on the response at the canyon edge.

Snapshots of the surface winds measured at the NOAA buoys and the near-surface water velocities measured by the moored array (Figures 6.4-2,3)

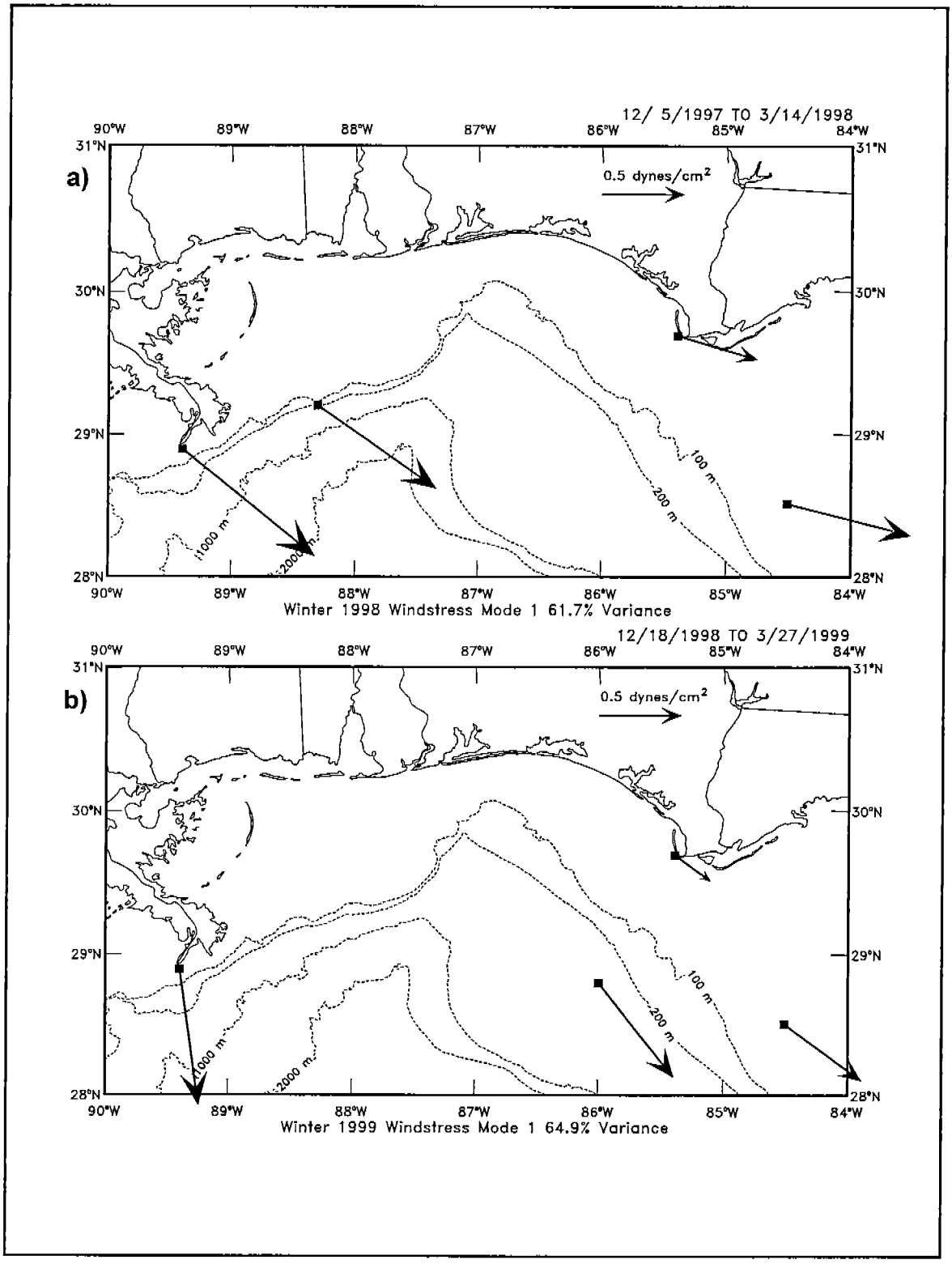

Figure 6.3-4. Time domain EOF eigenvector components represented as vectors multiplied by the standard deviation of the modes. Analysis is for the 40-HLP wind stress time series at the indicated stations. (a) winter 1998, and (b) winter 1999.

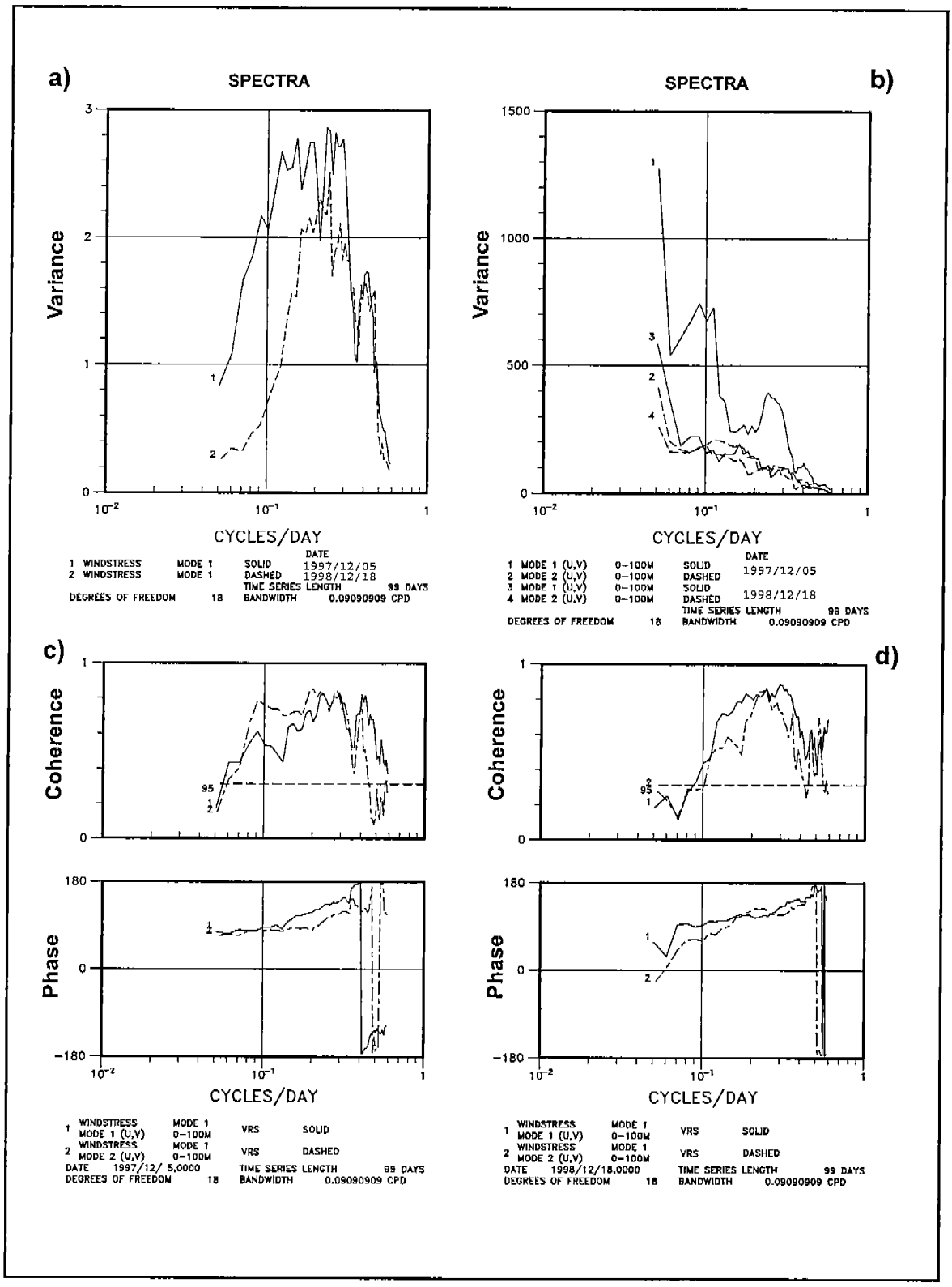

Figure 6.3-5. Variance preserving spectra for EOF (a) mode 1 wind stress, and (b) 0-100m depth mean current modes 1 and 2 for the winters of 1998 and 1999. Coherence squared and phase differences between the wind stress and current modes for the winters of (c) 1998 and (d) 1999.

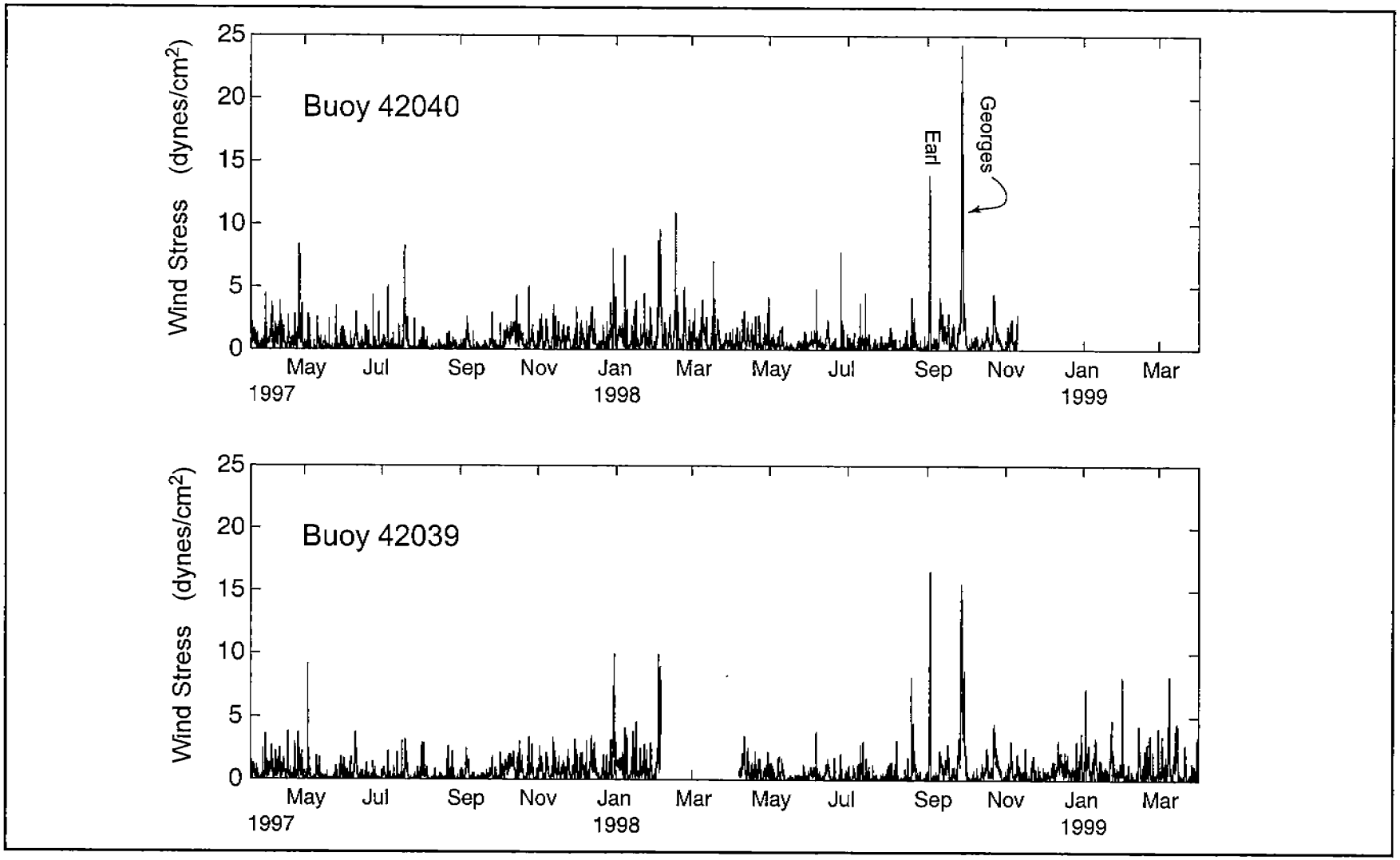

Figure 6.4-1. Estimated total surface wind stress at NOAA buoys 42040 and 42039 during the DeSoto Canyon study.

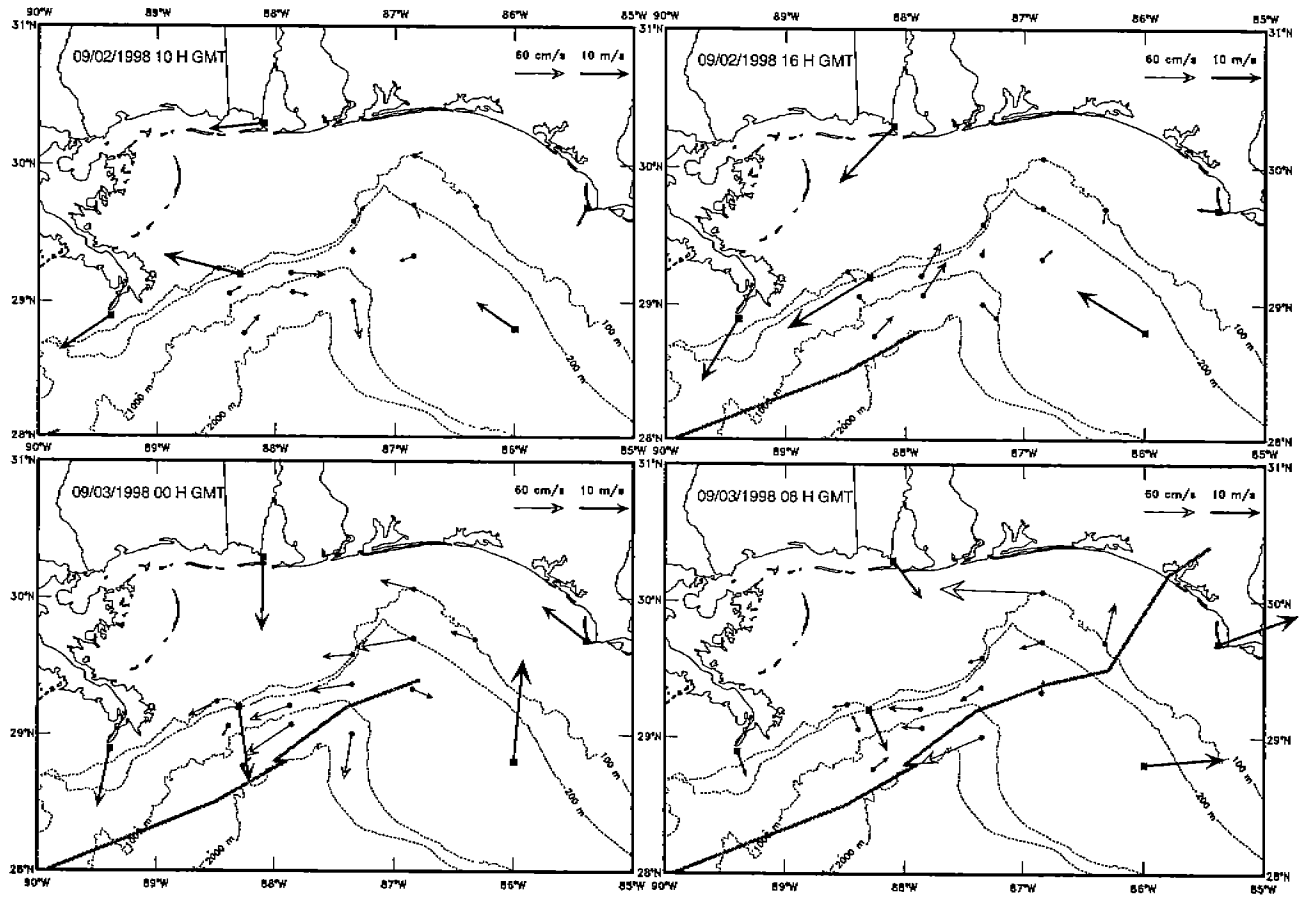

Figure 6.4-2. Wind velocities and near-surface currents (at 30 and 70m depth) measured during the passage of Hurricane Earl. The broader line going from SW to NE shows the approximate path of the hurricane center.

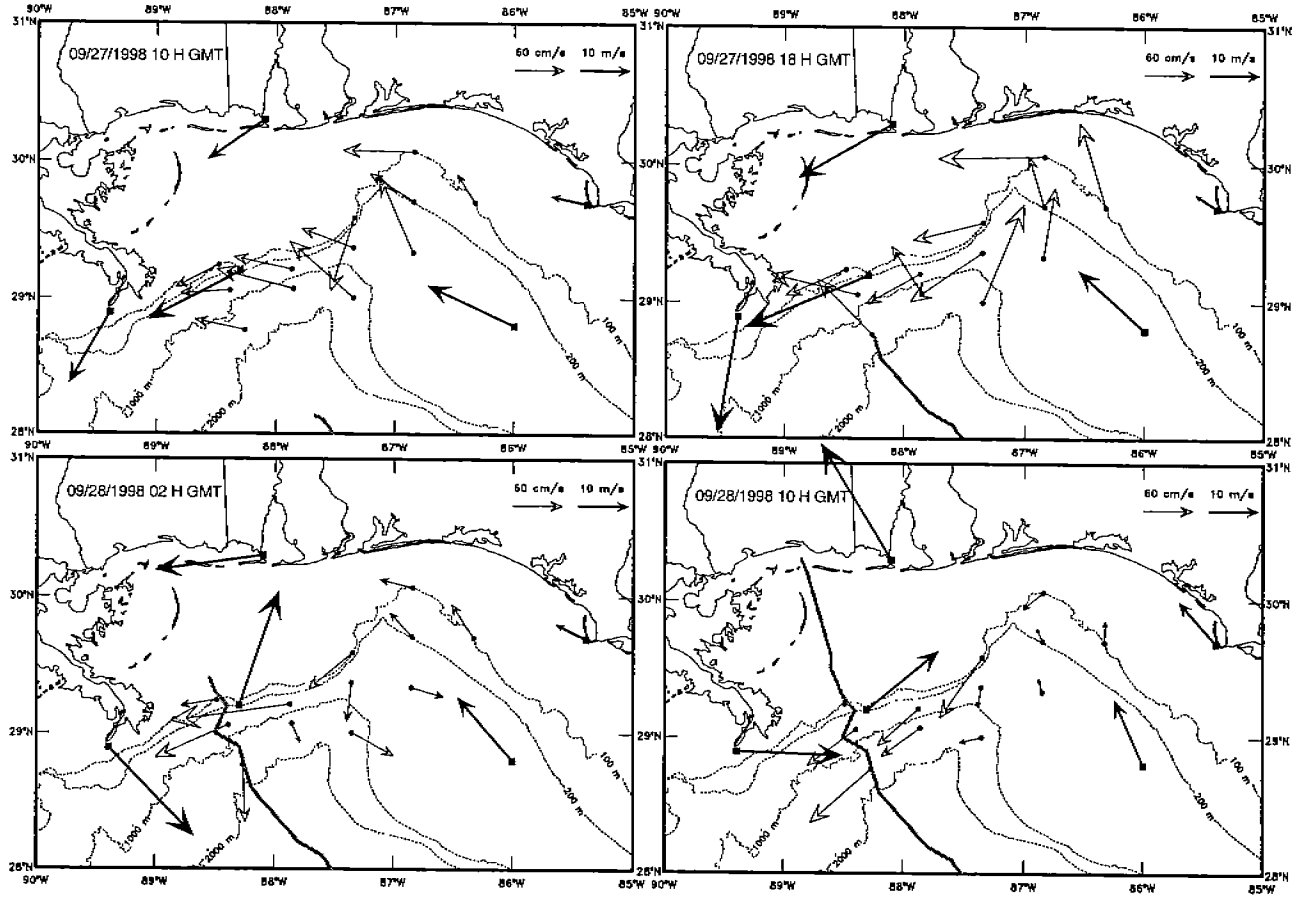

Figure 6.4-3. Same as Figure 6.4-2 except showing wind velocities and near-surface currents measured during the passage of Hurricane Georges as shown by the broader line going from SSE to NNW.

reveal that both storms had a spatially complex wind field over the canyon and that this generated a complex response in the near-surface flow field. Hurricane Earl approached the mooring array from the southwest. Over a period of approximately one day, the center of Hurricane Earl moved northeastward past the southern end of the array and made landfall over the Florida Panhandle. As the storm passed the array, its winds rotated cyclonically about the canyon. The spatial scale of wind variation was particularly short as the storm approached the Florida coast on September 3. At 00:00 on September 3, a northward wind was observed at the eastern end of the array (at buoy 42039) and a southward wind was observed at the western end of the array (at buoy 42040; see Figure 6.4-2). In spite of this short-scale variation in the wind field, near-surface currents over the upper canyon and canyon rim were fairly uniform in direction, tending toward the east. However, significant variations in the canyon currents were observed as the storm made landfall, with very large onshelf velocities appearing at the eastern canyon edge.

Hurricane Georges approached the array from the south. Its center moved northward along the western end of the array before making landfall near the Mississippi-Alabama border (Figure 6.4-3). As the storm's center approached the array, a well-organized, cyclonic wind field was seen over the canyon. However, as was observed during Hurricane Earl, winds over the canyon rapidly rotated and exhibited significant small-scale variations as Georges approached land. The near-surface currents driven by Georges over the canyon edge differed significantly from the storm-driven currents over the interior canyon. Currents over the deeper canyon rotated clockwise, at roughly the local inertial period, as the storm passed. By contrast, direction of flow at the canyon edge was relatively steady during the storm's passage. This flow appeared to move cyclonically along the canyon rim, following the early hurricane wind pattern.

6.4.2 The Canyon Edge Response

To illustrate the effect of the hurricanes at the canyon edge, Figures 6.4-4,5,6 show near-surface and near-bottom temperatures and velocities measured at the canyon rim moorings from late August through early October 1998. The plots of velocities have been rotated into along- and across-isobath components (see Table 6.4-1 for rotation angles). The coordinate system used has the positive along-isobath velocity directed such that deeper is to its right (i.e., to the northeast at moorings A1, B1 and C1; and to the southeast at mooring E1), and has the positive across-isobath velocity directed onshore.

Both storms generated a strong along-isobath flow near the surface. This moved from east to west along the canyon rim (Figure 6.4-4), opposite to the direction of the long-term mean flow. During Earl, the strength of this flow varied considerably as a function of position along the canyon edge. It was strongest at the canyon apex mooring, D1, where it exceeded 130 cm/s at 16m depth. The canyon edge flows were somewhat stronger during Georges than during Earl. Of particular significance were the strong near-bottom velocities seen at the canyon edge during Georges. Speeds in excess of 60 cm/s were measured at 5m

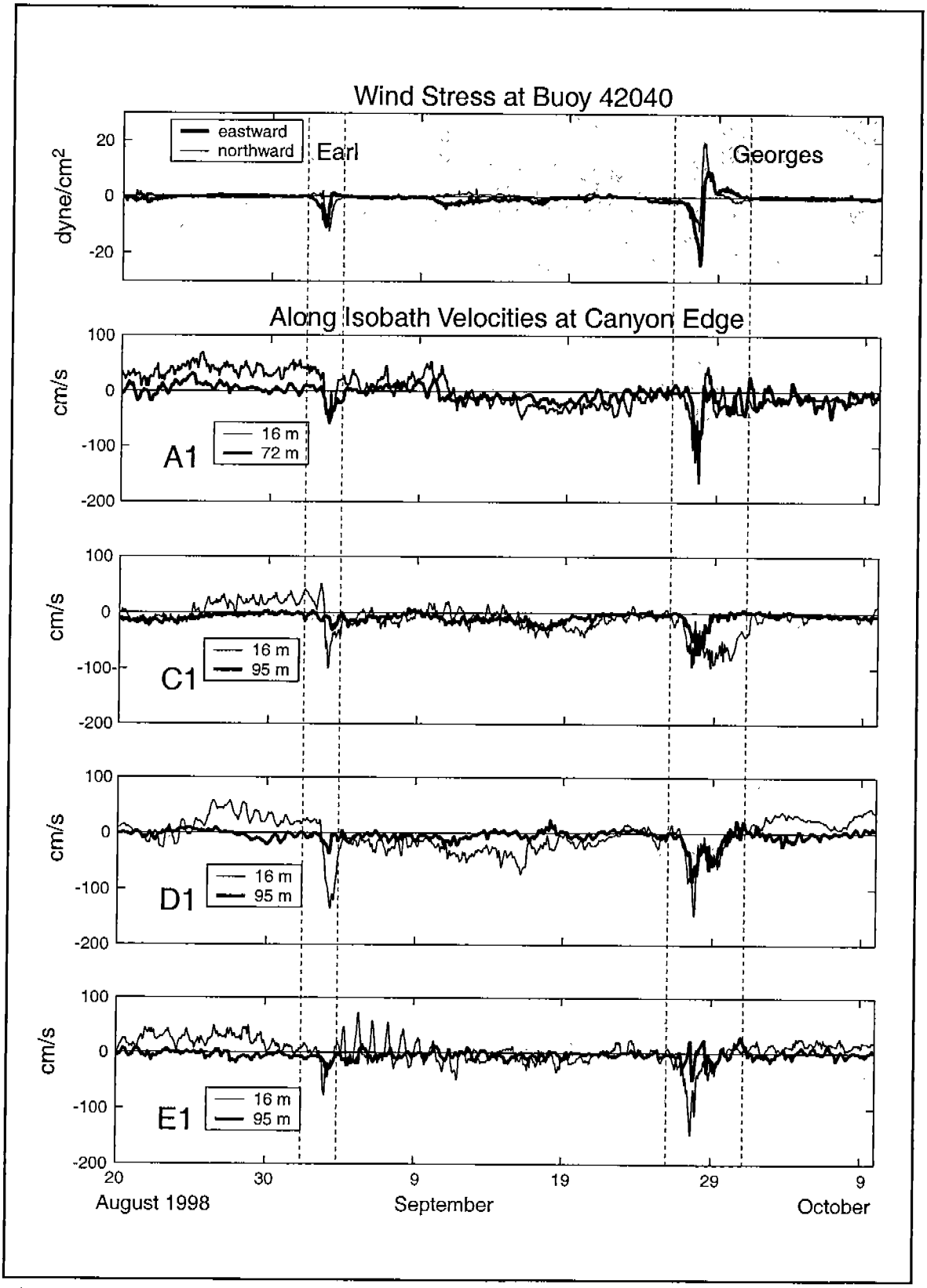

Figure 6.4-4. Time series of wind stress (top panel), and near-bottom and near-surface along-isobath current velocities (lower panels) measured at the indicated canyon-edge moorings during the passage of Hurricanes Earl and Georges.

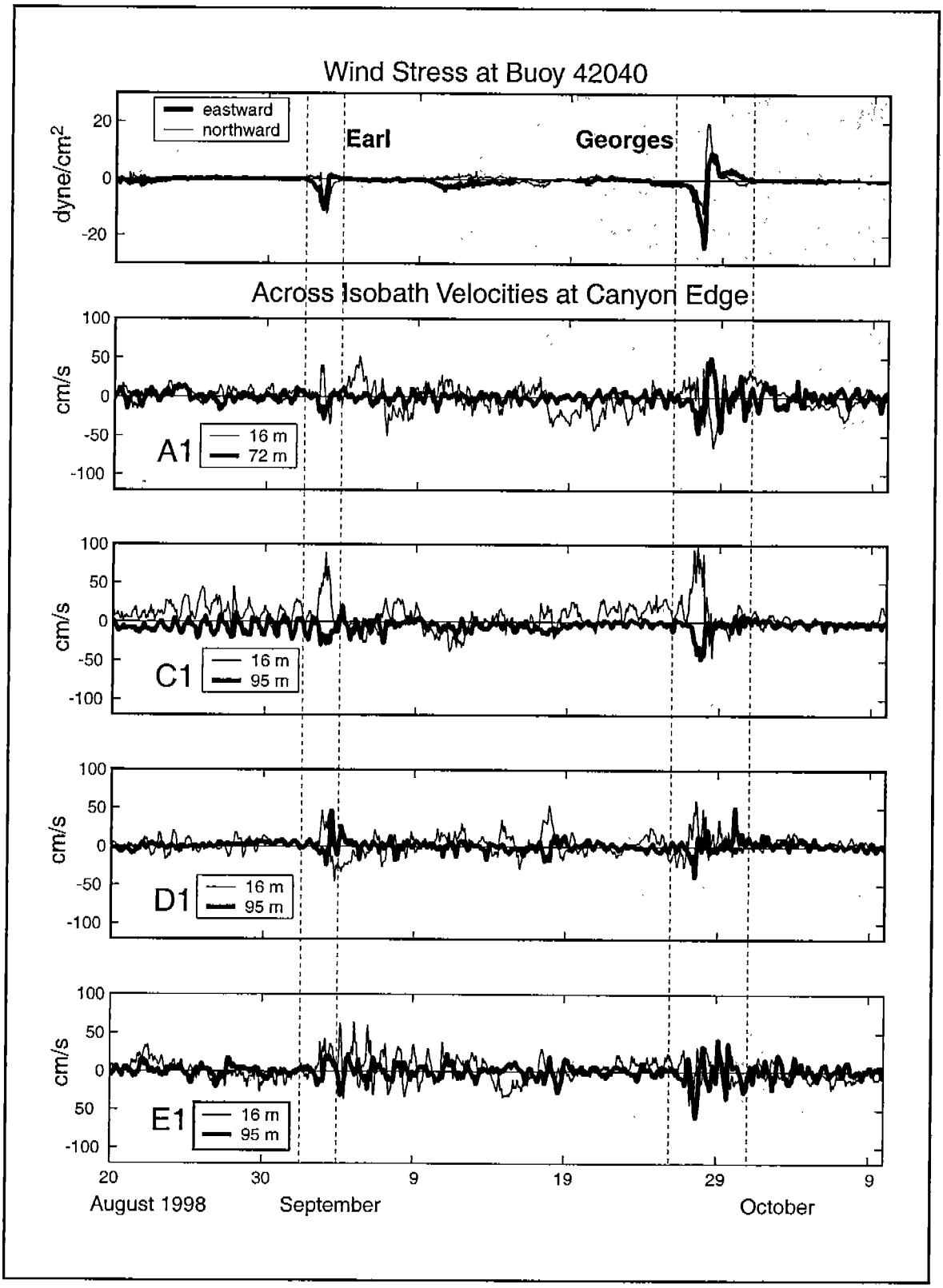

Figure 6.4-5. Same as Figure 6.4-4 except showing wind stress and across-isobath velocities measured during the passage of Hurricanes Earl and Georges. Positive velocities are directed onshelf.

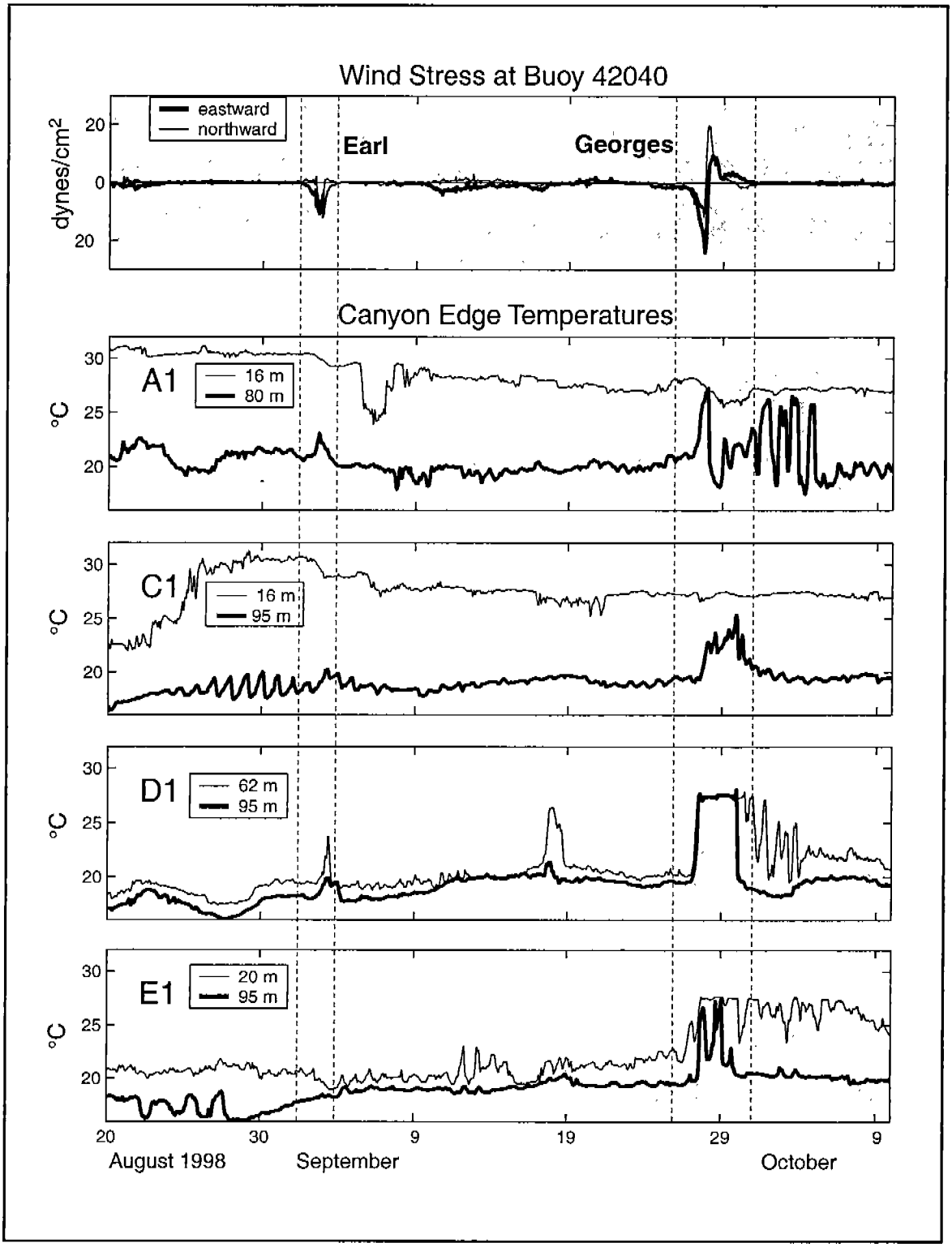

Figure 6.4-6. Same as Figure 6.4-4 except showing wind stress and temperatures measured during the passage of Hurricanes Earl and Georges.

above bottom at moorings C1, D1 and E1 as the storm approached the array. It is likely that these strong near-bottom currents may have mobilized a quantity of canyon edge sediments.

Strong and spatially varying across-isobath flows were seen at the canyon edge during both storms (Figure 6.4-5). Mooring C1 experienced the strongest cross-isobath currents, in excess of 60 cm/s during both storms. With very few exceptions, near-surface and near-bottom cross-isobath velocities measured at the canyon edge opposed each other during the hurricanes, evidence of a mode-1 baroclinic response to the storms.

Table 6.4-1. Net onshore and offshore volume transport per unit alongshelf distance measured at canyon edge moorings during early February 1998 storm and at mooring A1 during the presumed eddy passage of the mooring.

Even	Mrg.	Lnsh. Orient. *Ccw of East*	Dates 1998	Onshelf Trans. $(x10^6)m^2$	Offshelf Trans. $(x10^6)\ m^2$
February Storm	A1	20	Feb. 2-6	0.9	1.5
	B1	15	Feb. 2-6	1.2	0.9
	C1	45	Feb. 2-6	1.9	1.2
	D1	15	Feb. 2-6	2.7	0.1
	E1	-60	Feb. 2-6	0.8	2.3
Canyon Edge Eddy	A1	20	Jan. 10-16	2.6	2.8

Although no appreciable changes in canyon edge temperatures were observed during Earl, precipitous increases in near-bottom temperature were seen at the canyon edge moorings as Georges approached the array (Figure 6.4-6). These were not likely the result of local vertical mixing with warmer water from above because they were not matched by a coincident decline in near-surface temperatures at the canyon edge. They were probably the result of advection of warmer water from the shelf. All of the temperature increases coincided with offshelf near-bottom velocities. In addition, the large fluctuations seen in near-bottom temperature at moorings A1 and E1 during and after Georges were roughly 90° out-of-phase with cross-isobath velocities at the same level. This would be expected if the temperature fluctuations resulted from advection of a cross-shelf temperature gradient.

Details of the canyon edge velocity response to the two hurricanes can be seen in contour plots of velocity as a function of time and depth (Figures 6.4-7,8). During Earl, the highest velocities at the canyon edge tended to be concentrated in a near-surface jet. At moorings C1 and E1 this jet was particularly shallow, extending to about 30 m depth (Figure 6.4-7). By contrast, during Georges high velocities extended throughout the water column at all canyon edge moorings. A remarkable mid-depth maximum of along-isobath velocity was observed at mooring C1 during Georges (Figure 6.4-8). This suggests that the canyon edge

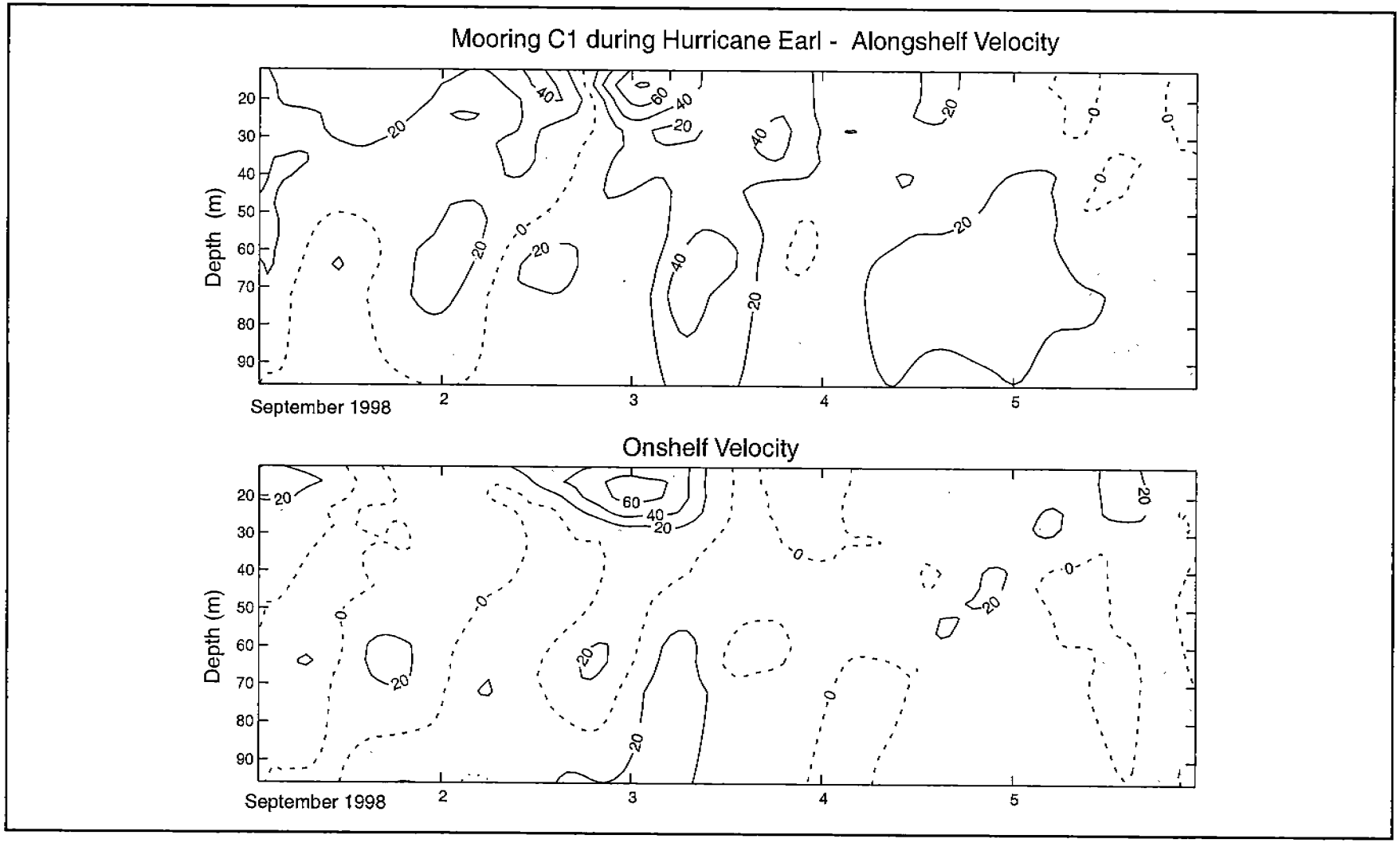

Figure 6.4-7. Contours of along-isobath (positive to the northeast) and across-isobath (positive onshelf) velocity recorded at mooring C1 during the passage of Hurricane Earl.

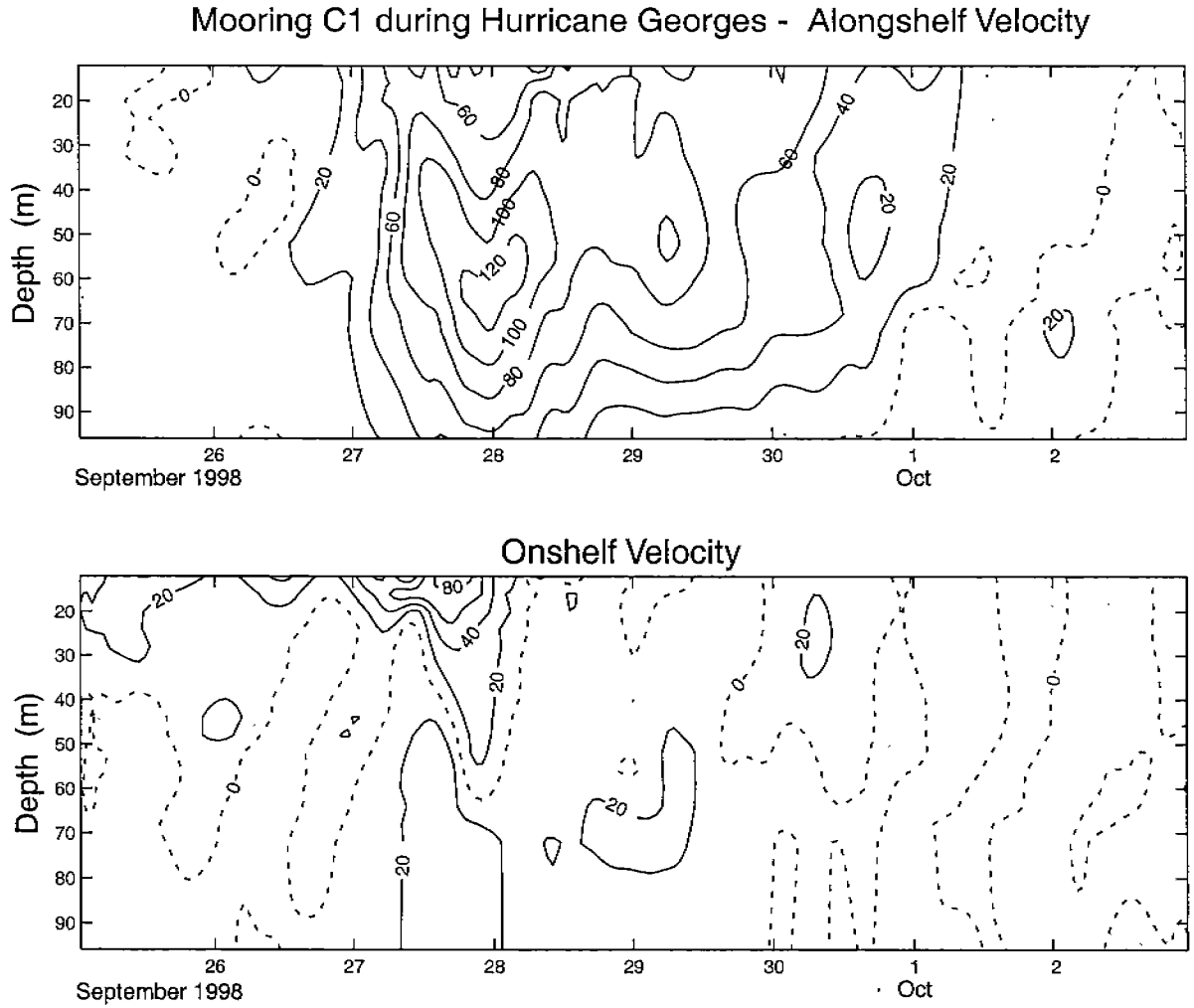

Figure 6.4-8. Same as Figure 6.4-7 except showing contours of velocity at mooring C1 during the passage of Hurricane Georges.

currents were not simply the product of vertical momentum transfer from local wind forcing at the surface.

No consistent trend was seen in cross-isobath velocities measured at the moorings during either hurricane. In fact, similarities in the hurricane-driven cross-isobath currents measured at the canyon edge moorings were hard to discern. During Georges, the cross-isobath flow measured at C1 was characterized by a strong and shallow onshelf current near the surface and a weaker onshelf current of greater vertical extent near the bottom (Figure 6.4-8). By contrast, near-bottom and near-surface cross-isobath currents measured at A1 changed sign during the passage of Georges (Figure 6.4-5) and were strongest in the 40-70m depth range. Still, different patterns were seen in the cross-isobath currents measured at the other canyon edge moorings during Georges.

6.4.3 Cross-margin Volume Transports at the Canyon Edge

An issue of importance to this study is the extent to which coastal and deep Gulf water masses were transported across the canyon rim as a result of the hurricanes. Unfortunately, the details of heat and salt transport at the canyon edge cannot be studied with the moored array data, due to the sparseness of temperature and salinity sensors in the array. However, the array data are well suited for the calculation of cross-margin volume flux at the canyon edge.

Using the velocity data from the canyon edge moorings, we computed the volumes of water transported on and off the shelf past each mooring during the passages of Hurricanes Earl and Georges. The volume of water transported onshelf (per unit of along-shelf distance) was computed by:

$$T_{on} = \int_{-D}^{0} \int_{t_1}^{t_2} u_{on}\, dt\, dz$$

Where u_{on} denotes the cross-isobath velocities measured at the mooring that were directed onshelf, D is water depth, and t_1 and t_2 bracket the time over which the hurricane affected currents at the mooring. The integration was carried out over the portion of the water column and times over which onshelf velocities were observed. A similar expression was used to compute offshelf volume transport. These integrations were carried out using the velocity data from moorings C1, D1 and E1 which extended over the depth range of 12-96m (no ADCP data were acquired at mooring B1 during the hurricanes, and no near-bottom velocities were measured at mooring A1 during the storms). It was assumed that the cross-isobath velocity in the surface and bottom layers lacking velocity measurements was uniform and equal to the velocity measured directly below (for the surface layer) or above (for the bottom layer). The along-isobath orientation at each mooring, on which the results of these calculations were sensitive, was chosen based upon the principal axes of the mooring's low-passed filtered velocity data. These orientations have an uncertainty of at least 5°. We found that changing the along-isobath orientation by 5° altered the computed transport by 10-35%.

The results (Table 6.4-2) indicate that Hurricane Georges generated significantly greater cross-margin volume transports than Hurricane Earl (by a factor of 2-3). These results also provide convincing evidence that hurricane driven onshore and offshore transports were not balanced at all locations on the canyon edge. A greater than 3:1 ratio of onshore to offshore transport was indicated at moorings D1 and E1 during Earl and at mooring D1 during Georges. This is a much larger imbalance than can be accounted for by the uncertainty in along-isobath orientation. These net onshelf transports, likely balanced by net offshelf transport elsewhere along the canyon rim, may have been the result of convergences and/or divergences in the flow along the canyon edge. This type of flow pattern may be expected in a region such as the canyon where the angle between wind direction and along-isobath orientation changes over relatively short distances.

Table 6.4-2. Net onshore and offshore volume transport per unit alongshelf distance measured at canyon edge moorings during Hurricanes Earl and George.

Storm	Mooring	Alongshelf Orientation *Ccw of east*	Dates Sept. 1998	Onshelf Transport $(x10^6)$ m^2	Offshelf Transport $(x10^6)$ m^2
Earl	C1	45	2-4	1.3	1.0
	D1	15	2-4	1.5	0.5
	E1	-60	2-4	1.4	0.4
Georges	C1	45	26.5-30	2.0	2.7
	D1	15	26.5-30	2.6	0.5
	E1	-60	26.5-30	1.4	2.0

6.4.4 The Inertial Wake

Previous investigators have found that storms passing over the Gulf of Mexico can leave vigorous inertial motions in their wake. Clear evidence of this was presented by Brooks (1983) who examined current meter and thermistor string records during and after Hurricane Allen's passage over the western Gulf of Mexico in 1981. Brooks found that the storm generated inertial currents with roughly 50 cm/s maximum amplitude, and that these decayed with an approximate time scale of 5 days. That analysis showed that the storm-driven inertial energy propagated downward through the thermocline at a rate which roughly accounted for the decay of the near-inertial currents in the surface mixed layer. A longer-term examination of inertial currents over the Texas-Louisiana shelf and upper slope was conducted by Chen et al. (1996). They found that pulses of near-inertial currents over the shelf tended to follow a sudden change in surface wind stress. Their analysis indicated that the vertical structure of near-inertial currents over the shelf typically conformed with that of a first baroclinic mode, with close to a 180° phase difference between the near-surface and near-bottom currents. The amplitudes of near-inertial currents observed by

Chen et al. (1996) were maximal near the shelf-edge, and decayed gradually toward the coast but rapidly offshore.

To examine the inertial current signal in the velocity records from the DeSoto Canyon array, we employed a method developed by Perkins (1971). Termed "complex demodulation", this method produces a time series of complex coefficients, D(_), according to:

$$D(\tau) = 1/(2T)\int_{\tau-T}^{\tau+T} [c(t) - \langle c \rangle]e^{ift}dt,$$

$$\text{where } c = u + iv$$

$$\text{and } \langle c \rangle = 1/(2T)\int_{\tau-T}^{\tau+T} c(t)dt,$$

In the above, c is a complex representation of the velocity series; f is the local inertial frequency; and T is the length of the demodulation window. In essence, D(_)is the Fourier transform of c over the period $-T<t<+T$ and at the frequency f. The magnitude and argument of D(t) thus approximate the amplitude and phase of the inertial velocity signal at time t.

The inertial current magnitude seen during and following the passages of Hurricanes Earl and George varied considerably from mooring to mooring (Figures 6.4-9,10). Hurricane Earl generated weak inertial currents along the canyon edge. As the hurricane passed the array, slight increases in inertial current magnitude were seen at moorings C1 and D1, while no appreciable changes in inertial current magnitude were observed at moorings E1 and A1 (Figure 6.4-9). By contrast, Hurricane Earl generated vigorous inertial currents within the interior of the canyon. These appeared to become stronger with increasing water depth. Along each mooring line their strength was greatest at the deepest mooring (near the 1300m isobath). The strongest inertial currents attributed to the storm were seen near the surface at mooring C3. Their magnitude peaked near 50 cm/s, roughly equivalent to the maximum strength of the inertial currents observed by Brooks (1983) in the wake of Hurricane Allen.

After the passage of Hurricane Earl, lengthy pulses of strong inertial currents appeared near the surface at moorings D2 and E1. When viewed as a function of time, the magnitude of these pulses resembled the magnitude of the inertial current pulse seen at mooring C3, except shifted forward in time (Figure 6.4-11). The time shift, relative to the C3 magnitude, was 1.2 days for the D2 pulse and 2.9 days for the pulse at E1. This suggests that the inertial current pulses seen at moorings D2 and E1 were not locally generated, but had propagated to the moorings from the western canyon. Based on the relative times of the pulse's first appearance at moorings C3, D2 and E1, we have determined pulse may have propagated with a group velocity of roughly 30 km/day to the ENE.

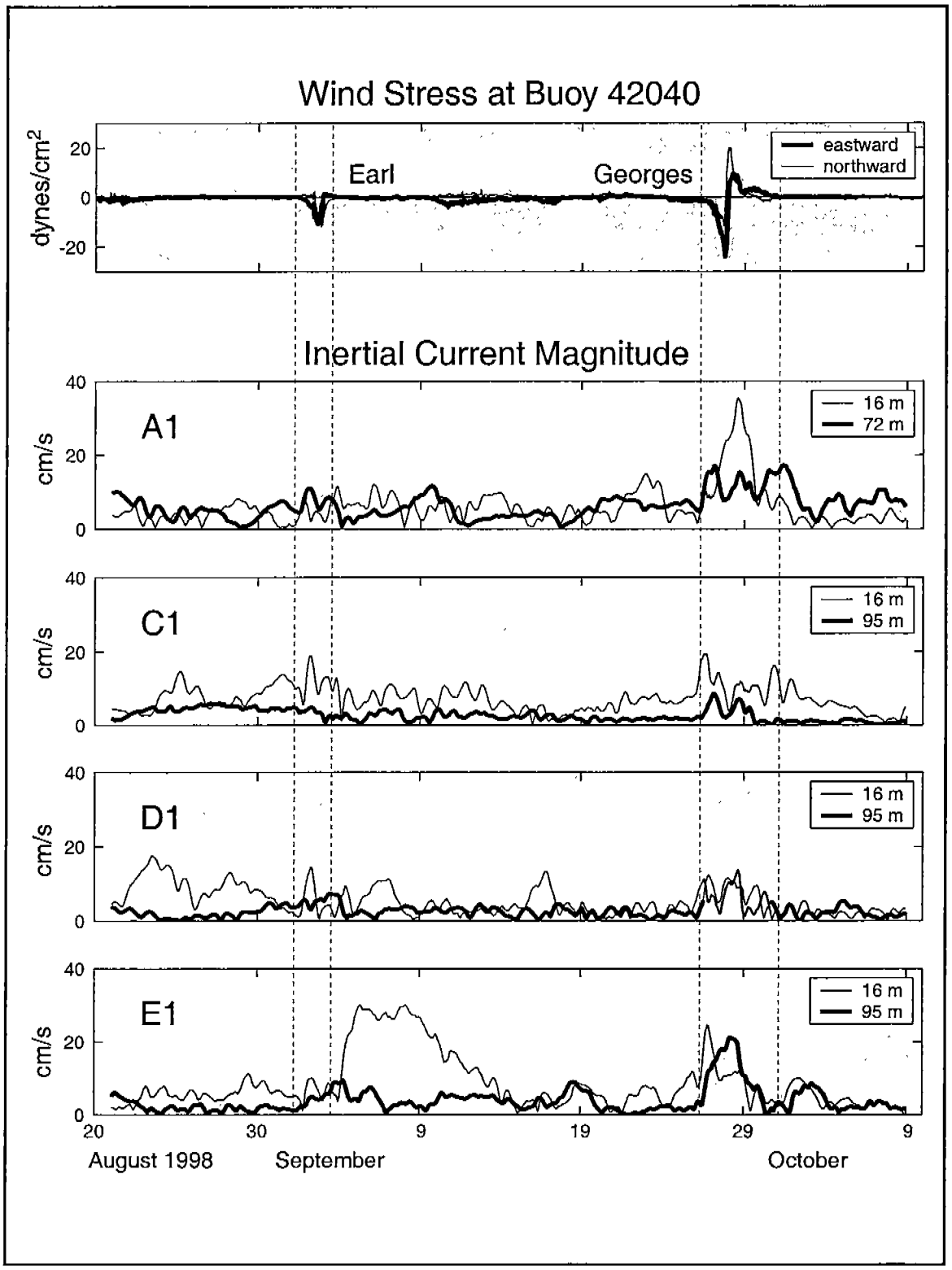

Figure 6.4.9. Surface wind stress (top panel) together with near-bottom and near-surface inertial current magnitude observed at the indicated canyon edge moorings during late summer-early autumn 1998.

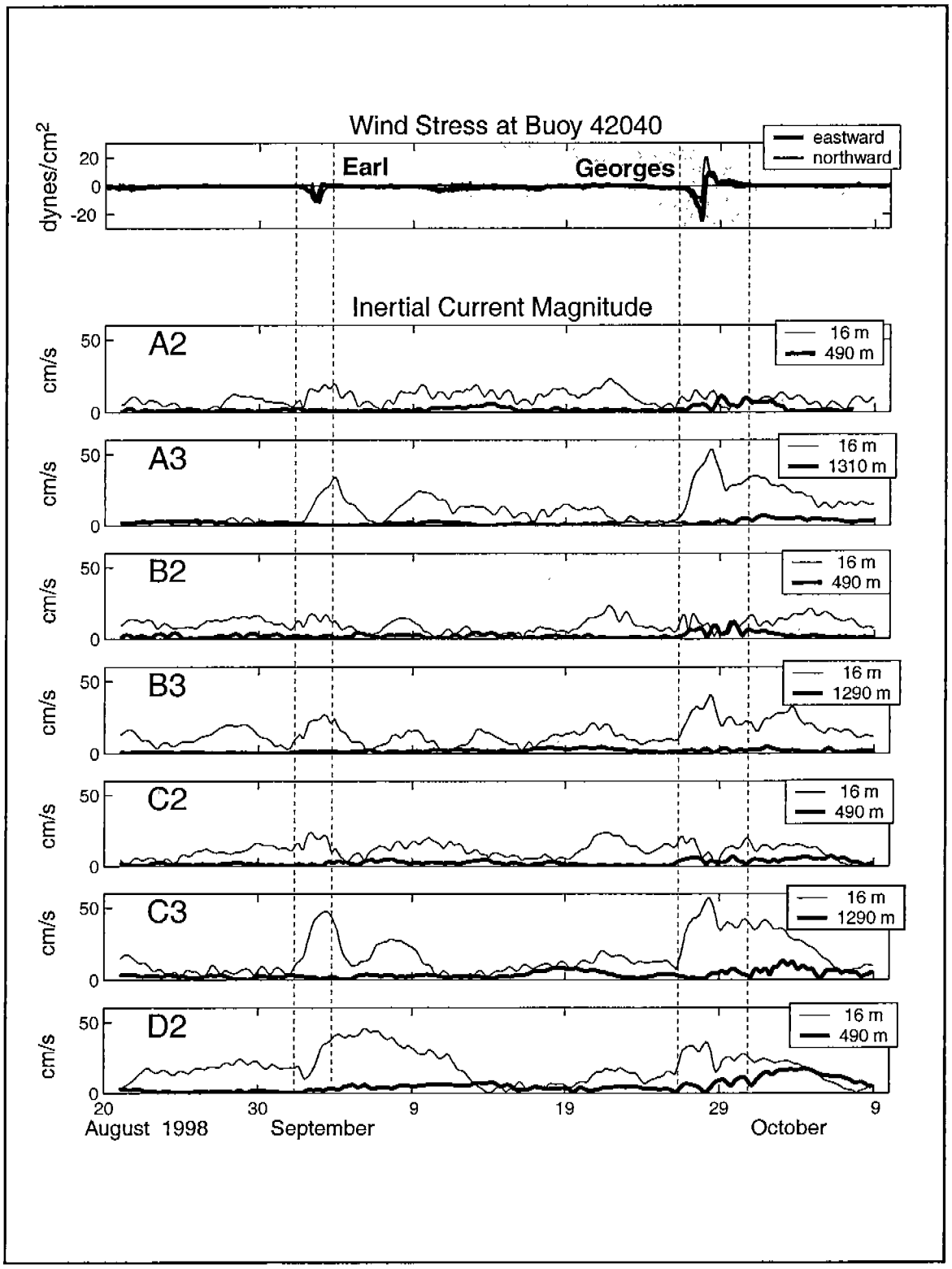

Figure 6.4-10. Same as Figure 6.4-9 except showing near-bottom and near-surface inertial current magnitude at interior canyon moorings. Note the strong and persistant near surface inertial currents during and following passage of Earl at Mooring D2.

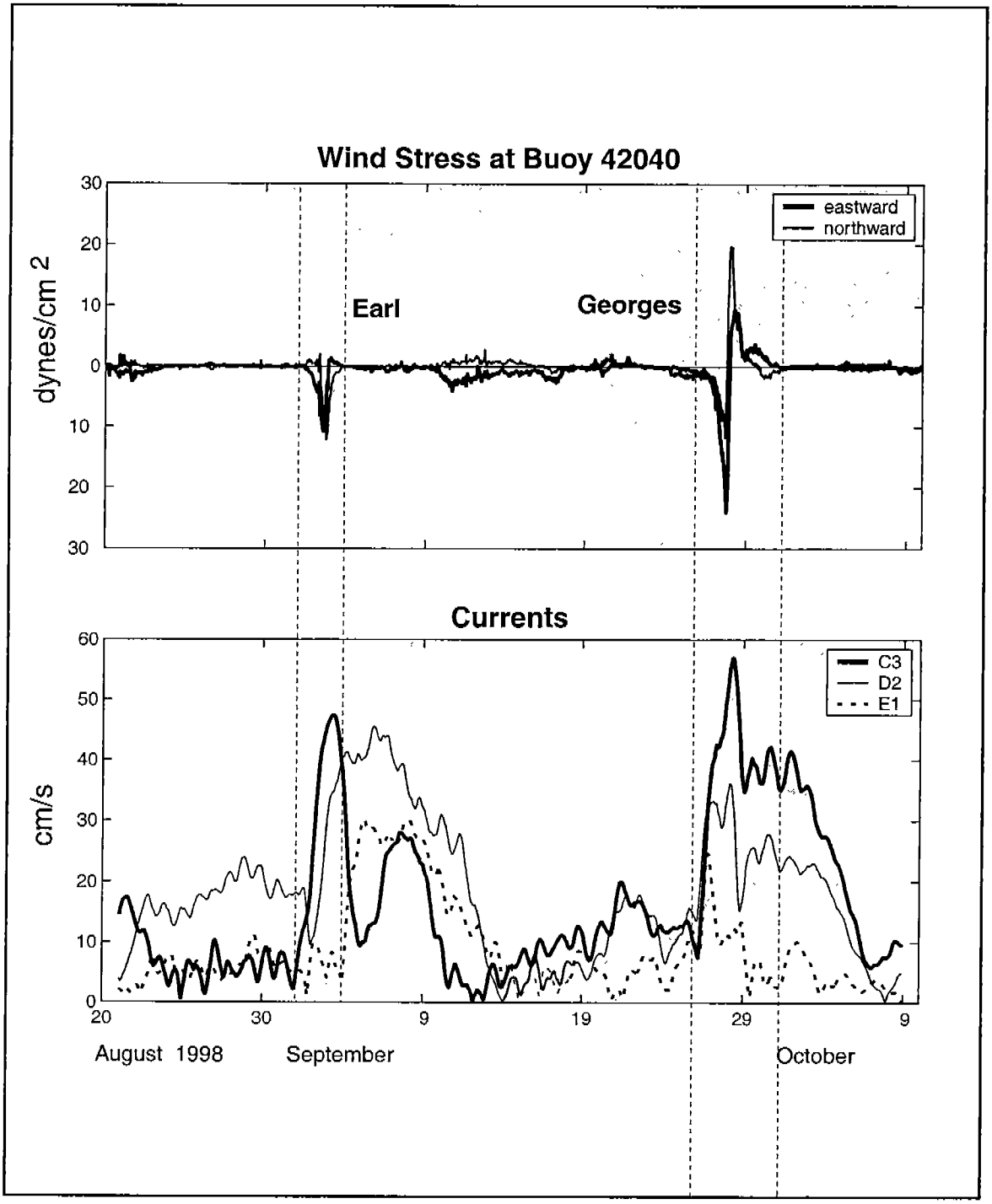

Figure 6.4-11. Comparison of inertial current magnitudes seen near the surface at moorings C3, D2 and E1 during late summer-early fall 1998

Hurricane Georges appeared to have generated strong inertial currents all along the canyon rim. Significant increases in inertial current magnitudes were observed at all canyon edge moorings during the hurricane's passage (Figure 6.4-9). However, the strongest inertial currents were again seen at the deepest moorings (Figure 6.4-10). Subsequent increases in near-bottom inertial current were also observed at the deepest moorings, suggesting that the hurricane-generated inertial motions propagated vertically to the deep canyon floor.

Strong near-bottom inertial currents were also seen at the canyon edge moorings following the passage of Georges. However, the relative phase of these currents was complicated and did not always conform with a mode-1 baroclinic structure (Figure 6.4-12).

To summarize, Hurricane Earl generated relatively weak inertial currents over the canyon edge but vigorous inertial currents over the deep canyon. The data suggest that the inertial motions generated over the deep canyon by Hurricane Earl may have propagated towards the ENE to the Florida shelf. Hurricane Georges generated vigorous inertial motions over the entire canyon, but these were again strongest over the deep canyon. The vertical phase of the inertial motions seen at the canyon edge during both storms were complicated and often bore little resemblance to a mode-1 baroclinic structure. These observations are in marked contrast to those of Chen et al. (1996), who found that storm-generated inertial motions over the Texas-Louisiana shelf have a mode-1 structure and decay rapidly in magnitude going off the shelf. The difference from our observations may be storm related or could reflect general differences in the character of inertial motions in the two study regions. Such differences might be expected given the drastic contrast in the bathymetric setting of the study regions.

To compare the strength of inertial currents generated by Hurricanes Earl and Georges to inertial currents generated by other storms, or by different mechanisms such as frontal instabilities, Figure 6.4-13 shows time series of near-bottom and near-surface inertial current magnitude at selected moorings for the duration of this measurement program. At some locations, inertial currents generated by Earl and Georges were the most vigorous of the study period (e.g., near the surface at mooring C3). At other locations, inertial currents due to Earl and Georges were matched or bested in strength by inertial currents due to other events, such as storms during February 1998. It is also seen that the decay of inertial energy going onshore to the canyon edge, seen during Earl and George, was typical of most inertial current events. Careful inspection of the wind stress and inertial current magnitude time series reveals that pulses of strong inertial motions were often associated with episodes of strong winds. However, there were times that strong inertial currents appeared when winds were weak (e.g., during May 1997 and April-May 1998). Likely causes of inertial currents during these times include eddy shedding from the LC and eddy-eddy interaction over the canyon.

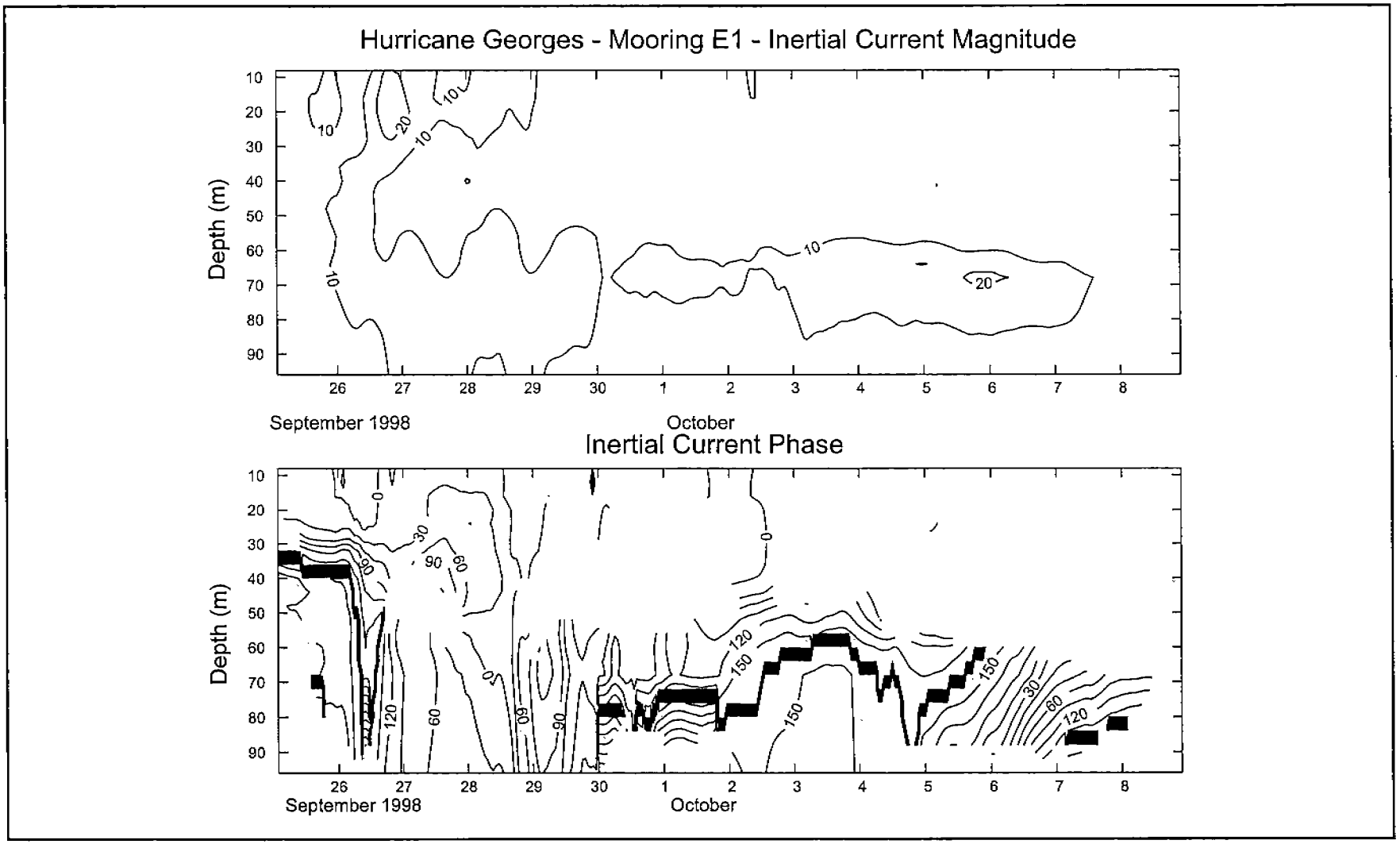

Figure 6.4-12. Contours of the magnitude and phase of inertial currents observed at mooring E1 during and after the passage of Hurricane Georges. Phase is relative to the current at the shallowest current meter and is contoured only where the magnitude exceeds 5 cm/s.

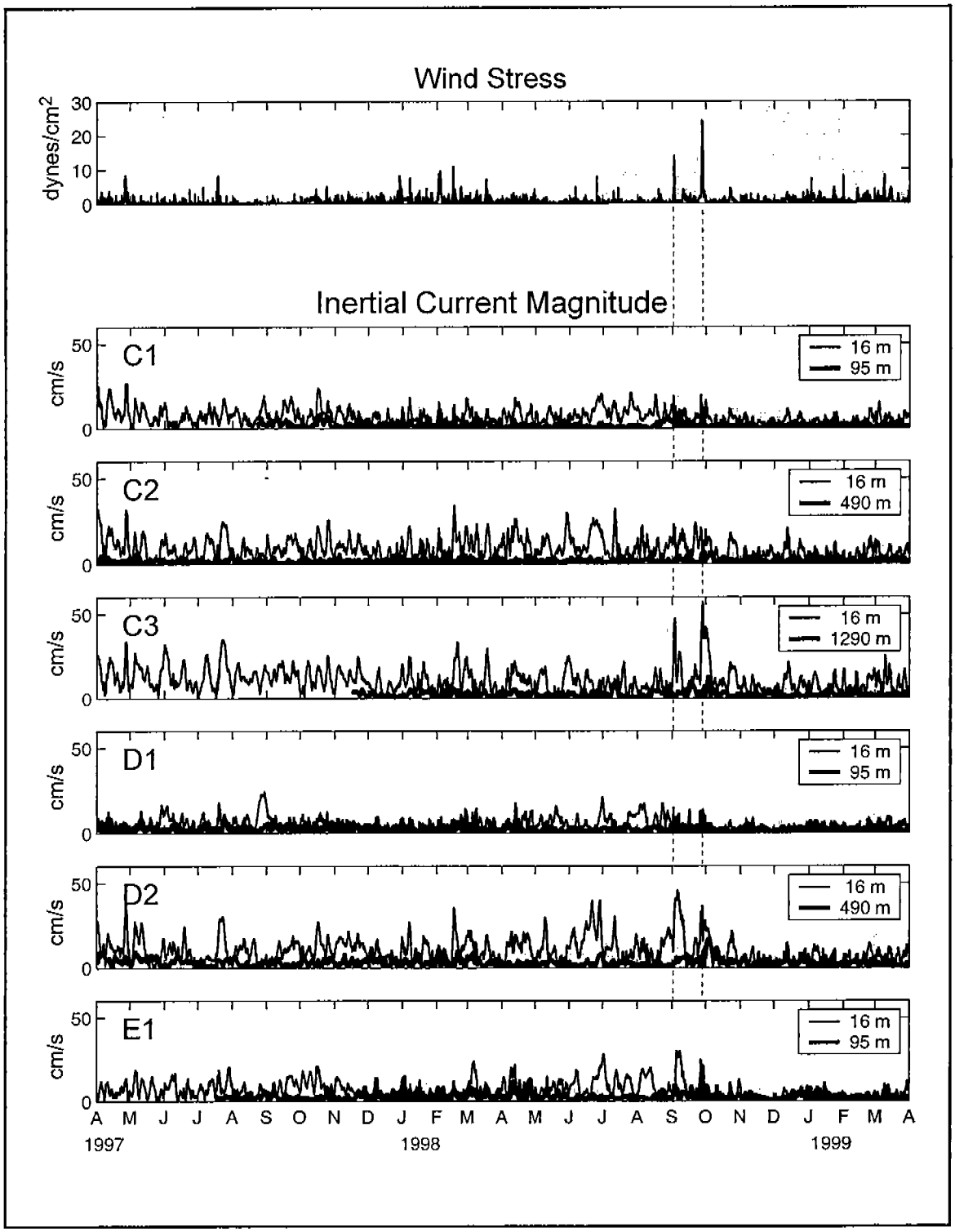

Figure 6.4-13. Surface wind stress together with near-bottom and near-surface inertial current magnitude observed at the indicated moorings over the study period. Because of gaps in the wind records, wind stresses over April 1997–November 1998 were computed from buoy 42040 wind velocities and subsequent wind stresses were computed using wind velocities from buoy 42039.

6.4.5 Storms vs. Canyon edge eddies during the winter of 1997-1998

When considering eddy vs. storm effects on the canyon rim, the winter of 1997-1998 is of particular interest. The strongest storms of the study period, not designated as hurricanes, passed over DeSoto Canyon during this time (Figure 6.4-1). The most intense of these storms occurred in early February 1998, with the second most intense storm traversing the canyon in late December 1997. Although severely limited by frequent cloud cover, satellite SST imagery of the period clearly showed a LC eddy extending northward into DeSoto Canyon and smaller eddies and/or frontal instabilities at the canyon rim (Figures 6.4-14,15). For example the STT image of January 16, 1998 shows an eddy (or frontal instability) at the western canyon rim in the vicinity of moorings A1 and B1 (Figure 6.4-15).

The effect of the storms and eddies on the canyon edge can be seen in near-surface and near-bottom velocities from the canyon edge moorings (Figures 6.4-16,17). The strongest winds of the late December 1997 storm were directed to the ESE. These appeared to have generated an eastward tending near-surface flow at the canyon edge (Figure 6.4-16). However, the effect of the storm on this current was not clearly defined by the moored array data, as they showed the strongest northeastward velocities occurring at moorings A1 and B1 shortly after the storm abated. The early February storm generated a relatively strong current that moved cyclonically along the canyon rim. Akin to Georges, this storm produced strong near-bottom currents at the canyon edge. As the storm passed the array, current speeds in excess of 30 cm/s were measured at 5 m above bottom at all canyon edge moorings. At mooring C1, near-bottom current speeds exceeded 45 cm/s for a full day during the storm's passage. Unlike Georges, a two-layer cross-margin exchange was not clearly evident over most of the canyon edge during the early February storm. It was only at mooring C2 that strong and opposing near-surface and near-bottom cross-isobath flows were observed at the canyon edge during this storm (Figure 6.4-17).

The canyon edge mooring data showed strong cross-isobath velocities during mid-January when winds were relatively weak and when SST imagery revealed eddies and/or frontal instabilities at the canyon edge (Figures 6.4-14,17). The strongest cross-isobath currents of this period were seen at moorings A1 and B1 where the SST imagery showed clearest evidence of eddy and/or frontal instability activity (Figures 6.4-14,15). A particularly strong and persistent flow, not related to wind forcing, was observed at mooring A1 during 14-20 January (Figure 6.4-18). This had subsurface maximum in its along-isobath component of roughly 60 cm/s within the 20-40 m depth range. It's cross-isobath component reached nearly 40 cm/s in magnitude and underwent an abrupt change in sign (direction) on 18 January. This is a velocity signal that may be expected due to the passage of an eddy or frontal meander.

To compare eddy and storm driven cross-margin volume transports, we used the method outlined in Section 6.4 to estimate these transports during the early February 1998 storm and during the presumed mid-January canyon

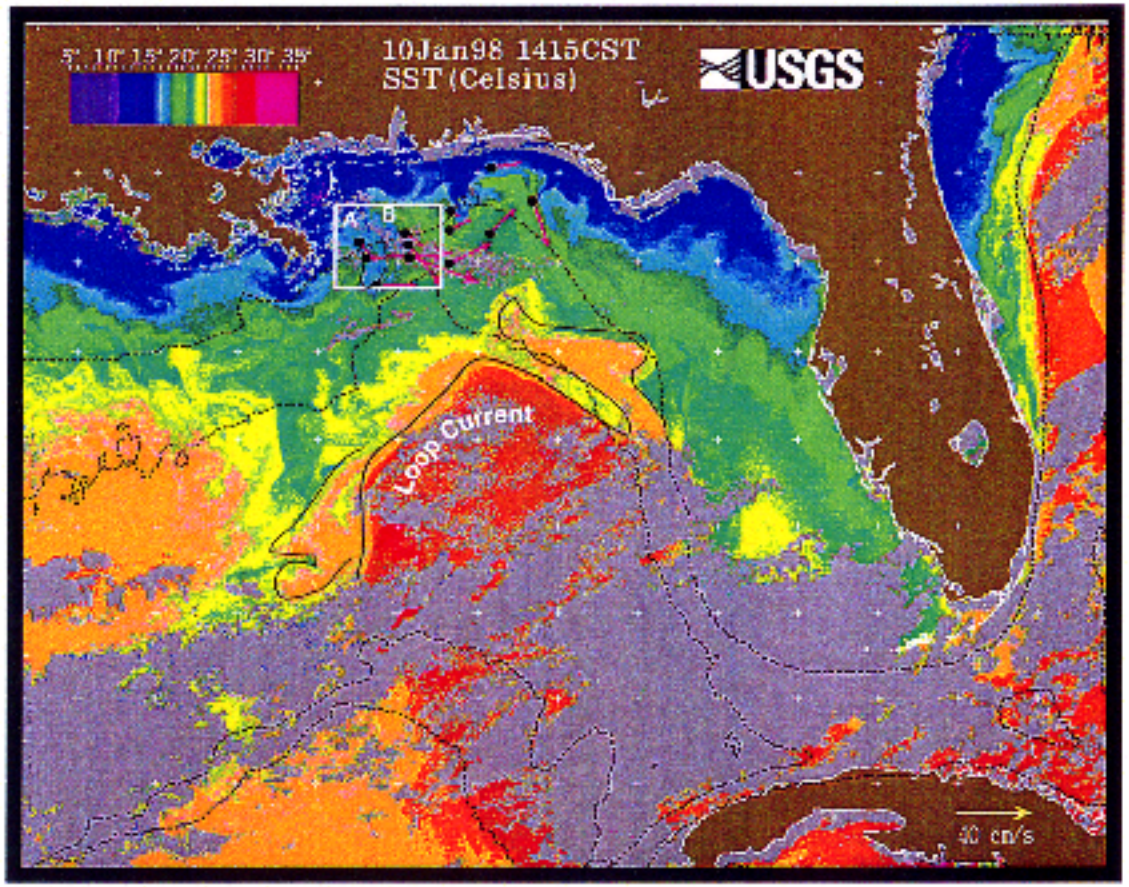

Figure 6.4-14. SST on January 10, 1998 (1414 CST) with measured near surface current velocities overlaid on the image. Some additional lines and notation have been added to help clarify the figure references in the text.

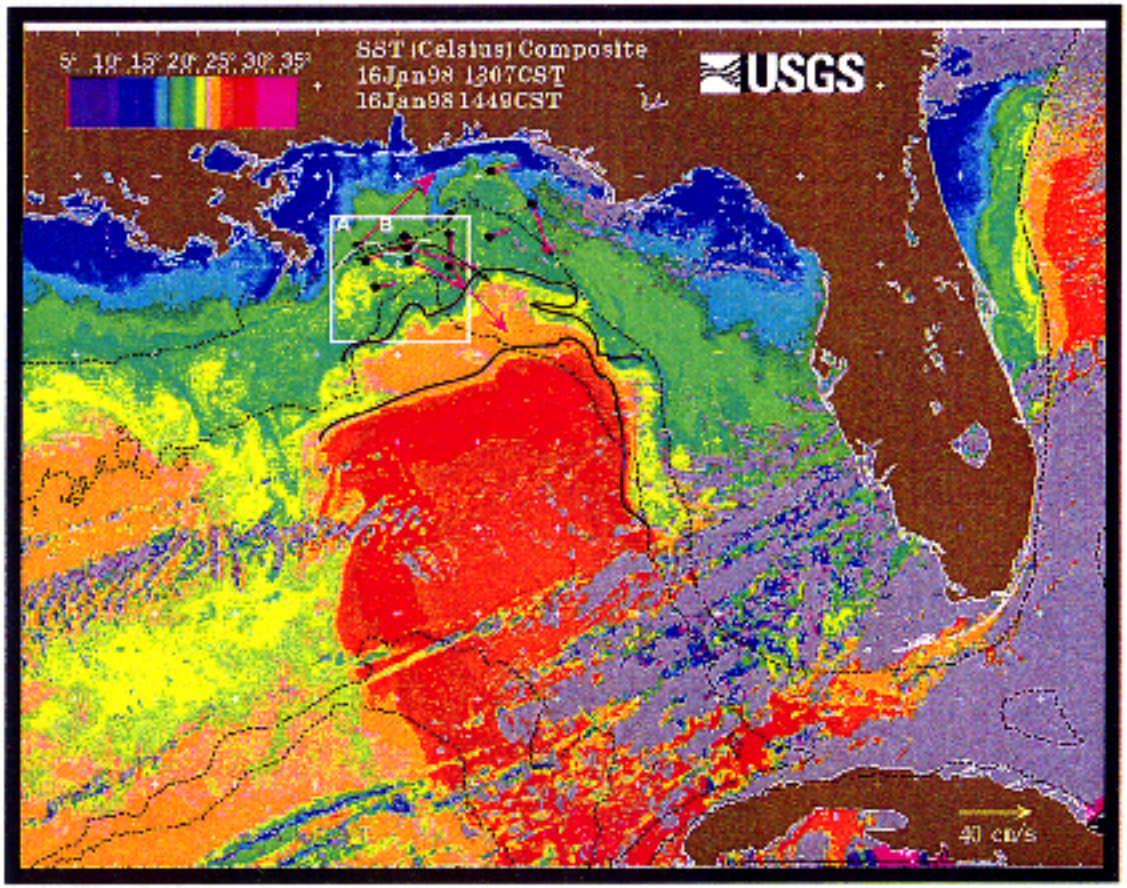

Figure 6.4-15. SST on January 16, 1998 (1307 CST) with measured near surface current velocities overlaid on the image. Some additional lines and notation have been added to help clarify the figure references in the text.

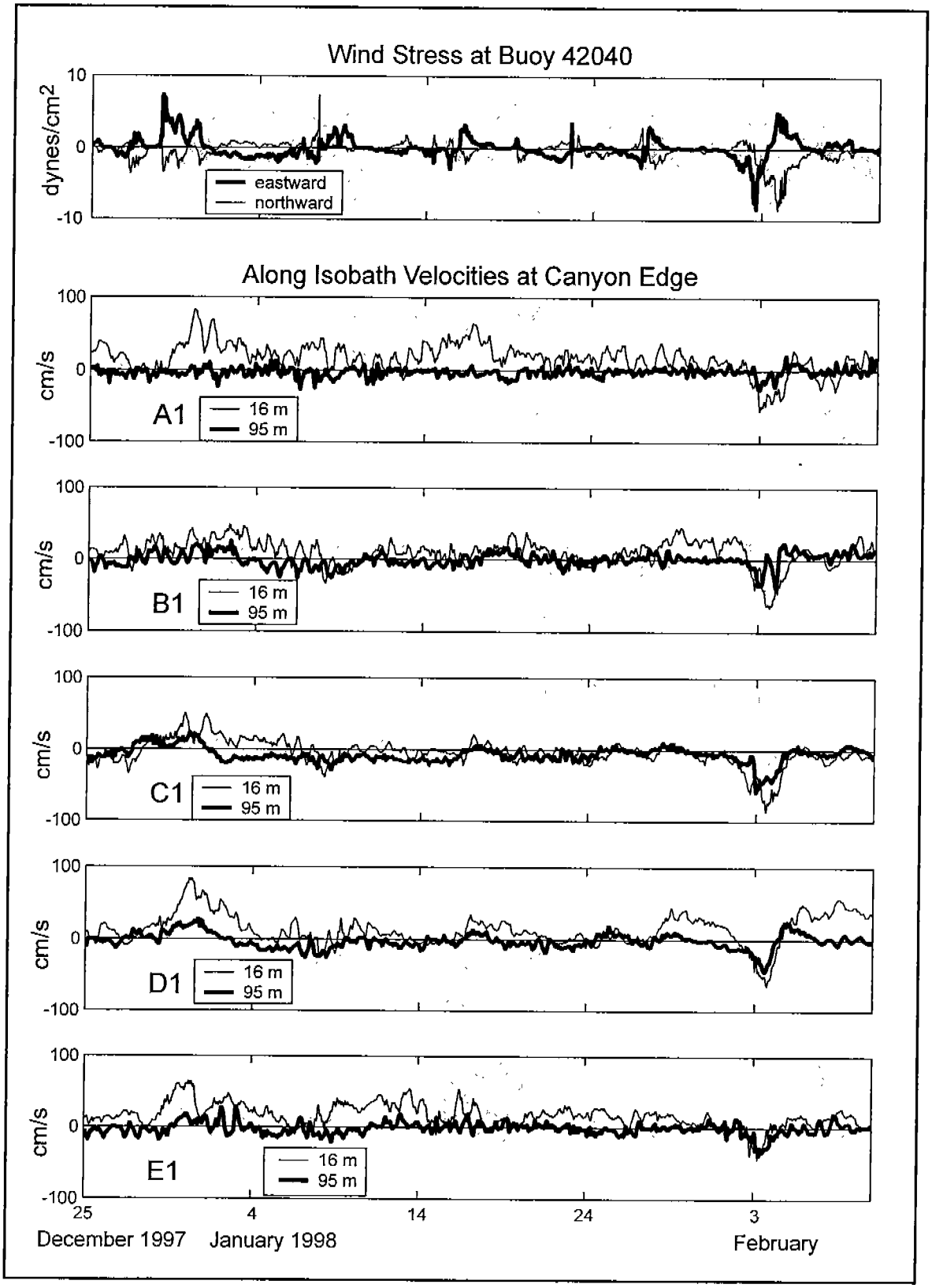

Figure 6.4-16. Near-bottom and near-surface, along-isobath velocities measured at the canyon edge moorings during the winter of 1997-1998.

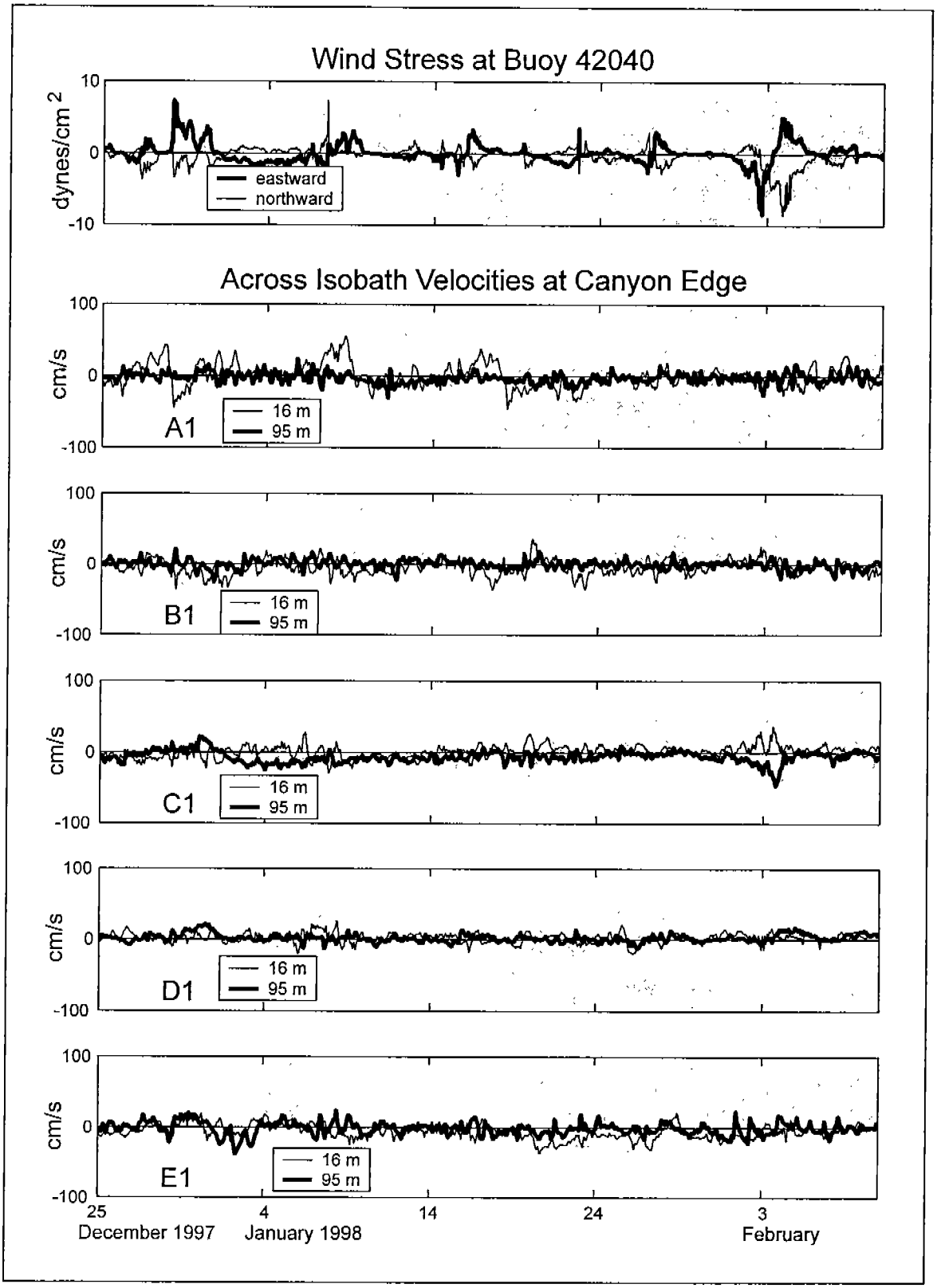

Figure 6.4-17. Same as Figure 6.4-16 except showing near-bottom and near-surface across-isobath velocities.

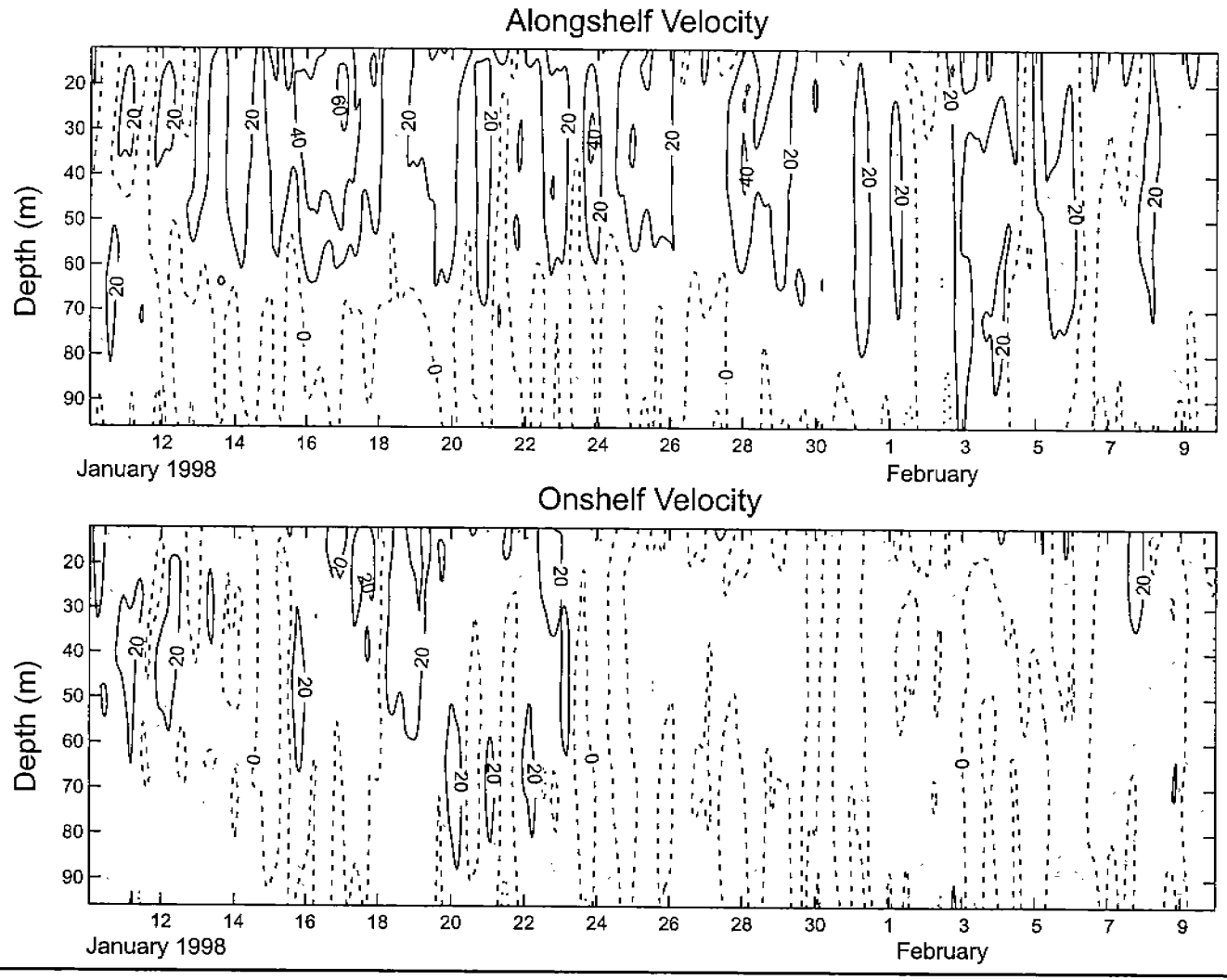

Figure 6.4-18. Contours of along-isobath and across-isobath velocity measured at mooring A1 during January and February 1998.

rim eddy event at mooring A1. Volume transports observed during the storm were of a magnitude similar to the transports observed during Hurricane Earl (Tables 6.4-1 and 6.4-2). Similar to the transport observed during Earl and Georges, onshelf and offshelf transports of the early February storm were approximately balanced at some moorings, and were grossly mismatched at others. The onshelf and offshelf transports observed at A1 during the presumed eddy passage were roughly equivalent and similar in magnitude, to transport observed during Hurricane Georges. A conclusion is that the canyon edge volume exchange generated by an eddy or frontal instability can be comparable to that generated by a hurricane.

6.5 Inertial Currents on the Slope

The velocity records often show large amplitude fluctuations with periods near 1 day. A typical example from the upper layer for the summer of 1997 is given in Figure 6.5-1. The across (U) and along (V) isobath currents have similar magnitudes and the velocity vector rotates clockwise (V leads U by ~90°). Because of their intermittent nature and variability with depth, these oscillations are attributed to wind-forced inertial-internal waves. This section describes the characteristics of these motions and their seasonal variability. The exceptional inertial currents that occurred in the wakes of Hurricanes Earl and Georges in September 1998 are discussed in Section 6.4. The inertial period ($2\pi/f$) at 29°N is 24.75 hours (0.97 cpd) which is in the center of the diurnal tide band. However, barotropic diurnal tidal currents over the slope have magnitudes < 1 cm/s. Internal tides may be present but should be phase-locked to the surface tide. The variability of the daily oscillations in Figure 6.5-1 does not show the regularity that would be expected from internal tide motions. The spectra also do not show distinct peaks at the K_1 or P_1 frequencies that would be expected for narrow band motions such as diurnal tidal currents. Therefore, the majority of the daily oscillations are considered to be caused by inertial-internal waves even though diurnal tidal motions are difficult to separate out from the records.

The time series of the velocity components have several interesting features (Figure 6.5-1). The strongest oscillations were at C3, the mooring furthest offshore and in the deepest water (1300m). Here, the inertial currents were present to some degree for most of this two-month period despite weak winds. There is little apparent correlation of the magnitude of the offshore oscillations with wind events. However, some of the abrupt shifts in wind direction (e.g. ~ August 1) seem to trigger bursts of inertial oscillations. Eddies could generate inertial currents by interactions with other flows, and flows with large horizontal shears that generate negative, relative vorticity anomalies can trap inertial oscillations by causing a local decrease in the effective planetary vorticity (f) (Mooers 1975; Kunze 1985). Thus, the eastward flowing upper-slope jet that is frequently found in the study region (see Section 5.2) could trap northward propagating inertial waves on its southern side (Kunze 1985). The summer 1997 clockwise rotary spectra (Gonella 1971) for two depth levels on transect C are given in Figure 6.5-2. The peaks around 1 cpd are broad, reflecting the

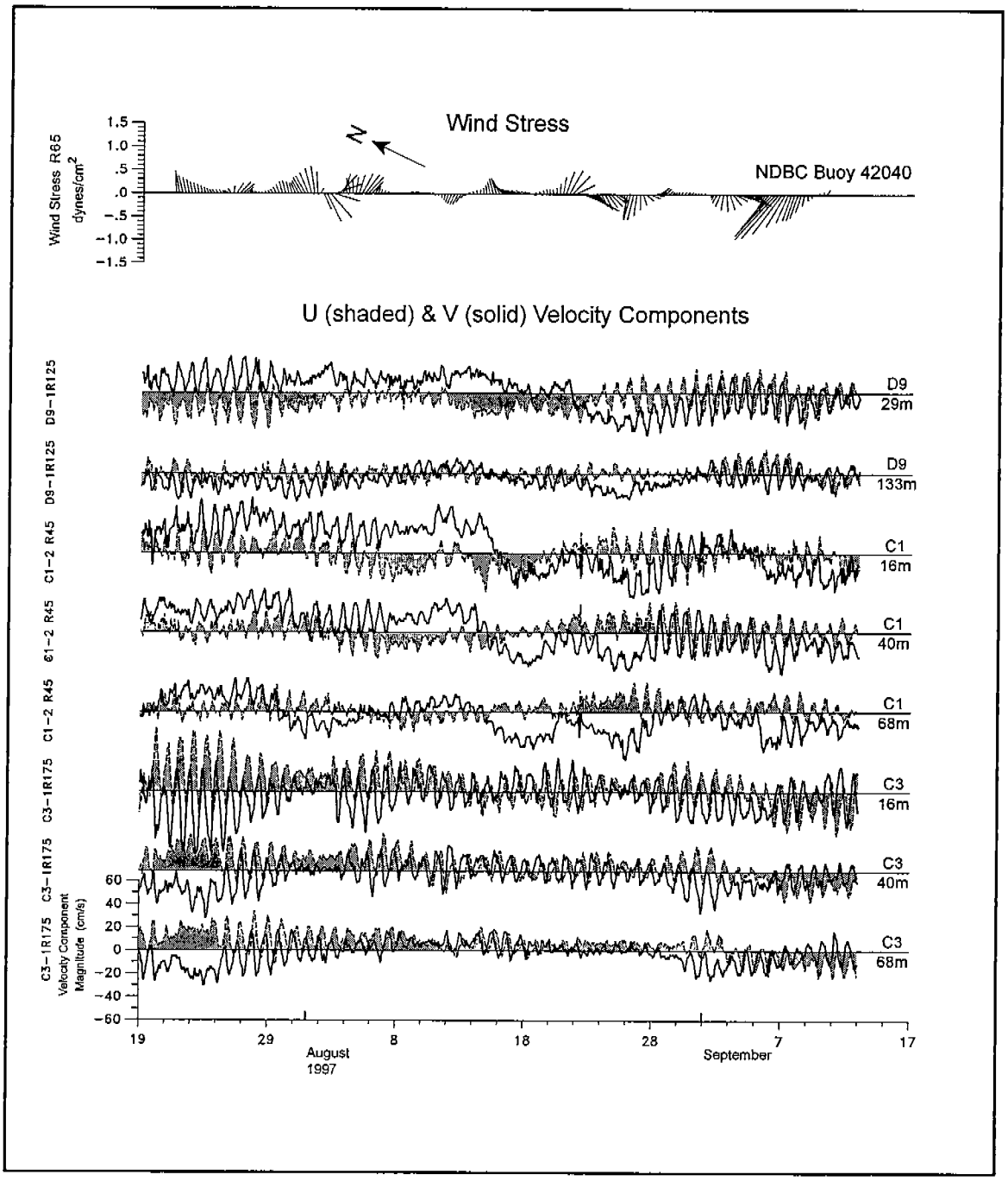

Figure 6.5-1. 3-HLP time series of the cross-isobath (U) component (dashed and shaded) and along-isobath (V) component (solid line) at selected depths on the indicated moorings during a two-month period in summer 1997. The top panel shows the 40-HLP wind stress vectors from buoy 42040. Current components are oriented so positive V has an easterly component and positive U is offshsore.

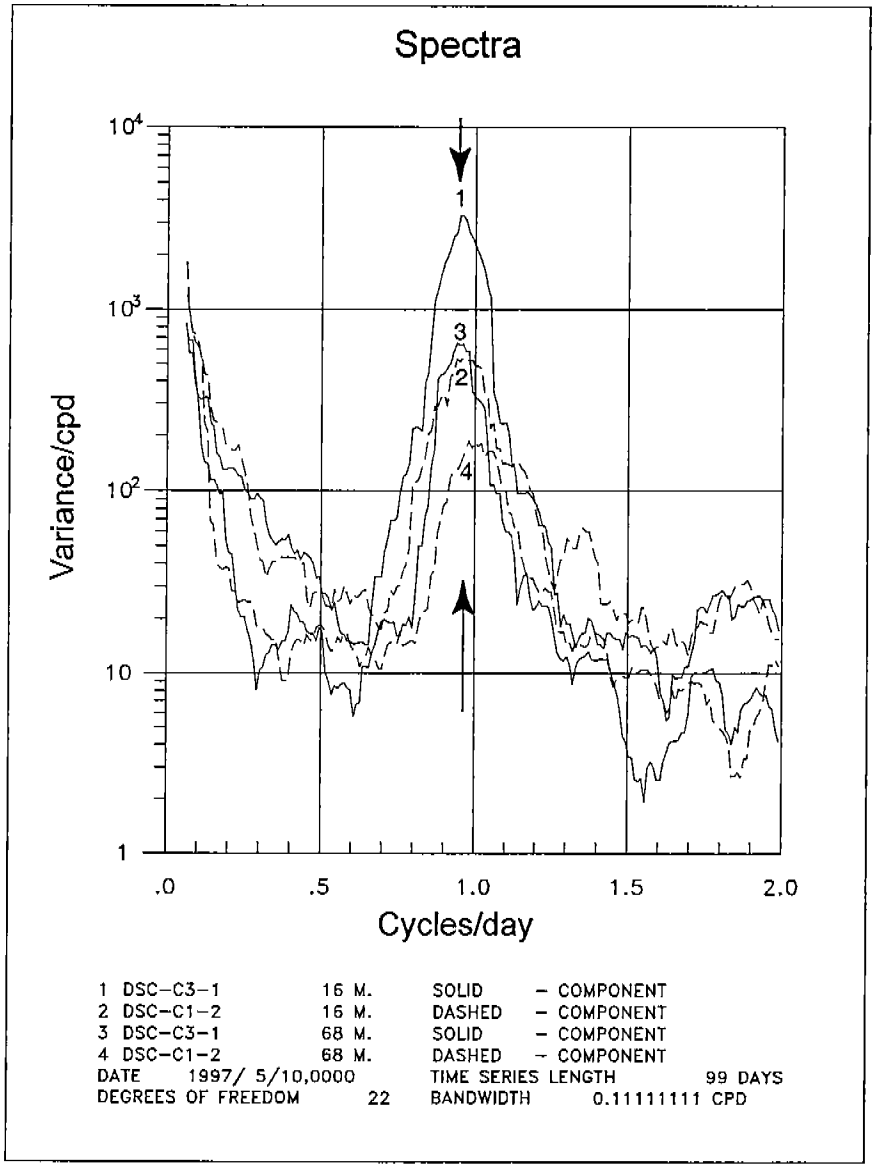

Figure 6.5-2. Clockwise (anticyclonic) rotary spectra for two depths on moorings C1 (dashed) and C3 (solid) for summer 1997. The frequency axis is linear to emphasize the inertial peak at approximately 1 cpd (see arrows).

intermittency of the inertial oscillations with the offshore being more energetic than the shelf break. The shelf break spectra maxima also occur at slightly higher frequencies than at the offshore mooring because of its more northerly position and thus larger value of f.

In contrast to the summer, the winter period had much less energetic inertial motions at the shelf break than the summer despite the more frequent passage of storms. The upper-layer subtidal currents during the winters of 1998 and 1999 were highly correlated with the local wind stress (see Section 6.2.3). Figure 6.5-3 shows the velocity components (U,V) for C1, D9 and C3 for a two-month period in the winter of 1999. Inertial oscillations were almost none existent at the three levels of C1, and intermittently present with small amplitudes at D9 and C3. The main reason for this is reduced stratification in the upper 100m, particularly at the shelf break. Inertial currents are not supported on the shelf if the water column is homogeneous (Kundu 1984). Figure 6.5-4 shows the inertial current amplitudes obtained by complex demodulation (see Section 6.4.4) at 30m depth at C1 and C3 for the two-year study period. The C3 record was almost always more energetic than C1 and the amplitudes have less seasonal variation. The exceptional peaks at the beginning and end of September 1998 were caused by Hurricanes Earl and Georges. The stratification at C1 is represented by the 16 and 80m temperature records. The temperature difference became very small at the beginning of January 1999 and there was correspondingly little inertial activity at C1 despite the rapid fluctuations of wind speed (Figure 6.5-4). In the previous winter, the vertical temperature differences were not quite so small, even though there were more high wind events. Therefore, the inertial amplitudes at C1 were not as well damped.

An EOF analysis was performed using the clockwise rotary spectra calculated for the summer 1997 interval (Figure 6.5-2). Five depths were used from the 13 ADCP's (16, 32, 44, 56 and 68m, except for D9 for which 29, 63, 89, 107 and 159m were used). The frequency band analyzed was 0.8 to 1.2 cpd. The first mode accounts for 32.5% of the total variance in the spectra and represents the large scale coherent inertial signal over the upper 100m of the study area. Phases and amplitudes consistently increase and decrease, respectively, with depth. The upward propagation of phase (positive phase angles lead) is consistent with surface generation and downward propagation of energy. Table 6.5-1 shows the mode 1 phase differences between the lowest and highest levels at each station. The least square estimated vertical wave lengths range from about 90 to 190m, and increase with the depth of water. The shelf break moorings show approximately 180° top-to-bottom phase differences as expected because of the shelf continuity constraint (Kundu 1984).

The horizontal distribution of amplitudes and phases for mode 1 are shown in Figure 6.5-5 for the depth of 30m. The other depths have similar patterns. The highest and lowest amplitudes are found on the offshore edge of the array and the eastern side of the canyon rim (D1 and E1), respectively. The phase distribution shows offshore propagation from the shelf break except around B3 which seems to be a focal point for propagating inertial waves. The trapping of energy in this area is also suggested by the high amplitudes found there.

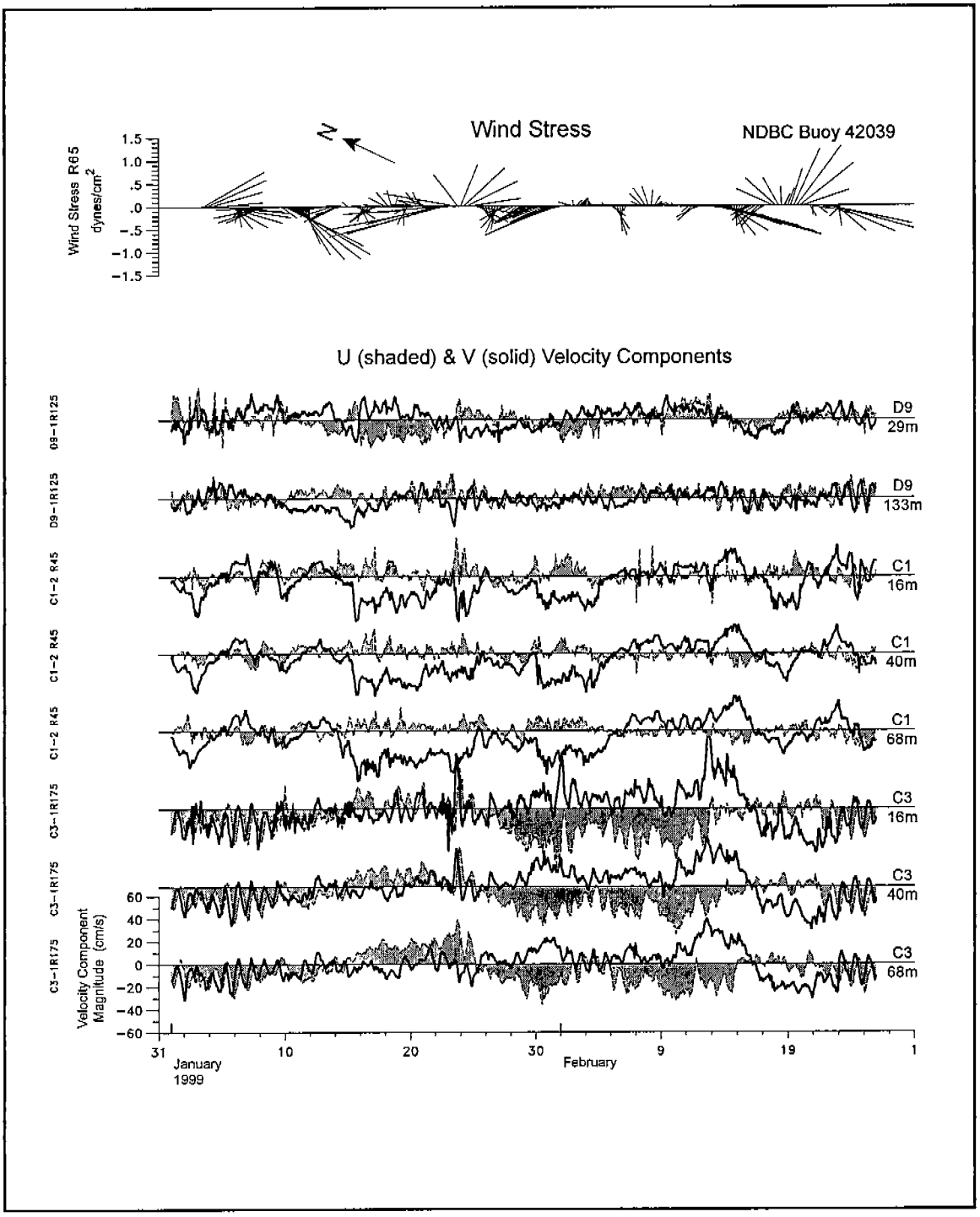

Figure 6.5-3. 3-HLP time series of cross-isobath (U) component (dashed and shaded) and along-isobath (V) component (solid line) at selected depths on the indicated moorings during a two-month period in winter 1999. The top panel shows the 40-HLP wind stress vectors from buoy 42039.

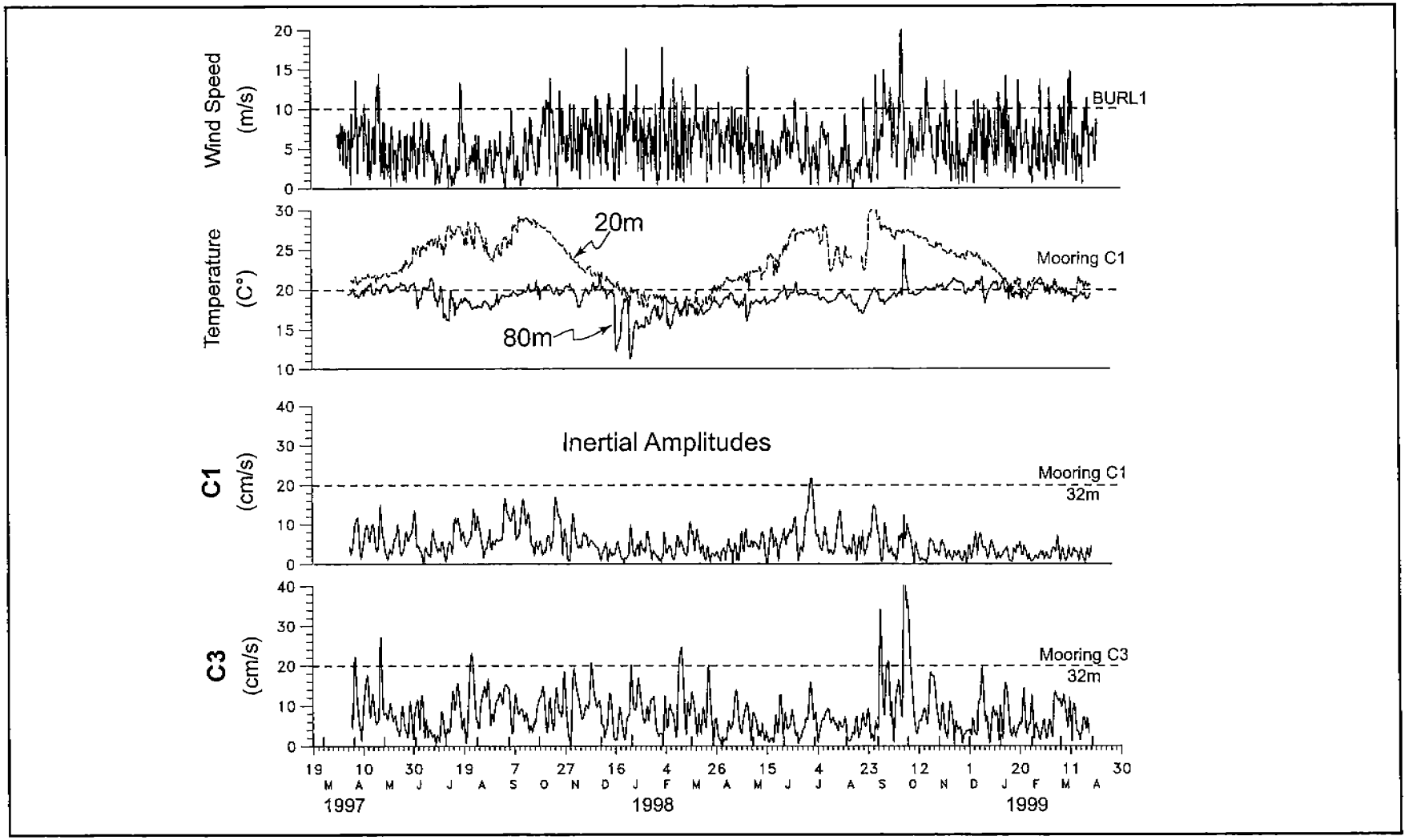

Figure 6.5-4. Bottom two panels show the inertial amplitude at the 32-m depth of the C1 and C3 moorings. The third panel shows the 40-HLP temperature records from the 20-m (dashed) and 80-m (solid) depths at C1, and the fourth panel shows the 40-HLP wind speed at the BURL1 CMAN meteorological station.

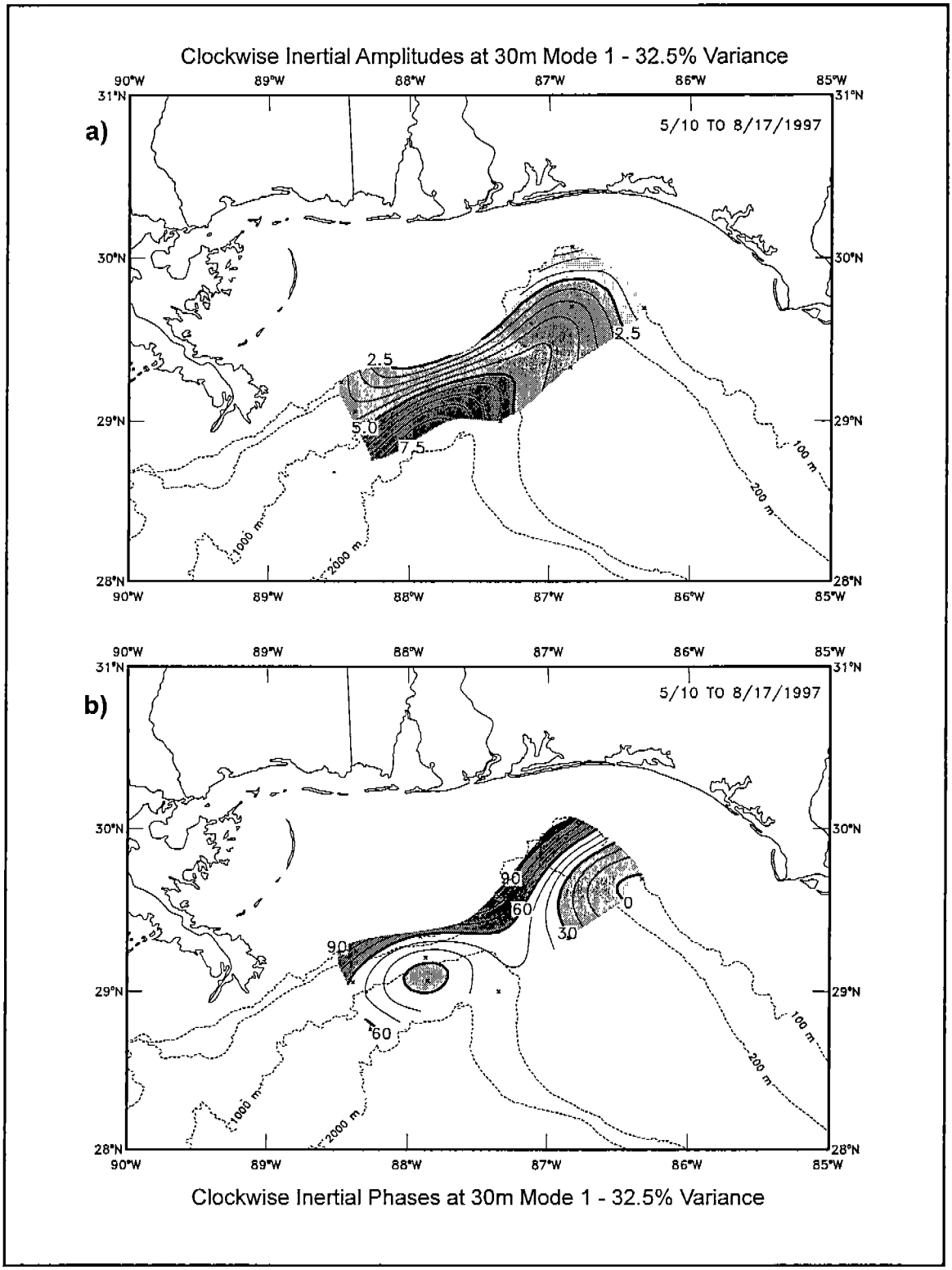

Figure 6.5-5. Mode 1 EOF amplitudes in cm/s (a) and phases in degrees (b) calculated from the inertial band of upper-layer clockwise spectra for the summer of 1997. Sub-sets for the 30-m depth level are contoured.

The mean flows for the upper-layer in the summer of 1997 are given in Figure 5.4-6. An instantaneous geostrophic current map for early July is given in Figure 5.4-1b. They indicate that the offshore region is between the northern edge of a cyclone and the eastward flowing upper-slope jet. This should generate a region of negative relative vorticity that may be trapping the offshore propagating inertial energy (Kunze 1986). Thus, eddy and jet flows may in some circumstances enhance inertial oscillations over the slope over those at the shelf break. Figure 6.5-4 seems to indicate that such offshore enhancement is the rule. An estimate of the horizontal wavelength from a least square fit of the 30 and 65m level phases gives 580 ±100 km directed along 155°±20°(T). Since the horizontal group velocity is proportional to the wave number, the large estimated horizontal wavelength implies the energy was primarily propagating in the vertical direction.
This preliminary investigation into non-hurricane inertial oscillations has shown that they dominated the high-frequency spectrum and were present in offshore waters throughout the year. Their spatial structure was complex because of the characteristic intermittency and the velocity and vorticity structure of the upper-layer flows on the slope. This is in contrast to the Texas-Louisiana slope where Chen et al. (1996) found that the inertial energy decayed rapidly seaward of the shelf-break.

Table 6.5-1 EOF Mode 1 inertial oscillation analysis vertical wavelength estimates from Mode 1 phase differences

Station	Water Depth (m)	Bottom-Top Level Phase Differences	Wavelength (m)
A1	100	190	105
A2	500	140	131
A3	1300	132	148
B1	100	174	110
B2	500	149	127
B3	1300	122	144
C1	100	124	146
C2	500	123	159
C3	1300	121	157
D1	100	230	86
D9	200	251	192
D2	500	153	120
E1	100	172	115
All	-	-	153

VII. CONCEPTUAL MODELS OF CIRCULATION PATTERNS

7.1 Introduction

The material presented in this chapter is a first effort to develop an integration of some of the observations made and used in this project. It is the beginnings of a conceptual model that will describe many of the various circulation patterns in an idealized/conceptualized model. The study region has many complex oceanographic processes of varying time and spatial scales; this is but a first attempt at a descriptive characterization.

7.2 Modes of LC and LC Rings

The discussion in Chapter 5 of Loop Current Frontal Eddies (LCFE), in conjunction with Table 5.3-1 that summarizes LCFE physical characteristics, reveals certain consistent and repeatable patterns in the evolution of observable features in the SST and SSH fields, and the responses in the flow and temperature measurements of the moored array that suggest distinct modes of interaction. The physical processes controlling these modes of interaction will be discussed with the aid of conceptual models.

- **Mode 1. Direct Interaction from LC or LC Ring**

Mode 1a. Mode 1a (Figure 7.2-1a) represents direct interaction of the northern edge of either the LC when it is near its maximum penetration into the eastern Gulf, or, a warm ring that is directly to the south of the array. In either case, the strong eastward flow near the northern boundary of the LC/ring will cause strong eastward flow and negative offshore temperature gradients in the array from near surface to at least 500m. A schematic model of this process is shown in Figure 7.2-1a. A good example of the current response to a warm intrusion of this type occurred for most of Period 7 (See Chapter 5) from early November 1998 to early January 1999 as shown by the strong, persistent eastward alongslope flow at all sites throughout the period (Figures 5.2-1b and -2d).

Mode 1b. Mode 1b is a form of remote ring interaction with the steep slope. SST imagery together with moored current vectors indicate that when a remnant warm LC ring interacts with the slope west of the Mississippi River delta, a warm eastward jet can develop over the slope and extend into the array region. A schematic representation of this process is shown in Figure 7.2-1b. The impingement onto the slope of strong eastward flow within the ring will set-up a negative alongslope pressure gradient that would be trapped over the slope by the steep topography and thus drive a warm eastward jet along the slope. A clear example of this mode of interaction occurred during November 1997 through January 1998 (Figure 5.2-6) and resulted in strong eastward flow over the upper 500m that continued for about 3 months at most sites in the array (Figures 5.2-1b and -2b).

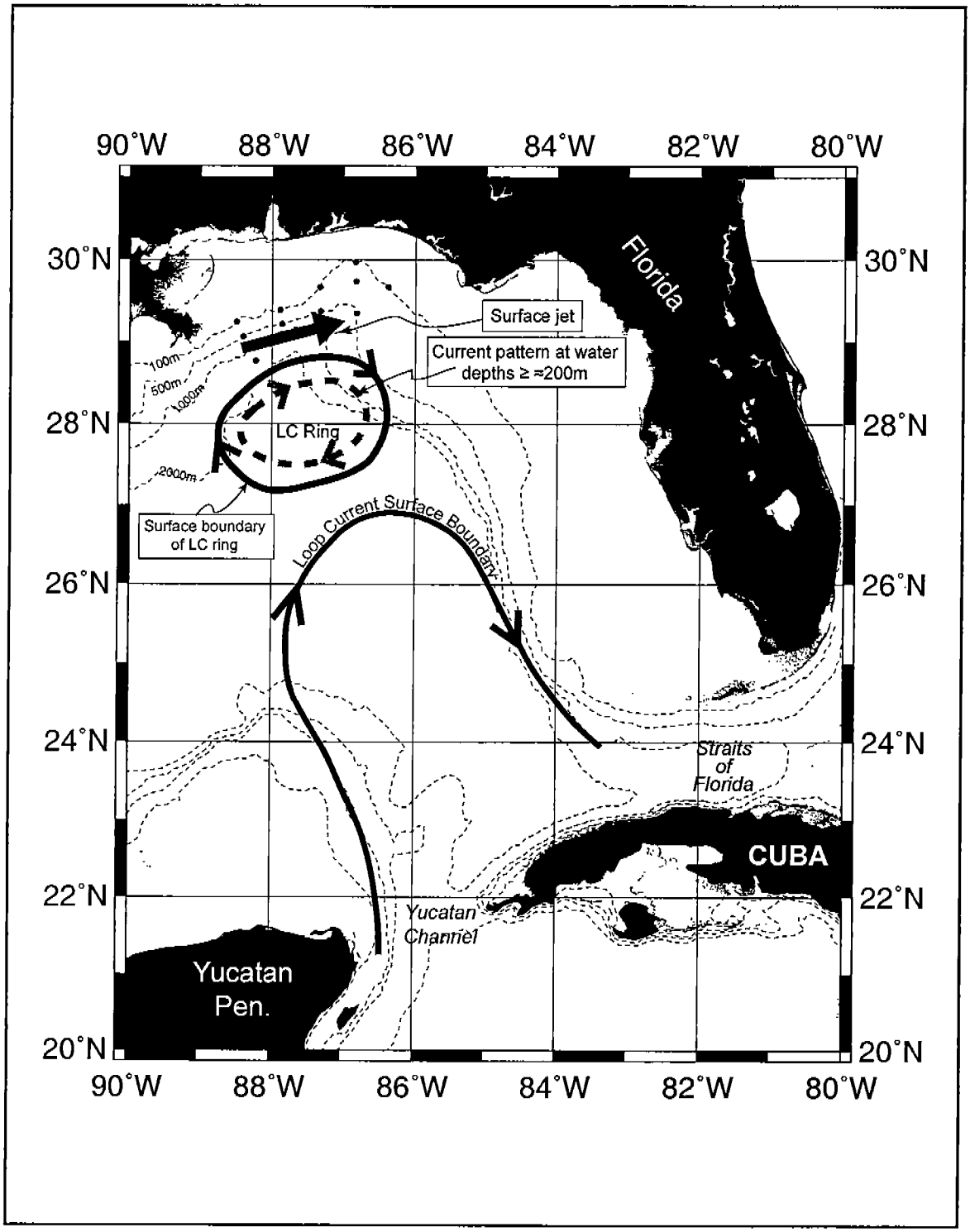

Figure 7.2-1a. Conceptual model of direct LC or LC ring flow interaction with the slope in the study region. The black solid line defines the boundary of the LC and a LC ring. The dashed line within the LC ring illustrates the pattern of currents below 200 m in the water column. The solid arrow through the mooring array illustrates the direction of flow at water depths of less than 100 m in the array.

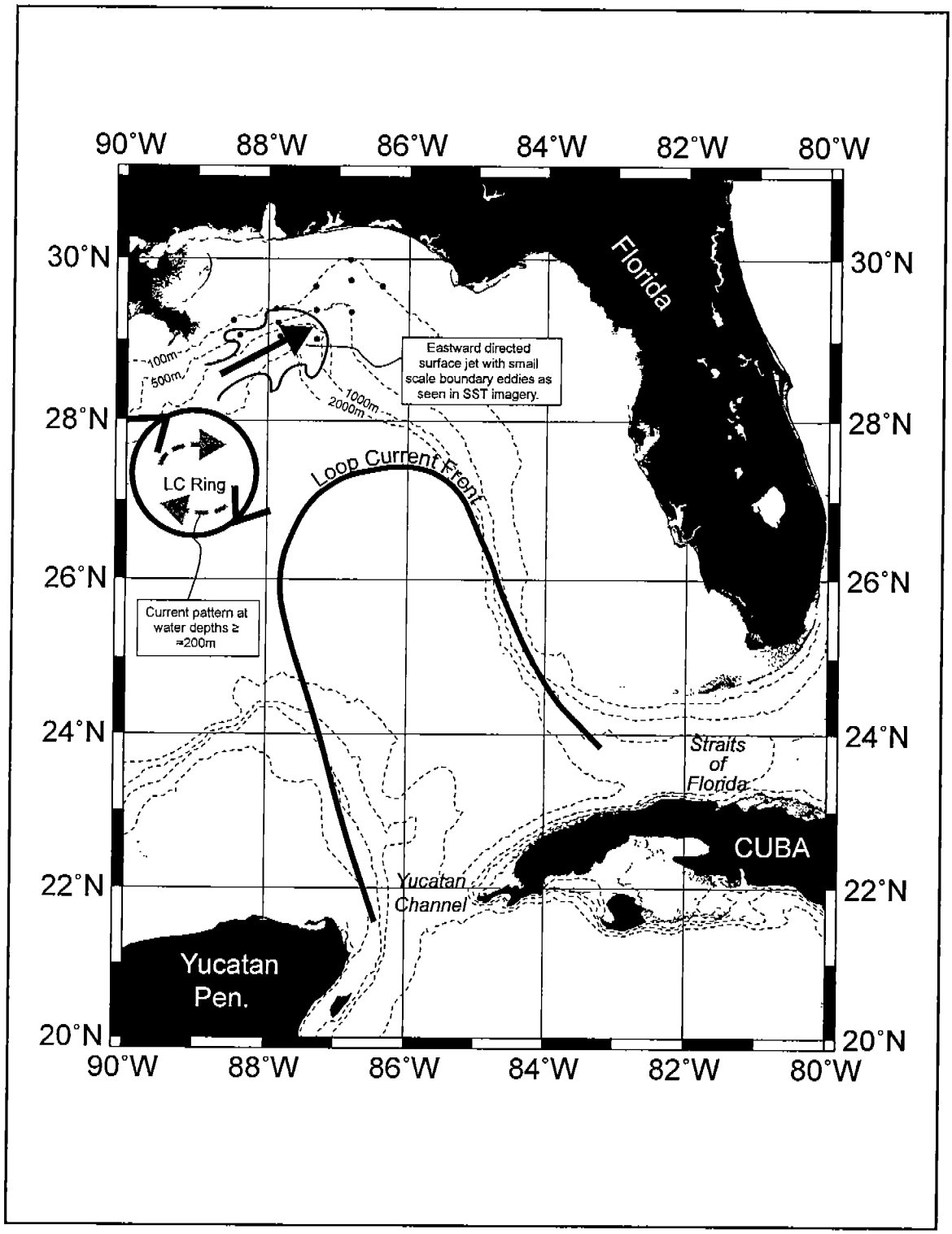

Figure 7.2-1b. Conceptual model of interaction of a LC ring located south and west of the Miss. Delta with the continental slope. Interaction creates eastward directed surface jet with small-scale eddies on either side.

- **Mode 2. LC Frontal Eddy Interactions**

Mode 2a. One of the more common events causing strong flow and temperature variability within the moored array comes from the interaction of LCFE's with the slope. Mode 2a represents the interaction that occurs from LCFE's moving around the northern boundary of a mature LC. This process is shown schematically in Figure 7.2-2a. LCFE's can have horizontal scales of several hundred km's and extend to depths of 600 to 800m. The cyclonic circulation in these features entrains warm LC water around their cold cores in the upper 100m. As the eddies move to the east around the LC and south of the array, they leave a long trailing warm streamer of upper level LC water that extends into the moored array. Isobaths curvature in the array shifts from a east-west orientation in the western part to more SE-NW alignment in the eastern part of the array. Thus, the northwest extension of a warm streamer will cross isobaths into shallower water. As a result the warm upper layer will shrink and vorticity constraints will cause an anticyclonic rotation. The streamer continues to pump warm water into the array region as the LCFE moves to the southeastcausing the eventual spin-up of a warm anticyclonic eddy over the array. This produces an eastward flow with a negative cross-slope temperature gradient in the upper 100m of the array. Below that depth, the cyclonic circulation in the LCFE causes strong, persistent westward flow. LCFE's 1, 2, 4, 5, 11 and 12 (Table 5.3-1) all produced this type of current and temperature response during their passage south of the array. Examples in SST imagery are given in Figures 5.2-3a, -10, -15, and -16. Intrusions of these warm streamers can sometimes result in strong up-canyon flows in the DeSoto Canyon (Figure 5.2-10a). Offshore flows can result from the convergence of the trailing wake of a LCFE with an approaching ring or LC crest (Figure 5.2-10a). Both processes can result in significant cross-slope exchange.

Mode 2b. Mode 2b is essentially the same as Mode 2a except the LCFE is located on the boundary of a LC ring south of the array instead of the LC itself (Figure 7.2-2b). LCFE 9 appears to have this mode of interaction.

Mode 2c. Mode 2c occurs when a LCFE is located close to the array and is directly interacting with the slope (Figure 7.2-2c). The warm streamer is more parallel to the slope bathymetry and is advected to the west around the cold core of the eddy. As a result the flow is westward throughout the array both above and below 100m. LCFE's 3 and 8 were of this type (Figure 5.2-9).

Mode 2d. Mode 2d represents the type of flow interaction that can occur from a LCFE on the eastern boundary of a warm ring, where its southward movement is blocked by a growing LC (Figure 7.2-2d). The LCFE produces westward flow in the deeper waters below 200m and eastward flow results in the upper 100m from the anticyclonic eddy that spins-up over the array from the warm streamer. Blockage of the movement of the LCFE can result in a near stationary eddy and prolonged influence on the flows in

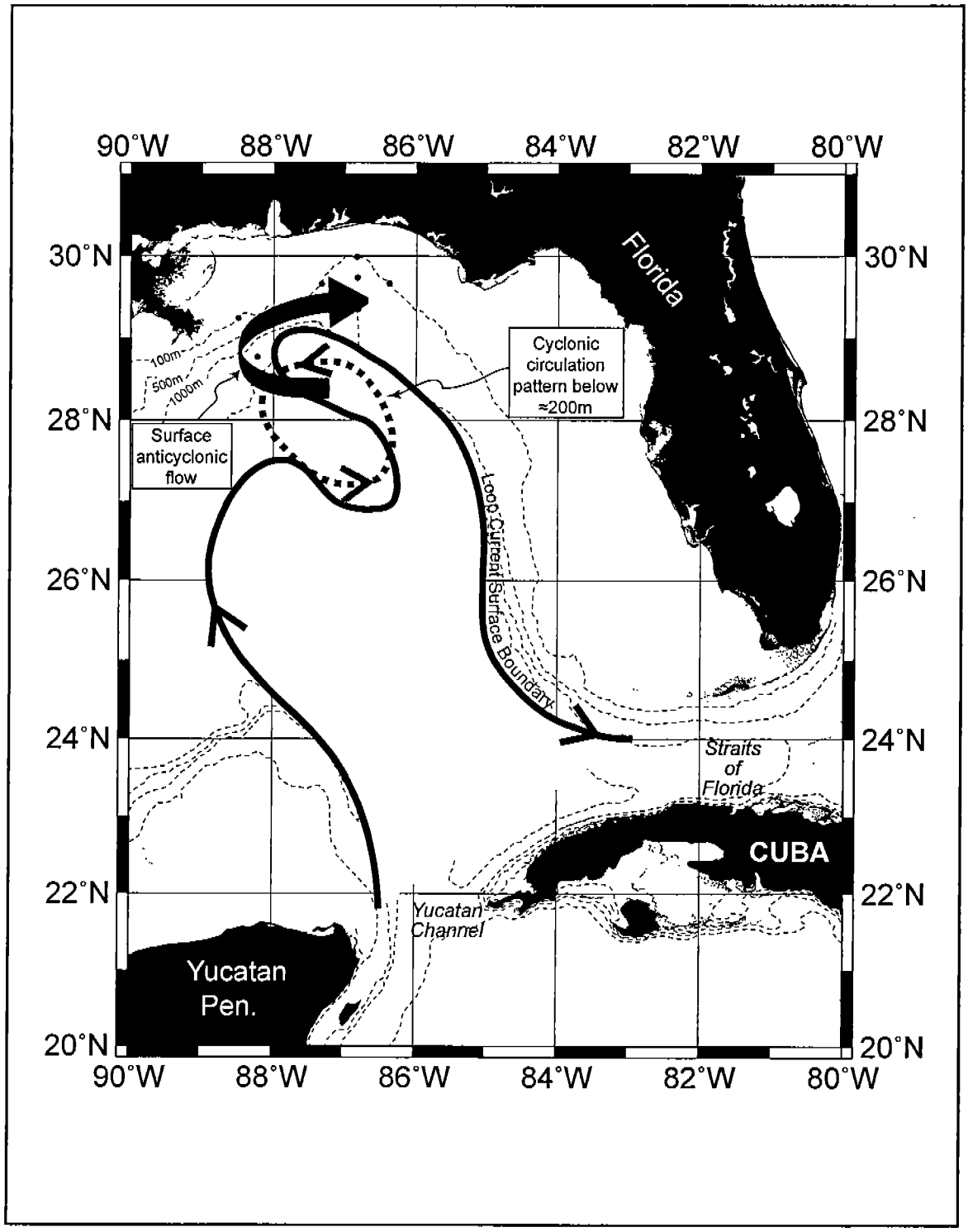

Figure 7.2-2a. Conceptual model of a LCFE flow interaction with the slope in the study region.

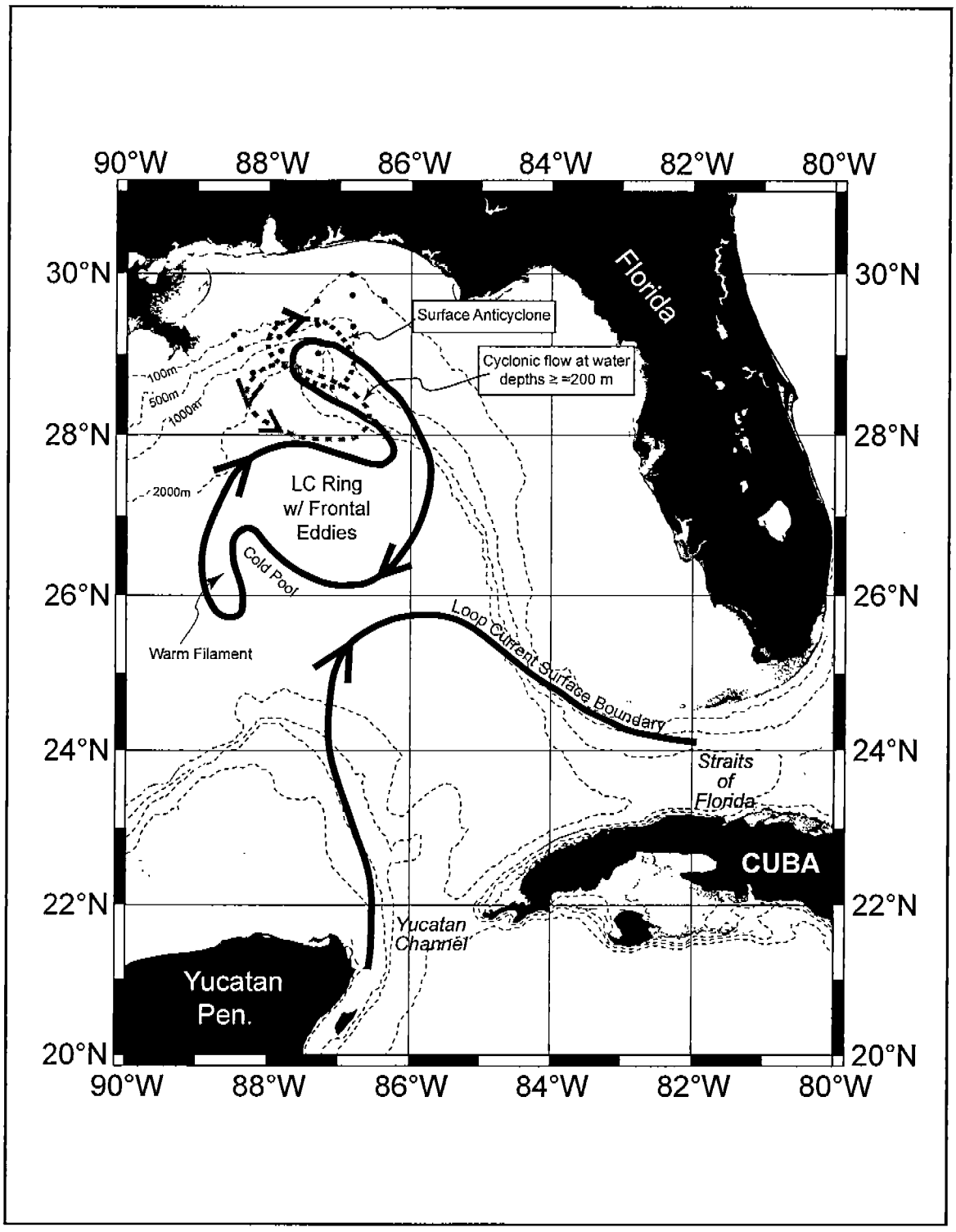

Figure 7.2-2b. Conceptual model of flow interaction with the slope in the study region from a LCFE on the boundary of a warm LC ring.

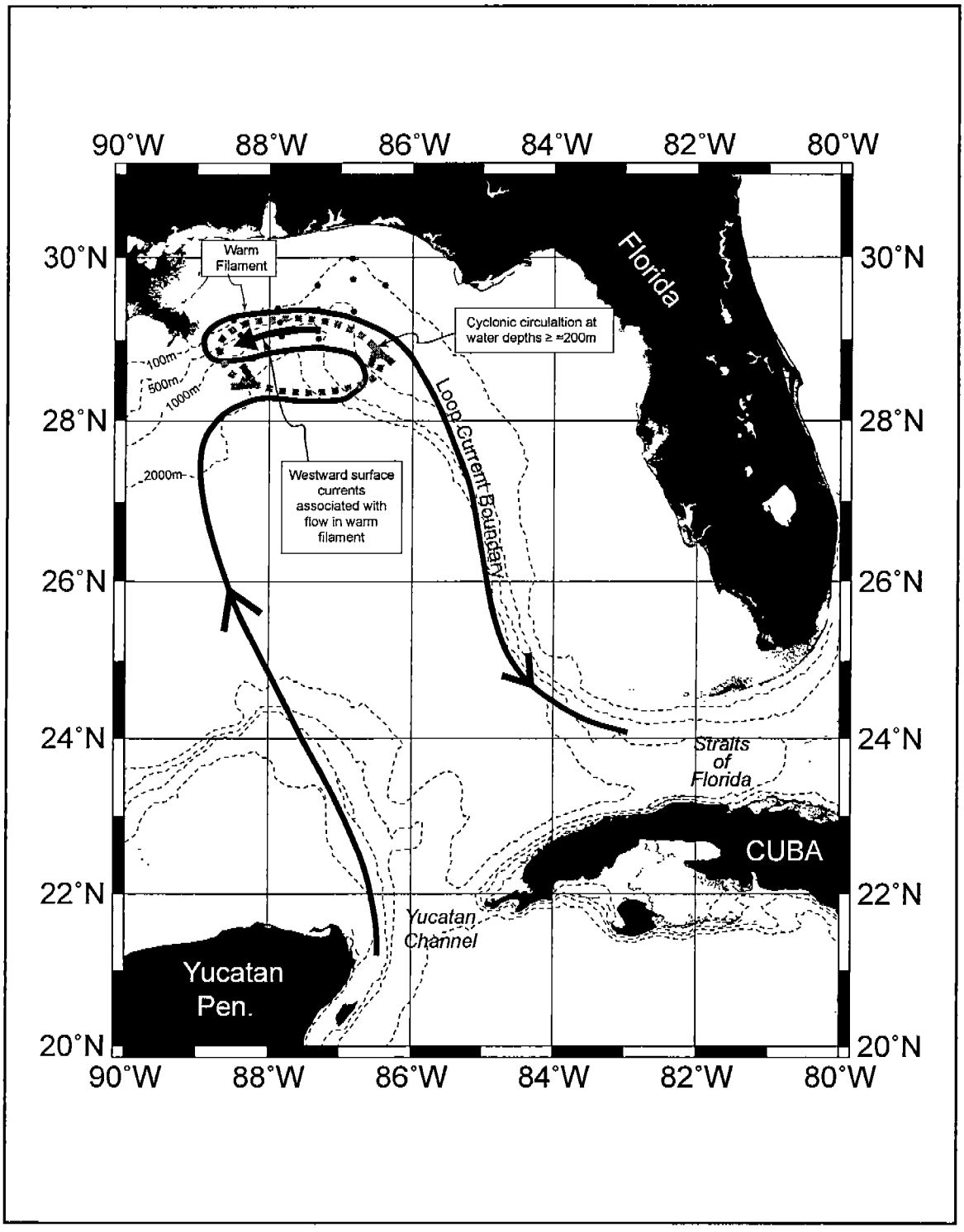

Figure 7.2-2c. Conceptual model of flow interaction with the slope from a LCFE close to the study region.

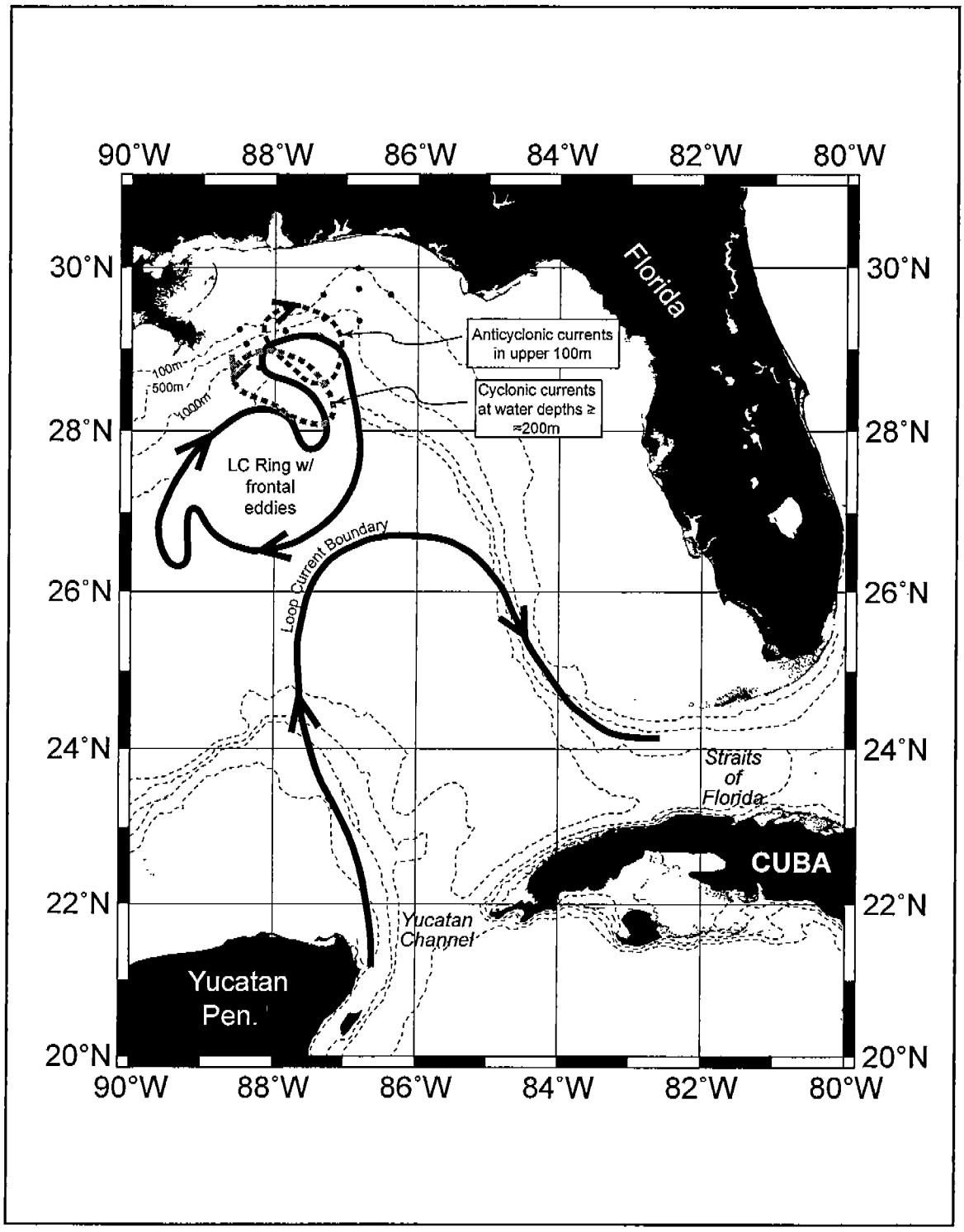

Figure 7.2-2d. Conceptualization of flow interaction with the slope from a LCFE on the boundary of a warm LC ring located south of the Mississippi Delta and blocking the LC.

the study region. LCFE's 3 and 10 had this mode of interaction (Figures 5.2-7, -9 and -10).

7.3 Regional Scale Patterns

The previous sections have discussed how LCFE's affect circulation on the lower slope, and contribute to the generation of anticyclones. The presence of eddies on the lower slope generates circulation patterns on the upper slope that can persist for periods of order weeks to months.

The most characteristic flow pattern is a two-layer jet with eastward flow at the surface and a return flow at depth. The transition between the upper and lower flows varies with the offshore forcing but is typically between 200 and 300m. The upper-layer jet along the Alabama slope can take various paths through the DeSoto Canyon, including bypassing the head of the Canyon or at the Florida slope. In the former case, the head of the canyon is often occupied by one or more eddies that can be cyclonic or anticyclonic. These jet-like flows are efficient at transporting Mississippi River water discharged near the delta out over the slope, and on occasion, injecting it onto the west Florida shelf.

The westward counter flow at depth is more complex and may have several causes including being an entrainment flow into a deep offshore cyclonic eddy, and the blockage of offshore eastward or northward flows by the west Florida escarpment that seems to turn these flows cyclonically into a westward current along the slope. This type of cyclonic turning at depth is often accompanied by a surface-layer cyclonic eddy in the head of the canyon. A sketch of this flow pattern is given in Figure 7.3-1. If a cyclonic frontal eddy associated with an extended LC or a recently detached LC ring moves onto the slope then the predominant eastward flows at the surface are replaced by westward flows of the cyclone.

Superimposed on these relatively steady flow patterns are fluctuating eddy-like currents that can alternately reinforce and oppose these circulations. The energetic parts of the spectrum can vary with position and season and the relatively poor coherence between adjacent moorings indicates that a good portion of these type motions are transitory and not well resolved even with the close spacing of the array. At long periods of ~100 days, there is evidence of the coherent propagating signal. This may indicate that the slope is acting as a topographic wave-guide allowing large-scale long-period disturbances, that may be initiated in the northeast Gulf, to propagate onto the Western Gulf slope.

Because the LC eddy shedding cycle is variable and does not have an annual component, the eddy field over the slope does not have a specific seasonal component. However, there is a difference in the circulation characteristics between summer and winter caused by wind-forcing. In winter (~December through March), there are frequent synoptic weather systems passing over the northeast Gulf. These systems produce energetic along-isobath, upper-layer flows that follow the canyon rim

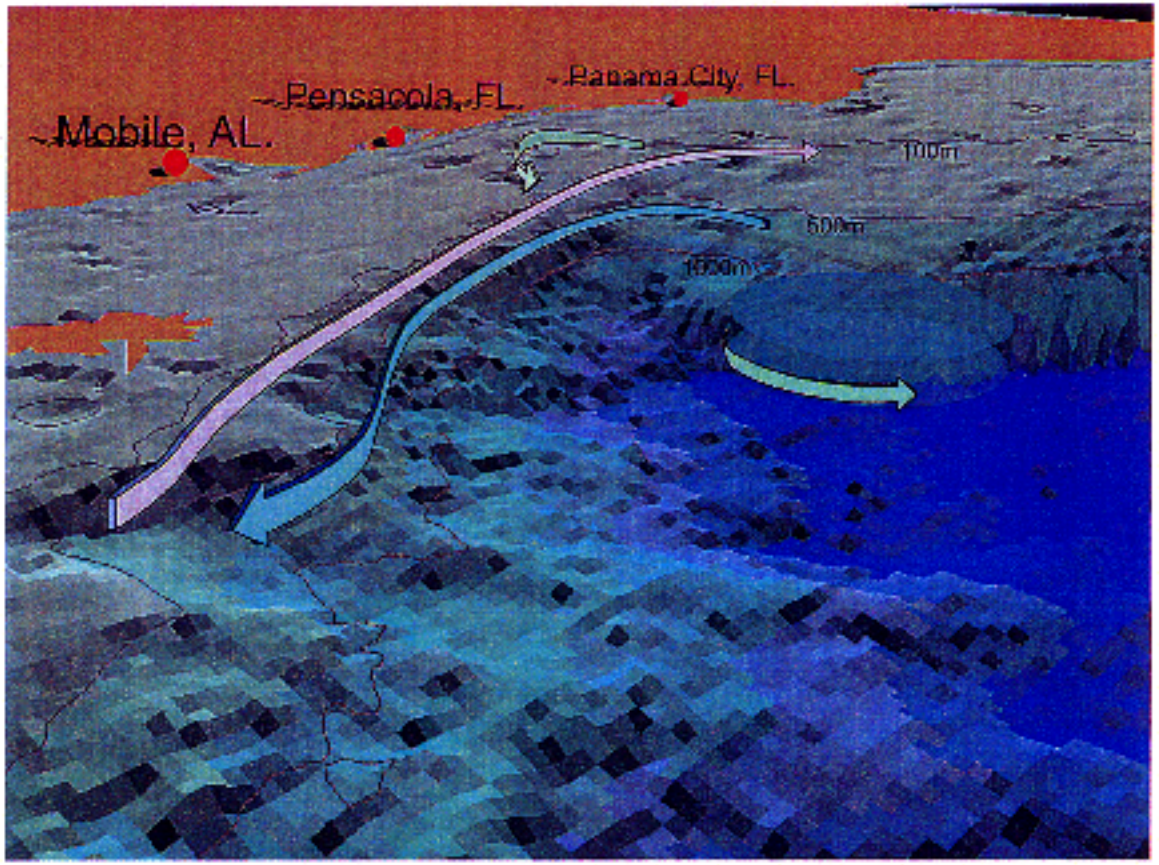

Figure 7.3-1 Conceptual schematic of the multilayered flow conditions in the DeSoto Canyon Study area.

with periodicities from ~3 to 15 days. These flows are largely absent in the summer. The wind component that is most effective in generating this slope response is directed parallel to the west Florida slope. The maximum current fluctuations are found over the Alabama slope with a lag of order one-day. The response is qualitatively that of an arrested topographic wave with that maximum response downstream (in a continental shelf-wave sense) of the maximum along isobath wind-stress. This is attributed to the relatively narrow shelf such that the cross-shelf length scale for continental shelf-waves extends over the slope. This is in contrast to the wide Texas-Louisiana shelf and slope where shelf-edge currents have little correlation with winter-storm winds (Nowlin et al. 1998).

Finally, the high frequency currents are dominated by inertial oscillations, with periods of ~1 day, that are present in deep water throughout the year. At the shelf break, inertial oscillations are present in the summer but not in the winter because of the lack of stratification in the latter. There is some evidence that inertial-internal wave energy is being trapped by the eddy-jet current systems of the slope. Hurricanes passing over the slope in summer produce a strong inertial response, which can persist for many days.

VIII. REFERENCES

Basic, T. and R. H. Rapp. 1992. Oceanwide prediction of gravity anomalies and sea surface heights using Geos-3, Seasat and Geosat altimeter data, and ETOPO5U bathymetric data, *Report 416*, Dept. of Geod. Sci., Ohio State Univ., Columbus.

Beardsley, R.C. and B. Butman, 1974. Circulation on the New England continental shelf: response to strong winter storms. *Geophys. Res. Lett.*, **1**, 181-184.

Bendat, J. S., and A. G. Peirsol, 1971. *Random Data: Analysis, Measurement and Procedures.* Wiley-Interscience, New York, 407 pp.

Berger, T., 1993. LATEX Program Newsletter, **2**, 25; College of Geosciences, Texas A. & M. Univ., College Station TX.

Berger, T., P. Hamilton, J.J. Singer, R.R. Leben, G.H. Born, and C.A. Fox, 1996. *Louisiana/Texas Shelf Physical Oceanography Program: Eddy Circulation Study, Final Synthesis Report. Vol. I: Technical Rpt.* OCS Study MMS 96-0051. U.S. Dept. of the Interior, MMS, Gulf of Mexico OCS Region, New Orleans, La. 324 pp.

Biggs, D., G. Fargion, P. Hamilton and R. Leben, 1996. Cleavage of a Gulf of Mexico Loop Current eddy by a deep water cyclone, *J. Geophys. Res.*, **101**, 20,629-20,642.

Bray, N.A. and N.P. Fofonoff, 1981. Available potential energy for MODE Eddies. *J. Phys. Oceanogr.*, **11**, 30-47.

Brooks, D. A., 1983. The wake of Hurricane Allen in the western Gulf of Mexico. *Deep-Sea Res.*, **13**, 117-129.

Callahan, P. S., 1993. TOPEX/POSEIDON NASA GDR Users Handbook JPL Publ. D-8590, rev. C, Jet. Propul. Lab., Pasadena, CA. 67pp.

Chen, C., R. O. Reid, and W. D. Nowlin, 1996. Near-inertial oscillations over the Texas-Louisiana shelf. *J. Geophys. Res.*, **101**, 3509-3524.

Chereskin, T. K. ; M.Y. Morris, P.P. Niiler, P.M. Kosro, R.L. Smith, S.R. Ramp, C.A. Collins, and D.L. Musgrave, 2000. Spatial and temporal characteristics of the mesoscale circulation of the California Current for eddy-resolving moored and shipboard measurements. *J. Geophys. Res.* **105(C1)**, p. 1245

Clark, A. J. and K. H. Brink, 1985. The response of stratified, frictional flow of shelf and slope waters to fluctuating large-scale, low-frequency wind forcing. *J. Phys. Oceanogr.*, **15**: 439-453.

Cochrane, J. D., 1972. Separation of an anticyclone and subsequent developments in the Loop Current (1969), in *Contributions on the Physical Oceanography of the Gulf of Mexico*, edited by L. R. A. Capuro and J. L. Reid, pp. 91-106, Gulf, Houston, Tex.

Cressman, G. P., 1959. An operational objective analysis system. *Mon. Weather Rev.*, **87**, 367-374.

Crosby, D. S., L.C. Breaker, W. H. Gemmil. 1993. A proposed definition of vector correlation in geophysics - theory and application, *J. Atmos. Oceanic. Tech.* **10**, 355-367.

Csanady, G. T., 1978. The arrested topographic wave. *J. Phys. Oceanogr.*, **8**, 47-62.

Davis, R. E. 1985. Drifter observations of coastal surface currents during CODE: The method and descriptive view, *J. Geophys. Res.*, **90**, 4741-4755.

Desai, S. D., and J. M. Wahr, 1995. Empirical Ocean tide models estimated from TOPEX/POSEIDON altimetry. *J. Geophys. Res.*, **100**, 25,205-25,228.

Drennan, K. L., 1968. Hydrographic studies in the northeast Gulf of Mexico. Report No., 68-0-1, Environmental Sciences and Engineering Laboratories, Gulf South Research Institute, New Iberia, Louisiana, 111 pp.

Elliott, B. A., 1982. Anticyclonic rings in the Gulf of Mexico. *J. Phys. Oceanogr.*, **12**, 1292-1309.

Foreman,M.G.G., 1979. Manual for tidal currents analysis and prediction. *Pacific Marine Science Report 78-6*. Institute of Ocean Studies, Partician Bay, Sydney, British Columbia. 70pp.

Fratantoni, P.S., T.N. Lee, G.P. Podesta and F. Müller-Karger, 1998. The influence of Loop Current perturbations on the formation and evolution of Tortugas eddies in the southern Straits of Florida. *J. Geophys. Res.*, **103(C11),** 24759-24799.

Gonella, J., 1971 A local study of inertial oscillations in the upper layers of the ocean. Deep-Sea Res., 18, 775-788.

Hamilton, P., 1990. Deep Current in the Gulf of Mexico, *J. Phys. Oceangr.*, 20, 1087-1104.

Hamilton, P., 1992. Lower continental slope cyclonic eddies in the central Gulf of Mexico. *J. of Geophys. Res.*, **97(C2),** 2185-2200.

Hamilton, P., T.J. Berger and W. Johnson, 2000. On the structure and motions of cyclones in the northern Gulf of Mexico. *J. of Geophys., Res., submitted.*

Hamilton, P. 1984. Topographic and inertial waves on the continental rise of the Mid-Atlantic Bigh. *J. Geophys. Res.*, **89**: 695-710

Hanawa, K., P. Rual, R. Bailey, A. Sy, M. Sxabados, 1995. A new depth-time evuation for Sippican or TSK T-7, T-6 and T-4 expendable bathythermographs (XBT). *Deep-Sea Research*, Vol. 42 No. 8, pp 1423-1451.

Hendricks, J.R., R. R. Leben, G. H. Born and C. J. Koblinsky, 1996. Empirical orthogonal function analysis of global TOPEX/POSEIDON altimeter data and implications for detection of global sea level rise. *J. Geophys. Res.*, **101**, 14,131-14,143.

Hogg, N.G., 1981. Topographic waves along 70°W on the continental rise, *J. Mar. Res.*, **39**, 627-649.

Hurlburt, H. E., 1986. Dynamic transfer of simulated altimeter data into subsurfaace information by a numerical ocean model. *J. Geophys. Res.*, **91**, 2372-2400.

Hurlburt, H.E., and J. D. Thompson, 1980. A numerical study of Loop Current intrusions and eddy shedding. *J. Phys. Oceanogr.*, **10(10),** 1611-1651.

Ichiye, T., H. Kuo and M. R. Carnes, 1973. Assessment of currents and hydrography of the eastern Gulf of Mexico, Control 601 Texas A & M University, College Park.

Kundu, P.J., 1976. An analysis of inertial oscillations observed near the Oregon coast, *J. Phys. Oceanogr.*, **6**, 879-893.

Kundu, P.K., 1984 Generation of coastal inertial oscillations by time varying wind, *J. Phys. Oceanogr.*, **14**, 1901-1913

Kunze, E., 1985. Near-inertial wave propagation in geostrophic shear. J. Phys. Oceanogr., **15**, 544-565.

Kunze, E., 1986. The mean and near-inertial velocity fields in a warm-core ring. *J. Phys. Oceanogr.*, **16**, 1444-1461.

Lee, T.N., 1975. Florida Current spin-off eddies. *Deep-sea Res.*, **22**, 753-763.

Lee, T.N., E. Williams, J. Wang and R. Evans, 1989. Response of South Carolina continental shelf waters to wind and Gulf Stream forcing during winter of 1986. *J. Geophys. Res.* **94**, 10715-10754.

Lee, T.N., K. Leaman, E. Williams, T. Berger and L. Atkinson, 1995. Florida Current meanders and gyre formation in the southern Straits of Florida. *J. Geophys. Res.*, **100(C5),** 8607-8620.

Leipper, D.F., 1970. A sequence of current patterns in the Gulf of Mexico. *J. Geophys. Res.*, **75(3),** 637-657.

Lillibridge, J., R. Leben, and F. Vossepoel, 1997. Real-time processing from ERS-2, *Proc. 3rd ERS Symposium*, Florence, Italy, Mar 11-14., 1997.

Maul, G.A. and F. M. Vukovich, 1993. The relationship between variations in the Gulf of Mexico Loop Current and Straits of Florida volume transport, *J. Phys. Oceanogr.*, **23**, 785 - 796.

Maul, G. A., 1977. The annual cycle of the Gulf Loop Current Part I: Observations during a one-year time series. *J. Mar. Res.* **35(1),** 29-47.

Maul, G. A., D. R. Norris and W. R. Johnson, 1974. Satellite photography of eddies in the Gulf Loop Current. *Geophys. Res. Lett.*, **1**, 256-258.

Maul, G.A., F. Williams, M. Roffer and F. M. Sousa, 1984. Remotely sensed oceanographic patterns and variability of bluefin tuna catch in the Gulf of Mexico. *Oceanol. Acta,* **7,** 469-479.

Mayer, D.A., and R. H. Weisberg, 1993. A description of the COADS surface meteorological fields for the Atlantic Ocean. *J. Phys. Oceanogr.*, **23**, 2201-2221.

Merrifield, M.A., and C.D. Winaut, 1989. Shelf circulation in the Gulf of California: A description of the variability. J.Geophys. Res., 94, 18133-18160.

Mitchum, G.T. and W. Sturges, 1982. Wind driven currents on the West Florida Shelf. J. *Phys. Oceanogr.*, **12,** 1310-1317.

Molinari, R. L., 1977. Synoptic and mean monthly 20°C topographies in the eastern Gulf of Mexico, *Tech. Memo. ERL AOML-27*, National Oceanic and Atmos. Admin., Silver Spring, Md. 32 pp.

Mooers, C.N.K., 1975. Several effects of a baroclinic current on the cross-stream propagation of inertial-internal waves. Geophys. Fluid Dgn., 6, 245-275.

Muller-Karger, F.E., J.J. Walsh, R.H. Evans, and M.B. Meyers. 1991. On the Seasonal Phytoplankton Concentration and Sea Surface Temperature Cycles of the Gulf of Mexico as Determined by Satellites. *Journal of Geophysical Research.* **96(C7)**. 12645-12665

Niiler, P., and W. S. Richardson, 1973. Seasonal Variability of the Florida Current. *Jour. Mar. Res.*, **31**(3), 144.

North, G.R., T.L. Bell, R.F. Calahan and F.J. Moeng, 1982. Sampling errors in the estimation of empirical or thogonal functions. Mar. Wealth. Rev. 110, 699-706.

Nowlin, W.D., Jr., and H. J. McLellan, 1967. A characterization of the Gulf of Mexico waters in winter, *J. Mar. Res.*, **25**, 29-59.

Nowlin, W.D., Jr., A.E. Jochens, R.O. Reid, and S.F. DiMarco. 1998. Texas-Louisiana Shelf Circulation and Transport Processes Study: *Synthesis Report, Volume I: Technical Report*. OCS Study MMS 98-0035. U.S. Dept. of the Interior, Minerals Mgmt. Service, Gulf of Mexico OCS Region, New Orleans, LA. 502pp.

Paluszkiewicz, T., L.P. Atkinson, E.S. Posmentier and C.R. McClain, 1983. Observations of a Loop Current frontal eddy intrusion onto the west Florida shelf. *J. Geophys. Res.*, **88,** 9639-9652.

Perkins, H., 1976. Observed effect of an eddy on inertial oscillations, *Deep Sea Res.*, **23**, 1037-1042.

Pichevin, T. and D. Nof, 1997. The momentum imbalance paradox. *Tellus*, **49A**, 298-319.

Pickart, R.S., 1995. Gulf Stream-generated topographic Rossby waves. J.Phys. Oceangr., **24**, 574-586.

Press, W.H., S.A. Tuekolsky, W.T. Vettering, and B.P. Flannery, 1992. *Numerical Recipes in FORTRAN, The Art of Scientific Computing*. Cambridge University Press. 2nd Edition, 963pp.

Reid, R. O., 1972. A simple dynamic model of the Loop Current. *In, Contributions on the physical oceanography of the Gulf of Mexico*, **2**, Capurro and Reid, eds., Texas A & M Ocean. Studies, Houston. 157-159.

Reid, R. O., B. A. Elliott and D.B. Olson, 1981. Available potential energy: a clarification. *J. Phys. Oceanogr.*, **11**, 15-29.

Rhines, P.B., 1970. Edge, bottom and Rossby waves in a rotating stratified fluid, *Geophys. Fluid Dyn.*, **1**, 273-302.

SAIC. 1989. Gulf of Mexico Physical Oceanography Program, *Final Report: Year 5. Volume II: Technical Report*. OCS Report/MMS-89-0068, U.S. Department of the Interior, Minerals Management Service, Gulf of Mexico OCS Regional Office, New Orleans, La. 333 pp.

Sato, O. T., and T. Rossby, 1995. Seasonal and low frequency variations in dynamic height anomaly and transport of the Gulf Stream. *Deep-Sea Res. I*, **42**, 149-164.

Scott, J. T., and G. T. Csanady, 1976. Nearshore currents off Long Island. *J. Geophys. Res.*, **81**, 5401-5409.

Shaw, P.T., and G.T. Csanady, 1988. Topographic waves over the continental slope. *J. Phys. Oceanogr.*, **18**, 813-822.

Silverman, B.W., 1986. *Density Estimation for statistics and data analysis.* Chapman and Hall, London & New York, 175 pp.

Stern, M. E., 1975. *Ocean Circulation Physics.* Academic Press, New York. 246 pp.

Sturges, W. and R. Leben, 2000. Frequency of ring separations from the Loop Current in the Gulf of Mexico: A revised estimate. *J. Phy. Oceangr.*, **30**, 1814-1819.

Sturges, W., 1992. The spectrum of Loop Current variability from gappy data. *J. Phys. Ocean.*, **22**, 1244-1256.

Sturges, W., 1994. The frequency of ring separations from the Loop Current, *J. Phys. Ocean.*, **24**, 1647-1651.

Sturges, W., J.C. Evans, W. Holland, and S. Welsh, 1993. Separation of warm-core rings in the Gulf of Mexico. *J. Phys. Oceanogr.*, **23**, 250-268.

Thompson, R.O.R.Y., 1977. Observations of Rossby waves near site D, *Prog. in Oceangr.*, **7**, 135-162.

Tierney, C. C., M. E. Parke and G. H. Born. 1998. An investigation of ocean tides derived from along-track altimetry, *J. Geophys. Res*, **103**, 10273-10287.

Van Meurs, P. 1995. The importance of spatial variabilities on the decay of near-inertial mixed layer currents: theory, observations and modeling, Ph.D. thesis, University of California, San Diego, 180 pp.

Vukovich, F. M. 1995. An updated evaluation of the Loop Currents eddy-shedding frequency. *J. Geophys. Res*, **100(5),** 8655-8659.

Vukovich, F. M., 1988a. Loop Current boundary variations, *J. Geophys. Res.*, **93**, 15,585-15,591.

Vukovich, F. M., 1988b. On the formation of elongated cold perturbations off the Dry Tortugas. *J. Phys. Oceanogr.*, **18,** 1051-1059.

Vukovich, F. M. and G. A. Maul, 1985. Cyclonic eddies in the eastern Gulf of Mexico. *J. Phys. Oceangr.*, **15**: 105-117.

Vukovich, F. M., B. W. Crissman, M. Bushnell and W. J. King, 1979. Some aspects of the oceanography of the Gulf of Mexico using satellite and *in-situ* data, *J. Geophys. Res.*, **84**, 7749-7768.

Welsh, S.E. and M. Inoue. 2000. Loop Current rings and the deep circulation in the Gulf of Mexico. *J. Geophys. Res.*, (C).

Winant, C. D., 1980. Coastal circulation and wind induced currents, *Ann. Rev. Fluid Mech.*, **12**, 271-301.

Yi, Y., 1995. Determination of Gridded Mean Sea Surface from Altimeter Data of TOPEX, ERS-1, and GEOSAT. Ph. D. Thesis. Department of Geodetic Science and Surveying, The Ohio State University, Columbus, Ohio, 140 p.

APPENDIX

A

APPENDIX A.

LCFE 1: When LCFE 1 was first observed in the SSH field of January 1, 1997 it was centered at about 26.8°N and 88.8°W and was already well-developed on the north side of a recently separated LC ring. During January and February the southward movement of this LCFE around the LC ring was blocked as the LC ring re-merged with the LC. Following this, the LC grew to the north and forced the LCFE to the northeast and closer to the moored array. LCFE 1 first began to influence the flow and temperature variability in the moored array in mid-March when a warm streamer was observed to wrap around the east side of the LCFE and extend into the array, causing strong eastward flow at A3 during March and April (Figure 5.2-3a). At this time the northern edge of the LC was at about 26.5°N or about 280 km south of the array. A smaller scale (100 km) cyclonic eddy was observed to develop on the warm front of the streamer causing cross-shelf exchange and recirculation within the array. During May and June the warm streamer appears to spin-up into a ACE over the array and LCFE 1 appears to have remained south of the array as estimated from the SSH fields. This causes strong eastward flow in the upper 100m at shelf break and mid-slope stations, and westward flow below 200m and at the 1500m stations. From mid-June to mid-August 1997, LCFE 1 translated around the eastern side of the LC at an increased forward speed of about 5 km/day. Its influence on observed currents appears to diminish in mid-July just as LCFE 2 approached the array. LCFE 1 was no longer observable after mid-August.

LCFE 2: LCFE 2 spun up just south of the array in the trough left by the departure of LCFE 1 around July 1, 1997. This eddy rapidly increased in size and continued the westward flow at the offshore sites and below 200m. LCFE 2 influenced the study area from mid-July to mid-September. Eddy 2 appeared to divide in mid-August with part moving away from the array to the southeast, travelling along the eastern side of the LC, which had an extreme tilt to the northwest at the time. The portion of the eddy that broke away was no longer identifiable in SSH by mid-October.

LCFE 3: LCFE 3 consist of the portion of LCFE 2 that remained near the array when it separated and moved southeast in mid-August 1997. LCFE 3 was located near the array in early to mid-September and caused westward flow at most locations. In mid-October this eddy started moving offshore along the eastern side of a warm ring that had separated previously from the LC and was located close to the shelf break southwest of the delta. Interaction of the warm ring with the steep topography appears to force a warm eastward jet that extends into the array causing strong eastward flow to depths of 500m. However, ring separation was not completed, which blocked the southward movement of the eddy causing it to remain near 27°N till mid-December at which time it began moving to the southeast around the LC at a speed of about 12 km/day (Figures 5.2-6 and -7), while LCFE 4 was approaching the LC from the southwest. A warm streamer wrapped around LCFE 3 and into the vicinity of the moored array. This streamer appears to have spun-up into a ACE over the array causing strong eastward flow to continue for most of Period 3. After mid-January this eddy was no longer identifiable in SSH fields.

LCFE 4: LCFE 4 was first observed on the west side of the LC in early December 1997 (Figure 5.2-7) and moved into the region south of the moored array in early January 1998. The eddy continued to move around the LC at speeds reaching 17 km/d and was midway down the LC off the west Florida shelf by early February 1998. The warm streamer from this LCFE continued to pump warm water into the upper layer of the study area and helped to maintain the eastward jet in the array. It is believed that the warm ring south of the delta would have produced eastward currents over the slope west of the array that may also have contributed to the warm eastward jet that occurred within the array.

LCFE 5: LCFE 5 was first observed on the west side of the LC on January 11, 1998. It moved around the LC reaching the crest just to the south of the array on February 5 (Figure 5.2-8) and was midway down the eastern side off the west Florida shelf by February 25. The rapid passage of this event with a translation speed of about 17 km/d caused increased variability of currents in the mooring array with transient westward flow at depths greater than 200m from about February 5 to 18, 1998.

LCFE 6: LCFE 6 was first observed in SST data on January 16, 1998. It moved up the north side of the LC and was near the array on February 25. The eddy influenced the study region from March 1 - 24. The LCFE enlarged to about 280 km in the east-west direction and caused significant westward flow in the mooring array as the warm filament was carried around the north side of the eddy and into the array (Figure 5.2-9). The cyclonic circulation of the eddy also appears to cause significant offshore transport of cooler slope water into the eddy core. The eddy moved rapidly around the east side of the LC and appears to have participated in separation of a large new ring toward the end of March 1998.

LCFE 7: SST imagery indicates that LCFE 7 was formed on the outer part of the Campeche Bank on February 5, 1998. It moved northward along the westward boundary of the LC reaching maximum size of 110 x 55 km on February 12 while still well south of the mooring array. On February 25 it had reached the northwest corner of the LC and was extending a long streamer into a remnant warm ring to the southwest. At a speed of about 24 km/d the eddy appears to catch up with and shear apart in the trough of LCFE 6, without impacting the currents in the moored array.

LCFE 8: LCFE 8 was first visible in SST images at the northwest corner of the LC on March 4, 1998. By March 20 the eddy was south of the array and had increased in size to 244 x 240 km (Figure 5.2-9). Westward flow on the north side of the eddy was causing strong westward flow within the moored array to depths of 500m. At this time the LC had separated into a large warm ring and the eddy was moving slowly to the east along the northern boundary of this ring at about 2.4 km/d. In early April, the southward movement of the eddy around the ring was blocked by the new growth of the young LC. Also a streamer extending around the eddy at this time appeared to have two smaller scale (100 km) cyclonic eddies form near the western tail and contributed to cross-slope exchange. On April 12, a large streamer wrapped around the east and north side of the eddy and into the array, where strong westward flow from the eddy continued (Figure 5.2-10a). By April 25, the eddy was on the eastern

side of the ring and had enlarged to 300 x 245 km. The warm streamer intruding into the array was causing flow splitting, with onshore flow on the line B, westward flow at line A and northeast, up-canyon flow along the lines C and D. In early May, the eddy appears to participate in further separation of the ring from the emerging LC and was no longer clearly identifiable in the SST fields. However, SSH data generally supports the same type of feature identification and indicates that the eddy was absorbed in the growing trough of ring separation in early June. The SSH fields also show the general pattern of the LCFE and streamer influencing westward flow in the array throughout March and most of April 1998. The cyclonic circulation within the eddy appears to have had a strong effect on movement of slope water into the eddy core, causing enhanced cross-slope exchange (Figure 5.2-10a).

LCFE 9: LCFE 9 was first observed in SST imagery March 23, 1998 on the southwestern extreme of the recently separated LC ring. It moved rapidly to the north along the ring western boundary at a speed of about 16 km/d. It reached the northwest area of the ring on April 12 and had dimensions of approximately 110 x 110 km (Figure 5.2-10a and -11). Its movement slowed to about 10 km/d as it traveled around the northern part of the ring and was south of the moored array in early May with a ridge wrapped around its eastern side and into the array. The ridge appears to have spun-up into a ACE that seems to have caused the eastward flow at the shelf break stations and westward flow offshore and at depths deeper than 200m. The combined influence of the newly formed ring and the young LC appears to have formed a ridge tilting toward the northwest. The SSH fields indicate that a series of LCFE's merged along the eastern side of the ridge during June 1998 and are difficult to identify separately in the imagery.

LCFE 10: SSH fields indicate that during July 1998 a cyclone formed south of the array on the northern side of the ring that separated in March. A ridge wrapped around the eastern side of the low and into the array (Figure 5.2-12a). The ridge intensified into an ACE near the array which caused eastward flow in the array that continued for most of Period 5. Westward flow developed below 300m for part of that period, presumably due to the cyclonic circulation in the offshore eddy. The cyclone remained more or less stationary until early February 1999. Apparently the interaction of the ring with the young LC caused a ridge that prevented movement of the cyclone around the ring.

LCFE 11: LCFE 11 was observed in SST fields on January 7, 1999 south of the array at about 26.5°N. A warm filament extended from the eddy to the region of the array and appears to have developed into an warm ACE. SST imagery of January 25 shows the eddy on the east side of the LC and a large streamer extending into the array (Figure 5.2-15). Apparently, only the northern edge of the ACE reached the offshore sites and caused eastward flow. Flow at the mid-slope and shelfbreak sites did not appear to be affected by this ACE. By February 8 the influence of the ACE on the study region was no longer apparent. Translation speed around the LC was approximately 10 km/d. On March 2 the eddy was located near 25°N and participated in narrowing of the LC neck, an indication of potential ring separation.

LCFE 12: LCFE 12 was first observed in SST fields of February 5, 1999 southwest of the array on the northwest curvature of the LC. SSH data show the eddy to be well-developed south of the array in mid-February This eddy moved eastward around the north side of the LC at a speed of about 9 km/d. A ridge developed around the east side of the eddy and extended into the array area. The SST data shows this ridge to consist of a warm filament that contributed to the ACE in the array area, producing eastward flow at the offshore mooring sites from February 20 to March 10 (Figure 5.2-18). The ACE moved southwest out of the array area in mid-to late March as the eddy moved down the eastern side of the LC, which was growing northward at the time. The eddy became difficult to detect in SSH data after April 1999.

The Department of the Interior Mission

As the Nation's principal conservation agency, the Department of the Interior has responsibility for most of our nationally owned public lands and natural resources. This includes fostering sound use of our land and water resources; protecting our fish, wildlife, and biological diversity; preserving the environmental and cultural values of our national parks and historical places; and providing for the enjoyment of life through outdoor recreation. The Department assesses our energy and mineral resources and works to ensure that their development is in the best interests of all our people by encouraging stewardship and citizen participation in their care. The Department also has a major responsibility for American Indian reservation communities and for people who live in island territories under U.S. administration.

The Minerals Management Service Mission

As a bureau of the Department of the Interior, the Minerals Management Service's (MMS) primary responsibilities are to manage the mineral resources located on the Nation's Outer Continental Shelf (OCS), collect revenue from the Federal OCS and onshore Federal and Indian lands, and distribute those revenues.

Moreover, in working to meet its responsibilities, the **Offshore Minerals Management Program** administers the OCS competitive leasing program and oversees the safe and environmentally sound exploration and production of our Nation's offshore natural gas, oil and other mineral resources. The MMS **Royalty Management Program** meets its responsibilities by ensuring the efficient, timely and accurate collection and disbursement of revenue from mineral leasing and production due to Indian tribes and allottees, States and the U.S. Treasury.

The MMS strives to fulfill its responsibilities through the general guiding principles of: (1) being responsive to the public's concerns and interests by maintaining a dialogue with all potentially affected parties and (2) carrying out its programs with an emphasis on working to enhance the quality of life for all Americans by lending MMS assistance and expertise to economic development and environmental protection.